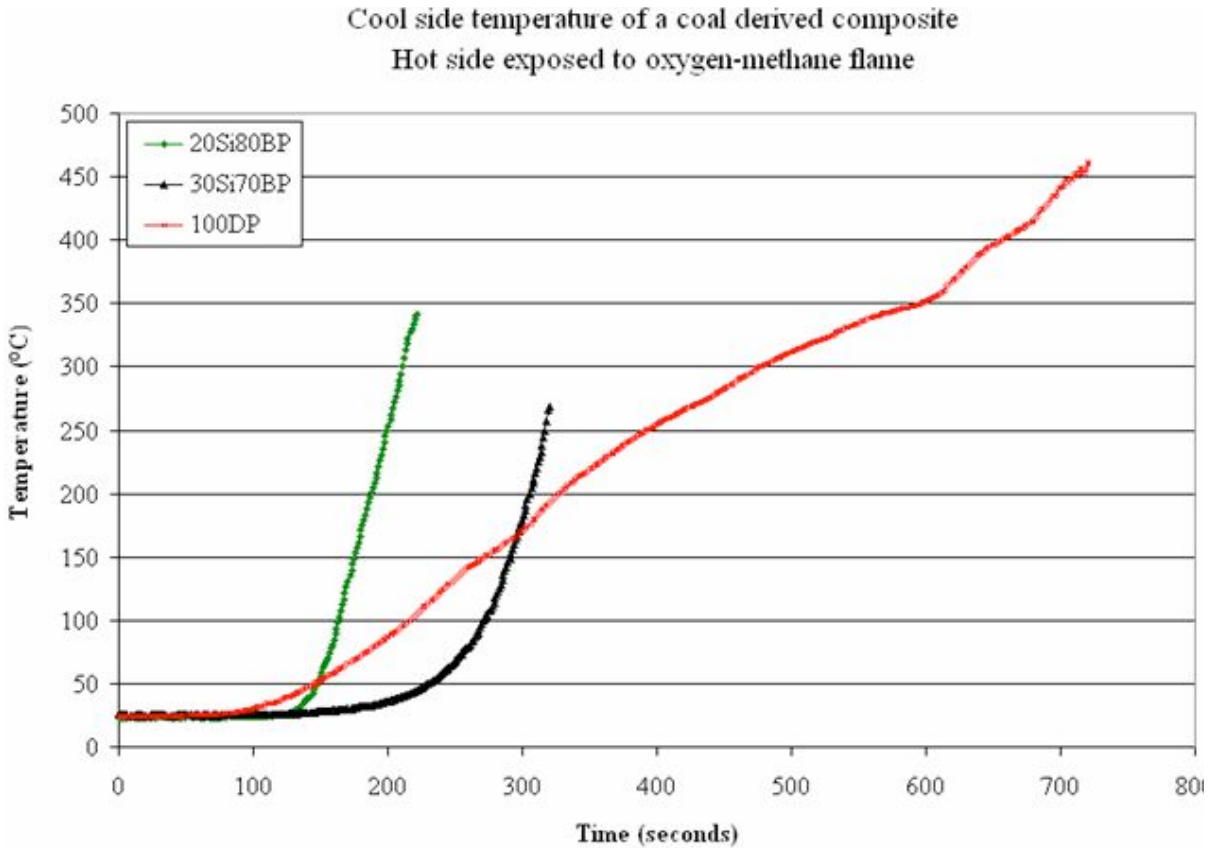

Figure 15. Relative temperature of composite cool side.

Appendix 1

Table 7. Fly Ash Composites

Sample Date	Sheet #	Number	Devol	BP	FA	Width (mm)	Height (mm)	Depth (mm)	Pre-weight (g)	Density (g/cc)	Post-weight (g)	wt loss	TTTD (s)	Stopwatch (s)	ABTT
6/14/2006	27		0%	75%	25%	72.63	56.51	27.41	30.36	0.270	26.63	12%	29.5	16	3.99
6/14/2006	28		60%	20%	20%	71.44	57.13	30.35	37.51	0.303	32.61	13%	54.7	20	5.95
6/14/2006	29		68%	17%	15%	72.73	55.22	45.85	28.55	0.155	25.91	9%	8.6	9	1.21
6/14/2006	30		78%	12%	10%	71.97	56.66	27.93	38.1	0.335			24.7	21	2.64
6/15/2006	31		50%	0%	50%	66.47	53.92	17.62	40.72	0.645	37.96	7%	72.4	61	6.37
6/15/2006	32		55%	0%	45%	67.69	56.78	21.28	38.95	0.476	36.74	6%	54.7	36	5.39
6/15/2006	33		60%	0%	40%	68.6	56.35	27.65	42.3	0.396	39.7	6%	37.3	39	3.40
6/15/2006	34		65%	0%	35%	71.34	56.31	24.39	38.72	0.395	36.46	6%	34.8	32	3.61
6/15/2006	35		70%	0%	30%	71.77	56.89	30.5	39.84	0.320	37.5	6%	24.9	26	2.55
6/15/2006	36		75%	0%	25%	72.28	67.55	37.05	46.05	0.255	43.82	5%	17.7	16	1.88
6/15/2006	37		80%	0%	20%	75.32	67.74	30.18	44.87	0.291	40.99	9%	30.0	24	3.41
6/15/2006	38		85%	0%	15%	73.86	65.3	32.18	46.04	0.297	42.03	9%	23.9	22	2.50
6/16/2006	39		0%	45%	55%	68.38	67.3	10.44	44.88	0.934	43.55	3%	38.3	34	3.93
6/16/2006	40		0%	40%	60%	65.14	56.36	8.61	30.18	0.955	29.18	3%	33.2	35	4.04
6/16/2006	41		0%	35%	65%	66.82	54.78	9.73	39.22	1.101	38.01	3%	44.2	33	4.13
6/16/2006	42		15%	20%	65%	63.6	62.24	12.87	46.78	0.918	44.86	4%	82.3	42	6.96
6/16/2006	43		20%	20%	60%	61.61	59.99	13.92	42.9	0.834	40.73	5%	41.0	29	3.53
6/16/2006	44		25%	20%	55%	66.92	52.54	14.34	41.54	0.824	39.55	5%	49.3	42	4.17
6/16/2006	45		30%	0%	70%	63.9	61.47	15.95	54.82	0.875	52.36	4%	43.4	32	3.11
6/16/2006	46		35%	0%	65%	62.91	47.32	13.48	38.98	0.971	37.21	5%	61.4	52	4.69
6/16/2006	47		40%	0%	60%	61.11	55.75	13.62	52.31	1.127	49.01	6%	109.9	73	7.16
6/16/2006	48		45%	0%	55%	60.7	64.96	12.05	38.72	0.815	36.39	6%	54.4	25	5.54

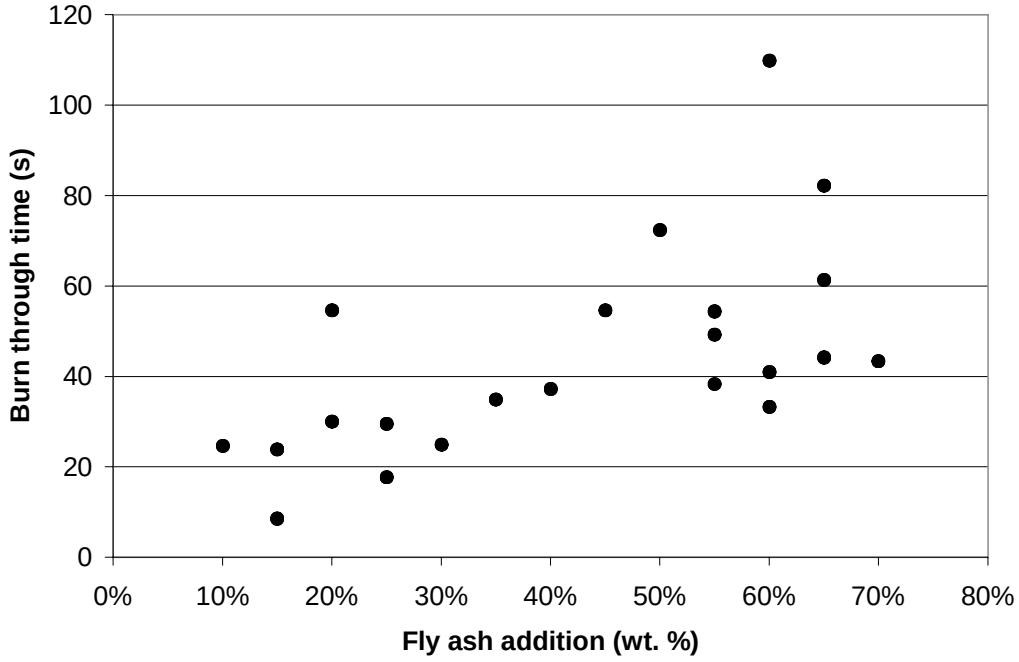

Figure 16. Burn through time as a function of fly ash content.

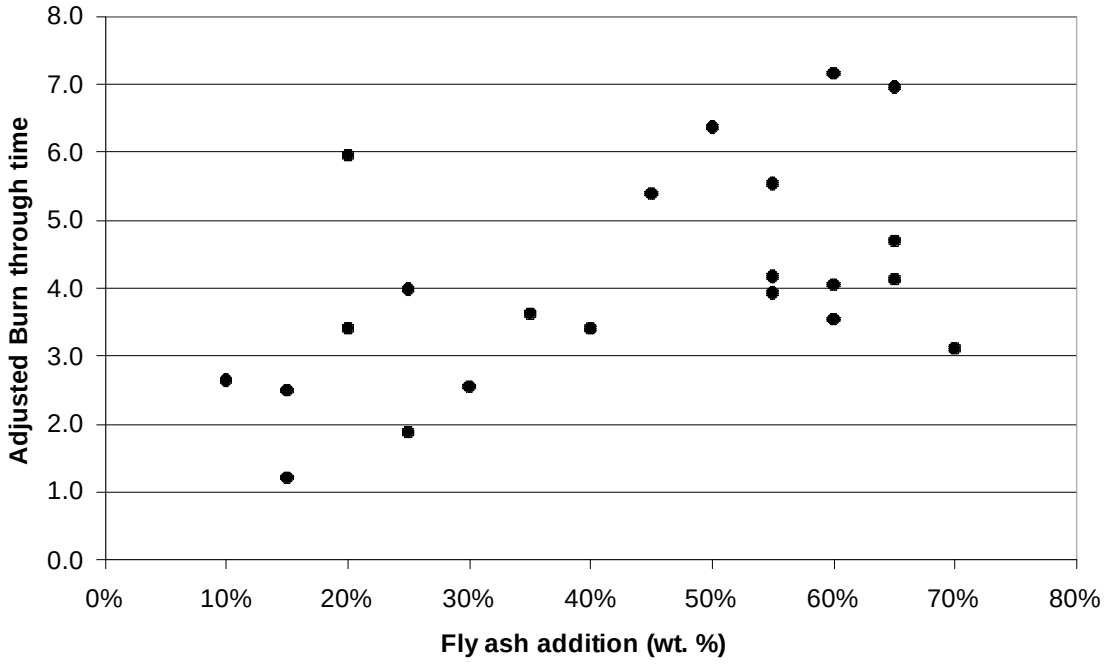

Figure 17. Adjusted burn through time as a function of fly ash content.

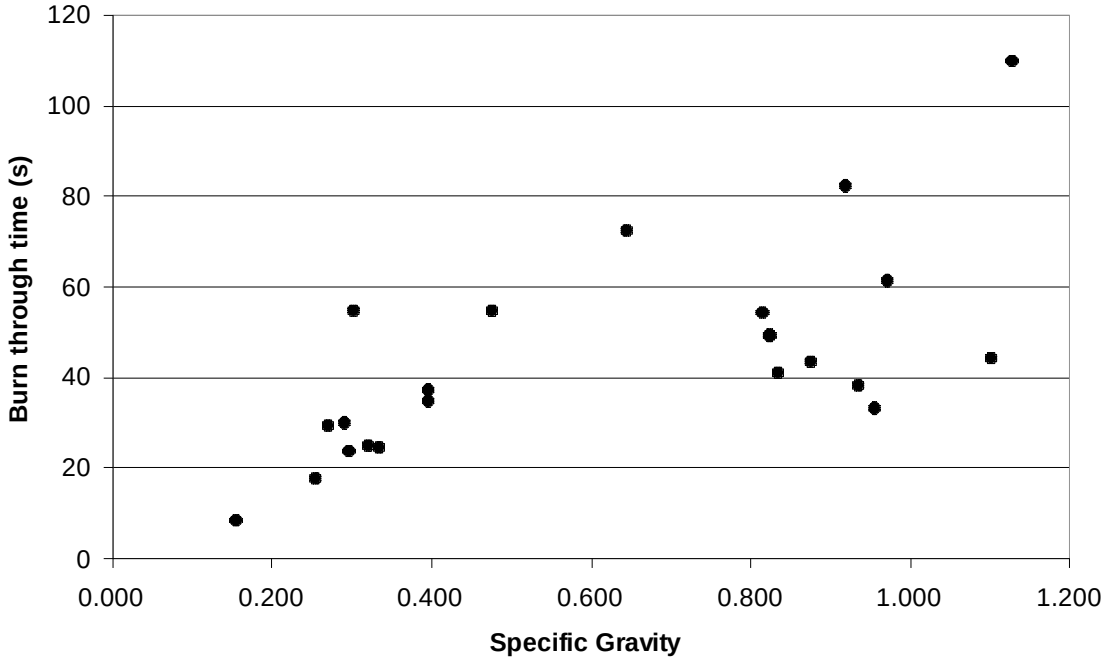

Figure 18. Burn through time as a function of specific gravity.

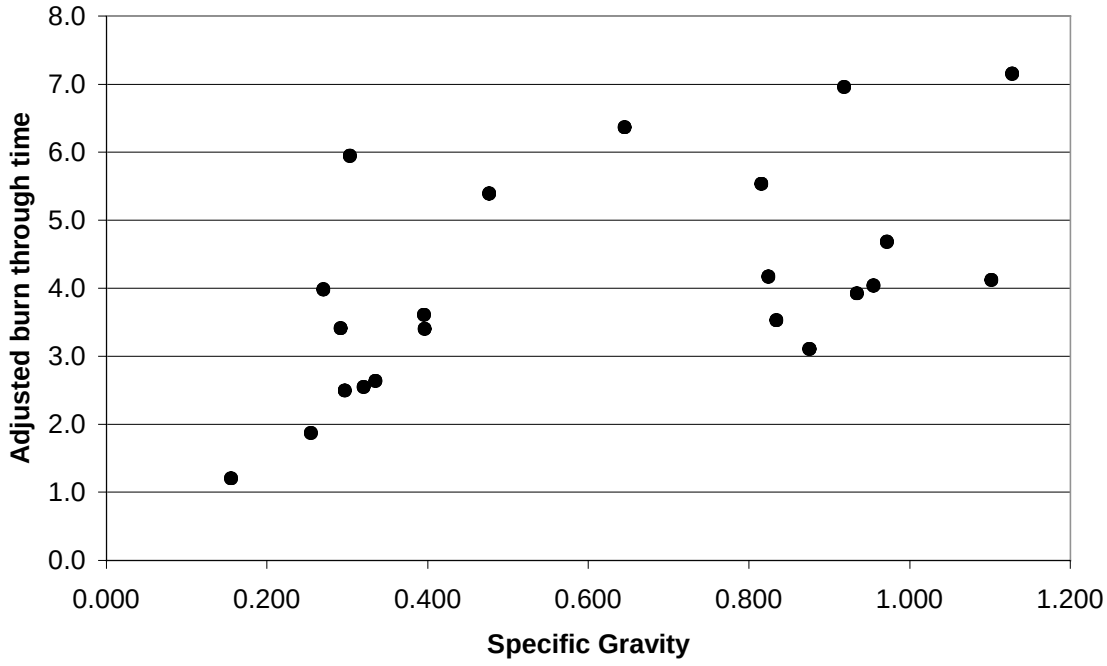

Figure 19. Adjusted burn through time as a function of specific gravity.

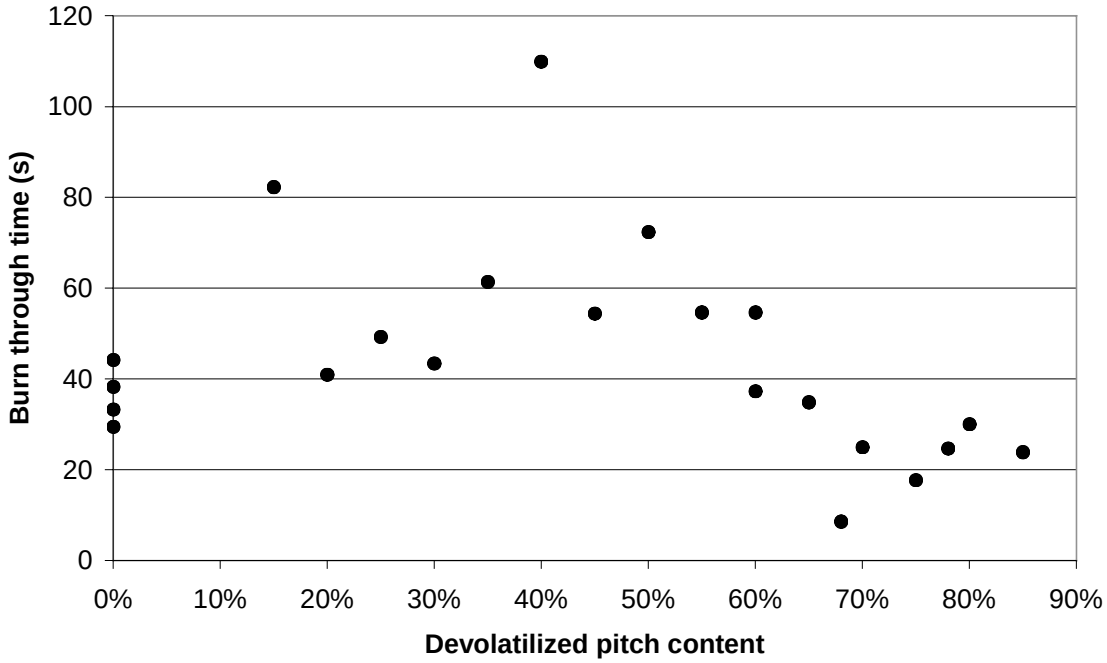

Figure 20. Burn through time as a function of devolatilized pitch content.

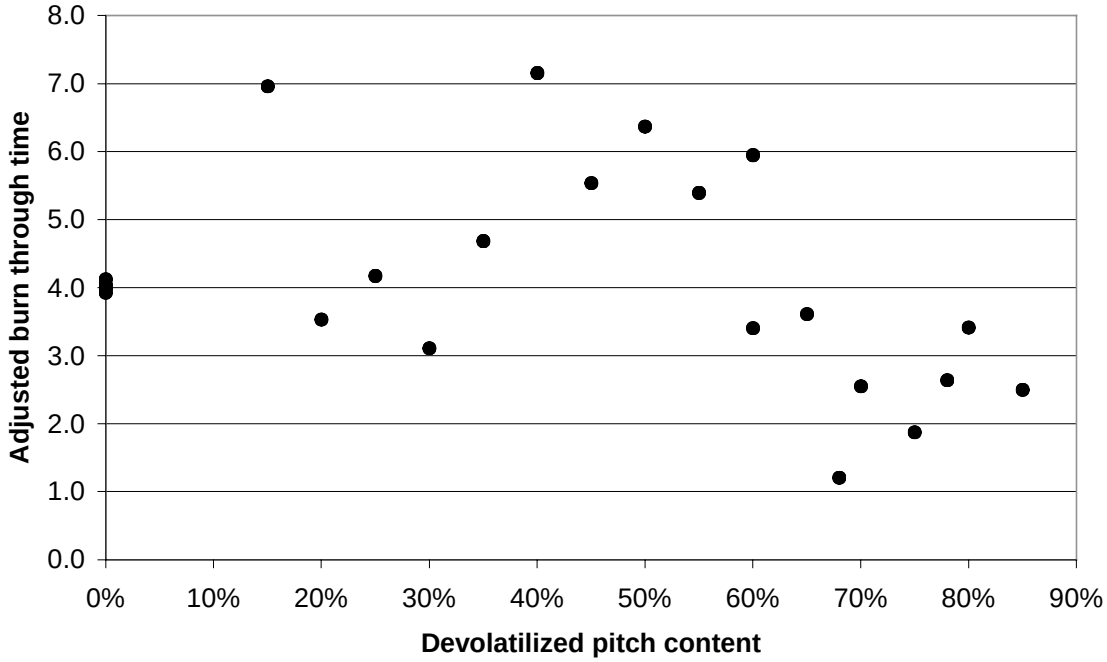

Figure 21. Adjusted burn through time as a function of devolatilized pitch content.

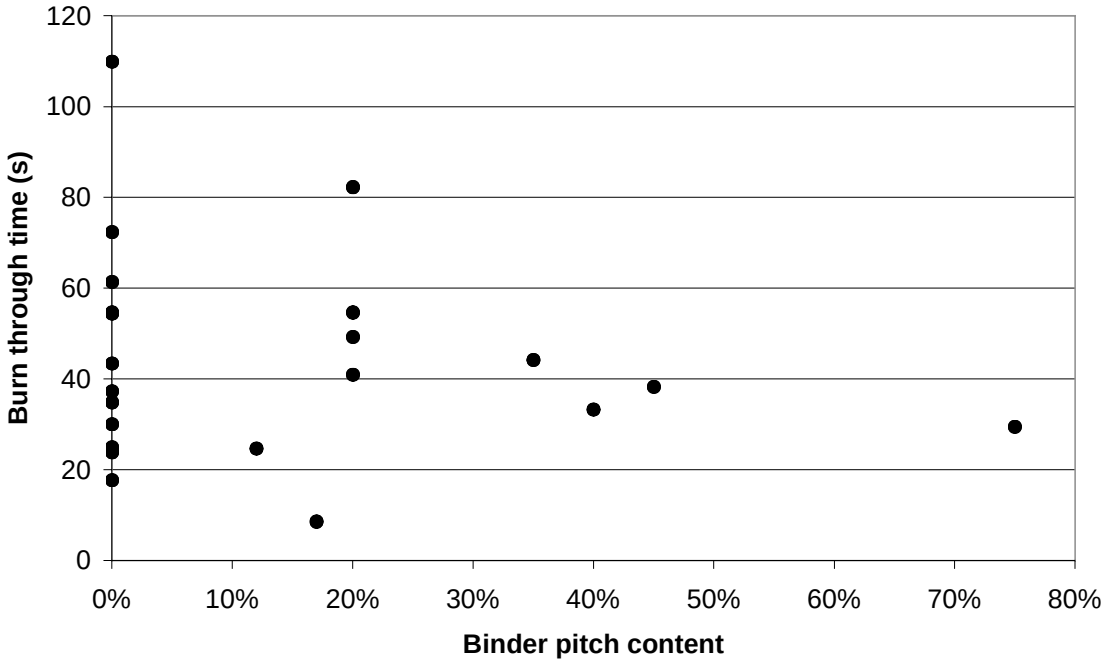

Figure 22. Burn through time as a function of binder pitch content.

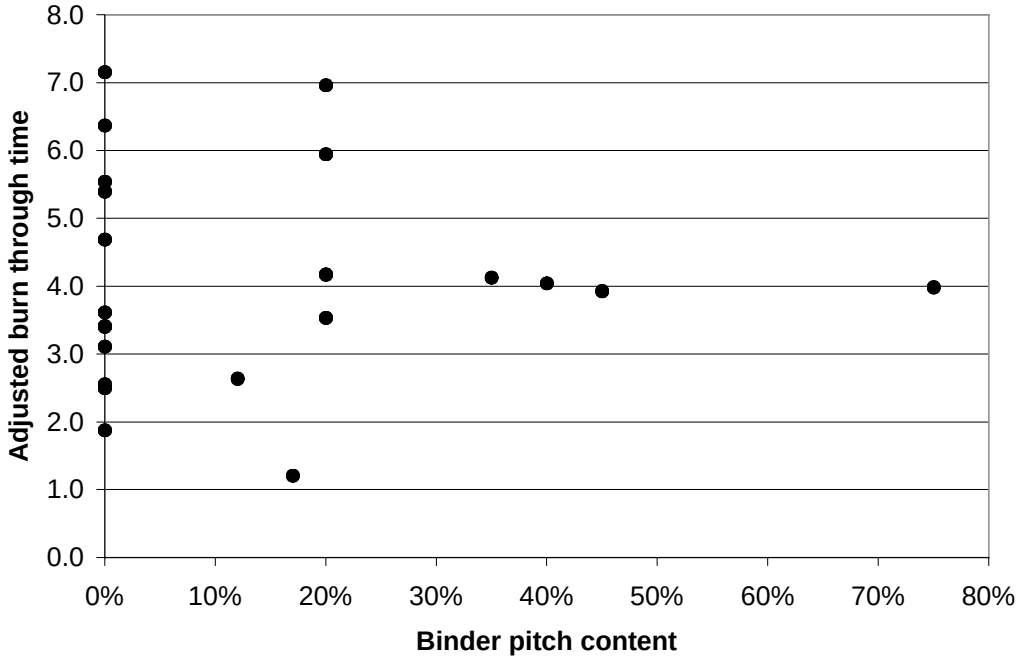

Figure 23. Adjusted burn through time as a function of binder pitch content.

Table 8. Silica Composites Summary.

Sample Date	Sheet #	Num-ber	De-vol	BP	Si	Width (mm)	Height (mm)	Depth (mm)	Pre-weight (g)	Density (g/cc)	Post-weight (g)	wt loss	TTTD (s)	Stopwatch (s)	ABTT
10/29/2005	1	1				55.38	56.07	24.83	13.58	0.176	12	12%	32.7	30	7.48
11/17/2005	2	1	0%	95%	5%	49.36	54.67	27.43	8.25	0.111	6.82	17%	10.2	3	3.33
11/17/2005	3	2	0%	93%	7%	51.34	52.48	25.25	9.42	0.138	7.85	17%	20.6	22	5.90
11/18/2005	4	1	0%	91%	9%	51.38	52.5	27.2	11.42	0.156	9.54	16%	30.3	32	7.15
11/18/2005	5	2	0%	89%	11%	53.71	54.99	25	8.4	0.114	7.27	13%	19.6	20	6.88
11/28/2005	6	1	0%	87%	13%	53.68	56	24.2	12.05	0.166	10.4	14%	34.8	32	8.69
11/28/2005	7	2	0%	85%	15%	47.16	56.2	28.54	12.08	0.160	10.44	14%	38.9	34	8.53
11/29/2005	8	2	0%	81%	19%	56.11	56.24	55.59	15.06	0.086	14.05	7%	21.7	15	4.55
11/30/2005	9	1	0%	85%	15%	57.98	54.89	26.45	10.52	0.125	9.52	10%	8.0	5	2.43
11/30/2005	10	2	0%	80%	20%	55.36	62.11	25.82	16.21	0.183	14.12	13%	34.8	34	7.39
12/1/2005	11	1	100%	0%	0%	59.29	68.25	32.52	40.59	0.308	36.62	10%	92.5	73	9.22
12/20/2005	12	1	60%	20%	20%	46.93	49.23	24.7	27.43	0.481	24.63	10%	79.9	77	6.73
12/20/2005	13	2	65%	20%	15%	48.29	56.02	27.8	32.71	0.435	29.62	9%	89.8	81	7.43
12/21/2005	14	1	58%	22%	20%	51.5	56.66	26.94	30.96	0.394	27.46	11%	93.3	89	8.79
12/21/2005	15	2	68%	17%	17%	48.79	57.02	27.36	32.17	0.423	28.87	10%	90.6	82	7.83
12/21/2005	16	3	45%	30%	25%	51.38	55.51	27.17	27.98	0.361	25.03	11%	95.7	78	9.75
12/22/2005	17	1	42%	33%	25%	50.63	56.77	27.04	27.57	0.355	24.81	10%	84.7	71	8.83
12/22/2005	18	2				48.93	54.59	25.45	22.42	0.330	20.02	11%	57.1	42	6.80
12/28/2005	19	1	38%	37%	25%	46.6	56.9	27.13	28.17	0.392	24.95	11%	85.0	67	8.00
12/28/2005	20	2	15%	55%	30%	49.71	54.88	27.22	22.37	0.301	19.93	11%	56.5	38	6.90
12/28/2005	21	3	0%	65%	35%	49.21	56.73	26.35	18.87	0.257	17.04	10%	41.3	20	6.11
1/9/2006	22	1	35%	40%	25%	54.51	54.29	26.43	22.78	0.291	20.45	10%	76.9	61	9.99
1/9/2006	23	2	15%	55%	30%	46.94	57.51	26.63	22.19	0.309	20.65	7%	31.1	16	3.78
1/10/2006	24	1	15%	60%	25%	55.09	56.16	23.73	27.76	0.378	25.71	7%	60.8	45	6.78
1/10/2006	25	2	0%	70%	30%	61.95	68.73	37.59	34.54	0.216	31.65	8%	56.5	39	6.97
1/12/2006	26	1				54	54.3	26.51	27.87	0.359	25.35	9%	65.4	49	6.88

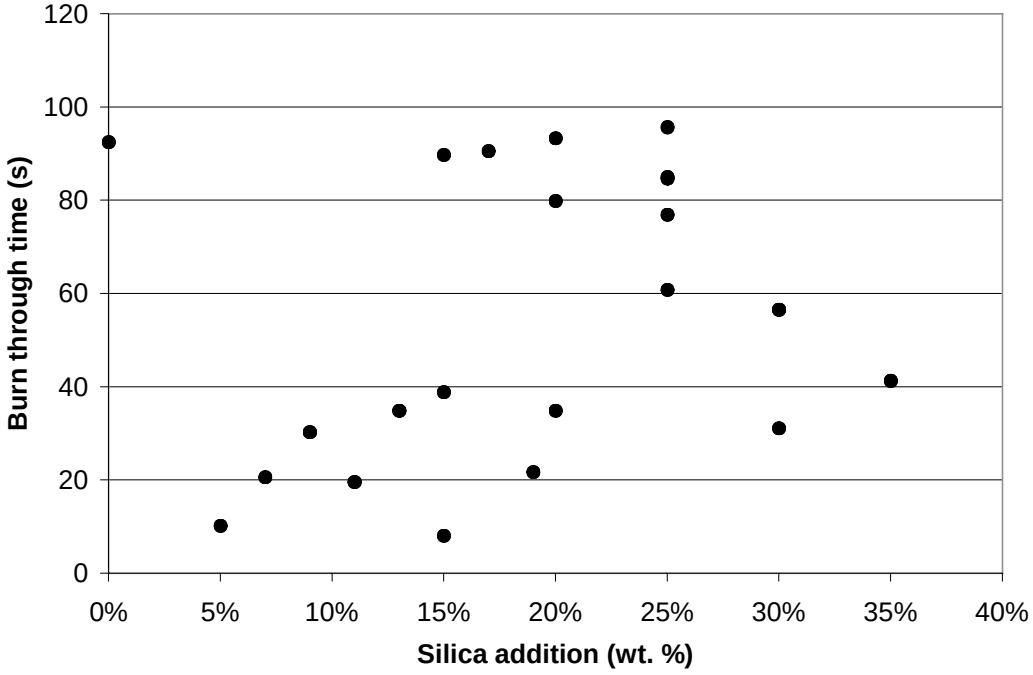

Figure 24. Burn through time as a function of silica content.

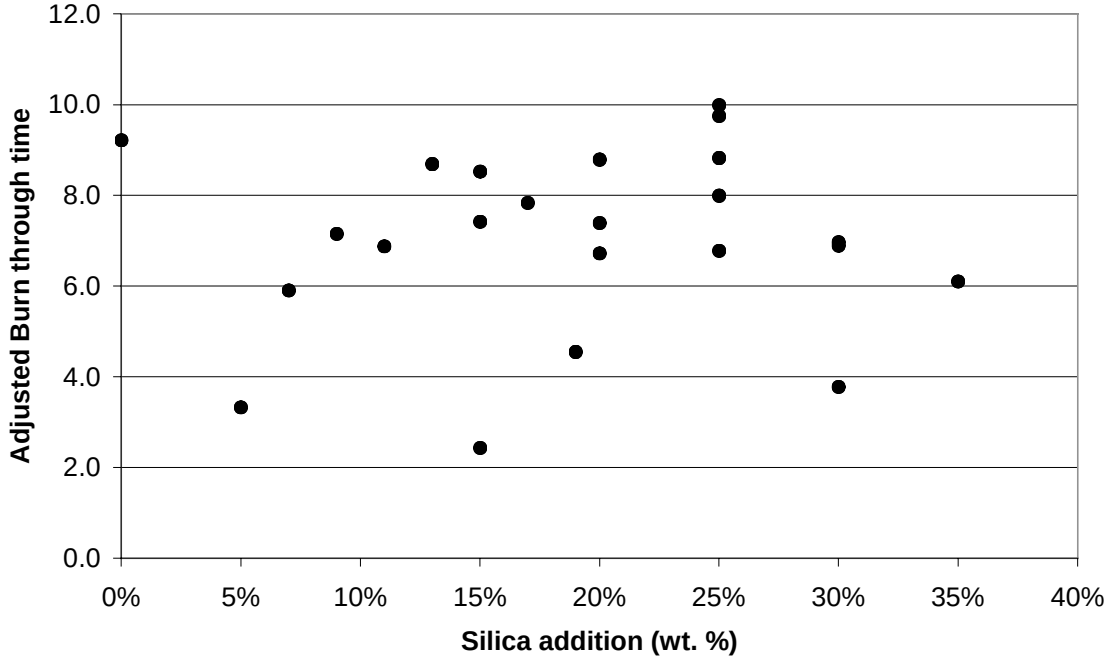

Figure 25. Adjusted burn through time as a function of silica content.

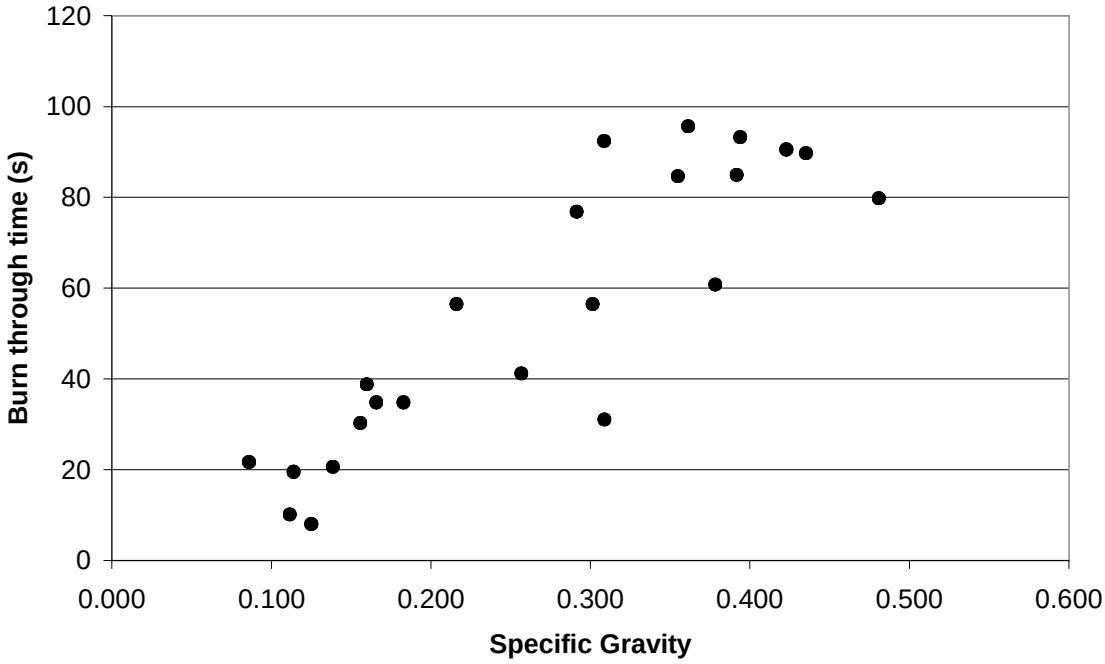

Figure 26. Burn through time as a function of specific gravity.

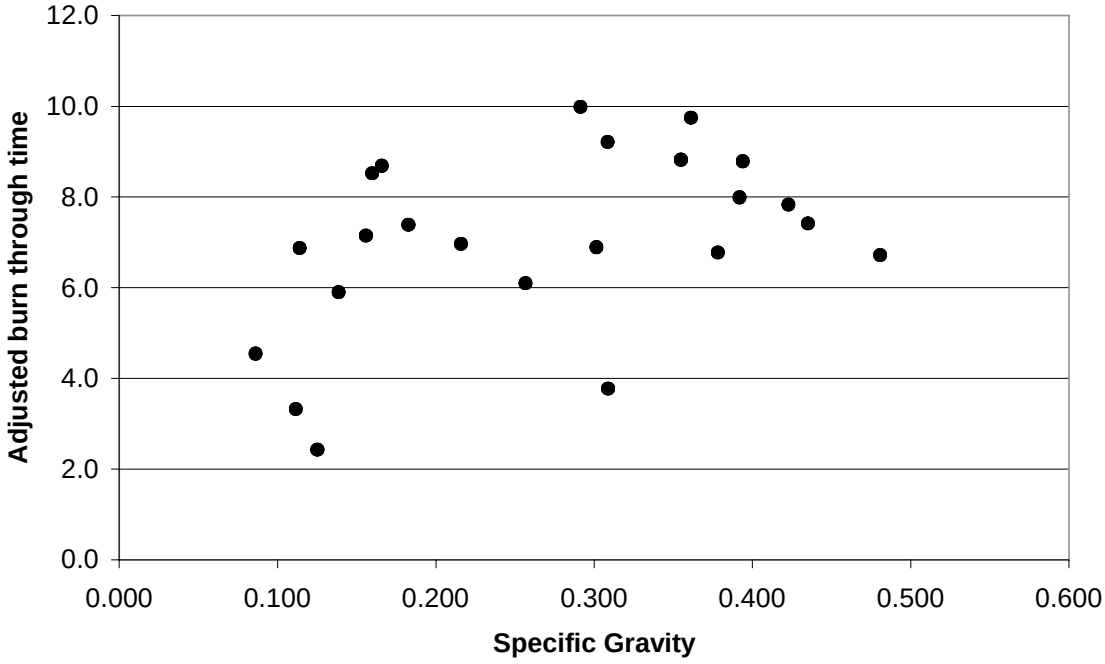

Figure 27. Adjusted burn through time as a function of specific gravity.

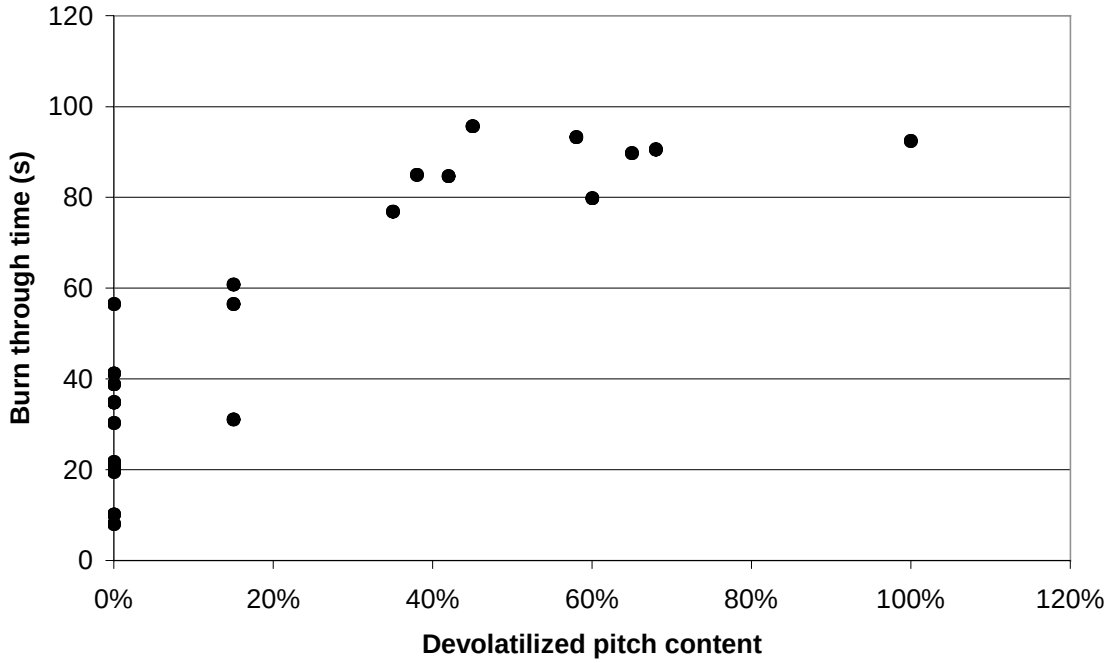

Figure 28. Burn through time as a function of devolatilized pitch content.

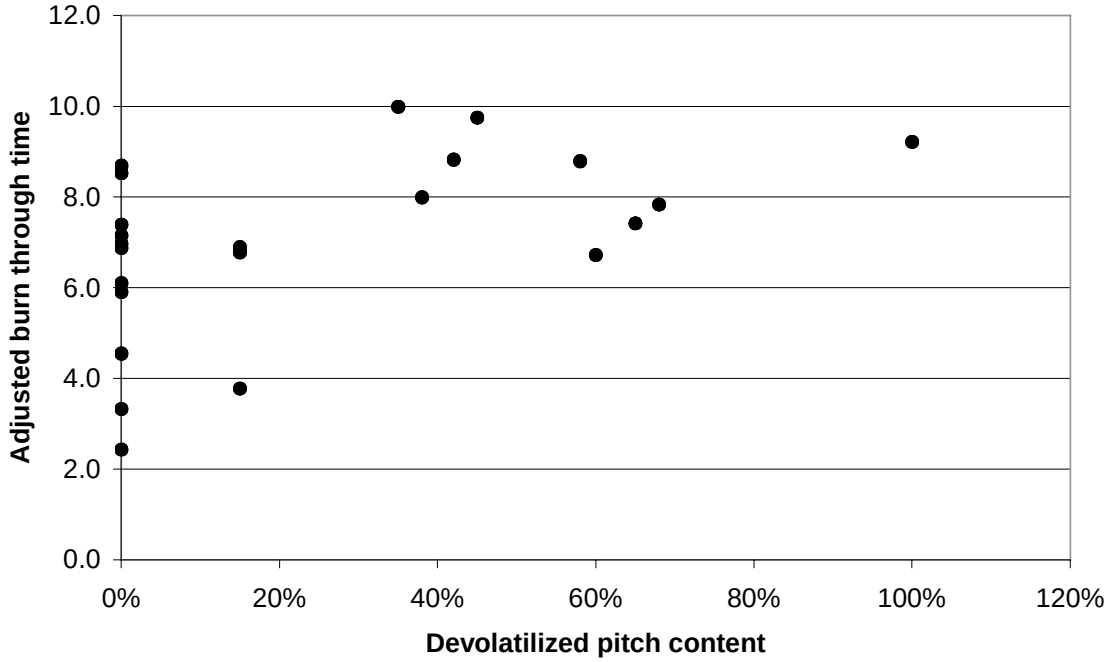

Figure 29. Adjusted burn through time as a function of devolatilized pitch content.

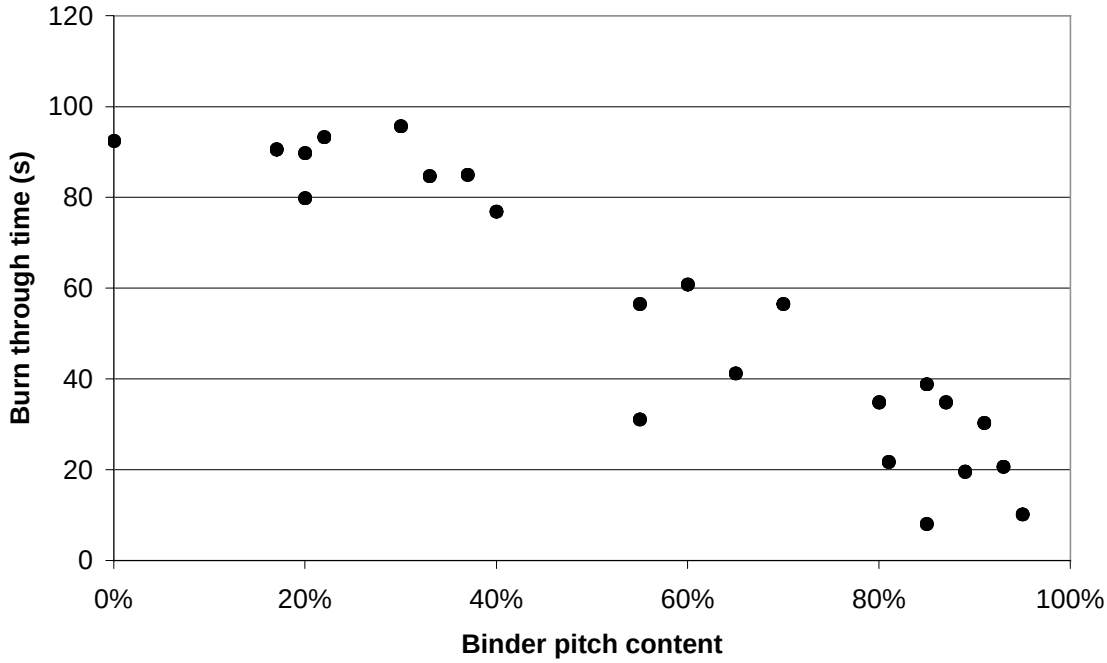

Figure 30. Burn through time as a function of binder pitch content.

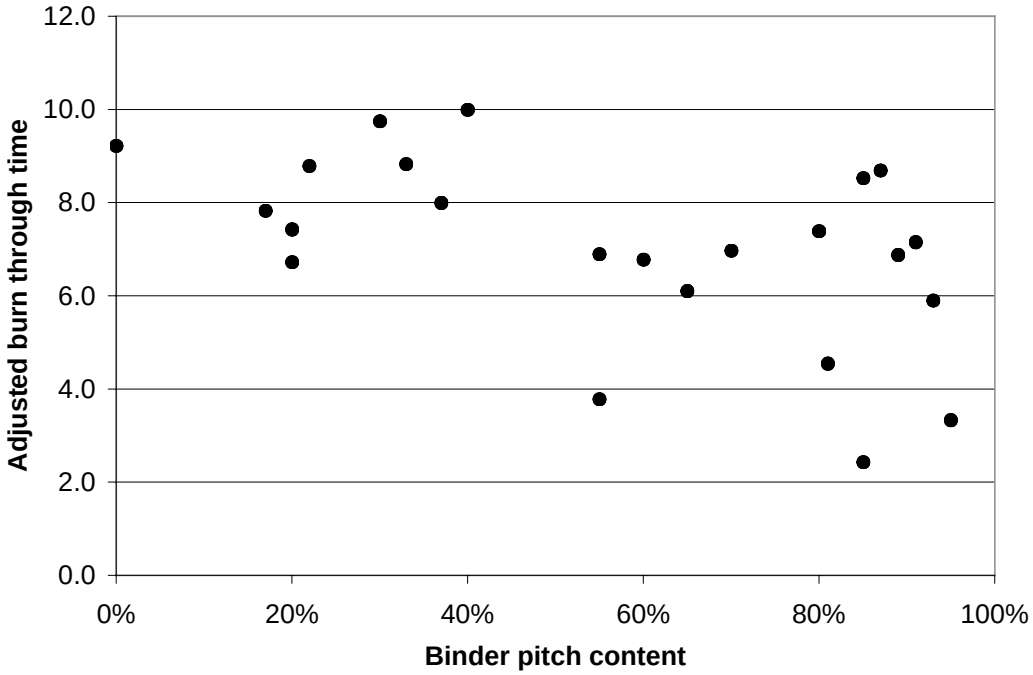

Figure 31. Adjusted burn through time as a function of binder pitch content.

V. Conclusion and Summary

Foams and monoliths were manufactured using a combination of coal tar pitch derivatives with reinforcement materials including pure silica as well as fly ash. These materials may be of interest for structural applications.

Carbon was shown to be a heat resistant material with possible uses for reentry shields and other very high temperature applications. However, the addition of fly ash or silica did not make a significant enhancement in the ability of the sample to resist burn-through in the presence of a high temperature oxyacetylene torch. It may be that oxidation of the carbon was too rapid and prevented the samples from achieving the necessary temperatures to form the silicon carbide phase.

VI. References

[1] Maria V. Pulsonetti, Richard A. Thompson, Stephen J. Alter, Prediction of STS-107 Hypervelocity Flow Fields about the Shuttle Orbiter with Various Wing Leading Edge Damage, NASA Langley Research Center, Hampton, Va.

[2] King, Nathan Douglas (2004). Chemical and Physical Modification of Petroleum, Coal Tar, and Coal-Extract Pitches by Air-Blowing, Master's Thesis, West Virginia University.

[3] "Final Technical Report". *Coal Based Nuclear Graphites for the New Production Gas Cooled Reactor. Task 1: Development of Coal-Derived Isotropic Coke and Nuclear Graphite*. West Virginia University, 1994.

"Needle Coke from Coal-Derived Feedstock"

Final Report

December 15, 2005 to June 30, 2006

Doug J. Miller, John C. Chang
Irwin C. Lewis, Rick T. Lewis
Harold Schobert*, Maria M. Escallon*, Leslie R. Rudnick*

GrafTech International Ltd.
UCAR Carbon Company Inc.
Parma R&D Center
12900 Snow Road
Parma, OH 44130
*** Pennsylvania State University**

Report Issued: June 30, 2006

Contract Number: 2867-GTIL-DOE-1874
Prime Award Number: DE-FC26-03NT41874

ABSTRACT

The main goal of this program was to demonstrate that coal tar distillate (CTD) is a highly suitable feedstock for needle coke. For this study, a heavy coal tar distillate from Koppers Co. and a reference petroleum-derived decant oil were transformed to coke using both a batch-scale autoclave at GrafTech and a continuous pilot coker at Penn. State University. Coking was also carried out on a CTD/decant oil blend. The raw cokes were characterized structurally and then calcined for use as filler in the production of 19mm diameter graphite electrodes. A graphite artifact produced using coke derived from batch coking of the CTD gave an extremely low CTE value of 0.04 ppm/°C, showing that the CTD would be an excellent needle coke feedstock. The CTD coke did show higher puffing during graphitization than the decant oil coke due to a higher nitrogen content.

The CTD and decant oil feedstocks and the liquid byproducts from the continuous coking runs were extensively characterized using a variety of analytical techniques. The CTD products are considerably more aromatic and exhibit much less side chain substitution than those from the petroleum-derived decant oil.

Table of Contents

Table of Figures

List of Tables

1. INTRODUCTION

Needle coke is the most important industrial raw material for producing graphite electrodes. Graphite electrodes are used in the electric arc furnace (EAF) for making steel from scrap metals. This EAF method of steel production is more energy efficient than the alternate process of producing steel from iron ore. There is currently a worldwide demand of one million metric tons of needle coke per year. Among those needle coke requirements, less than 15% of the coke needs are supplied by coal-based feedstock. In the United States, there is no coal-based needle coke producer at all. Two US needle coke producers, ConocoPhillips and Seadrift Coke, LP, are using petroleum-based feedstock to produce needle coke. Coal-based needle coke is available only in Japan and is based on a coal tar feedstock from metallurgical coking which has been previously treated for removal of quinoline insoluble (QI) solids.

Coal-based feedstock can have inherent advantages over petroleum-derived precursors because of its molecular composition. Coal-based feedstock, in general is more aromatic and has less side chains attached to the aromatic rings. If treated properly, the coefficient of thermal expansion (CTE), a major coke quality indicator, could be superior to that of petroleum-based needle coke. In this study, solid-free coal based distillate was used as the precursor for needle coke. Through use of a distillate material, the prior QI separation procedures used in Japan would not be necessary. Coal-based distillates are also readily available from commercial coal tar distillation processes. For comparison, a petroleum-based needle coke feedstock was also evaluated by itself and in a blend with the coal-based distillate.

Our approach was to perform a series of batch coking experiments in the high-pressure autoclave pilot plant at Parma using both coal and petroleum-based feedstocks individually and in a blend. The results of these batch-coking experiments were used to guide trial coking runs using the small continuous pilot coking unit at Pennsylvania State University for generating liquid by-products for analysis. The value of the liquid by-products is an important contributor to coking economics. Solid raw cokes were then calcined at the Parma pilot facility and characterized for needle coke quality. Liquid products were analyzed and evaluated for their suitability as fuels using the analytical capabilities at Penn. State University.

Graphite artifacts were manufactured from all the calcined needle cokes. The resultant coefficient of thermal expansion (CTE) was measured on these artifacts to assess the needle coke quality. Optical microscopy was used to characterize coke structure at various stages of production. Puffing tests of the batch processed cokes were conducted to determine the puffing behavior during the graphitization processes. All of the results are presented in the body of this Final Report.

2. EXPERIMENTAL

Coal and petroleum-based feedstocks were acquired for the program. The coal-based material is a high boiling coal tar distillate obtained from the Koppers Co. We had used this material in a previous CPCPC Program (2679-GITL-DOE-1874) as a precursor for mesophase pitch.

The petroleum-based feedstock was a decant oil derived from catalytic cracking of a gas oil distillate. We obtained a 55-gallon sample of this material from the Seadrift Coke, LP, at Seadrift, Texas. This facility has been used to produce needle coke.

2.1. Analytical Characterization Tests on Feedstocks

A variety of analytical tests were carried out on the original coke feedstocks and on coking liquid by-products using facilities at the Parma Testing Services Lab and at Penn. State University. The methods include: Modified Conradson Carbon (MCC), ash, C,H,N,S analyses, TGA weight loss, ^{1}H and ^{13}C NMR, GC, GC-MS and vacuum distillations. A description of the test methods used for this program follows:

2.1.1. Gas Chromatography / Mass Spectrometry (GC/MS)

The samples injected into the GC/MS were prepared as follows: Approximately 0.02-0.03 grams of the material was dissolved in approximately 1 gram of dichloromethane. The injection volume was 1.0 μL.

A Shimadzu QP-5000 GC/MS containing an XTi-5 column from Restek (30m x 0.25mm x 0.25 μm) was used. The instrument was programmed to run at 40 °C for 4 minutes, and then ramped up to 310 °C at a rate of 4 °C/min. This final temperature was held for 10 min.

The compound identification was made using the built-in library search and classified into eight different groups: paraffins, cycloalkanes, alkylbenzenes, indenes, naphthalenes, tetralins, decalins and polycyclic structures. The composition identification was made by peak to peak comparison with the built-in library and then classified according to the compounds mentioned above.

The summation of the area for each specific hydrocarbon type was divided by the summation of the areas of all the peaks. Hence, the percentage of each hydrocarbon type was obtained.

2.1.2. Simulated Distillation Gas Chromatography

Simulated distillation by gas chromatography (SimDist GC) was utilized in an attempt to determine the boiling-cut distributions of the original decant oil and coal-tar distillate and the liquid by-products from pilot coking. A Hewlett Packard HP 5890 GC Series II model was employed. The column was a Restek Sim. Dist. column (Carborane siloxane polymer).

The data obtained from this ASTM D2887 Method determined the yield by weight of any given fraction of liquid products examined. The first boiling range fraction was defined as liquids that had a boiling point of less than 175 °C. The second group was the jet fuel range and was defined as liquids with boiling points between 175° and 300 °C. The next group fell within the boiling range of 300-550 °C.

All of the samples were prepared as follows: Approximately 0.03-0.04 g of the material was dissolved in 1.2-1.5 grams of carbon disulfide. The samples were then placed in the Hewlett Packard automatic injection tray.

The sample was injected at 40 °C and held at this temperature for 4 minutes. The oven was then ramped up to 425 °C at a rate of 10 °C/min and held there for 15 minutes. The total run time was 57.5 minutes.

The data calibration was based on the use of n-alkanes as a reference. This procedure has been used previously for analysis of petroleum feedstocks, such as decant oil. However, as discussed later it was found inappropriate for the more aromatic coal tar distillate products. Therefore, we used regular vacuum distillation to characterize the liquids from the pilot coking runs.

2.1.3. Vacuum Distillations

The vacuum distillations were performed on the liquid by-products in order to obtain the true boiling point ranges. The use of vacuum minimizes sample decomposition. The distillations were performed using a 250 ml flask mounted in a heating mantle. A 100 ml quantity of the liquid was poured into a 250 ml vessel and a magnetic stirrer was used to assure a uniform temperature in the liquid inside the flask. The flask, glass bead packed column, distillation unit and liquid receiver were assembled; the pump hose was connected with the distillation system to provide vacuum. As the heating power was increased, the vapors were condensed and refluxed in the glass bead packed column. After passing through the packed column, the vapors were condensed and collected into the receiver flask.

Shown in Figure 1 is a nomograph, which was used to correlate the temperature at a given pressure (under vacuum) with the temperature at atmospheric pressure. The pressure and the temperature were constantly monitored during the distillation process.

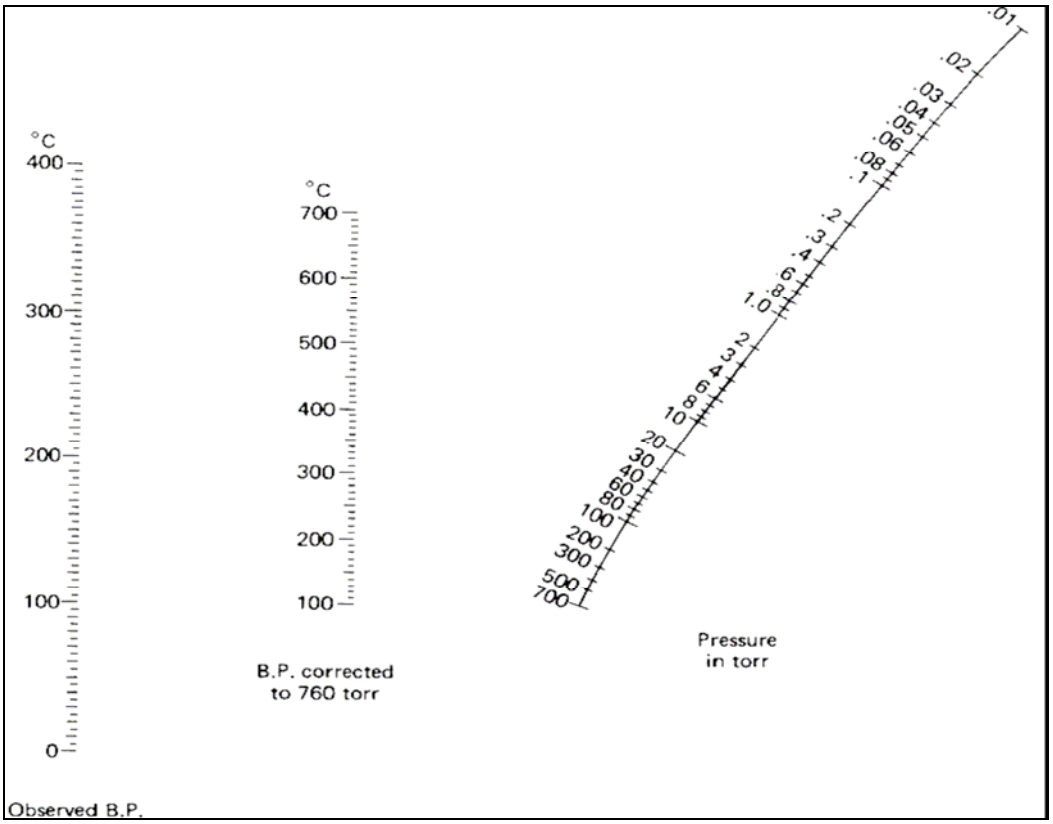

Figure 1: Nomograph for Calculation of Boiling Points

2.1.4. CHN Elemental Analysis

The LECO 600 CHN analyzer was used to measure total carbon, hydrogen and nitrogen contents in solid and liquid samples.

2.1.5. Total Sulfur Determination Analysis

The LECO SC 132 analyzer was used to measure total sulfur content in solid and liquid samples.

2.1.6. Automatic Determination of Proximate Analysis

The LECO MAC-400 analyzer was used to measure moisture, volatile matter and ash content by the loss of weight of the samples, after having been heated under atmospheric conditions.

2.1.7. Nuclear Magnetic Resonance – NMR

The measurements were made with a liquid-state NMR spectrometer with imaging capabilities. The samples were analyzed on a Bruker AMX 360 NMR spectrometer operating at 9.4 Tesla and a 70° tip angle. Liquid products were dissolved in $CDCl_3$ for analysis.

The NMR analysis was carried out on the original decant oil, coal-tar distillate, and the liquid coking by-products. Through the integration of the areas of the aromatic and aliphatic peaks in the spectrum, it was possible to establish differences between the two feedstocks (decant oil and coal tar distillate).

The regions for the integration of the spectra were defined according to the information in chemical shift tables for ^{13}C and ^{1}H[(1)]. For aliphatic and aromatic fractions, the regions were 8-65 and 125-150 ppm, respectively, for ^{13}C and 0.5-4.5 and 6-9 ppm for ^{1}H [(1)]. A detailed interpretation was applied following the peak integration procedure suggested by Rodriguez et al.[(2)] This is shown in Table I.

The description of functional groups peak assignments for ^{1}H NMR [(3)] is given as follows:

Total Aliphatic: This is the atomic percent of hydrogen atoms present in paraffinic or naphthenic components of the sample.
Total Aromatic: This is the atomic percent of hydrogen atoms present in mono two-, and three-ring aromatics.
Triaromatic: This is the atomic percent of hydrogen atoms on carbons adjacent to a bridgehead site in three-ring aromatics.
Diaromatic: This is the atomic percent of hydrogen atoms on carbons adjacent to a bridgehead site in a two-ring aromatic.
Monoaromatic: This is the atomic percent of hydrogen atoms in a single ring aromatic or on the periphery of a polynuclear aromatic ring.
Alpha (α)-CH: This is the atomic percent of hydrogen present on methyl groups directly attached to aromatic rings.
Beta (β): This is the atomic percent of hydrogen in CH or CH_2 groups in paraffinic or naphthenic groups, more than one carbon removed from an aromatic ring.
Beta-CH_2: This is the atomic percent of hydrogen present in naphthenic methylene groups or methylene groups in beta position to an aromatic ring.
Paraffinic-CH_2: This is the atomic percent of hydrogen present in paraffinic methylene groups.

Table I
^{1}H NMR Assignments for Functional Groups of Interest in Petroleum Carbonization Chemistry [(2) (3)]

Band TMS (ppm)	Assignment
0.5-1.0	CH_3 γ and further, some naphthenic CH and CH_2
1.0-1.7	CH_2 β and further, some β CH_3. Separation at 1.7 ppm is generally not base resolved
1.7-1.9	Most CH, CH_2 β hydroaromatic. This shoulder is one of the best available ways to estimate hydroaromaticity
1.9-2.1	α to olefinic
2.1-2.4	CH_3 α to aromatic carbons
2.4-3.5	CH, CH_2 α to aromatic carbons
3.5-4.5	CH_2 bridge (diphenylmethane)
4.5-6.0	Olefinic
6.0-7.2	Single ring aromatics
7.2-8.3	Two ring and most 3 ring aromatics
8.3-8.9	Some 3- and 4 ring aromatics
8.9-9.3	Some 4-ring aromatics

The description of functional group peak assignments for ^{13}C NMR which are shown in Table I and II follows[(3)]:

Aromatic Carbon: This is the atomic percent of carbons in aromatic groups.
Aliphatic Carbon: This is the atomic percent of carbons in naphthenic or paraffinic components.
Protonated Aromatic Carbon: This is the atomic percent of aromatic carbons with hydrogen attached.
Alkyl-substituted Aromatic Carbon: This is the atomic percent of aromatic carbons with alkyl groups attached.
Naphthenic-substituted Aromatic Carbon: This is the atomic percent carbon present as aromatic carbon substituted by naphthenic carbon groups.
Methyl-substituted Aromatic Carbon: This is the atomic percent carbon present as aromatic carbon substituted by a methyl group.
Internal Aromatic Carbon: This is the atomic percent carbon present as bridgehead aromatic carbons in polynuclear aromatics.

Table II
^{13}C NMR Assignments for Functional Groups of Interest in Petroleum Carbonization Chemistry [(2) (3)]

Band TMS (ppm)	Assignment
11.0-12.5	CH_3 γ and further from aromatic ring CH_3 in ethyl substituted cyclohexane
12.5-15.0	CH_3 γ and further from aromatic ring CH_3 α shielded by two adjacent rings or groups
15.0-18.0	CH_3 α shielded by one adjacent ring or group Some CH_3 α hydroaromatic and naphthenic CH_2
18.0-20.5	CH_3 α shielded by one adjacent ring or group Some CH_3 α hydroaromatic and naphthenic CH_2
20.5-22.5	CH_3 not shielded by adjacent rings or groups Some CH_3 α hydroaromatic and naphthenic CH_2
22.5-24.0	CH_2 γ and further adjacent to terminal CH_3 CH_2 β in unsubstituted tetralin structures
24.0-27.5	Some CH_2 naphthenic CH_2 α not shielded CH_2 β in propyl and indan groups CH_3 β in isopropyl
27.5-37.0	CH_2 not adjacent to CH in alkyl groups CH_2 adjacent to alkyl CH in some CH_2 α and CH_2 adjacent to terminal CH_3 in alkyl substituents with more than four carbons CH_2 in ring joining ethylene groups Some CH_2 naphthenic Some ring joining methylene (32-43 ppm)
37.0-60.0	CH alkyl groups (except isoalkyl) CH naphthenic CH_2 alkyl groups adjacent to CH Some ring joining methylene (32-43 ppm)
108.0-118.0	Some olefinic (others spread through aromatic region)
118.0-129.5	Protonated aromatics Some internal (quaternary) aromatics
129.5-133.0	Most internal aromatics. These carbons are present as bridgehead aromatic carbons in polynuclear aromatics
133.0-135.0	Methyl substituted aromatics
135.0-138.0	Naphthenic substituted aromatics
138.0-160.0	Alkyl (other than methyl) substituted aromatic heteroatom (N, O, S) aromatic

2.1.8. Asphaltene Content

The asphaltenes were quantified by following the ASTM Method D-3279.

2.1.9. Modified Conradson Carbon (MCC), Ash

The MCC was measured using procedure ASTM D-2416 and the ash content was determined employing a modification of ASTM C-561.

2.1.10. Thermogravimetric Analysis (TGA)

A special TGA method, which was adapted from ASTM E-2008, was used to estimate the boiling range of the feedstocks. The method uses a pan/lid assembly with a nominal 0.38 mm laser drilled hole in the lid. The heating rate is 5 °C/min from room temperature to 500 °C in a low flow rate of argon gas through the TGA. The measurements were made using a TA Instruments Model 2950 TGA.

2.2. Pilot-Scale Autoclave Batch Coking (Parma Technical Center)

The pilot-scale batch coking experiments were performed in an autoclave system with dimensions of 11.75" I.D. by 57" inside length. The autoclave is capable of 1500 psig pressure and up to 600 °C operating temperature. The temperature can be computer controlled for a pre-determined ramping rate, final hold temperature and hold time. Gas pressure was maintained during a run with an automatic control system. The pressure heat treatments were carried out on material contained in a covered stainless steel can with a capacity of about 16 liters. The can was partially filled with approximately 8,000 grams of coal tar distillate or petroleum-based feedstock.

The coking temperature was set to a nominal 475 °C. The autoclave was heated at a ramping rate of 50 °C/hr to the set point temperature of the autoclave, held at temperature for 20 hours, and then cooled down. The raw coke was weighed to obtain the coke yield, and samples were taken for analysis for MCC and optical microscopy.

2.3. Pilot Plant Calcination and Puffing Measurement

The raw cokes from the coking trials were crushed and heat treated (calcined) to 1,420 °C and held at the temperature for 30 minutes in a tube furnace. The calcined coke was then crushed and screened for further needle coke characterization.

Puffing is an irreversible expansion of carbon artifacts during the heat treatment to over 3,000 °C; it is attributed to the evolution of sulfur and nitrogen

containing species. A dilatometer was used to measure the expansion of the calcined coke particles during heat treatment up to 2200°C in a tube furnace for this project.

2.4. Coke Characterization by Microscopy

Raw and calcined coke specimens for metallographic observations by optical microscopy were prepared by encapsulating the particles in epoxy, grinding to a midline cross-section and polishing using standard procedures. Optical microscopy observations and photomicrographs in bright field and polarized light (crossed polarizers) were obtained with a Reichert MEF4 microscope. One coke specimen was also examined by a SEM JEOL JSM-5900LV coupled with EDX Oxford Model 7274.

2.5. CTE Rod Preparation

The calcined coke flours were hot-mixed with a typical coal tar binder pitch at 165 °C. The coke-binder mix was then extruded to a 19 mm diameter rod. The rods were heat-treated to about 850 °C in a baking furnace, and the baked rods were further graphitized to 3,000 °C in a tube furnace. The bulk density (ASTM C-559), specific resistance (ASTM C-611) were then measured on the graphitized rod.

2.6. CTE Measurement by PATE Machine

The CTE measurements of the graphitized rods were carried out using a PATE machine (Parma Apparatus for Thermal Expansion), which is based on the capacitance between two parallel plates of the ends of the rod. The details of the measurement have been published.[(4)]

2.7. Continuous Pilot Coking Experiments (Pennsylvania State University)

The delayed coking unit was designed after a unit developed at the PARC Technical Services, Harmarville, PA Pilot-Scale Laboratory Coker (PSLC) and consisted of a 7.5 cm ID x 102.5 cm cylindrical reactor unit having an internal volume of approximately 4.5 liters. The system pressure, temperature and flow rates are monitored by a number of computer-controlled devices, and data from these devices are recorded throughout the run.

The preheater was a 2.5cm OD x 51cm stainless steel tube fitted directly to the bottom of the reactor. This was fed by a 3/8” feed line that was outside the furnace and was heated to 238 °C using heating tape. This design configuration allows for essentially trouble-free pumping of the feedstock over a wide temperature range. The temperature gradient through this 51cm preheater is on the order of 200 °C with an outlet temperature of 420-460 °C. The preheater was connected to a 1/4” line that carried feedstocks from the feed pump.

The following operating conditions were used: coke drum inlet temperature 495 °C, coke drum pressure 50 to 100 psig, and feed rate 16.7 g/min for 6 hours. At the conclusion of feedstock Introduction period, the coke drum was maintained at a temperature of about 500 °C for an additional 24 hours to insure carbonization of non-volatile components. The pilot-scale laboratory coker and associated equipment is shown in Figure 2. The coke drum product temperature was maintained near 495 °C.

The feed is charged to a heated feedstock vessel that was continuously mixed throughout the coking experiment to achieve and maintain homogeneity. In these experiments the temperature was kept at 66 °C. The feed was incrementally heated along the feed line to the preheater. Feed was heated in the lines prior to the preheater to about 180 °C, and then to about 420 °C in the preheater. Heated feedstock from the preheater was fed to the coker drum. Thermocouples attached at different positions along the coke drum were used to measure and to control the temperature during the experiment. Light hydrocarbons that vaporized exit from the top of coker drum and pass through a series of condensers. Gases went through a mass flow meter and were either collected or sent to vent.

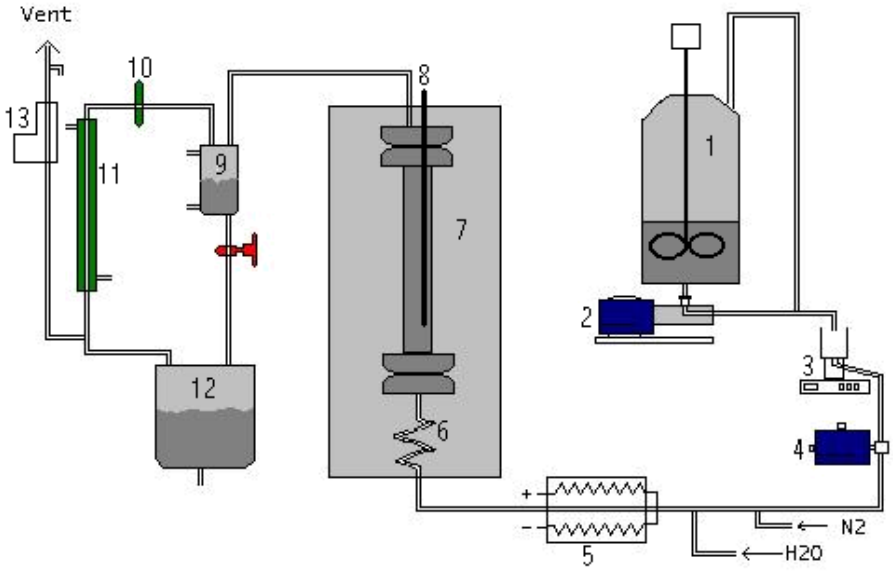

1. Heated Feedstock Tank
2. Feedstock Pump
3. Balance
4. Metering Pump
5. Superpreheater
6. Preheater
7. Coker Drum
8. Thermocouple Well
9. DP Cell
10. Back Pressure Regulator
11. Condenser
12. Receiver Tank
13. Mass Flow Meter

Figure 2: Coking Reactor Schematic

Liquid by-products from the coking runs were collected and analyzed using the following methods:

- Boiling point distributions by simulated distillation gas chromatography, with a Hewlett Packard 5890 Series II chromatograph, following the standard ASTM D2887 method.
- Direct vacuum distillation
- Elemental analysis using a Leco 600-CHN analyzer and a SC-132 sulfur analyzer.
- Gas chromatography-mass spectrometry for identification of specific compounds, using a Shimadzu QP-5000 instrument with Restek XTi-5 column .
- Solid-phase extraction for separation of polar species and their subsequent identification by GC-MS.
- Both ^{13}C and ^{1}H nuclear magnetic resonance spectrometry, for determining aromatic and aliphatic carbon and hydrogen distribution. The instrument used is a Bruker AMX 360.

All of this equipment is located in the laboratories of Penn State's Energy Institute.

2.8. X-Ray Diffraction

X-ray diffraction measurements were made on the graphite artifacts produced from the four different batch cokes. A description of the conditions used follows:

The samples were crushed in a Spex mill and screened to pass a ~375 mesh sieve. The powders were then loaded into holders for determining the XRD parameters. The measurements were made on a Scintag Diffractometer X2 with a theta-theta goniometer, graphite monochrometer, and a scintillation detector. Samples were powdered and mixed with 3% NIST 640c Silicon, which was used as an internal peak position standard. The samples were loaded using a front packing method with a spinning sample holder. Measurement conditions were as follows:

Accelerating Voltage	40 kV
Beam Current	40 mA
Slit size	0.015 mm
Step size	0.020 Deg
Count time	0.02 Sec
Range	5 to 100 Deg 2 Theta

The software used included Scintag DMSNT v 1.37 for data Acquisition and K-Alpha 2 Stripping, Peak-Fit V-4.11, and Table-Curve v- 5.01 for peak finding, background subtraction, goodness of fit and line fitting. Purified natural

graphite standard SP-1 was used to determine instrumental and inherent line broadening. A shape factor of .95 was used in the Scherrer equation.

3. RESULTS AND DISCUSSION

3.1. Feedstock Characterization

Characterization of the decant oil and coal-tar distillate was carried out using the techniques of ^{1}H and ^{13}C NMR, GC/MS, SimDis, elemental analysis and asphaltene content determination. The results are summarized in Tables III to IX.

The GC/MS date in Table III show that the coal tar distillate has a higher content of polycyclic aromatic structures than the decant oil and a lower content of paraffins, cycloalkanes, tetralins and decalins. In general, decant oil has more hydrogen-containing structures compared to those of the coal tar distillate. The results observed by GC/MS are supported by the elemental analysis where the H/C ratio is higher for the decant oil than for the coal tar distillate.

The ^{1}H and ^{13}C NMR data in Tables IV and V provide additional information about the chemical structures present in the two materials. According to the assignments for functional groups, ^{1}H NMR shows higher aromaticity for CTD compared to decant oil as well as a lower hydroaromaticity and lower degree of alkyl substitution. The number of CH, CH_2 and CH_3 groups attached to aromatic carbons is higher for decant oil than for CTD.

The ^{13}C NMR shows more alkyl groups and CH_3 α to hydroaromatic and naphthenic CH_2 for decant oil than CTD. The CTD has more internal aromatics than decant oil.

The simulated distillation data in Table VI show that the CTD has heavier components than the decant oil. The elemental analysis data in Table VII show that the CTD, in addition to being more aromatic, has a higher nitrogen content than the decant oil.

Table III
Hydrocarbon-Type Compounds Identified by GC/MS

	Decant Oil, %	Coal-Tar Distillate, %
Paraffins	9.91	0.03
Cycloalkanes	3.52	0.29
Alkyl benzenes	3.61	2.94
Indenes	2.47	4.90
Naphthalenes	3.42	5.87
Tetralins	1.88	0.34
Decalins	0.24	0.00
Polycyclic structures	74.94	85.63

Table IV
^{1}H NMR Determination of Group Types for Decant Oil and Coal-Tar Distillate
(Ref. Table I)

Band TMS (ppm)	Decant Oil	Coal-Tar Distillate
	%	
0.5-1.0	13.0	5.7
1.0-1.7	29.6	12.6
1.7-1.9	1.8	0.9
1.9-2.1	1.5	1.0
2.1-2.4	5.8	11.2
2.4-3.5	19.4	28.8
3.5-4.5	1.6	1.7
4.5-6.0	0.2	0.0
6.0-7.2	4.1	4.3
7.2-8.3	20.0	28.4
8.3-8.9	2.9	5.1
8.9-9.3	0.0	0.2
0.5-4.5	**72.8**	**61.9**
6.0-9.0	**27.2**	**38.1**

Table V
^{13}C NMR Determination of Group Types for Decant Oil and Coal-Tar Distillate

Band TMS (ppm)	Decant Oil	Coal-Tar Distillate
	%	
11.0-12.5	0.1	0.2
12.5-15.0	2.0	1.0
15.0-18.0	1.9	0.4
18.0-20.5	3.0	1.6
20.5-22.5	4.8	1.1
22.5-24.0	3.3	1.4
24.0-27.5	2.5	2.0
27.5-37.0	16.1	11.5
37.0-60.0	6.0	3.4
108.0-118.0	0.0	2.2
118.0-129.5	35.4	60.9
129.5-133.0	9.1	7.3
133.0-135.0	3.0	1.3
135.0-138.0	4.2	2.1
138.0-160.0	8.5	3.6
8.0-65.0	**45.4**	**32.9**
125-150.0	**54.6**	**67.1**

Table VI
Simulated Distillation Results

	Decant Oil	Coal-Tar Distillate
IBP, °C	113.5	173.5
10%, °C	123.8	203.4
20%, °C	135.6	243.9
50%, °C	216.9	353.5
95%, °C	489.1	497.9
FBP, °C	522.1	522.8
IBP-180, %	**40.50**	**2.30**
180-270, %	**19.04**	**23.41**
270-FBP, %	**39.53**	**73.34**

IBP=Initial Boiling Point, FBP=Final Boiling Point

Table VII
Elemental Analysis for the Decant Oil and Coal-Tar Distillate

	H,%	C,%	S,%	N,%	Atomic H/C
Coal-Tar Distillate	5.81±0.09	92.72±0.05	0.65±0.00	1.11±0.04	0.75
Decant Oil	7.86±0.10	91.68±0.26	0.48±0.01	0.44±0.01	1.02

Table VIII
Proximate Analysis for Decant Oil and Coal-Tar Distillate

	% Moist. Sample (As Recd.)	% Ash (Dry)	% VM (Dry)	%FC (Dry)
Coal-Tar Distillate	0.10±0.02	0.00±0.00	98.00±0.03	2.00
Decant Oil	0.21±0.05	0.03±0.03	93.79±0.20	6.19

Table IX
Asphaltene Content

	Wt. %
Coal-Tar Distillate	0.33
Decant Oil	1.63

3.2. Pinhole TGA Results on Feedstocks

Figure 3 shows the pinhole TGA curve for the Seadrift decant oil. The extrapolated onset temperature of 341 °C is consistent with the expected boiling range for a decant oil and the 7.2% residue after heating to 500 °C is also consistent with the measured MCC value of 8.8%.

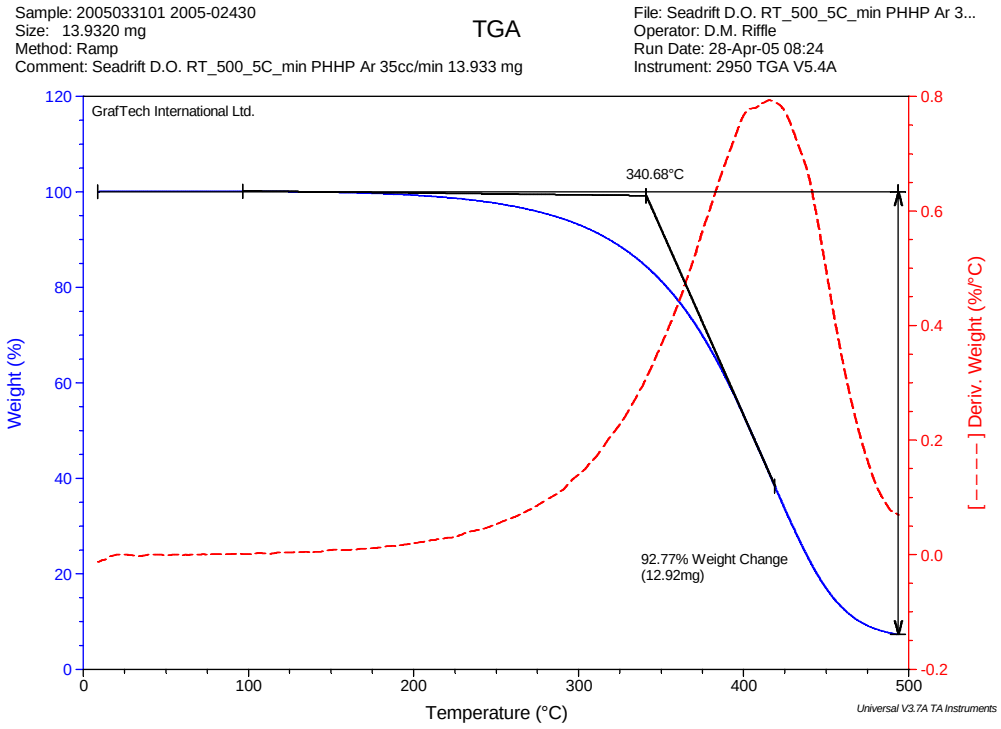

Figure 3: TGA Curve for Seadrift Decant Oil

Figure 4 shows the pinhole TGA curve for the coal tar distillate sample. The 325 °C extrapolated onset temperature is consistent with the expected boiling range for this distillate fraction. The very low (1.2%) residue after heating to 500 °C is consistent with the distillate origin of this material and is also consistent with the very low MCC value of 1.4% measured for this sample.

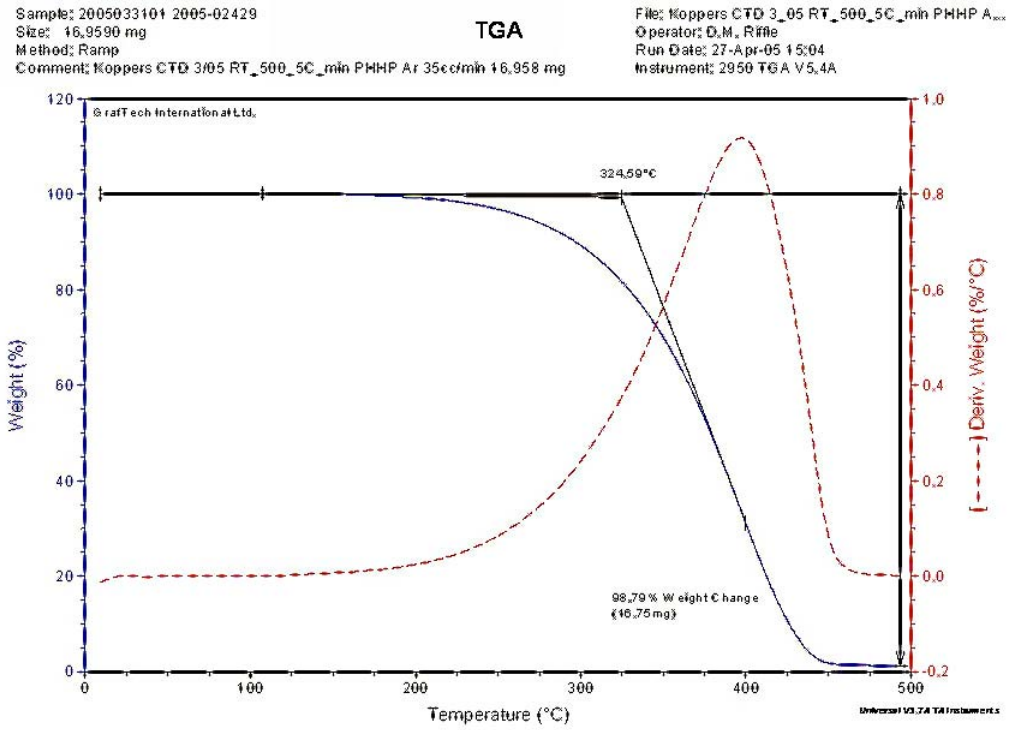

Figure 4: TGA Curve for Koppers Coal Tar Distillate

The boiling temperatures from the TGA method are appreciably higher than those calculated by the GC Simulation method in Table VI. The GC/Sim method employed paraffinic compounds as reference materials, which is apparently not appropriate for these more aromatic feedstocks.

3.3. Coking of Koppers Coal Tar Distillate and Seadrift Petroleum Feedstock

3.3.1. Pilot-Scale Autoclave Batch Coking at Parma

The first two batch coking runs were carried out under 100-psig gas pressure at a nominal product temperature of 475 °C with a ramping rate of 50 °C/hr and a hold time at 475 °C of 20 hours. The temperature vs. time curves for the thermocouples placed at the top and bottom external positions and the internal location (product temperature within the stainless steel can) for coking runs with the Koppers coal tar distillate and the Seadrift decant oil are shown in Figures 5 and 6, respectively.

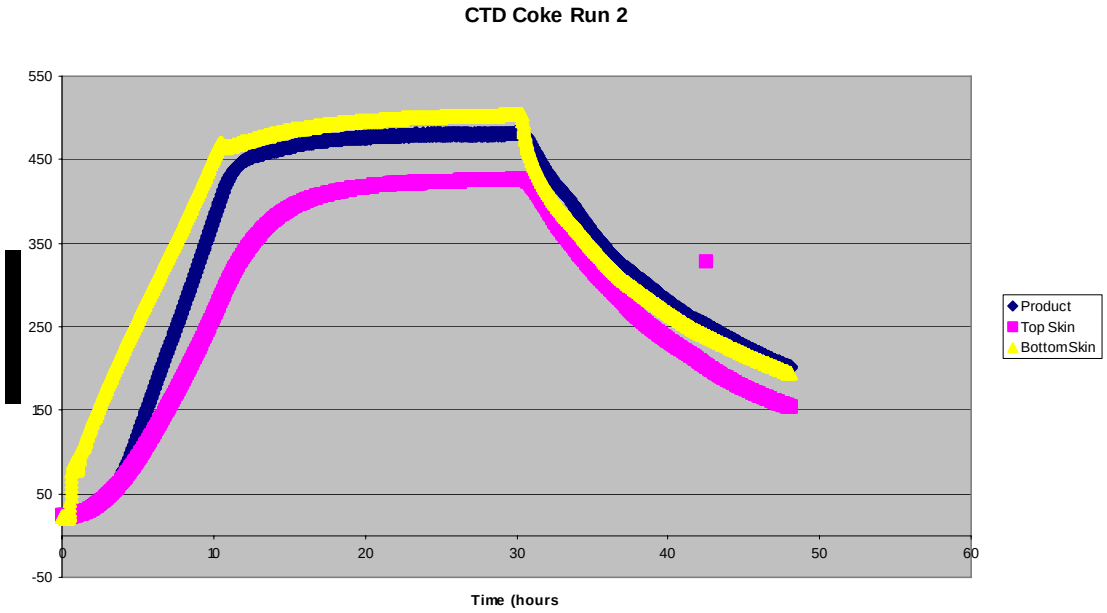

Figure 5: Temperature vs. Time for Batch Coking of Koppers Coal Tar Distillate at 100 psig in Coke Run 2

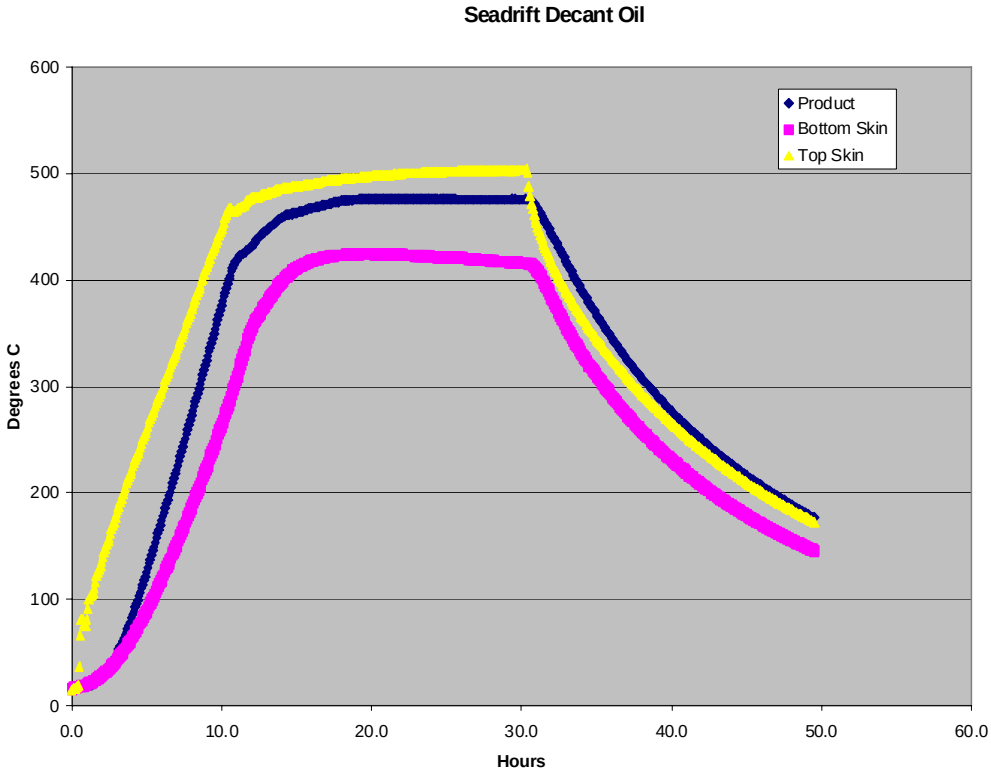

Figure 6: Temperature versus Time for Batch Coking of Seadrift Decant Oil at 100 psig for Coke Run 1

A third batch coking run was also carried out for the coal tar distillate (CTD) at 50 psig, and at 475°C for 20 hours. The purpose was to determine whether the high coke yield obtained at 100 psig could be duplicated at the lower pressure. A fourth batch coking run was performed with a blend of 80 wt.% CTD with 20 wt.% of decant oil using the same 50 psig and temperature conditions. The decant oil component would reduce the overall nitrogen content of the derived coke and, possibly lead to more orientation during coking as a result of gas evolution from the decomposing aliphatic side chains.

The temperature vs. time curves for the thermocouples placed at the top, bottom, and internal locations of the can for these two batch coking runs are shown in Figure 7a and 7b, respectively.

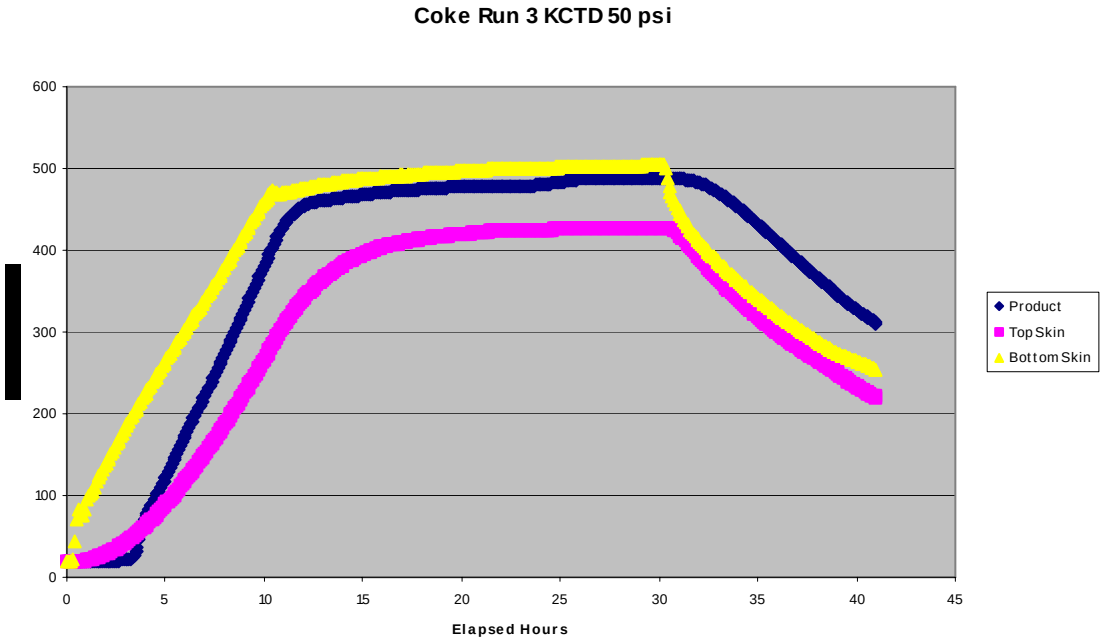

Figure 7a: Temperature vs. Time for Batch Coking of CTD at 50 psig for Coke Run 3

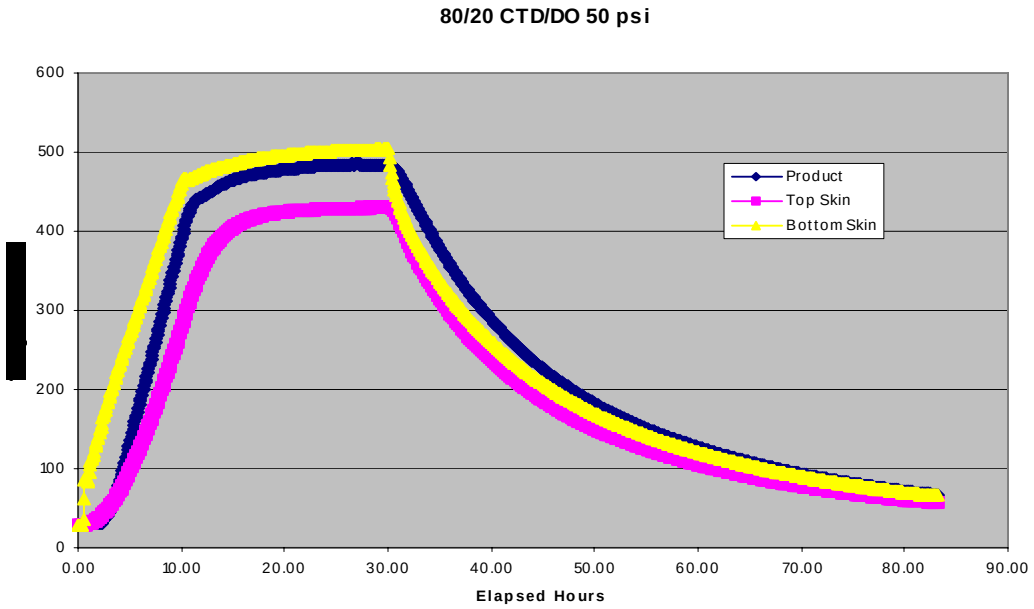

Figure 7b: Temperature vs. Time for Batch Coking of 80/20 CTD/DO at 50 psig for Coke Run 4

A summary of the operating conditions for the four batch coking runs is presented in Table X.

Table X
Summary of Operating Conditions for Batch Coking Runs

Sample	Pressure (psig)	Nominal Product Temperature (°C)	Coking Time (hrs)
100% CTD	**100**	**475**	**20**
100% DO	**100**	**475**	**20**
100% CTD	**50**	**475**	**20**
80% CTD/ 20% DO Blend	**50**	**475**	**20**

The summary of the green coke yields and their average MCC values is presented in Table XI.

Table XI
Summary of Green Coke Yields and Average MCC Values

Sample	Average Coke Yield, wt%	Average Green Coke MCC, wt%
(3823) 100% CTD 100 psig	**74.0**	**95.8**
(3806) 100% DO 100 psig	**49.2**	**99.3**
(5152) 100% CTD 50 psig	**75.3**	**97.3**
80/20 CTD/DO Blend 50 psig	**71.7**	**95.4***

* Average of middle and bottom sections in Table XII

Individual MCC values for different sections of each coke product were also determined by taking samples at the top, middle, and bottom of the coke bed in the stainless steel can. The results are shown in Table XII. The variations from top to bottom are very small, except for the last batch coking run with the CTD/DO blend, indicating that the temperature appeared to be uniform throughout the coke bed. Because of the

uniformity of the MCC values for the first three coke runs, the entire raw coke was combined and then calcined without any segregation. Subsequent optical microscopy examinations showed that the actual temperature was not uniformly high in some of these runs. For the fourth coke run with the 80/20 CTD/DO blend, the top portion had a significantly lower MCC value than the remaining material. Therefore, it was separated and calcined separately.

Table XII
MCC Values from Various Positions in the Coke Bed

Position	100%CTD 100 psig	100% DO 100 psig	100%CTD 50 psig	80/20 CTD/DO 50 psig
Top	**95.4**	**98.6**	**96.7**	**86.1**
Middle	**96.9**	**99.8**	**98.0**	**95.1**
Bottom	**95.1**	**99.5**	**97.1**	**95.7**

Note that the coke yield for the CTD at the pressure of 50 psig is equivalent to that obtained at the higher pressure of 100 psig. The use of a lower 50 psig pressure would be advantageous for a commercial coking operation.

3.3.1.1. Clausius-Clapeyron Estimate for Coal Tar Distillate Vapor Pressure; Effect of Pressure on Coke Yield

The surprisingly high batch coke yields found at both 50 and 100 psig for the coal tar distillate motivated a modeling effort to estimate the effective vapor pressure of distillate at the coking temperature of 475°C.

The nominal boiling range given in the literature for this type of distillate (heavy creosote oil) is >355°C. The literature data for boiling points of pure aromatic hydrocarbons were reviewed to select a suitable compound to represent this distillate. Pyrene was selected because it has a boiling point of 404°C and relevant thermodynamic data could be found in the literature to estimate the heat of vaporization from the liquid state to the gaseous state. Literature values for the heat of sublimation (22.5 kcal/mole) and the heat of fusion (4.2 kcal/mole) were combined to obtain an estimated value of 18.3 kcal/mole for the desired heat of vaporization. This value and the boiling point were entered into the classical Clausius-Clapeyron equation to calculate the constant term for pyrene.

The equation with the calculated constant was then used to estimate the vapor pressure at various temperatures of interest for pyrene as a model for our distillate. The result for the nominal

batch coking temperature of 475°C was 39 psig. Hence, we estimate that the distillate would develop this pressure at 475°C before any chemical pyrolysis and polymerization reactions occurred. Since the applied pressures in the two batch coking runs were 50 and 100 psig, the majority of the distillate should stay in the liquid state and have the opportunity to polymerize and convert to coke. This prediction is consistent with the high coke yields found at both pressures for the 475°C batch cokes.

The equation was also used to estimate the vapor pressure at the nominal temperature of 495°C used in the continuous pilot coking experiments to be discussed later. The result was 59 psig. This estimate indicates that the coke yield at 495°C could be significantly lower at 50 psig than it would be at 100 psig because a significant portion of the distillate could volatilize without reacting at the lower pressure.

3.3.2. Pilot-Scale Continuous Coking Runs at PSU

The apparatus and general operating conditions for the continuous pilot coking facility at PSU were described in Section 2.7. The same feedstock samples used in the batch coking runs were used in the continuous coking runs. The feed rate for each coking run was maintained at 16.8 g/min. After each coking run was completed, a hold period of 24 hours was maintained for the coke drum at 500°C to assure completion of the coking reactions.

A brief summary of the feedstocks and operating conditions for the four continuous coking runs performed during this program is presented in Table XIII.

Table XIII
Summary of the Operating Conditions of Continuous Coking Runs

Run #	Feedstock	Pressure (psig)	Nominal Product Temperature (°C)	Feedstock Introduction Time (hrs)
62	100% DO	50	495	6
63	100% CTD	50	495	6
64	80/20 CTD/DO Blend	50	495	6
65	100% CTD	100	495	6

After each coke trial (and holding 24 hours at 500°C), the entire raw coke log was carefully removed from the coke drum to preserve its integrity. The length and weight of the log were measured. The log was then shipped to Parma for further microscopy examination and subsequent calcinations and CTE measurement. The liquid by-products from each coking run were collected for analysis.

The coke and liquid yields are presented in Table XIV.

Table XIV
Summary of the Coke and Liquid Yields for the Continuous Coking Runs

Run #	Feedstock	Raw Coke Yield (Wt. %))	Liquid Yield (Wt. %)	Raw Coke Length (Inches)
62	100% DO	28.73	56.30	14
63	100% CTD	38.23	52.71	21
64	80/20 CTD/DO Blend	37.76	52.50	19.5
65	100% CTD	49.67	40.99	27

As in the case of the batch coking, the raw coke yield from decant oil is less than that of coal tar distillate at the same pressure, 50 psig. However, the coke yield for the continuous coking run is much less than from the batch coking of the same feedstock (cf..Table XI).. This is probably due to the higher coking temperature for the continuous runs (495°C vs. 475°C). Apparently, a long residence time at lower coking temperature is necessary to thermally react the less reactive, lower molecular weight components before they can volatilize. This is particularly true for the CTD feedstock.

3.4. Optical Microscopy Results on Raw Coke Samples

3.4.1. Raw Cokes from Batch Pressure Coking Runs at Parma

Optical microscopy examinations were undertaken on only a single large particle from each of the top, middle and bottom samples taken from the products from the first two batch pressure cokes produced at Parma. The primary goal was to confirm whether the coking conditions throughout the entire coke sample had been severe enough to fully convert the feedstocks to raw coke. The secondary goal was to assess the coke structural characteristics to verify that coking conditions were adequate for

producing needle coke from both feedstocks, which differ significantly in thermal reactivity. The number of particles examined from each sampling location was increased for some of the subsequent runs to provide better statistics and more information on whether coking was complete.

All three of the samples from Coke Run 1 at 100 psig with the Seadrift decant oil had essentially similar characteristics. No pockets of uncoked isotropic pitch-like material were detected in any of the particles, so the coking conditions in this run were adequate to ensure full coking of this feedstock. This is consistent with the high MCC values measured for all three samples. The overall structure was consistent with a needle coke material. There were many flow oriented areas, many large domain areas and some small domain regions. Figure 8 shows a typical area with flow orientation areas in polarized light.

Figure 8: Polarized Light Micrograph of a Predominantly Flow Oriented Region in the Bottom Sample from Coke Run 1 with Seadrift Decant Oil

A few pockets of catalyst particle fines were also detected, as shown in bright field (a) and polarized light (b) in Figure 9.

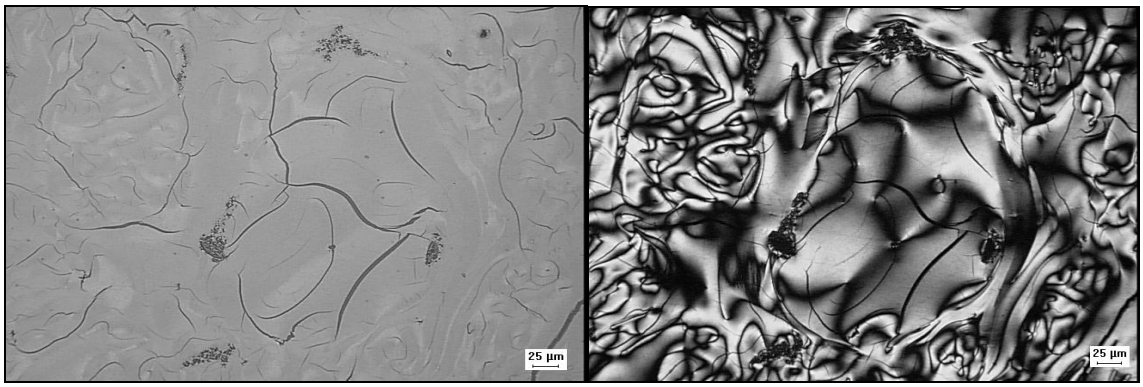

(a) (b)

Figure 9: Bright Field (a) and Polarized Light (b) Micrographs Showing Clusters of Catalyst Fines in Top Sample from Coke Run 1 with Seadrift Decant Oil.

The top and middle samples from Coke Run 2 at 100 psig with the Koppers coal tar distillate were similar to each other. They differed slightly from the Seadrift decant oil coke sample. The apparent bulk densities of these Koppers CTD raw coke samples were noticeably higher than those from the Seadrift coke and there was slightly less flow oriented material. A lower rate and volume of pyrolysis gas generated during coking is one possible explanation for these effects. The relative proportions of the large domain areas and small domain areas in these Koppers CTD coke samples were about the same as the Seadrift coke sample. Both samples were fully coked and contained no pockets of finely divided solids. The latter result is consistent with the distillate nature of this feedstock.

Figure 10 shows a typical area in the middle sample of the Koppers CTD coke under polarized light.

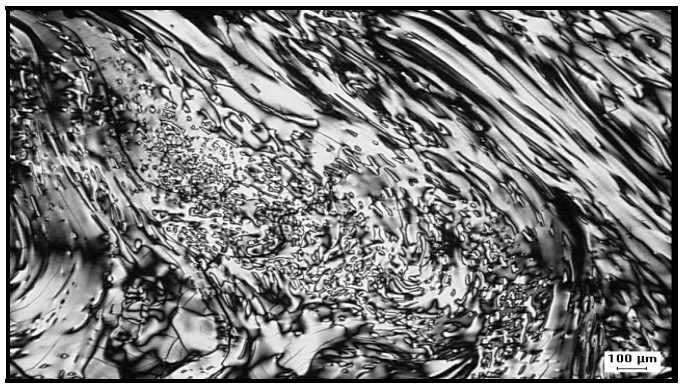

Figure 10: Polarized Light Micrograph showing Flow Oriented and Small Domain Areas in Koppers CTD Coke from Run 2.

Unexpectedly, the bottom sample from Coke Run 2 had several reasonably large pockets of isotropic pitch-like material, in addition to the normal fully coked areas.

Figure 11 shows area containing both types of material in bright field and polarized light.

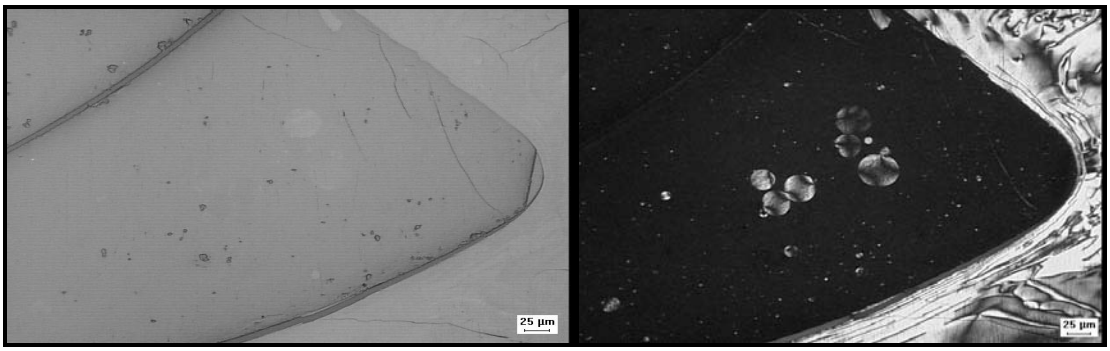

(a) (b)

Figure 11: Bright Field (a) and Polarized Light (b) Micrographs Showing a Large Pocket of Isotropic Pitch Containing a Few Mesophase Spheres in the Bottom Sample from Coke Run 2 with Koppers CTD.

The presence of these isotropic pitch pockets indicates that the coking conditions in at least a portion of the bottom section of the coking can were not sufficient to fully coke this feedstock, probably due to a slightly lower temperature in this local area. The very refractory nature of this coal tar distillate, compared to that for the decant oil, probably exacerbates the problem somewhat. In any case, the presence of a significant amount of uncoked pitch like material is undesirable because it can cause some volatile evolution problems and sintering of the raw coke particles during lab calcining.

Optical microscopy examinations were also performed on several particles from the top, middle and bottom sections of the product from Coke Run 3 at 50 psig with the Koppers CTD. Three particles taken from the top portion of the coke sample contained a mixture of raw coke and areas of isotropic phase that contained mesophase spheres. It appeared that at least two of these particles were taken from the original upper surface so they represent the true upper boundary of the coke sample. Either this top surface layer was significantly cooler than the bulk material or there was appreciable reflux of distillate at the top of the coking vessel. Figure 12a presents a polarized light photomicrograph of the top surface of the coke showing the isotropic pitch containing mesophase spheres. Figure 12b shows another area of the top coke particle that contains only well-oriented coke.

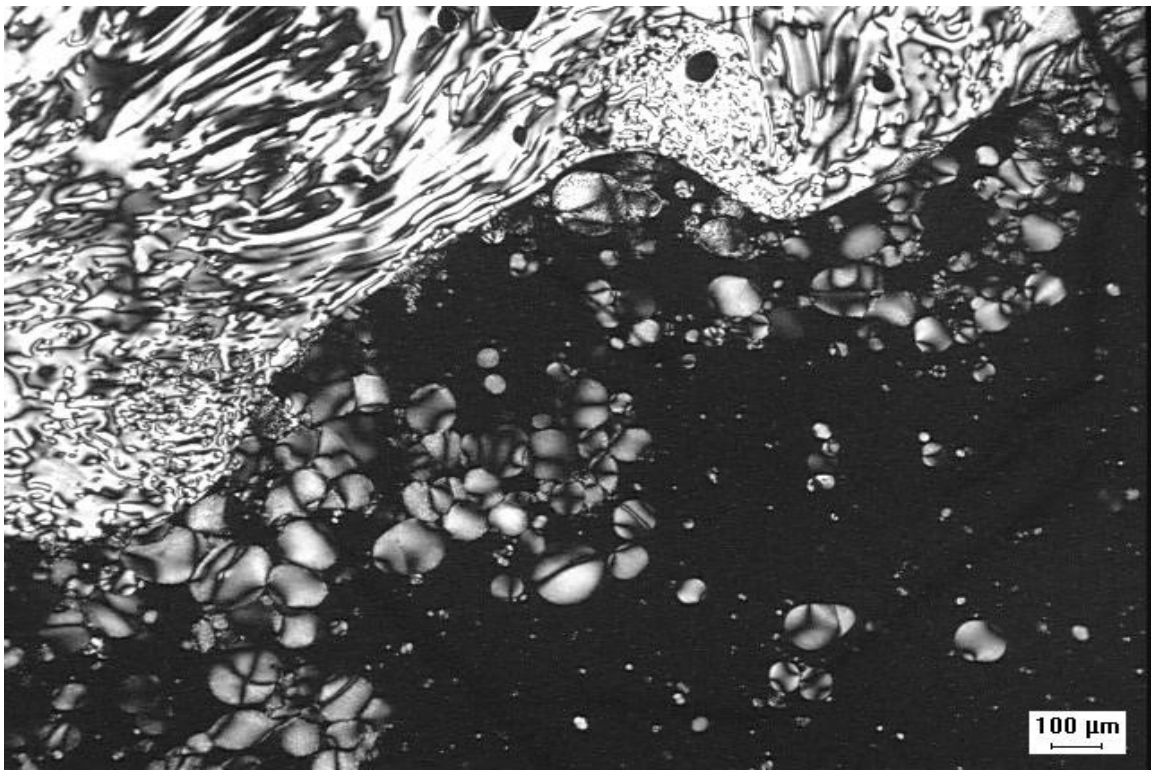

Figure 12a: Polarized Light Photomicrograph of Region at the Top Surface of Coke from Run 3 with CTD at 50 psig

Figure 12b: Polarized Light Photomicrograph Showing Well-Oriented Coke in the Top Region of Coke Obtained from Run 3 with CTD at 50 psig.

Both the middle and top sample of the coke from this run contained only raw coke with no isotropic pitch pockets. The particles taken from the middle section had significant amounts of both large domain and flow or needle structures. There were also some smaller domain areas as well, but these may be end-on or transverse sections of flow-oriented material.

A photomicrograph of the large domain region in the middle section of the coke is shown in Figure 13.

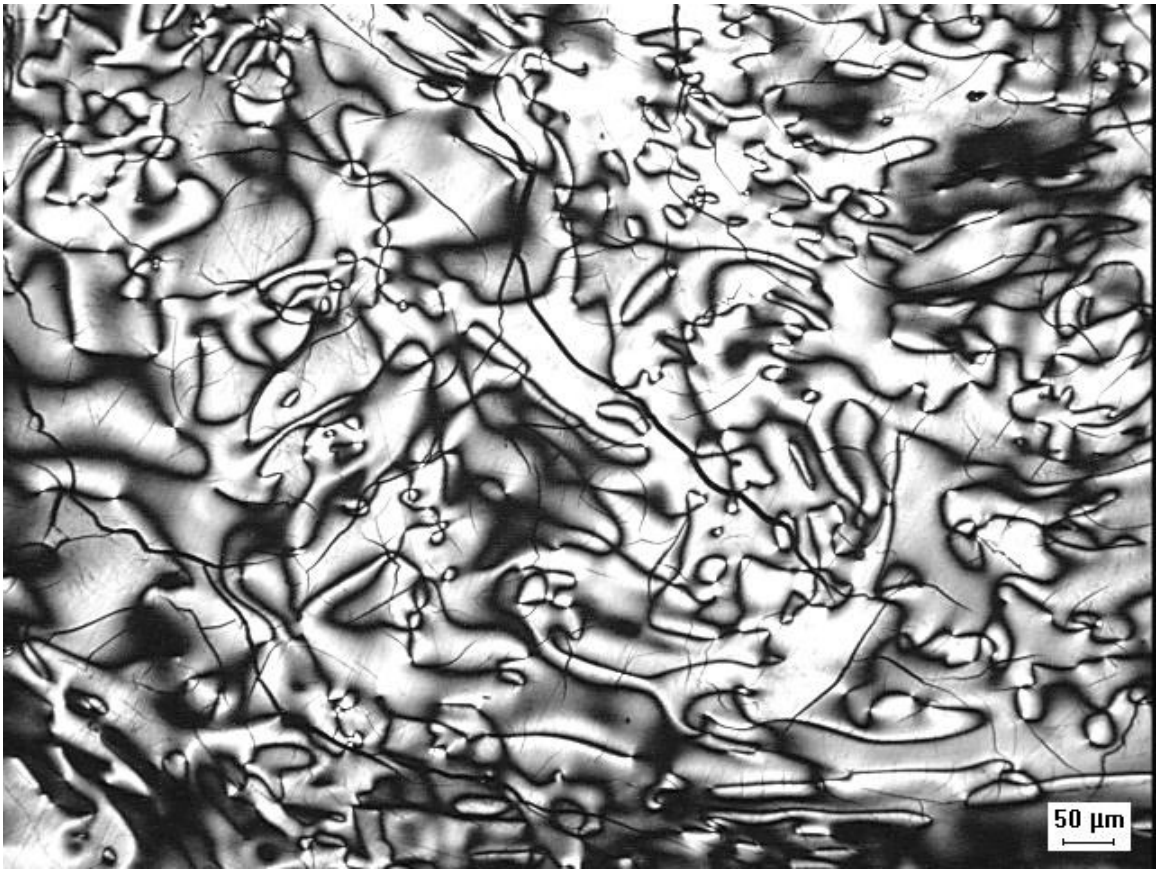

Figure 13: Polarized Light Photomicrograph Showing Large Domain Region in the Middle Sample from Coke Run 3 with CTD at 50 psig.

The bottom portion had considerably more flow structure and less large domain material than the middle sample.

A photomicrograph of a flow-oriented region in the bottom sample is presented in Figure 14.

Figure 14: Polarized Light Photomicrograph Showing Flow Orientation In a Particle from Bottom Portion of Coke Run 3 with CTD at 50 psig

Several large particles from the top, middle and bottom sections of the product from Coke Run 4 with an 80% CTD/20% Decant Oil blend at 50 psig were also examined.

Two of the particles from the top sample had conventional raw coke structures, but the third particle was essentially an isotropic pitch with a dilute concentration of mesophase spheres. This result is consistent with the relatively low MCC value for this top section of the coke log and justifies the decision to exclude this portion of the overall coke sample from the lab calcining because it could would have compromised the entire sample if it had been allowed to sinter and flow during calcining.

Most of the particles in the middle and bottom portions of this coke log exhibited typical needle coke structures with the expected mixture of needle (flow aligned), large domain and small domain areas. A few areas of uncoked material were also found in some of the particles, but the amount of uncoked material was much lower than that found in the top section. A photomicrograph illustrating the excellent flow oriented structure in one area in a particle from the middle portion of blend coke from Run 4 is shown below in Figure 15.

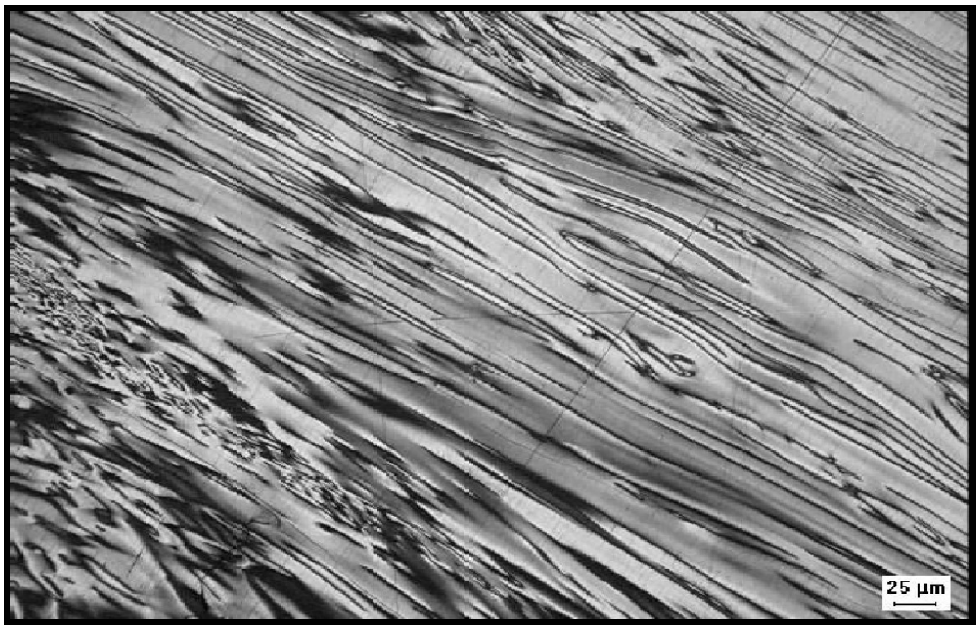

Figure 15: Polarized Light Micrograph Showing a Flow Aligned Structure in a Particle from the Middle Section of the 80% CTD/20% DO Raw Batch Coke from Coke Run 4

In general, the optical microscopy results indicated that at least some portions of the top and bottom samples from some of the batch pressure cokes were not fully coked. The most likely explanation is that the top and bottom portions of the sample container were at least slightly cooler than the bulk middle section. Refluxing of the volatiles from a cooler lid back down to the actual sample surface could be a factor for the top section, but the cause for the apparently cooler area at the bottom is not obvious. Undoubtedly, the relatively unreactive refractory nature of the CTD contributes to the incomplete coking problem.

3.4.2. Raw Cokes from Continuous Pilot Coking at PSU

Optical microscopy examinations were made on single large particles taken from each of the top and bottom sections of the raw coke logs produced in the PSU continuous pilot coker. Since only two particles from each log were examined, the statistics are very limited.

The initial objective of these microscopy observations was to verify that the logs were fully coked. In fact, all but one of the samples was fully coked with no obvious isotropic pitch phase areas. The exception was the top sample from the log from Run #65 at 100 psig with the CTD alone. Fairly large isotropic regions with some coalesced mesophase areas were detected. The only explanation that can be offered for the incomplete coking in this case is that the higher pressure, compared to the 50 psig level in the other runs, suppressed vaporization of more of

the CTD feedstock during the coking cycle. This is consistent with the higher apparent coke yield at 100 psig.

A very surprising result was that all particles from both sampling locations in all four coke logs appeared to be contaminated with an apparently platelet-shaped material, which severely degraded the mesophase formation behavior for a considerable distance adjacent to these platelet particles. A second problem is that a lot fine solids were generated or introduced in some unknown fashion during coking and produced localized small domain (high CTE) areas in these samples, all of which were taken from coke near the vessel walls or the upper free surface.

Figure 16 illustrates a platelet-shaped contamination particle in bright field and polarized light in the Top sample from PSU Coke Run #62 at 50 psig with Seadrift decant oil.

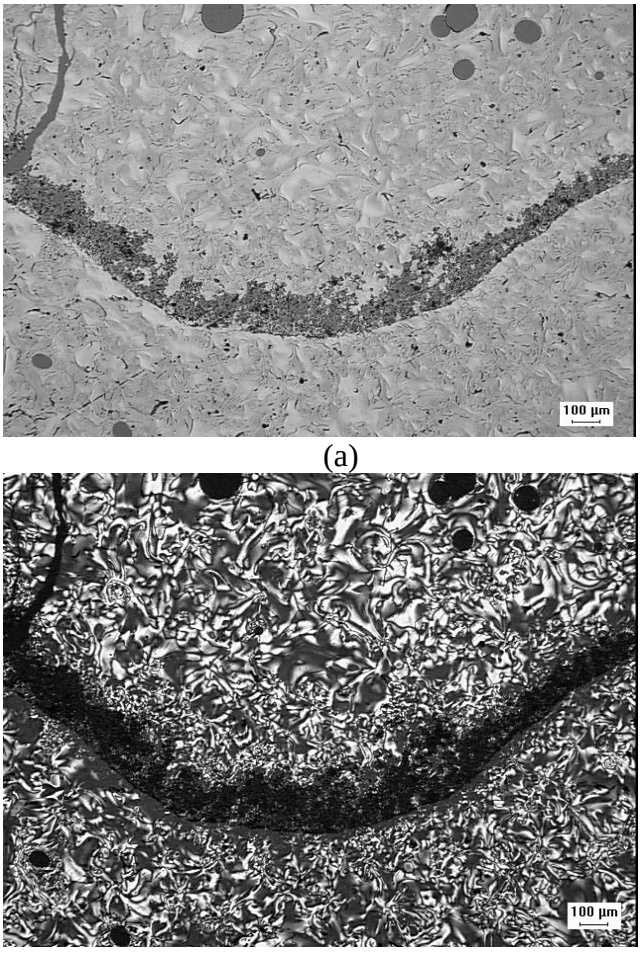

(a)

(b)

Figure 16: Bright Field (a) and Polarized Light (b) Micrographs of a Platelet-Shaped Particle in the Top Sample from PSU Coke Run #62 with Decant Oil Feedstock

Figure 17 shows higher magnification views of the apparently platelet-shaped particle in the same sample. These higher magnification views show that the platelet-shaped particles actually appear to consist of much smaller particles loosely held together in some manner.

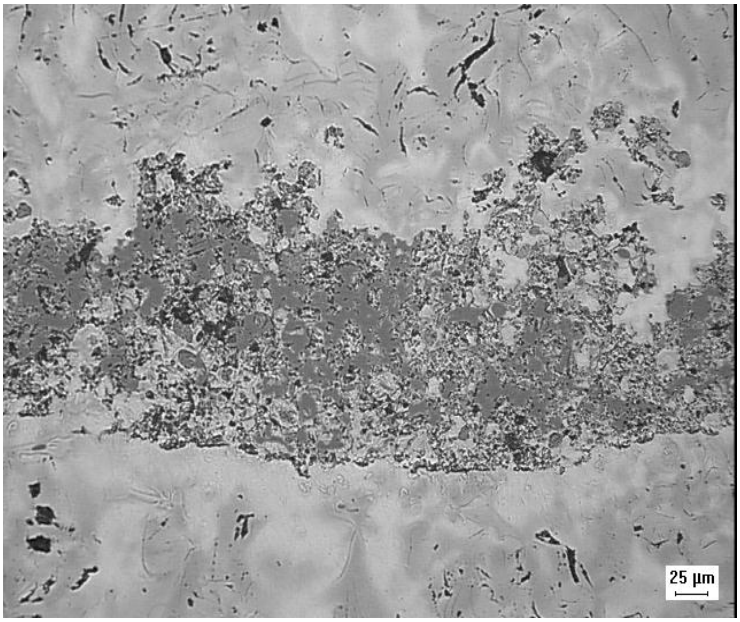

(a)

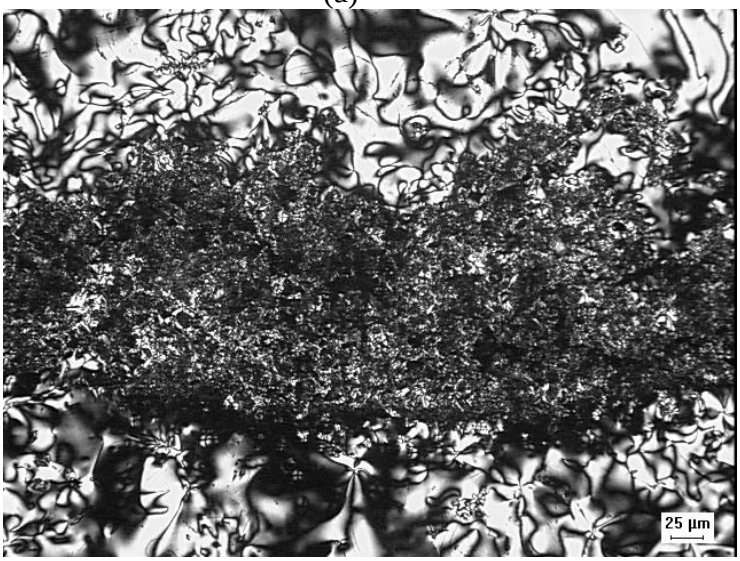

(b)

Figure 17: Bright Field (a) and Polarized Light (b) Higher Magnification Micrographs Showing Detailed Structure of Platelet-Shaped Particles in the Top Sample from PSU Coke Run #62

Figures 18 shows a very thin platelet-shaped particle at the wall interface in Bottom sample from PSU Coker Run #62 at 400X in bright field and polarized light. The porous nature of the platelet particles is evident in these high magnification images.

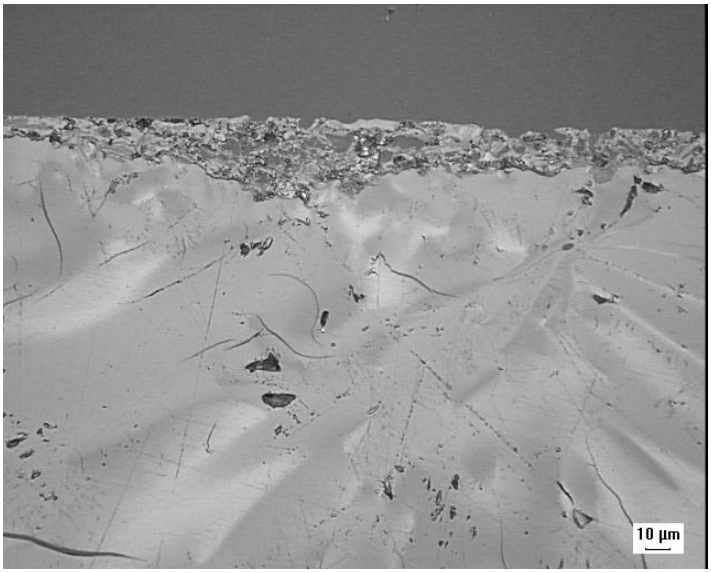

(a)

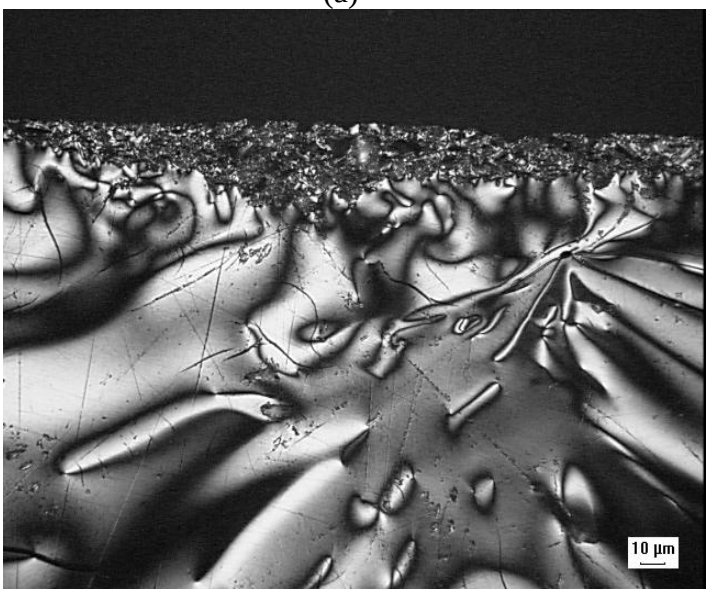

(b)

Figure 18: Bright Field (a) and Polarized Light (b) Micrographs Showing Porous Structure of Platelet–Shaped Particle Near Wall Surface in Bottom Sample from PSU Coke Run #62

Figures 19 and 20 illustrate both a platelet-shaped particle and a nearby very small domain region in the Bottom sample from PSU Coker Run #65 at 100 psig with the Coal Tar Distillate.

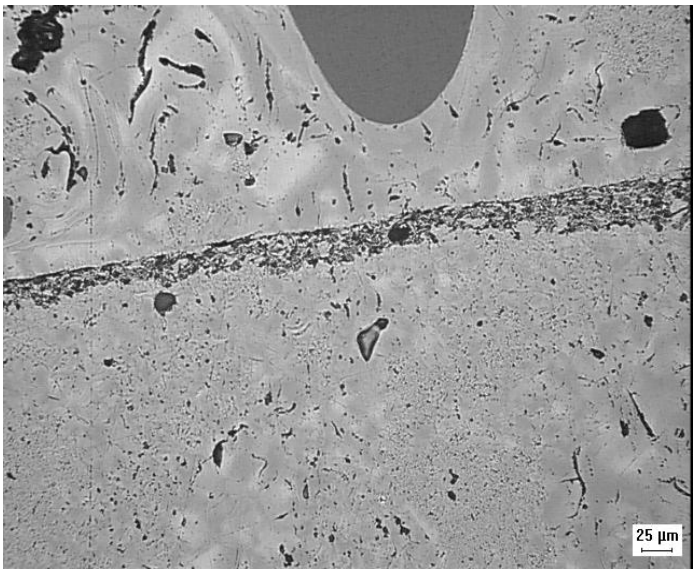

(a)

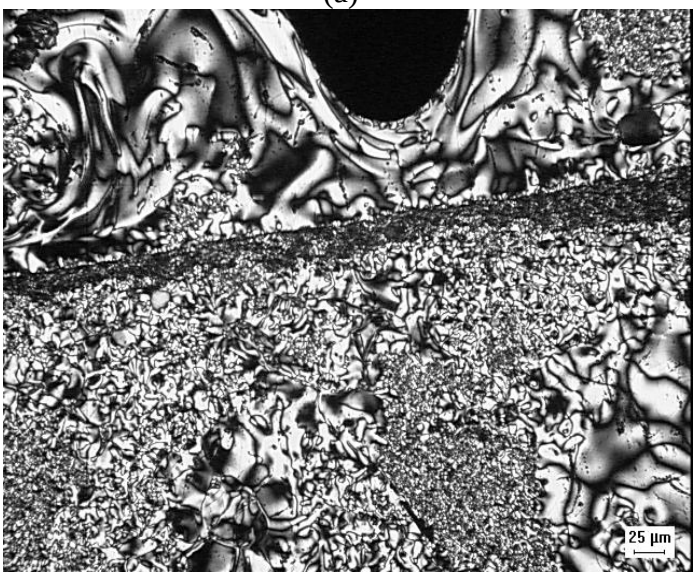

(b)

Figure 19: Bright Field (a) and Polarized Light (b) Micrographs Showing a Platelet-Shaped Particle in the Bottom Sample from PSU Coker Run #65 with Coal Tar Distillate.

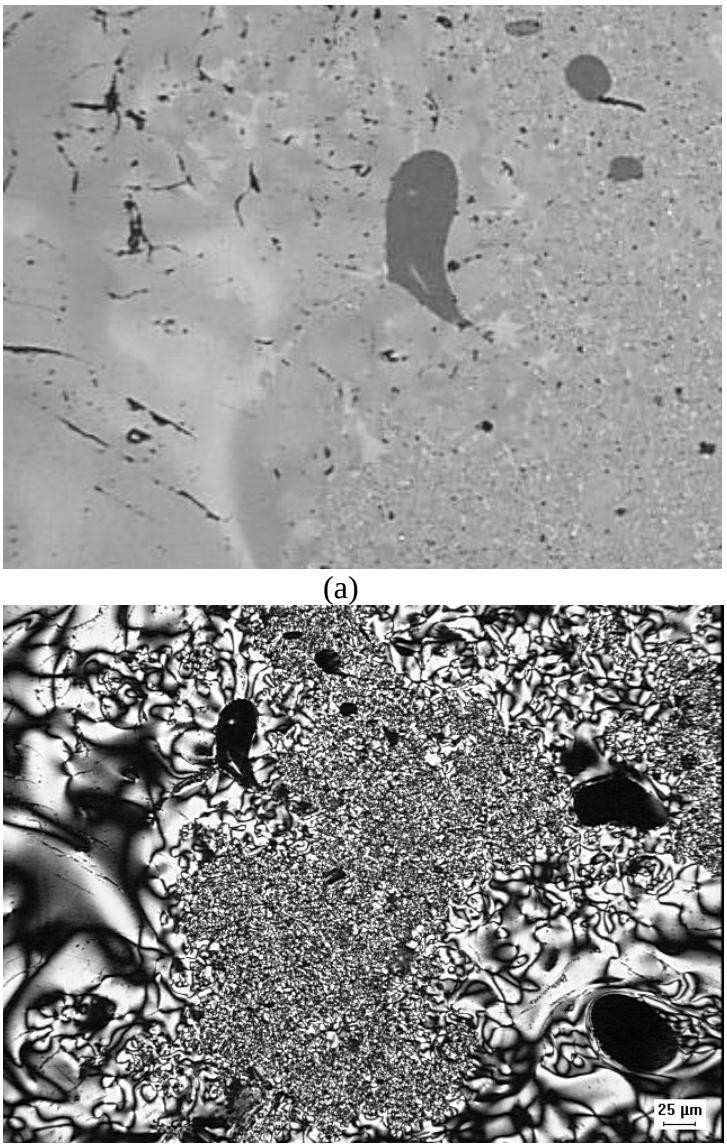

(a)

(b)

Figure 20: Bright Field (a) and Polarized Light (b) Micrographs Showing a Very Small Domain Area in the Bottom Sample from PSU Coker Run #65 with Coal Tar Distillate

One of the very large platelet-shaped particles found in the Bottom sample from Coker Run #64 at 50 psig with the 80/20 CTD/Decant Oil feedstock blend was examined briefly by SEM/EDS to assess its qualitative chemical composition to see if this would provide an explanation for the origin of these particles. The results summarized in Figures 21 and 22 show that the individual small particles in the larger platelet-shaped material are rich in Si and O. Some high Al and O areas are also present, but this may be an artifact from the alumina polishing compound used in preparing the specimens.

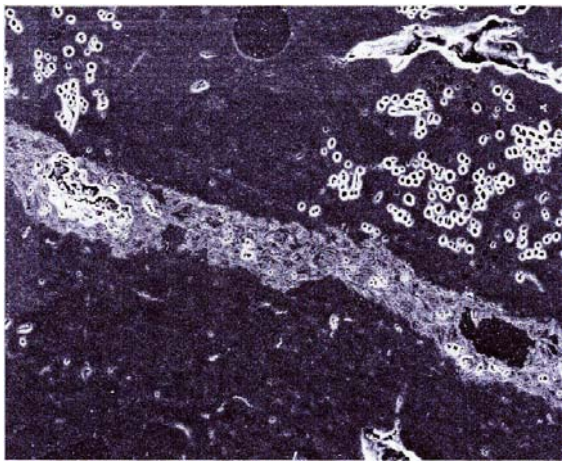

(a)

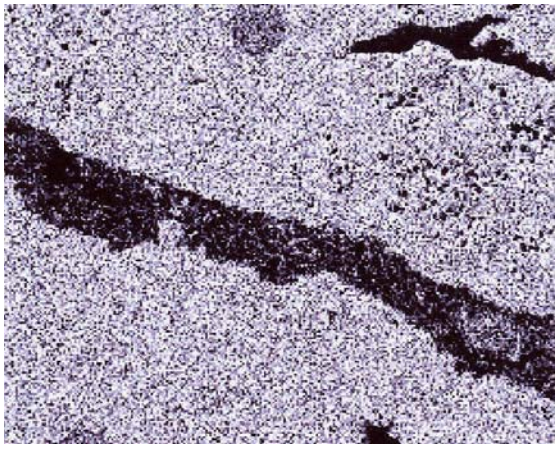

(b)

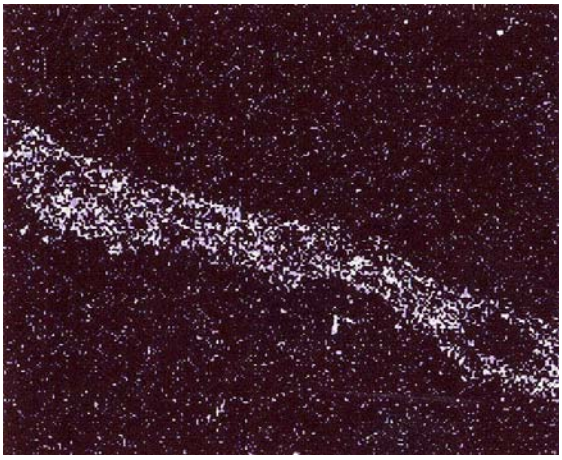

(c)

Figure 21: SEM Image at 250X (a), Carbon Dot Map (b) and Silicon Dot Map (c) for a Platelet-Shaped Particle in Bottom Sample from PSU Coke Run #64

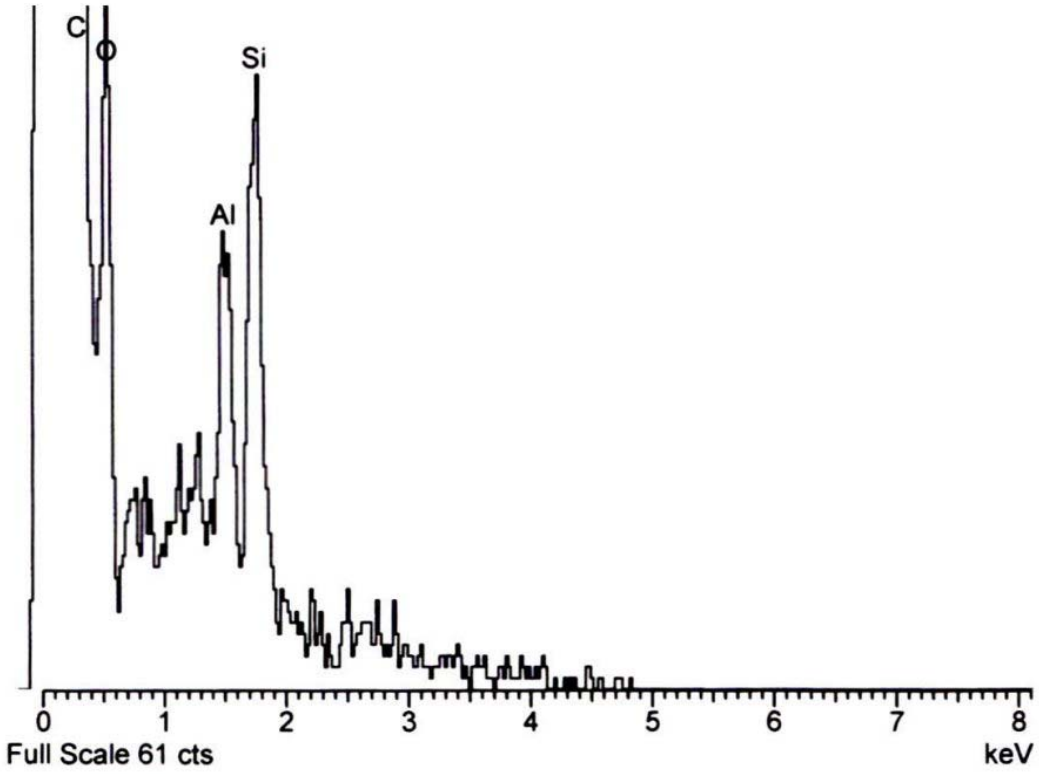

Figure 22: EDX Spot Spectra at 5 kv Acceleration Voltage for a Location in the Platelet-Shaped Particle Shown in Figure 21, (High Si, Al and O peaks apparent in this spot)

The individual particles do not appear to contain any of metallic elements, such as Fe, that one would expect if the walls of the pilot coker vessel itself were corroding. Also, they do not have a high S content, so corrosion of the wall by a conventional sulfidation mechanism can also be ruled out.

Subsequently, it was discovered that the walls of the PSU coker vessel were sprayed with a silicone release agent before each coking run to facilitate removal of the coke log. Apparently, the release agent decomposes and/or degrades at the high temperature used in the coking process. The final product from the degradation process appears to be a layer of finely divided particles containing high Si and O levels. It appears that this degradation phenomenon affects the raw coke to a distance of at least 0.5 inches from the walls, but it is hard to be more precise because the sampling pattern for the top and bottom samples was selected long before the contamination problem was detected. Unfortunately, these unusual and atypical coke features in all of the coke material in the vicinity of the walls of the coke vessel compromise the

validity of the overall coke evaluations because they produce very high CTE coke, which is NOT typical for these feedstocks.

Microscopy evaluations of randomly selected large particles (-3/+6 mesh) representing the entire (surface and central regions) of the lab-calcined samples derived from these PSU raw cokes will be reported in a later section of this report.

3.5. Liquid Analyses of the Continuous Pilot Coking Runs*

In a petroleum refinery, the liquid and gaseous by-products from delayed coking can be combined with other refinery products to provide high value materials. For example, in the production of anode coke, the liquid products have a higher value than the original feedstock[(5)]. In pressure coking of the CTD, about 25% of the original feedstock is evolved as liquid by-product. This is much lower than obtained for the petroleum decant oil. However, the economics of using the CTD as a needle coke precursor still depends on the commercial value of the liquid by-products. For this reason, we have carried out detailed analysis of the by-products collected during the continuous pilot coking trials performed at PSU.

3.5.1. Distillation Profiles

The distillation profiles were obtained for the liquid products collected from the continuous coking runs on the CTD and the decant oil using both the simulated GC method and by independent actual vacuum distillation. The boiling point cuts of the oils obtained after the coking of the decant oil alone are comparable for the two methods, as can be seen by comparing the data in Table XV and Table XVI (simulated and actual distillation); however, the boiling cuts of the oils obtained after the coking of the coal tar distillate (CTD) show a large difference between the simulated and actual distillation. The reason is that the CTD is richer in aromatic compounds when compared to the decant oil and the simulated distillation standard calibration is based on *n*-alkanes, which have lower boiling points than their aromatic counterparts. Therefore, the use of simulated distillation based on alkane standards for the boiling ranges is not reliable for the highly aromatic CTD.

*****Subsequent to the completion of this report, a more detailed description and analysis of the liquid byproducts from the continuous coking was prepared by Maria Escallon of Penn State University. This version is included as an appendix to this report.

Table XV
Simulated Distillation of Liquid By-products

Boiling Range, ^{o}C	Decant Oil - DO	Coal Tar Distillate - CTD
	%	%
ibp-180	5.46	0.86
180-270	11.11	7.26
270-332	12.80	24.27
332-fpb	69.66	66.64

ibp=initial boiling point; fbp=final boiling point

Table XVI
Actual Vacuum Distillation of Liquid By-products

Boiling Range, ^{o}C		DO	CTD	CTD/DO 4:1
		%	%	%
ibp-180	Gasoline	5.8	2.0	1.0
180-270	Jet Fuel	10.7	--	6.0
270-332	Diesel	14.6	--	---
332-fpb	Fuel Oil	68.9	98.0	93.0

For the actual vacuum distillations, the liquid products are classified as gasoline, jet fuel, diesel and fuel oil based on the boiling ranges. Actual vacuum distillation data are also presented in Table XVI for the liquids collected from coking of the CTD/DO blend.

The individual liquid products in Table XVI were analyzed using GC/MS and both ^{1}H and ^{13}C NMR. The results are presented in the Tables which follow.

3.5.1.1. Gasoline

The hydrocarbon types classified by GC/MS are shown in Table XVII for the three different gasoline products. For the CTD/DO blend the composition is expected to fall between that of the individual feedstocks.

There are some hydrocarbon-type compounds whose values or percentages are not in between the values shown for DO and CTD, such as benzene/alkylbenzenes, indenes, and polar compounds, suggesting a possible synergism by chemical interaction when the feedstocks are blended. The synergism is also evident in the NMR data presented in Tables XVIII and XIX.

The compound types where such synergism is possible are highlighted in the Tables.

Table XVII
Hydrocarbon-type compounds obtained by GC/MS – Gasoline

	Decant Oil, %	Coal-Tar Distillate, %	CTD/DO 4:1,%
Paraffins	57.70	30.47	43.42
Cycloalkanes	21.32	0.15	4.66
Benzene / alkylbenzenes	14.05	6.85	14.68
Indenes	1.67	0.79	3.05
Naphthalenes	5.25	40.00	21.67
Acenaphthylenes / acenaphthenes	--	11.65	0.35
Hydroaromatics	--	1.79	0.03
*Polar compounds	--	2.59	7.23
*Phenols	--	5.72	4.90

Table XVIII
Compounds obtained by ^{1}H NMR – Gasoline

Band TMS (ppm)	DO, %	Coal-Tar Distillate,%	80CTD/20DO, %
0.5-1.0	5.62	5.62	15.47
1.0-1.7	12.80	12.53	38.60
1.7-1.9	1.18	1.03	1.47
1.9-2.1	1.13	0.95	3.40
2.1-2.4	8.58	11.11	8.19
2.4-3.5	30.89	28.40	5.55
3.5-4.5	1.73	2.02	0.02
4.5-6.0	0.00	0.00	1.28
6.0-7.2	3.64	4.13	11.63
7.2-8.3	28.84	28.23	14.29
8.3-8.9	5.19	5.44	0.09
8.9-9.3	0.40	0.53	0.00

Table XIX
^{13}C NMR – Gasoline

Band TMS (ppm)	DO, %	Coal-Tar Distillate CTD, %	CTD/DO 80:20, %
11.0-12.5	0.62	0.61	0.43
12.5-15.0	4.74	4.81	5.08
15.0-18.0	1.66	1.66	1.81
18.0-20.5	5.17	5.26	2.93
20.5-22.5	4.00	4.07	2.70
22.5-24.0	4.88	4.95	5.32
24.0-27.5	4.63	4.69	2.97
27.5-37.0	27.88	28.23	25.34
37.0-60.0	11.78	11.40	5.51
108.0-118.0	0.09	0.15	3.41
118.0-129.5	20.68	21.25	29.92
129.5-133.0	4.05	4.00	4.32
133.0-135.0	3.25	3.18	4.33
135.0-138.0	2.20	2.11	1.32
138.0-160.0	4.37	3.64	4.61

The interpretation of the GC/MS and NMR data is as follows:

By ^{1}H and ^{13}C NMR it is observed that olefins are increased in the gasoline fraction when DO is blended with CTD (1.9-2.1 and 4.5-6 ppm ^{1}H NMR and 108-118 ppm ^{13}C NMR). Olefins increase the octane number and might be upgrading the gasoline fraction; however, olefins content needs to meet specification and these are reported in %v/v. Additional tests (ASTM) would have to be carried out to know the olefins composition in v/v %.

Aromatic content and single ring aromatics are higher for the blend, according to GC/MS, ^{1}H NMR (6.0-7.2 ppm) and ^{13}C NMR (118.0-129.5). The aromatics increase the octane number; however, the percentage has to be within the specifications range. Also, there are special restrictions for benzene (it has to be below 3% v/v).

3.5.1.2. Jet Fuel

The jet fuel in the blend should have no contribution from the CTD according to the distillation results presented

previously in Table XVI. However as observed in Table XX, the blend liquid product does show a contribution from the CTD in the presence of naphthalenes, fluoranthene, fluorenes and polar compounds. Hydrotreatment of the jet fuel fraction would lead to hydroaromatics and/or cycloalkane components that should improve the thermal stability of this jet fuel fraction. Hydrotreatment would also reduce polar components which would be beneficial for the use as jet fuel.

The GC/MS data in Table XX show that the percentages of the functional groups for the DO and CTD/DO are very much alike, which was expected because CTD is not contributing to this fraction. The NMR data in Tables XXI and XXII support this conclusion.

Table XX
Hydrocarbon-type compounds obtained by GC/MS - Jet Fuel

	Decant oil , %	**CTD/DO 4:1, %**
Paraffins	38.66	34.79
Cycloalkanes	10.00	1.75
Alkyl benzenes	7.07	5.21
Indenes	10.36	1.56
Naphthalenes	20.64	26.15
Bi-phenyls	5.91	2.93
Anthracenes / Phenanthrenes	2.14	1.96
Hydroaromatics	1.34	0.83
Pyrenes	0.03	0.00
Polar compounds	3.86	4.10
Fluoranthene	---	16.97
Fluorene	---	3.12

Table XXI
Hydrocarbon-type compounds obtained by ^{1}H NMR – Jet Fuel

Band TMS (ppm)	DO, %	CTD/DO 4:1,%
0.5-1.0	5.99	5.87
1.0-1.7	12.35	12.53
1.7-1.9	1.06	1.11
1.9-2.1	1.15	1.16
2.1-2.4	11.19	9.75
2.4-3.5	28.11	29.56
3.5-4.5	1.79	1.75
4.5-6.0	0.00	0.00
6.0-7.2	4.27	4.47
7.2-8.3	28.25	28.17
8.3-8.9	5.44	5.23
8.9-9.3	0.41	0.40

Table XXII
Hydrocarbon-type compounds obtained by ^{13}C NMR – Jet Fuel

Band TMS (ppm)	DO, %	CTD/DO 4:1, %
11.0-12.5	0.43	0.43
12.5-15.0	4.52	4.50
15.0-18.0	1.43	1.47
18.0-20.5	5.00	4.93
20.5-22.5	3.92	3.90
22.5-24.0	5.00	4.99
24.0-27.5	4.50	4.50
27.5-37.0	29.66	28.65
37.0-60.0	11.53	12.68
108.0-118.0	0.16	0.20
118.0-129.5	21.47	21.39
129.5-133.0	3.99	3.98
133.0-135.0	3.23	3.21
135.0-138.0	1.99	1.98
138.0-160.0	3.17	3.19

3.5.1.3. Diesel

The data in XVI show that no diesel oil fraction is obtained in the coking liquids from either the CTD or the CTD/DO blend, The GC/MS analysis for the Diesel fraction from the coking run on the straight decant oil is presented in Table XXIII. The NMR data for this fraction are summarized in Tables XXIV and XXV.

Table XXIII
GC/MS – Diesel

	Decant Oil – DO, %
Paraffins	10.84
Cycloalkanes	3.31
Alkylbenzenes	1.83
Indenes	1.67
Naphthalenes	4.37
Biphenyls	4.94
Anthracenes / Phenanthrenes	45.63
Pyrenes	4.50
Hydroaromatics	7.65
Polar compounds	13.37
Acenaphtylene	1.88

Table XXIV
Hydrocarbon-type compounds obtained by ^{1}H NMR – Diesel

Band TMS (ppm)	**DO, %**
0.5-1.0	6.22
1.0-1.7	12.49
1.7-1.9	1.11
1.9-2.1	1.24
2.1-2.4	11.52
2.4-3.5	27.57
3.5-4.5	1.57
4.5-6.0	0.00
6.0-7.2	4.61
7.2-8.3	28.15
8.3-8.9	5.21
8.9-9.3	0.30

Table XXV
Hydrocarbon-type compounds obtained by ^{13}C NMR – Diesel

Band TMS (ppm)	DO, %
11.0-12.5	0.43
12.5-15.0	4.48
15.0-18.0	1.45
18.0-20.5	4.91
20.5-22.5	3.88
22.5-24.0	4.96
24.0-27.5	4.46
27.5-37.0	28.50
37.0-60.0	12.55
108.0-118.0	0.06
118.0-129.5	21.12
129.5-133.0	4.05
133.0-135.0	3.26
135.0-138.0	2.11
138.0-160.0	3.76

3.5.1.4. Fuel Oil

The GC/MS and NMR data for the highest boiling fuel component in the liquid products are summarized in Tables XXVI-XXVIII. The percentages of compounds of the blend (CTD/DO) are closer to the CTD since this is the higher contributor to the blend (80%). The ^{1}H and ^{13}C NMR do not show a significant variation among DO, CTD and CTD/DO blend.

Table XXVI
GC/MS – Fuel Oil

	DO, %	CTD, %	CTD/DO 80/20,%
Paraffins	1.92	---	---
Cycloalkanes	0.09	---	0.06
Alkyl benzenes	0.00	1.67	0.00
Indenes	1.40	0.01	---
Naphthalenes, bi-naphthalenes	1.32	3.28	4.76
Bi, tri-phenyls	5.78	3.32	4.39
Anthracenes / Phenanthrenes (3-ring)	15.61	23.54	16.63
Pyrenes (4-fused ring)	39.60	13.67	16.65
Hydroaromatics	13.55	5.10	8.03
Polar compounds	3.67	1.60	1.41
Acenaphtylene	0.08	0.02	0.05
Fluorene	0.08	6.99	0.82
Fluoranthene	13.68	40.77	46.72
5-fused ring	2.38	0.02	0.39
6-fused ring	0.90	---	0.09

Table XXVII
^{1}H NMR – Fuel Oil

Band TMS (ppm)	Decant Oil-DO, %	Coal-Tar Distillate-CTD, %	CDT/DO 80:20, %
0.5-1.0	6.06	5.84	5.79
1.0-1.7	12.38	12.51	12.32
1.7-1.9	1.07	1.10	1.05
1.9-2.1	1.18	1.14	0.98
2.1-2.4	11.28	9.71	11.61
2.4-3.5	27.94	29.64	27.94
3.5-4.5	1.74	1.76	1.78
4.5-6.0	0.00	0.00	0.00
6.0-7.2	4.36	4.45	4.25
7.2-8.3	28.21	28.19	28.45
8.3-8.9	5.39	5.24	5.37
8.9-9.3	0.39	0.41	0.46

Table XXVIII
^{13}C NMR – Fuel Oil

Band TMS (ppm)	Decant Oil – DO, %	Coal-Tar Distillate – CTD, %	CTD/DO 80:20, %
11.0-12.5	0.51	0.45	0.47
12.5-15.0	4.63	4.53	4.58
15.0-18.0	1.55	1.48	1.47
18.0-20.5	5.08	4.96	4.48
20.5-22.5	3.96	3.91	4.54
22.5-24.0	4.96	4.97	4.97
24.0-27.5	4.56	4.49	4.54
27.5-37.0	28.36	28.51	28.58
37.0-60.0	12.02	12.40	12.25
108.0-118.0	0.10	0.08	0.18
118.0-129.5	21.16	21.20	21.33
129.5-133.0	4.03	4.03	4.01
133.0-135.0	3.25	3.25	3.23
135.0-138.0	2.09	2.08	2.02
138.0-160.0	3.74	3.65	3.34

3.6. Raw Coke Calcinations

3.6.1. Calcination of Raw Cokes From Batch Coking

The calcining yields at 1420 °C for all of the raw coke from the batch coking runs, including the separated portions of the 80/20 CTD/DO blend, are summarized in Table XXIX.

Table XXIX
Summary of Raw Coke Calcining Yields from Batch Coking Runs

	Calcining Yield, %
100% CTD 100 psig (3824)	90.3
100% DO 100 psig (3803)	94.1
100% CTD 50 psig (5551)	91.8
80/20 CTD/DO Blend (Top) (6288)	86.9
80/20 CTD/DO Blend (M&B) (6289)	91.7

As shown in Table XXIX for the 80/20 CTD/DO blend, the calcining yield for the top portion is significantly lower than that of the remaining material. Therefore, the mixed blend of the middle and bottom portion was selected as representative of this coking run. The low calcining yield of the top portion of the 80/20 CTD/DO blend is likely due to a somewhat lower temperature at the top of the drum during coking.

Optical microscopy results discussed earlier indicated that there was a substantial amount of uncoked pitch-like material in the top sample from the 80/20 CTD/DO run.

3.6.2. Calcination of Raw Cokes From the Continuous Coking Runs

The raw coke logs obtained from the continuous coking runs at PSU appeared to be reasonably uniform. It was therefore decided not to segregate the logs into different sections, but to blend the entire log for pilot plant calcinations. The calcinations were performed using the same procedures employed for the batch cokes and the yields of the four runs are presented in Table XXX.

Table XXX
Summary of Raw Coke Calcining Yields from Continuous Coking Runs

	Calcining Yield, %
100% DO 50 psig (#62)	95.4
100% CTD 50 psig (#63)	94.8
80/20 CTD/DO Blend 50 psig (#64)	95.4
100% CTD 100 psig (#65)	94.8

The calcining yields for the continuous coking runs are, in general, higher than those of the batch coking runs. This is likely due to higher coking temperature used for all of the continuous coking runs. This is also consistent with the microscopy results which found much less uncoked (pitch) material in the samples from continuous coking runs.

3.7. CTE Results

3.7.1. CTE Results for Batch Cokes

A summary of the CTE results for the graphitized rods from all of the batch coking runs is presented in Table XXXI along with the density and specific resistance values. The data for the 80/20 CTD/DO blend are for the mixture of middle and bottom portions of the coke drum.

The CTD was coked alone at two different pressures of 50 and 100 psig. As shown in Table XXXI, the CTE value for the 100% CTD coked at the lower 50 psig pressure was very low at 0.038. The higher CTE obtained at 100 psig for the CTD is the result of incomplete coking in the batch-scale run as discussed in the microscopy results in Section 3.4.1 and 3.8.1. The CTE value for the CTD/DO blend which was also coked at 50 psig pressure, falls between the values for the 100% DO and 100% CTD cokes. Based on the CTE values alone, the coal tar distillate could be used to produce a “super-premium” needle coke.

Table XXXI
Summary of CTE Rod Properties for Batch Cokes

Property	Unit	100% CTD 100 psig (3824)	100% DO 100 psig (3803)	100% CTD 50 psig (5551)	80/20 CTD/DO 50 psig (6289)
Bulk Density	g/cc	1.44	1.42	1.42	1.41
CTE	ppm/°C	0.286	0.169	0.038	0.074
Specific Resistance	micro-ohm-m	9.66	8.96	9.46	8.88

Evaluation data were also obtained for the separated top portion of the 80/20 CTD/DO coke run. We obtained a very high CTE value of 0.393 for this coke demonstrating the adverse effect of incomplete coking prior to calcining. Since this top coke sample is clearly anomalous and not representative of true delayed coke, no further work was carried out on this material.

3.7.2. CTE Measurement for Continuous Cokes

The calcined cokes from the continuous coking runs were processed into graphite artifacts using the same procedures described earlier for the batch cokes. The CTE values and the other properties for the graphites are presented in Table XXXII.

Table XXXII
Summary of CTE Rod Properties for Continuous Cokes

Property	Unit	100% DO 50 psig (#62)	100% CTD 50 psig (#63)	80/20 CTD/DO 50 psig (#64)	100% CTD 100 psig (#65)
Bulk Density	g/cc	1.48	1.51	1.48	1.53
CTE	ppm/°C	0.517	0.766	0.778	1.019
Specific Resistance	micro-ohm-m	10.74	9.58	11.05	11.22

All of the CTE values for these cokes were much higher than expected, especially for feedstocks, which normally produce needle cokes with low CTE's. The causes for these anomalous results will become apparent in the discussions of coke structure presented in the following sections.

3.8. Optical Microscopy Results on Lab Calcined Cokes

3.8.1. Microscopy Results on Calcined Batch Pressure Cokes

Five particles from each sample were examined at 50X magnification and the proportions of Needle, Large Domain and Small Domain structures in each particle were estimated visually by a single observer. The data for each individual particle were accumulated and calculated grand average values for the percentage of each structure in the overall sample were obtained. Some high magnification examinations were also made in selected areas, primarily to determine the cause (catalyst fines or natural QI) for any very small domain areas noted in some particles. The results for each sample are summarized below.

Coke Run #1 (3803) 100% Decant Oil, 100 psig: The overall structural results were 29% Needle, 37% Large Domain and 34% Small Domain. Most of the needle or flow regions showed local orientation only with little macro needle orientation for an entire particle. A few very small domain areas were found and high magnification examination showed that clusters of catalyst fines (or holes left behind by catalyst particles which reacted during calcining) were concentrated in these areas. The catalyst fines or holes are easily visible in bright field in Figure 23.

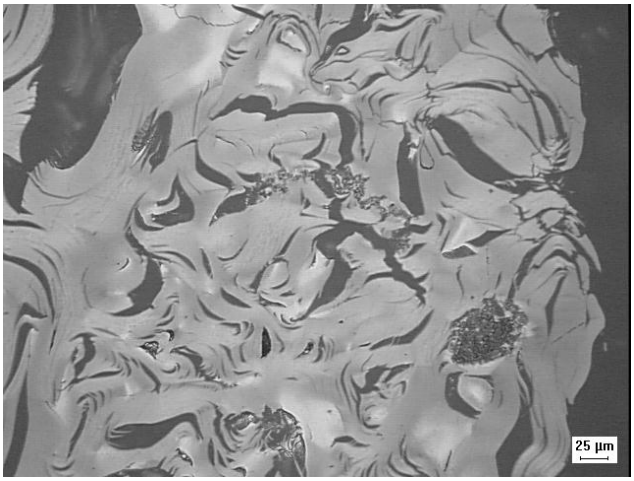

(a)

(b)

Figure 23: Bright Field (a) and Polarized Light (b) Micrographs Showing Catalyst Fines in a Local Small Domain Area in Calcined Batch Coke Sample 3803 Made from 100% Decant Oil

Coke Run #3 (5551) 100% Coal Tar Distillate, 50 psig: The overall structural results were 40% Needle, 40% Large Domain and 20% Small Domain. Some of the needle or flow regions showed macro orientation and a couple of the particles had a noticeable macro needle character. The greater amounts of Large Domain and Needle structures, compared to the 100% DO coke sample above, are consistent with the slightly lower CTE for this coke sample. A few pockets of very small domain material were also located in a few particles in this sample. Examination at high magnification showed that there were probably clusters of natural QI particles in these areas. The very small domain structures are visible in polarized light, but the QI particles are not readily

visible in bright field in a calcined coke because they are carbonaceous and blend in with the surrounding bulk coke matrix.

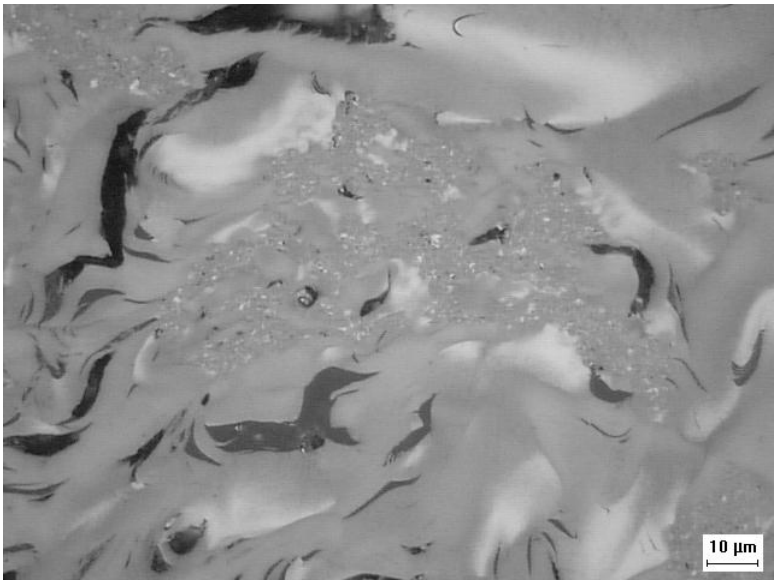

(a)

(b)

Figure 24: Bright Field (a) and Polarized Light (b) Micrographs Showing Very Small Domain Areas from QI Particles in Calcined Batch Coke 5551 Made with 100% Coal Tar Distillate

Coke Run #2 (3824) 100% Coal Tar Distillate, 100 psig: Several areas in most of the particles in this sample contained a composite structure where small individual particles of infusible raw coke had been surrounded by incompletely coked mesophase-derived material which flowed during the calcining process. One of the five particles contained at least 50% of this composite material and the others contained up to 20% of it. The texture of these composite areas is relatively small domain. The presence of a substantial amount of this fine domain composite material provides a very reasonable explanation for the surprisingly high CTE of this sample.

Figure 25 shows the appearance of the composite structure in one particle at low magnification, and Figure 26 shows the appearance of one of the sintered areas in this particle at higher magnification. The small individual fully coked particles cemented together by the uncoked material which flowed during calcining is shown clearly in Figure 26.

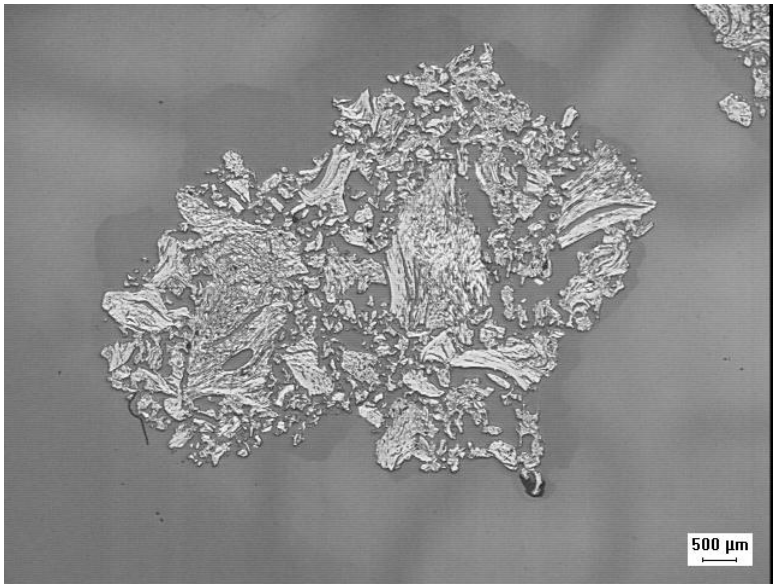

(a)

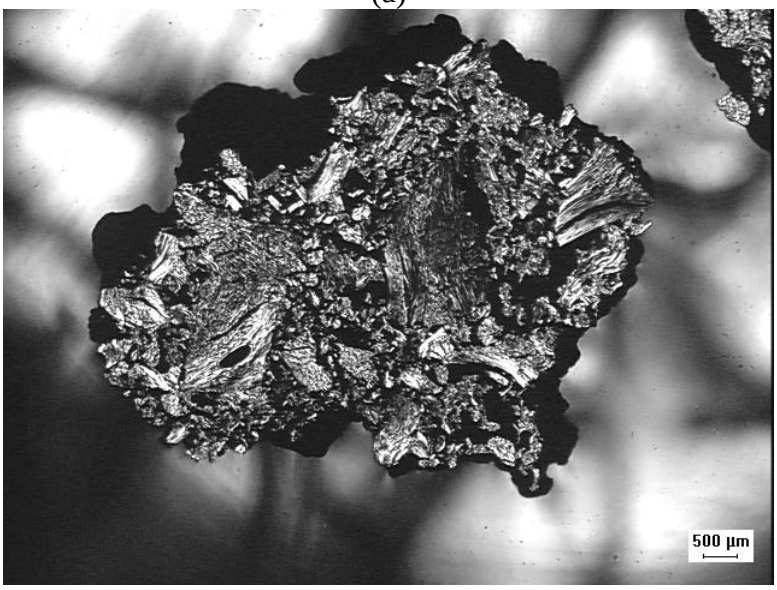

(b)

Figure 25: Bright Field (a) and Polarized Light (b) Micrographs Showing Loose Agglomerate Structure of One Large Particle from Calcined Batch Coke Sample 3824 Made with Coal Tar Distillate at 100 psig

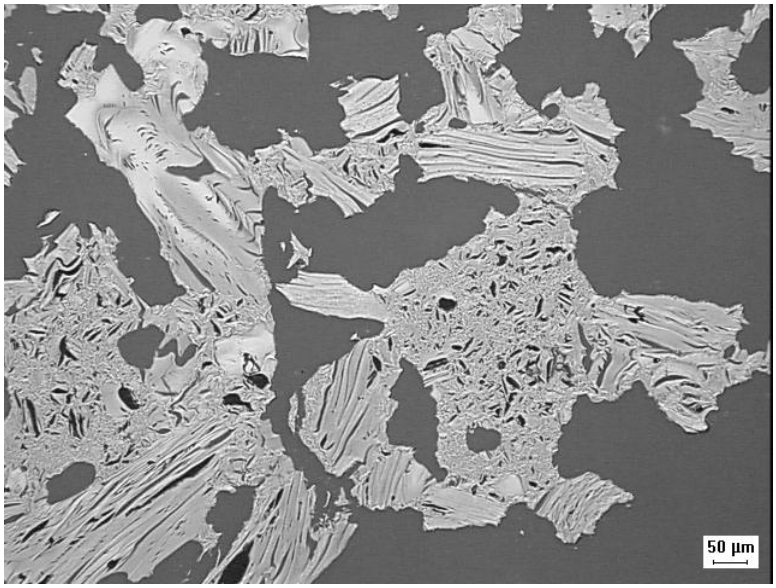

(a)

(b)

Figure 26: Bright Field (a) and Polarized Light (b) Micrographs Showing "Sintered" Area in Calcined Batch Coke Sample 3824 Made with Coal Tar Distillate at 100 psig

The bulk structure in the remaining particles in this sample looked normal. The overall structure ratings on this "normal" fraction were 42% Needle, 36% Large Domain, and 22% Small Domain, indicating that these portions of the sample are similar to those described above for the other 100% CTD coke sample.

Coke Run #4 (6289) 80% CTD/20% DO, 50 psig: The overall structure results were 33% Needle, 42% Large Domain and 25% Small

Domain. There was some macro needle or flow orientation in the particles, but most of the needle areas had only local flow orientation. Based on both the numerical structure data and its overall visual appearance, this sample appeared to be intermediate between the "good" 100% CTD sample and the 100% DO sample. This structure rating is consistent with its intermediate CTE value.

3.8.2. Microscopy Results on Calcined Continuous Pilot Coker Cokes

Five randomly selected -3/+6mesh particles of the lab calcined coke samples from the PSU raw coke logs were mounted and polished for examination. This is the GTI standard method for evaluating any commercial or lab calcined coke by microscopy. In contrast, the raw Penn State pilot coker samples were evaluated by examining only one large particle from the top and one from the bottom of the raw coke log. Hence, the results on the raw cokes, which were discussed in a previous section, are biased toward materials near the bottom wall and the top surface of coke log.

The first significant result is that there was no evidence for a substantial amount of "sintering" occurring during the lab calcining process with these continuous process cokes. Some of the Parma batch pressure cokes did soften and flow to some extent and give a sintering effect when they were lab calcined. The Penn State continuous cokes did not suffer from this problem.

The second significant result is that these "bulk" samples contained only a few areas that were clearly derived from the platelet-shaped contamination particles that were so prevalent in the corresponding raw coke samples from the top and bottom areas. Figure 27 shows low and high magnifications views of one these areas in the calcined PSU Coker Run #65 sample where it appears that much of the original silica-containing platelet shaped particle may have reacted with the surrounding coke during calcining and left a void region. There is some residual inorganic material visible on the boundary on one side of this area in the high magnification bright field view and the small domain character of that area is evident in the corresponding polarized light micrograph.

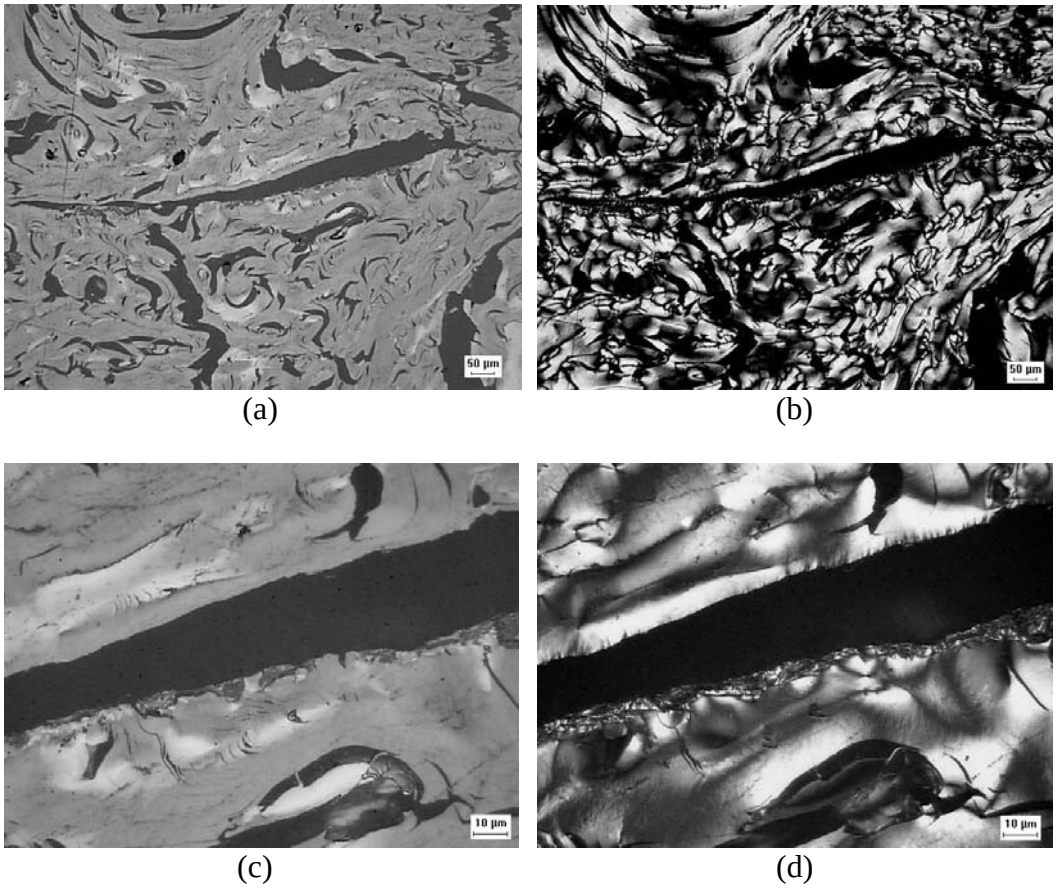

(a) (b)

(c) (d)

Figure 27: Low Magnification Bright Field (a) and Polarized Light (b) Micrographs and High Magnification Bright Field (c) and Polarized Light (d) Micrographs of an Area Showing Some Residual Contamination from a Platelet-Shaped Particle in One Large Particle in Calcined Continuous PSU Coker Run #65

In three of these samples, we did find a calcined coke particle with a partial flat edge, indicating that it was coked at a wall interface. All of these flat edge areas had very small domain structures and, in some cases, contained some clusters of finely divided solids. It seems clear that coke produced near the walls in this pilot coker was degraded by physical and/or chemical processes.

The third significant result is that all of these pilot-coke derived samples had much less needle or flow oriented areas than the corresponding calcined batch samples. They appeared to have a highly deformed structure in many areas from copious bubble percolation. Figure 28 shows one such area in the calcined coke from PSU Coker Run #63 with the Coal Tar Distillate at 50 psig.

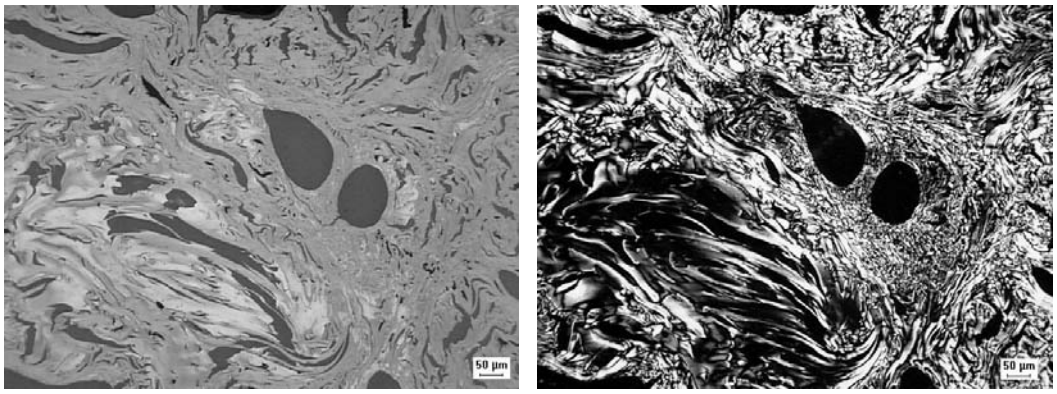

(a) (b)

Figure 28: Bright Field (a) and Polarized Light (b) Micrographs of a Highly Deformed Area in a Particle from Calcined Continuous PSU Coker Run #63 with Coal Tar Distillate

Based on our previous experience in carrying out coke structure studies under various coking conditions, it appears that the feedstocks were probably coked too quickly and did not develop the large domain character and flow characteristics that we normally see when these high quality feedstocks are coked commercially. Specifically, the coking temperature was probably too high and/or the feed rate was too fast.

These microscopy results on the calcined cokes from continuous coking runs indicate that there are probably two contributing causes for their relatively high CTE values: (a) a substantial degradation in the local coke quality near the walls from the contamination reactions with the residue from the silicone release agent and (b) a general degradation of potential coke quality from non-optimum coking conditions.

3.9. Elemental Analyses of Green and Calcined Cokes

All of the green and calcined batch cokes were milled to –200 mesh size flours. Elemental CHN analyses were obtained for these samples using the CHN analyzer and the data are reported in Table XXXIII. Sulfur contents were measured separately and are also reported in the Table.

Table XXXIII
Elemental Analyses of Green and Calcined Batch Cokes

Sample ID	Carbon Wt.%	Hydrogen Wt. %	Nitrogen Wt. %	Sulfur Wt.%
2005 3806 DO 100psig Green Coke	95.49	1.95	0.37	0.47
2005 3803 DO 100psig Calcined	98.85	0.00	0.15	0.41
2005 3823 CTD 100psig Green Coke	95.13	2.44	0.80	0.38
2005 3824 CTD 100psig Calcined	98.65	0.00	0.55	0.28
2005 5152 CTD 50psig Green Coke	96.4	3.48	0.89	0.35
2005 5551 CTD 50psig Calcined	98.8	0.04	0.59	0.24
2005 6196 CTD/DO Green Coke	96.8	3.36	0.78	0.37
2005 6289 CTD/DO Calcined	99.0	0.04	0.52	0.27

Note that the sulfur and nitrogen contents were reduced after calcination at 1420 °C for both the CTD and DO cokes. The nitrogen content for the CTD-derived needle coke is higher than that of coke derived from the decant oil. This could increase the puffing concern during the graphitization process step for graphite electrode production.

3.10. Puffing Results

3.10.1. Puffing Results of the Batch Coking Runs

Puffing is the irreversible expansion of carbon artifacts during the graphitization process. There are several factors affecting the puffing phenomena. One is the nitrogen and sulfur contents in the needle cokes. As the heat treatment temperature is increased to the range of 1,450 °C and 2200 °C, the nitrogen and sulfur-containing gases will evolve from the coke particles in the carbon artifacts. If there are significant nitrogen and sulfur contents in the calcined coke, the evolving gases can disrupt the carbon and graphite structure. The other factors affecting the amount of puffing are the crystallinity and pore structure of the coke.

The puffing results are presented in Table XXXIV as the relative volume expansion in the 1100 to 2200 °C range. The data indicate that coal tar distillate-derived needle coke, in general, exhibits more puffing than the petroleum-based needle coke. One can attribute this to the higher nitrogen content of the coal-based needle coke, as shown by the sulfur and nitrogen elemental analysis results included in the Table XXXIV.

Table XXXIV
Summary of Puffing Results for Calcined Batch Cokes

	Relative Volume Expansion, %	Sulfur, %	Nitrogen, %
100% CTD 100 psig (3824)	1.35	0.28	0.55
100% DO 100 psig (3803)	0.30	0.41	0.15
100% CTD 50 psig (5551)	0.55	0.24	0.59
80/20 CTD/DO Blend (M&B) (6289)	0.75	0.27	0.52

The result for the 100% CTD coke prepared at 50 psig is surprisingly low in puffing. It also has a very low CTE indicating high crystallinity which typically gives higher puffing for the same concentrations of sulfur and nitrogen.

Additional measurements were undertaken to see if the pore structure of these samples might give an explanation for the unusually low puffing behavior. Specifically, the envelope and helium densities of the same calcined coke materials used for the puffing tests were measured and the amount of open porosity was calculated for each sample. The results are summarized in Table XXXV.

Table XXXV
Summary of Density and Porosity Results for Calcined Batch Cokes

Sample Description	Envelope Density g/cc	Helium Density g/cc	Open Porosity
3803-DO, 100psig	1.596	2.128	25.0
3824-CTD, 100psig	1.578	2.082	24.2
5551-CTD, 50psig	1.619	2.095	22.7
6289-80CTD/20DO, 50psig	1.570	2.114	25.7

The results in Table XXXV show that the 5551 calcined coke from the batch coke run with the CTD at 50 psig is slightly denser and has less open porosity than the other coke samples. Increased particle density and lower open porosity are usually associated with higher puffing because it is more difficult for the sulfur- and nitrogen- containing gases to escape to the external surface of the particle without causing expansion. In this group of samples, the denser and less porous 5551 sample has surprisingly low puffing, so other factors must be dominating the relative puffing behavior.

3.10.2. Puffing Results of the Continuous Coking Runs

Puffing tests were initiated on calcined coke samples from the continuous coking runs before the contamination and structural problems with these cokes were discovered. Since it was clear that puffing tests on these materials would not be meaningful due to their anomalous structures, further testing was discontinued.

3.11. XRD of Graphites From Batch Cokes

The lattice parameters obtained for the graphite artifacts produced using the batch cokes as fillers are presented in Table XXVI. Of course, these artifacts contain about 15% by weight of a less graphitizable binder coke. The data in Table XXXVI do show a slight improved graphitizability for the CTD based graphites based on the d-002 and the L_C values.

Table XXVI
XRD Parameters for Graphites From Batch Cokes

Coke Filler	d-Spacing (002)(nm)	L_C (nm)-002	L_A (nm)- 101
Decant Oil 100 psig	3.361	202	181
CTD 100psig	3.360	220	158
CTD 50 psig	3.360	221	185

80%CTD/20%DO 50psig	3.360	204	242

4. CONCLUSIONS

1. Coal tar distillate has been shown to produce an excellent needle coke which can yield graphite with a lower CTE than petroleum-derived decant oil.

2. The high boiling CTD investigated in this program gives a very high yield of coke when coked at the relatively low pressure of 50 psig which is close to that used in commercial delayed cokers.

3. Both the quality and yield of the CTD-derived coke is sensitive to coking conditions. The CTD contains a narrow distribution of polynuclear aromatics. A long residence time at moderate coking temperatures is required to convert the lower molecular weight components to coke. The mild coking conditions employed in the batch coking trials allowed the slow development and alignment of large domained mesophase necessary for formation of low CTE coke.

Higher temperatures and shorter residence times, such as those used in the continuous coking trial, led to volatilization of the lower molecular weight aromatics and formation of finer-domained mesophase which gave a less oriented structure and produced a higher CTE graphite.

It is therefore important with this CTD material to allow slow thermal polymerization and to retain the lower molecular weight components, which can serve to plasticize the mesophase prior to completion of the coking process.

4. The coking behavior of the CTD material is related to its molecular composition which consists of polynuclear aromatic hydrocarbons and heterocyclics with a relative low degree of side chain substitution. As shown by the ^{1}H and ^{13}C NMR analyses, the petroleum-derived decant oil in contrast contains aromatics with a large degree of alkyl substituents of varying chain length. These alkyl substituents lead to a higher reactivity and possibly, a slightly lower graphitizability than shown by the aromatic components of the CTD.

5. The CTD has a much higher nitrogen content and a somewhat lower sulfur content than the petroleum-based decant oil. The nitrogen species contribute to a higher puffing rate for the CTD-based coke during graphitization which at present is not controllable by conventional inhibitors. This could have an adverse economic effect on the use of CTD coke for graphite electrodes.

6. Effective use of the liquid by-products is important in the economics of delayed coking. The chemical makeup of the by-products from coking of the CTD and the DO reflect the composition of the original feedstocks, with the CTD liquids showing few alkyl substituted aromatics as compared to the DO.

7. The liquid by-products from coking of the CTD are essentially all in the high boiling fuel oil range (BP>330^{o}C) with only ~2% in the lower boiling gasoline, diesel oil and jet fuel range. The CTD coking byproducts are likely the most volatile (least reactive) components of the original feedstock and would have economic value as a carbon black precursor or as fuel.

5. REFERENCES

(1) King, B. 1H and 13C Interpretation tutorial; http://www.wfu.edu/ylwong/chem/nmrc13/c13chemicalshift.html- 2003.

(2) Rodriguez, J.; W, T. J.; Irving, W. Evaluation of a delayed coking process by ^{1}H and ^{13}C n.m.r. spectroscopy: 2. Detailed interpretation of liquid n.m.r. spectra. *Fuel* 1994, 73, 1870-1875.

(3) http://www.process-nmrcom/liquidanalysis(2).html Analytical liquid-state NMR applications; Process NMR Associates, LLC, 2003.

(4) G. Wagoner, G. Sprogis, and D. G. Proctor, "Capacitance Bridge Measurement of Thermal Expansion", Carbon 1986 Proceedings, p. 234-236, Baden-Baden (1986).

(5) H.A.Adams "Delayed Coking – Practice and Theory" in Introduction to Carbon Technologies, Edited by H.Marsh, E.Heintz and F. Rodrigues-Reinoso, University of Alicante Press, (1997), p.491.

6. APPENDIX

"Needle Coke from Coal-derived Feedstock"

Oil analysis

December, 2005

Harold Schobert*, Maria M. Escallon*

***** Pennsylvania State University**

Contract Number: 2867-GTIL-DOE-1874
Prime Award Number: DE-FC26-03NT41874

Table of Contents

List of Tables

Abstract

100 g sample of each oil obtained from the coking of decant oil alone (DO), coal tar distillate alone (CTD) and the blend (CTD/DO) was subjected to vacuum distillation. Four boiling point cuts were obtained, gasoline, jet fuel, diesel and fuel oil. The boiling point cuts obtained from vacuum distillation were compared with the ones obtained by simulated distillation (SimDis).

The oil characterization was carried out at The Energy Institute, The Pennsylvania State University. Each boiling point cut was characterized by using chromatography-mass spectrometry (GC/MS) and nuclear magnetic resonance spectroscopy (^{1}H and ^{13}C NMR).

The characterization procedure was the same procedure followed for the feedtocks characterization (see the first submitted report).

1. Procedure of Analysis

1.1. Gas Chromatography / Mass Spectrometry (GC/MS)

The samples injected into the GC/MS were prepared as follows: Approximately 0.02-0.03 grams of the distillate was diluted in approximately 1 gram of dichloromethane. The injection volume was 1.0 μL.

A Shimadzu QP-5000 GC/MS containing an XTi-5 column from Restek (30m x 0.25mm x 0.25 μm) was used. The instrument was programmed to run at 40°C for 4 minutes, and then ramp up to 310°C at a rate of 4°C/min. This final temperature was held for 10 min.

The compound identification was made with the built-in library search and classified in eight different groups: Paraffins, cycloalkanes, alkylbenzenes, indenes, naphthalenes, tetralins, decalins and polycyclic structures. The composition was acquired by identifying peak by peak with the built-in library; then, the compound was classified according to the compounds above mentioned. The summation of the areas of specific hydrocarbon type was divided by the summation of the areas of all the peaks. Hence, the percentage of a particular hydrocarbon type was obtained.

1.2. Simulated Distillation Gas Chromatography

Simulated distillation by gas chromatography (SimDist GC) was utilized to determine the boiling-cut distributions of the decant oil and coal-tar pitch. A Hewlett Packard HP 5890 GC Series II model was used. The column was a Restek Sim. Dist. column (Carborane siloxane polymer).

The data obtained from this ASTM D2887 Method [1] determined the yield by weight of any given fraction of liquid products examined. The first boiling range fraction was defined as liquids that had a boiling point of less than 175°C. The second group was the jet fuel range and was defined as liquids with boiling points between 175-300°C. The next group fell within the boiling range of 300-550°C.

All the samples were prepared as follows: Approximately 0.03-0.04 g of the distillable oil was diluted with 1.2-1.5 grams of carbon disulfide. The samples were then placed in the Hewlett Packard automatic injection tray.

The sample was injected at 40°C; this temperature was held for 4 minutes and then ramped up to 425°C at a rate of 10°C/min. Once at 425°C, the oven remained there for 15 minutes. The total run time was 57.5 minutes.

1.3. Nuclear Magnetic Resonance – NMR

This equipment is a liquid-state NMR spectrometer with imaging capabilities. The samples were analyzed on a Bruker AMX 360 NMR operating at 9.4 Tesla and a 70° tip angle. Distillates were dissolved in $CDCl_3$ for analyses.

The NMR was carried out on the decant oil and coal-tar pitch samples. Through the integration of aromatic and aliphatic peaks in the spectrum, it was possible to establish differences between the two feedstocks (decant oil and coal-tar pitch)..

The regions for the integration of the spectra were defined according to the information in chemical shift tables for ^{13}C and ^{1}H. For aliphatic and aromatic fractions the regions were 8-65 and 125-150 ppm, respectively, for ^{13}C and 0.5-4.5 and 6-9 ppm for ^{1}H

[2]. A detailed interpretation was applied following the peaks integration suggested by Rodriguez et al.[3]. This is shown in

Table I and

Table.

The description of functional groups peaks assignments for ^{1}H NMR [4] is given as follows:

Total Aliphatic: This is the atomic percent of hydrogen atoms present in paraffinic or naphthenic components of the sample.

Total Aromatic: This is the atomic percent of hydrogen atoms present in mono-, di-, and tri-ring aromatic groups.

Triaromatic: This is the atomic percent of hydrogen atoms on carbons adjacent to a bridgehead site in a tri-ring aromatic.

Diaromatic: This is the atomic percent of hydrogen atoms on carbons adjacent to a bridgehead site in a di-ring aromatic.

Monoaromatic: This is the atomic percent of hydrogen atoms in a single ring aromatic group or on the periphery of a polynuclear aromatic group.

Alpha (α)-CH: This is the atomic percent of hydrogen present on methyl groups directly attached to aromatic groups.

Beta (β): This is the atomic percent of hydrogen in CH or CH_2 groups in paraffinic or naphthenic groups, more than one carbon from an aromatic group.

Beta-CH_2: This is the atomic percent of hydrogen present in naphthenic methylene groups or methylene groups in beta position to an aromatic group.

Paraffinic-CH_2: This is the atomic percent of hydrogen present in paraffinic methylene groups.

Table 1-1: ^{1}H NMR assignments for functional groups of interest in petroleum carbonization chemistry [3,4]

Band TMS (ppm)	Assignment
0.5-1.0	CH_3 γ and further, some naphthenic CH and CH_2
1.0-1.7	CH_2 β and further, some β CH_3. Separation at 1.7 ppm is generally not base resolved
1.7-1.9	Most CH, CH_2 β hydroaromatic. This shoulder is one of the best available ways to estimate hydroaromaticity
1.9-2.1	α to olefinic
2.1-2.4	CH_3 α to aromatic carbons
2.4-3.5	CH, CH_2 α to aromatic carbons
3.5-4.5	CH_2 bridge (diphenylmethane)
4.5-6.0	Olefinic
6.0-7.2	Single ring aromatic (or monoaromatic)
7.2-8.3	Diaromatic and most of tri- and tetraromatic
8.3-8.9	Some tri- and tetraromatic rings
8.9-9.3	Some tetraromatic rings

The description of the functional groups' peak assignments for ^{13}C NMR [4] shown in Table is given as follows:

Aromatic Carbon: This is the atomic percent of carbons in aromatic groups.
Aliphatic Carbon: This is the atomic percent of carbons in naphthenic or paraffinic components.
Protonated Aromatic Carbon: This is the atomic percent of aromatic carbons with hydrogen attached.
Alkyl-substituted Aromatic Carbon: This is the atomic percent of aromatic carbons with alkyl groups attached.
Naphthenic-substituted Aromatic Carbon: This is the atomic percent carbon present as aromatic carbon substituted by naphthenic carbon groups.
Methyl-substituted Aromatic Carbon: This is the atomic percent carbon present as aromatic carbon substituted by a methyl group.
Internal Aromatic Carbon: This is the atomic percent carbon present as bridgehead aromatic carbons in polynuclear aromatics.

Table 1-2: ^{13}C NMR assignments for functional groups of interest in petroleum carbonization chemistry [3,4]

Band TMS (ppm)	Assignment
11.0-12.5	CH_3 γ and further from aromatic ring CH_3 in ethyl substituted cyclohexane
12.5-15.0	CH_3 γ and further from aromatic ring CH_3 α shielded by two adjacent rings or groups
15.0-18.0	CH_3 α shielded by one adjacent ring or group Some CH_3 α hydroaromatic and naphthenic CH_2
18.0-20.5	CH_3 α shielded by one adjacent rings or group Some CH_3 α hydroaromatic and naphthenic CH_2
20.5-22.5	CH_3 not shielded by adjacent rings or groups Some CH_3 α hydroaromatic and naphthenic CH_2
22.5-24.0	CH_2 γ and further adjacent to terminal CH_3 CH_2 β in unsubstituted tetralin structures
24.0-27.5	Some CH_2 naphthenic CH_2 α not shielded CH_2 β in propyl and indan groups CH_3 β in isopropyl
27.5-37.0	CH_2 not adjacent to CH in alkyl groups CH_2 adjacent to alkyl CH in some CH_2 α and CH_2 adjacent to terminal CH_3 in alkyl substituents with more than four carbons CH_2 in ring joining ethylene groups Some CH_2 naphthenic Some ring joining methylene (32-43 ppm)

37.0-60.0	CH alkyl groups (except isoalkyl) CH naphthenic CH_2 alkyl groups adjacent to CH Some ring joining methylene (32-43 ppm)
108.0-118.0	Some olefinic (others spread through aromatic region)
118.0-129.5	Protonated aromatic Some internal (quaternary) aromatic
129.5-133.0	Most internal aromatic. These carbons are present as bridgehead aromatic carbons in polynuclear aromatics
133.0-135.0	Methyl substituted aromatic
135.0-138.0	Naphthenic substituted aromatic
138.0-160.0	Alkyl (other than methyl) substituted aromatic heteroatom (N, O, S) aromatic

2. Results and Discussion

2.1. Distillation

The distillation was carried out using the simulated distillation and actual distillation (under vacuum). The boiling point cuts of the oils obtained after the coking of the decant oil alone match when comparing Table 0-1 and

Table (simulated and actual distillation); however, the boiling cuts of the oils obtained after the coking of the coal tar distillate (CTD) shows a big difference between the simulated and actual distillation. The reason is because the CTD is richer in aromatic compounds when compared to the decant oil; the simulated distillation standard calibration contains *n*-alkanes which have lower boiling point when compared to their aromatic counterparts. Therefore, simulated distillation is reporting the present of compounds at lower boiling point cuts when actually those compounds do not belong to that cut.

Table 0-1: Simulated distillation

	Decant oil - DO	**Coal tar distillate - CTD**
	%	
ibp-180	5.46	0.86
180-270	11.11	7.26
270-332	12.80	24.27
332-fpb	69.66	66.64

ibp=initial boiling point; fbp=final boiling point

Table 0-2: Actual distillation

		DO	**CTD**	**CTD/DO 4:1**
		%		
ibp-180	Gasoline	5.8	2.0	1.0
180-270	Jet Fuel	10.7	--	6.0
270-332	Diesel	14.6	--	---
332-fpb	Fuel Oil	68.9	98.0	93.0

2.2. Boiling point cuts

The boiling point cuts are gasoline, jet fuel, diesel and fuel oil.

2.2.1. Gasoline

According to the yields of gasoline (

Table) and CTD/DO ratio, it is expected for the blend a mixture (roughly around 50:50) of the compounds present in DO and CTD.

Table 0-3: Hydrocarbon-type compounds obtained by GC/MS – Gasoline

	Decant oil - DO	Coal-tar distillate (CTD)	CTD/DO 4:1
paraffins	62.00	66.56	57.98
Cycloalkanes	22.91	0.33	6.22
Benzene / alkyl benzenes	15.10	14.96	19.60
Polar compounds	--	5.66	9.65
Phenols	--	12.49	6.54

There are some hydrocarbon-type compounds whose values or percentages are not in the range of the values reported for DO and CTD such as benzene/alkylbenzenes, and polar compounds, suggesting a synergism when the feedstocks are blended.

The synergism is shown in the different functional groups for ^{1}H NMR (Table 2-4). For the ^{13}C NMR the synergism is more evident in all the groups.

Table 0-4: Compounds obtained by ^{1}H NMR – Gasoline

Band TMS (ppm)	DO	Coal-tar distillate - CTD	CTD/DO 4:1
0.5-1.0	8.57	8.54	18.07
1.0-1.7	19.52	19.04	45.08
1.7-1.9	1.80	1.57	1.72
1.9-2.1	1.72	1.44	3.97
2.1-2.4	13.09	16.75	9.57
2.4-3.5	47.11	43.31	6.48
3.5-4.5	2.64	3.07	0.02
4.5-6.0	0.00	0.00	1.49
6.0-7.2	5.55	6.28	13.59

The components that show that synergism have been highlighted.

Table 0-5: ^{13}C NMR - Gasoline

Band TMS (ppm)	DO	Coal-tar distillate - CTD	CTD/DO 80:20
11.0-12.5	0.62	0.61	0.43
12.5-15.0	4.74	4.81	5.08
15.0-18.0	1.66	1.66	1.81
18.0-20.5	5.17	5.26	2.93
20.5-22.5	4.00	4.07	2.70
22.5-24.0	4.88	4.95	5.32
24.0-27.5	4.63	4.69	2.97
27.5-37.0	27.88	28.23	25.34
37.0-60.0	11.78	11.40	5.51
108.0-118.0	0.09	0.15	3.41
118.0-129.5	20.68	21.25	29.92
129.5-133.0	4.05	4.00	4.32
133.0-135.0	3.25	3.18	4.33
135.0-138.0	2.20	2.11	1.32
138.0-160.0	4.37	3.64	4.61

Discussion:

The components present in the GC/MS were revised. There are some components that do not correspond to the gasoline fraction; this suggested an overlapping with the jet fuel fraction. These components were removed of the table and the percentages were normalized.

The interpretation of the GC/MS and NMR is as follows:

By ^{1}H and ^{13}C NMR it is observed that olefins are increase in the gasoline fraction when DO is blended with CTD (1.9-2.1 and 4.5-6 ppm ^{1}H NMR and 108-118 ppm ^{13}C NMR). Olefins increase the octane number and might be upgrading the gasoline fraction; however, olefins content have to meet specification and these are reported in %v/v. NMR reports olefins in elemental percent (%H and %C). Additional test (ASTM) has to be carried out to know the olefins composition in v/v %.

Aromatic content and single aromatic are higher for the blend, according to GC/MS, ^{1}H NMR (6.0-7.2 ppm) and ^{13}C NMR (118.0-129.5). The aromatics increase the octane number; however, the percentage has to be within the specifications range. There are special restrictions for benzene (it has to be below 3% v/v).

Phenols and polar compounds are present in the blend; this is shown in the GC/MS and ^{13}C NMR (138.0-160.0 ppm) and this is contribution from the CTD. These components are undesirable for the gasoline for environmental purposes.

According to the analysis, the distillate resulting from after co-coke CTD and DO might not improve the gasoline. Phenols and polar compounds are present as a contribution from CTD. It is important to highlight that these data is not enough to know the possible improve of the gasoline fraction by blending CTD/DO 4:1. Additional test have to be carried out to get information about composition in v/v for specific components to see if they meet the specifications.

2.2.2. Jet Fuel

The jet fuel in the blend has no contribution from CTD according to

Table. However it is observed in Table 0-6 that the blend has a contribution from CTD in naphthalenes, and polar compounds. For ^{1}H and ^{13}C NMR

Table , shows the percentages of the functional groups for the DO and CTD/DO are very alike which was expected because CTD is not contributing to this fraction.

Table 0-6: Hydrocarbon-type compounds obtained by GC/MS - Jet Fuel

	Decant oil - DO	CTD/DO 80:20
paraffins	39.52	44.99
Cycloalkanes	10.22	2.26
Alkyl benzenes	7.23	6.74
Indenes	10.59	2.02
Naphthalenes	21.10	33.82
Bi-phenyls	6.03	3.79
Hydroaromatics	1.37	1.07
Polar compounds	3.95	5.30

Table 0-7: Hydrocarbon-type compounds obtained by ^{1}H NMR – Jet Fuel

Band TMS (ppm)	DO	CTD/DO 80:20
0.5-1.0	5.99	5.87
1.0-1.7	12.35	12.53
1.7-1.9	1.06	1.11
1.9-2.1	1.15	1.16
2.1-2.4	11.19	9.75
2.4-3.5	28.11	29.56
3.5-4.5	1.79	1.75
4.5-6.0	0.00	0.00
6.0-7.2	4.27	4.47
7.2-8.3	28.25	28.17
8.3-8.9	5.44	5.23
8.9-9.3	0.41	0.40

Table 0-8: Hydrocarbon-type compounds obtained by ^{13}C NMR – Jet Fuel

Band TMS (ppm)	DO	CTD/DO 4:1
11.0-12.5	0.43	0.43
12.5-15.0	4.52	4.50
15.0-18.0	1.43	1.47
18.0-20.5	5.00	4.93
20.5-22.5	3.92	3.90
22.5-24.0	5.00	4.99
24.0-27.5	4.50	4.50

27.5-37.0	29.66	28.65
37.0-60.0	11.53	12.68
108.0-118.0	0.16	0.20
118.0-129.5	21.47	21.39
129.5-133.0	3.99	3.98
133.0-135.0	3.23	3.21
135.0-138.0	1.99	1.98
138.0-160.0	3.17	3.19

Discussion:
Some components reported in the GC/MS that belong to a heavier fraction were removed, meaning that it was some overlapping in fractions when the vacuum distillation was carried out.
The result of the synergism between DO and CTD are the presence of naphthalenes. This is good for the Jet fuel fraction because further hydrotreatment of the jet fuel will give hydroaromatics and/or cycloalkanes, components that improve the thermal stability of the jet fuel. At the same time hydrotreatment might help in the reduction of polar components.

2.2.3. Diesel
According to

Table, diesel is not obtained in CTD and CTD/DO

Table 0-9: GC/MS – Diesel

	Decant oil - DO
paraffins	10.84
Cycloalkanes	3.31
Alkyl benzenes	1.83
Indenes	1.67
Naphthalenes	4.51
Bi-phenyls	4.94
Anthracenes / Phenanthrenes	50.00
Hydroaromatics	7.65
Polar compounds	13.37
Acenaphtylene	1.88

Discussion:
CTD does not contribute to the diesel fraction alone and do not have a synergetic effect on this fraction as it was for the jet fuel fraction; diesel fraction is not present in the blend.

Table 0-10: Hydrocarbon-type compounds obtained by ^{1}H NMR – Diesel

Band TMS (ppm)	**DO**
0.5-1.0	6.22
1.0-1.7	12.49
1.7-1.9	1.11
1.9-2.1	1.24
2.1-2.4	11.52
2.4-3.5	27.57
3.5-4.5	1.57
4.5-6.0	0.00
6.0-7.2	4.61
7.2-8.3	28.15
8.3-8.9	5.21
8.9-9.3	0.30

Table 0-11: Hydrocarbon-type compounds obtained by ^{13}C NMR – Diesel

Band TMS (ppm)	**DO**
11.0-12.5	0.43
12.5-15.0	4.48
15.0-18.0	1.45
18.0-20.5	4.91
20.5-22.5	3.88
22.5-24.0	4.96
24.0-27.5	4.46
27.5-37.0	28.50
37.0-60.0	12.55
108.0-118.0	0.06
118.0-129.5	21.12
129.5-133.0	4.05
133.0-135.0	3.26
135.0-138.0	2.11
138.0-160.0	3.76

2.2.4. Fuel Oil

The percentages of compounds of the blend (CTD/DO) are closer to the CTD since this is the higher contributor to the blend (80%). The ^{1}H and ^{13}C NMR does not show a significant variation among DO, CTD and CTD/DO.

Table 0-12: GC/MS – Fuel oil

	DO	**CTD**	**CTD/DO 4:1**
paraffins	1.92	---	---
Cycloalkanes	0.09	---	0.06
Alkyl benzenes	0.00	1.67	0.00
Indenes	1.40	0.01	---

Naphthalenes, bi-naphthalenes	1.32	3.28	4.76
Bi, tri-phenyls	5.78	3.32	4.39
Anthracenes / Phenanthrenes (3-ring)	15.61	23.54	16.63
Pyrenes (4-fused ring)	39.60	13.67	16.65
Hydroaromatics	13.55	5.10	8.03
Polar compounds	3.67	1.60	1.41
Acenaphtylene	0.08	0.02	0.05
Fluorene	0.08	6.99	0.82
Fluoranthene	13.68	40.77	46.72
5-fused ring	2.38	0.02	0.39
6-fused ring	0.90	---	0.09

Discussion:

The values for CTD/DO are in the range in between the DO alone and CTD such is shown in GC/MS and ^{1}H and ^{13}C NMR. For this fraction synergism is not observed except for Fluoranthene and naphthalenes/bi-naphthalenes.

Table 0-13: ^{1}H NMR – Fuel oil

Band TMS (ppm)	**Decant oil - DO**	**Coal-tar distillate - CTD**	**CTD/DO 80:20**
0.5-1.0	6.06	5.84	5.79
1.0-1.7	12.38	12.51	12.32
1.7-1.9	1.07	1.10	1.05
1.9-2.1	1.18	1.14	0.98
2.1-2.4	11.28	9.71	11.61
2.4-3.5	27.94	29.64	27.94
3.5-4.5	1.74	1.76	1.78
4.5-6.0	0.00	0.00	0.00
6.0-7.2	4.36	4.45	4.25
7.2-8.3	28.21	28.19	28.45
8.3-8.9	5.39	5.24	5.37
8.9-9.3	0.39	0.41	0.46

Table 0-14: ^{13}C NMR – Fuel oil

Band TMS (ppm)	**Decant oil - DO**	**Coal-tar distillate - CTD**	**CTD/DO 80:20**
11.0-12.5	0.51	0.45	0.47
12.5-15.0	4.63	4.53	4.58
15.0-18.0	1.55	1.48	1.47
18.0-20.5	5.08	4.96	4.48
20.5-22.5	3.96	3.91	4.54
22.5-24.0	4.96	4.97	4.97
24.0-27.5	4.56	4.49	4.54
27.5-37.0	28.36	28.51	28.58
37.0-60.0	12.02	12.40	12.25
108.0-118.0	0.10	0.08	0.18
118.0-129.5	21.16	21.20	21.33
129.5-133.0	4.03	4.03	4.01
133.0-135.0	3.25	3.25	3.23
135.0-138.0	2.09	2.08	2.02
138.0-160.0	3.74	3.65	3.34

Conclusions

- The characterization of the Decant oil and Coal-Tar pitch was carried out by using different techniques such as ^{1}H and ^{13}C NMR, GC/MS, SimDis.
- Oil coming from the CTD coking does not have cuts for jet fuel and diesel. Therefore, the final product (jet fuel and diesel) is very low in yield and the oil composition is more likely to the oil from DO.
- The presence of polyaromatics is observed in the jet fuel fraction. CTD has contributed to the blend even though this is not observed in the yields when CTD liquids from the coker are fractionated under vacuum; CTD alone does not have distillates falling in the jet fuel range. This suggests that there is a synergism effect when blending CTD and DO.
- ^{1}H and ^{13}C NMR show differences in the gasoline cut. Differences are not observed for the jet fuel, diesel and fuel oil. In jet fuel and diesel the differences are not observed because CTD alone does not have distillates falling in the jet fuel range.
- The possible improvement of the gasoline fraction by blending DO and CTD is not clear. There are present of compounds that increase the octane number but there is also presence of polar compound coming from the CTD. Some components for gasoline are strictly controlled for environmental purposes and those are not determined by GC/MS alone or NMR Additional techniques reported by the ASTM have to be carried out to get the information in volume percent.
- The jet fuel fraction might be improved by blending DO and CTD. The presence of naphthenic compounds, obtained after the hydrotreatment of the jet fuel fraction giving hydroaromatics and cycloalkanes, which improve the thermal stability of the jet fuel.

4. References

(1) ASTM/2887-84 In *Manual on Hydrocarbon Analysis*; A.W.Drews, Ed.; ASTM: Philadelphia, 1988; 551-555.

(2) King, B. 1H and 13C Interpretation tutorial; http://www.wfu.edu/ylwong/chem/nmrc13/c13chemicalshift.html, 2003.

(3) Rodriguez, J.; W, T. J.; Irving, W. Evaluation of a delayed coking process by 1H and 13C n.m.r. spectroscopy: 2. Detailed interpretation of liquid n.m.r. spectra. *Fuel* **1994**, *73*, 1870-1875.

(4) http://www.process-nmrcom/liquidanalysis(2).html Analytical liquid-state NMR applications; Process NMR Associates, LLC, 2003.

(5) ASTM/D3279-83 In *Manual on Hydrocarbon Analysis*; A.W.Drews, Ed.; ASTM: Philadelphia, 1988; 650-652.

Feasibility Study of Commercial Coal Gasifier Gases to Form Carbon Nanofibers

Final Report
March 1, 2005 - June 30, 2006

Thomas W. Hughes, Principal Investigator

Issue Date: September 2006

DOE Contract No. DE-FC26-03NT41874
Subaward No. 2868-ASI-DOE-1874

Applied Sciences, Inc.
141 W. Xenia Ave.
Cedarville, OH 45314

DISCLAIMER:

"This report was prepared as an account of work sponsored by an agency of the United States Government. Neither the United States Government nor any agency thereof, nor any of their employees, makes any warranty, express or implied, or assumes any legal liability or responsibility for the accuracy, completeness, or usefulness of any information, apparatus, product, or process disclosed, or represents that it use would not infringe privately owned rights. Reference herein to any specific commercial product, process, or service by trade name, trademark, manufacturer, or otherwise does not necessarily constitute or imply its endorsement, recommendation, or favoring by the United States Government or any agency thereof. The views and opinions of authors expressed herein do not necessarily state or reflect those of the United States government or any agency thereof."

Abstract

Carbon nanofiber growth trials were conducted using simulated gas mixtures based on products from commercial coal gasifiers as a feedstock for generating value-added carbon products from coal. This investigation evaluated several industrial scale coal gasification methods, including Winkler, Koppers-Totzek, Lurgi, and Wabash River. Production of value-added carbon nanofibers (CNF) from gasified coal, while maintaining generation of energy rich products such as electricity and hydrogen, is an attractive alternative sequestration technology of carbon and sulfur. The investigation demonstrated that CNF production from coal gasification is feasible, and also demonstrated the potential for considerable improvement in the efficacy and economy of the process. Efforts were made to boost CNF yield to above what was achieved from direct simulated coal gases through increasing the methane concentration in the gas feedstock stream. During the investigation into CNF production from coal gasification, it was found that methanation, a means of increasing the methane concentration, improved yields of CNF by a factor of two. However, as has been known for years, methanation catalysts are highly susceptible to sulfur poisoning, thus creating a challenge for high-yield CNF production from coal gasification. Sulfur thus plays a dual role as both an inhibitor and enabler in CNF production. Further work is needed to address the adverse consequence of sulfur in the presence of the methanation catalyst, so that sulfur in coal gas can be limited to simply that of an enabler of CNF production.

Table of Contents

Introduction

Coal gasification offers one of the most versatile and cleanest ways to convert the energy content of coal into electricity, hydrogen, and other energy forms. Rather than burning coal directly, gasification breaks down coal - or virtually any carbon-based feedstock - into its basic chemical constituents. Coal gasification is believed to be one of the best ways to produce clean-burning hydrogen for future automobiles and power-generating fuel cells. Hydrogen and other coal gases can also be used to fuel power-generating turbines or as the chemical "building blocks" for a wide range of commercial products. The Department of Energy's Office of Fossil Energy is working on coal gasifier advances that enhance efficiency, environmental performance, and reliability as well as expand the gasifiers' flexibility to process a variety of feedstocks, such as high-sulfur coal. Despite its merits, coal gasification produces sulfur and carbon byproducts which are regarded to be an environmental liability. The current study was undertaken to determine the feasibility of transforming these coal gasification byproducts into a commercially-viable, high value-added material – carbon nanofibers.

Carbon nanofibers, or CNF, are of the class of emerging nanoscale reinforcements which have captured the attention of the scientific community and the popular media. These nanoscale carbon reinforcements have properties which approach those of single crystal graphite, and are proposed for both substitutional and enabling applications. Molecular electronics is a field where nanofibers and nanotubes may play enabling roles as one dimensional quantum conductors, semiconductors and other devices. Such enabling applications are typically not cost sensitive. A large number of substitutional applications would be possible if nanofibers could be manufactured and priced at levels comparable to fillers such as milled carbon fiber, glass fiber, graphite flakes, or carbon black. Opportunity to insert CNF into the marketplace is fueled in part by the development of nanotechnology as a focal area, having generated considerable scientific, economic and political interest and investment, both in the U.S. and worldwide. The U.S. has dedicated close to a billion dollars in 2006 to the National Nanotechnology Initiative. The European Nanobusiness Association reports that spending for nanotechnology in the European Union is approximately equivalent to that in the U.S.

Currently CNF is marketed at a price of approximately $150 per lb. If in the future the price could be reduced below $10 per lb., CNF could invade the markets for graphite flake, milled carbon fiber, and even carbon black. Also, new markets for light-weight, fuel efficient automobiles would be enabled. In independent market studies, it has been projected that if the price of carbon nanofibers approaches the $3 to $5 range, then a market of over 100 million lbs per year could be realized for automotive polymers and other consumer applications. The role of gasified coal would be to capture economies of production necessary for low-cost production of carbon nanofibers.

A highly efficient and economical manufacturing technology has been developed which relies on a patented catalyst system, where an iron sulfide particle is used to nucleate the

growth of the nanofiber.[1] In this method, hydrogen sulfide generates the sulfur needed to form the iron sulfide catalyst. This formulation has suggested coal as the source of both carbon and sulfur for the CNF synthesis reaction, and since the hydrogen-rich off-gas is not used further, also suggests the advantages that can be gained in co-production of CNF and hydrogen from high-sulfur coal such as is abundant in the Midwest region of the US. This concept may be characterized as "coal refining" where, instead of burning the coal, the coal is processed to generate a suite of value-added products. Study along these lines originated from a small grant from the Ohio Coal Development Office about 12 years ago[2], and was subsequently expanded under a Department of Energy program.[3] Feasibility of this technology was first demonstrated in the laboratory in 1995 by Applied Sciences researchers.[4] Following that proof of feasibility, the OCDO contributed additional funding for a Pilot plant. In the pilot study, a coal gasifier contributed by the Battelle Memorial Laboratory in Columbus was used to generate syngas, and the investigation considered full utilization of high sulfur coal, including production of low carbon fly ash, which would be a value added product for cement reinforcement. The gasifier is designed to carry most of the carbon in the coal into the process gas. This gasifier was a smaller, higher-temperature counterpart to a larger gasifier at the same facility used primarily for biomass gasification. The integrated product line from coal would provide cost advantages enabling head on competition with carbon black and glass fiber.

Coal gasification has not been widely implemented for power production due to the disparity in cost in comparison to burning coal or natural gas for electrical energy production. The use of high sulfur coal also leads to a sulfur management problem. The alternative model would enable coal to be converted into carbon nanofiber, thus sequestering carbon and sulfur in the CNF, and generation of hydrogen and possibly low-carbon content fly-ash as value added products. The relatively high economic value of CNF, even if priced at $3 to $5 per lb., could provide powerful leverage on the economics of coal gasification.

The diagram in Figure 1 illustrates the process envisioned. High sulfur coal, oxygen, and steam would be fed to the gasifier, leading to a low-carbon fly ash and coal gas. The low-carbon fly ash would be sold as a reinforcement. Coal gas would then be used as the hydrocarbon and sulfur feedstock needed for carbon nanofiber synthesis. The effluent from the combined goal gasification / carbon nanofiber production process is rich in hydrogen, while poor in carbon, nitrogen and especially sulfur. Hydrogen would be separated from this gas stream and used for power production.

[1] U.S. Patent # 5,374,515, "Method for Making Carbon Fibers," Robert L. Alig, Gary G. Tibbetts and Daniel W. Gorkiewicz

[2] Ohio Coal Development Office, "Pilot-Scale Plant for Pyrgraf-III," Contract CDO/D-96-3

[3] Department of Energy, "Use of Coal Fines for Production of Clean Fuel and Vapor Grown Carbon Fiber," Contract DE-FG02-95ER81926

[4] U.S. Patent # 5,846,509, "Method for Producing Vapor Grown Carbon Fibers Using Coal," Robert Alig and David Burton, Applied Sciences, Inc.

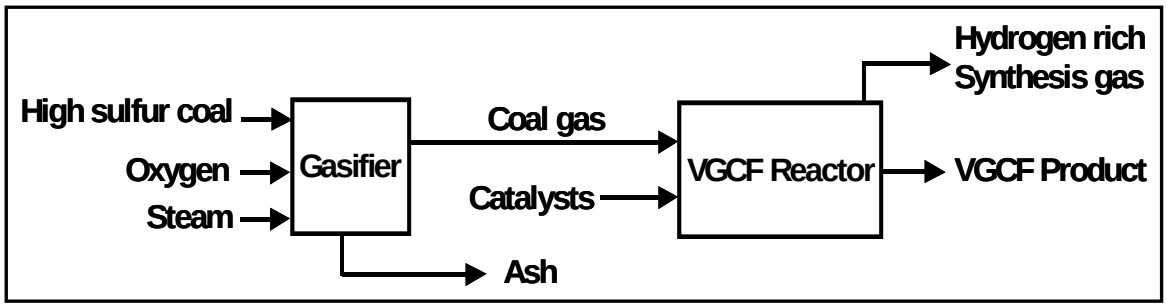

Figure 1. Process Flow Diagram depicting the means of producing vapor grown carbon nanofibers (VGCNF) from gasified coal. Along with producing the high value-added nanomaterials, the process also produces hydrogen-rich gas – the clean fuel source that is the primary goal of a coal gasifier facility.

The combination of these two high growth potential processes results in several economic and environmental benefits, and leaves few of the disadvantages which exist when considering each process independently.

The current study was focused on determining the efficiency of CNF synthesis from the various current coal gasification systems, and does not extend to consideration of fly-ash quality or hydrogen separation. The study was designed to build on this effort and demonstrate the feasibility of using gases typically produced in coal gasifiers to produce carbon nanofibers. This goal is significant because it demonstrates a process for using coal gasification byproducts in an environmentally-friendly manner, but it also transforms these byproducts into a commercially-viable, value-added material (carbon nanofibers), for which there is an established client base and strong commercial potential.

Methanation of coal gas has the potential of making any coal gas suitable for the production of carbon nanofibers or carbon nanotubes or any other carbon product such as carbon black. It appears that this would enable any coal gas, regardless of composition or pressure to be used for co-production of chemicals, electrical power, and hydrogen. Methanation would exploit the following chemical reactions.

$$CO + 3\ H_2 \leftrightarrow CH_4 + H_2O \qquad \Delta H = -\ 252\ kJ/mole\ CH_4\ formed$$

$$CO_2 + 4\ H_2 \leftrightarrow CH_4 + 2\ H_2O \quad \Delta H = -\ 257\ kJ/mole\ CH_4\ formed$$

The reaction examined was the methanation of carbon monoxide, however, both reactions are exothermic, that is, they give off heat as they progress. Both reactions are favored thermodynamically at low temperatures. The approach to be evaluated was to add hydrogen to the coal gases, allow them to react to form methane and water vapor, condense the water vapor, separate the methane gas from the liquid water, and use the methane to produce carbon nanofibers. Hydrogen would be produced as a byproduct in carbon nanofiber production and recycled to drive the methanation reaction. This proved to be high in potential, but requires an additional step prior to full feasibility is achieved.

That is, methanation must be performed in the absence of any form of sulfur. Therefore, a method for temporary removal of sulfur must be incorporated prior to methanation, followed by a reintroduction of sulfur prior to the production of carbon nanofibers.

Executive Summary

Coal gasification offers one of the most versatile and cleanest ways to convert the energy content of coal into electricity, hydrogen, and other energy forms. Rather than burning coal directly, gasification breaks down coal - or virtually any carbon-based feedstock - into its basic chemical constituents. Despite its merits, coal gasification produces sulfur and carbon byproducts which are regarded to be an environmental liability. The current study was undertaken to determine the feasibility of transforming these coal gasification byproducts into a commercially-viable, high value-added material – carbon nanofibers. Carbon nanofibers, or CNF, are of the class of emerging nanoscale reinforcements which have captured the attention of the scientific community and the popular media. These nanoscale carbon reinforcements have properties which approach those of single crystal graphite, and are proposed for both substitutional and enabling applications.

Carbon nanofiber growth trials were conducted using simulated gas mixtures based on products from commercial coal gasifiers as a feedstock for generating value-added carbon products from coal. This investigation evaluated several industrial scale coal gasification methods, including Winkler, Koppers-Totzek, Lurgi, and Wabash River. Production of value-added carbon nanofibers (CNF) from gasified coal, while maintaining generation of energy rich products such as electricity and hydrogen, is an attractive alternative sequestration technology of carbon and sulfur. The investigation demonstrated that CNF production from coal gasification is feasible, and also demonstrated the potential for considerable improvement in the efficacy and economy of the process. Efforts were made to boost CNF yield to above what was achieved from direct simulated coal gases through increasing the methane concentration in the gas feedstock stream. During the investigation into CNF production from coal gasification, it was found that methanation, a means of increasing the methane concentration, improved yields of CNF by a factor of two. However, as has been known for years, methanation catalysts are highly susceptible to sulfur poisoning, thus creating a challenge for high-yield CNF production from coal gasification. Sulfur thus plays a dual role as both an inhibitor and enabler in CNF production. Further work is needed to address the adverse consequence of sulfur in the presence of the methanation catalyst, so that sulfur in coal gas can be limited to simply that of an enabler of CNF production.

Very encouraging results were obtained during this investigation that will guide efforts for future work. Quite small CNF yields of sooty fibers were obtained with the initial gasifier mixtures used. However, fiber quality and yields were considerably increased by modifying the feedstock to decrease the fraction of CO_2. Fibers produced using this modified feedstock were in several ways superior to those produced with our standard production gas mixture, in that they exhibit a smaller and more uniform diameter, a smaller amount of adsorbed polynuclear aromatics, and were mixed with less soot. Experimentation with varying CO/CH4 mixtures was done, to incorporate and optimize

the observed benefits into our standard production techniques. It was found that increasing the carbon monoxide concentration results in a lower CNF yield. This led to an effort to convert the carbon monoxide present in the coal gases to methane in order to change the carbon nanofiber feed gases to more closely match the ratio of methane to other constituents in natural gas. Trials were attempted using methanation chemistry at atmospheric pressure. Tests showed some conversion of carbon monoxide to methane without a catalyst being present.

The observed sulfur poisoning effect on methanation catalysts currently limits the incorporation of a methanation step and thus limits the potential of CNF from coal gas. Therefore, an opportunity for future work has been realized in this investigation. That is, utilizing a means for temporary removal of sulfur from the gas stream in order to convert carbon monoxide to methane, then reintroducing sulfur for use in the CNF growth process in an economical manner. The most significant challenge to overcome in future work is to prevent the poisoning effect that sulfur has on the methanation reaction while still utilizing the benefits sulfur provides for CNF nucleation. One approach under consideration is to include temporary sequestration of sulfur through the conversion of H2S to FeS, which would then drop from the gas stream. This would be followed by re-introduction of FeS into the process gas after the methanation step. If this approach can be reduced to practice, the use of coal gas for co-production of carbon nanofiber, clean hydrogen, and other value-added products will have high prospects for economic exploitation of coal gas.

Generally, carbon nanofiber production from gasified coal is regarded to have great economic and environmental potential. Producing CNF from coal gases removes the costly need to sequester carbon and sulfur and replaces those costs with high vale-added products, namely, carbon nanofibers, low-carbon fly-ash for cement reinforcement, and hydrogen. Due to the energy-inhibiting effects of carbon monoxide that results in comparably lower CNF yields, methanation is an attractive method of increasing the methane concentration in the gas stream, and thereby improving CNF yields.

Experimental

Simulated coal gases were acquired from Delille Industrial and Specialty Gases, along with calibration gases to be used for micro-gas chromatographic analysis of the feed gases and process gases.

Carbon nanofiber production was done in tube furnaces using a floating catalyst method and is conducted at ~1100^{o}C. Nanofiber production trials were performed using simulated coal gases, varying the compositions corresponding to the stage of unit operations present in commercial coal gasification plants.

Metrics for evaluation used in this study were scanning electron microscopy (SEM), the bulk density of the CNF produced, the electrical conductivity of a CNF pellet, the iron content in the CNF product, and the total yield of CNF from the production reaction. The CNF was analyzed using SEM for physical dimensions and structure. The bulk density of the CNF product was used as a first order metric to determine the quality of CNF production, since the bulk density is influenced by the ratio of CNF to other carbon products, such as soot. A second metric used was the electrical conductivity of a pellet of CNF, since the electrical conductivity is related to the degree of graphitic perfection of the sample. The third metric used was the residual iron content in the CNF product. The yield of CNF is defined as the ratio of carbon which is converted into CNF to the total carbon admitted into the reaction, and is an assessment of the production efficiency.

A Varian CP 2003 Micro-GC was used to measure the gas concentrations in the effluent of the carbon nanofiber growth reactor. The Micro-GC is fitted with two separation columns. The first is the column module 10 meter Molsieve 5A backflush heated injector CP739995, which can separate CH_4, H_2, CO, N_2, O_2, etc. The second column module is the Pora Plot U 10 meter heated injector CP739691 which can separate CH_4, H_2S, C_2H_6, CO_2, etc. Ultra high purity Argon purchased from Delille Oxygen Co. is used as the carrier gas which is set to 80 psi and the Varian Inc. Chrompack Gas-Clean filter CP17973 is used for filtering O_2 and H_2O. Once separated, the individual gas species are detected with a thermal conductivity detector. The sample line used to inject the gases into the inlet of the Micro-GC is a 1/16" outer diameter stainless steel tubing with 0.010 wall thickness. Within this line is a Varian Inc. external sample filter kit CP736729 used to filter out fine particulate from the sample gas. CH_4, H_2, CO, and CO_2 at 100% concentration levels were measured.

The first trials conducted simulated coal gases downstream of the acid gas removal systems but upstream of the water gas shift reactors in commercial scale coal gasifiers. The next set of trials conducted simulated coal gases upstream of the acid gas removal systems. Acid gas removal can be used to remove both hydrogen sulfide and carbon dioxide. Removal of hydrogen sulfide is normally achieved via standard Claus reactors whereby a portion (one third) of the gas stream containing hydrogen sulfide is oxidized to create sulfur dioxide. Sulfur dioxide then reacts with the remaining two thirds of the

hydrogen sulfide to produce sulfur vapor which is condensed from the gas stream. Oxidation of a portion of the gas stream to produce sulfur dioxide also produces carbon dioxide. It has been hypothesized that the creation of carbon dioxide has two adverse effects: 1) carbon dioxide is formed as a co-product in the carbon monoxide disproportionation reaction as shown below which could reverse the chemical equilibrium of the reaction and 2) carbon dioxide, being a green house gas, absorbs much of the input energy required to pyrolyze methane to carbon nanofibers.

Carbon monoxide disproportionation:

$$2\ CO(g) \rightarrow C(s) + CO_2(g) \qquad \Delta H = -172.5\ kJ/g\text{-mole C formed}$$

Methane pyrolysis:

$$CH_4(g) \rightarrow C(s) + 2\ H_2(g) \qquad \Delta H = +74.89\ kJ/g\text{-mole C formed}$$

In order to overcome the effects of carbon monoxide on the CNF production process a methanation process was investigated. Methanation of carbon monoxide was attempted at atmospheric pressure in the presence of a nickel methanation catalyst. The methanation catalyst used was provided by Sud-Chemie, Inc, which was C11-PR-3 nickel methanation catalyst in 4.7 x 4.7 mm tablets. The methanation catalyst was loaded into the reaction chamber, shown below in Figure 2. Catalyst screens used were 316L stainless steel wool (part #7155512) from Palmer Manufacturing. The catalyst was activated under a mixture of hydrogen and nitrogen at 450 ^{o}C at a space velocity of 500 hr^{-1} prior to methanation. Methanation was conducted by flowing hydrogen and carbon monoxide at a ratio of 3:1 into the reaction vessel with initial operating temperatures ranging from 100-200 ^{o}C. Trial operating temperatures were recorded by computer. Trials were run for 30 minutes, allowing reaction to occur for sufficient time for an appreciable amount of water to form. Following each trial, nitrogen was flowed through the reaction system in order to purge the system of reactants, as well as to push any water formed into the cold trap for collection. Any water formed from the reaction was collected and measured.

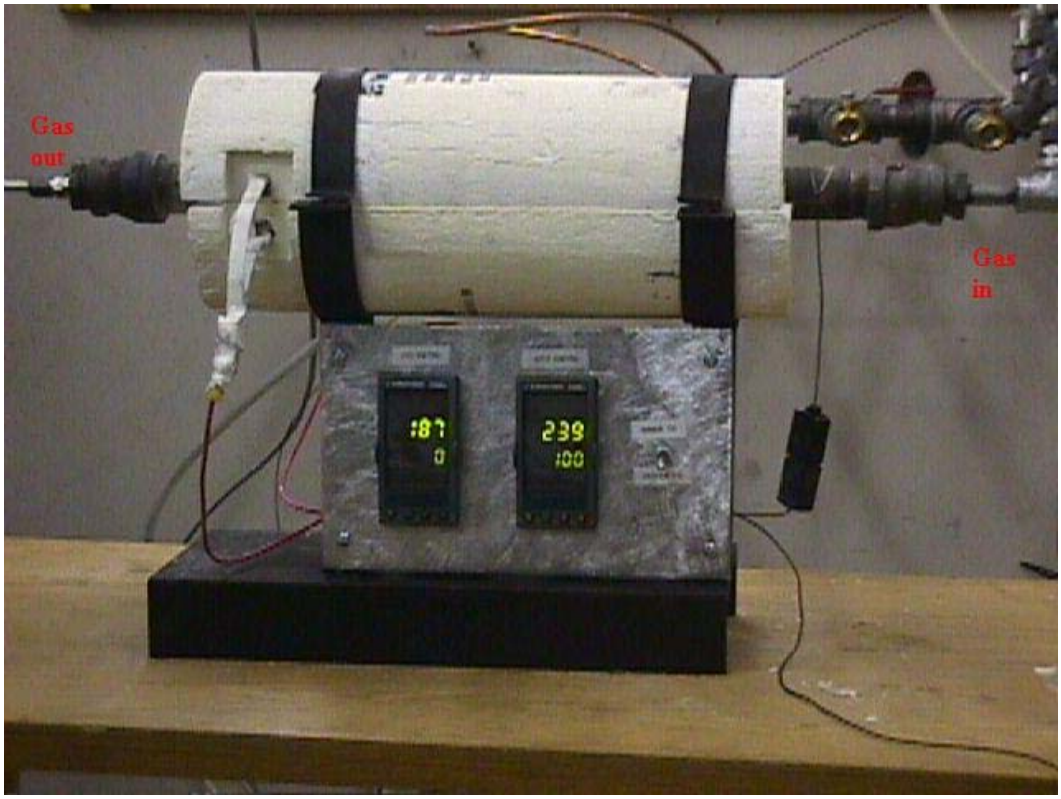

Figure 2. Self contained catalyst reduction and methanation chamber

After additional sets of methanation trials were completed using lower reactant flow rates and cooling air, additional trials were conducted using small amounts of 5% H_2S in H_2 mixed with hydrogen and carbon monoxide, to determine the influence very low levels of sulfur in the reduced form play on the methanation reaction studied.

Results & Discussion

Table 1 below summarizes all of the CNF production trials from simulated coal gases. It can be seen that producing CNF from coal gases eliminates the need for sulfur sequestration. Also, it can be noted that CNF production directly from simulated coal gases reduces carbon sequestration.

Description	GAS COMPOSITION TESTED, VOL. %					Carbon sequestered, %	Sulfur sequestered, %
	CO	CO_2	H_2	CH_4	H_2O		
PR-19 Control	9.0%	1.0%	0.0%	81.9%	8.1%	21.5%	100.0%
PR-19 & H2, 1X Tan, same BTU	9.0%	0.0%	5.0%	86.0%	0.0%	32.4%	100.0%
PR-19 Base	9.0%	1.0%	0.0%	90.0%	0.0%	38.0%	100.0%
PR-24 Base	9.0%	1.0%	0.0%	90.0%	0.0%	39.7%	100.0%
PR-24 Basewith 1x H2 Tangential	9.0%	0.0%	5.0%	86.0%	0.0%	28.2%	100.0%
PR-19 Basewith 1X H2 Tangential	9.0%	0.0%	9.5%	81.5%	0.0%	32.4%	100.0%
PR-19 Basewith 2X H2 Tangential	9.0%	0.0%	13.6%	77.4%	0.0%	26.8%	100.0%
PR-19 Basewith 3X H2 Tangential	9.0%	0.0%	5.0%	86.0%	0.0%	22.1%	100.0%
Battelle Syn Gas	17.0%	18.8%	13.8%	50.5%	0.0%	37.3%	100.0%
Lurgi - upstream of acid gas removal	59.6%	2.3%	29.7%	0.0%	0.0%	4.2%	100.0%
Winkler - upstream of acid gas removal	25.0%	18.0%	49.5%	3.0%	0.0%	1.4%	100.0%
Koppers - upstream of acid gas removal	58.7%	7.1%	32.8%	0.0%	0.0%	2.9%	100.0%
Wabash - upstream of acid gas removal	45.0%	14.0%	26.0%	2.0%	0.0%	3.6%	100.0%
Lurgi - downstream of acid gas removal	0.2%	37.4%	58.3%	0.0%	0.0%	0.0%	100.0%
Winkler - downstream of acid gas removal	25.0%			3.0%	0.0%	10.7%	100.0%
Koppers - downstream of acid gas removal	58.7%			0.0%	0.0%	0.0%	100.0%
Wabash - downstream of acid gas removal	50.0%	8.0%	21.0%	5.0%	0.0%	4.3%	100.0%
1	0.0%	5.0%	0.0%	95.0%	0.0%	23.9%	100.0%
2	0.0%	5.0%	0.0%	95.0%	0.0%	22.3%	100.0%
3	0.0%	0.0%	5.0%	95.0%	0.0%	30.2%	100.0%
4	50.0%	0.0%	0.0%	50.0%	0.0%	36.1%	100.0%
5	25.0%	0.0%	0.0%	75.0%	0.0%	36.2%	100.0%
6	25.0%	0.0%	0.0%	75.0%	0.0%	29.7%	100.0%
7	25.0%	0.0%	0.0%	75.0%	0.0%	34.2%	100.0%
8	50.0%	0.0%	0.0%	50.0%	0.0%	32.2%	100.0%
9	100.0%	0.0%	0.0%	0.0%	0.0%	33.3%	100.0%
10	100.0%	0.0%	0.0%	0.0%	0.0%	34.0%	100.0%
11	100.0%	0.0%	0.0%	0.0%	0.0%	27.7%	100.0%
12	50.0%	0.0%	50.0%	0.0%	0.0%	42.2%	100.0%
13	25.0%	0.0%	75.0%	0.0%	0.0%	37.0%	100.0%
14	25.0%	0.0%	75.0%	0.0%	0.0%	35.0%	100.0%
15	0.0%	0.0%	25.0%	75.0%	0.0%	33.2%	100.0%
16	0.0%	0.0%	20.0%	80.0%	0.0%	32.0%	100.0%
17	25.0%	0.0%	0.0%	75.0%	0.0%	40.4%	100.0%
18	25.0%	0.0%	0.0%	75.0%	0.0%	42.3%	100.0%
19	25.0%	0.0%	0.0%	75.0%	0.0%	37.0%	100.0%
20	33.0%	0.0%	0.0%	67.0%	0.0%	36.7%	100.0%
21	50.0%	0.0%	50.0%	0.0%	0.0%	30.0%	100.0%
22	0.0%	0.0%	50.0%	50.0%	0.0%	36.7%	100.0%

Table 1. Summary of carbon nanofiber production trials with coal gases

Initial results of using coal gas downstream of the acid gas removal systems showed low yields of carbon nanofibers (CNF).

Component	Lurgi	Koppers-Totzek	Winkler	Wabash River
Nitrogen	4.1%	1.4%	3.0%	11.7%
Argon	0.9%			0.0%
Hydrogen	29.7%	32.8%	49.5%	26.0%
Carbon monoxide	62.2%	58.7%	25.0%	45.0%
Carbon dioxide	2.3%	7.1%	18.0%	14.0%
Water	0.0%			0.0%
Methane	0.0%		3.0%	2.0%
H_2S & COS	0.8%		1.5%	1.3%
Total	100.0%	100.0%	100.0%	100.0%
Carbon nanofiber yield, %	13.0%	4.3%	9.0%	11.2%

Table 2. Results of producing carbon nanofibers using coal gas upstream of the acid gas removal equipment at commercial gasifiers

Improved yields in carbon nanofiber production were observed by using coal gas upstream of the acid gas removal section in the coal gasification plant. However, the yields were still low, compared to results from the direct pyrolysis of high sulfur coal, where substantially higher yields of carbon nanofibers were obtained, as shown in Table 3.

Component	Volume percent
Hydrogen	30.5%
Carbon Monoxide	22.8%
Carbon Dioxide	8.0%
Methane	23.4%
Ethane	2.7%
Ethylene	6.6%
Acetylene	5.0%
Hydrogen Sulfide	1.0%
Total non-nitrogen gas	100.0%
Carbon nanofiber yield, %	33%

Table 3. Feedstocks used and yields obtained with coal gas derived from indirect pyrolysis of high sulfur coal

To test the theory that carbon dioxide adversely affects carbon nanofiber yields, a series of tests were conducted where CO2 was eliminated from the gas stream, and the concentrations of CH_4 and CO were varied to determine the effect on CNF yield. Figure 3 shows the results of the trials. The data show how the relative proportions of methane to the total of methane and carbon monoxide effects yields. For comparison purposes, we overlaid the results of the commercial coal gas trials (before and after acid gas removal sections) as well as the data from carbon nanofiber production from coal gases derived from indirect pyrolysis of high sulfur coal.

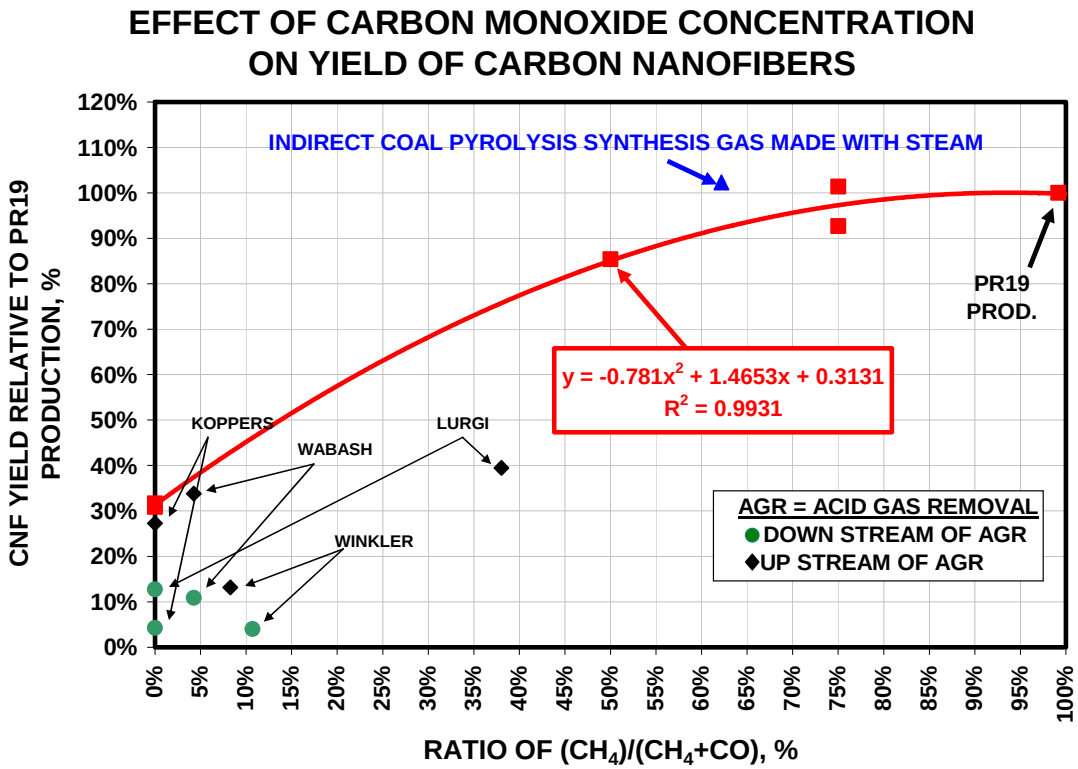

Figure 3. Results of methane and carbon monoxide trials conducted to see if carbon dioxide could be causing adverse yield results

Based on the data shown in Figure 3, it appears that reducing the concentration of carbon dioxide in the coal gas stream does indeed increase the yields of carbon nanofibers relative to the yields observed in commercial production. Also, it appears that the ratio of methane to carbon monoxide plays a role.

The data represented by the red regression fit line and red markers represent mixtures of methane and carbon monoxide without any carbon dioxide. The blue data point represents the actual datum obtained with the coal gas derived from the indirect pyrolysis of high sulfur coal in the 1990's by Applied Sciences. These regressed data probably represent the maximum yields of carbon nanofibers to be obtained from coal gases containing carbon monoxide and methane. Additional experimentation is needed to truly certify this assertion.

H_2 Flow (ccm)	CO Flow (ccm)	H_2S Flow (ccm) [8% H_2S in H_2]	Total H_2S % Concentration	H_2O Formed (cc)	Avg. Operating Temperature (^oC)	Conversion %
369	123	0	0	0.5	102	23
369	123	0	0	0	117	0
701	234	0	0	3	181	89
701	234	0	0	3	170	87
701	234	0	0	3	150	83
701	234	0	0	3.5	153	97
653	234	52	0.45	3	163	85
701	234	0	0	2.5	156	70
653	234	52	0.45	1	155	28
701	234	0	0	0	168	0

Table 4. Representative results of methanation trials conducted using a nickel based catalyst.

From the table above it can be observed that methanation is a viable means of converting carbon monoxide to methane and thereby allowing for improved CNF yields to be achieved. However, as expected, introduction of sulfur, even at very low concentrations has a detrimental effect on the conversion of carbon monoxide due to catalyst poisoning. Therefore, it is clear that a solution must be realized which would provide temporary removal of sulfur from the gas stream, methanation, followed by reintroduction of sulfur into the gas stream for use in the carbon nanofiber growth reactors.

Conclusions

Very encouraging results were obtained during this investigation that will guide efforts for future work. Quite small CNF yields of sooty fibers were obtained with the initial gasifier mixtures used. However, fiber quality and yields were considerably increased by modifying the feedstock to decrease the fraction of CO_2. Fibers produced using this modified feedstock were in several ways superior to those produced with our standard production gas mixture, in that they exhibit a smaller and more uniform diameter, a smaller amount of adsorbed polynuclear aromatics, and were mixed with less soot. Experimentation with varying CO/CH4 mixtures was done, to incorporate and optimize the observed benefits into our standard production techniques. It was found that increasing the carbon monoxide concentration results in a lower CNF yield. This led to an effort to convert the carbon monoxide present in the coal gases to methane in order to change the carbon nanofiber feed gases to more closely match the ratio of methane to other constituents in natural gas. Trials were attempted using methanation chemistry at atmospheric pressure. Tests showed some conversion of carbon monoxide to methane without a catalyst being present.

The observed sulfur poisoning effect on methanation catalysts currently limits the incorporation of a methanation step and thus limits the potential of CNF from coal gas. Therefore, an opportunity for future work has been realized in this investigation. That is, utilizing a means for temporary removal of sulfur from the gas stream in order to convert carbon monoxide to methane, then reintroducing sulfur for use in the CNF growth process. The most significant challenge to overcome in future work is to prevent the poisoning effect that sulfur has on the methanation reaction while still utilizing the benefits sulfur provides for CNF nucleation. One approach under consideration is to include temporary sequestration of sulfur through the conversion of H2S to FeS, which would then drop from the gas stream. This would be followed by re-introduction of FeS into the process gas after the methanation step. If this approach can be reduced to practice, the use of coal gas for co-production of carbon nanofiber, clean hydrogen, and other value-added products will have high prospects for economic exploitation of coal gas.

Generally, carbon nanofiber production from gasified coal is regarded to have great economic and environmental potential. Producing CNF from coal gases removes the costly need to sequester carbon and sulfur and replaces those costs with high vale-added products, namely, carbon nanofibers, low-carbon fly-ash for cement reinforcement, and hydrogen. Due to the energy-inhibiting effects of carbon monoxide that results in comparably lower CNF yields, methanation is an attractive method of increasing the methane concentration in the gas stream, and thereby improving CNF yields.

CONSORTIUM FOR PREMIUM CARBON PRODUCTS FROM COAL

Continued Development of Pitch/Nanotube Foam and Fiber Composites

Subcontract No. 2869-UK-DOE-1874

Final Report

1st March 2005 – 30th June 2006

University of Kentucky

Center for Applied Energy Research

&

West Virginia University

November 2006

Disclaimer

Abstract

The principal objectives of the program were to develop new carbon materials to satisfy the increasingly exacting requirements needed for thermal management of electronic and electric power devices. Such high performance carbon materials offer attractive potential alternative solutions to other more severe duty applications, including blast mitigation and nuclear/chemical warfare protection. The inclusion of carbon nanotubes in a range of pitches was studied and the conversion of the derived composite materials to foams and/or fibers was expected to open up opportunities for developing other high performance carbon materials. The key to achieving these aims and to more fully exploit the extraordinary physical properties of the carbon nanotubes was to generate MWNT/carbon composites from a range of different pitches containing well dispersed carbon nanotubes. It was planned to promote the interaction between the nanotubes and the continuous matrix by surface activation of the nanotubes and in particular for the synthesis of carbon fibers to ensure that nanotube dispersion was complete by separating the nanotubes down to individual tube level.

These studies were conducted under DOE Subcontract No. 2869-UK-DOE-1874. This contract is with the University of Kentucky Research Foundation, which supports work with the University of Kentucky Center for Applied Energy Research and West Virginia University.

Table of Contents

Figures

Summary

A series of nanotube/pitch composite materials were prepared using three samples of isotropic pitch, a low QI pitch, a coal tar pitch and a Koppers low volatile pitch with softening points ranging from 120 to 170^{o}C. Synthesis of the nanotubes was carried out at CAER using the continuous reactor developed on-site. Multiwall carbon nanotubes (MWNTs) were dispersed into the pitches at concentrations of 0.5, 1.0 and 2.5wt% using conventional melt processing techniques. A reference sample without the addition of nanotubes was also prepared from each pitch using the same mixing conditions. An additional composite was prepared using surface treated nanotubes at a concentration of 2.5wt% in one of the pitches. Surface activation of the nanotube sample was carried out by refluxing in concentrated nitric acid. The MWNT/pitch composite samples were converted into carbon foams through a carefully controlled heating and pressure control regime designed to regulate the fluidity of the pitches and the development of a stable bubble structure. The foams were carbonized at 1000°C for testing and characterization.

A different approach was used to prepare MWNT/pitch composite materials for carbon fiber synthesis. The presence of any agglomerates in the composite disrupts the fiber forming process during melt spinning and introduces stress concentration defects into the fiber. Although melt mixing is a method that is able to generate carbon nanotube (CNT) composites with a uniform distribution of MWNTs, it is unlikely to yield a pitch composite with the quality of CNT dispersion required for the synthesis of carbon fibers that exhibit significantly enhanced properties. Hence, a more complex approach was used that had better prospects for achieving the required aims. This involved the dispersion of nanotubes in a carrier solvent followed by accelerated sedimentation to remove any agglomerates. The supernatant fraction was then mixed with a solution of the pitch to produce a nanotube/pitch composite following solvent recovery. This material was then melt spun into fine filament and converted into carbon fiber by thermal processing. The properties of the carbon fibers were measured and compared to similar fibers produced from the parent pitch.

Introduction

It is the exceptional mechanical strength and stiffness and high thermal and electrical conductivity of carbon nanotubes that provide the basis for generating new high performance materials. The tensile strength of carbon nanotubes has been reported to be as high as 200GPa with an elastic modulus of up to 1TPa. Nanotubes also possess one of the highest thermal conductivities known, lending themselves for use in thermal management and flame suppression applications. Their dispersion into a continuous matrix allows the production of new composite materials with exciting properties. The current program, *"Continued Development of Pitch/Nanotube Foam and Fiber Composites"* was initiated in order to build upon the promising results obtained in earlier studies[(1)]. The main objectives were to promote the fabrication of a range of pitch/nanotube based composites, particularly aimed at the development of new materials for thermal management and electromagnetic shielding applications. Such carbon based composite materials also offer distinct advantages as construction materials, including strength, toughness, impact resistance, EMI shielding and high thermal conductivity. Hence, they could be used to produce lighter, stronger, cheaper and more effective materials. Multifunctional carbon materials based on carbon foams could be developed for modular assembly as wall treatments to provide blast mitigation and nuclear/chemical warfare protection as well as enhanced electronic security. An important feature in the synthesis of the foams and fiber composites is that they are derived from coal, a low cost feedstock with extensive domestic reserves.

In the previous study[(1)], carbon nanotubes were dispersed into isotropic pitches and the derived composites used to produce fibers and foams. In this current study, it was intended to further develop this approach by producing pitch/nanotube composites with different properties and explicitly to explore methods that promote the interaction between the pitch matrix and the embedded nanotubes in order to more fully exploit the extraordinary properties of carbon nanotubes. It was expected that the work conducted in this project would produce results that could be used to demonstrate how the formation of coal-derived carbon fibers and foams containing well dispersed nanotubes could be fabricated, exhibiting enhanced structural, thermal management and electrical shielding properties. The component materials, coal extract pitches from WVU and UK and high purity multiwall carbon nanotubes from UK, were produced, blended and formed into fibers (UK) and foams (WVU). The materials were heat treated and tested for their physical, electrical and thermal properties.

Experimental

Feedstocks

Preparation of Multiwall Carbon Nanotubes

CAER has developed a chemical vapor deposition process for selectively producing high purity (>95%) multiwall carbon nanotubes (MWNTs); virtually no amorphous carbon is co-generated with the nanotubes. The pilot-scale unit operates in a truly continuous manner without the need for difficult and expensive post-synthesis purification of the product, producing ~2.5kg of MWNTs per day. The synthesis proceeds by the reaction of a hydrocarbon vapor over a dispersed iron catalyst that is deposited in situ on quartz substrates[(2)]. Commonly, a xylene-ferrocene liquid mixture is injected continuously into a pre-heater zone and is swept into the reactor by an argon or nitrogen carrier gas. Operating conditions are varied to control the type

and form of the nanotubes required. The reaction zone is typically controlled at a temperature of ~800℃. The carbon nanotubes (CNTs) grow perpendicular to the quartz plates in parallel alignment, forming thick mats (Figure 1) that can be readily harvested. Since the CNT mats are so well aligned, their dispersion into liquid or solid matrices is less difficult compared to the entangled nanotube products manufactured through other routes. However, it is the transfer of their unique properties from nanoscale materials into the realm of high performance composite materials that is the challenge that needs to be resolved for their practical exploitation.

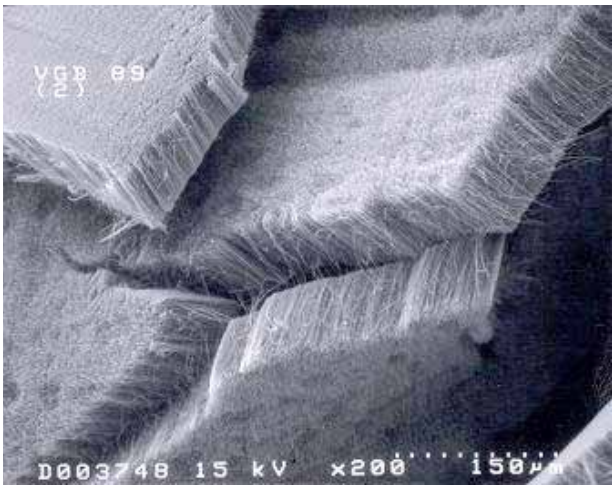

Figure 1 MWNT Produced at CAER

The nanotubes are removed from the quartz substrates in a continuous washer/scrubber unit and the wash liquor filtered to recover the MWNTs in the form of a filter cake which is then dried at 65^{o}C in an air oven. One of many appealing qualities of this low temperature CVD nanotube synthesis process is that the MWNTs (as produced) are of such high purity that they can be utilized directly without recourse to any further treatment. However, the nanotubes do contain ~7wt% Fe in the form of discrete catalyst particles in the core of the tubes. If required, this can be removed by heating to a temperature above 2000^{o}C. This procedure has the beneficial effect of simultaneously annealing some of the lattice defects in the structure of the nanotubes[(3)].

Nanotube Surface Activation

Dispersion of the MWNTs uniformly and individually throughout the matrix is probably one of the most critical parts of composite fabrication, since previous studies have shown that there has been a failure to fully realize the extraordinary properties of carbon nanotubes. The ability to produce homogeneous dispersions of nanotubes in a continuous matrix can be significantly enhanced by chemically altering the nanotube surface to augment the pitch MWNT interaction. Surface treatment of the nanotubes can not only be used to aid the dispersion process but also to promote interfacial bonding with the matrix and thereby maximizing interaction between the MWNTs and matrix for efficient load transfer and thermal transport. This may be accomplished by a variety of methods including the use of surfactants, chemical dispersing agents and chemical functionalization. Attaching functional groups to the graphite lattice comprising the tube surface or more reactive tube ends of the CNTs can be used to promote interaction between the otherwise unreactive nanotubes and the continuous matrix. However, a simpler and effective

method of achieving this objective is by an oxidative activation of the nanotube surface by methods including the use of strong oxidizing reagents or by subjection to oxygen plasmas. Alternatively, mechanical processing of nanotubes (ball milling, shatter milling) results in shorter nanotubes with vastly improved dispersibility. Shatter milling for 10minutes results in tube shortening from ~50μm to lengths in the range 1 to 5μm. The shortened tubes are much easier to disperse into fluid media, and have many more exposed, reactive edge sites than an equal mass of the as-produced carbon nanotubes. The aspect ratio of the tubes is reduced by this action but is still high at a value of around 100. More importantly, the exposed edges provide active sites that can be used in a variety of oxidation and electrophilic substitution reactions.

In the present study, nanotube surface activation was achieved by oxidation in nitric acid. About 50g of as-produced MWNTs were mixed into 3liters of 70% nitric acid and refluxed by heating to ~100^{o}C in a stirred flask for 8hours. The mixture was allowed to cool to room temperature and then stirred into 20l of de-ionized (DI) water to dilute the acid. The nanotubes were allowed to settle for 30minutes and the supernatant liquid containing few nanotubes then siphoned from the vessel. More DI water was added to make up to 20l, the mixture stirred and again allowed to sediment. This procedure was repeated multiple times in order to reduce the acidity of the water. The settling rate noticeably decreased as the pH approached neutrality (after ~10 dilutions). Following the final dilution cycle (pH ~5) the mixture was filtered through Whatman cellulose filter paper mounted in an array of Buchner funnels arranged in parallel. The series of filter cakes were collected together and the surface treated nanotubes dried at 65^{o}C in an air oven. The yield was ~92% of the as-produced MWNTs. Most of the weight loss can be attributed to the dissolution of the Fe catalyst contained in the core of the nanotubes.

Pitch Sources

Three samples of coal-derived isotropic pitch were selected for the preparation of composite materials containing carbon nanotubes from which carbon foams were fabricated. The three pitches: (a) a WVU low QI synpitch, (b) a Koppers coal tar pitch and (c) a Koppers low volatile pitch were selected for their different characteristics. The softening points were measured by DMA.

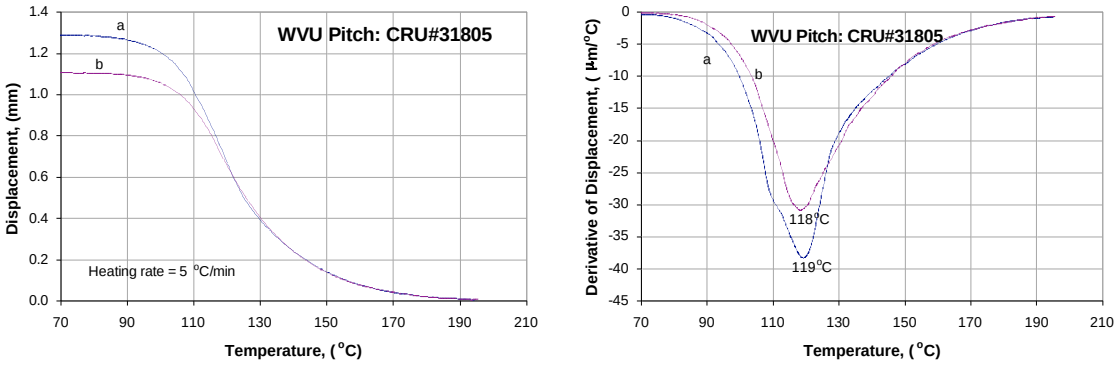

Figure 2 DMA Controlled Force Determination of Softening Characteristics

(Softening Point determined from the Inflexion Point of the Derivative)

This is a very simple, accurate and repeatable method for determining the softening characteristics of a pitch and has been used to determine the optimum conditions for dispersing the nanotubes into the pitch matrix by high shear mixing. In the method, "Controlled Force Mode" a single particle of the pitch is subjected to a static load of typically 0.2N and the displacement monitored as the temperature is increased at a rate of 5^{o}C/min over the temperature range of interest. A typical DMA displacement plot is shown in Figure 2. The derivative of this function with respect to temperature can be used to determine the inflexion point and define a characteristic softening temperature, Table 1.

Sample No	Pitch Type	Softening Point (^{o}C)
WVU#012506	Low QI Synpitch	140
CRU#031805	Koppers Coal Tar Pitch	120
WVU#031706	Koppers Low Volatile Pitch	170

Table 1 Pitch Softening Point

Unfortunately, the pitches and MWNT/pitch composite materials produced for the fabrication of carbon foams were not ideal for conversion into carbon fibers. The softening temperature needs to be as high as practicable without introducing insuperable problems for the fiber forming step. In practice, a compromise is found by producing a pitch with a softening temperature in the range 230 to 300^{o}C, required to facilitate conversion of the pitch matrix into carbon without melting, usually achieved through an oxidative stabilization step. A pitch with characteristics suitable for conversion to carbon fiber was produced by vacuum distillation of a coal solution prepared by the solvent extraction of a Western Kentucky coal, WKy#6. UKCAER has developed a bench scale mild solvent extraction process for converting bituminous and sub-bituminous coals to pitch[(4)]. A simplified schematic of the process is shown in Figure 3. Previous studies have demonstrated that the conversion of coal to pitch can be achieved at high efficiency using anthracene oil (a coal tar distillate) as the solvent at mild extraction conditions and without recourse to the introduction of a hydrogen atmosphere at high pressure, expensive catalysts or the use of exotic solvents. Dissolution of the coal in the digestion reactor allows the mineral matter and undissolved coal fraction to be removed from the coal solution by a solids separation step. Filtration is generally used for this purpose as the ill-defined separation between the dissolved coal and the boiling point distribution of the heavy process solvent make the use of alternative anti-solvent de-ashing techniques impractical. Virtually all of the mineral matter present in the coal is removed during the filtration stage.

A 2liter reactor was used to prepare the coal solution from a slurry of WKy#6 in anthracene oil. The conditions used 410^{o}C with a residence time of 60minutes and a solvent to coal ratio of 2:1 produced a digest that was filtered without difficulty. The specific cake resistance was <25x10^{10}m/kg with a filtration rate of ~70kg/m^{2}/h. Flow rates are based on a notional system in which filters are operated in parallel with one set on-stream while the others are off-line for cake discharge, stripping and cleaning, allowing 30minutes for each part of the cycle. At the end of the filtration phase the filter was allowed to drain and then blown with nitrogen to recover the coal solution from the cake; no attempt was made to wash the cake with solvent and vacuum dry to recover the useful products from the 'wet' cake. However, analysis of the cake (proximate,

ultimate and quinoline insolubles {QI}) allowed calculation of the dissolved coal and solvent content. The conversion of the coal WKy#6 to liquid products during solvent extraction was high, yielding a conversion of around 85%daf.

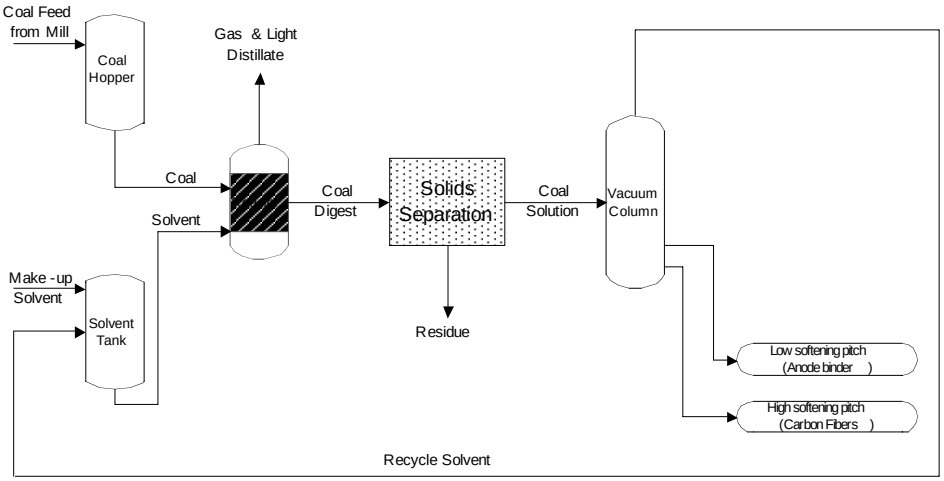

Figure 3 The Production of Pitch by the Solvent Extraction of Coal - Schematic

The amount of residual solids in the coal solution was determined by measurement of the quinoline insolubles. Quinoline is an excellent solvent for the dissolution products from coal extraction and does not normally result in precipitation of any of the dissolved coal. The value, <0.1% showed that the filtration was effective, removing virtually all of the undissolved solids to yield a coal solution that was suitable as a feedstock for the preparation of a 'clean' pitch. A sample of the coal solution was vacuum distilled to remove most of the solvent to generate a pitch with the required softening characteristics. The softening point (~270^{o}C) of the sample produced for these experiments was again measured by DMA.

Methods of Nanotube Dispersion

The purpose of dispersion is to homogeneously distribute individual nanotubes throughout the matrix material. By this means the extraordinary properties of CNTs can be fully exploited, allowing an applied load to be uniformly distributed among the nanotube population for example. The same argument applies to the development of CNT composite materials in thermal management applications. The melt mixing used here relies on the shearing forces generated during the mixing of molten pitch to disperse the nanotubes[(5)]. Nanotubes, however, are known to increase the viscosity of fluids due to their large aspect ratio, high stiffness, and ability to form entangled networks[(6,7)]. An alternative method for dispersing the CNTs throughout the matrix, ultrasonic stimulation uses high frequency sound waves to induce cavitation in low viscosity fluids containing CNT agglomerates. The energy released upon cavity collapse breaks up the CNT agglomerates dispersing the nanotubes into the carrier fluid[(8,9)]. Pitch can be dissolved into the CNT/solvent dispersion to produce a CNT/pitch composite material once the solvent has been removed. In either case the quality of CNT dispersions has a profound impact on the resulting composite properties. Initial property enhancements at low loadings, ~1wt% CNT often do not continue or are reduced at higher loading[(10,11)]. Agglomerates of CNTs can act as a stress concentrating points and reduce the mechanical properties of the matrix[(12)]. However, once

dispersed in the continuous melt or solution, dispersions of CNTs can be processed via conventional processing techniques such as fiber spinning.

Nanotube shortening through fracture and breakage is an unavoidable result in all dispersive processes, a result of the forces acting on the CNTs. However, this effect may enhance the dispersion of the CNTs as their ability to entangle is dependent on their aspect ratio. Conversely, reduction of the CNT length may negatively impact their reinforcing capacity. A reduction in MWNT length was previously found to accompany shear mixing, but CNT aspect ratios of >200 remained.

The orientation of the embedded CNTs relative to the direction of the applied load or thermal gradient, as in all fiber composites, has a major influence on the properties that are measured. The process of shear-mixing or ultrasonic stimulation results in random orientation of the CNTs throughout the pitch matrix. Without the intervention of strong uni-directional shear, this random orientation is preserved throughout further processing. However, a high degree of CNT alignment within a pitch matrix can be achieved through the action of a shear field, by forcing the composite material through a spinneret die and drawing down into fibers. Melt spun CNT composite fibers have been shown to be very effective in aligning the CNTs with the direction of flow, i.e., the fiber axis. However, the ability to sustain stable CNT-pitch composite fiber spinning is largely dependent on the homogeneity of the dispersion. CNT agglomerates can disrupt the flow as fiber attenuation is applied leading to breakage during processing, or in the case of large agglomerates, complete blockage of the small diameter orifices through which the fibers are extruded. Achieving large attenuations or draw ratios, which serve to orient the CNTs with the fiber axis with resulting improvement in fiber properties, is primarily dependent on the quality of the initial CNT dispersion. Thus, for the synthesis of carbon fibers it is crucial that very high quality nanotube dispersion is achieved, approaching separation down to individual nanotube level. Methods of preparing MWNT/pitch composite materials with these properties have been developed and a significant amount of effort has been focused on the development of MWNT/pitch precursor materials which contain an absolute minimum of MWNT agglomerates. This work has built upon parallel studies investigating factors affecting dispersion and settling in various liquid media.

Preparation of MWNT/Pitch Composite Materials

(i) Materials for carbon foam fabrication. For the preparation of carbon foams a simple melt mixing procedure was used to disperse the carbon nanotubes (CNTs) into the pitch using a Haake 3000P high shear mixer unit fitted with roller rotors. The measured softening points were used to determine the temperature at which the unit was operated. The capacity of mixing chamber is 310ml, although for optimum mixing conditions the unit is operated at a maximum loading of 70%. Two batches at each condition were prepared and then combined to produce sufficient material for the foaming tests. Composites were prepared from each pitch by dispersing as-produced multiwall carbon nanotubes (MWNTs) into the pitches at concentrations of 2.5, 1.0 and 0.5wt%. Previous work has shown that at the optimum pitch viscosity (controlled by operating temperature and pitch characteristics) a residence time of 40minutes at a rotor speed of 20rpm is adequate to produce a homogeneous composite material with well dispersed MWNTs. Inspection of polished sections of the composite materials by optical microscopy has shown that this is valid on the macro scale. However, it is most unlikely to produce complete dispersion of the CNTs – there will still be many small agglomerations at the sub-μm level.

Separate tests were performed to produce reference materials with 0% nanotubes under the same operating conditions.

An additional experiment was conducted to prepare a composite material containing the surface activated MWNTs. Koppers low volatile pitch was used into which 2.5wt% surface treated nanotubes were dispersed. There was a noticeable disparity in the dispersion behavior for the two types of nanotubes. Under virtually identical mixing conditions the torque required to achieve the dispersion by melt shearing was significantly different for the two types of nanotubes, Figure 4. The lower torque associated with dispersion of the acid treated MWNTs implies that they are more readily separated than the as-prepared tubes and should therefore produce a composite material with improved CNT dispersion.

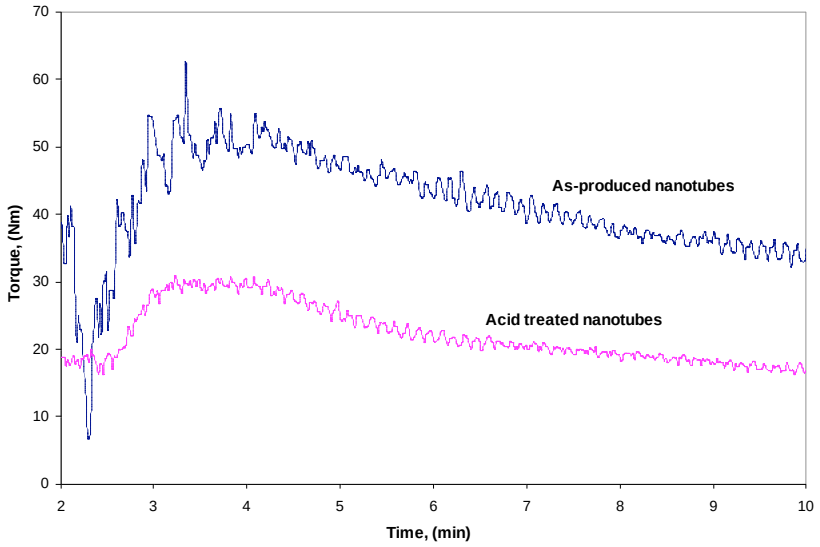

Figure 4 Torque Generated by Dispersing MWNTs into a Common Pitch

(ii) Composite samples for carbon fiber synthesis. A more complex procedure was devised in order to prepare nanotube/pitch composites for fiber synthesis. The CNTs were dispersed in a solvent using ultrasonic excitation followed by accelerated sedimentation to remove any remaining CNT agglomerates. The supernatant fraction was then mixed with a solution of the pitch in the same solvent. In theory, recovery of the solvent from the dispersion would then yield a MWNT/pitch composite material with the absolute minimum of agglomerates. Tests were initiated using a petroleum derived pitch, A500 (softening point 260^{o}C) in order to preserve the coal derived pitch that was available for use once the procedure had been validated. Tetrahydrofuran (THF) was selected as the solvent for the pitch rather than quinoline, as later removal of the solvent would be more tenable with the lower boiling solvent. The effect of the presence of a third phase, the small fraction of the pitch that was THF insoluble was accepted as a necessary compromise in order to achieve the principal objective. A procedure was developed that included dispersion of 0.25wt% MWNTs in THF by ultrasonic excitation for 5min using a 550w wand dismembrator (Fisher Scientific 550) at 20kHz and 250w power input, followed by 2h in an ultrasonic bath at 40kHz and then repeating the wand dismembrator application for a further 5min. A centrifuge was then used to remove agglomerates by accelerated sedimentation.

After centrifuging for 1hour at 10ġ the supernatant liquid had the same clarity as the starting solvent; apparently there were no CNTs present in the supernatant either in a dispersed phase or as agglomerates.

The use of a dispersant was therefore deemed to be a necessary adjunct to the procedure. A dispersant used in the motor oil industry was selected for testing. Unwanted carbonaceous material is produced as a byproduct of combustion within the confines of the internal combustion engine. Some of this colloidal carbon is retained in the engine oil, where agglomeration can occur increasing the viscosity of the oil and significantly diminishing its lubrication performance. In time a harmful sludge can form to severely degrade the effectiveness of the lubricant. To reduce this agglomeration dispersants are added to the oil; these adsorb on the surface of the carbon particles thereby stabilizing them. A commonly used dispersant is a polyamine (PAM) with a polyisobutylene succinimide (PIBSI) tail; the PAM adsorbs on the surface of the carbon particles, while the PIBSI tail provides steric stabilization[13]. These function well for the purpose for which they were designed but their ability to disperse CNTs in pitch is unknown. In addition, the temperature dependence of the efficacy of the stabilization of the dispersant is an important issue in engineering motor oils and their performance over the temperature range needed for spinning pitch into fiber could be crucial. PIBSI formulations are closely guarded commercial secretes and samples are not readily available. However, a sample solution of polyisobutylene succinimide (PIBSI) in naphtha was kindly donated by the ‘Specialty Chemicals Division’ of BASF in Germany and has been used as a dispersant to stabilize MWNT/THF mixtures.

The inclusion of a small amount of PIBSI to the MWNT/THF mixture was decisive – supernatant dispersions of MWNTs in THF were produced using the procedure described above with no evidence of CNT agglomeration. To produce sufficient MWNT/pitch composite material for the carbon fiber synthesis tests four mixtures were prepared by adding 0.25wt% MWNTs to ~100g of THF containing PIBSI at a concentration of 4wt% relative to the weight of MWNTs used. The ultrasonic dispersion technique was used. After centrifuging for 1 hour at 10ġ the supernatant fraction contained only well dispersed MWNTs with few, if any agglomerates. The four supernatant fractions were then combined and the CNT concentration determined by thermal gravimetric analysis (TGA). For an accurate determination it was necessary to monitor the weight loss from the sample immediately on transfer to the weighing pan and prior to weight stabilization for the instrument to initiate the temperature ramp, as evaporation of the THF at room temperature was significant. By this means the weight lost as a function of time was determined, enabling calculation of the original composition of the supernatant dispersion by extrapolation to zero time (before the TGA commenced logging the weight change of the sample). The concentration of MWNTs in the supernatant fraction was determined as 0.05wt%, compared to the 0.25wt% in the original mixture, showing that 80% of the CNTs were lost in the sedimentation process, either as agglomerates or through capture by the migrating agglomerates.

Sufficient pitch was crushed such that when combined with the supernatant fraction it would yield a MWNT/pitch composite containing 0.5wt% MWNTs, following removal of the carrier solvent (THF). A finely divided sample of the pitch was dissolved in THF and mixed for 2h in an ultrasonic bath. The solution was further mixed at 5000rpm for 10minutes using a Silverson high shear mixer. This instrument is capable of milling any remaining particles of pitch to produce a

pitch solution containing a dispersion of minute insoluble particles. The supernatant fraction of the MWNT/THF dispersion was then combined with the pitch solution and the resulting dispersion further mixed for 1 hour in an ultrasonic bath and then at 5000rpm for 10minutes using the Silverson. The resulting dispersion was poured into a shallow glass dish floating in the ultrasonic bath in order to evaporate most of the THF while inhibiting agglomeration of the MWNTs. To remove the last of the THF from the pitch/MWNT dispersion the glass dish was heated in an oven at 120ºC for 30minutes in a nitrogen atmosphere. Any residual volatiles, including the naphtha originally in the PIBSI were removed by vacuum distillation at 200ºC and 2.5torr. Removal of the naphtha and THF was confirmed from TGA analysis of the resulting MWNT/ pitch composite. This convoluted process was necessary to produce a MWNT/pitch composite containing ~0.5wt% of MWNTs that was in a condition that had promise for conversion to a MWNT/carbon composite fiber.

Preparation of Carbon Foams

For the successful fabrication of carbon foams it is crucial that the test material exhibit specific characteristics in terms of the fluidity and dilatation rate in a defined temperature range. During the foaming process the volatiles from the light fractions and decomposition products serve as the blowing agent. However, the fluidity of the test material needs to be in a narrow well defined range at a temperature where the onset of polymerization reactions promotes the stabilization of bubble shape and structure, resulting in the formation of a stable foam[(14)]. Unfortunately, commercially available Koppers coal tar pitch and WVU SynPitch were not suitable for making carbon foam directly because the average molecular weight is not high enough, and the fluidity is too high for adequate foaming. Therefore, the pitches were modified to increase their molecular weight and viscosity (decrease their fluidity). Heat treatment is a simple and effective way of modifying the properties of pitches to meet the requirements of foaming. It can be used to increase molecular weight and fluid viscosity mainly through polymerization and condensation reactions but also via de-hydrogenation and de-volatilization. The heat treatment is performed under an inert atmosphere (nitrogen) prior to initiation of the foaming operation.

Tests were performed on the pitches and MWNT/pitch composite materials prepared at CAER. The pitches were weighed and transferred to aluminum pans for insertion into the pressure vessel used for the foaming process. The vessel consisted of 200mm diameter stainless steel pipe with flanges welded at both ends to enable closure of the reactor. Grafoil® gaskets were used as seals between the end plates and the flanges with bolts tightened to a torque of 95Nm. The pressure vessel was installed in a kiln and purged with nitrogen before the temperature was raised to 350°C at 4°C/min. The pitch was held at this temperature for 45minutes to reduce its fluidity. Following this heat soak period the pressure was increased to 700kPa (100psi) using nitrogen and the temperature further increased to 550°C at 4°C/min and held at this temperature for 1hour. At the end of this process the furnace was turned off and allowed to cool to room temperature while the sample was retained under 700kPa (100psi) nitrogen. At completion the carbon foam samples were carbonized by heating to 1000°C in nitrogen for 1 hour. The samples were then allowed to cool before recovery for testing and characterization.

The electrical resistivity of the carbonized foams was measured by a method conforming to ASTM C611-98 using the apparatus is shown in Figure 5.

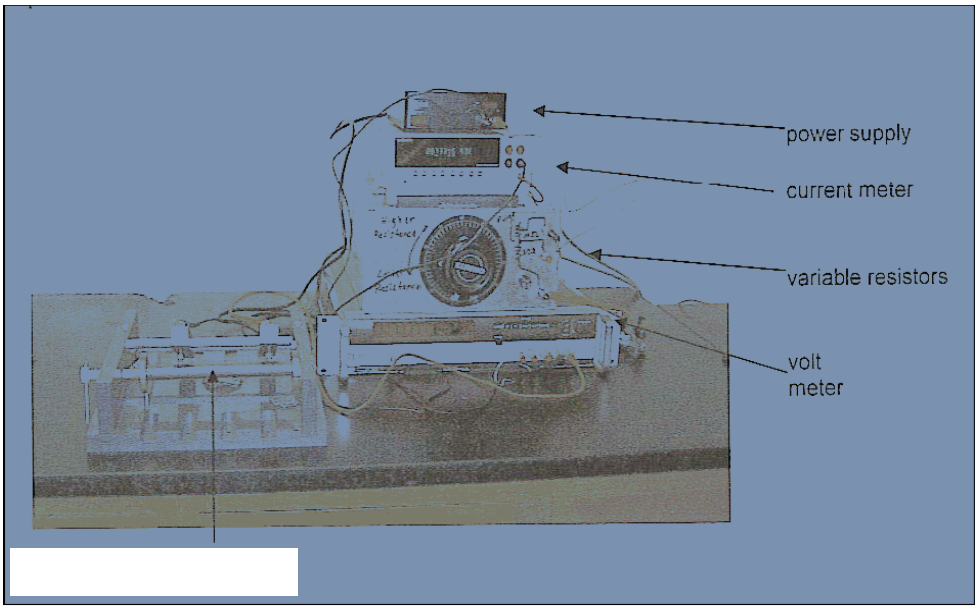

Figure 5 Apparatus used for Measuring Electrical Resistivity.

The resistivity of the carbonized foams was calculated from:

$$\rho = R\frac{A}{L}(1000) = \frac{VA}{IL}(1000)$$

where,

ρ = resistivity, (μΩ-m), R = resistance, $(\Omega) = \frac{V}{I}$,

V = electric potential between probes (volts), I = current passing through foam (amps),

A = sample cross-section area (mm^2), L = distance between probes (mm)

The voltage drop (V) was measured between probes a known distance apart, L, with a current (I) passing through the sample. The resistance, R, is the quotient of the voltage and the current and A, is the cross-sectional area of the sample face through which the current is applied.

Compressive strength and modulus of samples cut from the carbon foams were also determined using an Instron 5869 load frame.

Electromagnetic shielding measurements were conducted on carbon foam samples cut to the specification required by ASTMS D4935. Measurements were made at room temperature over the frequency range 100 to 1500MHz.

Carbon Fiber Synthesis

Samples of the parent pitch and the MWNT/pitch composite were crushed to provide a size fraction (0.2 to 1.2mm) suitable as a feed to a Wayne single screw bench-scale extruder fitted with a 6.2mm diameter screw and 0.3mm diameter x 1mm capillary die. Tests were conducted to determine the conditions under which the samples could be successfully extruded to produce a continuous thread. Feed size distribution and the temperature profile along the barrel and die zone were crucial to this task. Samples were melt spun to produce continuous filament by

forcing the molten pitch through the die. The extruded thread was attached to a wind-up drum rotating at speeds up to 1700rpm (12m/s) to draw filament of 15 to 40μm diameter. In the normal approach to fiber spinning it is essential to remove any entrained particulates by a solids separation process as the ability to produce fine filaments from a pitch is very sensitive to the rheological properties of the pitch. Here, a foreign material (the MWNT) was deliberately introduced into the pitch matrix and unless well dispersed could pose additional problems to successful fiber formation.

Tows of green fiber cut from the drum were thermally processed into carbon fiber. In an initial step the 'green' pitch fibers were rendered infusible (stabilized) to prevent the fibers melting during carbonization. The most practical and economic method of stabilization is by oxidation in air at a progressively increasing temperature to about 300℃, resulting in weight increases of typically 5 to 10%. To avoid fiber softening and deformation, the cross-linking reactions must be initiated below the glass transition temperature, T_g typically about 50℃ lower than the measured softening temperature. As oxidative cross linking reactions proceed T_g and the softening temperature both increase, and hence the reaction temperature can be raised until the fibers are rendered infusible. For these 'green' fibers produced from a high softening pitch stabilization was achieved by heating in air to 200ºC at 5ºC/min and then at 1ºC/min to 310ºC with a dwell of 1 hour at this temperature. Once stabilized the fibers were carbonized by heating in an inert atmosphere (nitrogen) to a temperature of 1000℃ at a heating rate of 20^{o}C/min and held at this temperature for 1 hour. The yield and linear dimensions of the fibers were measured after each stage to monitor the major changes that were occurring during stabilization and carbonization.

The physical properties of the carbonized fibers, including diameter (by optical microscopy), tensile strength, elastic modulus were then measured using a single fiber tensile testing method, (ASTM D3379, D638M). A random selection of ten single filaments was made from the tow of fiber. The filaments were center-line mounted on custom-made slotted paper frames using epoxy resin. The frames were gripped so that the test specimen was aligned axially in the jaws of a constant-speed movable crosshead test machine. The sides of the paper frames were then cut to leave the fiber spanning the gap between the jaws. The fibers were stressed to failure at a constant strain rate of 1mm/min.

Gauge lengths of 20, 30, 40 & 50mm were used in the tests in order to adjust the results for system compliance. Carbon fibers can fail at very low imposed strain and hence small strains in the load cell and mounting system need to be allowed for in order to determine the true elastic modulus of the fiber. System compliance can be determined from the change in measured compliance with the gauge length.

$C_a = \frac{L}{E_a.A}$ where C_a is the apparent compliance, E_a is the measured (apparent) elastic modulus, L is the gauge length and A is the cross sectional area of the fiber. By plotting C_a against L the system compliance C_s can be determined by extrapolation to $L = 0$, and the true fiber compliance (C) and hence true modulus determined from $C = C_a - C_s$ and $C = \frac{L}{E.A}$

Results and Discussion

Carbon Foams

The foam samples were weighed between each processing step in order to monitor the loss of volatile matter during foaming and thermal processing. The concentration of nanotubes in each sample increased as a result of the loss of volatile matter during processing, Table 2

Foam Precursor	Initial Nanotube Content (wt%)	Wt loss during		Final Nanotube Content (wt%)
		Foaming (wt%)	Carbonization (wt%)	
Koppers CTP	0.0	14.4	4.1	0.0
	0.5	12.0	4.4	0.6
	1.0	12.4	4.4	1.2
	2.5	14.2	3.8	3.2
WVU Synpitch	0.0	28.9	5.0	0.0
	0.5	28.6	5.0	0.8
	1.0	28.8	5.2	1.5
	2.5	31.4	6.2	3.9
Koppers Low Vol Pitch	0.0	ND	ND	ND
	2.5*	28.9	4.5	3.7
	2.5#	20.3	4.3	3.3

* untreated nanotubes, # HNO_3 treated nanotubes ND = Not determined

Table 2 Weight loss During Foaming and Thermal Processing

The high softening point coal tar pitch from Koppers (Koppers Low Vol) was only foamed with nanotubes in the pitch. The sample labeled “untreated nanotubes” contains the same type of untreated nanotubes as used in the previous experiments. The other low volatility sample from Koppers includes nanotubes that were surface activated in nitric acid before they were introduced into the pitch.

Figure 6 Scanning Electron Microscope at West Virginia University.

The adhesion between the nanotubes and the pitch matrix is critical to the enhancement of the foam properties. Otherwise, the nanotubes become discontinuities within the foam matrix and serve as physical weaknesses within the structure. Scanning Electron Microscopy was used to visually inspect whether the nanotubes bond well with the foam matrix. The Hitachi S-4700 field emission SEM used at West Virginia University is shown in Figure 6.

SEM images were taken before and after carbonization to observe if thermal expansion created a substantial problem with the foam/nanotube adhesion. Figure 7 shows SEM micrographs of both green and carbonized Koppers Coal Tar Pitch foam with 0.5 % wt nanotube addition.

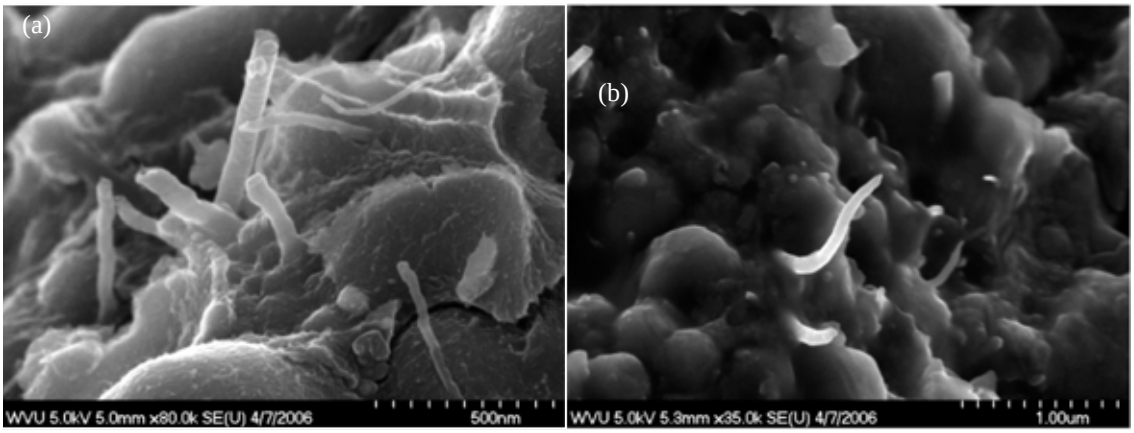

Figure 7 Koppers Coal Tar Pitch Foam (0.5wt%MWNT), (a) Green (b) Carbonized

Inspection of the SEM micrographs suggests that there is an interaction between the foam matrix and the dispersed nanotubes. This is apparent in both images where wetting of the CNTs by the matrix at the base of the nanotubes can be seen and where the foam matrix seems to be drawn up the nanotube wall. This observation suggests that the foam matrix is bonding to the nanotubes and therefore some enhancement of the foam properties should be observed.

Foam Precursor	Initial Nanotube Content (wt%)	Resistivity (μ Ohm-m)	Bulk Density (g/cm^3)
Koppers CTP	0.0	366	0.47
	0.5	328	0.40
	1.0	359	0.38
	2.5	277	0.44
WVU Synpitch	0.0	257	0.41
	0.5	250	0.45
	1.0	333	0.37
	2.5	354	0.53
Koppers Low Vol Pitch	0.0	ND	ND
	2.5*	241	0.52
	2.5#	229	0.54

* untreated nanotubes, # HNO_3 treated nanotubes ND = not determined

Table 3 Resistivity of Foam Samples

Carbonization significantly changes the properties of the foams by removing volatile matter to fix the carbon structure, resulting in increases in strength and electrical conductivity (lower resistivity). The resistivity measurements for the foam samples are summarized in Table 3.

The results from the resistivity measurements are somewhat confusing. For the foams fabricated from the Koppers coal tar pitch containing nanotubes there is apparently a small beneficial decrease in resistivity with increasing nanotube content. However, the opposite trend is observed for the WVU Synpitch. The problem of interpretation of the data is that any small changes in resistivity due to the inclusion of CNTs in the pitch precursors is masked by the dominating influence that changes in foam bulk density has on the measured values of the resistivity. With the exception of two outliers in the complete data set there is a strong correlation between resistivity and bulk density, the resistivity declining as the bulk density increases. Further there is no correlation between bulk density and CNT concentration. Thus, under the conditions studied here there is no evidence for improvement in electrical conductivity of the carbon foams due to the inclusion of the MWNTs into the pitch matrix.

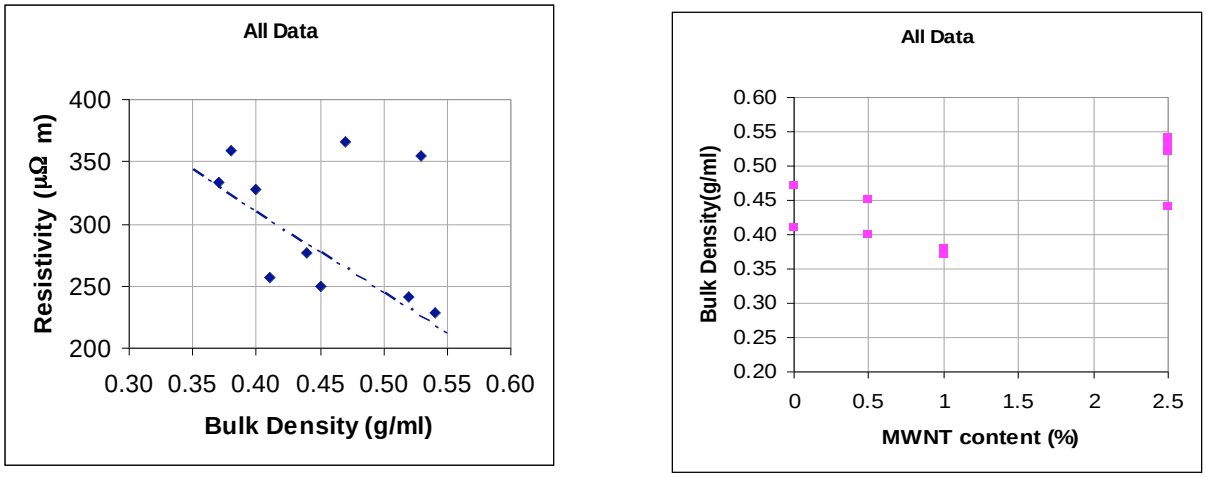

Figure 8 Electrical Resistivity & Bulk Density of Carbon Foams

Inferences can be drawn by studying the SEM micrographs of the carbonized Synpitch foams. Figure 9 shows that the matrix of the foam becomes more ordered than the coal tar pitches. It is apparent from Figure 9a that the Synpitch matrix forms plate-like structures, which is more conducive to forming graphite at high temperature. Unfortunately, the interfacial bonding between the nanotubes and the matrix does not appear to have been sustained during the foaming process and particularly carbonization, Figure 9b. The matrix has not bonded with the nanotubes, instead holes are visible where the nanotubes have pulled out.

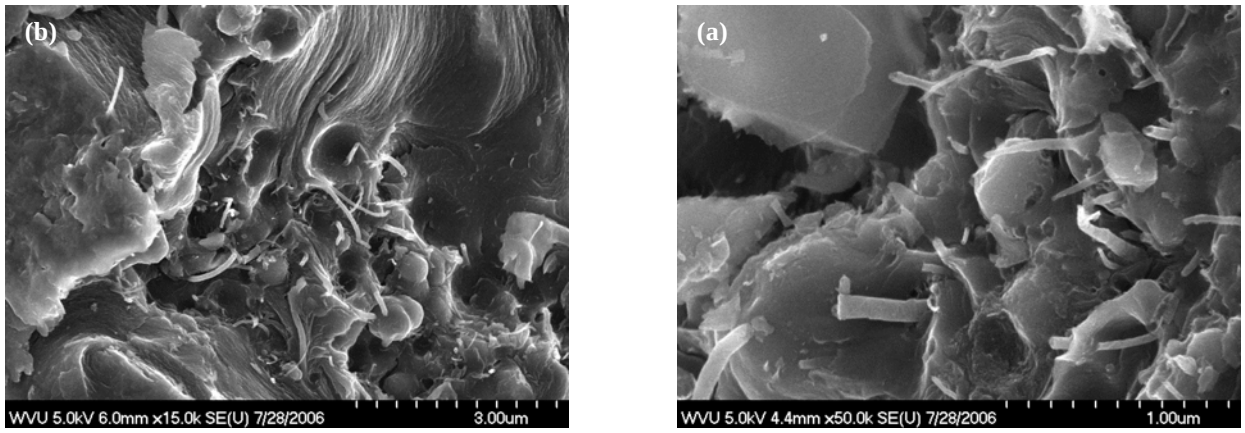

Figure 9 Carbonized WVU Synpitch Foam, (a) 0wt% MWNT, (b) 2.5wt% MWNT.

The Koppers high softening point pitch with the nanotube additions did not seem to show much difference between the treated nanotubes and the untreated nanotubes. The SEM micrographs in Figure 10 show that there visually does not seem to be much, if any, difference in the matrix-nanotube interactions between the two surface treatments.

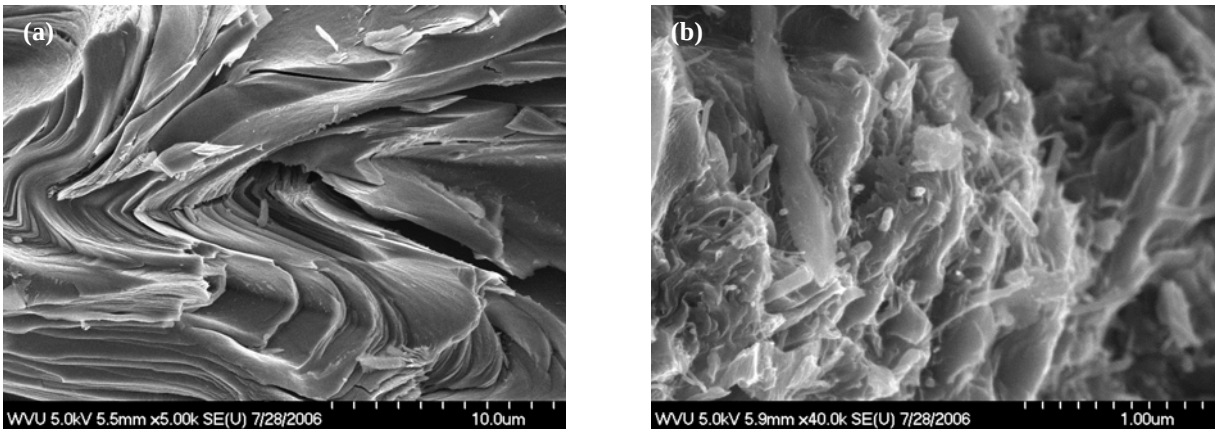

Figure 10 HSP Koppers CTP with (a) 2.5wt% HNO_3 MWNT, (b) 2.5wt% MWNT.

Compression testing was performed on the foams using an Instron 5869 load frame to determine if the nanotubes increased the mechanical compressive strength of the materials, Table 4. The method[15] developed by Carpenter at West Virginia University was employed to complete these measurements since there is no current ASTM method for compression testing for carbon foams. Unfortunately, there was not enough material to run more than one test per sample and two of the original foam samples (Koppers CTP 0.0wt% and Synpitch 2.5wt%) were not large enough for the sample preparation used for the compression test.

The Synpitch results are the most conclusive of the three pitches showing a decline in strength and modulus as the nanotube content was increased. This view is supported by the SEM micrographs showing the matrix structure of the calcined foam which shows a higher order carbon material being formed, which would become graphitic at high temperatures due to the plate-like formations.

Foam Precursor	Initial Nanotube Content (wt%)	Compressive Modulus (MPa)	Yield Strength (MPa)	Bulk Density (g/cm^3)
Koppers CTP	0.0	ND	ND	0.47
	0.5	107	3.5	0.40
	1.0	74	5.6	0.38
	2.5	122	3.2	0.44
WVU Synpitch	0.0	33.5	5.8	0.41
	0.5	22.7	4.3	0.45
	1.0	23.0	3.7	0.37
	2.5	ND	ND	0.53
Koppers Low Vol Pitch	0.0	ND	ND	ND
	2.5*	94.1	6.0	0.52
	2.5#	92.9	5.9	0.54

* untreated nanotubes, # HNO_3 treated nanotubes ND = Not determined

Table 4 Compression Test Data

In comparison with other performance tests the CNT doped carbon foams performed well in the EMI shielding tests. Measurements were made on the Koppers coal tar pitch containing CNTs from 0 to 2.5wt% over the frequency range 100 to 1500MHz. The results, Figure 11 demonstrate the effectiveness of dispersing carbon nanotubes into the pitch on the shielding properties of the derived carbon foam. There is a progress improvement in shielding effectiveness as the nanotube content in increased from 0 to 2.5wt%. At the highest loading the shielding approaches that required for cell phone protection. -40 to -50dB at the peak intensity 1050MHz.

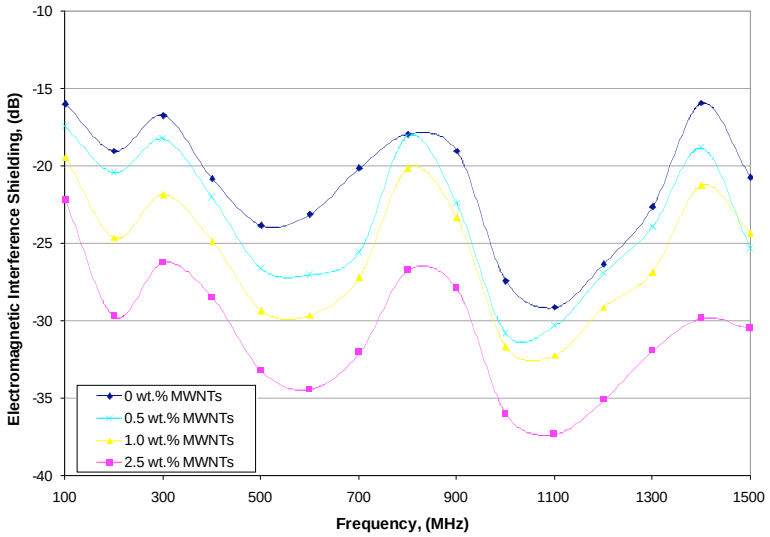

Figure 11 EMI Shielding of MWNT/Carbon Foams

Carbon Fibers

The complexity of the methods developed for preparing a pitch containing 0.5wt% CNTs with an absolute minimum of agglomerates surprisingly did not hinder the fabrication of carbon fibers. Extrusion of the pitch through a narrow die was achieved with few problems, producing 'green' fibers with diameters in the range 15 to 40μm. Fiber diameter was controlled by varying the speed of the wind-up spool in the range 20 to70% of maximum. These were successfully converted to carbon fibers by the thermal program defined above and characterized by measurement of their physical properties, (diameter, tensile strength, elastic modulus and strain energy to break). Unfortunately, the results were disappointing. There was no improvement in the physical properties compared with fibers prepared from the parent pitch. Tensile strengths increased as fiber diameter decreased but within the range of values previously determined for the carbon fibers derived from the parent pitch, Figure 12. Similarly the elastic modulus of the carbon fibers fabricated from the MWNT/pitch composite were indistinguishable from those produced from the untreated pitch.

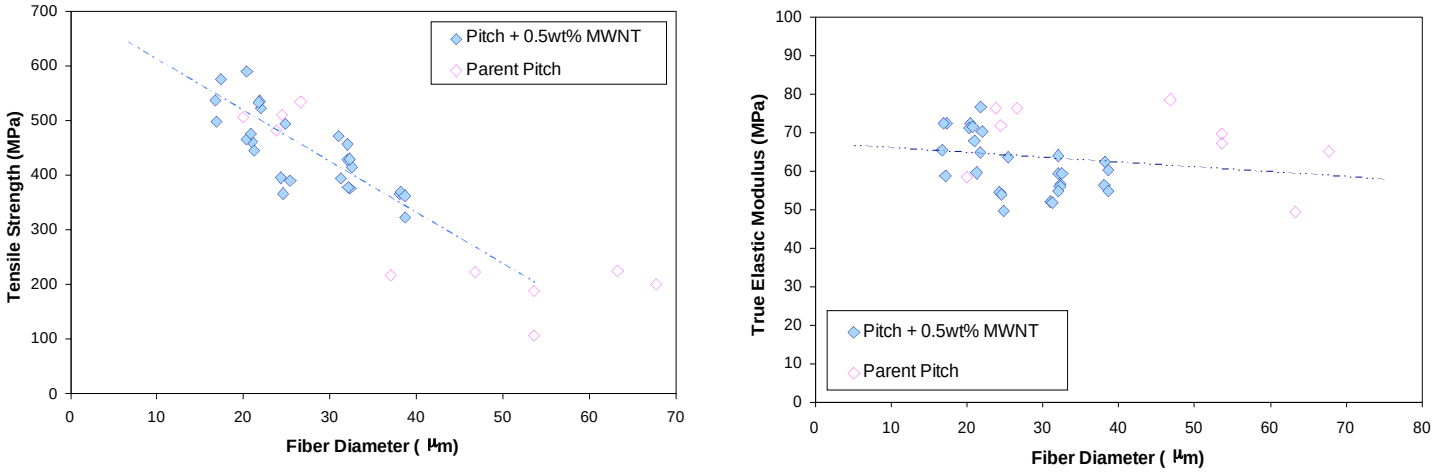

Figure 12 Tensile Strength & Elastic Modulus of MWNT/Carbon Fibers

The elastic modulus measurements have been adjusted to remove errors introduced by system compliance. This was achieved by measurement of fiber properties using samples with a wide range of gauge lengths, 20 to 50mm. The true elastic strain was approximately half of the measured value and the modulus therefore twice the measured value. Although these experiments have not produced the desired improvement in the physical properties of the fibers the work has shown how an agglomerate-free dispersion of carbon nanotubes in a pitch can be produced and could be the first step towards generating high performance fibers. It may be necessary to use the embedded carbon nanotubes as templates to build a graphitic structure from within the fiber by thermal processing at much higher temperatures (>2000^{o}C) and simultaneously imposing strain to retain the CNT alignment with the fiber axis. However, time did not allow for this theory to be tested under the current program.

Conclusions

Multiwall carbon nanotubes (MWNTs) were dispersed into three discrete samples of isotropic pitch at concentrations of 0.5, 1.0 and 2.5wt% by a conventional melt mixing technique. Reference samples of pitch containing no MWNTs were also prepared under the same conditions. One composite was also prepared using surface activated MWNTs at a concentration of 2.5wt%. The nanotubes were refluxed in concentrated nitric acid to promote surface interaction between the MWNTs and the pitch matrix. These composites materials were converted into carbon foams by a precisely controlled heating and pressure regulated process, followed by carbonization to 1000^{o}C.

Characterization of the Koppers Coal Tar Pitch showed some small improvement in physical properties due to the inclusion of the MWNTs, but little significance could be drawn as the effect was masked by the dominating influence of other variables. For example the small decrease in resistivity of the carbon foam (or increase in conductivity) was certainly measurable but was masked by changes in bulk density which had a more significant affect on resistivity. The inclusion of MWNTs in the pitch apparently had no effect on the mechanical properties of the derived carbon foam. However, other factors can affect the mechanical strength such as bulk density interior bulk matrix and precision of sample preparation. Ideally, the dimensional tolerance of the samples should be to less than 0.25mm. However, this was not possible with the equipment and methods that were available and could have an adverse affect on the characterization measurements. In contrast, measurement of the electromagnetic interference shielding gave very encouraging results with a progressive increase in the shielding performance as the concentration of MWNTs in the carbon foam was increased from 0 to 2.5wt%. At the peak frequency, 1050MHz the shielding achieved with carbon foam containing the 2.5wt% MWNTs approached that required for cell phone protection. -40 to -50dB.

There was no significant difference in the results from tests with the Koppers high softening point pitch containing surface activated MWNTs and the carbon foam containing as-produced nanotubes. The electrical resistivity, compressive modulus and the yield stress values were all similar. Analysis of the SEM images provides no evidence to prove otherwise. It appears that the untreated nanotubes adhere to the foam matrix just as well as the HNO_3 treated nanotubes.

A complex method for preparing MWNT/pitch composite materials suitable for the synthesis of high performance carbon fibers has been developed. The technique was based on dispersion of the MWNTs in a carrier solvent using ultrasonic excitation and a PIBSI dispersing agent followed by accelerated sedimentation to produce a high quality stable dispersion containing an absolute minimum of nanotube agglomerates. The procedure was completed by mixing a solution of the pitch in the same solvent with the supernatent fraction and recovering the solvent by evaporation and distillation. This series of steps enabled the required MWNT/pitch composite material to be derived. The synthesis of carbon fibers from the composite followed established methods with carbonization to 1000^{o}C. Unfortunately, measurement of the physical properties of the fibers produced disappointing results with no improvement in tensile strength or elastic modulus of the fibers compared with measurement of the fibers derived from the parent pitch alone. It may be necessary to thermally promote aligned graphitic structure within the composite fibers by heating to a temperature of >2000^{o}C while imposing strain to retain alignment with the fiber axis.

References

(1) "*Nanotube Enhancement of Coal Extract Pitches: Fibers and Foams*", CPCPC Report No 2480-UK-DOE-0350, August 2004.
(2) Andrews R, Jacques D, Rao A.M, Derbyshire F, Qian D, Fan X, Dickey E.C & Chen J, "*Continuous production of aligned carbon nanotubes: A step closer to commercial realization*". Chemical Physics Letters 1999, 303, 467-474.
(3) Andrews R, Jacques D, Qian D & Dickey E.C, "*Purification and Structural Annealing of Multiwalled Carbon Nanotubes at Graphitization Temperatures*". Carbon 2001, 39, 1681-1687.
(4) "*Technical and Economic Assessment of Mild Coal Extraction*", CPCPC Report No 2691-UK-DOE-1874, October 2005.
(5) Gorga R.E & Cohen R.E, "*Toughness enhancements in poly(methyl methacrylate) by addition of oriented multiwall carbon nanotubes*". J. Polym. Sci.: Part B: Polym. Phys. 42, 2690–2702 (2004).
(6) Advani S.G & Fan Z, "*Materials Processing and Design: Modeling, Simulation, and Applications*", NUMIFORM 2004 (eds. Ghosh, S., Castro, J. C. & Lee, J. K.) 1619–1623 (American Institute of Physics, 2004).
(7) Shaffer M.S.P & Windle A.H, "*Analogies between polymer solutions and carbon nanotube dispersions. Macromolecules*" 32, 6864–6866, (1999).
(8) Weisenberger, M.C, Grulke E.A, Jacques D, Rantell T. & Andrews R. "*Enhanced mechanical properties of polyacrylonitrile/ multiwall carbon nanotube composite fibers*". J. Nanosci. Nanotechnol. 3, 535–539, (2003).
(9) Ding W. et al., "*Direct observation of polymer sheathing in carbon nanotube-polycarbonate composites*". NanoLett. 3, 1593–1597, (2003).
(10) Zeng J, Saltysiak B, Johnson, W.S, Schiraldi D.A & Kumar S, "*Processing and properties of poly(methyl methacrylate)/carbon nano fiber composites*". Compos. Part B: Eng. 35, 173–178, (2004).
(11) Fisher F.T, Bradshaw R.D & Brinson L.C, "*Fiber waviness in nanotube-reinforced polymer composites-I: Modulus predictions using effective nanotube properties*". Compos. Sci. Technol. 63, 1689–1703, (2003).
(12) Hammel, E. et al, "*Carbon nanofibres for composite applications*", Carbon 42, 1153–1158, (2004).
(13) Kearns J.C. & Shambaugh, R.L, "*Polypropylene fibers reinforced with carbon nanotubes"*. J. Appl. Polym. Sci. 86, 2079–2084, (2002).
(14) Chen C, Kennel E.B, Stiller A.H, Stansberry P.G & Zondlo J.W. "*Carbon Foam Derived from Various Precursors*", Carbon 44, (2006), 1535-154.
(15) Carpenter, S.P, "*Development of a Constrained Piston Method for Compression Testing of Carbon Foams*", Master's Thesis, West Virginia University, (2005).

COAL DERIVED NANOFIBER SHEET DEVELOPMENT

CONSORTIUM FOR PREMIUM CARBON PRODUCTS FROM COAL
FINAL REPORT

Performance Period March 1, 2005 – August 30, 2006
Principal Author: Dr. David W. Firsich

Submitted Aug 30, 2006

Subcontract No. 2870-ISI-DOE-1874
"Coal Derived Nanofiber Sheet Development"

Inorganic Specialists, Inc.
P.O. Box 181
720 Mound Ave.
Miamisburg, Ohio

Disclaimer

Abstract

This project is focused on the development of paper sheets made from coal-derived carbon nanofibers from Applied Sciences, Inc. (ASI). The paper form adds value to this coal-derived product. Applied Sciences currently produces coal nanofibers from a gasified coal feedstock; their mainstream products are nanofibers made from hydrocarbon gases. The reaction conditions employed to make the coal material are similar to those which produce one of ASI's mainstream products (PR-19), and so its not surprising that SEM characterization shows that the coal-derived nanofibers are similar (but not exactly the same) as hydrocarbon-derived PR-19.

It has been found that coal-derived nanofiber paper has a strength comparable to its hydrocarbon analog PR-19, which is not very strong. The ASI product PR-24 makes a paper more than twice as strong. But even with the modest strength of the current type of coal nanofibers, it was possible to fabricate a number of demonstration papers of coal-derived nanofibers, including sheets that were as large as 12"x12".

One emphasis of this project was to examine uses for coal-derived nanofiber papers. The applications we investigated showed some promise and some drawbacks. It was generally found that the coal-derived nanofibers of today did not perform as well as the hydrocarbon variety. For example, a coal-derived electrochemical capacitor electrode with good performance was synthesized, but there are caveats due to coal impurities introducing self-discharge. We performed one test of a coal material as a fuel cell component and observed reduced performance relative to hydrocarbon-derived nanofibers. These issues may disappear in the future, as there is a move underway at Applied Sciences to make coal-derived nanofibers by a process that would utilize a relatively pure feedstock of hydrocarbon gases derived from a coal-burning power plant. If the same gas composition as is now used in their commercial nanofiber production can be achieved, ASI could make their current product at a much lower cost.

Since a limited amount of coal-derived nanofibers were provided to us by ASI, development work was often done with their commercial hydrocarbon-derived nanofiber, with the expectation that future coal-derived nanofibers would have identical properties. Development work such as experiments with binders to add strength, studies designed to improve paper conductivity, evaluation of filter membranes for paper manufacture, and additional applications testing were all performed for this project.

The advances of this project include a better knowledge of binders, the development of improved conductivity, the demonstration of various applications (fuel cells, composites, EMI shielding, electrochemical capacitors), and a clear route to making nanofiber sheet material on a continuous basis. Further development effort will be appropriate when Applied Sciences implements their plans to make nanofibers that are identical to their current products, using coal-derived hydrocarbon gases as their feedstock.

TABLE OF CONTENTS

Introduction

A method for the bulk preparation of carbon nanofibers from gasified coal has recently been developed by Applied Sciences Inc. (ASI) in Cedarville Ohio. The synthetic technique produces coal-derived nanofibers in the form of low-density, spongy clumps, similar to other carbon nanofiber products made by ASI. This raw material has the potential for use in high-value products, but only after suitable processing.

ASI nanofibers can be made into pure sheet form using a method created by Inorganic Specialists in Miamisburg Ohio. Freestanding sheets between 2 and 20 mils thick have been produced. It is thought that sheet form will add value and make the product marketable for applications such as membranes, electrodes, composite pre-forms, fuel cell components, etc. The sheet fabrication method is currently a laboratory process similar to papermaking; it needs to be improved to make it suitable for scale-up, and useful applications need to be demonstrated. Such development efforts are the focus of this project, testing fabrication options to make a manufacturable product as well as examining new applications for the product. The preparation of pure nanofiber sheets was principally studied, although some effort pursued the incorporation of binders. Imparting improved toughness/conductivity to these sheets will increase their commercial appeal and improve the prospects for mechanical scale-up of sheet fabrication.

Applied Sciences Nanofibers and Coal-Derived Nanofibers

Applied Sciences "nanofibers" are actually large diameter nanotubes with an uncommon morphology. In contrast to conventional nanotubes that consist of concentric tubes of graphite sheets (**A**), the ASI nanofibers consist of stacked cups of graphite sheets (**B**), with edge sites along their length.

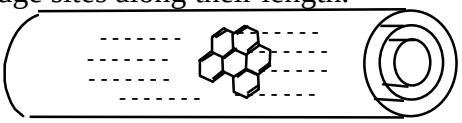

A

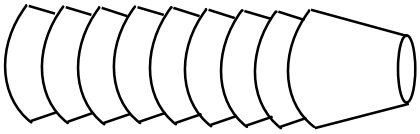

B

ASI produces two types of nanofibers in bulk. One is a 60 nm diameter nanofiber with structure **B**, and the second consists of structure **B** coated with a thick layer of turbostratic carbon (**C**), giving it a much larger diameter (200 nm). This distinction is noted because to date, the nanotubes ASI has made from coal have been produced with the recipe that produces structure **C**, and structure **C** makes a paper with different properties than structure **B**.

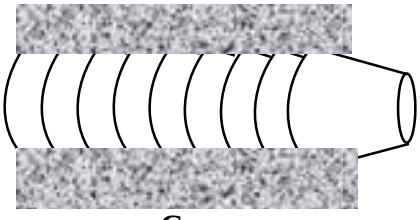

C

As synthesized by Applied Sciences, the coal-derived nanofiber contains more contaminants (metal, soot, sulfur) than its hydrocarbon-derived analog. These can be reduced with processing, but our study was not overly concerned with this- we did not want to add extra processing steps to make a very pure paper, we simply wanted to explore the basics of sheet preparation and strength. Happily, during the course of this program, the coal-derived nanofibers made by ASI became cleaner, less contaminated with carbon soot, as shown below.

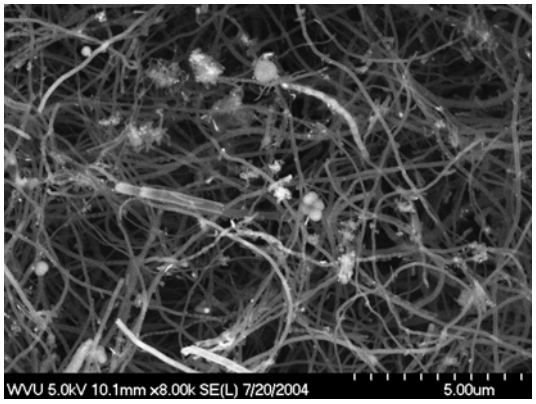

Early batch of coal-derived nanotubes

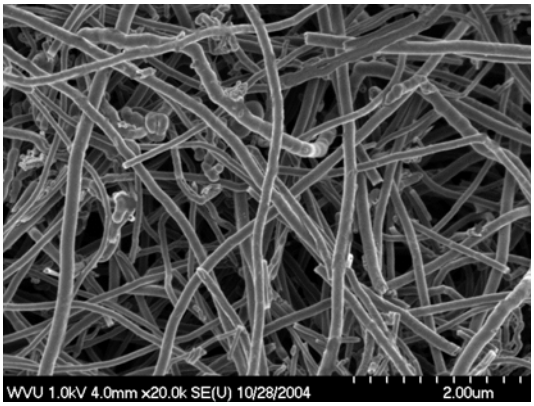

Cleaner coal nanotubes from later batch

The sheets we are producing with our papermaking procedure can vary significantly in density, depending on the fiber used and the way it is dispersed in its stock solution. We have observed paper densities over the range of 0.12 g/cc to 0.37 g/cc. Since the density of an individual ASI nanotube has been calculated as ~1.5 g/cc, this corresponds to a volume packing density of 8% to 25%.

EXECUTIVE SUMMARY

This project is focused on the development of paper sheets made from coal-derived carbon nanofibers from the company Applied Sciences,Inc. (ASI). The ultimate goal is to develop a higher-value form of coal nanofibers by finding ways to make them into papers or monoliths, and then demonstrate applications for these materials. Applied Sciences produces the coal nanofibers from a gasified coal feedstock instead of the hydrocarbon gas that they normally use.

Here is a synopsis of the development activities carried out for this project:

Monolith Preparation, SiC composite preparation
A 1" thick slab of nanofiber was prepared by the papermaking route and fired to 1500 C. It shrank uniformly without cracking, showed a high conductivity, and was subsequently used to make a SiC composite by infiltrating the porous slab with a pre-ceramic.

Binder Development
We have previously encountered severe conductivity and flexibility reductions when the paper is modified with binders to add strength. These problems were mitigated by changing the binder application technique and by using a latex binder.

Scrim-Based Paper
Making the coal-derived nanofibers into a paper using a carbon fiber web reinforcement (a nonwoven scrim) was found to be an excellent way of adding strength, flexibility, and conductivity to coal-derived nanofiber papers.

All-Coal Electrochemical Capacitor Electrode
Carbon electrodes made out of coal nanofibers or a mixture of coal nanofibers and coal powder were evaluated as electrochemical capacitor electrodes. The mixed electrode showed excellent power features, but the concern is that impurities in the coal could hurt its performance over time.

Nanofiber Paper as a Fuel Cell Catalyst Support
Hydrocarbon-derived nanofiber paper was found to have extremely beneficial properties in both methanol and hydrogen fuel cells, showing a catalyst utilization improvement of 1600% in one case. The coal-derived paper severely underperformed these results.

EMI Shielding
Nanofiber paper has been shown to provide electromagnetic shielding at high frequencies, but whether is provides enough shielding to be of interest to the military remains to be seen.

Scale Up Activities
A 50 liter reactor was purchased to handle larger feedstock quantities. After much searching, a filter medium suitable for continuous papermaking was identified. This is the key component that will allow us to design a papermaking machine for continuous nanofiber paper production.

General Experimental

All starting materials were purified with acid before making them into paper. This allowed the resulting papers to be further modified and tested without a concern that contaminants were harming the results. After removal of contaminants, nanotube samples were further treated to make them suitable for papermaking, and then our basic proprietary papermaking process was applied. The samples prepared for this project were generally 5-15 mil in thickness. Pure nanofiber papers and papers with additives (vide infra) were prepared, analyzed, and sometimes post-treated to assess the treatment impact on strength or conductivity.

Strength tests were performed by a tensile test procedure on a "dogbone" shaped nanofiber paper sample that was tape-reinforced on either end. The apparatus shown below was used, and the procedure was to suspend one end of the dogbone from the underside of an analytical balance, while the other end was attached to a lab jack. The sample was gradually stretched by lowering the lab jack, and the force applied to the dogbone measured by the analytical balance. The balance was interfaced to a computer to collect 5 points per second until sample rupture.

Strength Measurements

Strengths were compared by evaluating the force necessary to pull apart a dogbone sample of a constant size, and then normalizing the results for the weight of the dogbone. This procedure gives a weight-based comparative measure of strengths for different nanofiber paper samples.

Results and Discussion

During the course of this project we were supplied with relatively small samples of coal-derived nanotubes (there is simply not much of this material available, as the production of coal nanotubes is a development effort at Applied Sciences). At the same time, we had available large quantities of Applied Sciences' bulk-produced nanotubes made from hydrocarbon gas, and so we frequently used these materials to develop techniques for improving nanopaper strength. What we learned from working with the hydrocarbon-derived nanotubes was then tested in experiments on coal-derived nanotubes.

The hydrocarbon derived nanofibers from Applied Sciences have structures **A** and **B**. **B** makes a weaker paper than **A**. The coal-derived nanofiber paper has a strength comparable that of fiber **B**, and a similar structure. Our expectation is that future coal fiber development can produce a nanofiber comparable to **A**, which will lead to a stronger coal-derived nanofiber paper.

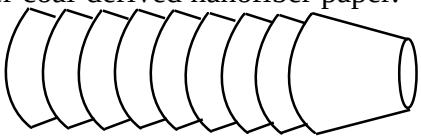

A

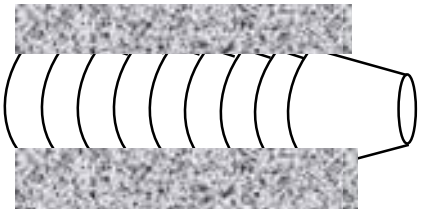

B

A) NEW PAPER EMBODIMENTS

1) Coal Nanofiber Block

A monolith of coal nanofibers was formed by filtering a large amount of suspension to form a thick sample. This brick was then fired to 1500 C under vacuum to partially graphitize it. The sample did not crumble upon firing, and in fact formed a strong porous monolith. Its measured electrical conductivity (4-point probe) was equal to the highest conductivity seen for analogous monoliths of hydrocarbon-derived nanofibers (2 S/cm). As good as this result was, it was still disappointing that the bulkier coal-derived nanofibers did not conduct better than the smaller-diameter hydrocarbon nanofibers. It is somewhat odd that nanofibers of different diameter and structure seem to become equivalent conductors when they are fired to a sufficiently high temperature.

Monolithic porous blocks of coal nanofibers are of interest as pre-forms for composites. Composites would seem to be a good application for coal-derived nanofibers. Unlike some applications where high purity is required (some battery applications), composites are compatible with some of the naturally-occurring silicon oxides or metals in coal.

2) Conductivity Reduction by Binders, and Overcoming this Problem

As reported at the CPCPC meeting in May 2005, the incorporation of binders that provide tensile strength enhancement can diminish the conductivity of the nanofiber sheet, as seen in the example below.

	Binder Content	**Relative Resistance, ohms**
Plain Nanofiber Paper	0	3.2
Paper with Binder 1	.5%	400
Paper with Binder 1	1.5%	1800
Paper with Binder 1	7.0%	3300

This apparently happens when the binder deposits between individual nanofibers or groups of nanofibers, creating a insulating layer between them. This can be seen in the SEM below, where webs of binders are evident at fiber junction points.

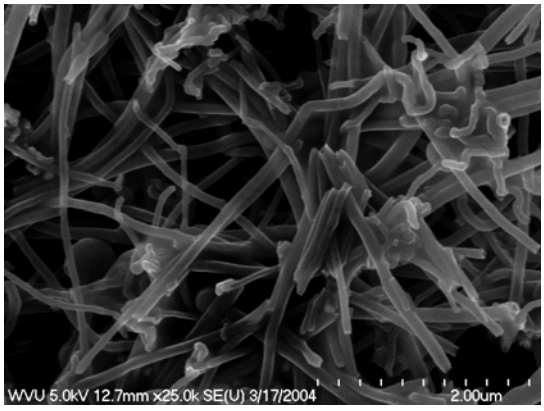

Recent work has shown that this problem can be overcome by changing the way the binder is applied, and by incorporating a conductive additive ('binder 2' in the list below). This strategy not only allow one to overcome the resistance added by binders, they actually make the paper more conductive than the original binderless paper. The series of samples below shows the effect- it compares binderless paper, papers with binders, and papers with binders combined with conductive additive.

	Nanofiber Paper with No Binder	**Relative Resistance with Binder**	**Relative Resistance with Binder, Conductive Additive, and New Processing**
Binderless	200 ohm		
Binder 1		460 ohm	150 ohm
Binder 2		265 ohm	76 ohm

Furthermore, by using a flexible binder such as a latex, the paper retains its flexibility. The ability to make a nanofiber paper with the best combination of strength, flexibility, and conductivity is what will make nanofiber paper a commercial success. Applied Sciences, who makes the raw nanofibers, is interested in obtaining nanofiber papers for developing a number of applications (EMI shielding, composites, host material, others). However, instead of using papers tailored for each application, they want to work with one variety. This illustrates how creating an optimized blend of properties is an important goal.

3) Preparation of a Coal Nanofiber Sheet on a Carbon Scrim

A different approach to achieving a strong, flexible, conductive nanofiber sheet was examined in this program, the strategy of forming the nanofiber sheet on a nonwoven mesh of larger carbon fibers. We tested a very thin (2-mil), extremely open mesh nonwoven as a reinforcing material, filtering the nanofiber suspension directly onto the mesh to form the reinforced paper. This works extremely well. When a 10-mil nanofiber sheet is prepared with the mesh reinforcement, the mesh reinforcement only represents 10% of the weight of the paper, and yet the paper has more conductivity than that produced by any other strategy we have tested. No binders were added in this process. The resulting sheet is flexible and extremely strong. At this time, this appears to be the most promising way to create a robust coal-derived nanofiber sheet that shows excellent conductivity. This type of nanofiber paper has shown good performance as a fuel cell catalyst support.

Graphitized Nanofibers on a Carbon Scrim

Past testing on nanofibers as lithium ion anodes has shown that the graphitized form of the nanofiber works better than other nanofiber varieties. However, a graphitic nanofiber by itself will not form a nanofiber paper that has good cohesion. Therefore we tested making the material on a scrim, in a process similar to that described above. The resulting sheet did not cleanly release from its filter backing, and so the experiment was tried again using a 20% content of non-graphitized nanofibers as a sort of binder. This proved more successful, creating a strong sheet that is mostly graphitized nanofibers. Applied Sciences is currently investigating the lithium ion application in an NSF program, with participation by General Motors.

B) APPLICATIONS DEVELOPMENT

1) A Coal Nanofiber/SiC composite

The monolith of coal nanofibers described in the Section A of this report was used as the starting material to make a composite. This disk, ~3" in diameter and 5mm thick, was infused with a commercial pre-ceramic organometallic for making silicon carbide (from the Starfire corporation), and the infused monolith was fired to 800^0C according to the manufacturer's directions to convert the liquid organosilicon to silicon carbide. After firing, it was found that the resulting disk of nanofiber-reinforced silicon carbide was about 15% smaller than the original disk. The infused disk had shrunk during the course of conversion to a SiC composite, but retained its shape. It is clearly not fully dense (density ~1.6 g/cc), but this was expected, as Starfire's instructions call for iterations of infusion/firing to achieve a fully dense SiC/carbon sample. We approached Applied Sciences with this information and furnished them a sample, because ASI was doing a project on SiC/nanofiber composites at the time. However, ASI chose not to engage us to pursue this approach, preferring their in-house strategy of infiltrating nanofiber compacts with SiO vapor.

2) Coal-Derived Papers as Electrochemical Capacitor Electrodes

Two types of coal electrochemical capacitor papers were prepared. One was simply made from the coal nanofibers alone, and the second was a 55/45 mixture of coal nanofibers and a high-surface-area mesoporous carbon made from coal by Prof. John Zondlo. Disks were punched out of each for testing as electrochemical capacitor electrodes. Sealed coin cells consisting of two identical electrodes wetted with sulfuric acid and separated by a polypropylene battery film were prepared, and these single-cell units were electrochemically evaluated.

The initial evaluation was done with cyclic voltammetry because our Impedance instrument was out for repair. This analysis showed that the coal nanofiber alone stored about the same amount of energy as their hydrocarbon analogs, about 29 F/g. The coal mixture showed a value of 105 F/g, and by back-calculating it was determined that the mesoporous coal powder showed ~200 F/g. This seemed too good to be true, and so the value was conservatively reported as >175 F/g at the May CPCPC meeting.

Subsequent impedance analysis showed that these energy values were indeed too high. It was found that the coal nanofibers are 24 F/g, the mixed electrode is 75 F/g, and the mesoporous powder alone is 140 F/g. Its easy to rationalize these discrepancies: Cyclic voltammetry does not discriminate between true capacitance and faradaic components, so that electroactive impurities in the material can skew the CV results too high.

To some degree, the energy discussion above is moot, because what really matters in electrochemical capacitors is power. Energy is only important if it can be delivered quickly. We find that the electrode made from 2 coal components (the mix of nanofibers and mesoporous powder) has excellent power. To quote the numbers here won't mean much to the average reader (a 4.2 mil thick electrode shows 75 F/g with a -45 deg phase angle of 35 Hz). However, this is comparable to the best carbon samples I've worked with over the past 5 years in terms of power. This electrode can release its energy in less than a tenth of a second, and it would be even faster if it were thinner. So it is a very respectable material, and the only question is whether the processing involved in making it and reducing its metallic impurities would render it too expensive.

One of the recent CPCPC proposals selected for funding is a University of Kentucky program that involves electrochemical capacitors. We have prepared all-coal capacitor electrodes like the ones mentioned above and furnished them to UK for inclusion in that program. These proved a bit too fragile because we incorporated a heavy powder content in them. Any additional samples that we provide for them will be furnished gratis, in the spirit of helping a fellow CPCPC member, but not a part of our own CPCPC project .

3) Nanofiber Paper as a Fuel Cell Catalyst Support

The data shown below is from a test of nanofiber paper as a methanol fuel cell anode. In this test, a methanol/water fuel mixture is fed into the fuel cell.

Three different anode configurations were tested in order to compare the effect of support material on methanol oxidation current. Each of the tests below used the standard 50:50 PtRu catalyst (Johnson Matthey). In all cases the catalyst was deposited by air spraying a solution of 12wt% Nafion ionomer and 80mg of PtRu suspended in 600μL of isopropanol. The different configurations are illustrated in the figure below.

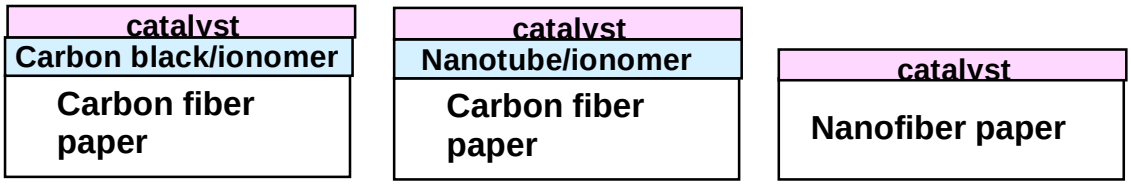

Configurations **A** and **B** used the Toray Carbon Paper (CP) (0.09 mm thickness, De Nora Inc.) as a support, whereas C used the nanofiber paper support.

Type **A** samples (corresponding to the traditional DMFC Nuvant standard [1-3]) were produced by spraying the Toray CP with a carbon black (Alfa Aesar)/Nafion ionomer solution, followed by drying, and subsequent deposition of the PtRu catalyst (4mg/cm^2).

In Type **B** samples the Toray CP was sprayed with a solution of single-wall carbon nanotubes (Carbon Nanotechnologies, Inc.) and Nafion ionomer (the nanotubes serving as an alternative to carbon black as a pore-filler and catalyst-support material), followed by drying, and subsequent deposition of the PtRu catalyst (.9mg/cm^2).

For Type **C** samples the PtRu catalyst was directly deposited onto the nanofiber paper (1.1 mg/cm^2).

Analysis by Scanning Electron Microscopy showed that in each case the surfaces were fairly uniform, and the catalyst well-dispersed. These samples were simultaneously evaluated for electrochemical performance towards MeOH oxidation in the commercial Nuvant test cell; a multi-array instrument that has been shown to yield data that correlate well with real fuel cell performance [1].

Samples prepared as described above were analyzed simultaneously in triplicates in order to determine their activity toward methanol oxidation. The test was run under half cell condition in which the anode array had 0.5M Methanol flowing over the backside of each anode at 8mL/min. The cathode had humid hydrogen gas at ~180sccm. Figure 1 shows Linear Sweep Voltammetry (LSV), at scan conditions of 2mV/sec over the voltage range 0 to 1.0V versus Dynamic Hydrogen Electrode (DHE).

It is seen in Figure 1 that the nanofiber electrode produces 16 times the current compared to the standard catalyzed Toray paper (the plot has been normalized for catalyst content. It also performs twice as well as the single-wall-nanotube-modified Toray paper at about the same catalyst content. This data has been reproduced in triplicate, and its standard deviation falls within 10% of the mean.

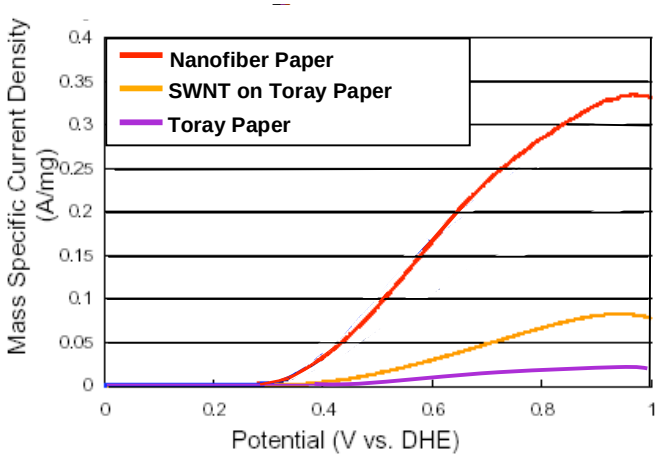

FIGURE 1. Comparative performance of different anode types in direct methanol fuel cell testing. The nanofiber paper (C) shows about 8 times the current compared to the Toray paper standard, an eight-fold improvement in catalyst utilization.

These results (obtained on conventional hydrocarbon-derived nanofibers) prompted us to test the coal-derived nanofibers in this application. The results (below) show that while a coal-derived nanofiber catalyst support gives about 2.5 times more current than the Toray paper standard (50 vs. 20 mA per mg catalyst), the hydrocarbon-derived nanofibers outperform them.

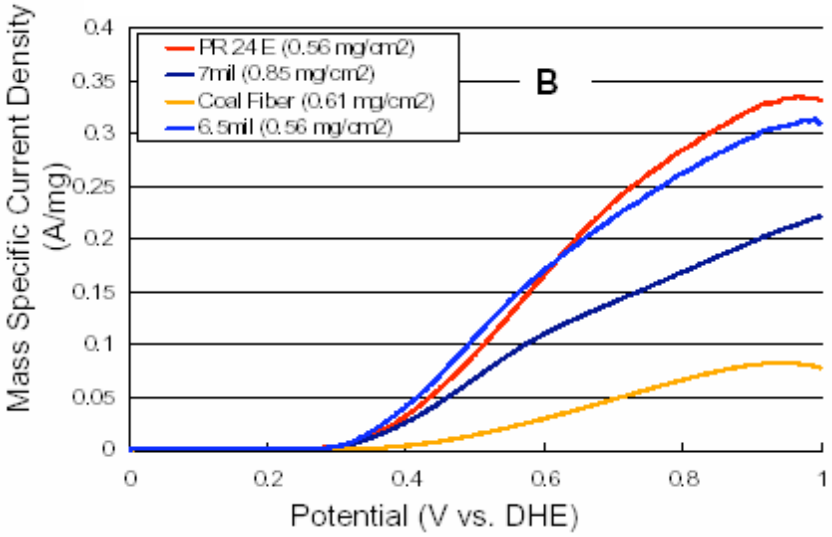

A Second Fuel Cell Application: Cathode for Oxygen Reduction

The cathode is the limiting factor in power output for a hydrogen fuel cell, so much so that the performance of a complete H2 fuel cell essentially mimics the cathode. Here we compare a commercial ELAT bi-layer support to the same material modified with a nanofiber paper layer. The same catalyst was applied in the same way to each sample, and the two samples were run at the same time in the same cell against a common anode.

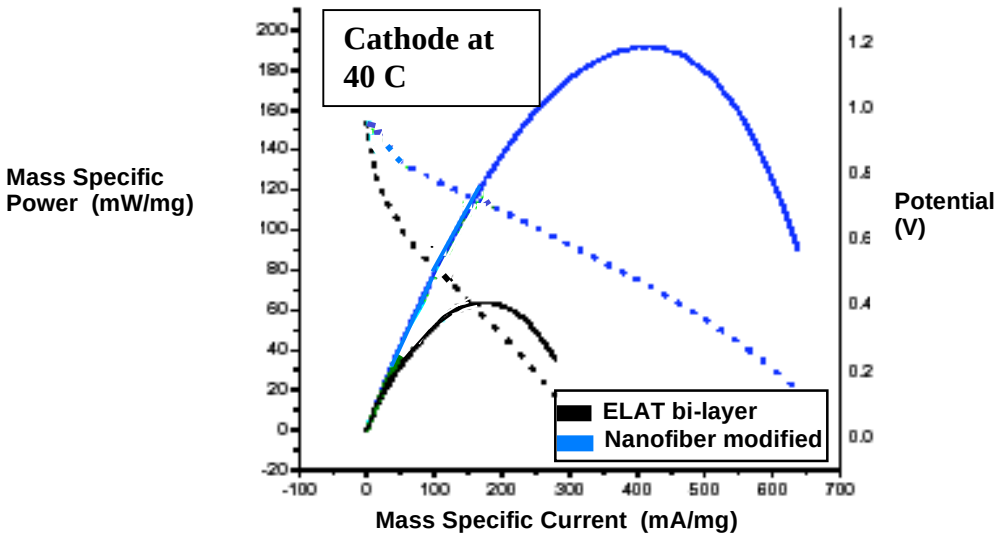

It is seen that the nanofiber material exhibits about 3 times the power output per gram of catalyst. This significant improvement was obtained using a hydrocarbon-derived nanofiber; the coal nanofiber (as currently produced) was not deemed pure enough to test. This data was taken at 40 C, and it was found that at 60 C the improvement dropped to a doubling of power. It seems that in fuel cells, everything works better at higher temperatures.

4) Nanofiber Paper EMI Shielding Data

One application for nanofibers is as an electromagnetic shielding material, in particular, a shielding layer that operates in a very high frequency range. There is currently a solicitation from the Dept of Defense to develop a composite material with carbon nanofibers for shielding in the 8-18GHz range. They ask for a shielding layer that is about 50 mils thick, which is thicker than the paper we typically make (at this thickness it is more like cardboard), but it is readily prepared.

To see if nanofiber paper works for this purpose, a few different varieties have been submitted to Wright Patterson Air Force Base for high-frequency shielding tests. The data shown below is typical of the data seen over the range of 8-12GHz.

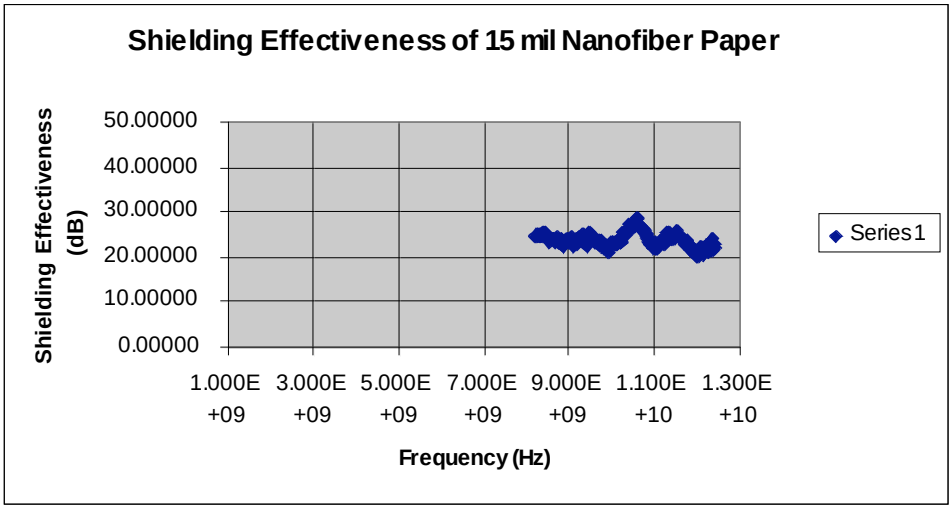

The Dept. of Defense is asking for a shielding level of 60dB for a 50-mil thickness, and this sample showed 24dB at a 15 mil thickness. Since shielding effectiveness goes up exponentially with thickness, it was thought likely that a thicker specimen will meet the 60dB goal. However, doubling the sample thickness gave no better result, which may be an artifact of the measurement method, since no good explanation for this behavior has emerged from colleagues who work in this area.

We considered making a composite version of nanofiber paper by incorporating fine-particulate thermoplastic into the paper as it was made (using the type of powdered polymer made for powder coating). However, a few conversations with the local Air Force and with a scientist from Boeing made it clear that end-users had their own in-house methods of introducing polymer, and so that effort was shelved.

In related work, an article from the University of Alabama has been published on the topic of using nanofiber paper for energy damping (4).

5) General Development Work

The strategy of incorporating finely-divided acetylene black as an additive to improve conductivity was examined. A 5% content of acetylene black produced a ~30% reduction in resistance, and a 20% acetylene black content produces an 80% reduction in resistance, while still allowing the formation of a freestanding sheet. This is a cheap way to enhance conductivity, and a sample of this higher-conductivity sample is currently being tested in a methanol fuel cell. Another method of making the sheet conductive (heat treating) makes the resulting sheet hydrophobic; a methanol fuel cell test with this material gave much poorer results compared to a standard sheet.

Another development activity involved treating the basic paper with a conductive polymer (polypyrrole) to enhance its conductivity. This approach works, but not any better than the acetylene black addition, and conductive polymers are expensive. Furthermore, the paper becomes brittle if the polymer is applied in large quantity.

C) Scale-up and Commercialization Activities

Large amounts of nanofiber feedstock are needed to pursue scale-up activities, and so a customized 50 liter reactor was purchased for preparative purposes. It is similar to the unit seen here, but with a larger volume and a high-horsepower stirrer to handle viscous solutions. This reactor was used during the CPCPC program to process 10 liter quantities of coal nanofiber papermaking feedstock, but it was not purchased only for the CPCPC program. We have accordingly included only ¼ of its cost in our upcoming CPCPC invoice.

Beyond the CPCPC work, this reactor's capacity supports the development activity of building a continuous papermaking machine. Our current plan is to contract Southeast Nonwovens in South Carolina to design and build a pilot-scale papermaking unit that would produce a nanofiber paper roll about 12"-16" wide. This size is large enough to produce an introductory commercial product. The development process that we go through as we build the unit will yield crucial information that could be applied to even larger scale-ups in the future.

We are currently seeking funding to pursue this venture, which we expect to take one year. Cost estimates have been developed, and a confidentiality agreement with Southeast Nonwovens is in place. We have met with Southeast Nonwovens at their plant in South Carolina and discussed the project.

One key component of a successful unit will be the forming sheet. It needs to have the right sheet-release properties, sufficient durability, and appropriate pore size. It also has to be commercially available in a length and width that will allow its use on a continuous manufacturing line that makes a sheet at least 14" in width. During this program we examined numerous polymer membranes and nonwovens from different manufacturers. These all had different advantages and disadvantages- some gave great release but made a non-uniform paper. Some filtered too slowly, while others allowed nanofibers to permeate into the membrane. After many failures, we tried to adapt some underperforming materials by using a double thickness of a durable roll-stock filter material to even out the inhomogeneities in filtration. But this unsatisfactory solution was later abandoned when we finally found a suitable material, whose identity we consider proprietary.

Consult with Commercial Papermaker

Discussions were held with a commercial papermaker (Hollingsworth and Vose) at their R&D unit in Massachusetts. The purpose of the visit was to establish a relationship with this specialty paper manufacturer as well as developing insight into tailoring our process

for compatibility with standard manufacturing methods. This company is a potential licensee for making nanofiber paper, and they generously offered tips to further develop the process. They suggested specialty binders suitable for carbon nanofibers, furnished references to small developmental facilities, and provided a tour of their wet-laid pilot operation. The pilot unit is currently used for glass-fiber papermaking, but it would be suitable for the process used with nanofibers.

Conclusion

The limiting factor on the development of coal-derived nanofiber papermaking is the present state of coal-nanofiber production. Applied Sciences has made a limited quantity of nanofibers from a gasified coal feedstock, with no plans to continue that work unless there is support for more development. They are currently pursuing a large Ohio initiative that will integrate their nanofiber production with a fuel source from a coal-burning power plant. If they can successfully refine that fuel so that they can make an exact duplicate of the nanofibers they currently make from hydrocarbons, it will make sense to revisit coal-derived nanofiber applications development.

This CPCPC program has shown that carbon nanofibers can be used in a number of applications, and that paper made from nanofibers (coal-derived or otherwise) can be made in a variety of ways (with either binders or a reinforcing scrim) and scaled up to a continuous production process. In applications requiring high purity (such as fuel cells or electrochemical capacitors), a coal-derived nanofiber paper may not be as suitable as one made from hydrocarbons. But for composites or EMI shielding, coal derived nanofiber papers could represent a less expensive and equally effective option.

The promise of carbon nanofibers is clear, and the ability to add value to them by making them into a paper is a good step towards mainstream introduction. The scale-up activities done during this program have solved most of the problems associated with creating a continuous papermaking machine that can make nanofibers a cost effective material available in significant quantity. The identification of a moving filtration medium suitable for this unit was a key accomplishment of this project- it establishes the feasibility of creating a papermaking machine, which we now anticipate building. In the interim, our company will begin selling nanofiber paper at our website that will shortly be operational, at inorganicspecialists.com.

References

1) Carbon, Electrochemical and Physiochemical Properties, Kim Kinoshita, Wiley Interscience (1988).
2) Introduction to Nonwovens, Albin Turbak, Tappi Press (1998).
3) Chan, B., et al., *Comparsion of High-Throughput Electrochemical Methods for Testing Direct Methanol Fuel Cell Anode Electrocatalysts.* J. Electrochem. Soc., 2005. **152**(3): p. A594-A600.
4) Jihua Gou et al, *Journal of Nanomaterials*, Vol 2006, Article ID 32803 (2006).

"TiO_2-Coated Activated Carbon"

Final Report

Reporting period start: March 2005
Reporting period end: September 2006
Principal Author: David W. Mazyck
Date report issued: September 30, 2006
DOE Award Number: 2871-UF-DOE-1874

Submitting organization:

University of Florida
PO Box 116450
Gainesville, FL 32611

DISCLAIMER

ABSTRACT

During Quarter 1, several coal-based sorbents were coated with TiO_2 using a boil deposition procedure to determine if the physical and/or chemical properties of these sorbents impacted photocatalysis of phenol. It was hypothesized that as the conductivity of a sample increased, so would photocatalysis. Another variable of interest was to assess if the ash content of the samples impacted photocatalysis. Results showed that as the ash content of the samples decreased, the rate of photocatalytic oxidation increased.

During Quarter 2, additional batch photocatalysis studies and characterization of the samples were completed. The objective was to learn what constituents of the ash might be responsible for enhancing photocatalytic oxidation of phenol. The results were inconclusive, for the overall performance of the various samples tested under a variety of conditions did not result in performances that were notably different.

During Quarter 3, the focus switched from lower surface area carbons to commercially available carbons to investigate the impact morphology, conductivity, and carbon precursor had on phenol removal. All three variables proved to be important variables.

During Quarter 4, the focus of the research was on the efficacy of using the TiO_2-activated carbon in an in-situ regenerative system whereby the TiO_2-activated carbon would adsorb phenol and then, once exhausted, be exposed to UV irradiation to regenerate the activated carbon surface. Results indicated that this approach was plausible, but the mechanism of regeneration is first desorption of the phenol proceeded by oxidation.

TABLE OF CONTENTS

LIST OF TABLES

LIST OF FIGURES

EXECUTIVE SUMMARY

The ultimate goal of the proposed research program was to develop a cost-effective and reliable air emission control system. The focus of the research was the manufacture and testing of a composite material consisting of activated carbon coated with a photocatalyst, titanium dioxide (TiO_2); herein referred to as titania-coated activated carbon. Activated carbon has been shown to be effective in removing synthetic organic chemicals (SOCs), volatile organic compounds (VOCs), and hazardous air pollutants (HAPs) from various sources, and its effectiveness is attributed to its high surface area (e.g., typically greater than 600 m^2/g) and tunable surface chemistry. Despite its ability to effectively adsorb organic compounds, activated carbon does have a finite service life, and, once exhausted, regeneration is necessary to return it back, or as close as possible, to its initial capacity. The proposed system accomplishes regeneration by photocatalytically oxidizing sorbed pollutants via irradiation of the TiO_2 coating. While the applications for air treatment are clear, of equal importance is its use in the purification of water where traditional treatment practices are unacceptable (e.g., space missions, military maneuvers, developing nations, disaster response, etc.). Therefore, this research contributed to the CPCPC mission through the development of a premium material manufactured from coal suitable for solving a plethora of environmental problems.

The objectives of the research program were:

Objective 1: Identify why the adsorption/oxidation behavior of irradiated titania-activated carbon composites differ depending upon the core carbon material, as shown in previous studies.

Objective 2: Develop and optimize a titania coating procedure that (a) uniformly coats the carbon and (b) does not hinder adsorption.

Objective 3: Apply the fundamentals learned from Objectives 1 and 2 to produce a coal-based titania-activated carbon (coal raw material collected from West Virginia from a prior CPCPC project) to demonstrate the efficacy of commercialization.

Research activities focused on fundamentally understanding the 3 objectives. A host of analytical techniques were employed to quantify carbon's characteristics that explain why one particular carbon worked better than others. Afterwards, three titania coating strategies were employed and the resulting titania-activated carbons were characterized. Finally, titania-activated carbons manufactured from West Virginia coal were produced to demonstrate the efficacy of manufacturing possibilities.

INTRODUCTION

Currently, various volatile organic compounds (VOCs) and hazardous air pollutants (HAPs), for example methanol, formaldehyde, acetaldehyde, and methyl ethyl ketone (MEK), are emitted into the atmosphere from industrial sources such as pulp and paper mills and the automotive industry. The Environmental Protection Agency (EPA) has mandated that these industries develop and implement air emission control strategies by December 2006 to control the current release of these potentially harmful organic chemicals.

The goal of the proposed research program herein is to develop a cost-effective and reliable air emission control system. The focus of the research is a composite material of activated carbon coated with a photocatalyst, titanium dioxide (TiO_2); herein referred to as titania-coated activated carbon. Activated carbon has been shown to be effective in removing SOCs, VOCs, and HAPs from various sources, and its effectiveness is attributed to its high surface area (e.g., typically greater than 600 m^2/g) and tunable surface chemistry. For example, the Department of Defense chose to use activated carbon to remove VOCs and HAPs, such as MEK and methyl isobutyl ketone (MIBK), from military paint spray booths in Barstow, CA (Cannon et al. 1996). Despite its ability to effectively adsorb organic compounds, activated carbon does have a finite service life, and, once exhausted, regeneration is necessary to return it to (or as close as possible to) its initial capacity. Typically, regeneration is performed ex-situ by exposing the carbon to high temperatures in an oxidizing environment. To minimize the down time due to regeneration and lower the energy requirements and costs associated with ex-situ regeneration, a goal of this work is to coat the activated carbon with a photocatalyst and use UV light to regenerate the carbon in-situ. In traditional thermal or microwave regeneration, pollutants are simply desorbed. Regeneration in the proposed system is achieved by photocatalytic oxidation of pollutants (Sadeghi et al. 1996; Wu et al. 1998), thus no post-treatment is needed for desorbed pollutants. Additionally, titania can photocatalytically oxidize high molecular weight organics, hence preventing the glazing coating problem commonly encountered in an adsorption bed (Fujii et al. 1997).

Many researchers (Torimoto et al. 1996, Tryba et al. 2003, Tsumura et al. 2002), including some preliminary studies by the PI (Khan et al. 2002), have focused their attention towards titania-coated activated carbon. However, even though there is great interest in this composite material and there are numerous applications for this technology, to the PI's knowledge, titania-coated activated carbon is currently not manufactured by any carbon manufacturer throughout the world. This is likely true because (a) carbon properties (e.g., surface chemistry, pore size distribution, ash content, etc.) that are best suited for this application are unknown, (b) the coating techniques discussed in the literature lack details, thereby preventing reproducibility, and (c) there is not a full understanding of how to design a system that could utilize this composite. Therefore, this work set out to solve the first two of these fundamental questions.

EXPERIMENTAL

Pitch coke, graphite, anthracite, and lignite samples were collected from Asbury Graphite Mills, Inc. and were subsequently coated with titania. These materials were chosen because of their variation in electrical conductivity and low surface area. Low surface area was desired because it was of interest to investigate just photocatalysis versus photocatalysis and adsorption. Table 1 lists the BET surface areas, carbon content, ash content, and relative conductivity for each sample.

Table 1 - Comparison of raw material properties.

Sample	Carbon Content (%)	Ash %	Density[1] (g/mL)	Conductivity[2] (S/cm)	BET Surface Area (m^2/g)
Pitch Coke	93.5	6.5	2.13	331.7	<10
Graphite	99.4	0.6	2.51	197	<10
Anthracite	89.7	10.3	1.85	50.4	<10
Lignite	74.3	25.7	1.76	NA	<10

[1]When coated with 3% by mole TiO_2
[2]Literature derived values

TiO_2 Coating Procedure:

The carbons were coated with TiO_2 via the following procedure:

1. The sample is first washed with DI water.
2. The sample (approximately 2-4 grams) along with the TiO_2 (3% by mass) is placed in a 250 mL Erlenmeyer flask. Adding the TiO_2 on a mole basis was also investigated.
3. Approximately 200-220 mL of DI water is poured into the Erlenmeyer flask.
4. The mixture is then placed on a hot plate and allowed to boil until all the water has been evaporated.
5. The flask is then placed in an oven (105 ºC) for at least 12 hours to remove any residual water that may be present.

Phenol Batch Photocatalytic Oxidation Studies:

Mass Basis: During the boil deposition step, the TiO_2 was added to the carbon so that its mass was 3% of the mass of each of the carbons used. After the boil deposition step, 80 mg of each carbon which was now coated with 3% (w/w) of TiO_2 was placed in its respective reactor. The reactors consisted of 100 mL syringes. In addition to the TiO_2 carbons, 80 mL of phenol solution (~ 60ppm) was also added to each reactor. The reactors were then supported on a rotator capable of supporting 4 reactors at a time. The entire setup consisting of the reactors and the rotator was surrounded by 3 UV lamps (365 nm), 120° apart which were at a minimum distance of 1 cm from the reactors.

Experiments were carried out for 24 hrs after which the final concentration of phenol in each reactor was determined via GC/MS. Similar experiments were also carried out without the presence of UV in order to observe the amount of pure adsorption of phenol to each sample.

Mole Basis: For coating the carbon with TiO_2 on a mole basis, the amount of elemental carbon (C) in each sample was found (Table 1) by performing an ash analysis in which the carbon samples were heated to 575 – 600 °C for 4 hours . The difference between the initial mass and the final mass (of the ash) provided the amount of elemental carbon in each sample. With the amount of carbon per sample known, the carbon samples were coated with TiO_2 by the boil deposition procedure introduced above. However, the samples were coated on a mole/mole basis. Hence, each carbon was coated with TiO_2 such that the number of moles of TiO_2 was 3% of the number of moles of elemental carbon in the sample. This was done to normalize the carbon to titania ratio in each sample. Another difference in this experiment was the fact that the TiO_2 coated carbons were added to the reactors on a volume basis as opposed to a mass basis. Hence, each reactor contained 0.05 mL of the respective sample as opposed to a fixed mass. The remainder of the experimental procedure remained the same as above.

The pitch coke, graphite, anthracite, and lignite samples that were collected from Asbury Graphite Mills, Inc., and were subsequently coated with titania. These materials were chosen because of their variation in electrical conductivity and low surface area. Low surface area was desired because it was of interest to investigate just photocatalysis verses photocatalysis and adsorption. Table 1 lists the BET surface areas, carbon content, ash content, and relative conductivity for each sample.

RESULTS AND DISCUSSION

Preliminary research with activated carbon manufactured from different coal precursors demonstrated that the oxidation of phenol was quite different for each sample. However, because it was not possible to separate whether the phenol was simply being adsorbed or adsorbed and oxidized in these previous studies, it was desired to study the raw materials that were used to create the activated carbons. Using the bituminous coal and anthracite coal samples that were coated with TiO_2 (3% by wt), they were tested for their ability to oxidize 60 ppm of phenol over 24 hours. Figure 1 demonstrates that the titania-coated bituminous coal performed significantly better than the anthracite coated sample. Also included is how the bituminous coated sample performed in the absence of UV (i.e., adsorption only). The data indicates that very little of the phenol removal can be contributed to adsorption.

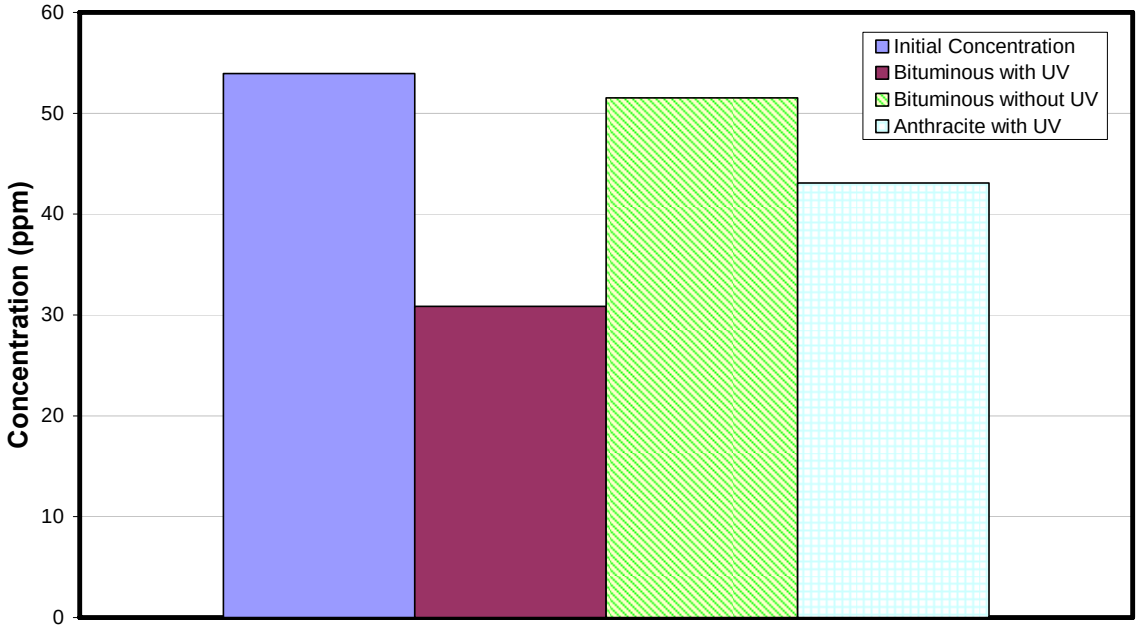

Figure 1 - Comparison of selected samples for oxidation of phenol when coated with 3% TiO_2 (wt/wt) and added to the phenol solution on a mass basis.

Because the densities of the samples are different (Table 1), it was of interest to compare the photocatalytic effectiveness of the samples when they were coated on a molar basis and added to the water volumetrically versus gravimetrically. Figure 2 plots the percent removal via photocatalysis for the pitch coke and graphite samples, and although not shown the performance of the anthracite coated sample was very similar.

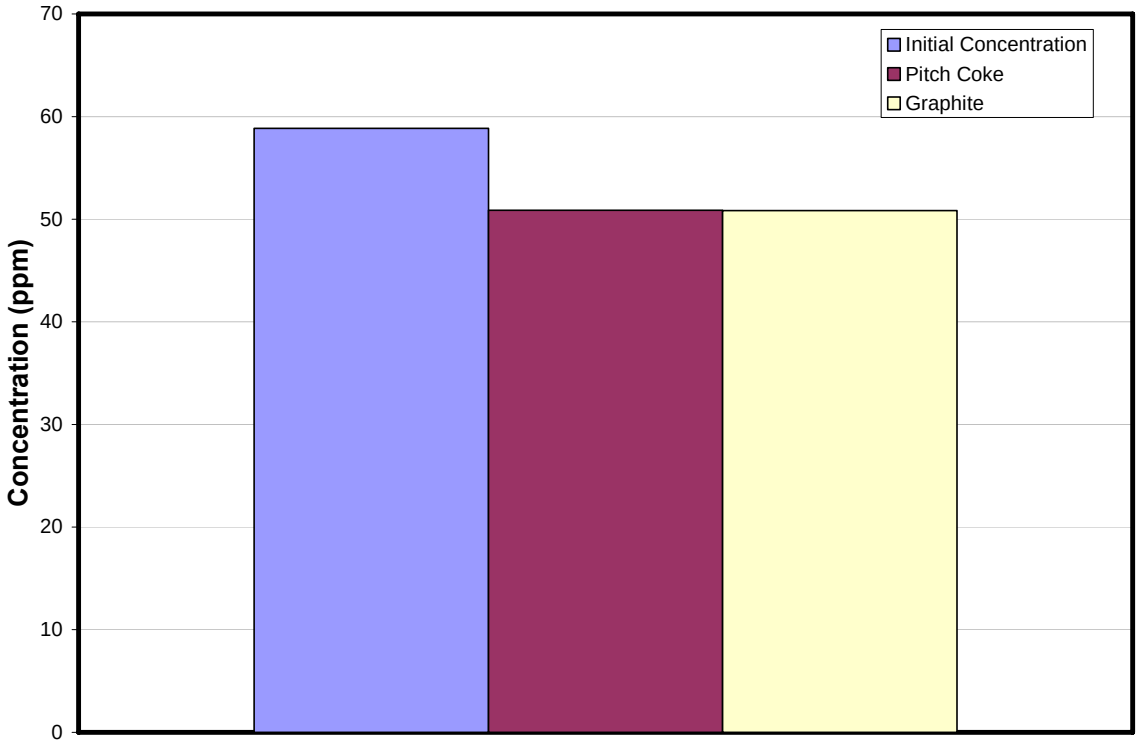

Figure 2 - Comparison of pitch coke and graphite coated with 3% (by mole) and added to the phenol solution on a volume basis.

Figure 2 suggests that the conductivity of the samples does not impact photocatalysis. However, the initial concentration of phenol is quite high and may be overwhelming the TiO_2.

Another variable of interest was the ash content of the samples. Pitch Coke, which had an approximate ash content of 7%, was acid washed with nitric acid for 1, 3, and 5 hrs. As the time increased, the amount of ash removed would also increase. Figure 3 demonstrates that slight improvements were realized as the ash content was removed from the sample.

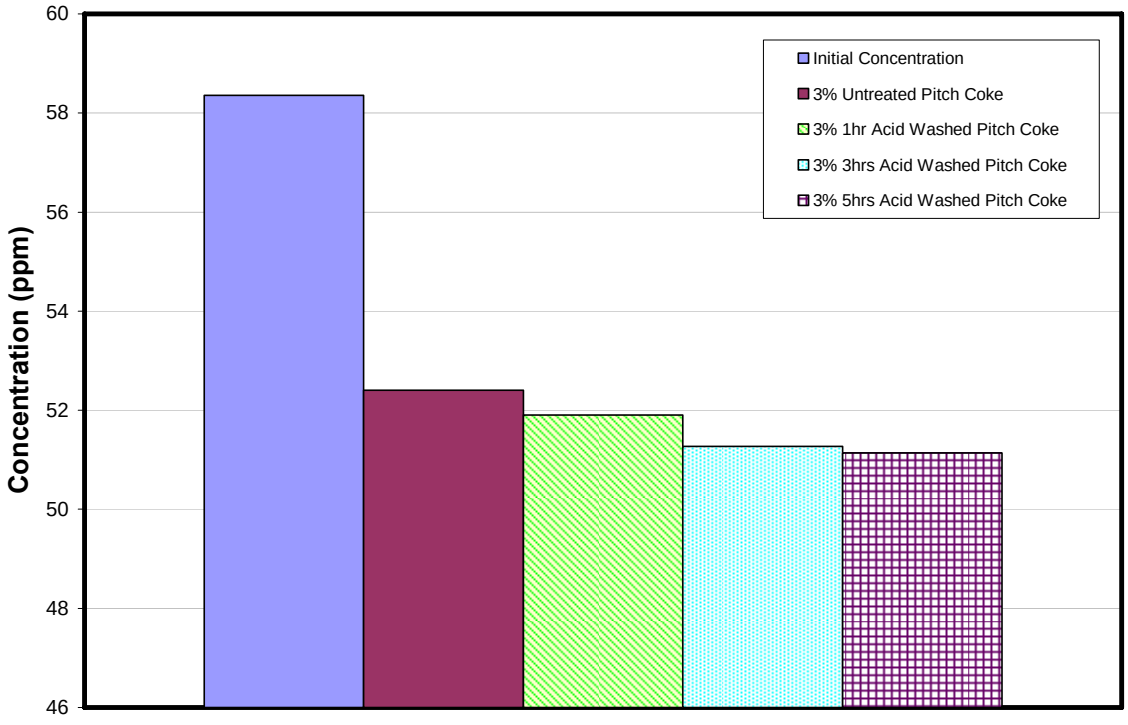

Figure 3 - Comparison of pitch coke samples that have been acid-washed for various times.

During first quarter activity, high carbon content materials (e.g., bituminous coal, anthracite coal, and pitch coke) were coated with TiO_2 and subsequently tested for their ability to oxidize phenol (ca. 55 mg/L) via photocatalysis. During the second quarter, similar batch studies were undertaken.

The multitude of variables observed in the performance of activated carbons (ACs) with respect to adsorption and photocatalysis led to the investigation of carbon substrates having low surface areas in order to separate adsorption affects from other carbon properties that may impact photocatalysis. By selecting a variety of carbons with different properties that were hypothesized to be conducive or inhibitive to photocatalysis, it would be possible to relate these specific properties of the carbons to the synergy observed with some activated carbons. As hypothesized by Khan (2003), the reason for the superior photocatalytic performance of certain titania-coated ACs is the presence of ionic metals. These metals act as electron sinks, which hinder electron-hole recombinations, thus enhancing photocatalysis. As interpreted by this author, enhanced photocatalytic activity is a function of electrical conductivity primarily due to specific sites on the carbon surface where metals are present. In theory, the presence of titania in the vicinity of a conductive site (metal) will result in a favorable difference in Fermi energies between the titania and the metal. The resulting effect is the change in the distribution of electrons of the semiconductor (titania). The formation of the Schottky barrier will cause the migration of electrons from the titania to the metal, increasing the electron-hole recombination times and therefore enhancing photocatalysis. Thus, to further test whether conductivity and metals play a role in enhancing photocatalysis, low surface area carbons (< 10 m^2/g) with varying conductivities were chosen.

It should be noted that, in general, the addition of conductive materials to semiconductors or insulators has a positive impact on their conductivity. This property may be approximated as a summation of the conductivities of the materials involved. However, at the same time, it is important to note that metals content is by no means the sole factor influencing electrical conductivity. In the case of graphite, a major influence of its electrical conductivity is its crystalline structure. Crystalline graphite consists of parallel sheets of carbon atoms, each sheet containing hexagonal arrays of carbon atoms. Each carbon atom exhibits sp^2 hybridization and forms sigma bonds with its three nearest neighbors. There is also distributed pi bonding between the carbon atoms in the sheet. This delocalized pi system is responsible for the electrical conductivity of graphite. The disruption of this graphitic structure is the cause for a loss in electrical conductivity in carbonaceous materials.

With this in mind, carbon materials having varying electrical conductivities were selected. The carbons selected for the studies were graphite, pitch coke, bituminous coal and anthracite coal. The gradient in electrical conductivity between the selected carbons, graphite being the highest and bituminous the lowest is shown in Table 2. These conductivities were measured as resistivities by compacting the carbons in a column at pressures between 125-150 psi and measuring their resistivity to charge (Data provided by Asbury Carbons, NJ). Hence the resistance of the compacted powdered carbons was measured and obtained, which was then easily translated to electrical conductivity by the reciprocal of the resistivity.

Table 2 - Electrical conductivity values for low surface area carbons

Carbon	Conductivity ($m\Omega^{-1}cm^{-1}$) (mho)
Graphite	20-50
Pitch Coke	~ 10
Anthracite	0.001-0.01
Bituminous	< 0.001

Metals Content of Low Surface Area Carbons

Before discussing how the titania-coated low surface area carbons performed for phenol adsorption, it was of interest to also investigate the ash contents of these samples. To determine if conductive metals were indeed present in any of the carbons, an EDS study was performed. Prior to that, the quantity of ash for each carbon was determined. This would enable us to analyze the EDS scans with more perspective. The ash contents of the low surface area carbons are provided in Table 3.

Table 3 - Elemental carbon and ash contents of low surface area carbons

Carbon	Elemental carbon (%)	Ash (%)
Graphite	99%	1%
Pitch coke	93%	7%
Anthracite	90%	10%
Bituminous	65-72%	28-35%

EDS scans of all the carbons were performed with the exception of graphite. The electrical conductivity of graphite is extremely high and its ash content is negligible. Hence, the amount of impurities found in graphite (metals) would be negligible and would not make any significant difference. However, it is interesting to see whether the conductivity due to its structure plays a role in photocatalysis.

The EDS scan of the ash residue of the anthracite coal is shown in Figure 4. It shows prominent peaks corresponding to aluminum and iron. These metals have very high electrical conductivities (376/mohm-cm and 102 /mohm-cm respectively) as compared to titanium (23 /mohm-cm). A smaller peak of sodium is also seen. Another peak present is that of silicon (electrical conductivity of silicon = 0.012 /mohm-cm). A number of such EDS scans were taken, all of which showed similar results.

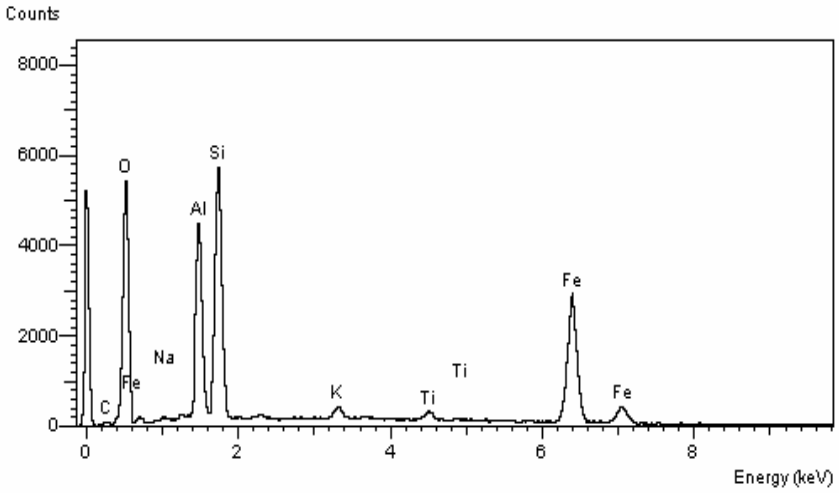

Figure 4 - EDS scan of ash residue of uncoated anthracite coal

Again, it must be noted that EDS is by no means a quantitative analytical tool and is at best semi-quantitative. However, the images do show a greater prominence of some elements over others.

Figure 5 shows an EDS scan of the ash residue of bituminous coal. The image shows a prominent aluminum peak. In addition to this, smaller peaks of iron, calcium, magnesium and sodium are also seen. Again, as in the case of anthracite, a silicon peak is noticed.

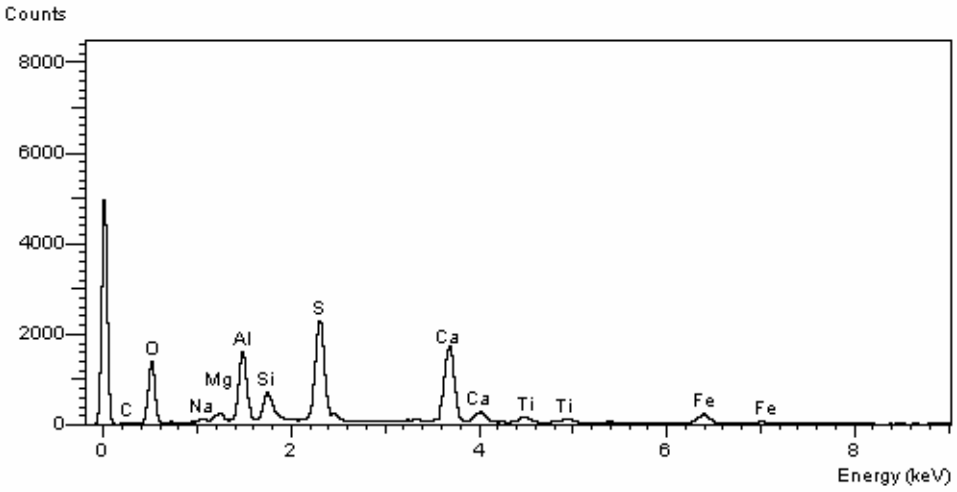

Figure 5 - EDS scan of ash residue of uncoated bituminous coal

Although anthracite and bituminous are low conductivity carbons, the presence of metals such as aluminum and iron means that there is a high probability of a number of conductive sites on the surface of these carbons. The amount of ash contained in these carbons (10% and 28-35%, respectively) also points towards there being a relatively large amount of these metals in these carbons.

A similar scan was performed on the ash of pitch coke (Figure 6). Small peaks of aluminum and silicon in addition to small peaks of sodium and sulfur are seen.

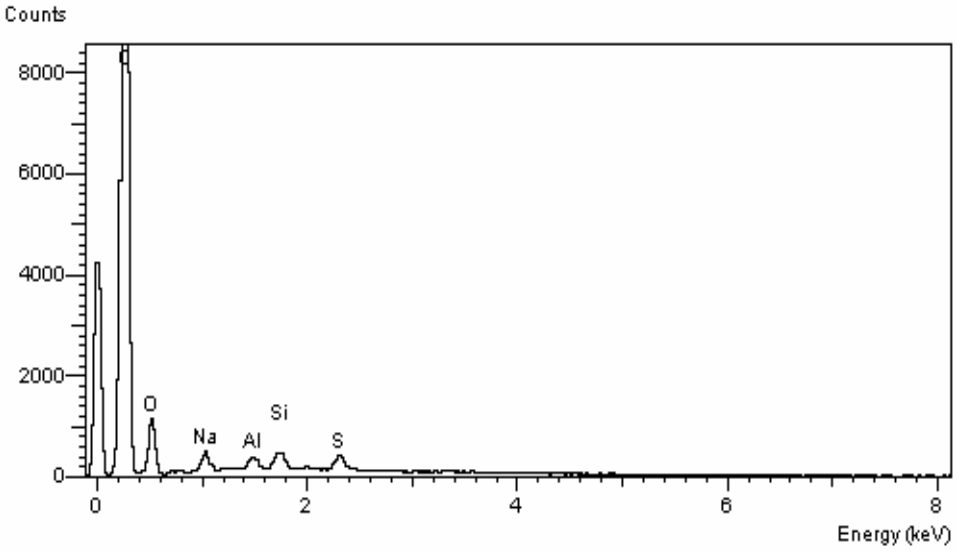

Figure 6 - EDS scan of ash residue of pitch coke

From the EDS scans of the low surface area carbons, it is evident that aluminum is commonly found in each of the carbons. A very prominent iron peak is seen in anthracite coal with the bituminous sample also showing some presence of iron. Recalling the study by Khan (2003), which hypothesized metals (specifically iron) to be the cause of increased photocatalysis, it may be expected that anthracite and bituminous should show the greatest removal when the carbons are subjected to batch adsorption-oxidation studies.

Batch Studies with Low Surface Area Carbons

Batch studies were performed with low surface area carbons. The carbons used were sieved to 35 x 200 in order to normalize the external surface area of the carbons. Titania was coated on the ACs via boil deposition (3% by mass). A mass of 80 mg of each sample was used with 80 mL of 55 ppm phenol solution.

Adsorption studies performed on coated low surface area carbons in the dark

In order to verify the negligible adsorption capacity of the carbons, equilibrium adsorption studies were performed on each carbon using a batch reactor in the absence of UV light. In addition to the carbons, a titania (Degussa P25) slurry was also tested as a comparison to the coated substrates. The titania was weighed such that its mass was equal to the theoretical mass of the titania on the surface of the carbons (3% of 80 mg, i.e., 2.4mg). It was expected that all the samples including the titania slurry would show negligible adsorption. Figure 7 shows the results of the adsorption studies.

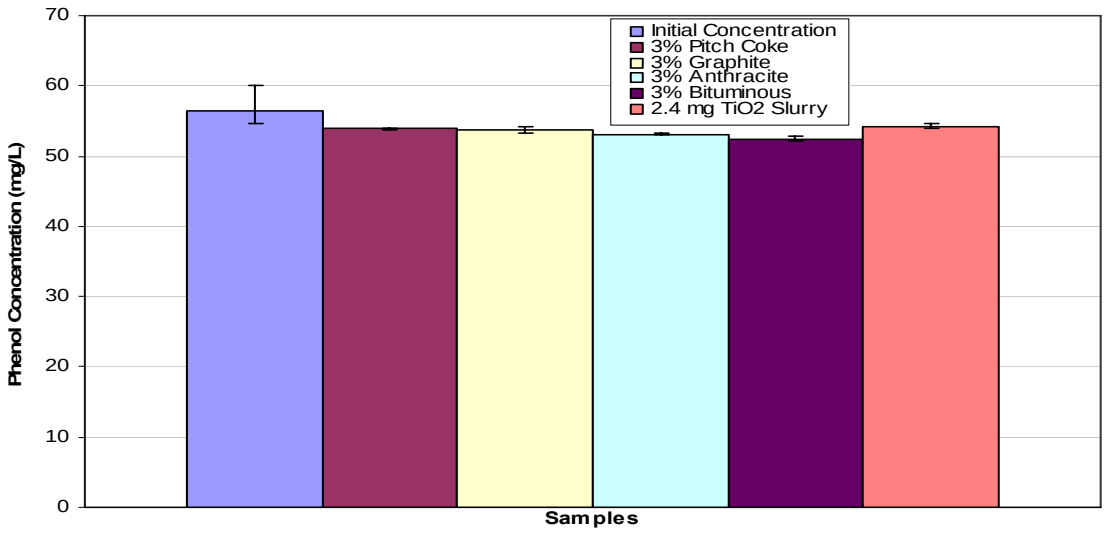

Figure 7 - Adsorption studies of coated low surface area carbons and titania slurry

The adsorption seen in each of the carbon samples including the slurry is negligible. In fact, the maximum removal seen is only 4.6%. This emphatically proves that the carbon composites are indeed of low surface area, incapable of any significant adsorption.

Photocatalysis studies performed with coated low surface area carbons

The carbons and the titania slurry were then made to undergo photocatalysis studies. Using an identical configuration, the samples were exposed to 365 nm UV light. It was expected that carbons containing a larger concentration of metals in their matrices would perform better than those with a lower content of metals (Khan, 2003). Although all the carbons with the exception of graphite contained a considerable amount of metals, due to the presence of metals and the relatively high natural conductivity of pitch coke, it was expected to perform better than the other carbon composites. Due to better mass transfer, the titania was also expected to perform relatively well. The results of the experiment are shown in Figure 8.

Although there was little distinction in the performance of the carbons, the titania-coated bituminous coal showed the greatest removal of 20%. Anthracite coal with 18% removal also performed relatively well. Pitch coke, which was expected to perform well, only removed 6% of the phenol. The graphite, which is the most electrically conductive although lacking in ash content, showed a removal of 13%. However, a surprising result was that of the titania slurry which only accounted for 11% removal. This was attributed to a reduction of the surface area of titania available for irradiation. It was thought that the amount of titania loaded was too high.

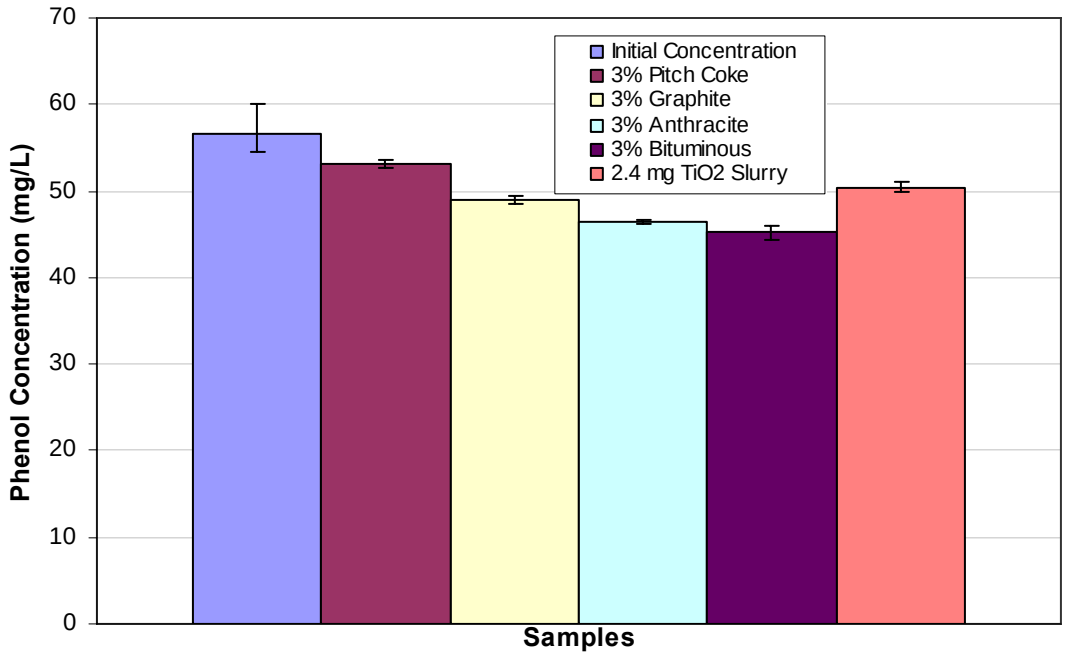

Figure 8 - Batch photocatalysis studies of carbons and titania slurry (m/m)

Hence for the specific configuration of the reactor, the titania concentration in the slurry was greater than the optimal loading, causing low penetration of UV through the slurry.

Comparing the oxidation studies to the adsorption studies in the absence of UV, it is evident that there is photocatalysis taking place. A comparison between the carbon-titania particles shows no trend with respect to conductivity or metals content in their ash residues. However, a trend was noticed in the difference in performances being similar to the carbons' differences in densities. Due to this, the volume of carbons and hence the amount of titania in each reactor would be different. Higher density would result in a smaller volume of that particular carbon resulting in a lower titania dose in the respective reactor. Table 4 summarizes the densities of the coated carbons.

Table 4 -Average densities of 3% (m/m) titania coated carbons

Carbon	Density g/m^3
Bituminous	1.37
Anthracite	1.93
Pitch coke	2.25
Graphite	2.58

From Table 4 it can be seen that bituminous coal and anthracite coal are the two carbons with the least density. This difference in density is reflected in the difference seen between the performances of the carbons. Since the adsorption capacities for all the carbons were negligible, the coated carbons were loaded on the basis of volume in order to normalize the volumes and titania loaded to each reactor. This was expected to

magnify differences in phenol decomposition between the carbons. The following graph shows the results of the batch studies in which the carbons were coated with titania on the basis of mass and loaded to the reactors such that their volumes equaled 0.05 mL. This set, shown in Figure 9, is referred to as 'mass-volume' or 'm/v'.

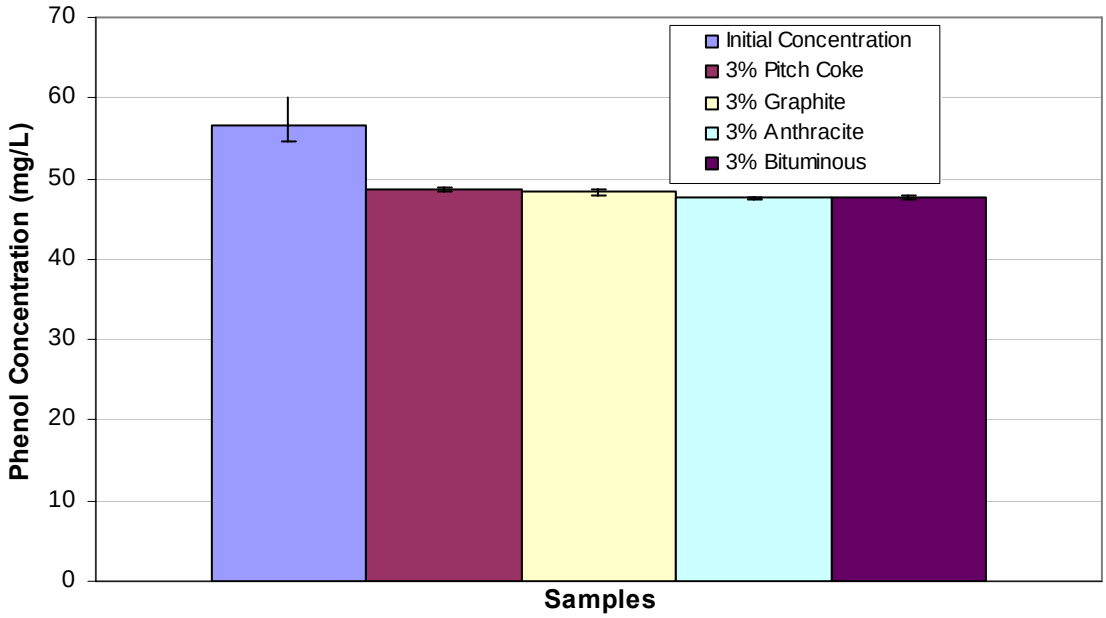

Figure 9 - Photocatalysis studies of titania-coated low surface area carbons in the presence of UV (m/v)

To further verify these results and normalize the amount of carbon and titania in each reactor, tests were performed using a molar basis for coating the carbons with titania. This basis consists of coating the carbons such that the mole ratio of titania to carbon is 3%. The carbons were then loaded to their reactors on the basis of volume as in the earlier case (0.05 mL). This set of samples has been referred to as 'mole-volume' or 'mol/v'. The results from these tests which were otherwise performed in an identical manner to the previous batch tests are shown in Figure 10. For the mass-volume and the mole-volume sets, it was deemed unnecessary to perform control studies in the absence of UV light as the carbons contained no internal pore structure. Hence, a higher concentration of TiO_2 coated on the carbon surface would not make any noticeable difference to adsorption. The results from these tests showed a slight increase (less than 2%) in the photocatalytic degradation of phenol. However, this was seen in all the samples, resulting again in no significant distinction between the samples.

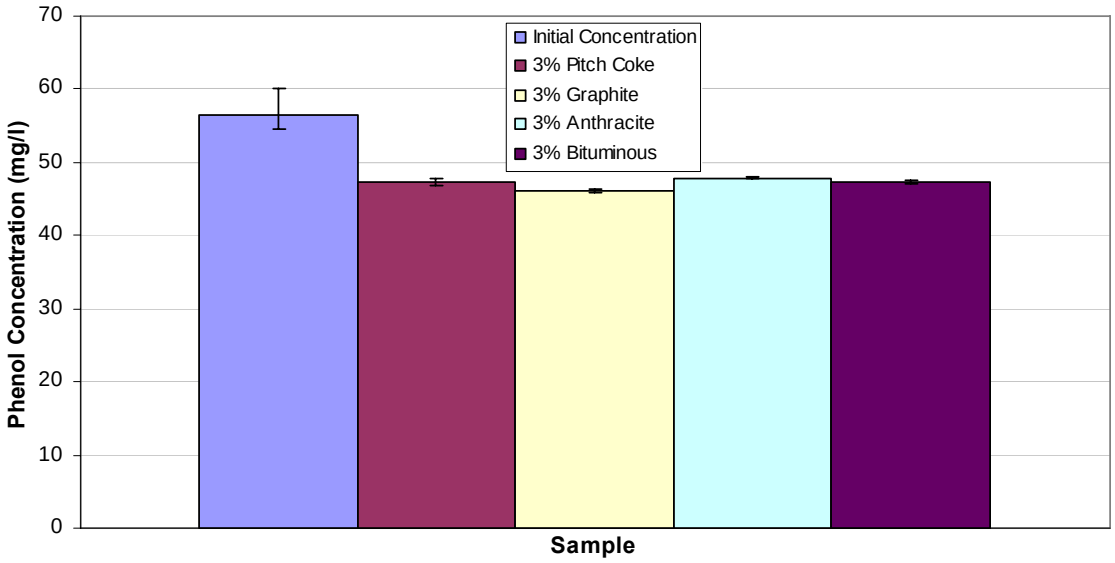

Figure 10 - Photocatalysis studies of titania-coated low surface area carbons in the presence of UV (mol/v)

The influence of metals on photocatalysis was also questioned as clearly, there was no distinction seen in photocatalysis between the carbons even though they differed in the content and composition of metals. It may be noticed that the performances of the ACs with the exception of the 'mole-volume' samples which showed a slight increase in performance, remains relatively constant. The only considerable distinction can be made in the case of the 'mass-mass' carbons. However, this has been explained by the differences in their densities. It is evident from these studies that when titania is coated on a substrate such as carbon, adsorption plays a very important role. More importantly, what is shown by the low surface area carbon tests is that as previously hypothesized by this author, conductivity may not play any significant role in the enhancement of photocatalysis. Even though carbons were selected whose conductivities varied by orders of magnitude, there was no significant effect or even any trend that was noticed in the performance of the titania-coated carbons. Hence, the conclusion by Khan (2003) about metals such as iron enhancing photocatalysis due to their role as electron traps is uncorroborated. At the same time, the theory by Matos et al. (2001) regarding the synergy seen in the case of titania systems containing H-type ACs is also unsubstantiated.

Furthermore, the experiments conducted with the AC composites and the low surface area carbonaceous composites show that a slight synergy may be noticed in titania-AC composites, primarily driven by adsorption. The difference in the electrical conductivities of the low surface area substrates did not show any considerable synergy.

Evaluation of Carbon Coating Strategies

Titanium dioxide was coated on the activated carbons using 4 different coating techniques: boil deposition, pore volume impregnation (PVI), chemical attachment, and mechanical attachment.

Boil deposition was by far the easiest and most convenient coating technique as it required using a commercially available TiO_2 (Degussa P25), water and heat. It was nevertheless a very inconsistent and unpredictable coating method as the TiO_2 deposited not only on the AC but also on the beaker in which it was being carried out. Therefore, although a known mass of titania was used in the coating process, the actual amount of TiO_2 deposited on the carbon was likely less than the targeted value. The average phenol removal observed for HD4000 coated with titania was 78%.

Pore volume impregnation resulted in the immobilization of the TiO_2 within the pores of the AC. The titania depositing in the pores of the ACs was considered a disadvantage for this coating technique, particularly due to the opacity of activated carbon and the random orientation of its pores. It was hypothesized that due to titania deposition within the pores it would result in a low probability of the UV light reaching the titanium dioxide, resulting in a system with reduced photocatalytic activity. The results obtained seemed to agree with this hypothesis. The photocatalytic tests which were performed with HD4000 showed a removal of only 42%.

Chemical attachment of the TiO_2 to the carbon was also attempted to manufacture a more rigid composite. Although this coating technique would provide a more consistent coating on the surface of the ACs, the performance of the ACs coated by this technique did not show any marked improvement over the boil deposition technique. The sol-gel coated HD4000 resulted in 81% removal via adsorption and photocatalysis, which was comparable to the removal seen with the boil deposition method.

Mechanical attachment was achieved through impaction using the Theta Composer instrument (Tokuju Inc., Japan) which resulted in the attrition of the granular activated carbon (GAC) particles, which originated as approximately 1 mm in size, to particles less than 45 μm (Powdered Activated Carbon or PAC). The technique also resulted in separation of the TiO_2 particles from the substrate upon introduction in water. The advantages and the disadvantages of each technique are summarized in Table 5. It must be noted that multiple batches of the TiO_2-AC composites were tested. Based on these results, the boil deposition technique was selected for coating the carbons with titania. This decision was predicated on its simplicity, but for full-scale manufacturing the chemical attachment sol-gel method may provide the most plausible route.

Table 5 - Summary of coating techniques

Coating technique	Performance	Advantages	Disadvantages
Boil deposition	78%	Simple procedure Good performance	1) Inconsistent coating 2) Poor control of TiO_2 loading
Pore volume impregnation (PVI)	62%	Good coating control	1) Requires additional hydrolysis and calcination steps 2) Titania deposition in macropores 3) Poor performance
Chemical attachment	81%	Good coating control Good performance	1) Requires additional hydrolysis step 2) Experimental setup is cumbersome
Mechanical attachment	--	--	1) Attrition of AC particles 2) TiO_2 separation from substrate

Analysis of Titania-Coated Activated Carbons for Phenol Removal

Khan et al. (2003) showed that F400 and HD4000 showed a synergy when coated with TiO_2, whereas Bionuchar did not. The authors concluded that metals, naturally occurring in activated carbon may have been responsible for the observed synergy (i.e., removal of target pollutant increased when titania was coated on AC as compared to activated carbon alone). Nevertheless, they did not investigate this phenomenon in further detail. It was hence a viable exercise to investigate whether metals, in particular electrically conductive metals such as iron and aluminum, could be a plausible mechanism for creating the described synergy.

Ash Analyses of Activated Carbons

To determine the metallic content of Bionuchar, F400 and HD4000, the ACs used by Khan (2003), the uncoated (i.e., virgin) carbons were combusted in air at 575°C until only an ash residue remained. The ash residue of each AC was then analyzed by a scanning electron microscope (SEM) to perform an energy-dispersive spectroscopy (EDS) study. EDS was also used to verify the presence of titania on the surface of the coated ACs. Note that the ACs of which the ash residues were examined were not coated with titania prior to ashing. Even though the EDS data cannot be used as a complete

quantitative comparison, it is still useful as a semi-quantitative as well as a qualitative tool for characterizing elemental composition. The percentage of ash (by weight) in each sample is provided in Table 6. Also provided in the table is the amount of titania (as a percentage) by weight actually coated on the AC samples. This was quantified simply as the difference between the weight of the ash residue of a virgin AC and that of a coated AC sample. The theoretical amount of titania which was to be coated on the surface of each of the ACs was 3% (i.e., weight of titania added equals 3% of the weight of the AC sample). Table 6 shows the inconsistency of the boil deposition procedure in coating the ACs. On an average it is seen from the data provided in Table 6 that Bionuchar has the lowest TiO_2 deposited on its surface. This is attributed to morphological differences between the wood based Bionuchar and the coal based F400 and HD4000.

Table 6 - Ash contents of ACs and mass % of titania deposited (m/m) on AC surface

Activated carbon	Precursor	Carbon% (virgin ACs)	Ash% (virgin ACs)	TiO_2 %
Bionuchar	Wood	92-98%	2-8%	0.5-1.3%
F400	Bituminous	86-94%	6-14%	1.6-2.2%
HD4000	Lignite	82-88%	12-18%	1.4-2.3%

The ash analyses of the ACs provided an estimate as to the magnitude of the composition of elements seen in the EDS scans. Figures 11(A-F) show the EDS scans of the ash residues of the virgin ACs and the scans of the coated ACs.

The EDS scan of the Bionuchar ash residue (Figure 11A) shows that it consists of primarily phosphorous, silicon and sodium. A very faint trace of aluminum as well as a peak corresponding to iron is also observed. The phosphorous peak is likely remnant from the chemical activation technique using phosphoric acid.

Figure 11B represents an EDS image of a Bionuchar sample coated with titania. It can be seen from the scan that smaller peaks corresponding to phosphorous, silicon and sodium are again observed. A titanium peak is also seen in addition to the peaks seen in the ash residue of the same AC. It is important to note than the total ash content of the Bionuchar samples is a maximum of only 10% of the weight of the sample which is inclusive of the titania coated on the surface. Hence, coupled with the results from the EDS scan, it may be concluded that a very small amount of each of the elements is present in Bionuchar. Hence the low presence of conductive metals such as aluminum in Bionuchar (also observed by Khan (2003)) may result in very few conductive sites on the surface of Bionuchar.

The residual ash sample of F400 (Figure 11C) consisted of very large peaks of aluminum and silicon. Smaller peaks pertaining to iron, sodium, magnesium and calcium were also noticed. In comparison to the EDS scan performed on the ash of the Bionuchar sample which showed an aluminum peak of about 200 counts (in replicate sets of scans), the F400 ash residue showed aluminum peaks having magnitudes between 3800 and 4000 counts in the replicate sets of scans preformed. The presence of iron should also be noted.

The activated carbon sample of TiO_2-F400 (Figure 11D) shows the presence of aluminum, silicon, iron and titanium. What is interesting to note is the extremely high titania peak of about 5000 counts. It may be recalled that the corresponding peak in the Bionuchar sample did not have a magnitude of even 2000 counts. This suggests that the morphological difference between the wood based Bionuchar and the coal based F400 resulted in a difference in TiO_2 coating. For instance, variations in roughness may cause the titania to adhere to AC surfaces differently. This would then affect the adsorption of phenol as well as photocatalytic mechanisms. Another observation to be made is the higher ash content of F400 (6-14%) as compared to Bionuchar. This indicates the presence of larger quantities of the elements seen in the EDS scans of F400 relative to Bionuchar.

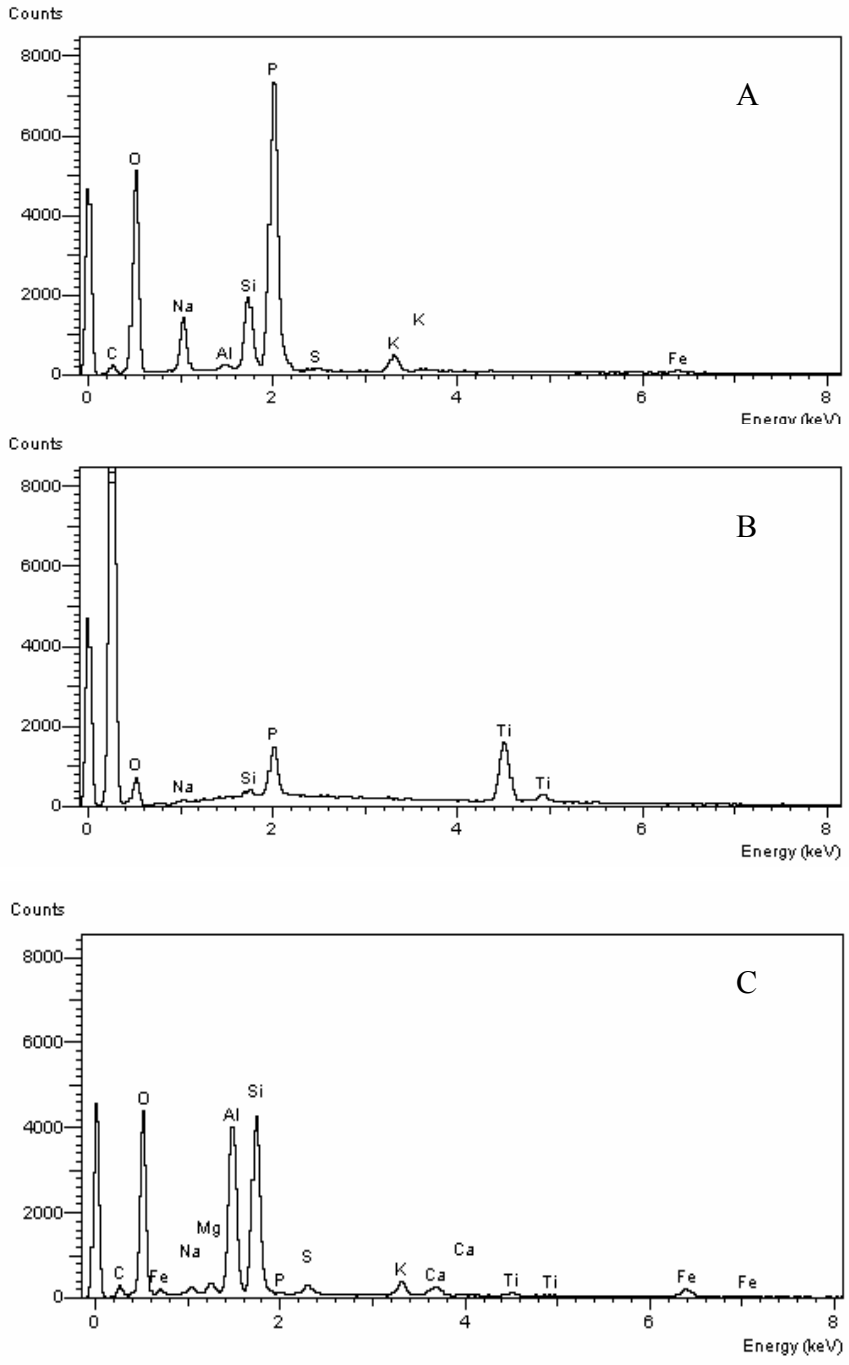

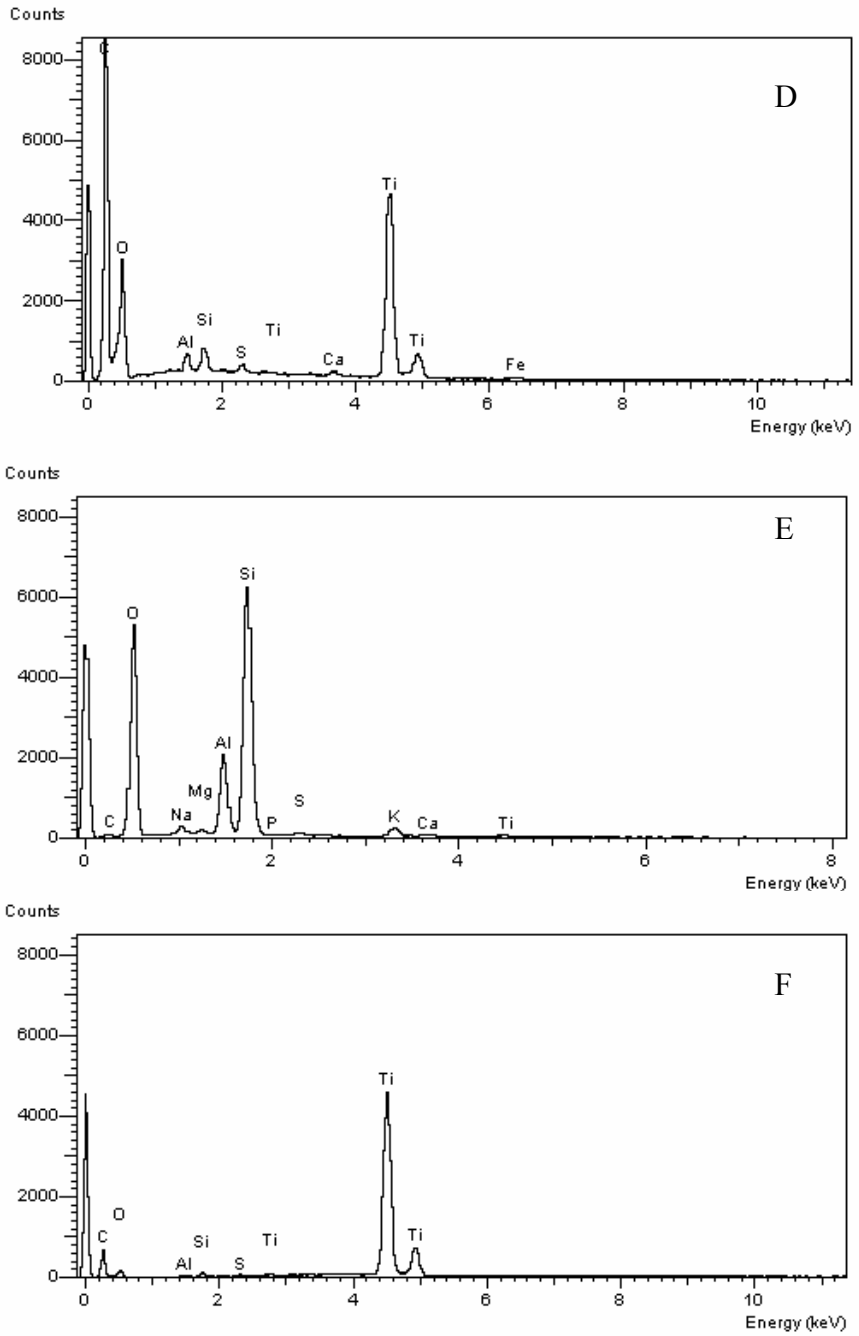

Figure 11 - EDS of A) ash residue of uncoated Bionuchar, B) Bionuchar coated with TiO_2, C) ash residue of uncoated F400, D) F400 coated with TiO_2, E) ash residue of uncoated HD4000, F) HD4000 coated with TiO_2

The differences in the ash compositions as well as the compositions of the ACs (Bionuchar and F400) are noticed, with the prominent peak of aluminum and the presence of iron being the most pertinent to this study. The relatively high conductivity of aluminum and iron may play a role in the distinction between the performances of Bionuchar and F400 that were observed in the work of Khan (2003). This may be a possible cause for F400 showing a synergistic phenomena with respect to dyes. The results of the EDS scan of F400 also agree with Khan (2003) about the presence of iron in F400.

F400 would have different metals contents because it is a coal-based activated carbon that originated as bituminous coal. Therefore, metals that are present in the subterranean environment would be inherent in the coal. However, Bionuchar is a wood based activated carbon that not only would have different metals than coal-based activated carbons, but since it is chemically activated, during the chemical impregnation step at low pH, some of the metals would become soluble and leach out of the wood.

In the case of HD4000 the EDS image (Figure 11E) of the ash residue prominently consisted of silicon and aluminum. In addition, magnesium and sodium were also fairly prominent. However, iron that was hypothesized to be important for the observed synergy in the work of Khan (2003), was absent in the EDS scan.

The presence of aluminum and silicon were also detected in the TiO_2 coated HD4000 sample (Figure 1F). The EDS image also showed a very high titanium peak (about 5000 counts). In replicate sets which provided reproducible results, counts as high as 8000 were found for titanium. The EDS scans for the HD4000 samples also showed a relatively low carbon peak indicating that a titanium dioxide agglomerate may have been focused on. The fact that this was the case in replicate sets between different TiO_2 coated HD4000 samples may also indicate to some extent a uniform coating on the surface of this AC. Noteworthy is the fact that HD4000, like F400 is also a coal based AC. This strengthens the argument that morphology may play a role in the deposition of titania on the AC. This can also be attributed to the enhanced performances seen in the coal based carbons with respect to adsorption and photo-oxidation of dyes (Khan, 2003). The fact that HD4000 also contains highly conductive metals such as aluminum strengthens the argument that conductivity may play a role in enhanced photocatalysis. Also, the fact that the ash content of HD4000, a lignite based AC, is relatively high (12-18%) increases the probability of the coated titanium dioxide being in the vicinity of a site on the AC which possesses a higher conductivity (due to the presence of conductive metal ions).

SEM Images of Titania Coated ACs

SEM images were used to further characterize the coating of titania on the ACs. The images showed a variation in the deposition of titania on the activated carbons as well as the degree to which each AC had been coated. Figure 12 shows an image of titania coated Bionuchar.

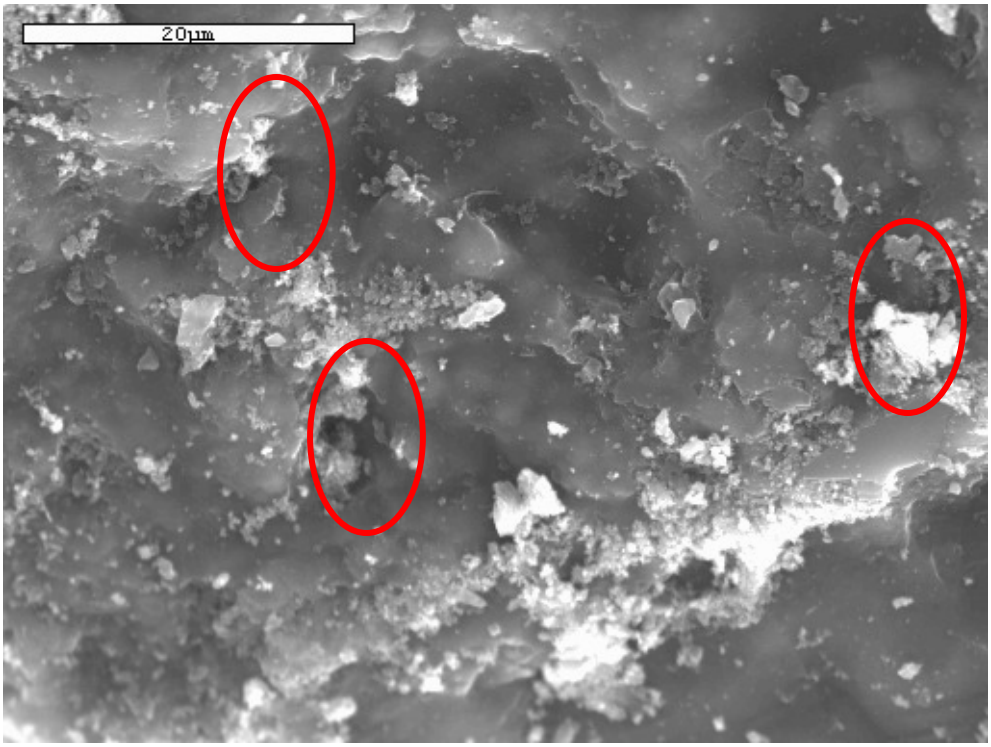

Figure 12 - Titania coated Bionuchar with the TiO_2 blocked pores circled

It can be noticed from the image that the surface of Bionuchar seems very smooth. The smooth nature of the AC surface may cause a lack of adherence of the titania to the AC surface which may result in decreased photocatalytic activity. Another notable aspect of this image is the fact that a number of pores (shown circled) appear to be partially or completely blocked by the titanium dioxide. This may in fact be due to the poor adherence of the TiO_2 surface resulting in the titania being deposited inside the pores of the AC. Deposition in the pores would of course reduce the diffusion of phenol to adsorption sites, thereby decreasing the adsorption of phenol (as discussed in subsequent sections). The wood based nature of this AC is evident in Figure 13.

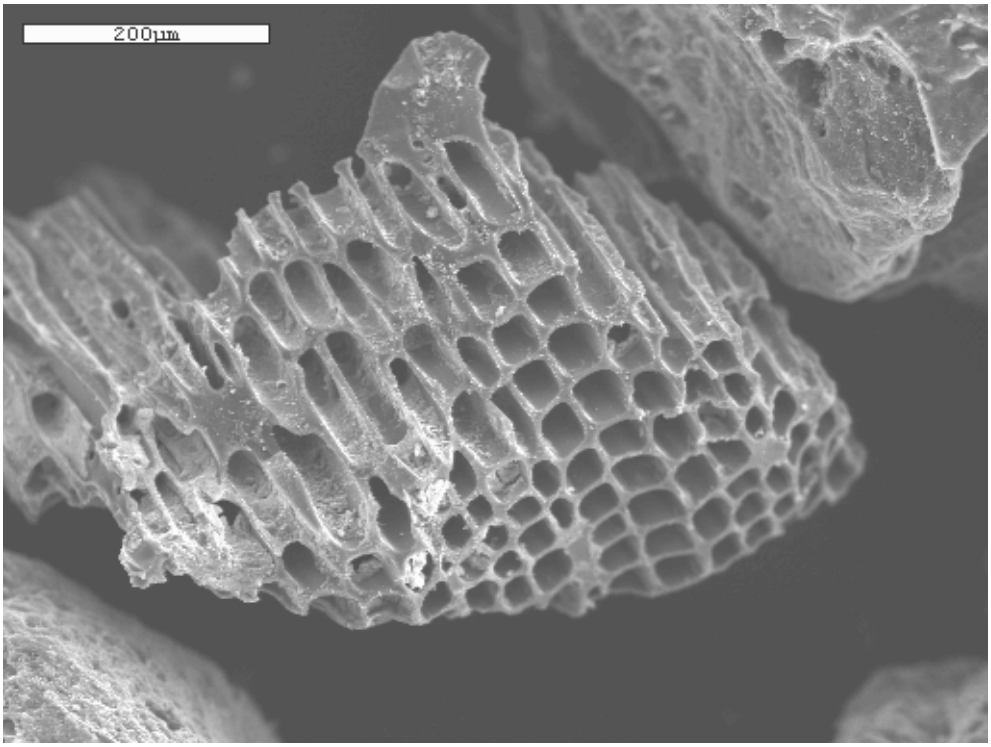

Figure 13 - Bionuchar showing cellulose structure of the wood based AC

The Bionuchar AC particle seen in this image shows what seems to be a cellulose-like structure due to the wood precursor. It may also be noticed that the particle appears to have a smooth honeycomb structure which as mentioned earlier may not allow TiO_2 to adhere well to its surface. The PI considers the morphology of the Bionuchar surface to be one of the reasons why a relatively small titanium peak is detected in the EDS of Bionuchar and its ash residue. Indeed, Table 6 showed that the percentage of titania on the Bionuchar samples was less than the other two samples.

In contrast to the morphology of Bionuchar, the titania seems to be uniformly coated on the surface of F400 (Figure 14).

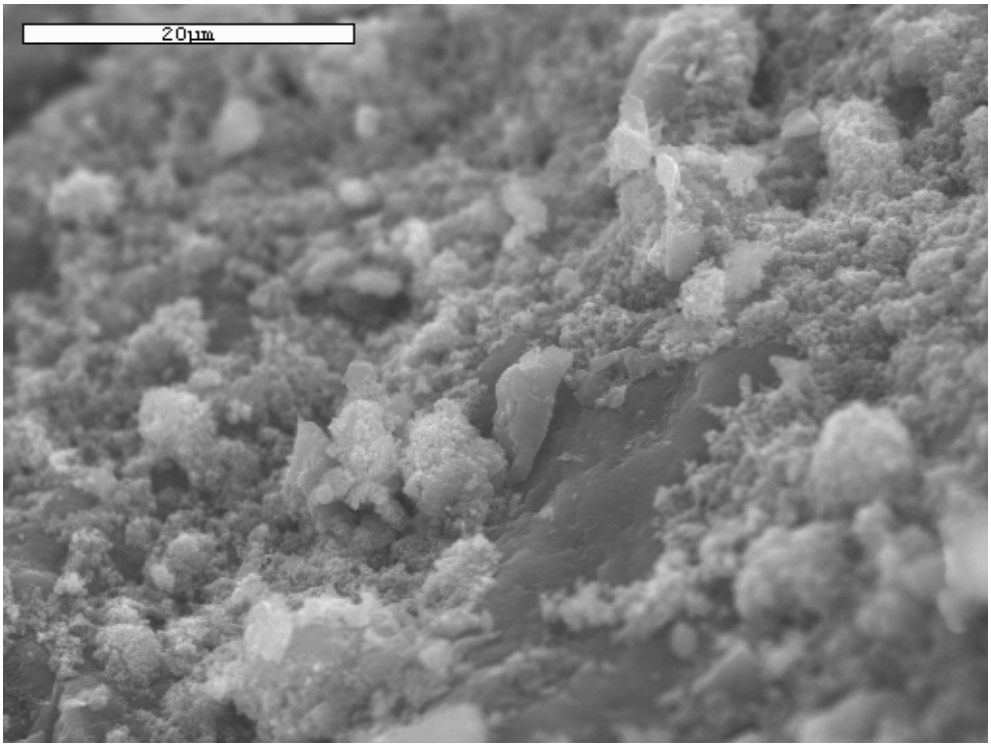

Figure 14 - Titania coated on the surface of F400

The uniformity in coating is thought to be an explanation for the well defined peaks of titania seen in the EDS scans of F400 and could also be an explanation for the synergy seen in the study by Khan (2003). A uniform coating would increase the probability of titania contacting metals present on the AC surface which could hypothetically improve photocatalysis.

An SEM image of HD4000 coated with titania is shown in Figure 15-16. It may be noticed that the TiO_2 agglomerates on the surface of HD4000; here the TiO_2 agglomerate is near the opening of a macropore (see circled region). The size of the TiO_2 agglomerates (about 15 μm) is observed to be much larger than the individual TiO_2 particles (i.e., 27 nm) (Li et al., 2004).

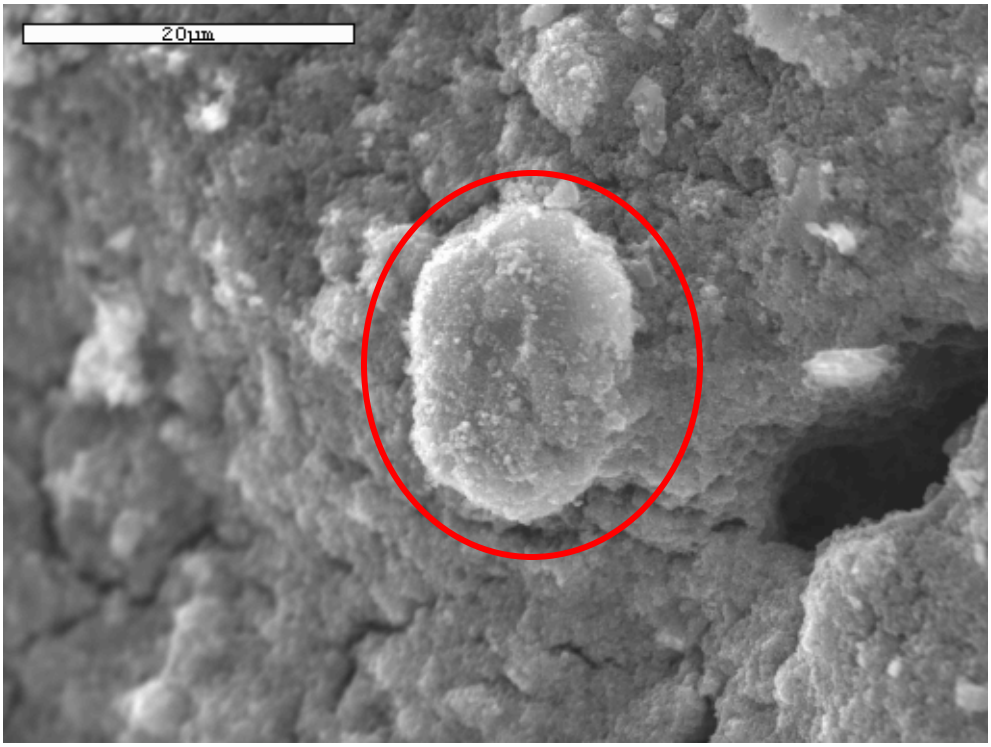

Figure 15 - TiO_2 agglomerate (shown circled) near a macropore on the surface of HD4000

However, it may also be noticed that similar to the case of F400, the titania is coated more uniformly on the surface than in the case of Bionuchar; a phenomenon believed to be dictated by the morphology of HD4000 (a lignite-coal). Figure 16 shows the uniform coating and the agglomeration of titania particles along with the rough surface of HD4000. As in the case of F400, the uniformity in coating may be an explanation for the large titania presence seen in the EDS scans for HD4000. This may also be a possible explanation for the synergy noticed by Khan (2003) for the same reasons as mentioned for F400.

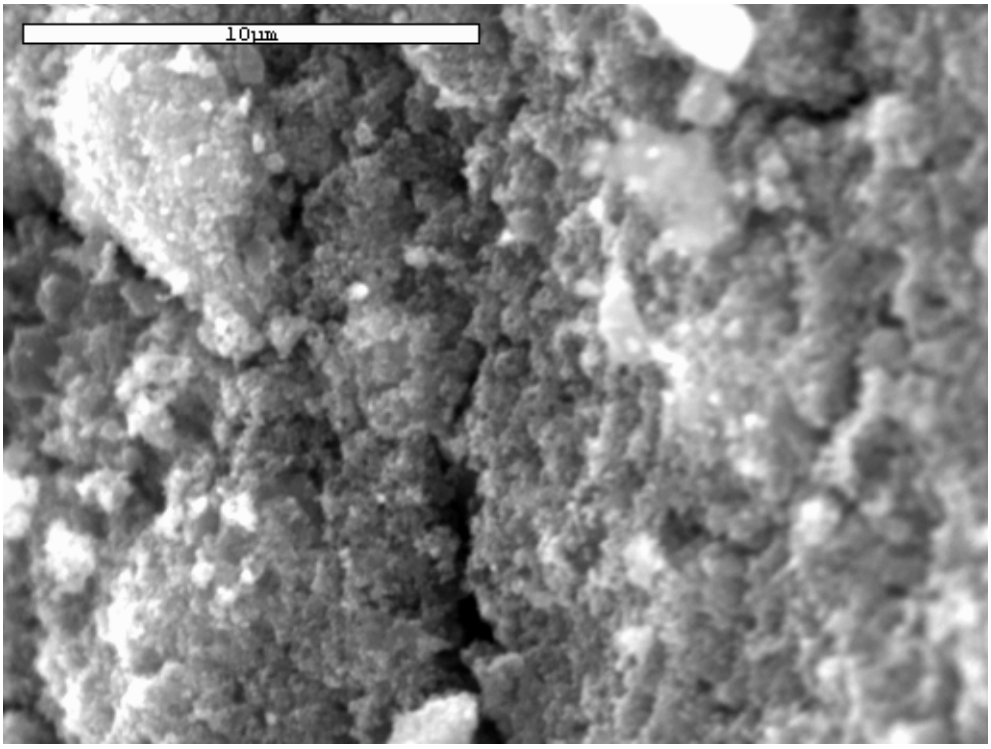

Figure 16 - Surface of HD4000 showing uniform coating of TiO_2 which tends to form agglomerates

Hence, it may be summarized that the wood based carbon and the coal based carbons differ morphologically. Titania coated on Bionuchar seems to concentrate around the pores. It is also believed that due to the smoothness of the Bionuchar surface, there is less adherence of the TiO_2 particles to the Bionuchar surface. However in the case of both F400 and HD4000, a more uniform coating of titania is observed with the titania forming agglomerates on the surface of HD4000.

The ash analysis, EDS scans and the SEM images together provide us with some possible explanations for the synergistic phenomenon of certain TiO_2-AC particles observed by Khan (2003). Both F400 and HD4000 contain relatively high ash contents as compared to Bionuchar. Their EDS scans also show a very high titanium presence on their surface in addition to the higher presence of electrically conductive metals (i.e., aluminum, iron).

It may be concluded that there is a greater possibility of titania being in contact with a conductive site in the case of F400 and HD4000 relative to Bionuchar.

Activated Carbon Batch Studies

The results of the batch tests conducted on the activated carbons which compared the performance of the ACs (or the TiO_2-AC composites) as a function of the removal of phenol are presented. It must be noted that differences in phenol removal of less than 4-5% were not considered significant.

Virgin activated carbons

In the work of Khan (2003), the focus was on the removal of dyes. Herein, the focus was on a model aromatic adsorbate (phenol) and the intent was to learn if the conclusions made by Khan (2003) and as previously discussed, were applicable to the removal of phenol.

To determine the adsorption capacity of the ACs, batch tests were performed in the dark for a period of 24 hours. The studies were first performed with virgin ACs. Three activated carbons were used: Bionuchar, F400 and HD4000. The results of the tests performed with the virgin ACs are presented in Figure 17.

It can be seen from the results that the virgin F400 showed the most adsorption capacity with 87% removal whereas Bionuchar showed the least adsorption capacity with only 52% removal. HD4000 performed relatively well with about 76% removal. The high adsorption capacity of F400 may be explained by the fact that its pores are predominantly (60%) microporous. The molecular size of phenol is about 6 Å (0.6 nm). Therefore, it is expected to adsorb mainly in pores having a microporous size range. The low adsorption capacity observed for Bionuchar is attributed to the acidity of its surface. The surface of Bionuchar is highly acidic. It is well documented in the literature that 'L-type carbons' or 'acidic' activated carbons show reduced adsorption of organics such as phenol (Matos et al., 1998; Salame et al., 2003; Coughlin et al., 1968, Mattson et al., 1969).

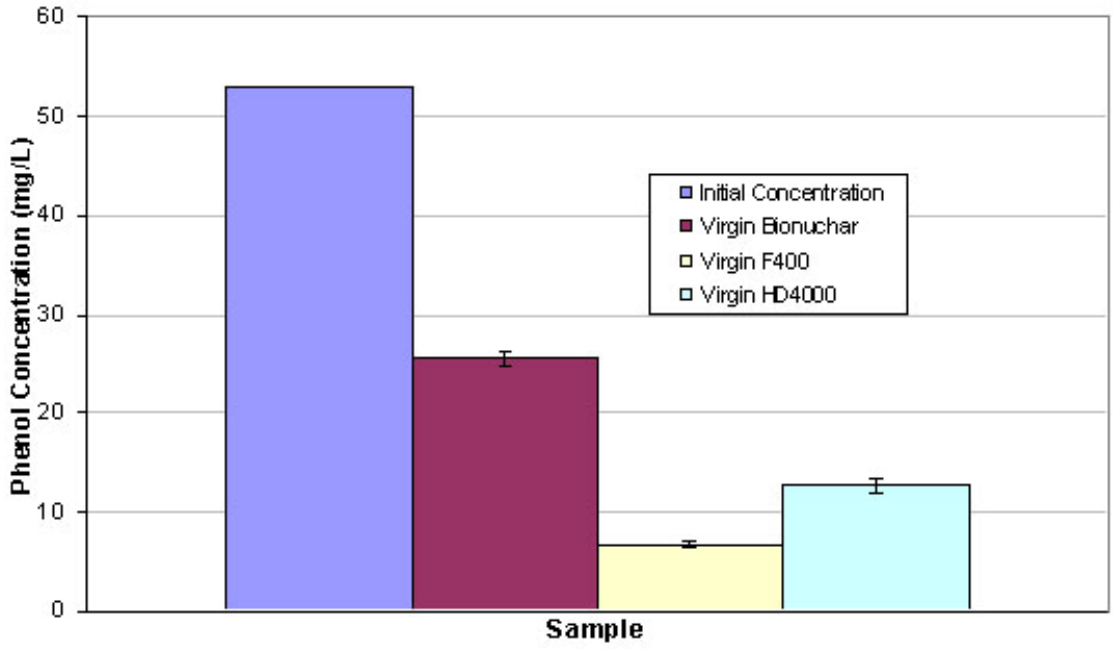

Figure 17 - Batch adsorption studies of virgin ACs in the absence of UV

It is thought that carboxyl and other such electron withdrawing functional groups result in a lowering of phenol adsorption capacity by removal of the π-electron from the AC

aromatic ring. This decrease in the density of the electron cloud in the carbon basal planes causes a decrease in the strength of interactions between the benzene ring of phenol and the basal planes of AC. Phenol also reacts with carboxylic groups on the carbon surface forming ester bonds which contributes to this phenomenon (Salame et al., 2003; Nevskaia et al., 1998). As a result, there is decreased adsorption of phenol on the basal planes of carbon. The case of HD4000 however is peculiar at first glance. HD4000 is acidic due to its activation procedure, but this acidity is a function of residual acid used for acid-washing versus the presence of oxygenated functional groups located on the edge sites. Therefore, although it displays characteristics of an L-type carbon, the manner in which this is manifested is different than "traditional" L-type carbons. At the nano-scale, HD4000 behaves more like an H-type carbon, which suggests that π-π bonding is the dominant adsorption mechanism.

Adsorption capacity for titania-coated activated carbons

Similar trends were seen when batch adsorption studies were performed in the dark with 3% (m/m) (i.e., mass of titania per mass of activated carbon) titania-coated AC samples (Figure 18). Note that the targeted titania loading was 3%, but as was shown earlier the actual amount of titania on the surface of each AC was less than 3 %.

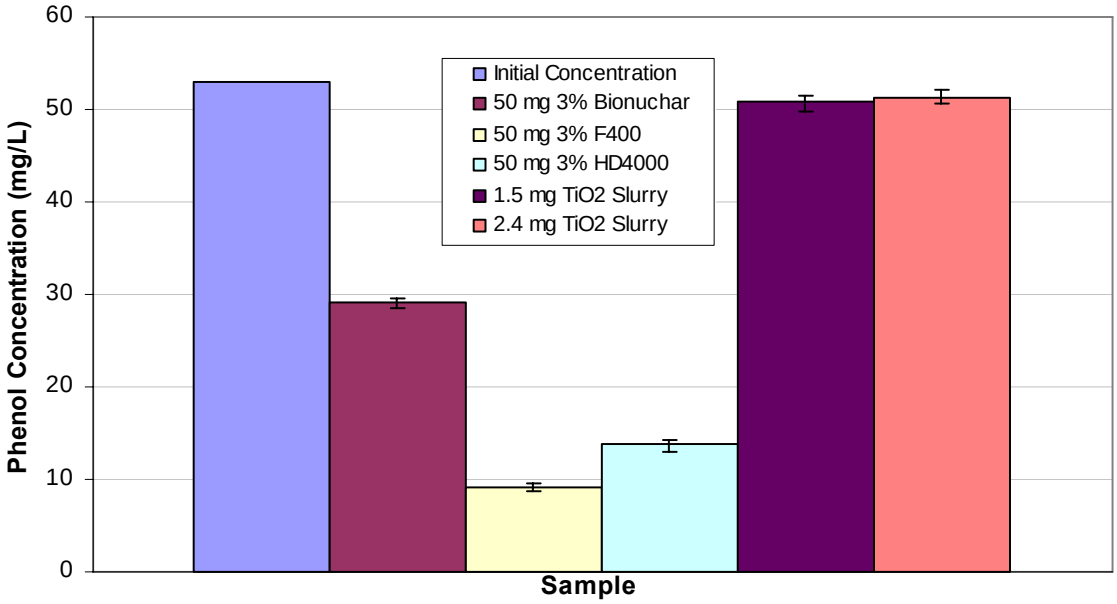

Figure 18 - Batch adsorption studies of 3% (m/m) coated ACs in the dark compared to TiO_2 slurries

A slight decrease in adsorption capacity as compared to the virgin ACs was observed in all the ACs. This was attributed to the partial blockage of pores and hence reduced surface area and active sites available for adsorption. In addition to the ACs, Figure 18 presents the adsorption capacities of two titania slurries (no AC). These masses of titania were chosen because they are very near the masses of titania that was present on the ACs.

Clearly the titania slurries show very low adsorption capacities (approximately 8% removal). In fact, it is noticed that even when a higher amount of titania is loaded to the reactor, the decrease in phenol concentration does not change.

Adsorption and photocatalysis for titania-coated activated carbons

The next step was to determine the performance of the coated ACs in the presence of UV light. As in the earlier experiment, performances of two titania slurries were also included. It was expected that UV would initiate photocatalysis and therefore considerably enhance the removal of phenol through the combined functions of adsorption and photocatalysis.

The tests with the titania coated ACs were conducted in a sequence which would eventually normalize the amount of carbon and titanium dioxide for each sample. The initial batch tests consisted of ACs coated with titania on the basis of mass. The AC's were loaded to their respective reactors such that each reactor contained 50 mg of the titania-coated AC. These samples have been denoted in places as 'mass-mass' or 'm/m'. The amounts of titanium dioxide for the slurry systems were 1.5 (3% of 50 mg) and 2.4 mg (3% of 80 mg as a comparison) respectively. It must be noted that the ACs do not have the same density which resulted in each reactor having different volumes of ACs. The results of the tests are shown in Figure 19.

The irradiated Bionuchar composite with only 39% removal performed poorly compared to HD4000 (78% phenol removal) and F400 (88% phenol removal). The performance of both titania-HD4000 and titania-F400 composites slightly improved in the presence of UV; a fact that is attributed to photocatalysis by UV. However, this refutes Matos et al. (1998, 2001) who claim that an L-type AC inhibits photocatalysis whereas an H-type AC enhances photocatalysis. The surface of HD4000 is acidic and can therefore be categorized as an L-type carbon, but as was previously mentioned, the manner in which HD4000 exhibits a low pH is mechanistically different than "traditional" L-type carbons.

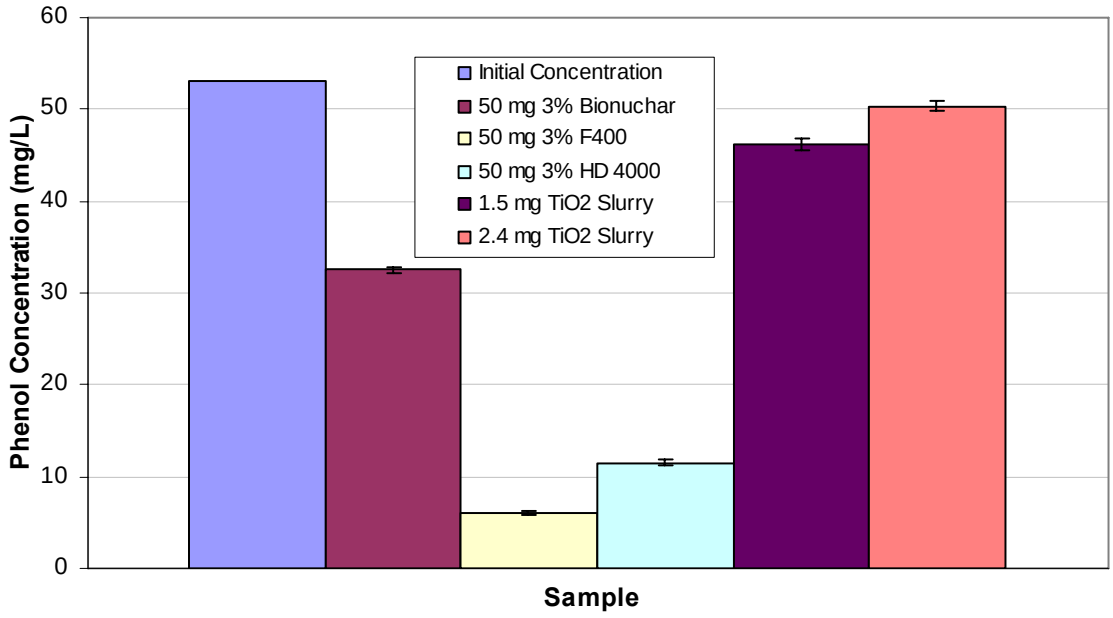

Figure 19 - Batch adsorption-photocatalysis studies of 3% (m/m) coated ACs in the presence of UV

Matos et al. (1998, 2001) clearly erred in their oversight that L-type carbons exhibit less adsorption than H-type carbons. Therefore, decreased adsorption was actually responsible for their results as opposed to decreased photocatalysis.

As was previously discussed in detail, a possible explanation as to why the coal-based carbons behaved synergistically is because both contained conductive metals. The enhanced performance of the ACs may point to a favorable difference in Fermi energies between the titania coated on their surface and a conductive metal in their vicinity, resulting in longer recombination times and improved photocatalysis. As explained earlier, due to the relatively large ash content and metals composition, there is a greater probability of the titania on the surface of AC being in the vicinity of a conductive metal.

Contrary to the performance of the coal based carbons, the performance of the irradiated Bionuchar-titania composite, which is acidic, was considerably worse than the performance of the virgin Bionuchar (13% difference). Whereas this phenomenon may be attributed to pore blockages in the coated Bionuchar, the observation that the irradiated Bionuchar composite performed worse than the Bionuchar composite (6% difference) in the absence of UV makes for an interesting discussion (Figure 19).

A trend similar to the one seen in Figures 18 and 19 was noticed in the experiments performed by Khan (2003). It was found that irradiated dyes (denoted as Dye^*) showed tendencies to adsorb differently than dyes which had not been irradiated (denoted as Dye). According to Khan (2003) and Khan et al. (2006), the irradiation of the dye caused the excitation of the delocalized electrons in the aromatic structure which would affect the adsorption of the compound (Dye^*). These delocalized electrons in the aromatic structure would then interact with the carbon basal planes of Bionuchar which due to

acidic functional groups would contain a less dense electron cloud resulting in decreased uptake (due to decreased π-π interactions). The decreased uptake would also result in decreased photocatalysis. Hence, ACs which preferentially adsorbed the unadulterated dye compounds had reduced uptake for 'Dye*' would have a reduced overall performance. This was due to the fact that their affinity for the unadulterated dye compound resulted in the overall hindrance to adsorption of the dye compound. Hence, in the case of dyes, the two theories cumulatively may explain the reduced performance of titania-Bionuchar composites in the presence of UV. Continuing in the same vein, the synergy observed with F400 and HD4000 in the presence of UV was attributed to their relative affinity for 'Dye*'. In the case of ACs that showed good removal, a situation of augmented adsorption was theorized wherein activated carbons having an affinity to adsorb both 'Dye' and 'Dye*' at comparable levels showed increased decolorization of the dye solution (Dye + Dye*). Whether the same theory may apply to phenol (hence forming phenol*) was thought to be an idea worth investigating and is discussed later.

Regarding the performance of the titania coated ACs and titania alone, each of the ACs showed more removal of phenol than the titania slurries. In fact, the titania slurry containing a lower concentration of titania slightly outperformed the slurry with a higher concentration. Although this may be attributed to decreased penetration of UV with increasing TiO_2 concentration, the fact still remains that the removal was considerably lower than the AC-TiO_2 composites. Therefore, it must be noted that although titanium dioxide may result in a decrease in adsorption capacity when coated on ACs, the ACs coated with titania provide for better overall removal of phenol in the presence of UV as compared to the titania slurry.

Volumetric loading of the reactors and mol/mol coating

Due to the variation in the densities of the ACs, it was deemed necessary to normalize the differences in the volumes of ACs loaded to the reactors. In other words, since the wood-based carbon was less dense than the coal based carbons, the mass of carbon added for each experiment was less. Since the mass of carbon was less, then mass of titania would be less. Therefore, the system could be normalized by adding the carbons to the reactor based on their volumes versus mass. Hence, 0.025 mL of AC was loaded to each of the respective reactors.

The results of the experiment carried out under these conditions are shown in Figure 20.

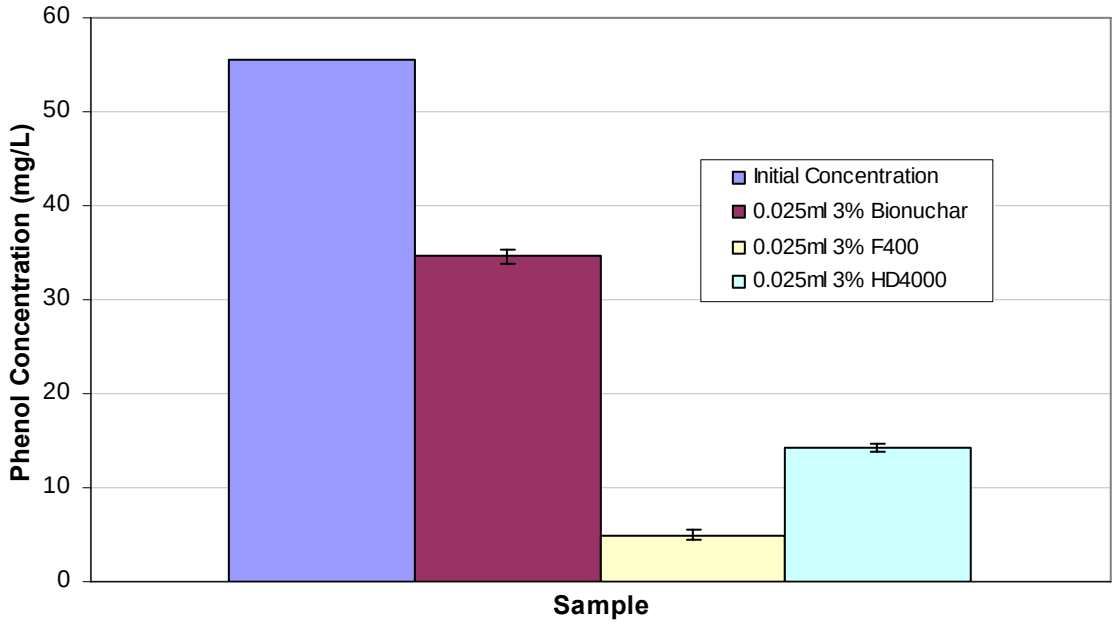

Figure 20 - Batch adsorption-photocatalysis studies of 3% (m/m) coated ACs loaded to the reactors on a volume basis in the presence of UV

The tests did not result in any significant difference in performance of the ACs. A trend similar to the one seen in Figure 19 was seen for this experiment as well. With this said, the change in basis of loading from mass to volume only succeeded in normalizing the amount of AC in each reactor. It was also of interest to learn if normalizing the amount of titania on each AC based on titania to carbon would impact the results. This ratio would be different for each carbon because of the different ash contents. To normalize the titania to carbon loading, the ACs were coated such that 3 moles of titania were present for every 100 moles of elemental carbon. In doing so, the titania to elemental carbon ratio in each AC remained constant. In addition to the change in coating basis, the titania-coated ACs were continued to be loaded by volume into their respective reactors. Using these bases for coating the titania on the ACs and loading them to the reactors, tests were performed in the absence as well as in the presence of UV light.

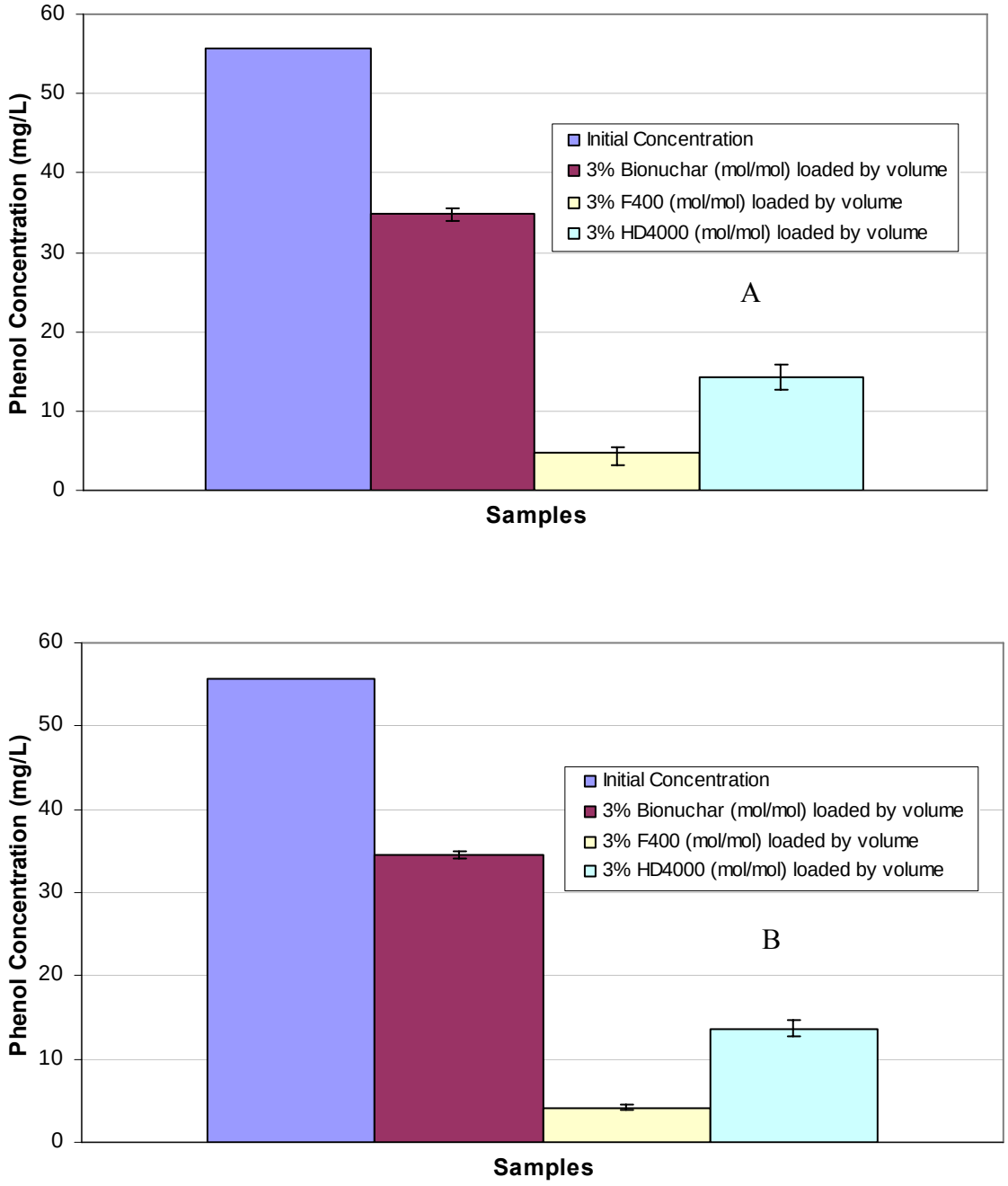

Figure 21 - Batch adsorption studies: A) 3% (mol/mol) coated ACs in the absence of UV loaded to the reactors by volume, B) Photocatalysis studies of 3% (mol/mol) coated ACs in the presence of UV loaded to the reactors on a volume basis

Tests in the absence of UV were performed to assess as to how much the change in the basis of coating affected adsorption of phenol since in each case the amount of coated titania increased. Similarly, tests in the presence of UV were performed to assess the effect that the increased titania coating on the ACs had on simultaneous adsorption-photocatalysis. Figures 21a and 21b show the results of the experiments in the absence and presence of UV light respectively.

As in the earlier tests, an analysis of the data revealed no significant differences in the trends of their performances. Although there are signs of photocatalysis having some effect on phenol removal, the differences noticed in the trends are not of sufficient magnitude to arrive at any definite conclusion with respect to how photocatalysis was influenced by the variations.

The results seemed to show that adsorption dominated over photocatalysis as a mechanism. Hence, the extent to which photocatalysis plays a role in the removal of phenol in a co-adsorbent with high surface area was questioned. Unlike results shown by Matos et al. (1998) in the case of organic compounds and Khan (2003) in the case of dyes, the results seen herein failed to show any clear evidence of a synergy of any kind existing between ACs and TiO_2 with respect to performance. The premise that a co-adsorbent with high surface area would result in an increase in photocatalytic efficiency of titania (Matos et al., 1998; Takeda et al., 1995) can hence be questioned. The theory by Matos et al. (2001) that L-type ACs inhibit photocatalysis whereas H-type ACs enhance photocatalysis has also gone unfounded based on the data that has been presented. The failure by Matos et al. (2001) to perform adsorption control studies seems to be the cause of the unverifiable hypothesis.

Previous data contained in quarterly reports indicated that the TiO_2-coated bituminous coal provided the most encouraging results with respect to phenol adsorption and oxidation. Therefore, it was chosen as the candidate for testing the efficacy of regenerating the activated carbon (once exhausted) with phenol in a column adsorber.

Figure 22 plots the adsorption profile for the virgin TiO_2-coated activated carbon and adsorption profile for two carbons that were regenerated with DI water or UV plus DI water. (The breakthrough curves were purposely designed to load the carbon with phenol rapidly, which is why there is no period where the carbons removed 100% of the influent phenol (C_o =10 mg/L)). As the two regeneration curves indicated, when flowing just DI water or DI water with UV irradiation, the subsequent adsorption for the carbon was much less than for the virgin carbon. Furthermore, when operating in a single pass configuration, DI water alone (i.e., simply desorption) worked as well at removing phenol than did DI water plus UV.

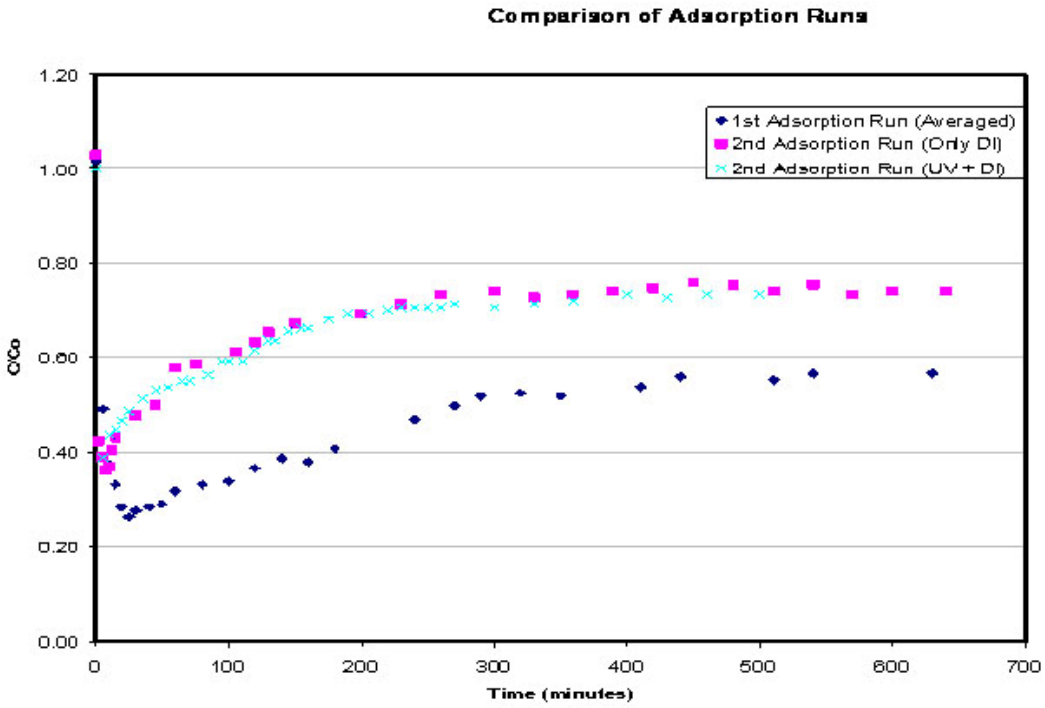

Figure 22 - Comparison of virgin and regenerated carbon for phenol removal.

The regeneration experiments for Figure 22 demonstrated that desorption of phenol is a phenomena that requires a solution. Therefore, the column adsorber was operated in a recirculation mode whereby the effluent (i.e., desorbed phenol) would be reintroduced in to the influent of the reactor to be oxidized by the titania on the carbon surface. Three different approaches were tested: packed bed (Figure 23), bubbling bed (Figure 24), and fluidized bed (Figure 25). The fluidized bed was hypothesized to work the best because most of the carbon would be exposed to the UV versus in the packed bed approach whereby only the carbon nearest the UV would be irradiated.

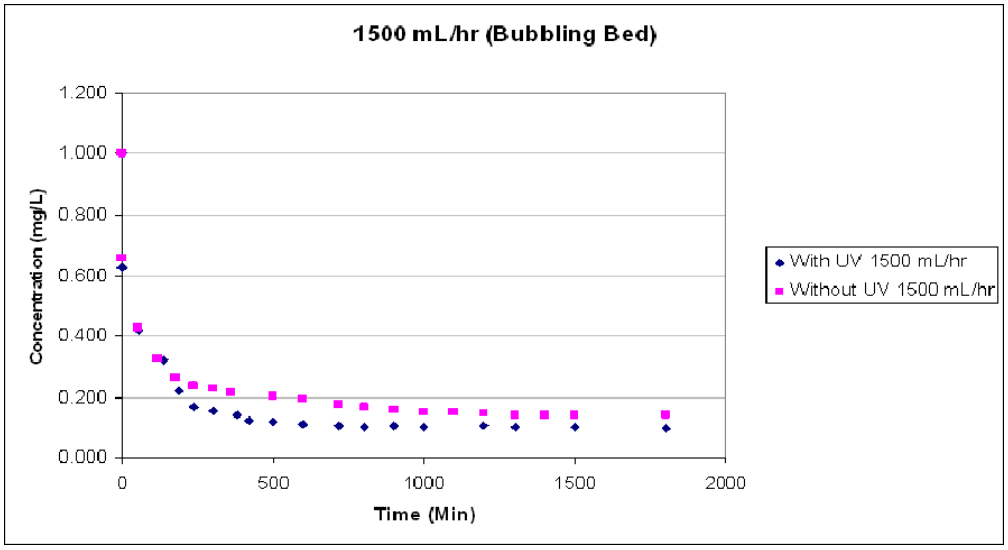

Figure 23 - With and without UV regeneration (packed bed)

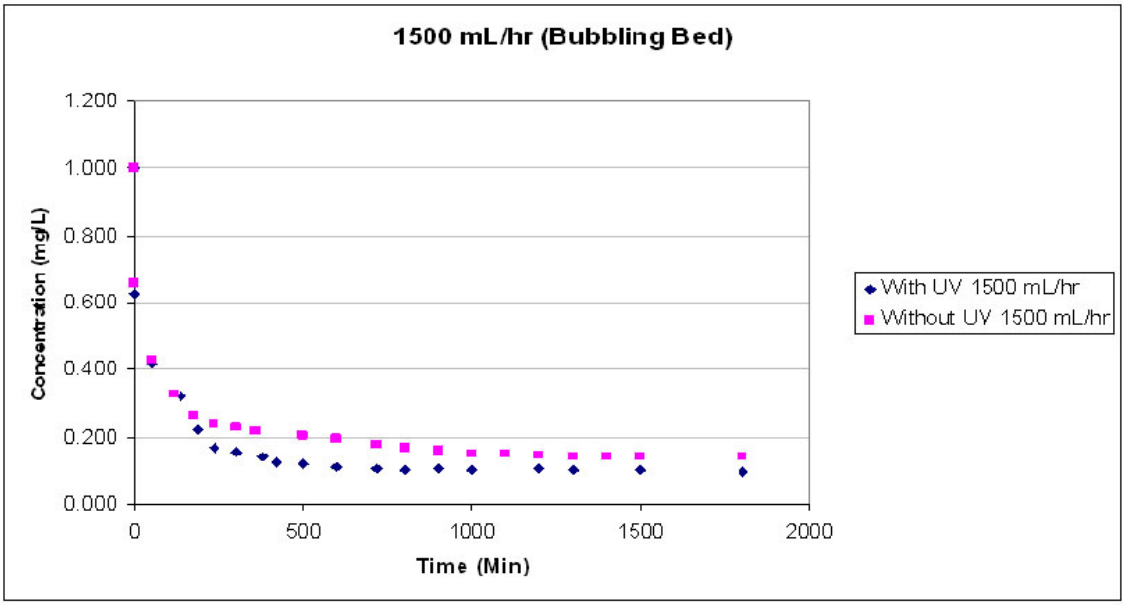

Figure 24 - With and without UV (bubbling bed)

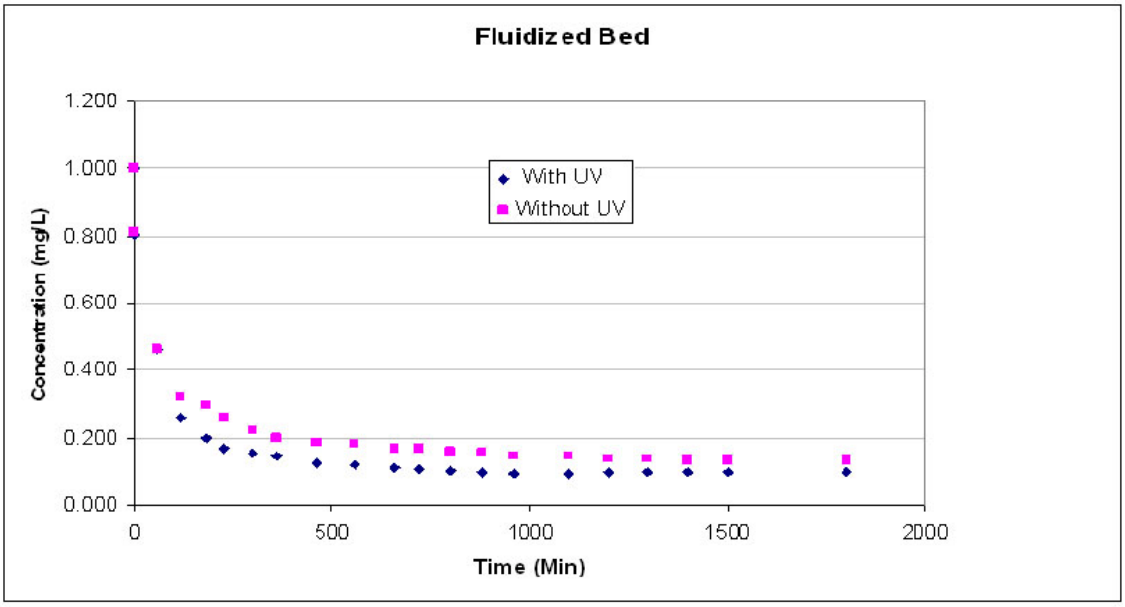

Figure 25 - With and without UV (fluidized bed)

In the bubbling bed and fluidized bed scenarios, the with UV condition performed better (i.e., the effluent concentration was closer to zero). In both cases (i.e., with and without UV), the phenol was removed well from the activated carbon surface, but in the case of the with UV scenario, the phenol was oxidized to as verified with GC and spectrophotometric analyses.

CONCLUSIONS

Prior to the initiation of the research presented herein, it was hypothesized that the conductivity of the carbon and/or the conductivity of metals inherent in the materials tested would enhance photocatalysis. However, this theory was disproved. On the contrary, the morphology of the carbon that is to be coated with photocatalysts is most important. A rough surface resulted in a uniform coating, which was proven to enhance photocatalysis of the test adsorbate (phenol).

Contrary to the literature, adsorption was proven as the key variable responsible for the decrease in phenol concentration. Therefore, when coating activated carbon, a carbon should be selected that demonstrates the greatest uptake of the contaminant(s).

Finally, a series of coating strategies were investigated to determine the efficacy of these coatings while keeping commercialization in mind. Although the boil deposition proved the simplest, it resulted in an un-even coating. Therefore, even though the performance was not as promising, the pore volume impregnation technique offers the greatest potential for commercialization.

REFERENCES

Cannon FS, J Dusenbury, D Paulsen, J Singh, D Mazyck, D Maurer. Advanced Oxidant Regeneration of Granular Activated Carbon for Controlling Air-phase VOCs. *Ozone Sci. Engr.,*1996, 18:417- 441.

Celzard A., Mareche JF, Payot F, Furdin G. Electrical conductivity of carbonaceous powders. *Carbon* 2002; 40:2801-2815.

Coughlin RW and Ezra FS. Role of surface acidity in the adsorption of organic pollutants on the surface of carbon. *Environmental Science and Technology*. 1968; vol.2; No. 4: 291-297

Fujii, T., T Suzuki and K Sakamoto, "Simultaneous Removal of Gases and Particulates by Photocatalyst and UV/Photoelectron Method", *Kuki Seijo*, 1997, 35(3), 169-176.

Khan AY, DW Mazyck, CY Wu. TiO_2 Coated Activated Carbon: A Regenerative Technology for Water Recovery. NASA ICES Conference July 2002.

Khan AY. Titanium dioxide coated activated carbon: A regenerative technology for water recovery. 2003. *Masters Thesis*. The University of Florida, Gainesville, FL-32611.

Khan AY and Mazyck DW. The effect of UV irradiation on adsorption by activated carbon/TiO_2 composites. *Letters to the Editor/Carbon*. 2006; 44: 158-193.

Li W, Ni C, Lin H, Huang CP, Shah IS. Size dependence of thermal stability of TiO_2 nanoparticles. *Journal of Applied Physics*. 2004; Vol.96; No.11.

Matos J, Laine J, Herrmann JM. Synergy effect in the photocatalytic degradation of phenol on a suspended mixture of titania and activated carbon. *Applied Catalysis B: Environmental.* 1998; 18: 281-291.

Matos J, Laine J, Herrmann JM. Effect of the type of activated carbons on the photocatalytic degradation of aqueous organic pollutants by UV-irradiated titania. *Journal of Catalysis*. 2001; 200: 10-20.

Mattson JS, Harry MB Jr., Malbin MD, Weber WJ Jr., Crittenden JC. Surface chemistry of active carbon: specific adsorption of phenols. *Journal of Colloid and Interfacial Science*. 1969; Vol. 31; No.1; 116-130.

Nevskaia DM, Castillejos-Lopez E, Munoz V, Guererro-Ruiz A. Adsorption of aromatic compounds from water by treated carbon materials. *Environmental Science and Technology.* 2004; 38: 5786-5796.

Salame II and Bandosz TJ. Role of surface chemistry in adsorption of phenol on activated carbons. *Journal of Colloid and Interfacial Sciences*. 2003; 264: 307-312.

Sadeghi, M., W Liu, T Zhang, P Stavropoulos and B Levy, "Role of Photoinduced Charge Carrier Separation Distance in Heterogeneous Photocatalysis: Oxidative Degradation of CH_3OH Vapor in Contact with Pt/TiO_2 and Cofumed TiO_2-Fe_2O_3", *J. Phys. Chem.*, 1996, 100, 19466-19474.

Torimoto T, Ito S, Kuwabata S, Yoneyama H. Effects of adsorbents used as supports for titanium dioxide loading on photocatalytic degradation of propyzamide. *Environ Sci Tech.* 1996;30:1275-1281.

Tryba B, Morawski A, Masahiro T, Inagaki M. TiO_2-mounted activated carbon for the elimination of organic pollutants in water. *Res Adv in Water Research*. 2003;4:35-42.

Tsumura T, Kojitani N, Umemura H, Toyoda M, Inagaki M. Composites between photoactive anatase-type TiO_2 and adsorptive carbon. *Applied Surface Science*. 2002;196:429-436.

Wu, CY, TG Lee, G Tyree, E Arar and P Biswas, "Capture of Mercury in Combustion Systems by InSitu Generated Titania Particles with UV Irradiation", *Env. Eng. Sci.*, 1998, **15(2)**, 137-148.

PAPERS PUBLISHED FROM RESEARCH

Khan AY, Mazyck DW. The Effect of UV Irradiation on Adsorption by Activated Carbon/TiO_2 Composites. *Carbon* 2006; 44:182-184.

PRESENTATIONS FROM RESEARCH

Khan A, Shyamasundar V, Mazyck D. TiO_2-Activated Carbon: A Novel Approach to the Removal of Aqueous Metals. July, 2006 The International Carbon Conference. Aberdeen, Scotland.

Bach MT and Mazyck DW. Tailoring of a Powdered Activated Carbon through Manipulation of Dissolved Oxygen. July, 2006 The International Conference on Carbon. Aberdeen, Scotland.

Design of nanoporous carbon derived from coal tar pitch/polymer blends for ultracapacitors

Final Report

July 31, 2006

Ramakrishnan Rajagopalan and Henry C. Foley

Subcontract No. 2872-TPSU-DOE-1874

Project Starting Date: 03/01/2005

Project Ending Date: 07/31/2006

Pennsylvania State University
University Park, PA 16802

Disclaimer

Abstract

This project was aimed at developing novel nanoporous carbon materials from activated coal tar pitch/ polymer blend precursors with very high surface area and optimum porosity to use as an electrode in electrical double layer capacitors (EDLCs). The project successfully demonstrated the synthesis of nanoporous carbon with very high surface area in the order of 1000-1500 m^2/g upon CO_2 activation. Electrical double layer capacitance was measured using both cyclic voltammetry and electrochemical impedence spectroscopy. There is a strong correlation between the surface area of the carbon and the specific capacitance. Carbon that had surface area smaller than 1000 m^2/g had specific capacitance less than 50 F/g while the carbons having surface area from 1000 – 1500 m^2/g showed specific capacitances in the order of 200 -250 F/g. It was shown that the mesoporosity and macroporosity in the parent carbon are critical for both activation and as well as the specific capacitance of the material. The use of these carbons in EDLCs was also demonstrated by fabricating a two-electrode ultracapacitor.

TABLE OF CONTENTS

Executive Summary

The main physical properties of interest while designing a carbon materials as use as electrodes in EDLCs are surface area, pore volume, pore size distribution, density and surface functional groups. We began our quest for developing novel nanoporous carbon with these properties in mind. Our goals were to synthesize a carbon that has the following properties:

i) High surface area in the order of 1000 – 1500 m^2/g

ii) Adequate micro- and mesoporosity

iii) High micropore volume (> 0.5 cc/g)

We employed two distinct approaches to synthesize the carbon with desired properties. The first approach was to use coal tar pitch (supplied by Koppers Inc.), which has about 16% quinoline insoluble (QI) content and has a softening point of 110℃ as a precursor and blend it with polymer precursor like polyethylene glycol diacid (pore former) and carbonize. The resultant carbon was then activated using CO_2 at 900℃. The second approach was to activate the carbon formed using blends/copolymer of polyfurfuryl alcohol (micropore former) and polyethylene glycol diacid (mesopore former). Both these methods resulted in carbons with very high surface area (1000 – 1500 m^2/g).

Our choice of coal tar pitch with high QI content (16%) was based on the fact that the presence of QI impedes the development of mesophases in the pitch. Since our primary goal was to develop high surface area carbon, we thought that the high QI content would aid in the formation of disordered carbon. Carbonization of CTP by itself yielded a carbon (~50% yield) that has no micro-/mesoporosity. Our initial approach was to just blend the coal tar pitch with different polymer precursors such as polyfurfuryl alcohol, polyethylene glycol and sucrose and vary the composition of the polymer blends. This resulted in carbon with very few micropores, which was very resistant to CO_2 activation. The surface area of these carbons was in the order of 10 -15 m^2/g. Our next goal was to change the character of the pitch. We achieved this by blending the pitch with polyethylene glycol diacid and adding sulfuric acid (oxidizing agent) to the mixture. The addition of sulfuric acid to CTP results in oxidation of low volatile aliphatic compounds to form organic acid and phenol structures. Upon heat treatment in the presence of

H_2SO_4, they can further undergo polycondensation and thereby increase the yield of condensed aromatic structures [1]. Indeed, the carbonization of these materials showed almost 90 -100% yield/g of CTP. We also saw that these materials could now be easily activated using CO_2 at 900℃. The resulting carbon had surface areas in the order of 600 – 900 m^2/g. The next step was to isolate the component of the CTP that upon carbonization could be activated. We did this by first extracting and separating the soluble and insoluble components of CTP in tetrahydrofuran. Both the components were then mixed separately with polyethylene glycol diacid and H_2SO_4, carbonized and then activated. The THF soluble fraction yielded carbon with surface area in the order of 900 m^2/g while the THF insoluble fraction resulted in carbon with surface area upto 1500 m^2/g. The micropore volume in these carbons was as high as 0.8 cc/g.

In our second approach, we start with polyfurfuryl alcohol, which upon carbonization yields a carbon that is microporous (4 - 5Å). Blending with another polymer like polyethylene glycol results in inducing mesoporosity in the carbon along with microporosity. In the past, we have shown that the mesoporous volume scales with the molecular weight of polyethylene glycol. We set out to improve on the properties of the carbon derived from these blends. The first important objective is to ensure good miscibility of both the polymer components. Hydrogen bonding is the main interaction between the two polymers. We enhanced the possibility of hydrogen bonding and also promote possible covalent bonding between the two polymers by using polyethylene glycol diacid instead of polyethylene glycol. The carbon synthesized using polyfurfuryl alcohol/polyethylene glycol diacid blends were easy to activate. The surface area of the activated carbon were in the order of 1000 – 1500 m^2/g. The micropore volume of these carbons was as high as 0.6 cc/g. We also varied the molecular weight of polyethylene glycol diacid (PEG acid). The time required for activation in order to synthesize high surface area carbon (> 1000 m^2/g) decreased with increase in the molecular weight of PEG acid.

The synthesized high surface area carbons were then analyzed using cyclic voltammetry and electrochemical impedance spectroscopy. Carbons with surface area ranging from 300 m^2/g – 1500 m^2/g were tested using both these methods. The specific capacitances of the carbon were 10 – 50 F/g for carbon with surface area less than 1000

F/g. As the surface area of the carbon increased above 1000 m^2/g, the specific capacitance increased dramatically and was about 200 – 250 F/g for carbons derived from both PFA/PEG diacid and CTP/PEG diacid blends. Finally, the use of these carbon materials as electrodes in EDLCs was successfully demonstrated by fabricating a two-electrode electrochemical capacitor.

In this report, we have successfully demonstrated the use of polymer-derived carbons and coal tar pitch derived carbon as use as electrodes for electrical double layer capacitors using aqueous electrolyte. There is enormous commercial potential to engineer the physical properties of these carbons to extend its use in organic electrolytes, which would increase the energy density of the capacitor.

Experimental

i) Synthesis of coal tar pitch derived carbons

a) Coal tar pitch polymer blends

Blends of coal tar pitch and polymer precursors such as sucrose, polyfurfuryl alcohol and polyethylene glycol were prepared by simply mixing them in a ratio of 1:3 by weight. They were then placed in a quartz boat, which was in turn placed in a tube furnace under flowing argon atmosphere. The samples were then heated to 800°C slowly and maintained at 800°C for 8 hours.

b) Modification of coal tar pitch

3g of coal tar pitch was mixed with 9g of PEG600 diacid and 3ml of H_2SO_4. The resultant mixture was then allowed to stir overnight. As the reaction proceeded, the viscosity of the solution increased. The viscous solution was then transferred onto the quartz boat for carbonization at 800°C.

In another experiment, 5g of coal tar pitch was dissolved in 50 ml of tetrahydrofuran (THF) and allowed to stir for 2 hours. The dissolved mixture was then filtered using suction filtration and the residue (THF insoluble) and the filtrate (THF soluble) were collected separately. After the extraction, 3g of THF insoluble and THF soluble were separately mixed with 10g of PEG600 diacid and 2ml of H_2SO_4. The solution was stirred overnight and the mixture was carbonized at 800°C.

ii) Synthesis of polymer derived carbons

a) Synthesis of polyethylene glycol diacid

PEG diacid (PEG with end carboxylic acid groups instead of alcohol groups) were synthesized according to the procedure introduced by Ferruti et al [2]. 10 mmol of PEG (MW: 1000, 2000, 3350 and 6000 g/mol) , 50 mmol succinic anhydride, and 50 mmol of pyridine also from Aldrich were mixed in Chloroform for 48 hours at 55 °C. The reacted solution was then evaporated and redissolved in a 10% sodium bicarbonate solution and filtered to remove residue. The mixture was then chilled to 0 °C - 5 °C and acidified using 0.3 mol of hydrochloric acid. The product was then extracted using chloroform and recrystallized using diethyl ether.

b) Synthesis of polyfurfuryl alcohol/polyethylene glycol diacid

0.1M p-toluenesulfonic acid (p-TSA) was dissolved in 5 ml THF and cooled down to 0°C using an ice bath. 10 ml of furfuryl alcohol was slowly added to this solution using a syringe pump at 10 ml/hr. The solution was then stirred and the reaction was allowed to proceed for 48 hours. To this solution, polyethylene glycol diacid (600 g/mol) was mixed in a ratio of 1:2 by weight. The polymer blend was then carbonized at 800°C.

iii) CO_2 activation of carbon

The carbon was placed in a quartz boat and placed in a tube furnace. The sample was heated under argon atmosphere to 900°C in one hour and soaked for another hour. This was followed by activating under CO_2 atmosphere at 900°C. After activation, the sample was cooled down to room temperature under argon atmosphere.

iv) Characterization of activated carbon

a) Pore size distribution

The pore size distribution of the carbon was calculated using a methyl chloride adsorption tests. The pore size was calculated using H-K model described elsewhere [3].

b) Surface area measurements (BET)

The surface area measurements were made using BET equation using nitrogen adsorption experiments at 77K. Approximately, 0.2 g of sample was used for the experiment and the samples were baked at 100°C overnight before the experiment.

c) Electrochemical characterization

Electrode preparation

0.2g of carbon was mixed with polyvinyledene powder (0.02g) and grinded using a mortar and pestle. The resultant powder was dispersed in 1 ml of N-methylpyrrolidone. The solution was ultrasonicated for half hour and the resultant paste was applied onto a gold foil (1 cm^2) and blow dried to form a thin carbon film. The weight of the carbon film was ~ 20 mg for every experiment.

Cyclic Voltammetry

All electrochemical measurements were done using a 263A Potentiostat/Galvanostat. The experiments were doing using a three-electrode electrochemical cell. The carbon film was used as the working electrode while a platinum wire was used as a counter electrode. A Ag/AgCl was used as a reference electrode. 1M Sulfuric acid was used as electrolyte. The voltammograms were measured using a scan range of 0 to 0.9V vs Ag/AgCl and at different scan rates ranging from 2 mV/sec to 20 mV/sec. The capacitance was measured as follows:

$C = \frac{I}{\upsilon m}$ where I – average current in A

υ - scan rate in V/sec

m – mass of the electrode

Electrochemical Impedance Spectroscopy

EIS measurements were done using a model 5210 Lock-in amplifier coupled with 263A Potentiostat/Galvanostat. The experiments were done using a three-electrode electrochemical cell. A dc voltage of 0.5V vs Ag/AgCl was applied. To this an ac perturbation of 10 mV was applied. The frequency of the ac perturbation was varied from 10^5Hz to 10^{-3}Hz. The impedance was calculated by measuring the resulting current. The specific capacitance was then measured from the impedance data at very low frequencies (10^{-3} Hz) where the sample is almost purely capacitive in nature as follows:

$C = \frac{1}{|Z|\omega}$ where |Z| is the magnitude of the impedance and ω is the angular frequency and is equal to 2πν (ν is frequency in Hz).

v) Fabrication of double layer electrochemical capacitor

Two-electrode electrochemical capacitor was fabricated by sandwiching a Celgard 5400 membrane between two identical carbon electrodes. The carbon electrodes were prepared by mixing 90wt% carbon with 5wt% Teflon solution and 5wt% acetylene black. The resultant mixture was kneaded into dough and pressed into a 50μ thick carbon film. Two gold-coated stainless steel meshes were used as the current collector. The assembly was then immersed in 1M H_2SO_4 for 2 hours before begining any testing. One

of the carbon electrodes acted as both the counter electrode and as well as the reference electrode. The capacitor was then tested using both galvanostatic charge-discharge experiments, cyclic voltammetry and electrochemical impedance spectroscopy.

Results and Discussion

i) Carbon derived from coal tar pitch

The carbon derived from the parent coal tar pitch has almost no microporosity or mesoporosity. The surface area of this carbon is very low (0.6 m^2/g). The carbon could not also be activated easily by CO_2 at 900°C. We then tried to blend coal tar pitch with polymer precursors such as polyfurfuryl alcohol, polyethylene glycol and sucrose. Table 1 summarizes the surface area of the carbons. The surface area for most of these carbons was below 50 m^2/g. The next step was to change the character of the coal tar pitch. When coal tar pitch was carbonized, the yield of the carbon was about 50%. We tried to incorporate the low volatile organics by trying to polymerize them using oxidizing agent like H_2SO_4 [1]. Coal tar pitch was mixed with PEG600 acid and H_2SO_4 and carbonized, this resulted in increasing the yield of the carbon to almost 95% per g of coal tar pitch. A systematic study of the activation showed that the surface area of these carbons could be increased upto 900m^2/g as shown in Figure 1. It scales up with activation time but does not increase much beyond 900 m^2/g. We used 5 hours as an upper limit for activation time. The next objective was to figure out the component in the carbonized pitch that aids the activation. We did this by isolating the components of the coal tar pitch that are insoluble in tetrahydrofuran. Both the insoluble and the soluble fractions were mixed with PEG600 diacid, carbonized and then activated using CO_2 at 900°C for 3 hours. Table 2 summarizes the surface area of the carbons pyrolyzed under different conditions. Coal tar pitch pyrolyzed at 900℃ had a surface area of 150 m^2/g. When we added sulfuric acid to the coal tar pitch and activated the sample, the surface area increased to 409 m^2/g. If we were to mix PEG 600 diacid with CTP in the absence of sulfuric acid, we could obtain a carbon with surface area as high as 870 m^2/g. We then dissolved the CTP in tetrahydrocarbon and extracted both the soluble and insoluble fraction of coal tar pitch. The soluble fraction of CTP when mixed with sulfuric acid and PEG600 diacid showed a surface area of 900 m^2/g while the insoluble fraction showed surface area of 1680 m^2/g.

The micropore volume of this material was about 0.6 cc/g while the mesopore volume was about 0.1 cc/g as shown in Figure 2.

Figure 3 (a) shows the cyclic voltammogram of carbon that has a surface area of 1476 m^2/g. The specific capacitance measured was a function of scan rate (Figure 3(b)). This suggested that although the surface area of the carbon was very high, the specific capacitance of the carbon was limited by the diffusion of the electrolyte anion into the pores. We believe that this could be due to the blockage of pores by PVDF, the binder. Nevertheless at very low scan rates (2 mV/sec), specific capacitance was as high as 170 F/g. The diffusion limitation was also seen from the Electrochemical Impedance Spectroscopy (EIS) measurements. Figure 4 shows the magnitude and phase angle plot of the impedance versus frequency. It was seen that at very high frequencies, the electrode is completely resistive but as the frequency is lowered, the anions start to permeate through the pores and the double layer capacitance is measured. Interestingly, the phase angle does not become 90° as is the case with purely capacitive material. There seems to be another resistive component, which seems to impede this behavior. This might be due to the pore resistance offered by the blockage of the micropores and hence the diffusion limitation. By reducing the concentration of PVDF from 10wt% to 5wt%, we saw that the capacitance increased from 81 F/g to 147 F/g (Figure 5). Capacitance as measured using EIS was 265 F/g for 5wt% binder and 135 F/g for 10wt% binder.

Our results are in agreement with our primary hypothesis that the presence of high QI content aids in development of microporous carbon by forming disordered carbon. Previous investigations have shown that THF soluble fraction was almost QI free and generally consisted of low molecular mass compounds [4]. However, the exact composition of the THF insoluble fraction is very difficult to study and might be worth studying to prepare better microporous carbon.

ii) Carbon derived from PFA/PEG diacid blend

Table 3 summarizes the results of activation, the corresponding surface area and specific capacitances achieved. These carbons did not have any diffusion limitations. We believe that this might be due to the fact that the bulk density (presence of macropores) of these carbons were very low and hence the binder does not block the pores. Another

noticeable feature was that the activation required considerably very less time. It took only about two hours of activation to achieve a surface area of about 1500 m^2/g. As we increased the molecular weight of PEG diacid, it even took lesser time to activate.

Figure 7 shows the pore size distribution of carbon derived from PFA/PEG600 diacid blend. We chose three different carbons activated for different times to compare. The surface areas of the carbon were 330 m^2/g, 920 m^2/g and 1360 m^2/g. It is seen that the micropore volume increases with increase in the surface area of the carbon. The micropore volume for the 1360 m^2/g was about 0.6 cc/g and the mesopore volume was 0.11 cc/g. Both the micropore and the mesopore volumes increased with increase in the surface area. The ratio of the mesopore/micropore volume was 0.069, 0.072 and 0.1474 respectively.

We also looked at the effect of pyrolysis temperature on the surface area of the activated carbon. Figure 8 shows a plot of the surface area of carbons activated under similar conditions versus the pyrolysis temperature of the precursor. The samples were pyrolyzed from 900℃ - 1800℃. It was seen that the surface area of the sample increased with increase in the pyrolysis temperature upto 1200℃. The surface area of the carbons were as high as 2300 m^2/g. However, when the pyrolysis temperature was increased further, the surface area begins to decrease due to the collapse of the pores in the carbon at such high temperatures.

Figure 9 shows the overall plot of specific capacitance versus surface area made from different precursors. It was seen that the specific capacitance was proportional to the surface area. For surface areas less than 1000 m^2/g, the specific capacitance was less than 100 F/g. However, when the surface area was increased above 1000 m^2/g, the specific capacitance increased appreciably to 200 – 250 F/g. We see that the mesopore/micropore volume in this material almost doubles for carbon greater than 1000 m^2/g as compared to carbon less than 1000 m^2/g. This suggests that the presence of mesopores is very critical to have higher specific capacitance.

Carbon derived from PFA/PEG diacid shows lot of promise to develop high surface area carbon for capacitors. Our experiments show that the role of functional groups on PEG (-OH or –COOH) plays an important role in determining the character of the derived carbon. The –OH terminated PEG when blended with PFA leads to carbon

with very little macroporosity and mesoporosity. This material is difficult to activate using CO_2. On the other hand, -COOH terminated PEG results in carbon with very high surface area. The mechanism for this dramatic difference is still unknown and is under study. Our hypothesis is that there is change in the nature of interaction of PEG with PFA. With PEG diacid, there could be more hydrogen bonding, possible covalent bonding (ester formation) resulting in better mixing with PFA. The better-mixed blend can then undergo much more controlled reaction induced phase separation at higher temperatures.

Figure 10 shows the comparison of the pore size distribution of our carbon with a commercial activated carbon (BP-20) used in ultracapacitors. The experiments were done in Rohm and Haas using Argon porosimetry and DFT analysis. Based on the DFT analysis the coal tar pitch blend samples and polymer blend samples have similar peak in the distribution as BP-20 near 14Å. However, the polymer blend sample has a broad peak in the range 100 - 2500Å while the coal tar pitch have a small tail in the region extending upto 1000 Å. This suggests that the coal tar pitch sample can be used for high energy density capacitor applications while the carbon derived from polymer blend sample can be used for fast charge/discharge capacitor applications.

iii) Demonstration of double layer electrochemical capacitor

The capacitor was tested using Galvanostatic charge/discharge experiments, Cyclic voltammetry and Electrochemical Impedance Spectroscopy. We tested the capacitors made using both coal tar pitch/PEG 600 diacid blends and polymer blends. The capacitor was made using a carbon prepared using PFA/PEG600 diacid that has a surface area of 1360 m^2/g while the coal tar pitch/PEG600 diacid had a surface area of 1500 m^2/g. Our electrochemical measurements showed that carbon derived from polymer blends had a specific capacitance of 180 F/g while carbon derived from coal tar pitch blends had a specific capacitance of 130 F/g. Figure 11, 12 and 13 shows the cyclic voltammogram, Bode plot of the tested capacitor and Constant current charge/discharge measurements.

Conclusions

Nanoporous carbons were derived from two different precursors such as CTP/PEG diacid blend and PFA/PEG diacid. Our investigation showed that surface areas ranging from 1500 – 2000 m^2/g could be achieved upon activation of these carbons using CO_2. The specific capacitances for these carbons can be as high as 250 F/g. THF insoluble fraction of CTP when carbonized can be activated to yield a very high surface area carbon that can be potentially used as electrodes in capacitors. We believe that this carbon can be used to make high energy density capacitors as the bulk density of these carbons can be as high as 0.5 – 0.8 g/cc. PFA/PEG diacid blends also acts as excellent precursor to develop high surface area carbons. This carbon can be used to make capacitors that have fast charging/discharging capabilities. The developed carbons were systematically studied using cyclic voltammetry and electrochemical impedance spectroscopy. We have also fabricated a two-electrode electrochemical double layer capacitor using these carbons as electrodes. Using sulfuric acid as electrolyte, we were able to make capacitors with capacitances as high as 150 -180 F/g. These are very promising and we believe that there is potential to extend the use of these capacitors in organic electrolyte system to achieve higher energy densities.

References

1. Ferruti, P.; Tanzi, M. C.; Koleske, L.; Cecchi, R.; *Makromol. Chem.* **182**, 2183 (1981).
2. Petrova B., Budinova T., Petrov N., Yardim M.F., Ekinci E. and Razvigorova M., *Carbon*, **43**, 261 (2005).
3. R.K. Mariwala and H.C. Foley, *Ind. Eng. Chem. Res.*, **33**, 2314-2321 (1994).
4. Andresen J.M., Martin Y., Moinelo S.R., Maroto-Valer M.M. and Snape C.E., *Carbon*, **36**, 1043 (1998).

.

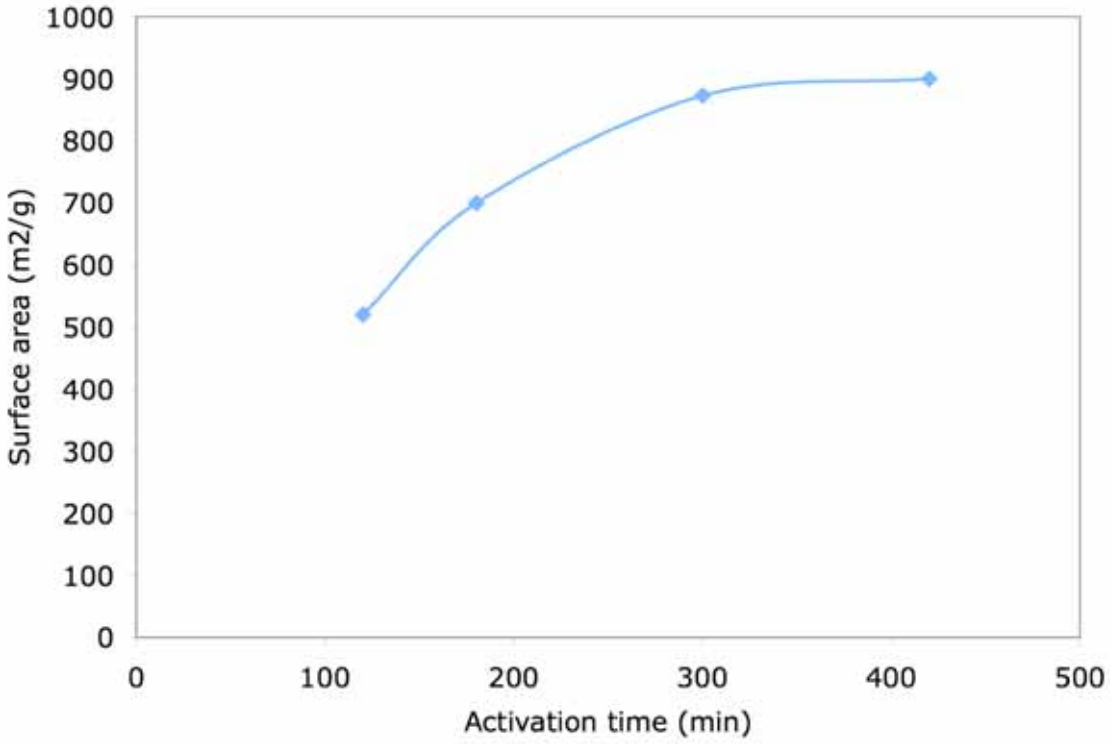

Figure 1. Surface area of carbon derived from CTP/PEG600 diacid blend mixed with H_2SO_4 as a function of activation time using CO_2 at 900°C

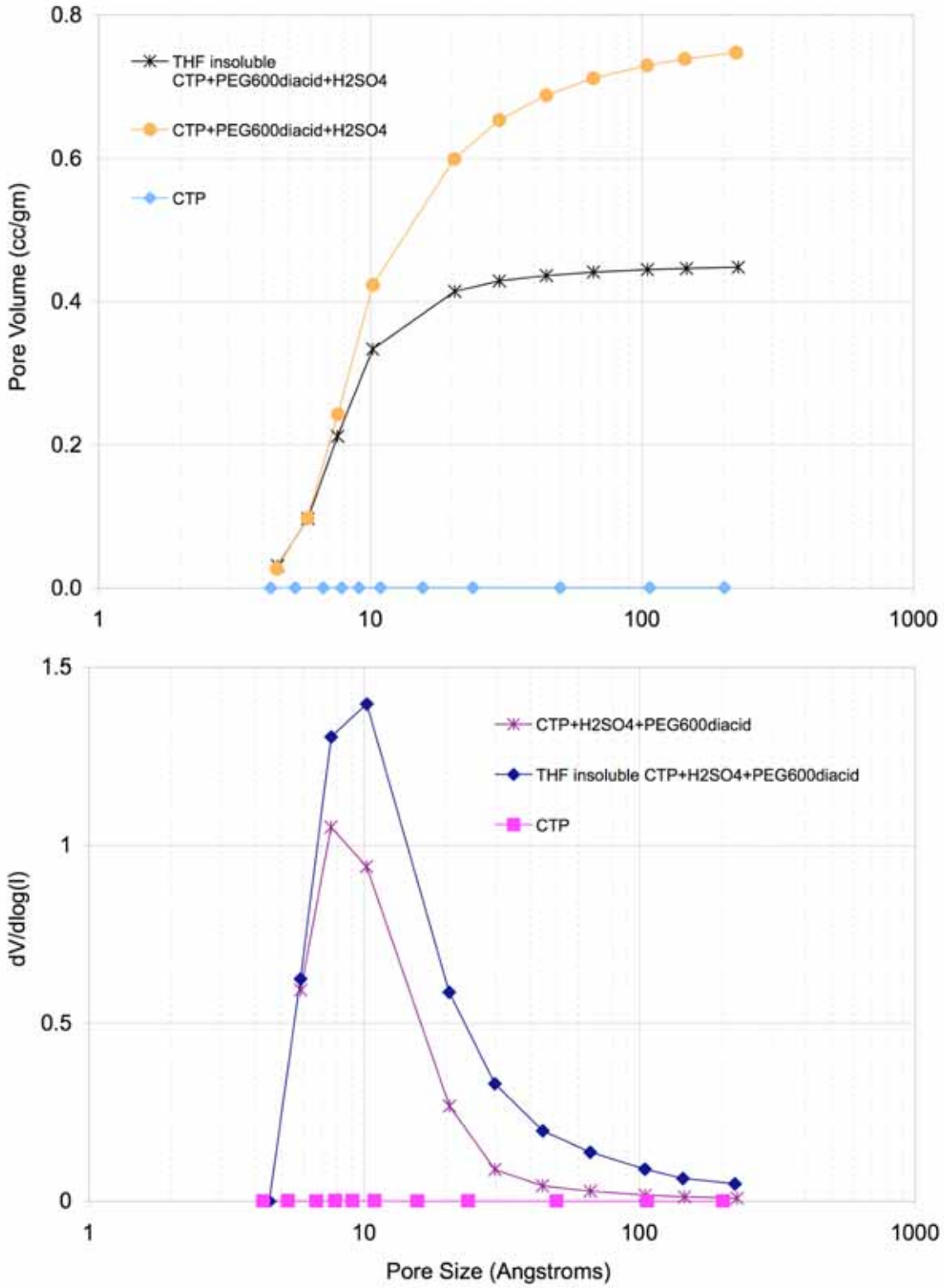

Figure 2 Pore size distribution of carbon derived from coal tar pitch

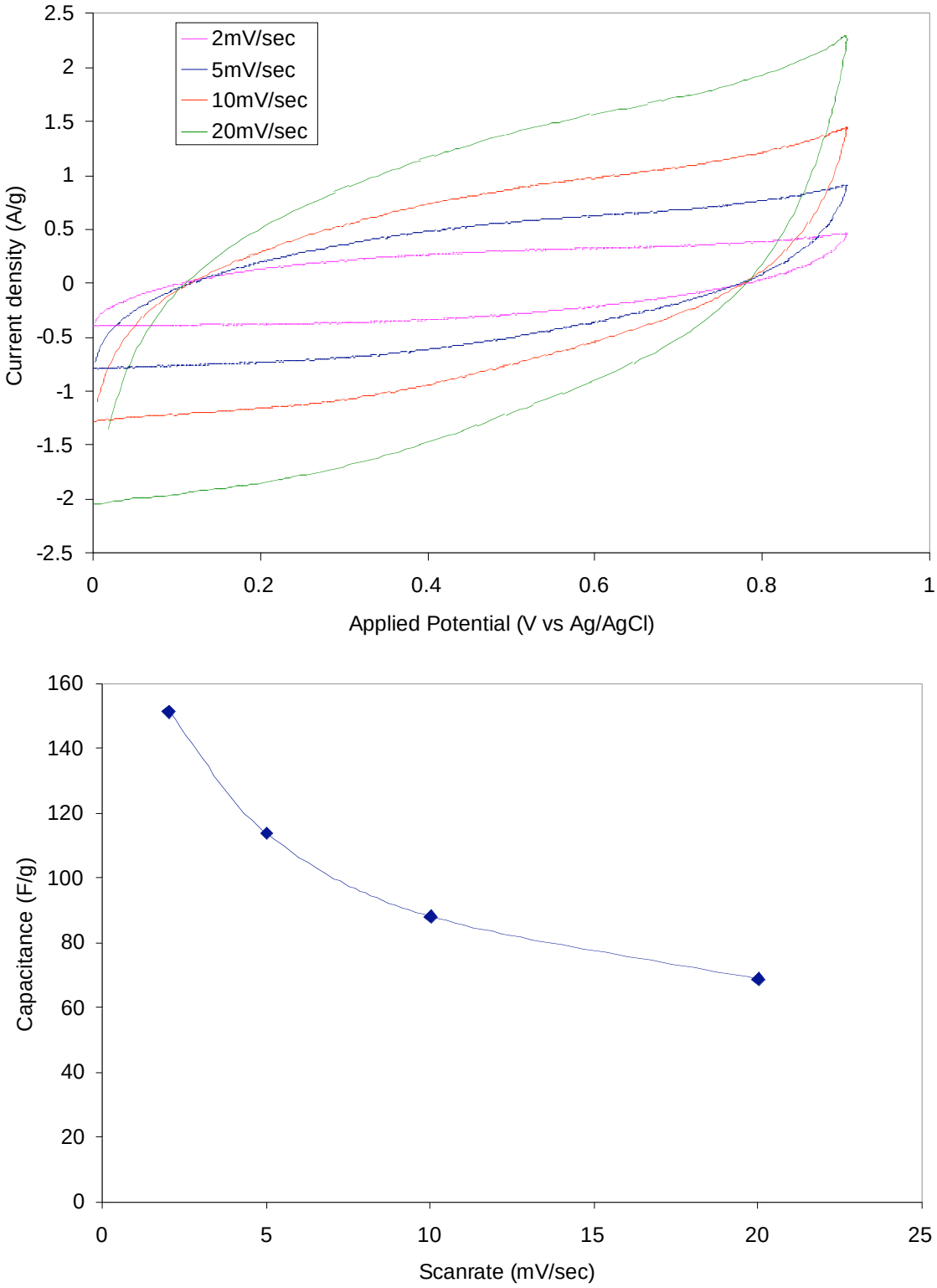

Figure 3 (a) Cyclic voltammogram of carbon derived from CTP having a surface area of 1476 m^2/g using 10wt% PVDF as binder and (b) Specific capacitance of carbon derived from CTP having a surface area of 1476 m^2/g using 10wt% PVDF as binder

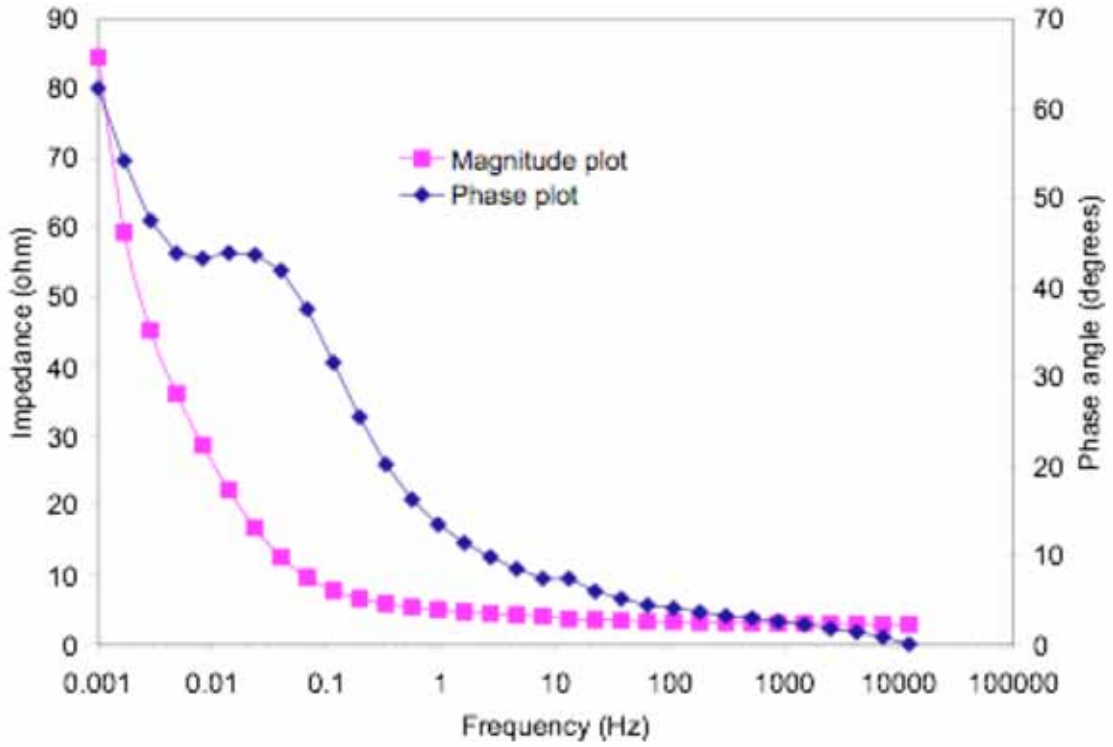

Figure 4. Bode plot of carbon derived from CTP using 10wt% PVDF as binder

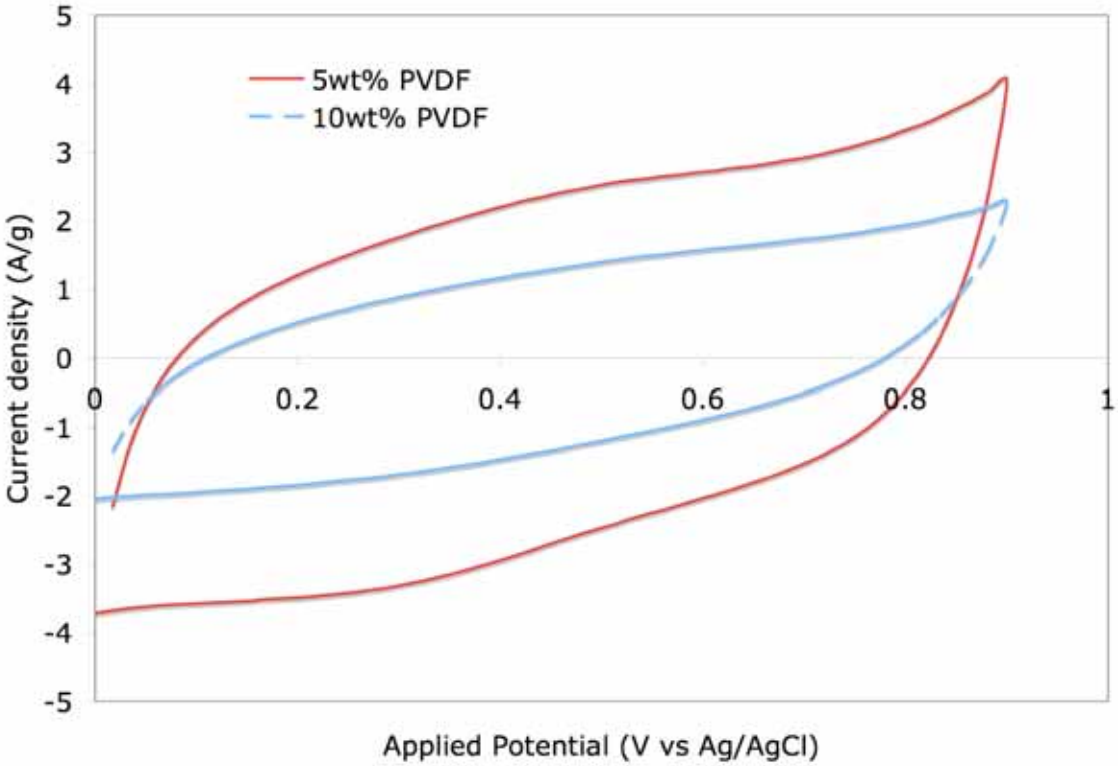

Figure 5. Cyclic voltammogram of carbon derived from CTP as a function of PVDF concentration

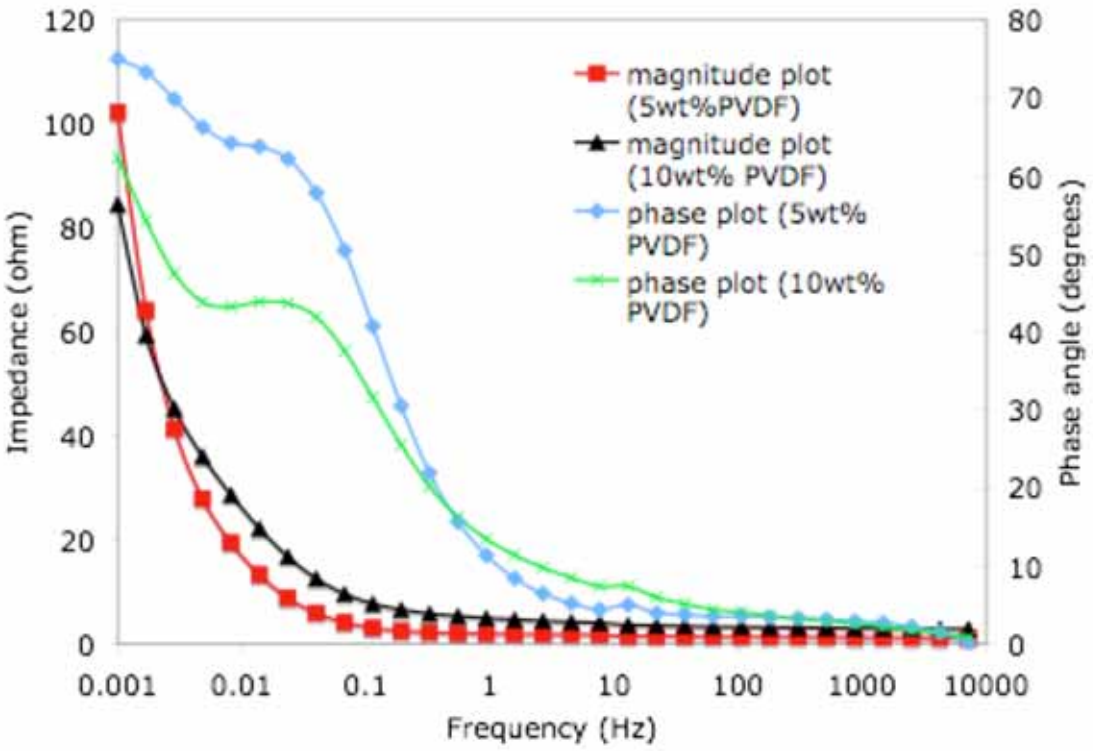

Figure 6. Comparison of bode plot of carbon derived from CTP that has a surface area of 1476 m^2/g using two different binder concentrations

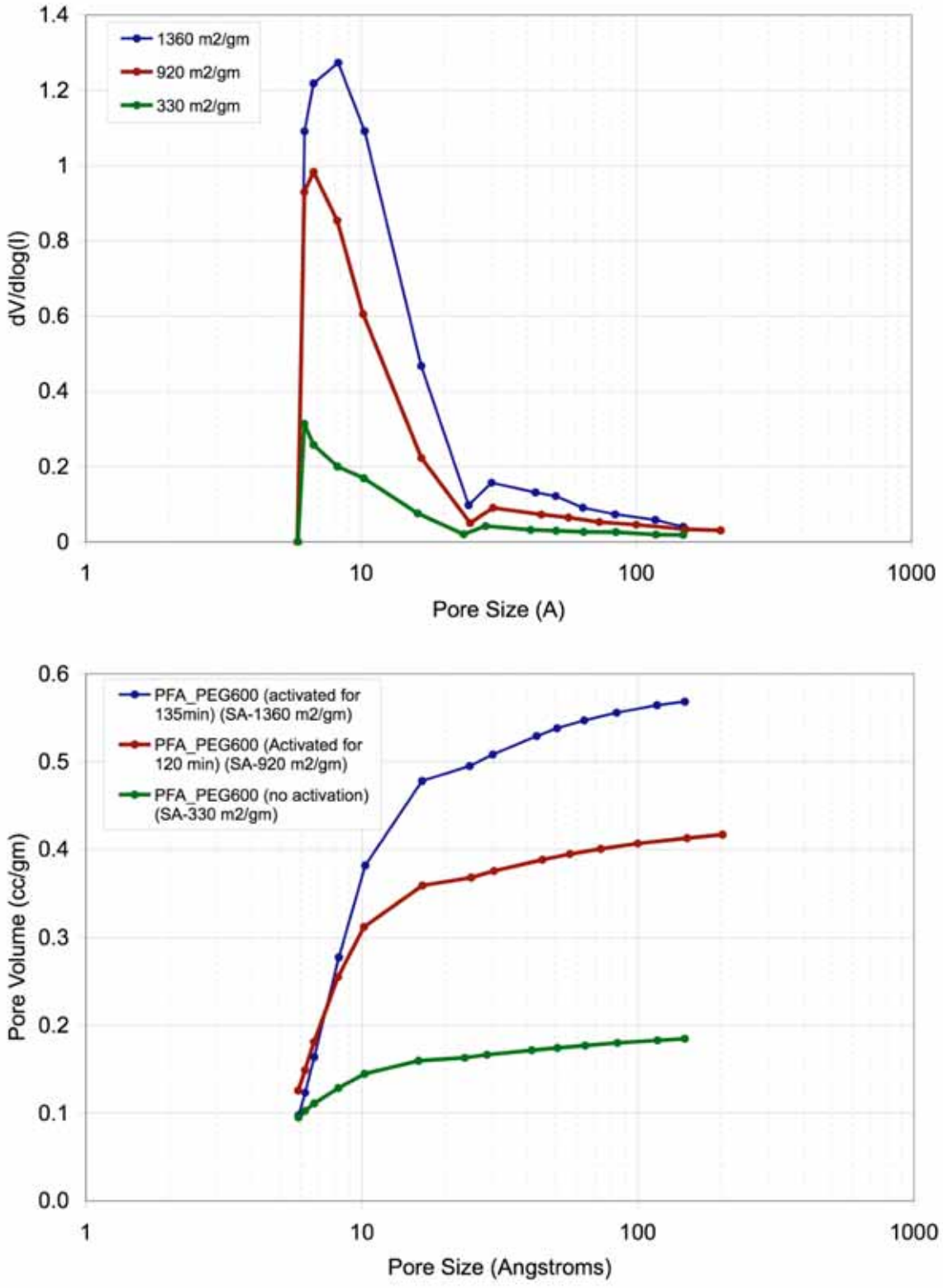

Figure 7. Pore size distribution of carbon derived from PFA/PEG600 diacid blend

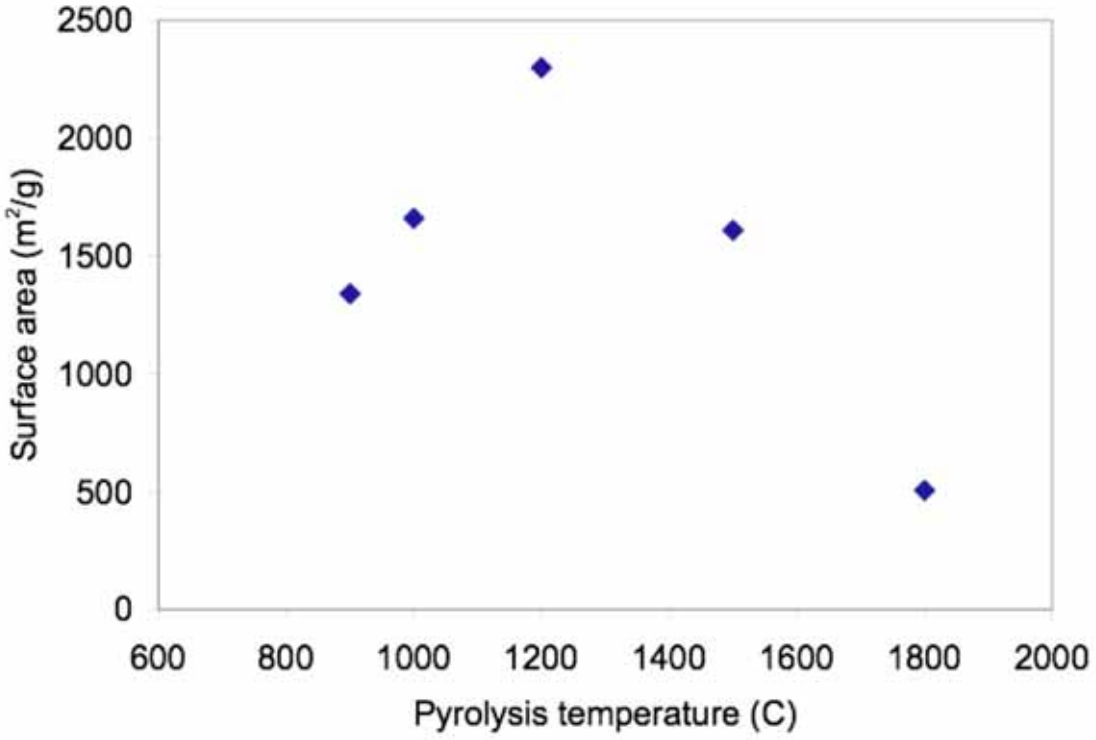

Figure 8. Surface area of the activated carbon as a function of pyrolysis temperature of polyfurfuryl alcohol/polyethylene glycol diacid blend precursors

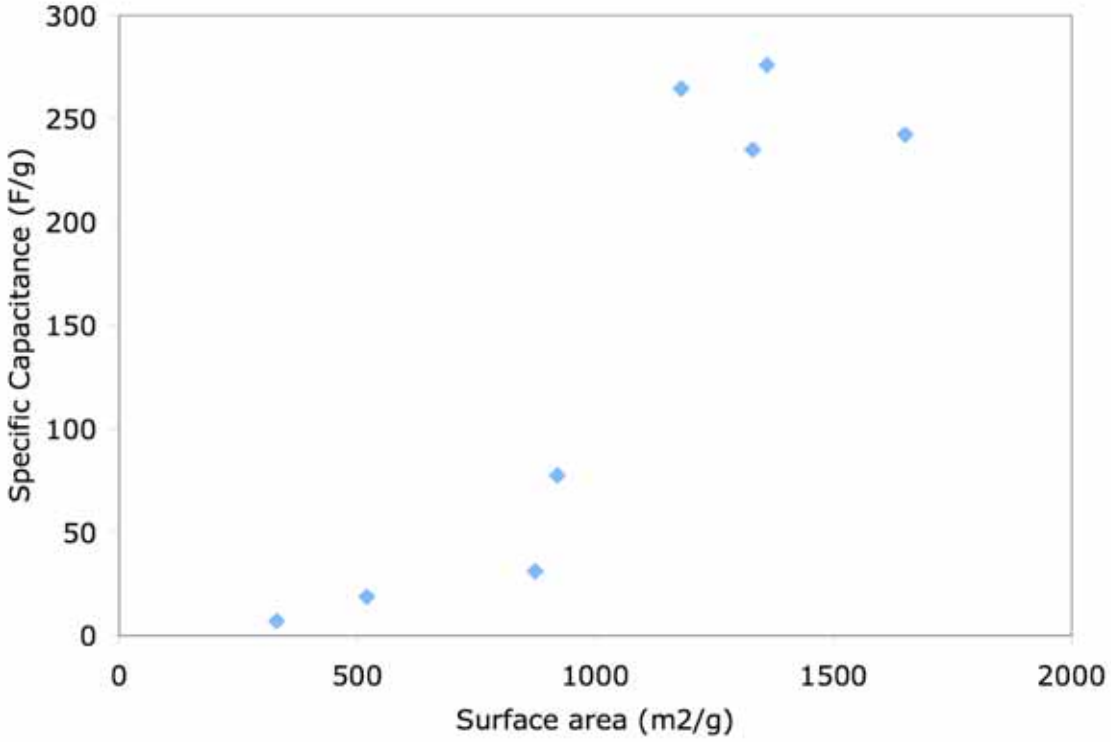

Figure 9. Specific capacitance of different carbons and their corresponding surface area.

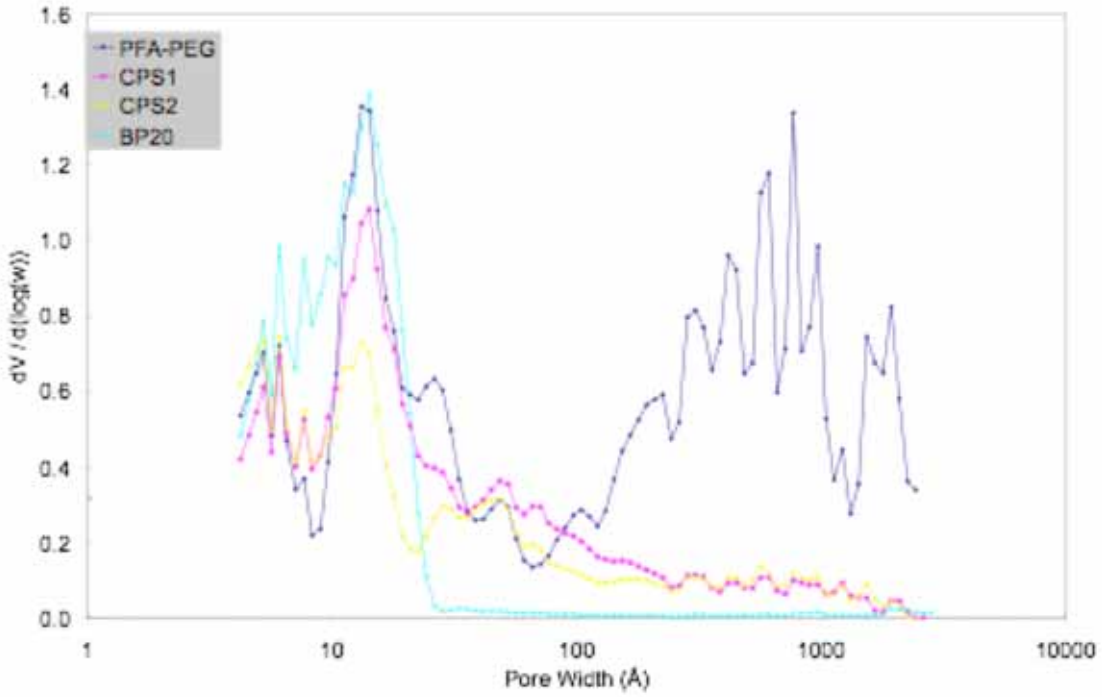

Figure 10. Comparison of the Pore size distribution using DFT analysis of carbon derived from coal tar pitch blends, polymer blends and commercial activated carbon BP-20

(a)

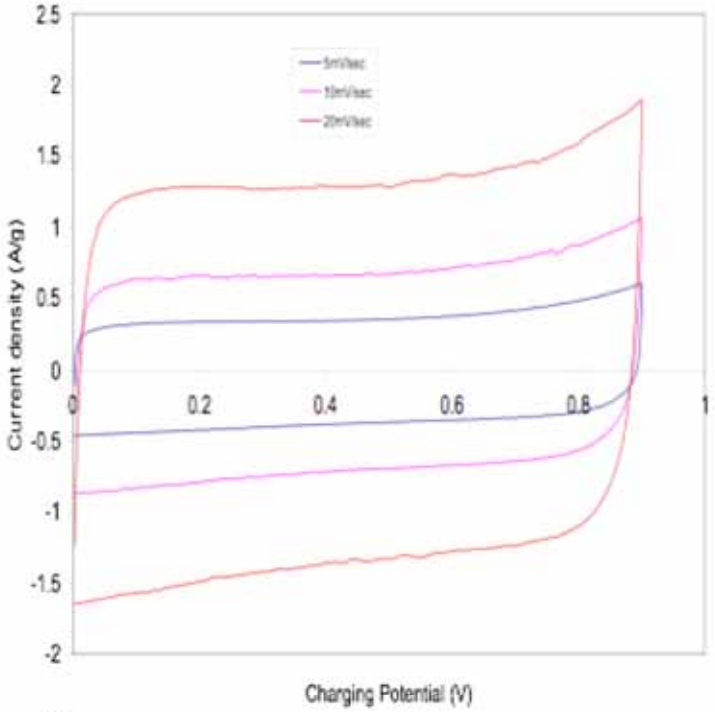

(b)

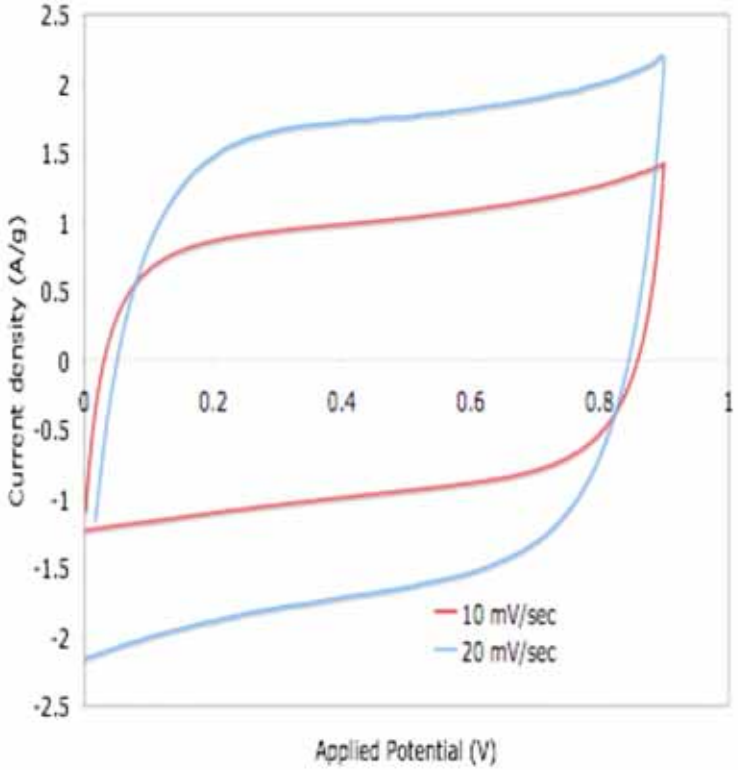

Figure 11. Cyclic voltammogram of a capacitor made with a) PFA/PEG 600 diacid carbon and b) CTP/PEG 600 diacid carbon

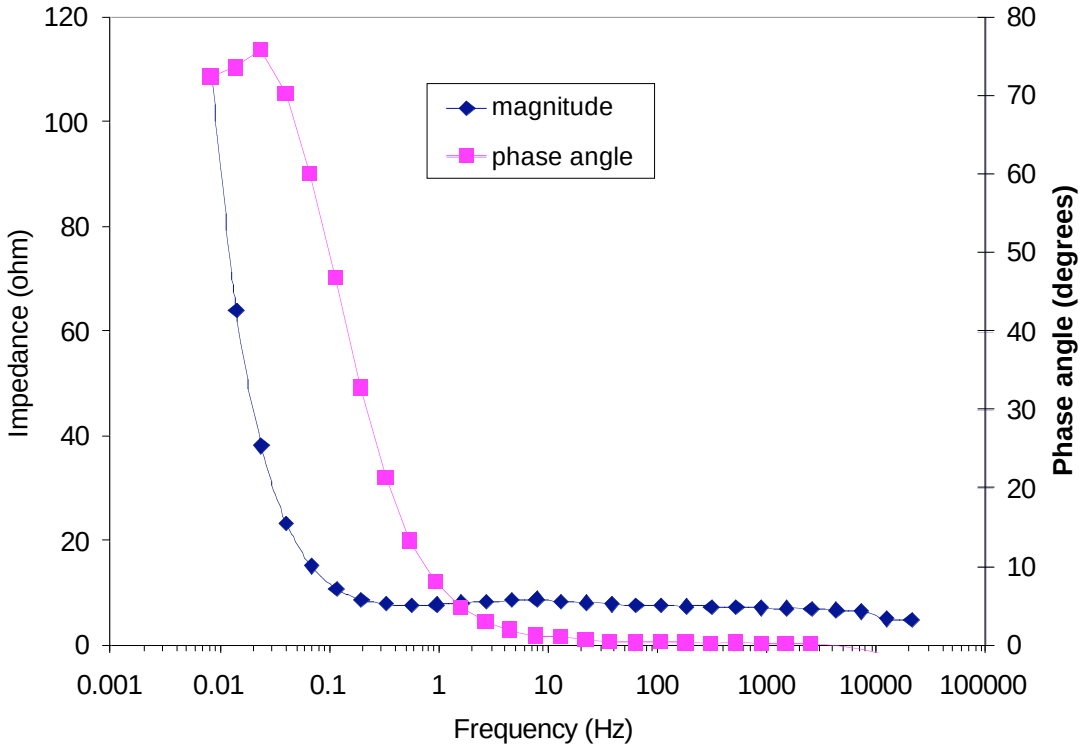

Figure 12. Bode plot of a capacitor made with carbon that has a surface area of 1360 m^2/g

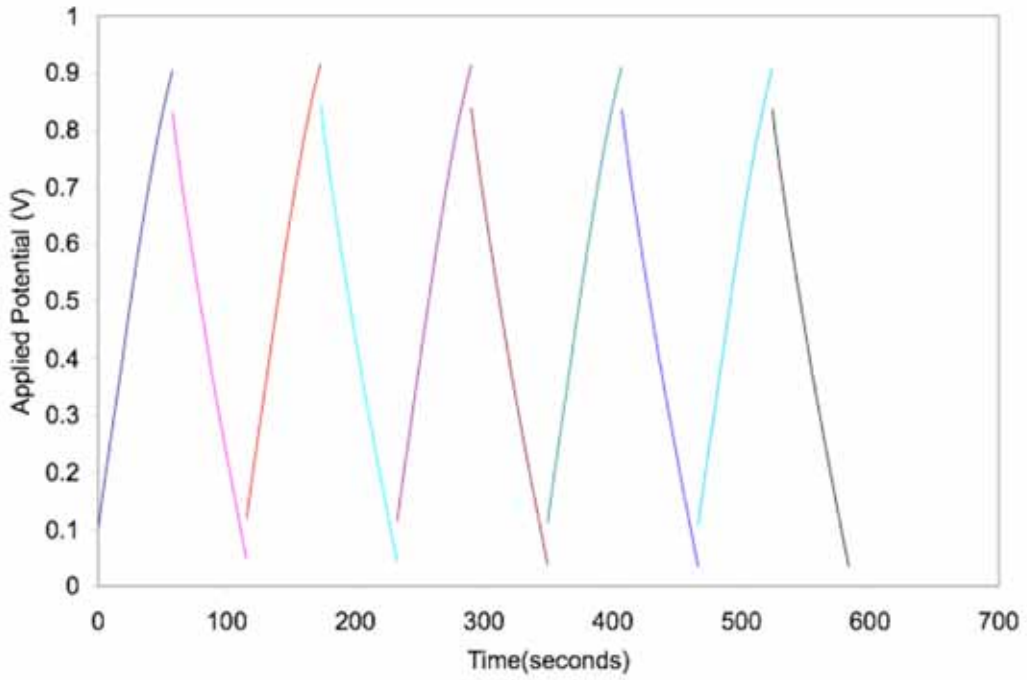

Figure 13. Constant current charge-discharge measurements on a capacitor under a constant current load of 1A/g

Samples	Surface area (m^2/g)
CTP	0.3
CTP_PEG2k	0.46
CTP_PEG6k	1.07
CTP air activated	20
CTP_PFA	13
CTP_PFA_KOH	37.23
CTP_sucrose	18

Table 1. Surface area of coal tar pitch and coal tar pitch/polymer blend

Samples	Surface area (m^2/g)
Coal tar pitch	115
Coal tar pitch + H_2SO_4	409
Coal tar pitch + PEG600 diacid	873
THF soluble + PEG 600 diacid + H_2SO_4	920
THF insoluble + PEG 600 diacid + H_2SO_4	1680

Table 2. Surface area of activated coal tar pitch/polymer blends

PFA blended with	Activation time (min)	Surface area (m^2/g)	Specific Capacitance (F/g)
PEG 600	-	330	7
PEG 600	120	920	77.6
PEG 600	135	1360	276
PEG 1000	120	1330	235
PEG 2000	60	1180	264.7
PEG 2000	120	1650	242.35
PEG 3350	45	1200	-

Table 3. Specific capacitance and surface area of carbon derived from PFA/PEG600 diacid

ADAPTING ANTHRACITE COAL AND STOCKPILED ANTHRACITE FINES TO GREEN SAND IRON FOUNDRIES

CPCPC Final Report

Reporting Period Start Date: March 1, 2005
Reporting Period End Date: June 30, 2006

Principal Author(s) from Penn State: Fred Cannon
He Huang
Yujue Wang
Robert Voigt
Jason Clobes

Principal Author(s) from Neenah Foundry: Jeff Goudzwaard

Report Issued: July 2006
DOE Award Number: 2873-TPSU-DOE-1874

Principal Investigator: Fred S. Cannon, Professor
Department of Civil and Environmental Engineering
The Pennsylvania State University
212 Sackett Engineering Building
University Park, PA, 16802
Tel: 814-863-8754
Email: fcannon@psu.edu

DISCLAIMER

Abstract

Characterization of properties and performance of bituminous coal (highly volatile) currently used in foundry green sand molds provides the baseline from which the foundry performance of anthracite coal substitution can be evaluated. Then lab scale experiments discovered that lignite-based in-situ pyrolyzed carbon can robustly contain more pore volume and surface area than bituminous coal-based and anthracite-based in-situ pyrolyzed carbon. Full scale experiments found a 32% percent removal of VOCs emission by using regenerated commercial activated carbon. The emission characteristics of the highly volatile bituminous coal and the potential substitute carbonaceous additives were evaluated. Knowledge of this would help the foundry personnel to choose the proper material, and provide guidance for process modifications in the foundry to minimize their HAP emissions.

Table of Contents

1. Project Introduction

1.1 Advanced Oxidation Processing in Green Sand Foundries

Iron casting green sand foundries produce "green sand" molds by compacting silica sand bonded with wet bentonite clay mixtures (with dry clay content about 6-12% by weight). The bentonite clay is "activated" (hydrated) by mixing in "temper" water at approximately 35% of the weight of the clay—or about 2-5% of the total green sand weight—and by mechanically shearing the wet clay and sand mixture ("mulling"). The wet clay holds the sand particles together in the compacted mold during the casting process. Carbonaceous materials, typically highly volatile bituminous coal, are also added to the mixture at various levels (generally 2-10% of the mold), primarily to prevent the molten metal from wetting the sand and clay in order to facilitate removal of the solidified casting from the mold and to improve the casting surface finish.

When molten metal is poured into a green sand mold, the heat from the metal dissipates outward into the mold. As the heat progresses into the mold, carbonaceous materials are both volatized and combusted, and the clay dries. The heat volatilizes organic gases from the bituminous coal at the mold/metal interface. These gases provide a barrier between the casting surface and the mold materials and also produce a reducing atmosphere around the casting. The coke that is produced also helps to prevent molten metal from penetrating the mold. The bentonite clays "dry" in three ways: (i) the external surface water is readily lost at low temperatures (<110°C); (ii) water adsorbed around the cations in the interlayer is also lost at relatively low temperatures (~100-150°C); and (iii) at temperatures greater than about 500°C, a portion of the clay can also "calcine", where the hydroxyls in the clay combine to release water (dehydroxylation), and the clay is changed into a non-functional aluminosilicate (Cartage.org, 1984).

Advanced oxidation (AO) processing in green sand foundries is designed to facilitate the recycling of used clay and coal materials in sand system baghouse dusts and to decrease volatile organic compound (VOC) emissions during molten iron pouring and casting cooling and shakeout processes. Typical AO processing in the foundry employs ozone aeration and hydrogen peroxide additions to tap water or blackwater slurries (aqueous mixtures of green sand system fines recycled from baghouses); combined with acoustic sonication and hydro-cavitation of the water/slurry to produce advanced oxidant-containing water/slurry. Ozone (O_3) aeration is produced through electric discharge ozone generators that produce a concentration of about 1-3% ozone in streaming oxygen (American Foundrymen's Society, Inc, 1976). The ozone aeration is intended to produce aqueous saturation of ozone at about 5-10 ppm. The hydrogen peroxide is added with typical concentrations of 100-500 ppm H_2O_2. Acoustic cavitation, or "sonication," is produced within the water/slurry by submersion of acoustic horns that are vibrating at frequencies typically ranging from 10 to 40 kHz at a total energy input of over 10 kW (American Foundrymen's Society, Inc, 1976). "Hydro-cavitation" is produced by forcing the water/slurry from high pressure to low pressure through a Venturi nozzle. Additionally, some AO units utilize underwater plasma and/or ultraviolet (UV) radiation units for hydroxyl radical generation. Chemically, the processing goal of the AO green

sand foundry systems is to produce large amounts of highly reactive hydroxyl radicals, $OH^{\bullet}$, for use in reactions with green sand mold components both at room temperature and at elevated temperature (during metal pouring and mold cooling).

There are two different AO system designs currently used in full-scale foundries—the AO-clean water system ("AO-CW") and the AO-dry dust to black water system ("AO-BW" or "AO-DBW"). The AO-CW system treats tap water with the advanced oxidation processes described previously, and the resulting "clean water" is added to the sand system at the sand coolers and/or the sand muller instead of tap water. A schematic of the AO-CW system is presented in Figure 1-1.

AO-BW processing utilizes chemical and physical treatment of recovered mold materials (primarily baghouse dusts, which are rich in clay and coal), and separates valuable, reusable materials (clay and coal) from waste silica and silicate materials (including calcined or "dead" clay). Foundry AO-BW systems directly treat slurries (10-17 volume% solids (American Foundrymen;s Society, Inc., 1994) of baghouse dust in water with the advanced oxidation processes described previously. A gravitational clarifier separates suspended particles (which are returned to the system in the temper water) from larger, higher density particles (which are removed from the system as sediment sludge via a drag chain). The suspended particles are a collection of clay, organic materials (mainly coal), and some silica fines, while the waste sludge consists mainly of larger silica fines and other silicates, with little clay or organic materials. Figure 1-2 presents a schematic of the AO-BW system. An example of the clay and coal recovery possible from an AO-BW clarifier is presented in Table 1-1.

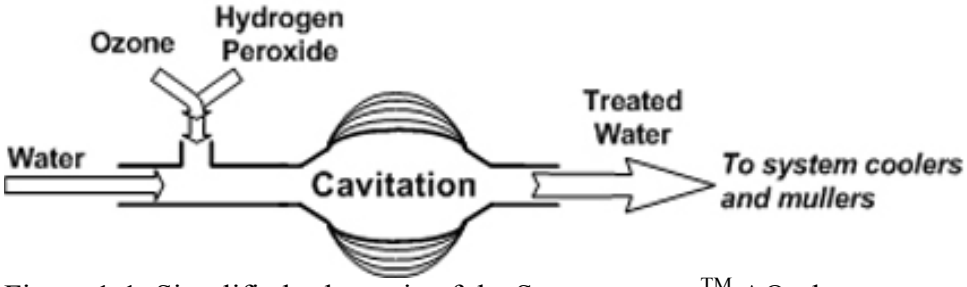

Figure 1-1: Simplified schematic of the Sonoperoxone™ AO-clean water system (modified from Cannon, Furness, and Voigt, 2000 (Cannon et al., 2000).

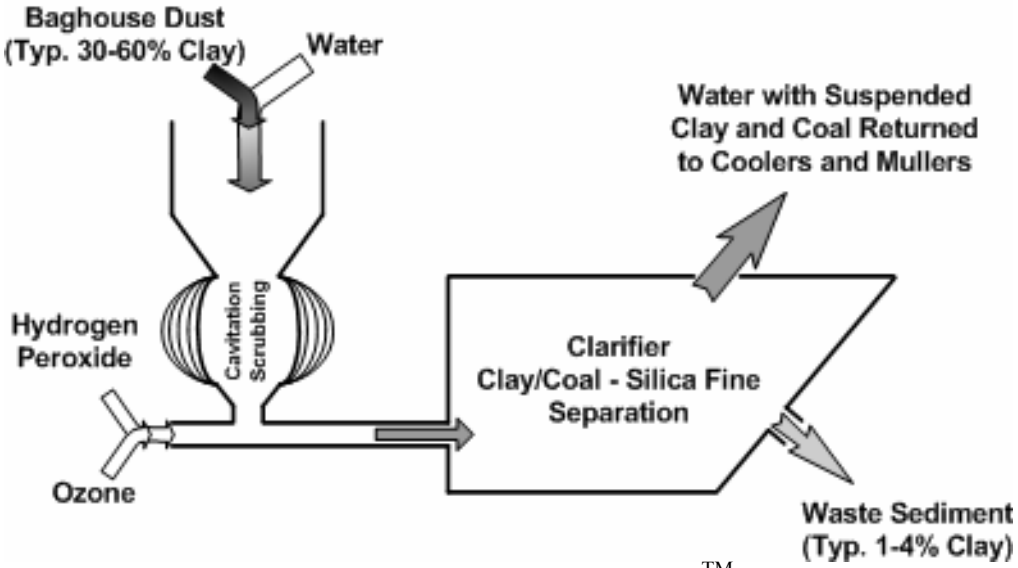

Figure 1-2: Simplified schematic of the Sonoperoxone™ AO blackwater system (modified from Cannon, Furness, Voigt, 2000 (Cannon et al., 2000))

Table 1-1: An example of clay and coal recovery in a foundry AO-BW system. (Glowacki et al., 2003)

	Weight Percent of Solids		
	Silica and Silicates	Bentonite Clays	Carbonaceous Materials
Baghouse dust (source)	30-50%	34-45%	20-23%
Blackwater solids (returned)*	5-30%	50-65%	20-30%
Waste sludge (disposed)	>85%	1-4%	4-11%
* Blackwater solids content was approximately 5-6% by weight in water			

The advanced oxidation system can be incorporated into a green sand foundry process as shown schematically in Figure 1-3. In AO-CW systems, tap water is subjected to AO treatment, and the AO-treated tap water is added to the sand mullers and/or the sand coolers. In AO-BW systems, foundry baghouse dust is added to tap water. This slurry is then subjected to AO treatment, and the AO-treated slurry of suspended particles from the top of the blackwater clarifier is added to the sand mullers and/or the sand coolers. Green sand returning from the sand coolers is physically mixed with new makeup sand, clay, and coal (as well as other additives), and AO-treated water or slurry in the muller. The conditioned green sand is subsequently compacted by high pressure molding machines into the desired mold shapes, and then any cores are added. Molten metal is poured into the mold cavity, and the casting solidifies and cools in the mold as the heat transfers outward from the casting. Once the casting is sufficiently cooled, the mold is broken off from around the casting, and vibrating machines shake the green sand off of

the casting ("shakeout"). The loose sand is then cooled and sent to the muller to be reused. Exhaust systems draw fine particles along with the exhaust air from the pouring, cooling and shakeout areas and the sand cooling and muller system to prevent the buildup of silica fines within the green sand. The exhaust passes through baghouse particulate collection systems before being exhausted through the stacks. The particulate fines collected in the baghouses (termed **baghouse dust**) are then reusable in AO-BW systems.

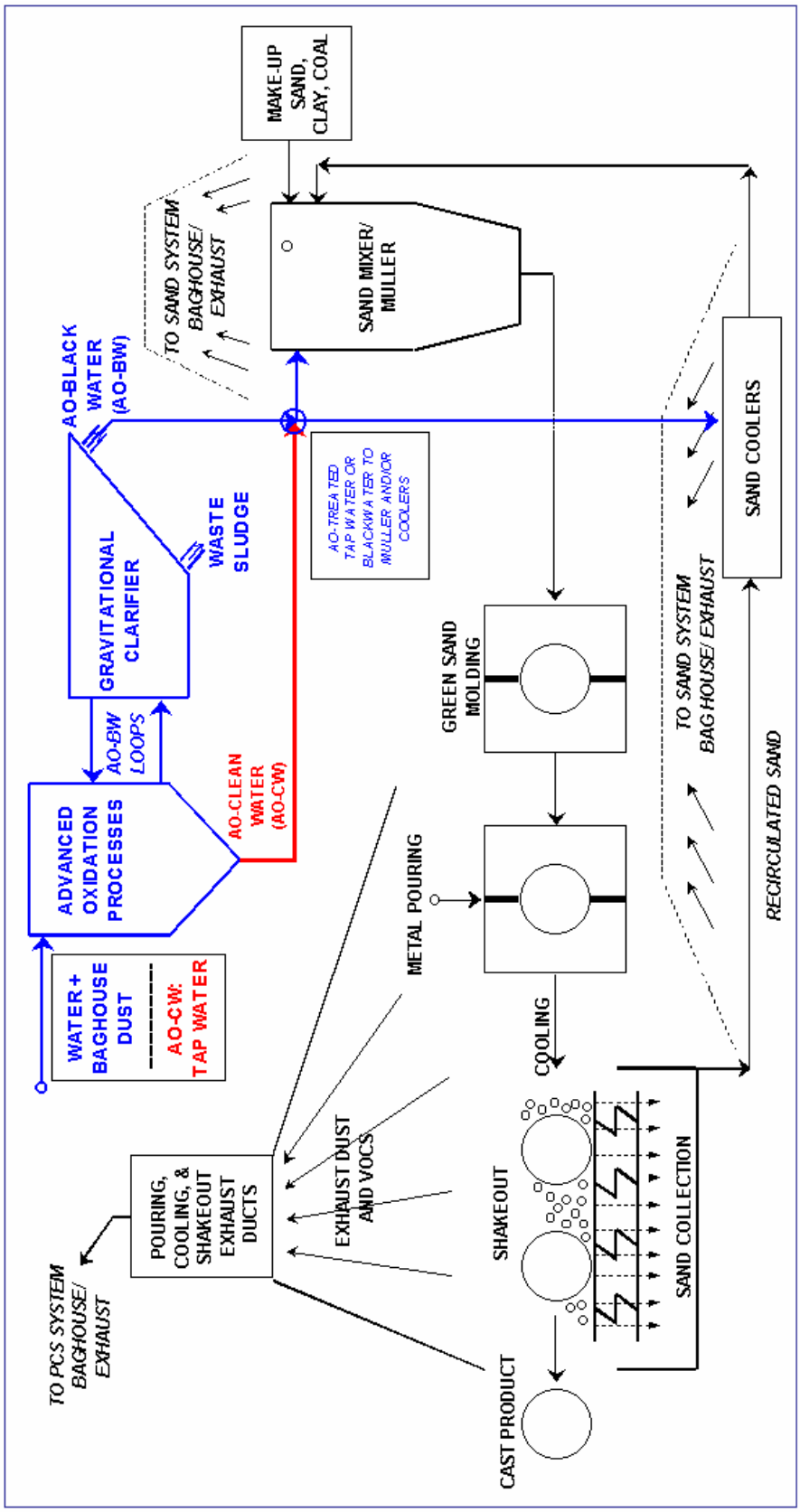

Figure 1-3: Schematic of a foundry casting process (modified from Neill et al., 2001 and Glowacki et al., 2003

1.2 Mold and Baghouse Dust Material Organic Materials

Organic materials, typically coal, are also mixed into the green sand for iron casting. These materials can provide a non-wetting barrier between the molten iron and the mold surface and can improve casting finish, eliminate surface defects, and improve sand handling characteristics. Additionally, organic-bonded sand matrix core residuals (often phenolic urethane-bonded sand) are a component of green sand systems when complex, cored castings are produced in the foundry.

Carbonaceous materials improve the casting process in many ways. These materials liberate volatile matter at the mold/metal interface and also deposit a film of pyrolitic graphite at the mold surface when contacted with hot molten metal. Coking of these materials (loss of the volatiles) also swells the carbon, filling voids between the sand grains. Each of these processes helps to prevent the metal from wetting the mold surface. The decomposition of the carbonaceous materials also creates a reducing atmosphere that combats metal oxidation and reduces the extent of iron-silica reactions. However, due to the low carbon content necessary for steels, cereals instead of carbonaceous materials (such as highly volatile bituminous coal) are usually used for steel casting.

The main carbonaceous material used in iron casting green sand foundries is “highly volatile bituminous coal,” which is mainly bituminous coal with amorphous carbon. A schematic model of this bituminous coal is presented in Figure 1-4. Bituminous coal contains a large amount of aromatic material in the form of linked compact aromatic clusters. Because bituminous coal is not a high-grade coal, it inherently contains a greater concentration of nitrogen, oxygen, and hydrogen atoms than anthracite.

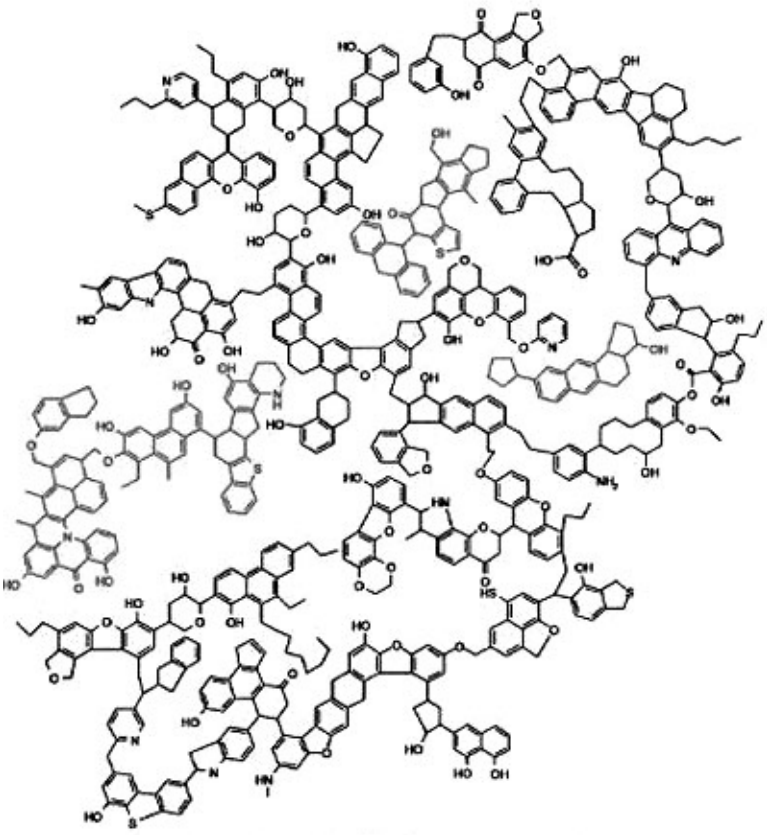

Figure 1-4: Model of bituminous coal.

Highly volatile bituminous coal can also be replaced in part by asphalt or gilsonite, causticized lignite, or other carbon-based materials. Asphalt and gilsonite release high amounts of volatile matter quickly and therefore cause excessive air pollution; however they have been used to improve casting peel, and also produce low amounts of ash. However, excessive use may "waterproof the green sand." Causticized lignite can be added to enhance clay dispersion and reduce the viscosity of the sand system. It also acts as a "cushion material" to reduce mold expansion defects. Other petroleum distillates are also occasionally used in foundries as partial highly volatile bituminous coal replacements.

Other types of organic materials are also used in metal green sand casting, such as cellulose (fibrous plant matter), which is used as a cushioning agent, to control sand expansion defects, and to improve sand shakeout and flowability; cereals and starches (gelatinized organic carbohydrates), which are used to enhance the ease of pattern drawing and reduce sand erosion; and synthetic polymers, which are used to improve dispersion of the clays into the sand mixture. Additionally, cellulose, cereals and starches absorb water, and thus broaden the water temper range at which acceptable mold properties can be achieved. Mold release agents, such as silicones, fatty acids, paraffins combined with hydrocarbons, or linseed oils may also be used in small quantities to enhance pattern/mold separation during mold making.

Other green sand system additives may be used to enhance either the mulling or molding performance of green sand systems. Soda ash (sodium carbonate) is a common inorganic additive which is added mainly to keep the sand system from becoming acidic due to the recycled spent core/mold sand or the degraded organic sand additives. Organic or inorganic wetting agents (non-ionic, cationic, or anionic) can be added to the temper water to allow the water to better infiltrate the clay during mulling, or to enhance clay dispersion.

1.3 In-situ Pyrolyzed Carbon for VOC Adsorption

Air pollution is one of the most important environmental issues in iron foundries, and volatile organic compounds (VOCs) represent a major component of air pollutants. VOCs can be produced both from the coal and the phenolic urethane cores that are included in the green sand mold during the process. Foundries are required by EPA to diminish the air pollution. Activated carbon can be used to adsorb these emissions in the foundries, but using commercial activated carbon would pose a cost problem to the foundries. In conventional iron foundries, in order to melt the iron, high temperatures are required in the cupola. The exhaust gas from the cupola travels through a drop-out box, and then cools in an air-to-air heat exchanger followed by a wet scrubber system. Commonly these extra heat sources in the foundries are wasted. The temperature in the drop-out box is 815-1150˚C, and this compares favorably to the 800-1000˚C temperature at which activated carbon is commercially manufactured. Also, in some foundries, nitrogen gas is used to provide a gas blanket to protect the molten metal against oxidation during iron pouring. This operation heats the nitrogen temperature to 1300˚C. This gas flow could also be valuably reclaimed as heat and protection of the carbon pyrolysis. One objective of our research is to investigate the feasibility of reclaiming this commonly wasted heat and nitrogen gas, and use it to produce in-situ pyrolyzed carbon. This in-situ pyrolyzed carbon could be used to treat the air pollution in foundries. The proposed raw material of this in situ pyrolyzed carbon is coal, and we have thus far tested anthracite, bituminous, and lignite coals. We observed that pyrolysis will induce less mass loss for anthracite coal than for bituminous or lignite.

Our field scale proposal in foundries is to protrude a heat exchanger tube (HEX) through the drop box, and then pass coal, and wasted hot nitrogen gas through this tube. The first step has been to investigate the pyrolysis of the coals in the lab scale, in order to get the best operation conditions. In the lab scale experiments, thermogravimetric analyzer (TGA) was used to simulate the proposed situation of a drop-out box with heat exchange tube.

Thus, our field-scale aim has been to: (a) Use the waste heat from cupola exhaust air and the heated waste nitrogen gas from the metal nitrogen blanket, (b) pass waste nitrogen gas and pulverized coal through a HEX that resides within the drop box, (c) employ pyrolysis conditions (i.e. without added gas streams of CO_2, H_2O or air), which facilitates a rather uniform robust product over a broad range of temperature and contact time, (d) although the pyrolyzed coal product may have less pore volume and surface area than conventional activated carbon, it robustly and inexpensively contains enough porosity to adsorb the VOCs.

1.4 Hydrocarbon emission characteristics of typical carbonaceous additives in green sand foundries

Hazardous air pollutant (HAP) emissions from green sand foundries pose considerable hazards to the environment and human health. Among the 189 HAPs listed in the 1990 Clean Air Act Amendment (CAAA), some 40 compounds have been identified in the air emissions from the foundry (Technikon, 2000). And organic HAPs that are released from mold making, metal pouring, casting shakeout comprise over 90% (by weight) of the total HAPs in the typical foundry emissions (Schifo et al., 2003). Research has shown that one of the major sources of the HAPs is the pyrolysis of carbonaceous additives that are added into the green sand mold to improve casting quality and facilitates casting shakeout (Allen et al., 1991; McKinley et al., 1993; Fox et al., 2002; Schifo et al., 2003).

Although there are many different theories on the functions of carbonaceous additives in casting process, most of them rely on the ability of carbonaceous additives to release volatiles during the pyrolysis (Wang et al., 1973; Green et al., 1980; Dempsey et al., 1997). Upon casting heat, carbonaceous additives undergo pyrolysis reaction and release large quantities of volatiles. These volatiles are rich in hydrocarbon gases, together with certain amount of CO, CO_2, and etc. These gases form a gaseous blanket between the molten metal and the sand, and thus prevent their direct contact (Green et al. 1980). The hydrocarbon gases are further pyrolyzed to deposit a thin graphitic carbon layer (called as lustrous carbon in foundries) at the metal-mold interface. This lustrous carbon film keeps sand grains from sticking to the castings and prevents the formation of iron silicate (Wang et al. 1973).The pyrolysis of the carbonaceous additives and hydrocarbon gases also provide a reducing atmosphere at the metal-mold interface and prevent the oxidation of the hot casting surface (Green et al. 1980). From many years' experience, foundry personnel perceive that a certain amount of volatiles from the carbonaceous additives must be present in the green sand for the production of quality castings. When there are insufficient carbonaceous additives in the green sand to provide the volatiles, the extent of sand adherence to the casting surface increases (Volkmar et al., 2000); while when there are excessive carbonaceous additives, castings surface may generate wrinkles due to the piling up of lustrous carbon film (Naro, 2002).

The most commonly used carbonaceous additive is finely crushed high volatile bituminous coal due to its superiority to release large quantities of volatiles during pyrolysis. However, it was found that significant amount of hazardous air pollutants (HAPs) are present in the volatile emissions of the highly volatile bituminous coal, with benzene, toluene, xylene (BTX) compounds composing the major part. As a response to the ever stringent regulations on air emissions, foundries are seeking alternative carbonaceous additives to partially or totally replace the highly volatile bituminous coal in the green sand. Among many highly volatile bituminous coal replacements that have been tested in foundries or pre-production foundries, anthracite, lignite, and cellulose have shown some promising results of producing casting with acceptable quality (LaFay et al., 2004; Thiel et al., 2005). However, few emission data are available regarding the HAP emission characteristics of these materials. The reliabilities of the stack emission tests are generally poor. Considerable variations in HAP emissions were often observed

for stack tests (Lafay, et al. 2004; Thiel et al., 2005; Land et al., 2004; Schifo et al., 2003). This unavoidable variability in stack test results makes it difficult to estimate true emission levels and verify the emission reduction. In addition, many samples must be taken because of the large variation from one test to the next, which makes stack test expensive and time consuming to conduct. In comparison, laboratory analytical pyrolysis can be easily conducted under strictly controlled conditions that closely simulate the thermal conditions that carbonaceous additives experience in the green sand mold. And the emissions can be easily analyzed with laboratory instrument. These laboratory evaluations delivered key information to the present understanding of actual metal casting process (Bachmann et al., 1982; LaFay et al., 2000). Our previous study has shown thermogravimetric analyzer (TGA) was capable of simulating the emission trends that were observed in the full-scale foundry (Wang et al., 2004).

In this light, the objective of this research is to evaluate the emission characteristics of the highly volatile bituminous coal and the potential substitute carbonaceous additives with laboratory facilities. Knowledge of this would help the foundry personnel to choose the proper material, and provide guidance for process modifications in the foundry to minimize their HAP emissions.

2. Executive Summary

At first, initial experimental work characterizing the properties and performance of highly volatile bituminous coal currently used in foundry green sand molds has been completed. This characterization provides the baseline from which the foundry performance of anthracite coal substitution can be evaluated. The work summarized here includes ESEM characterization of highly volatile bituminous coal-containing baghouse dusts from a typical production foundry before and after treatment with advanced oxidants. ESEM and EDS measurements confirmed that AO and sonication treatments greatly separate surface clays from the large particles of silica and coal and reduce the size of the clay agglomerates. The physical characteristics of baseline bituminous coal particles in these baghouse dust suspensions have been characterized so that the relative performance of anthracite-based green sand mixtures can be similarly characterized in the later portions of the study.

Bench-Scale experiments regarding producing in-situ pyrolyzed carbon and full-scale tests using activated carbon to adsorb VOCs in Neenah foundry were studied. It was found that lignite will develop more surface area and pore volume during pyrolysis than did the anthracite and the highly volatile bituminous coal. Also, the pores developed in lignite are more robustly generated at a broad range of temperatures; and this is more favorable than for the highly volatile bituminous coal which yields considerable less pore volume at 600 ˚C or 900˚C than it does at 800 ˚C. Full-scale test shows that the VOCs emission in Neenah foundry can be diminished by 32% by applying reactivated carbon from NORIT Americas.

Further lab scale experiments were conducted to produce in-situ pyrolyzed carbon by using lignite as raw material with focuses on the different lignite resources, the effect of temperature and the effect of pyrolysis time on final product. The lignite from Sabine Mine provide the highest micro-pore volume and surface due to its highest fixed carbon contents among the lignites tested. It was also found that the in-situ pyrolyzed carbon contains the highest pore volume and surface area after being treated at 800 °C. As the pyrolysis time increases, the pore volume and surface area of the in-situ pyrolyzed carbon decrease. The best in-situ pyrolyzed carbon produced in the experiments so far contains surface about as much as 80% of the commercial activated carbon HD4000. Preliminary adsorption experiment using the in-situ pyrolyzed carbon suggests the in-situ pyrolyzed carbon is feasible to be used as an adsorbent for VOCs adsorption.

Finally, experiments were conducted to evaluate the emission characteristics of the highly volatile bituminous coal and the potential substitute carbonaceous additives, such as anthracite, lignite, and cellulose, with laboratory facilities. It is found that the hydrocarbon gas yields in the TGA slow pyrolysis are much lower than them in the flash pyrolysis for all the samples tested herein. Also, it is found that the heating rates have a more pronounced effect on the cellulose compared with other carbonaceous additives. Knowledge of this would help the foundry personnel to choose the proper material, and provide guidance for process modifications in the foundry to minimize their HAP emissions. As shown, the cellulose HAP emissions are much lower than them of other

carbonaceous additives tested herein. This would offer a great opportunity for the foundry to cut down the HAP emissions.

3. Experimental

3.1 Advanced Oxidation Processing of Baghouse Dust Slurries

Three of the main foundry advanced oxidation (AO) processing methods— acoustic sonication, ozone aeration, and the addition of hydrogen peroxide—were used to treat baghouse dust obtained 5/20/2002 from the Victaulic-Alburtis foundry (Victaulic Co. of America, Alburtis, PA). The baghouse dust from the Victaulic-Alburtis foundry was collected about one month after the introduction of an AO system into the foundry. Advanced oxidation (AO) processing of baghouse dust was performed in a *bench-scale* batch reactor (i.e. beaker). A slurry of baghouse dust was made by adding 30 grams of baghouse dust (approximately 62% clay and fine silicates with 28% hydrated clay, 25% silica, and 13% carbon, by weight) to 450 mL of distilled water (Sodium-free distilled water, bottled by Meyer Bros., West Seneca, NY) in a 600 mL Teflon beaker (4.75 in. height x 3.25 in. inside diameter) subjected to continuous stirring with a magnetic stirrer. The addition of the dust produced a 5% by weight slurry. This is a lower particle concentration than in most foundry blackwater clarifiers, where the solids concentration has been reported as 10-17 vol% (American Foundrymen's Society, Inc., 1994). The lower particle concentration used in these experiments amplified the effects found from the bench-scale AO setup.

"**Non-AO**" **treatment** for the experiments performed herein refers to simple stirring in water. Stirring was created via a magnetic stirrer and large stir bar (2.5 in. x 0.5 in.). The stirring was fast enough to create a vortex, but slow enough that the angle of the vortex was less than a few degrees. "**Untreated**" powders are different than "non-AO" powders herein in that untreated refers to as-received powders.

"**AO**" **treatments** for the experiments performed herein included acoustic sonication, ozonation, and hydrogen peroxide additions, emulating a simple foundry AO-BW system on a small scale. In cases where multiple components were used, the slurry was created under magnetic stirring as described for non-AO treatment above; then ozonation was applied to the reactor, followed quickly by acoustic sonication and then the addition of various amounts of a 2 wt% hydrogen peroxide solution to obtain the desired peroxide concentration. Figure 3-1 presents a sketch of the bench-scale reactor used for the AO treatment.

In these experiments, acoustic sonication was intentionally applied for very long durations; ozone was bubbled at a high rate through the slurry and hydrogen peroxide was added at high concentrations compared to that found in typical foundry AO-BW systems. AO component levels and treatment durations were increased in these experiments to overload the system with sonication and oxidants in order to amplify the effects from AO. Other differences between the batch scale reactor and full scale AO-BW systems include the lack of hydro-cavitation and turbulent flow capability and the lack of hydroxyl radical production enhancers (such as UV, plasma, etc.) in the batch-scale studies. Therefore, comparisons between the results of these experiments and that found in full-scale foundry AO systems cannot be directly made.

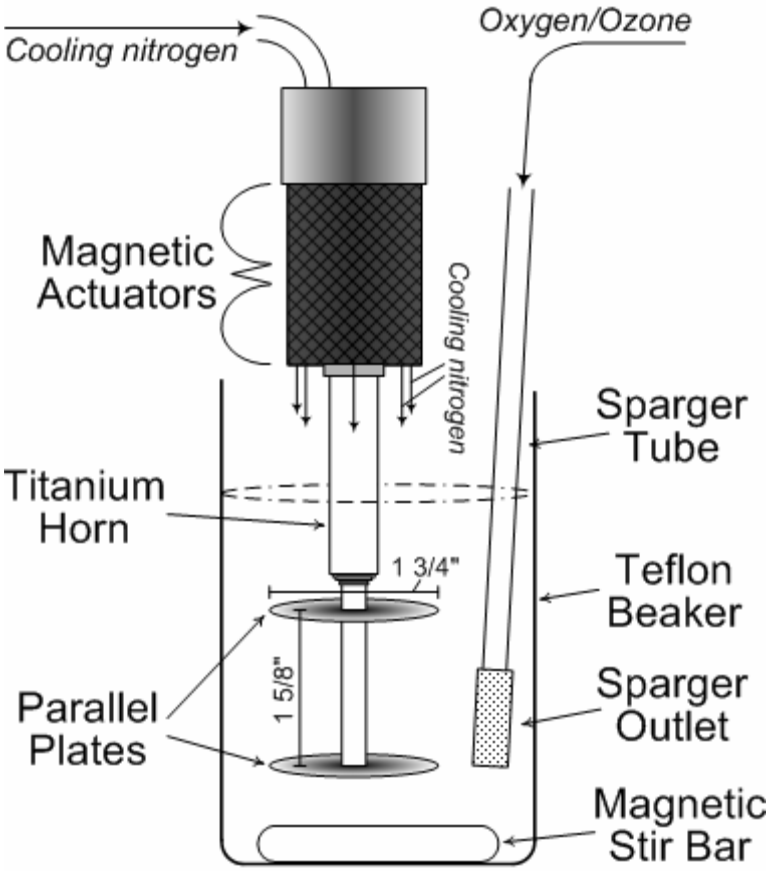

Figure 3-1: The bench-scale AO reactor setup (1/2-scale).

Acoustic sonication was applied via a frequency generator (Titan Series Manual Oscillator MOS-01 with AC power system) attached to a parallel plate titanium horn (Furness-Newburge, Inc., Versailles, KY). The horn plates were circular in shape, 1 3/4 inches in diameter, 1/16 inches thick; and were 1 5/8 inches apart, parallel to one another, and set perpendicular to the base of the beaker. The plates were welded to a 1/4 in. titanium rod—tapered up to 1/2 in.—that attached to the magnetic actuators. The horn was submerged into the slurry such that the bottom plate of the horn was approximately 1 inch from the bottom of the beaker. With 400-450 mL of slurry, the top of the horn was then about a 3/8 in. to 1/2 in. from the top slurry surface.

The frequency of the sonic unit was set at 10.75 kHz for all experiments. This frequency was chosen after trial and error experimentation, where the frequency was varied to find the most significant cavitation with the sonic horn immersed in water. Thus, 10.75 kHz was determined to be a frequency antinode that produced sufficient cavitation in water. The intensity of the sonication was controlled by the output current on the frequency generator. The output current was generally set at 100%, unless otherwise noted. The acoustic intensity varies approximately as the square of the output current (Intensity output = (Eff.) x Intensity input = (Eff.) x Power/Area = (Eff.) x I^2R/Area), where *I* is the current, *R* is the resistance, and *Eff*. is the efficiency of the device compared to the input.

The acoustic intensity should thus be approximately proportional to the square of the electrical current input to the device. Therefore, when the current to the actuators was halved, the acoustic intensity should have been approximately one-fourth of the original intensity. However, this relationship does not necessary hold for energy output of a device such as a sonic horn. The efficiency of the sonic horn output power is variable, depending on the power applied. Furthermore, the energy coupled to the slurry material can vary with the power as well. Variables and phenomena that can affect the acoustic intensity in the slurry include "temperature, viscosity, chemistry, cavitation, and pressure" (American Foundrymen's Society, Inc., 1976).

Nitrogen gas flowed through the acoustic actuator housing to cool the actuators and streamed downward (softly) onto the surface of the stirring slurry; however it is assumed that the relatively inert nitrogen would not chemically affect the slurry contents. Ozone (O_3) was generated via a "two-pack" corona-discharge generator (Furness-Newburge, Inc.), as shown schematically in Figure 3-2. In the corona-discharge generator, oxygen flows between two parallel plate electrodes between which a voltage is applied. The corona discharge produces the reaction shown in Eq. 0.1 to convert oxygen to ozone.

$$\begin{aligned} O_2 &\rightarrow 2\,O^{\bullet} \\ O^{\bullet} + O_2 &\rightarrow O_3 \end{aligned} \qquad 0.1$$

where the superscript "•" denotes a chemical radical. The "two-pack" produces a maximum of about 2-4% ozone in streaming oxygen. For the purposes of this report the incorporation of any amount of ozone in the reactor will be called "ozonation" or "ozone aeration."

The power to the electrode plates was held constant for every run at 50% of full power. Therefore, the gas entering the reactor was actually mostly oxygen with about 1-3% ozone. The oxygen/ozone mixture was bubbled through the reactor at a flow rate of about 10-12 scfh (standard cubic feet per hour)—the minimum recommended by the manufacturer (American Foundrymen's Society, Inc., 1976). Ozone (as a small percentage of the carrier oxygen) was released into the reactor through a 1 in. length x 1/2 in. diameter Pyrex sparger (12 C, ASTM 40-60) consisting of hundreds of tiny holes along the side and bottom surfaces. The oxygen/ozone gas exited through the holes in the sparger set about 1 inch from the bottom of the beaker. This produced vigorous bubbling through the stirred slurry.

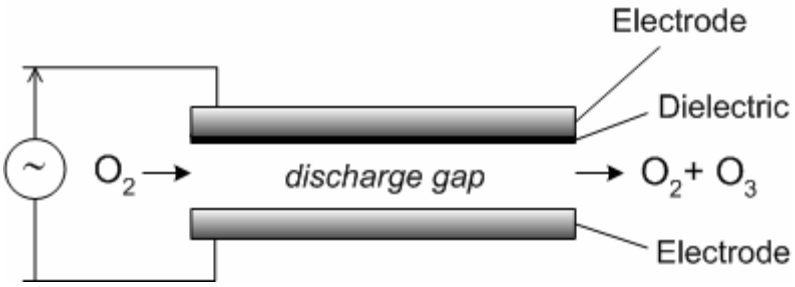

Figure 3-2: Schematic of corona-discharge ozone generation.

Hydrogen peroxide concentrations were produced by pipetting a specified amount of 2% hydrogen peroxide (Lot. 44215434, VWR International, West Chester, PA) aqueous solution into the stirring beaker. The peroxide was added slowly so that the peroxide would be dispersed into the slurry.

Two other sonication sources were also examined for baghouse dust slurries – a high-intensity sonic unit ("Sonifier") and a sonic bath. The high-intensity (400 watt) Sonifier (Sonifier Model 450, Branson Ultrasonics Corp., Danbury, CT) included a 1/2-inch diameter titanium surface through which all sonic power was transmitted. Because of the shape and size of this horn, the slurry to be sonicated had to be reduced in volume to less than 250 mL. The slurry was stirred for one hour previous to sonication, and then was stirred continuously during sonication. The sonic output cycle was set at about 50% pulse (pulsed on for about a half second, then off for about a half second) and 60% output control. The slurry was sonicated for a total duration of 1, 2, 5, 10, 20 and 30 minutes, stopping for particle size analyses at each interval.

The other sonication source that was tested herein was an ultrasonic bath (Branson Model 1510 Ultrasonic Cleaner, Branson Ultrasonics, Danbury, CT). The Branson 1510 vibrates a water bath at 40 kHz to transmit sonic power into a beaker of sample immersed in the bath. A 600 mL stainless steel beaker containing 450 mL of slurry (at normal solids concentration) was immersed into the vibrating sonic bath for 1 hour of sonic treatment. The temperature of the bath and the sample increased over time due to the sonic energy input—with the slurry in the beaker warming faster than that of the bath. To control the temperature the bath water was replaced with cool water every 10 minutes. Stirring of the sample was performed manually about every five minutes using a plastic stirring rod. It should be noted that the large particles quickly settled to the bottom of the beaker since there was no continuous stirring. Therefore, the large particles at the bottom of the beaker were hit not only by sonic waves traveling through the water, but also by the vibration of the bottom of the stainless steel beaker.

After AO treatment, the pH and temperature of the treated slurries were measured. The pH was measured using a Beckman Φ10 pH meter (Beckman Instruments, Inc., Fullerton, CA) with a Corning "3 in 1" Combo electrode (Corning, Inc., Corning, NY) standardized by 7.00 and 10.00 pH buffers (Ricca Chemical Company, Arlington, TX). The temperature was measured with a 1.55 volt digital thermometer probe (VWR International). The treated slurry was then transferred quantitatively (using aliquots of distilled water when necessary) into a 500 mL glass bottle for transportation, including capturing most of the small iron particles from the baghouse dust that had adhered magnetically to the stir bar.

3.2 Freeze-Drying of Suspensions

All slurries were freeze dried to obtain powders similar in both chemical and physical characteristics to the particles as they were when suspended in the slurries. Freeze drying has been used in the past to dehydrate montmorillonite and other clays. A 30-40 mL sample of the slurry was transferred from the stirring slurry to two 125-mL Nalgene wide-mouth plastic bottles just after the particle size analyses were completed. This

bottle was then mixed and immediately put into a bath of liquid nitrogen. The liquid nitrogen has a theoretical temperature of about -196°C. The freeze-dryer (Lyph-Lock 6 Freeze Dry System, Labconco, Kansas City, MO) chamber was large enough to dry up to about 8 125-mL bottles at the same time. The refrigerated collection coils cooled to -50°C; and the vacuum pump (GE Motors) brought the pressure inside the dryer to less than 10×10^{-3} mbar (however, the pressure in the chamber rose as ice collected on the coils). The samples inside the vacuum chamber were not refrigerated, however the applied vacuum and the endothermic sublimation of the ice (~ +46.7 kJ/mol) kept the samples below the melting point until the ice fully sublimated. The freeze dryer was typically run for 48-72 hours to sublime the 30-40 mL of ice from each bottle. The dry powder residue was then stored in capped bottles in desiccators.

3.3 Environmental SEM Imaging and Energy Dispersive Spectroscopy

Environmental scanning electron microscopy (ESEM) was used to view the microstructure of treated and untreated dusts. The ESEM is similar in use to a standard SEM, however the ESEM does not require high vacuum and its specimens do not need to be electrically conducting. The ESEM permits a low pressure of a variety of gases within the sample chamber. Therefore, the ESEM is a nearly ideal instrument for use in imaging materials containing hydrated, hydrophilic clays. The ESEM focuses on a specimen with a primary electron beam, which causes the specimen to emit secondary electrons. The secondary (or backscattered electrons) are then detected and an image is formed from the intensity of the detected electrons.

Energy Dispersive Spectroscopy (EDS) can also be performed simultaneously with ESEM imaging to determine the relative concentration of an element within the selected beam area. EDS works by the detection of characteristic x-rays (using a solid state detector) produced by a sample bombarded with an electron beam. The depth of penetration for EDS is about 1μm and the spatial resolution is also about 1μm (both depending on sample composition, beam accelerating voltage, etc.), therefore the composition returned by EDS is representative of the sample within a few cubic microns of the area of focus.

Samples for ESEM imaging and EDS were produced by taking a standard SEM aluminum mounting stub and applying either carbon or copper double-sided tape to the surface. The stubs were then pressed softly into the sample powder to get a “random” particle distribution adhering to the surface. Excess particles were then blown off of the stub using a canister of compressed air. The copper tape was used for baghouse dust samples because it had a lower carbon content (though not “zero” carbon because of the adhesive) than the standard carbon tape often used in SEM mounting. The lower carbon content in the tape was useful when performing EDS elemental analyses—especially with respect to carbon on the particle surface—to attempt to lessen scattering contamination from the mounting tape itself. For the bentonite samples, standard carbon tape was used and carbon peaks during EDS were simply removed from the analyses.

The ESEM (FEI Quanta 200, FEI Company, Hillsboro, OR) uses a tungsten electron source filament and a gaseous secondary electron detector ("lower fill detector"). (The backscatter detector was not used in this research.) The samples were placed into the ESEM chamber and the system was set to "low-vacuum" with a typical pressure of 0.62 torr water vapor. The working distance (focal distance) was set at about 8.0 mm. The accelerating voltage was 20 kV and the spot size was generally set at "3.5". The image resolution was set to 1024x884 and an average of 16 frames was used to obtain better image quality. A variety of treated and untreated freeze-dried powder samples were viewed under the ESEM.

Simultaneous to the ESEM imaging, EDS was performed to determine the constituents of the sample being viewed. The EDS instrument (Oxford Inca 200, Oxford Instruments Analytical, Concord, MA) spectra acquisition time was set at 60 or 90 seconds and the process time was 5 seconds with a spectral range of 0-10 keV.

3.4 Coal Resources

Three types of coal were studied, anthracite, bituminous and lignite. The grain size distribution and the composition of the anthracite we used are listed in Table 3-1 and Table 3-2 respectively.

Table 3-1 The grain size distribution of anthracite

Mesh number	Retained %	Passing %
28 (0.60 mm)	60.0	40.0
35 (0.42 mm)	18.5	21.5
60 (0.25 mm)	14.5	7.0
100 (0.15 mm)	4.5	2.5
200 (0.075 mm)	1.5	1.0
300 (0.045 mm)	0.5	0.5

Table 3-2 Composition of anthracite

Contents	Weight Percentage (%)
Moisture	13.25
Ash	11.00
Sulfur	0.38
Volatile	4.33
Fixed Carbon	71.42

The bituminous coal we tested is the highly volatile bituminous coal that has been used at Neenah Foundry (Neenah, WI). The grain size distribution and the composition of the highly volatile bituminous coal we used are listed in Table 3-3 and Table 3-4 respectively.

Table 3-3 The grain size distribution of highly volatile bituminous coal

Mesh number	Retained %	Passing %
28 (0.60 mm)	5.1	94.9
35 (0.42 mm)	7.1	87.8
60 (0.25 mm)	15.8	71.9
100 (0.15 mm)	16.3	55.6
200 (0.075 mm)	21.9	33.7
300 (0.045 mm)	10.7	23.0

Table 3-4 Composition of highly volatile bituminous coal

Contents	Weight Percentage (%)
Moisture	5.18
Ash	8.56
Sulfur	0.79
Volatile	32.67
Fixed Carbon	53.69

Three lignite resources were obtained and the approximate details of these raw materials are listed in Table 3-5. These raw lignite coals were grinded and sieved to keep the grains which passed sieve #40 for the following pyrolysis experiments

Table 3-5 Approximate analysis of the raw lignites

Name	Red Hills	Red Rivers	Sabine
Location	Ackerman, MS	Coushatta, LA	Hallsville, TX
Ash (%)	14.64	14	12.1
Sulfur (%)	0.58	0.6	0.61
Moisture (%)	42.75	32	34.35

3.5 In-situ Pyrolyzed Carbon

The thermogravimetric analyzer (TGA) we employed is a Cahn TG131 from THERMO Electron Corporation (Newington, NH) with a 2 inch (in diameter) x 8 inch (length) furnace reactor tube. The lignites were pyrolyzed in the reactor tube, where they were exposed only to N_2 and inert gas. The temperature was increased from room temperature to the desired final temperature (treatment temperature) at a rate of 50˚C/min and maintained at the final temperature for certain time. After this period, nitrogen gas was provided until the temperature dropped to room temperature.

3.6 Pore Volume Distribution and Surface Area

The character of the pyrolyzed carbons such as surface area and pore volume distribution were measured by the Accelerated Surface Area and Porosimetry System (ASAP) 2010 (Micromeritics. Inc, Norcross, GA). Argon was used as the analysis gas in the ASAP to measure the surface area and pore volume distribution of the pyrolyzed coals. These tests employed 0.3-0.5 g of pyrolyzed coal. Free space and volume adsorbed in the tube with the coal were measure at first. Then the pore volume distribution was analyzed, per our standard Penn State protocol.

3.7 Adsorption Experiment

Adsorption Experiment was conducted in a system simulating the emission from foundry. Highly volatile bituminous coal which is used in green sand mode was pyrolyzed in the TGA and the emission from highly volatile bituminous coal during pyrolysis was passed through a column with two sections. The first section of this column was packed with the pyrolyzed Sabine lignite, while the second section was packed with activated carbon to check the breakthrough. After the adsorption, the pyrolyzed Sabine lignite and the activated carbon packed in the column were washed by CS_2 respectively to extract the adsorbed VOCs. Then the CS2 solutions were injected into a Hewlett Packard 5890 Series II Gas Chromatography to detect the VOCs.

3.8 Material and Method for Evaluation of hydrocarbon emission characteristics

The highly volatile bituminous coal used in this research was shipped from a full-scale foundry. The anthracite was from Jeddo Coal Company (Wilkes-Baree, PA). The lignite was from Mississippi Lignite Mining Company (Ackerman, MS). The cellulose was from Spilltech ltd. (Alpharetta, GA). The highly volatile bituminous coal, anthracite, and lignite were grounded to pass through a 75μm sieve. Cellulose with a particle size about 100 μm was used in the test. All the samples were dried at 105 ^{o}C overnight and stored in a desiccator prior to use. The elemental analysis of these samples is shown in Table 3-6.

Table 3-6 Elemental Analysis of the Carbonaceous Additives

Sample	C	H	N	O
Highly volatile bituminous coal	77.0	5.11	1.50	16.4
Anthracite	82.2	1.97	0.78	15.1
Lignite	51.0	3.93	0.83	44.3
Cellulose	44.2	5.56	0	50.2

It is noted that carbonaceous additives are heated in quite different conditions at the different locations within a green sand mold. At the metal-mold interface, green sand is heated to above 1000 ^{o}C (depending on metal pouring temperature) instantly after the metal is poured into the mold. The temperature ramping rates could be thousands ^{o}C/sec. Then during the casting solidification and mold cooling, as the heat dissipates outwards through the green sand mold, green sand further away from the metal-mold interface is heated orderly, but at much lower heating rates (several to hundreds ^{o}C/min depending on the distance from the metal-mold interface and casting size). The peak temperatures also decrease quickly as the distances from the metal-mold interface increase (Zeng et al., 1985; Chen et al., 1990; Shih et al., 1996; Hsiau et al., 1998; Wang et al., 2006). The huge difference in the heating conditions could profoundly affect the volatile yields and distributions of the carbonaceous additives. To simulate the different heating conditions that the carbonaceous additives experience in the different locations within green sand molds, a thermogravimetric analyzer (TGA) and a Curie-point pyrolyzer were used in this research to pyrolyze the samples.

3.8.1 TGA pyrolysis of carbonaceous additives and hydrocarbon emission characterization.

About 20 mg of the samples were placed in a TGA 2050 (TA instrument, DE) and pyrolyzed at 20 ^{o}C/min from ambient temperature to 1000 ^{o}C under a nitrogen atmosphere. This simulated the slow heating conditions that carbonaceous additives experienced at the further away from the metal-mold interface within the green sand mold. The effluent from the TGA was transported to a downstream mass spectroscopy (MS) (Thermostar GSD 301T, Pfeiffer, NH) for emission kinetics analysis.

To quantify the hydrocarbon emissions, the samples were pyrolyzed in a quartz-glass reactor of a TGA (Cahn TG-131, Thermo Electron Inc., CA) with a heating rate of 20 ^{o}C/min from ambient temperature to 1000 ^{o}C under a nitrogen atmosphere. During the heating, granular activated charcoal (GAC) tubes were used to capture the emissions in the TGA effluent. Then the emissions were desorbed with carbon disulfide solvent for 24 hr to ensure full extraction. The solvent with analytes was then analyzed for hydrocarbon emissions by the GC-FID.

3.8.2 Flash pyrolysis of carbonaceous additives and hydrocarbon emission characterization.

About 1.5 mg sample was tightly wrapped in a ferromagnetic foil that was then placed in a small quartz reactor (4.0 mm i.d.) in the Curie-point pyrolyzer. The foil could be rapidly heated to its specific Curie-point temperature by an induction heating coil. In our experiment, the foil is heated to 920 ^{o}C at the heating rate of 3000 ^{o}C/sec in a helium atmosphere, and then the temperature was held for three sec for complete pyrolysis of the carbonaceous additives. This closely simulated the fast heating conditions that carbonaceous additives experienced at the metal-mold interface. The gases emitted from the sample were carried to a GC-FID (HP 5890) for hydrocarbon emission analysis through a heated tube by the helium carrier gas flowing through the reactor to the GC. The pyrolyzer reactor and the transporting tube were maintained at 200 ^{o}C to prevent condensation of the volatile emissions.

4. Results and Discussion

4.1 On Characterization of the Properties and Performance of Highly volatile bituminous coal Used in Foundries

4.1.1 Environmental Scanning Electron Microscopy and Energy Dispersive Spectroscopy of Treated Baghouse Dust Powders

Environmental Scanning Electron Microscopy (ESEM) imaging was performed to determine any visual differences in the bentonite particles due to the various AO component treatments. ESEM was performed using the secondary electron detector to obtain 3-dimensional images of the treated particles. Simultaneous with the imaging, Energy Dispersive Spectroscopy (EDS) was performed to determine the relative elemental concentration of the particles being imaged. The depth of penetration of the EDS is approximately 1μm, and the spatial resolution is also about 1μm—therefore the composition returned by the EDS is representative of the sample in the corresponding ESEM image within a few cubic microns of the area of focus. EDS elemental analysis of these fine particles should only be considered semi-quantitative, particularly for the non-uniform baghouse dust samples.

Several different treated baghouse dusts were viewed under the ESEM, and hundreds of images were captured and many EDS spectra were acquired. Representative images and spectra representative are presented herein.

ESEM images and EDS analyses were performed on the as-received baghouse dust (BHD) in order to obtain information on the starting material before any treatment. Figure 4-1 presents a representative ESEM image of the untreated baghouse dust, along with a corresponding EDS analysis. Figures 4-2 shows some typical montmorillonite agglomerates within the as-received baghouse dust.

The as-received baghouse dust is generally a conglomeration of large silica and coal particles that are surrounded and coated with montmorillonite clay. The untreated BHD particles were generally quite spherical in shape. The EDS spectra were dominated by silicon and oxygen from the silica; carbon (and other impurities, including sulfur) from the coal; and silicon, oxygen, aluminum and magnesium from the montmorillonite. The lesser identified elements generally included sodium, calcium and iron from the clay, sulfur from the coal, and iron from the iron castings themselves. The as-received BHD particles are light and porous with a low bulk density. The porosity inherent in the dust was evident in some ESEM images. The porosity within some of the BHD agglomerates could partially be due to carbon volatilization from inside the particles, or due to the expansion and/or contraction of wet and dry montmorillonite.

The initial thickness of the clay layers that surrounds most of the untreated BHD particles is not known with accuracy, but from the particle size analyses discussed previously, it likely ranges up to 25μm in radius. The thickness of the clay coating is greater than 1 μm

(the typical depth of penetration for EDS), as the EDS spectra of the untreated BHD consistently showed a large concentration of montmorillonite elements.

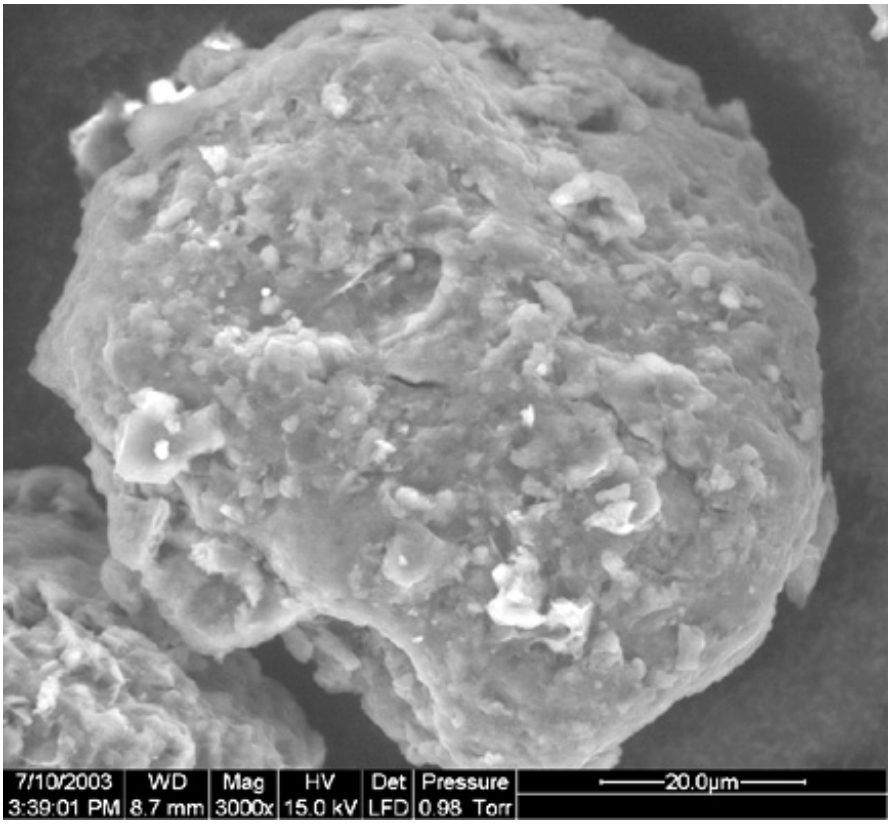

Figure 4-1: ESEM image and EDS analysis of an as-received BHD particle (3000x).

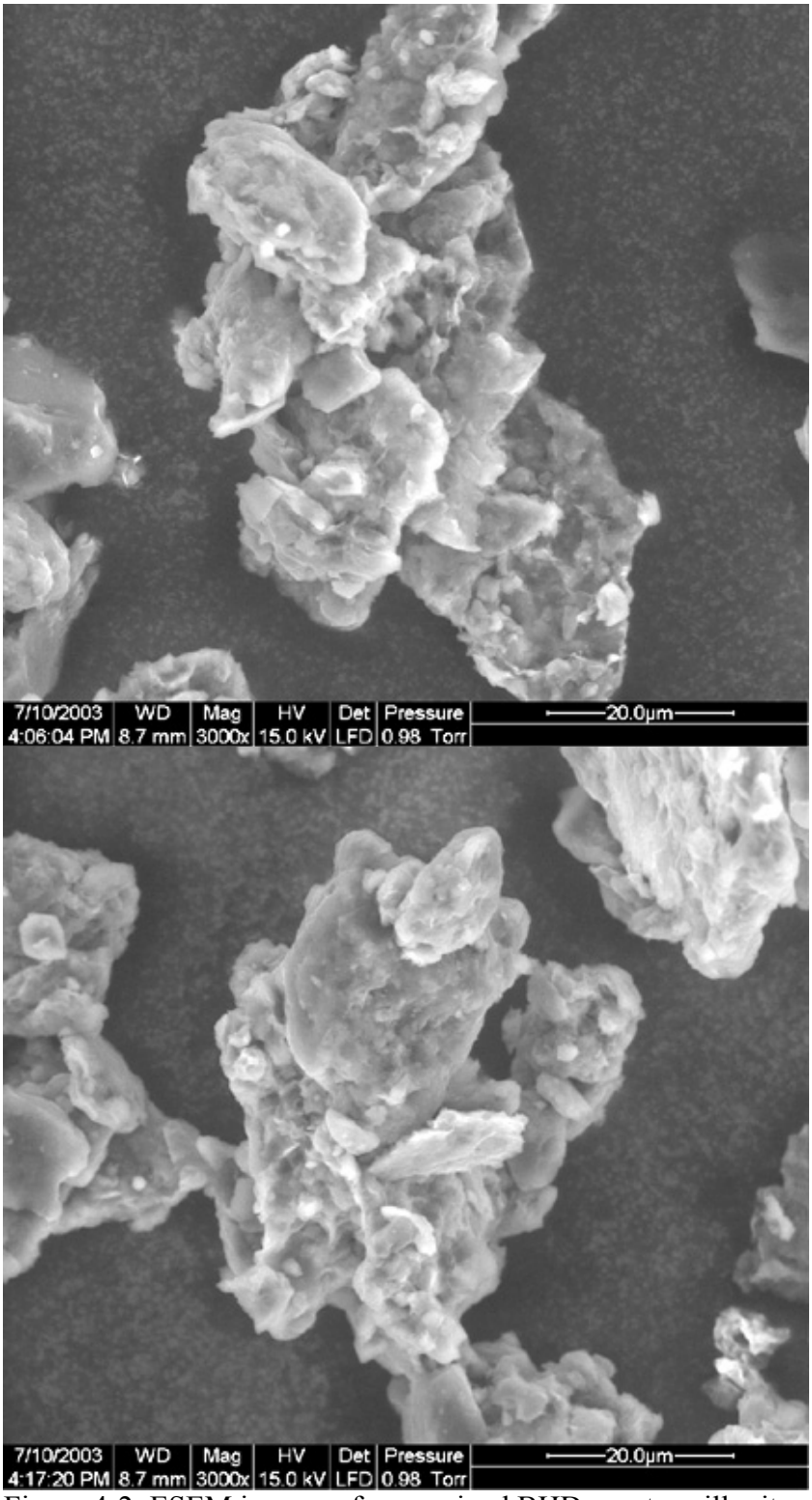

Figure 4-2: ESEM images of as-received BHD montmorillonite agglomerates (3000x).

ESEM/EDS of Non-AO (Stirred) Baghouse Dust

Numerous ESEM images and EDS analyses were obtained for the 60 min. stirred baseline baghouse dusts to maintain a baseline for comparison between the various treatments. Figures 4-3 to 4-10 present representative ESEM images of the stirred (and subsequently freeze-dried) BHD, along with corresponding EDS analyses. Figure 4-3 is a representation of the smaller montmorillonite particles that could be found in the freeze-dried slurry. Figures 4-4 to Figure 4-7 are representative images and elemental spectra of the common agglomerates found in the stirred BHD. The low-shear stirring does not produce enough force to break apart the bulk of the particles, and therefore much clay agglomeration is present in these particles. Figures 4-8 to 4-10 show examples of the large silica and coal particles within the BHD. Coal particles were generally free from clay coatings. On the other hand, silica particles were sometimes found clean (Figure 4-10), and other times found with some degree of montmorillonite coating on the surface (Figure 4-8). The images clearly show that stirring alone can clean much of the clay coating off of a significant amount of the large silica and coal particles in the dust.

The EDS-determined carbon concentration at the surface of the non-AO treated BHD "montmorillonite" agglomerates was approximately 25-35 wt% for the typical BHD montmorillonite agglomerate. The EDS-determined carbon concentration on the surface of silica particles was significantly less than on that of the montmorillonite agglomerates, as shown by comparisons of the EDS results in Figures 4-8 and 4-10 with those in, i.e., Figure 4-4.

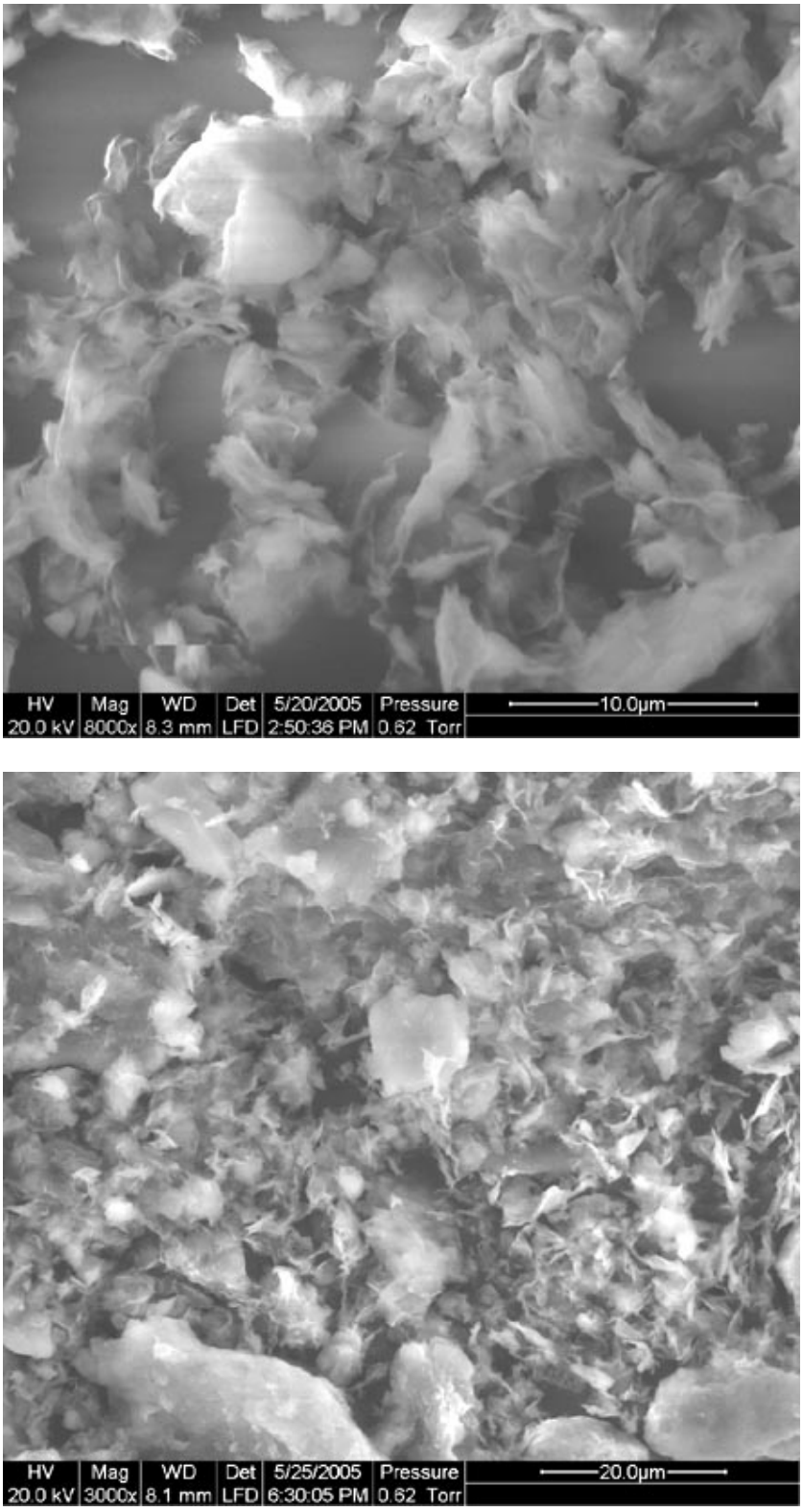

Figure 4-3: ESEM images of montmorillonite particles for non-AO (stirred) BHD.

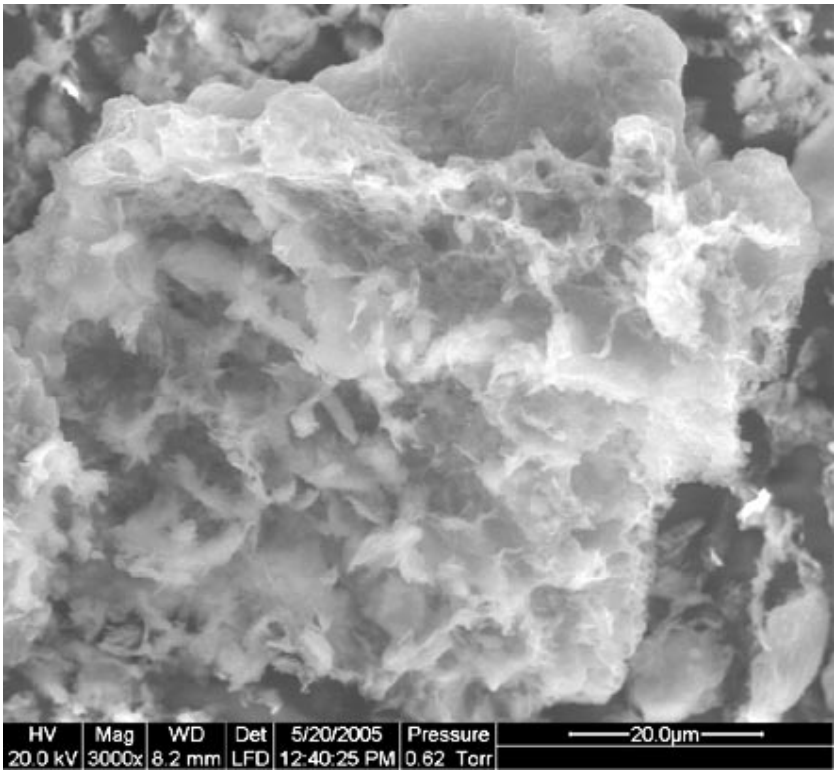

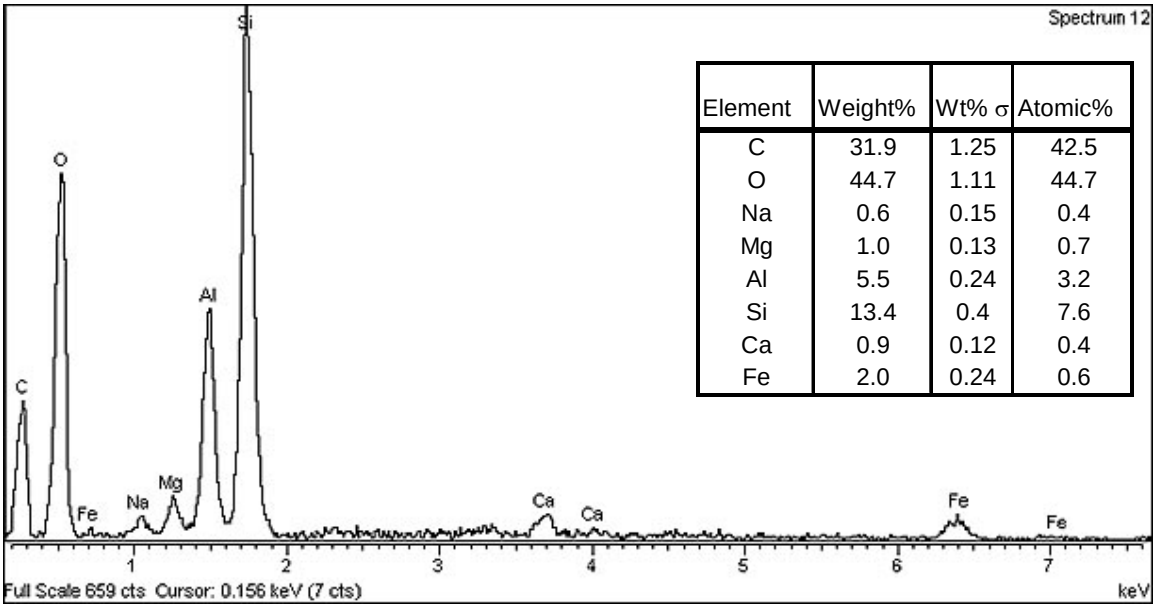

Element	Weight%	Wt% σ	Atomic%
C	31.9	1.25	42.5
O	44.7	1.11	44.7
Na	0.6	0.15	0.4
Mg	1.0	0.13	0.7
Al	5.5	0.24	3.2
Si	13.4	0.4	7.6
Ca	0.9	0.12	0.4
Fe	2.0	0.24	0.6

Figure 4-4: ESEM image/EDS analysis of a montmorillonite agglomerate for non-AO (stirred) BHD. (σ is the standard deviation for the weight analysis.)

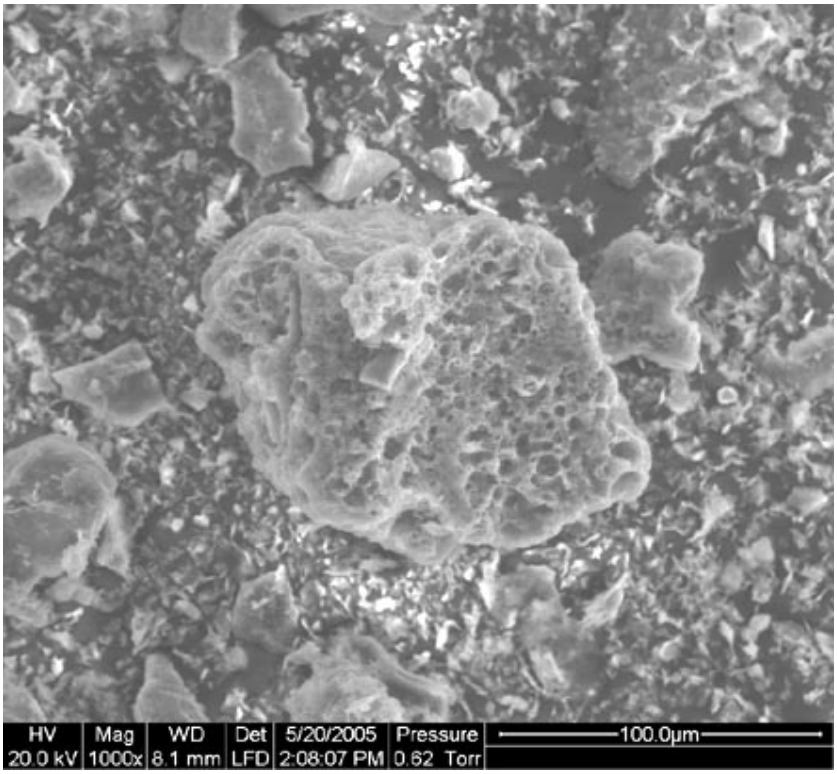

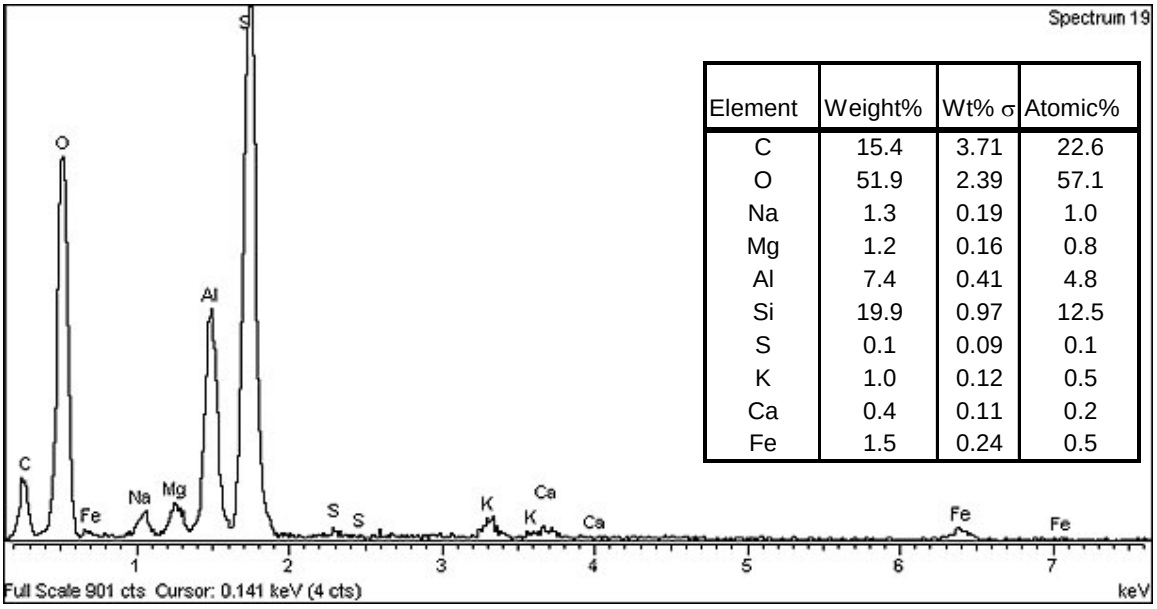

Element	Weight%	Wt% σ	Atomic%
C	15.4	3.71	22.6
O	51.9	2.39	57.1
Na	1.3	0.19	1.0
Mg	1.2	0.16	0.8
Al	7.4	0.41	4.8
Si	19.9	0.97	12.5
S	0.1	0.09	0.1
K	1.0	0.12	0.5
Ca	0.4	0.11	0.2
Fe	1.5	0.24	0.5

Figure 4-5: ESEM image/EDS analysis of an agglomerate for non-AO (stirred) BHD.

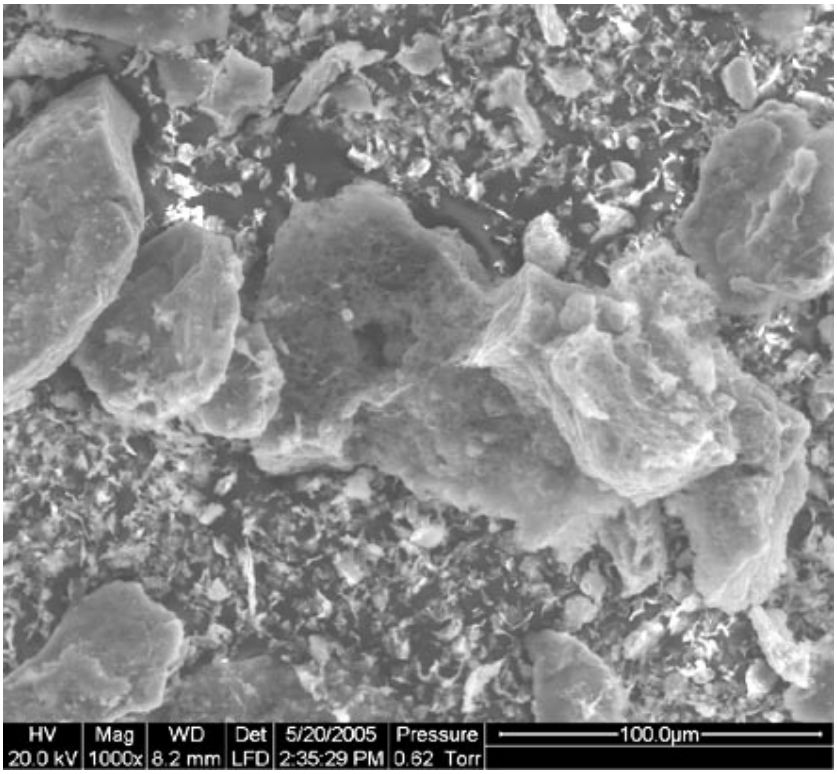

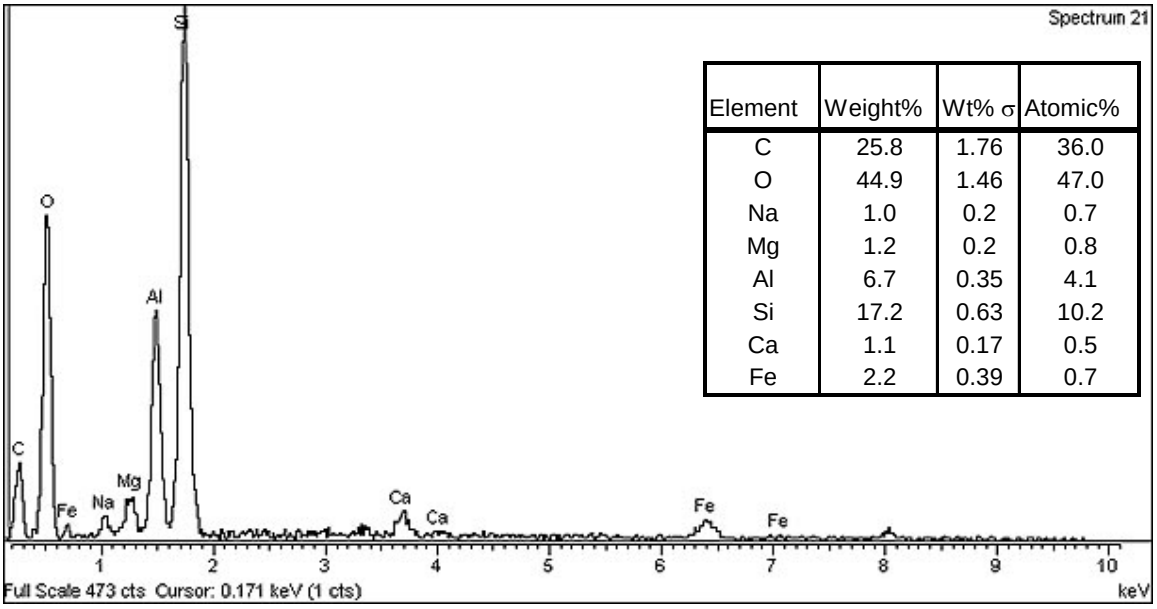

Element	Weight%	Wt% σ	Atomic%
C	25.8	1.76	36.0
O	44.9	1.46	47.0
Na	1.0	0.2	0.7
Mg	1.2	0.2	0.8
Al	6.7	0.35	4.1
Si	17.2	0.63	10.2
Ca	1.1	0.17	0.5
Fe	2.2	0.39	0.7

Figure 4-6: ESEM image/EDS analysis of an agglomerate for non-AO (stirred) BHD.

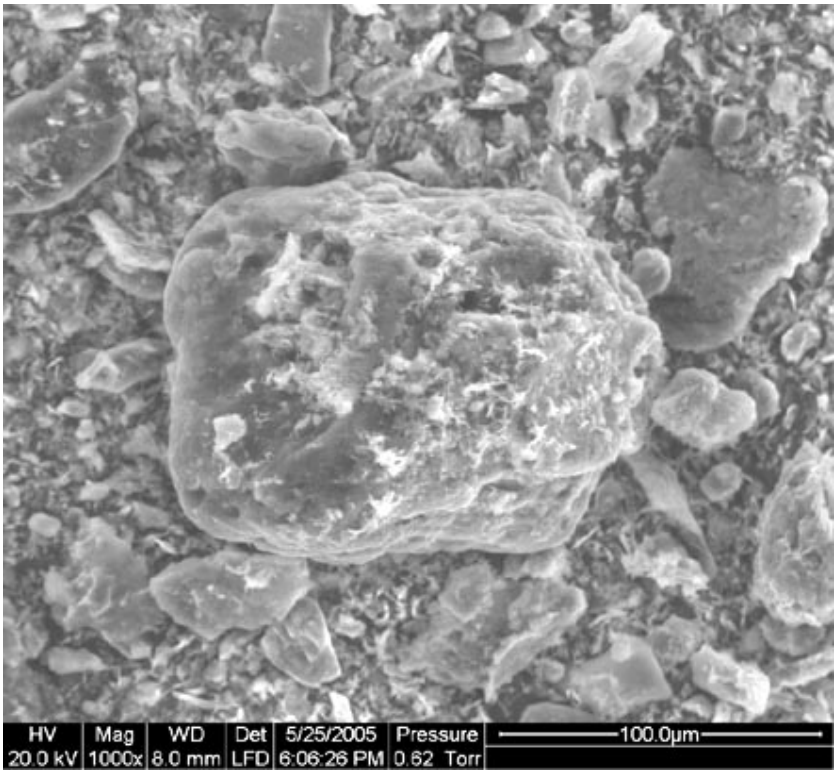

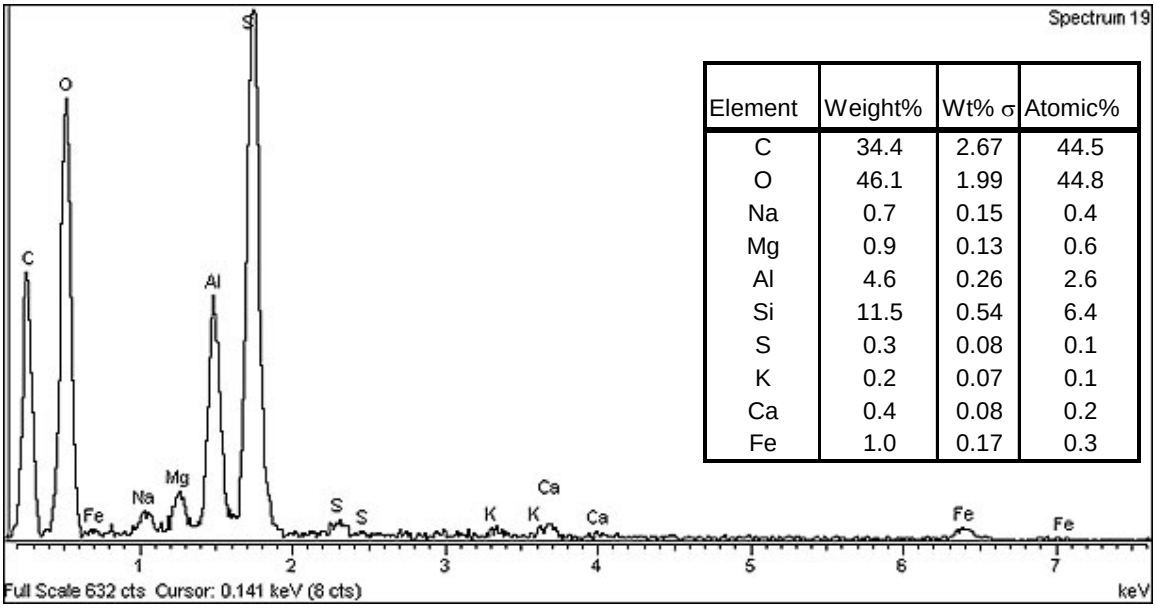

Element	Weight%	Wt% σ	Atomic%
C	34.4	2.67	44.5
O	46.1	1.99	44.8
Na	0.7	0.15	0.4
Mg	0.9	0.13	0.6
Al	4.6	0.26	2.6
Si	11.5	0.54	6.4
S	0.3	0.08	0.1
K	0.2	0.07	0.1
Ca	0.4	0.08	0.2
Fe	1.0	0.17	0.3

Figure 4-7: ESEM image/EDS analysis of an agglomerate for non-AO (stirred) BHD.

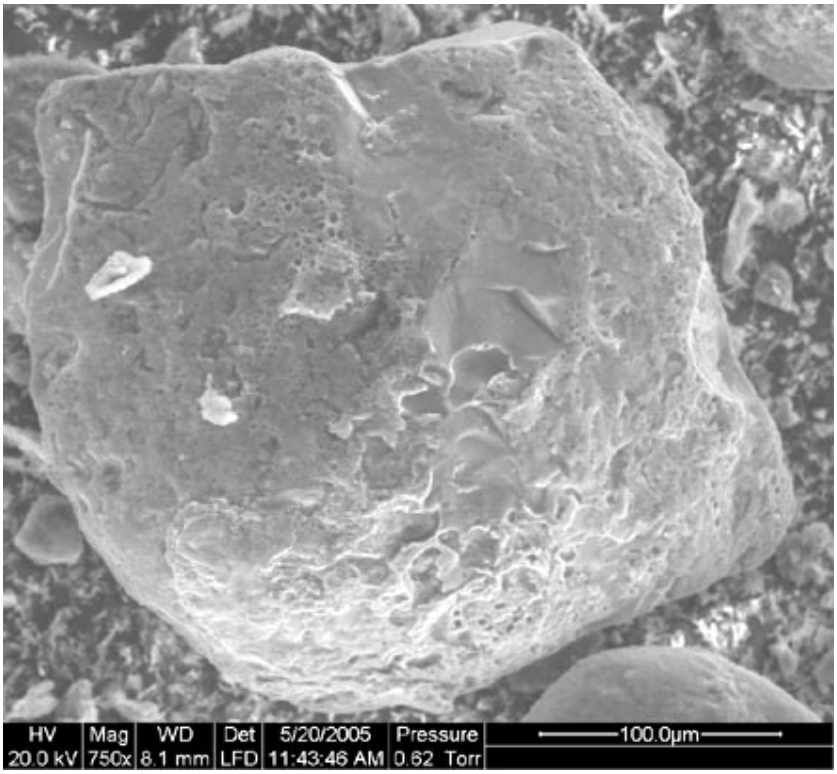

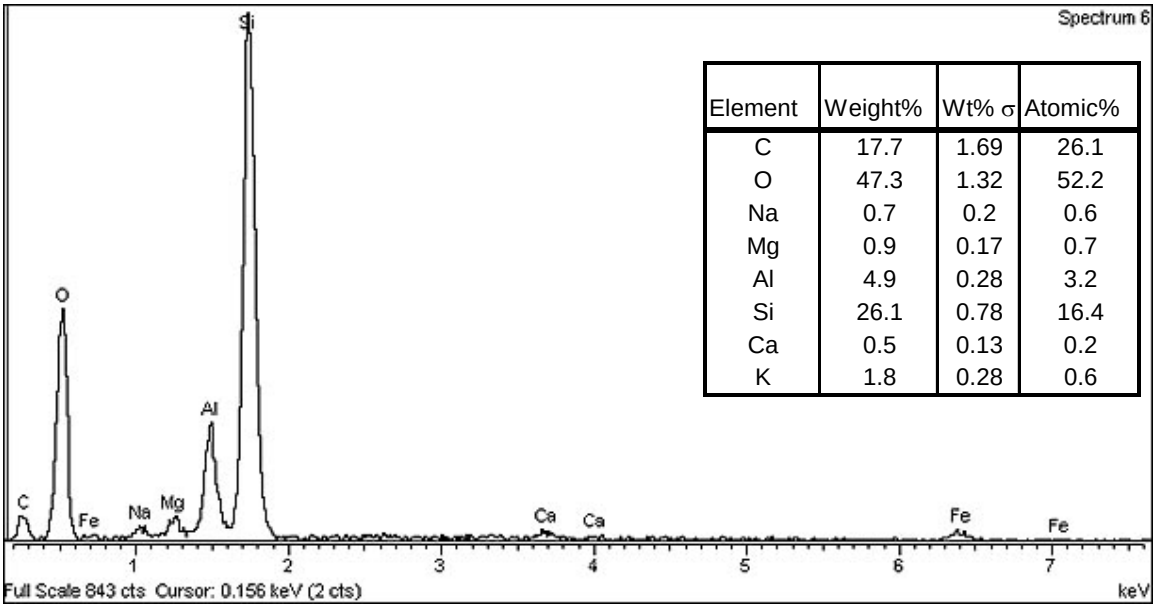

Element	Weight%	Wt% σ	Atomic%
C	17.7	1.69	26.1
O	47.3	1.32	52.2
Na	0.7	0.2	0.6
Mg	0.9	0.17	0.7
Al	4.9	0.28	3.2
Si	26.1	0.78	16.4
Ca	0.5	0.13	0.2
K	1.8	0.28	0.6

Figure 4-8: ESEM image/EDS analysis of a silica particle for non-AO (stirred) BHD.

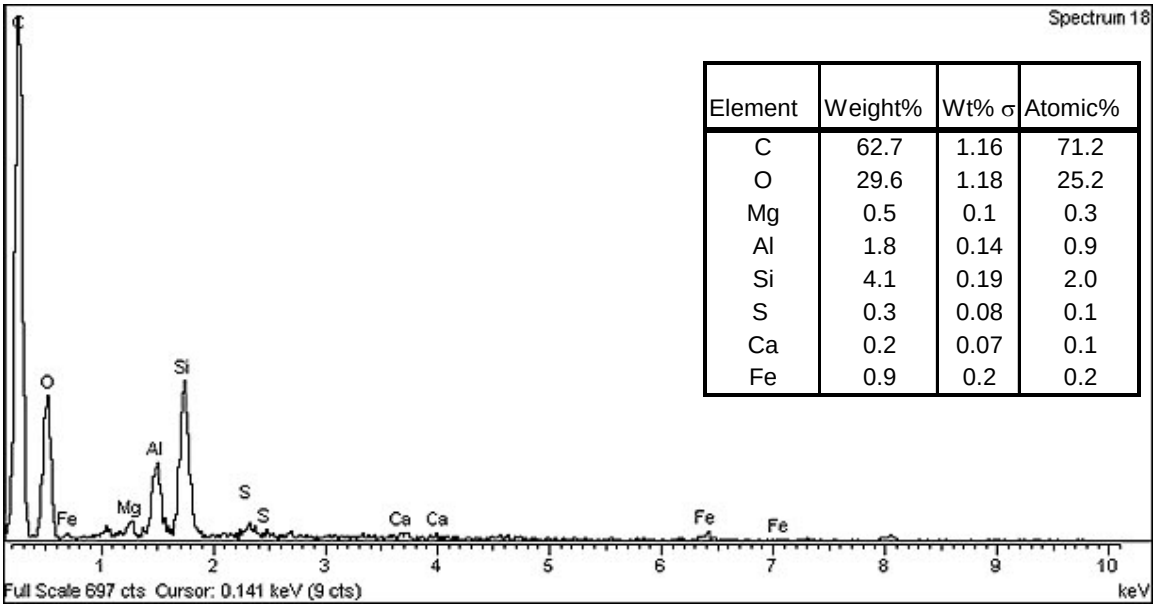

Element	Weight%	Wt% σ	Atomic%
C	62.7	1.16	71.2
O	29.6	1.18	25.2
Mg	0.5	0.1	0.3
Al	1.8	0.14	0.9
Si	4.1	0.19	2.0
S	0.3	0.08	0.1
Ca	0.2	0.07	0.1
Fe	0.9	0.2	0.2

Figure 4-9: ESEM image/EDS analysis of a coal particle for non-AO (stirred) BHD.

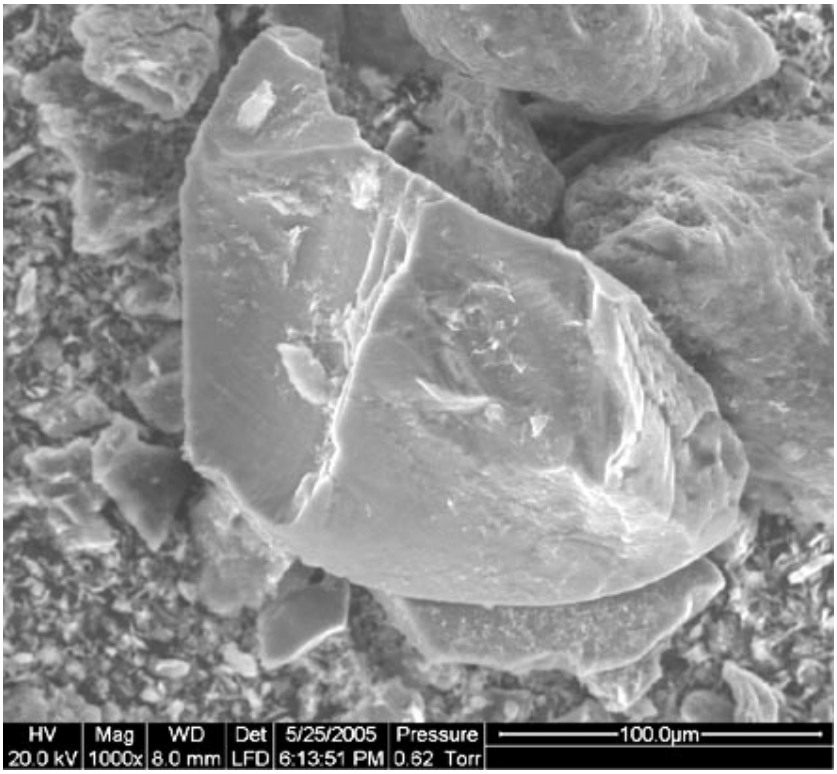

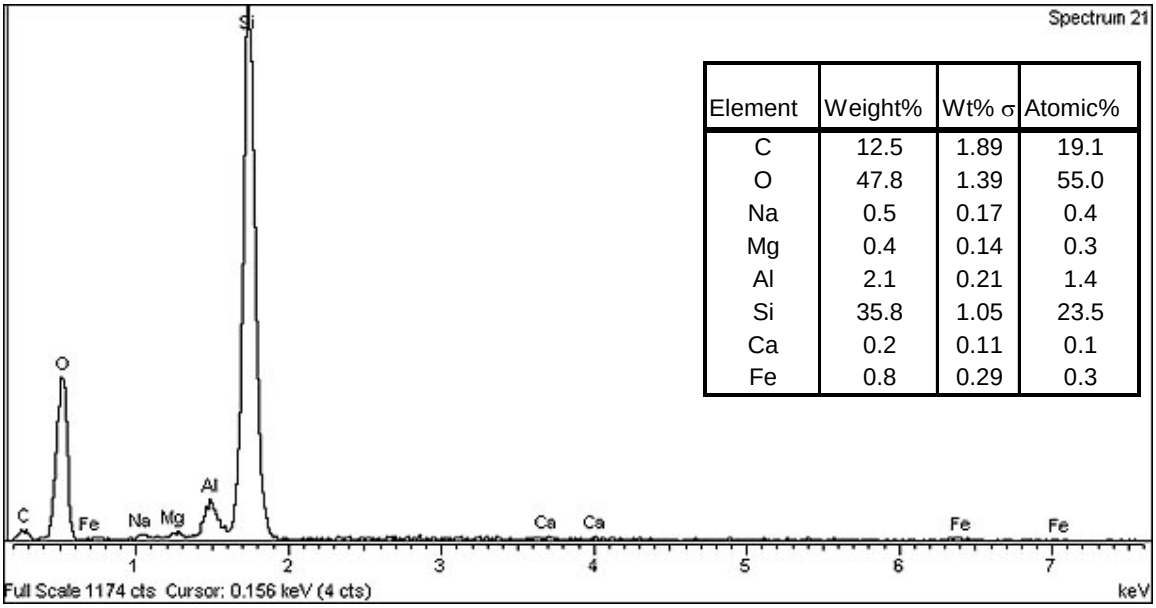

Element	Weight%	Wt% σ	Atomic%
C	12.5	1.89	19.1
O	47.8	1.39	55.0
Na	0.5	0.17	0.4
Mg	0.4	0.14	0.3
Al	2.1	0.21	1.4
Si	35.8	1.05	23.5
Ca	0.2	0.11	0.1
Fe	0.8	0.29	0.3

Figure 4-10: ESEM image/EDS analysis of a silica particle for non-AO (stirred) BHD.

ESEM/EDS of Treated Baghouse Dust

Various treatments of AO and AO components were applied to the baghouse dusts, as described throughout. The following is a selection of ESEM images and EDS spectra meant to compliment the discussion provided throughout the rest of this report. It should be noted that the montmorillonite particles became much too small with sufficient

treatment (i.e. sonication) to obtain proper EDS analyses (without garnering contamination from their surroundings).

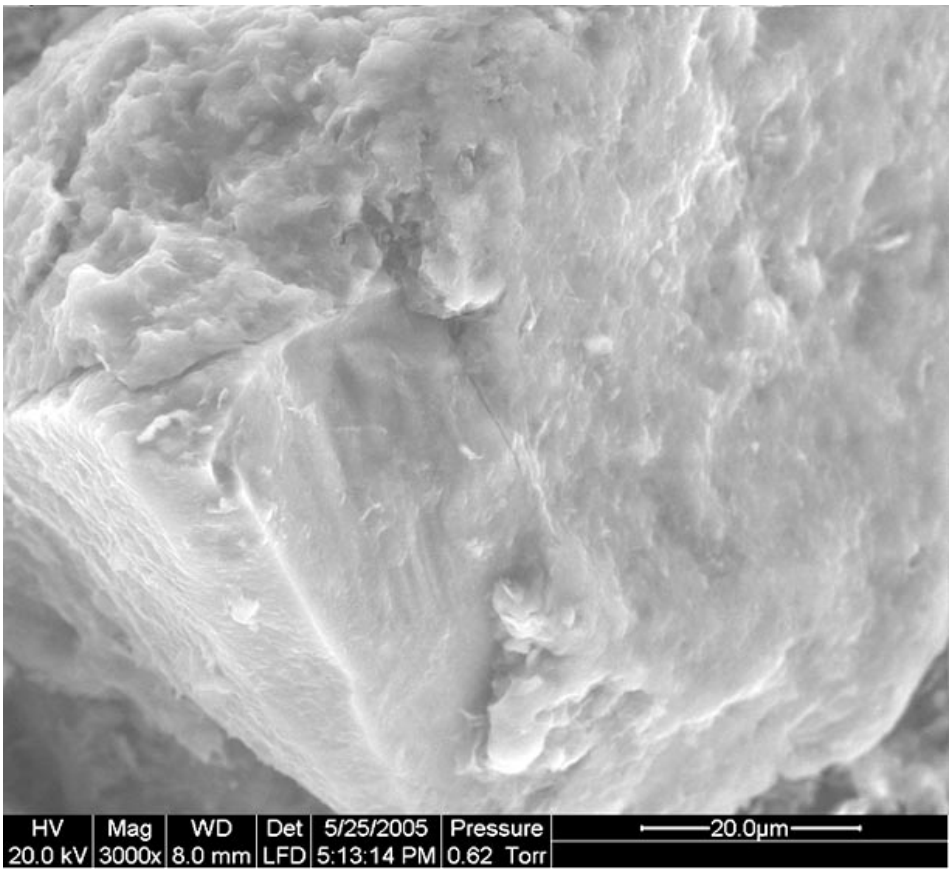

Figure 4-11: Silica-based particle treated with 4000 ppm H_2O_2 with coating of montmorillonite.

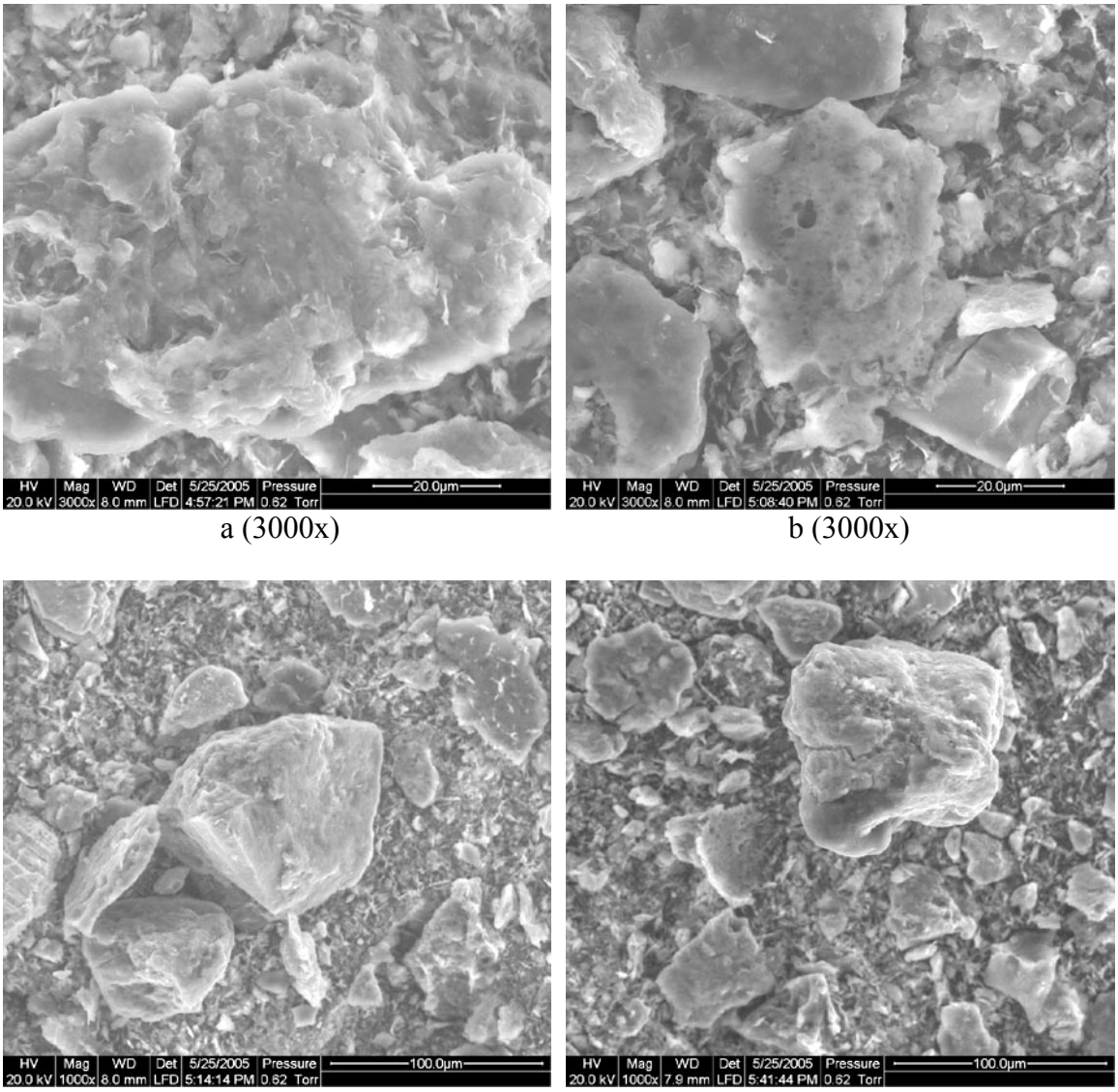

a (3000x) b (3000x)

c (1000x) d (1000x)

Figure 4-12: Hydrogen peroxide-treated BHD (4000 ppm).

Hydrogen peroxide has been shown to have little to no effect on the physical properties of the baghouse dusts. As shown in Figure 4-12, (a) shows a large montmorillonite agglomerate, (b) shows the inner porosity inherent in the BHD particles, (c) shows a chunk of montmorillonite that has cleaved off of the bulk particle surface, and (d) shows another such particle where cleavage has not yet fully occurred.

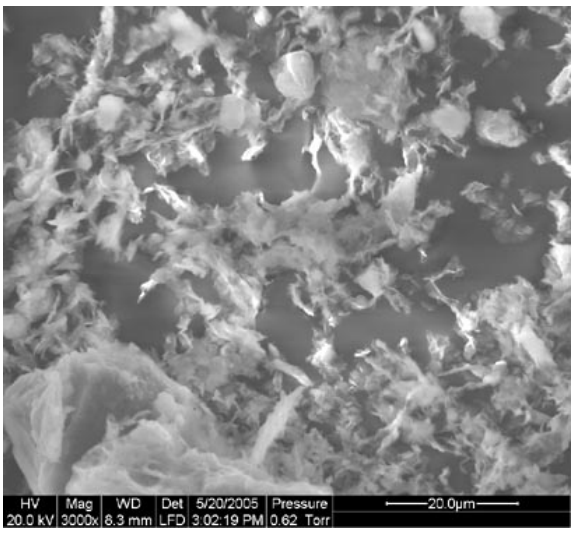

a (AO, 15 min., 3000x)

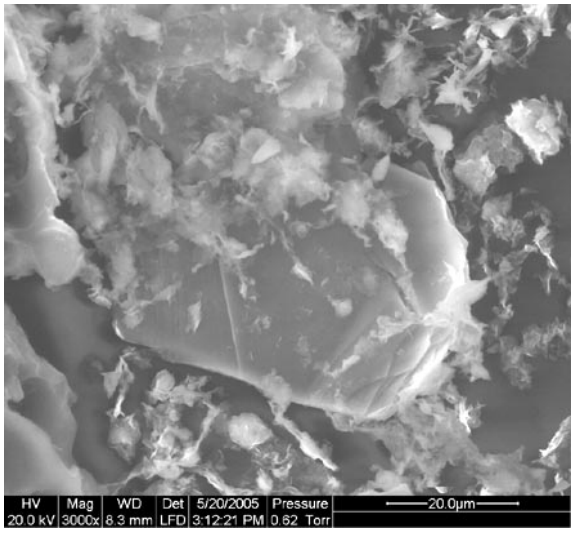

b (AO, 15 min., 3000x)

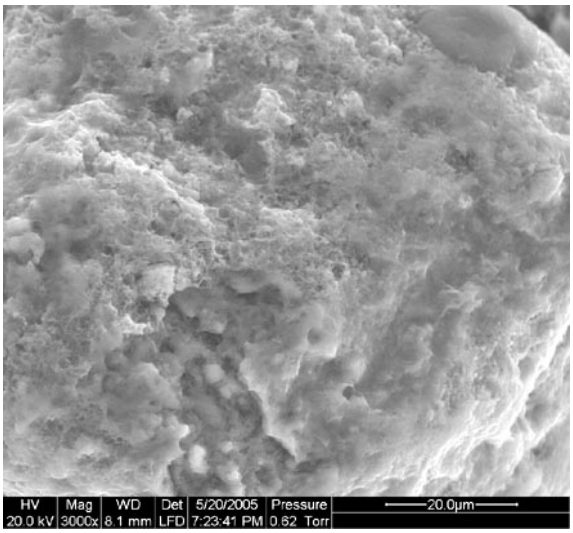

c (low-intensity sonication, 3000x)

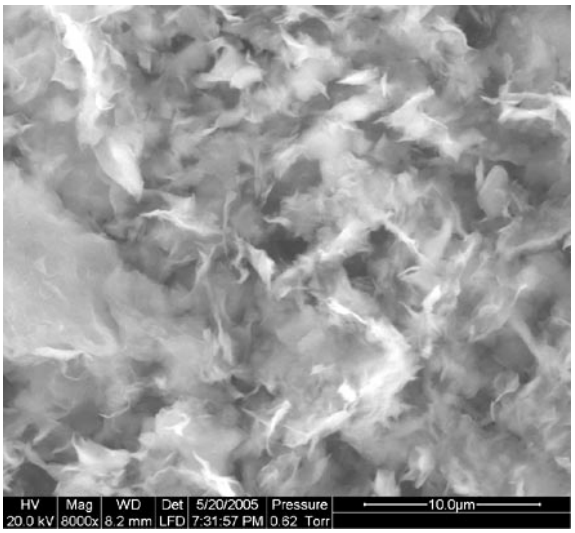

d (low-intensity sonication, 8000x)

Figure 4-13: (a) and (b): Full AO treatment 15 minutes; (c) and (d): Sonication at only ~1/16 of normal intensity for 60 minutes.

Figure 4-13 shows the effect even 15 minutes of intense treatment has on the particle morphology. The montmorillonite particles for the 15 minutes of AO treatment are beginning to diminish in size and break apart from each other and from large particle surfaces. Image (b) shows a large coal particle surrounded by relatively small montmorillonite particles. Image (c) shows the surface of a silica particle coated with clay. Image (d) shows the morphology of montmorillonite particles as they are just beginning to be broken apart by low-intensity sonication. Figure 4-14 presents two images of BHD treated for one hour with the parallel-plate sonic horn. The particles are greatly broken apart and are starting to attain thin plate-like appearances, as were found for sonication and AO treatment of bentonite alone. The bottom image in Figure 4-14 shows a Si and K-rich particle (possibly illite) with obvious clay edge bonding at the surface of the larger particle.

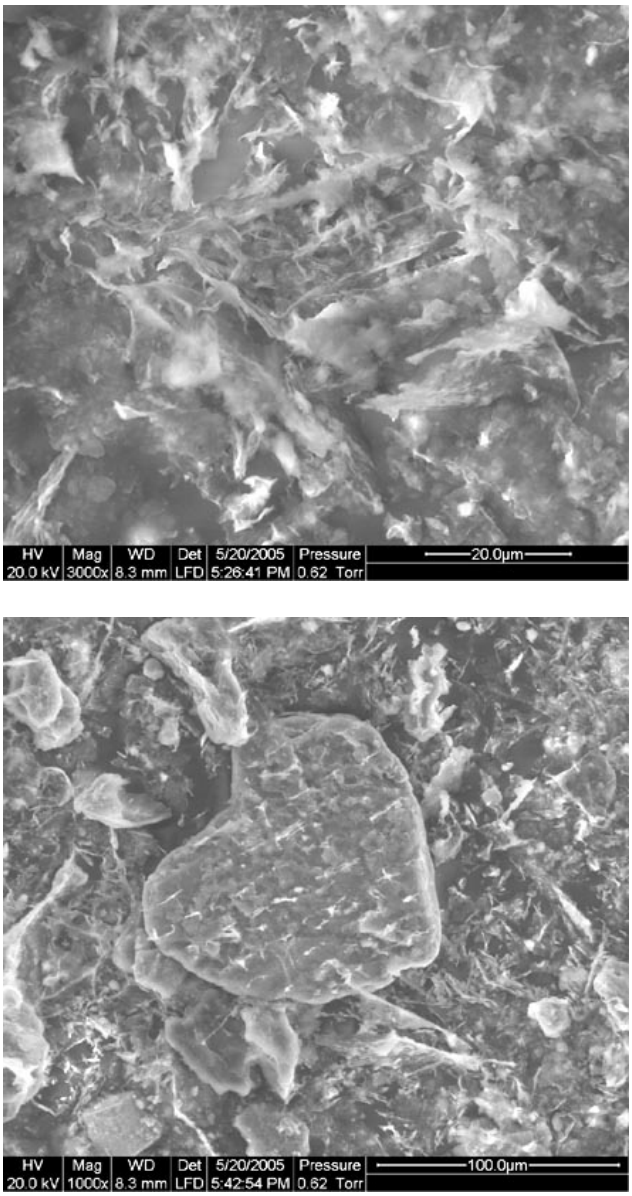

Figure 4-14: Parallel-plate horn acoustic sonicated BHD (60 min., 100% intensity).

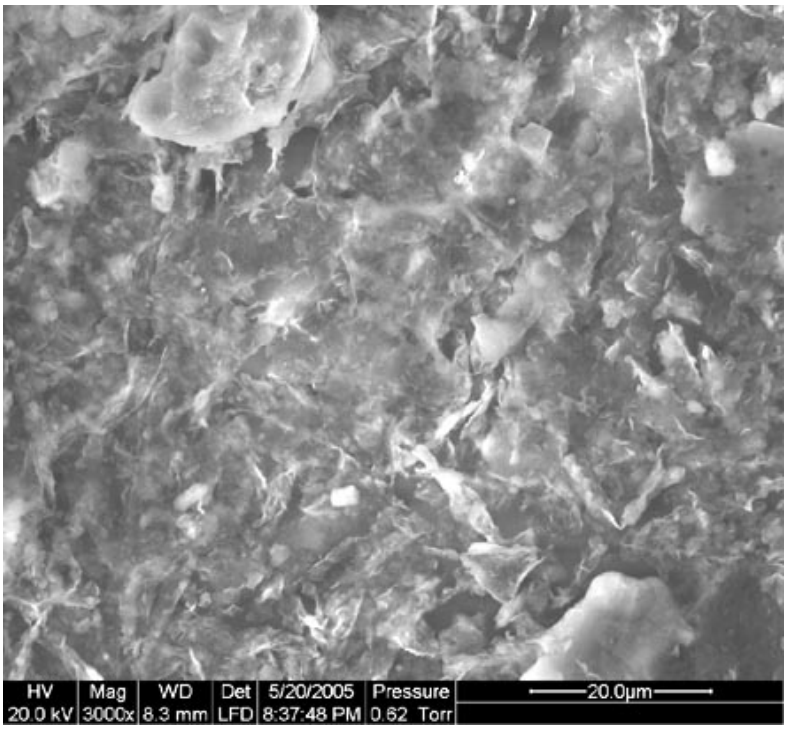

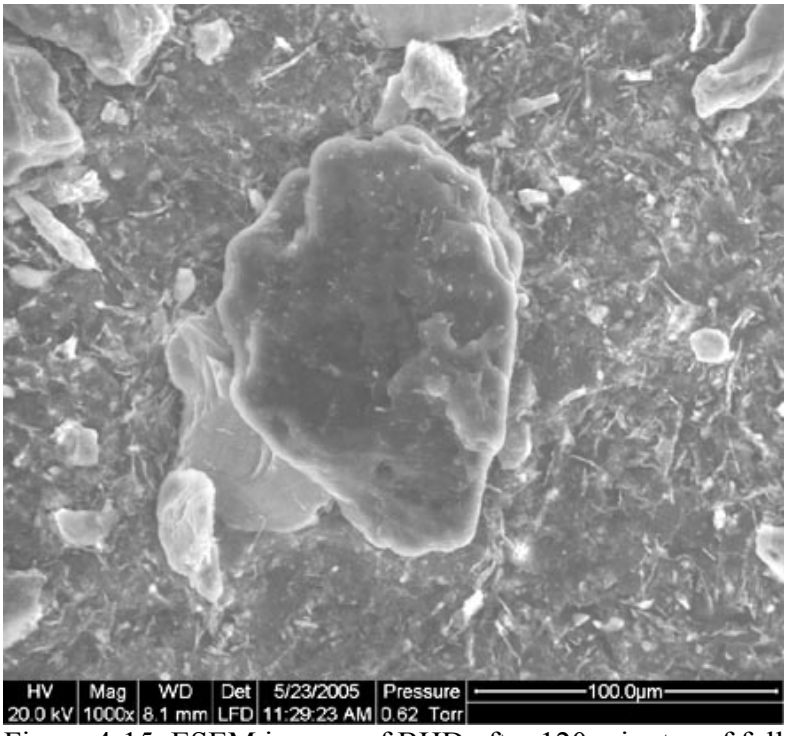

Figure 4-15: ESEM images of BHD after 120 minutes of full AO treatment.

Figure 4-15 shows two ESEM images from baghouse dust treated for 120 minutes with full AO. After this intense treatment, the large particles appear to be almost fully clean throughout the samples (as shown by many of the background particles in the images). Furthermore, the montmorillonites are shown to be forming the platy shapes found for

full AO treatment of the western bentonite. It is not known whether this phenomenon is a manifestation of the processing or a manifestation of clay edge-to-edge type bonding driven by the freeze-drying process. The final images presented herein are of baghouse dust that was treated by the high-intensity sonic unit for a total of 30 minutes. The ESEM images for this sample show very thin platelet agglomerates, similar to that attained by the bentonite after full AO or sonication processing. The platelets shown in Figures 4-16 and 4-17 are shown to have very high aspect ratios and appear to be partly transparent through the cross-section.

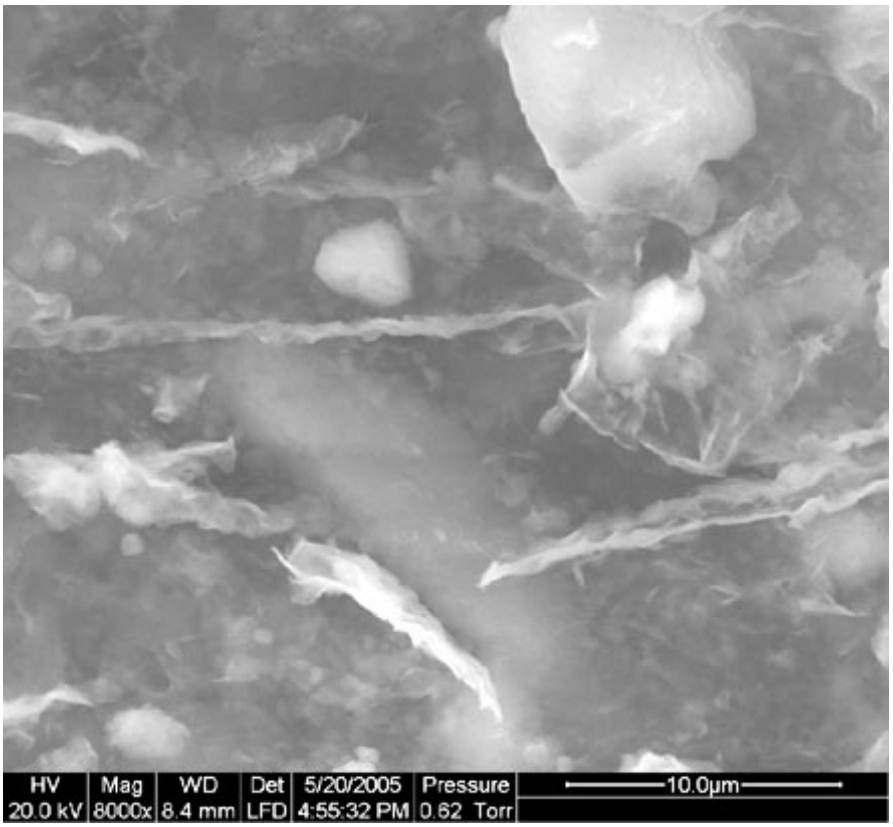

Figure 4-16: ESEM images for BHD treated with high-intensity sonication (Sonifier unit) (8000x).

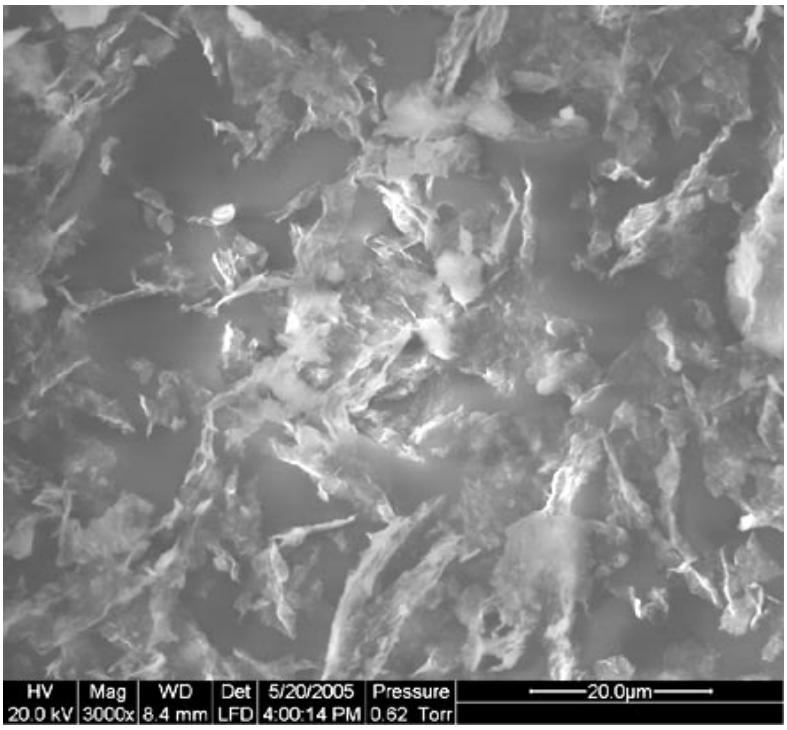

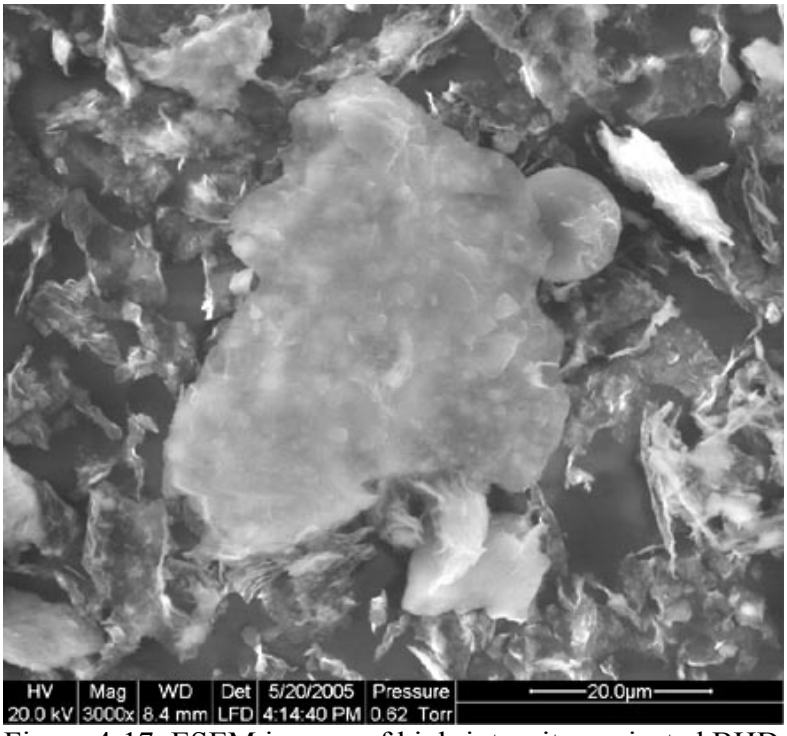

Figure 4-17: ESEM images of high-intensity sonicated BHD.

4.2 On Searching of the Optimal Raw Material for in-situ Pyrolyzed Carbon

4.2.1 Pyrolysis of Anthracite

Anthracite was pyrolyzed under nitrogen at 950˚C, with mass loss response as shown in Figure 4-18. The anthracite lost 6.5% of its mass during temperature ramp up, and only 0.5% more under the 1 hour pyrolysis.

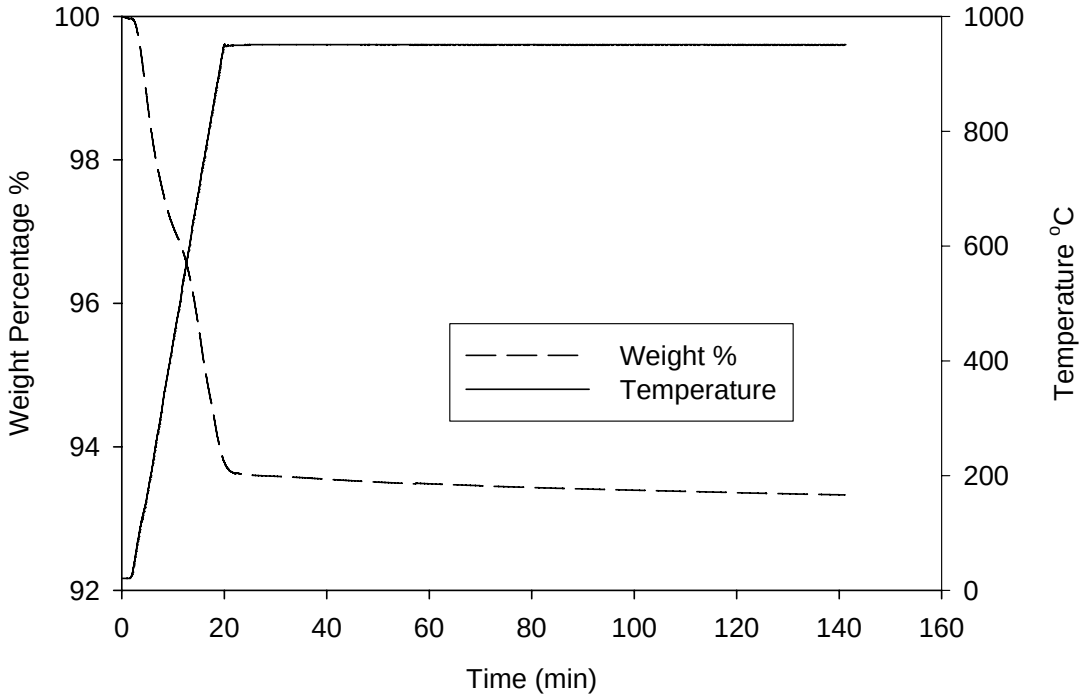

Figure 4-18 Mass loss profile during pyrolysis of anthracite

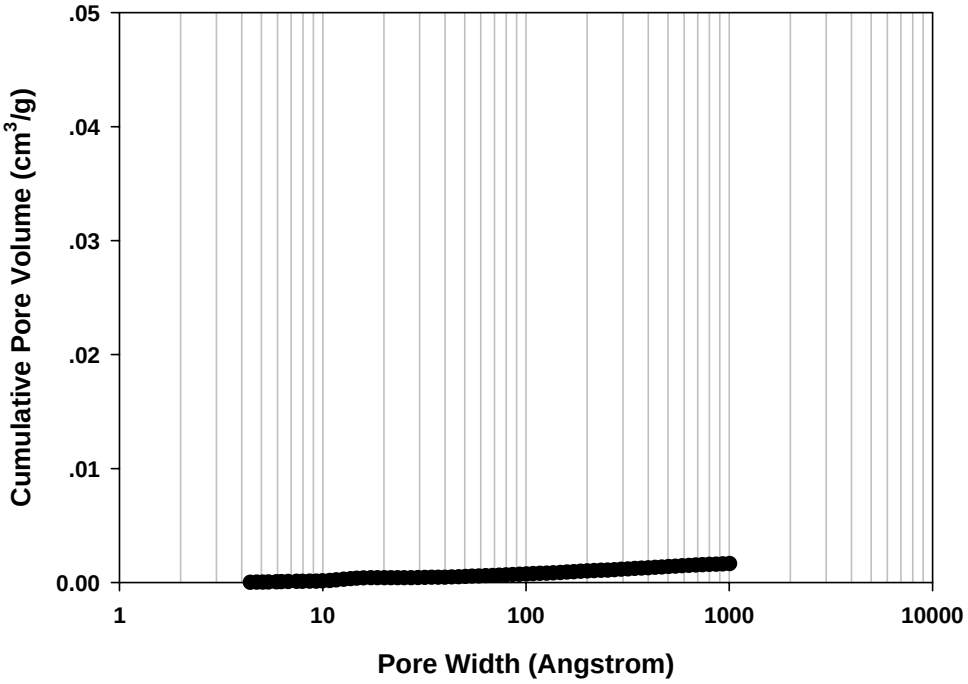

Figure 4-19 The cumulative pore volume of pyrolyzed anthracite

The experimental results from the pyrolysis of anthracite showed that this protocol did not develop very much pore volume. It is well known that anthracite has the highest carbon content and lowest volatile matter content among the three types of coals, and anthracite is the densest coal.

4.2.2 Pyrolysis of highly volatile bituminous coal

Figure 4-20 shows the pyrolysis of highly volatile bituminous coal (i.e. bituminous coal) under nitrogen and the treatment temperatures of 600˚C and 900˚C.

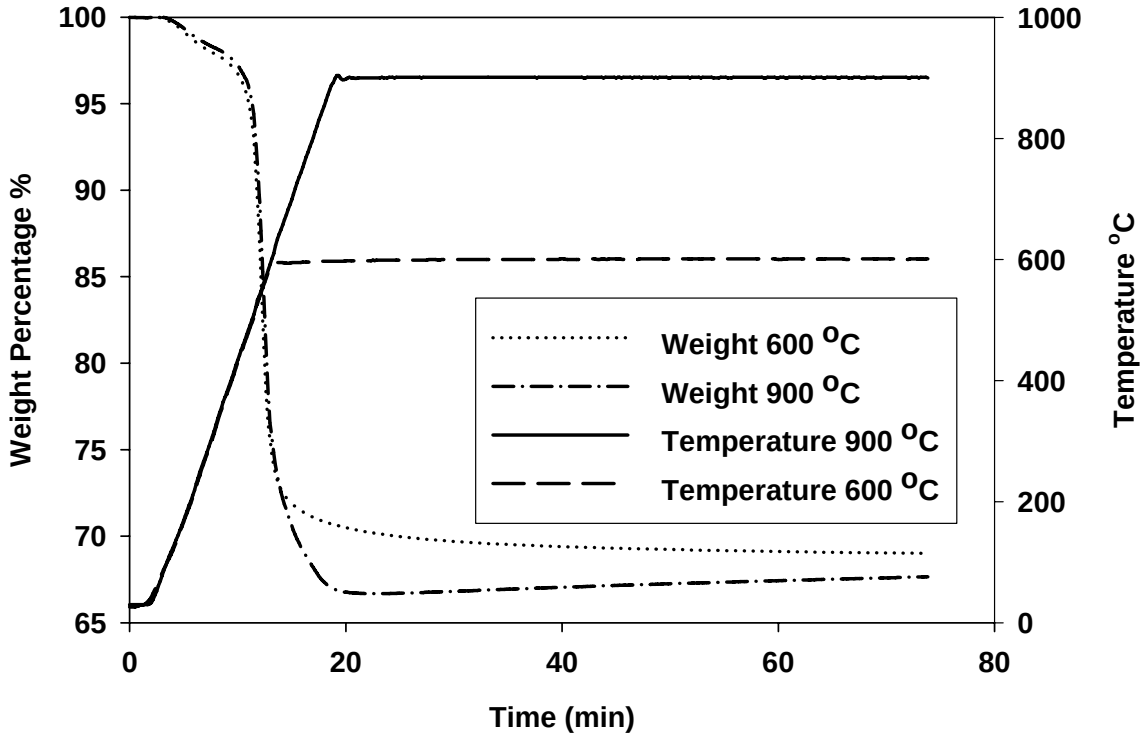

Figure 4-20 Mass loss profile during pyrolysis of highly volatile bituminous coal

During the pyrolysis, the highly volatile bituminous coal lost about 1/3 of its weight. And the mass loss of the highly volatile bituminous coal is about the same under different treatment temperatures, per Table 4-1.

Table 4-1 The mass loss of highly volatile bituminous coal during pyrolysis, with a 1-hour holding time at the noted temperature

Treatment Temperature (˚C)	Mass Loss (% of Weight)
600	30.98
800	32.37
900	32.26

The authors observed that while the highly volatile bituminous coal experienced thermal treatment, the coal grains fused together to form a single chunk of pyrolyzed coal. We crushed these chunks so as to measure the surface areas and pore volume distributions. These characteristics for the pyrolyzed highly volatile bituminous coal are shown in Figure 4-21 and Figure 4-22 respectively.

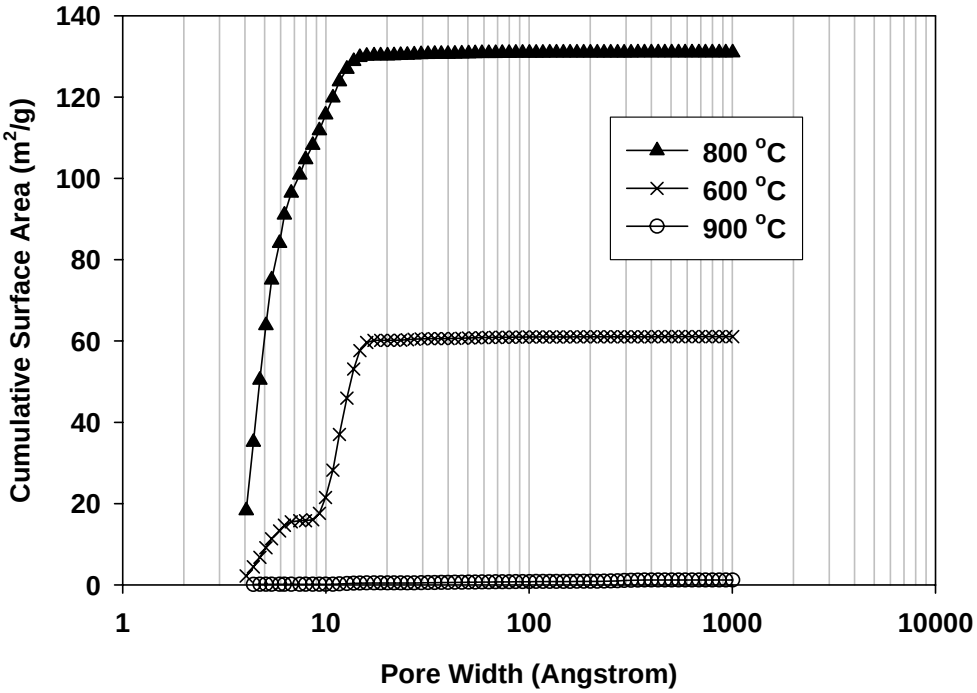

Figure 4-21 The cumulative surface area of pyrolyzed highly volatile bituminous coal at various temperatures, listed in descending order of surface area

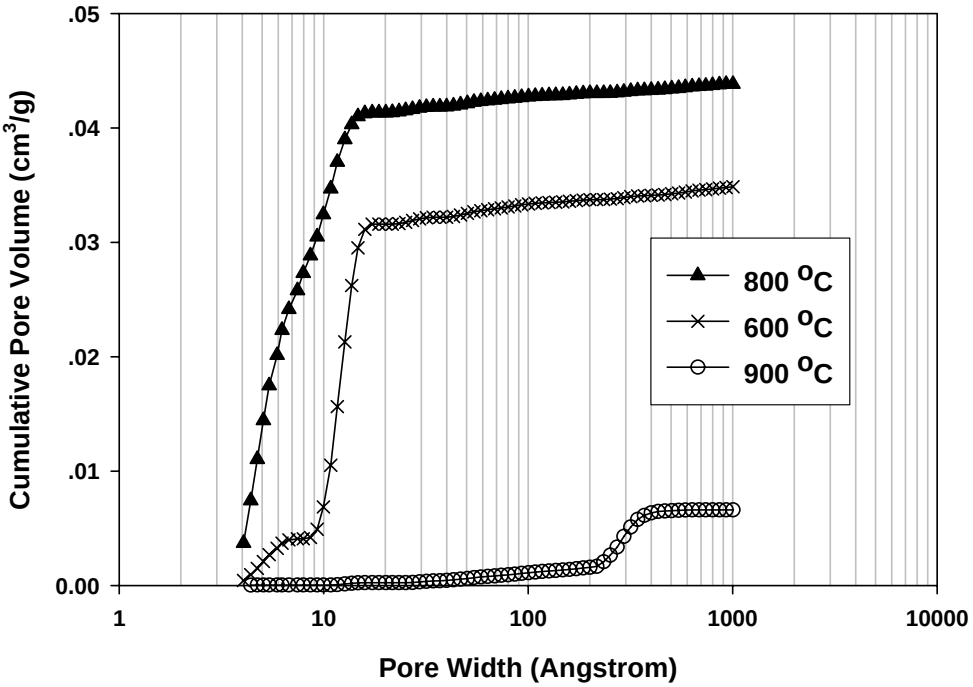

Figure 4-22 The cumulative pore volumes of pyrolyzed highly volatile bituminous coal at various temperatures, listed in descending order of pore volume

It can be seen that the pyrolyzed highly volatile bituminous coal provides more surface area and more pore volume than the anthracite. Under the treatment temperature of 800˚C for an hour, a cumulative surface area about 130 m^2/g and a cumulative pore volume of about 0.045 cm^3/g were achieved.

Also, we can get from the cumulative pore volume curve that almost all the pores developed in the pyrolyzed highly volatile bituminous coal are micropores (pore with the pore width less than 20Å).

The effect of treatment temperatures on the surface area and pore volume distribution of pyrolyzed highly volatile bituminous coal is interesting. At first, it seems that with the increase of treatment temperature, the cumulative surface area and cumulative pore volume increase. That can be seen from the figure that more surface area and pore volume were produced under 800˚C than that of 600˚C. It is a straight forward that cracks in the carbon will increase with the increase of pyrolysis temperature. And some of the carbon content that remains at the lower temperature will be pyrolyzed at higher temperature (although the amount of this content is very small, most of the mass was lost below 600˚C). But as the treatment temperature increased to 900˚C, the pyrolyzed highly volatile bituminous coal lost 90% of it pore volume and almost all of it surface area. This phenomenon indicates that the carbon sintered and experienced some coking as temperatures progressed to 900˚C.

The surface area and pore volume of the 800 ˚C pyrolyzed highly volatile bituminous coal was about 1/10 of that for conventional activated carbon. But compared to the results for anthracite, the experimental results of the highly volatile bituminous coal showed a favorable tendency, namely that coals with more volatile matter and moisture provided more surface area and pore volume during the pyrolysis.

4.2.3 Pyrolysis of Lignite

Figure 4-23 shows the pyrolysis mass loss profile for lignite under treatment temperature of 600˚C and 900˚C.

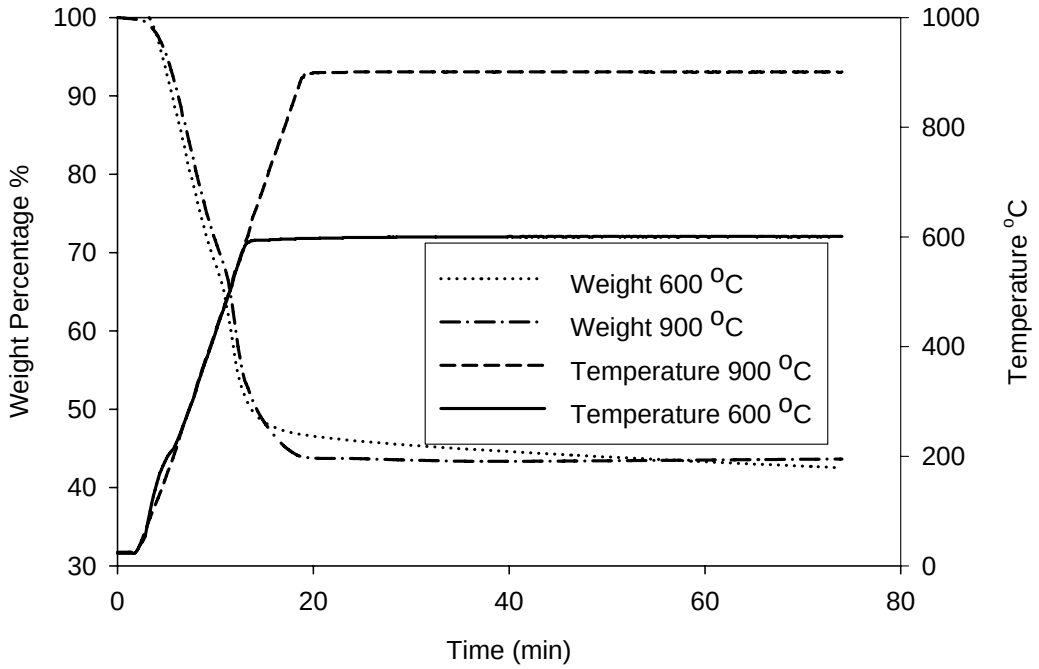

Figure 4-23 Mass loss profile during pyrolysis of Red Hill lignite

The Red Hills lignite lost 57-60% of its mass by weight during these pyrolysis conditions. Also as the mass loss effect of sustained holding at the treatment temperatures was slight (Table 4-2).

Table 4-2 The mass loss of Red Hills lignite during pyrolysis for 1 hour

Treatment Temperature (˚C)	Mass Loss (% of Weight)
600	57.48
800	59.96
900	56.32

The authors also observed that when the lignite grains experienced thermal pyrolysis, they remained as discrete grains, and they did not agglomerate into larger chunks. The surface areas and pore volume distributions of pyrolyzed Red Hills lignite are shown in Figure 4-24 and Figure 4-25 respectively.

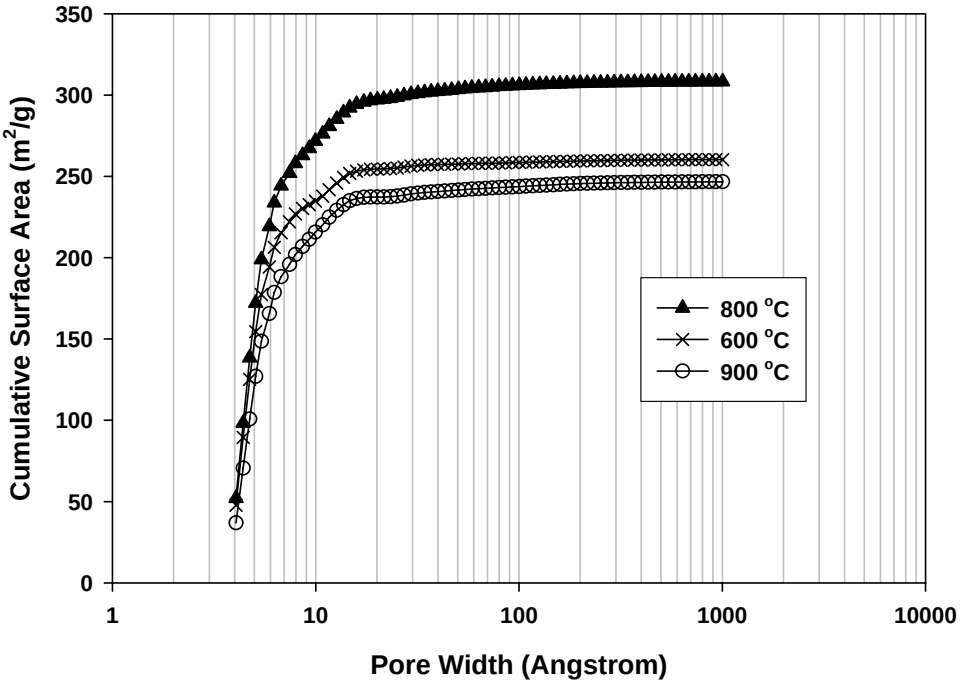

Figure 4-24 The cumulative surfaces of pyrolyzed Red Hills lignite at various temperatures, listed in descending order of surface area

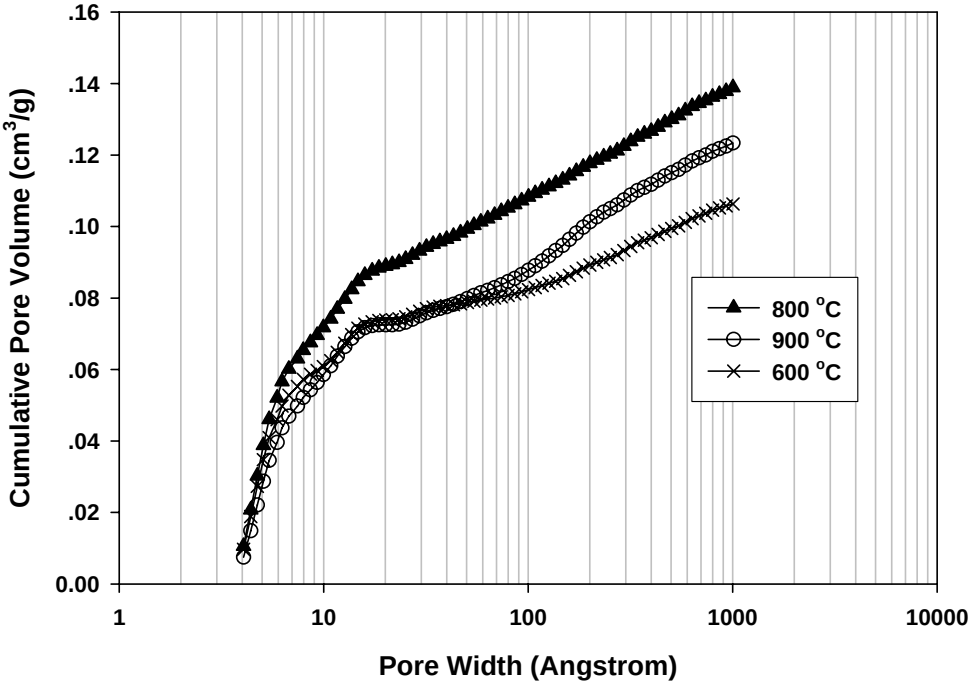

Figure 4-25 The cumulative pore volumes of pyrolyzed Red Hills lignite at various temperatures listed in descending order of pore volume

It is clear that the pyrolyzed lignite developed yet more cumulative surface area and pore volume than did pyrolyzed highly volatile bituminous coal. Treatment temperature conditions at 800˚C yielded cumulative surface area of about 310 m^2/g and a cumulative pore volume of about 0.145 cm^3/g.

As is shown in the cumulative pore volume curve, both micropores and mesopores were developed in the pyrolyzed lignite. This distinguishes the lignite from the highly volatile bituminous coal, where predominantly micropores developed. In general, more mesopores enhance the mass transfer of VOCs into the pyrolyzed coals, while more micropores enhance the extent of adsorption.

In one way, the effect of treatment temperatures on the surface area and pore volume distribution in the pyrolyzed lignite is similar to that of the highly volatile bituminous coal. Specifically, the largest cumulative surface area and pore volume were achieved at 800˚C. Also, sintering of the micropores occurred at 900˚C for the lignite. However the lignite exhibited a far smaller decrease of cumulative surface area and pore volume at 900 ˚C than did the highly volatile bituminous coal. From the cumulative pore volume, it can be seen that only a fraction of the micropores were lost as temperature rose from 800˚C to 900˚C. From this perspective, lignite will be more robust than highly volatile bituminous coal when full-scale operations dictate somewhat variable treatment temperature.

4.2.4 Full-scale Emission Testing When Employing Activated carbon

As an in-kind contribution to this CPCPC study, Neenah foundry has conducted full-scale testing to discern how stack gas emissions can be affected by introducing activated carbon and zeolite. In this testing, activated carbon and zeolite were injected into process stack gases, collected and exhausted from a primary mold cooling process. The activated carbon was a reactivated carbon that has been provided by NORIT Americas (900 m^2/g N_2-BET surface area). The zeolite utilized was 100 mesh Clinoptilolite from Badger Mining. The dosage rate for zeolite was 8.0 mg/scf. The dosage rate of GAC was 3.0 mg/scf in combination in addition to 1.5 mg/scf zeolite. The location where these materials were injected was approximately 24 feet upstream of the Bag House. The contact time was approximately 0.56 s ahead of the bag houses and 0.32 seconds within the bag house fabric's accumulated solids.

This effect of injecting these materials on VOC emissions is illustrated in the following figure. All tests were performed at a production foundry while utilizing the same core resin, similar green sand properties and production parts employing similar core loading. VOC emissions were captured from the exhaust stack, after a baghouse, utilizing GAC absorbent tubes. Captured non-methane/ethane VOCs were measured as hexane with a GC-FID. Samples employing GAC /zeolite injection measured VOCs at 410 and 420 μg VOC. The test method's reporting limit was 1.3 μg VOC. Comparative test measurements without injection are illustrated in blue. The GAC/zeolite injection samples are illustrated in pink while the zeolite injection samples are illustrated in yellow. While considerable scatter is present, the GAC samples illustrate a 32.86% reduction from the non-injection population mean. Similarly the zeolite injection samples illustrate a 6.14% reduction.

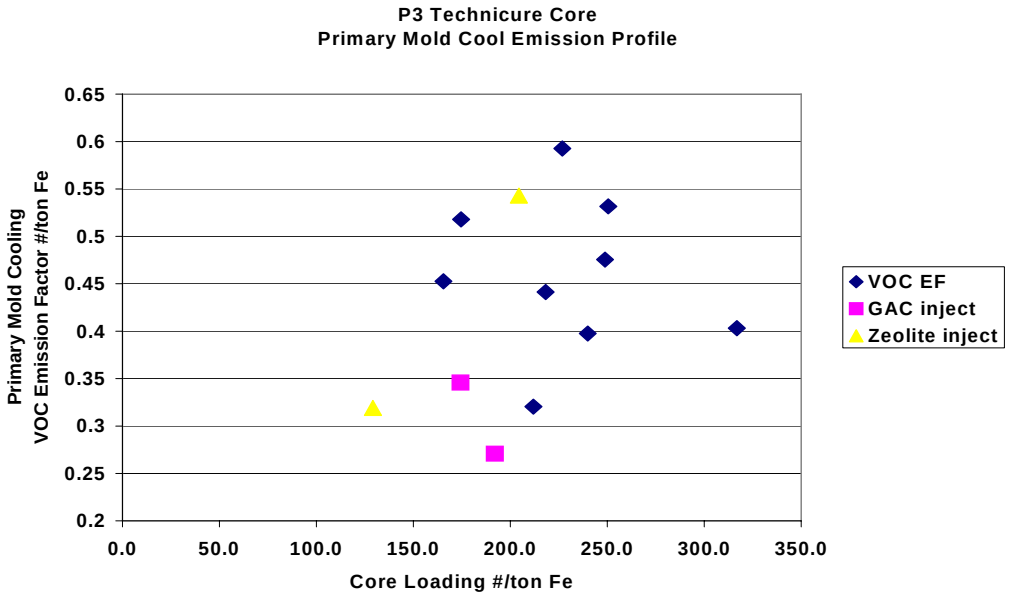

These full-scale results, coupled with the Penn State bench-scale results provide us the optimism that if we were to produce pyrolyzed lignite carbon in-situ from the foundry's waste heat, and introduce this in-situ pyrolyzed carbon into the exhaust ducts at a dose of 3 times that which was employed in these preliminary trials, then we can likewise diminish VOC's by 1/3. Moreover, this VOC-loaded pyrolyzed carbon can provide the coal source for the make-up materials that are added to the next cycle of green sand any may provide additional adsorption of VOC emissions.

4.2.5 TGAs of Bag House Dust

Parenthetically, as part of collaborative work with Neenah foundry, we conducted some thermogravimetric analysis (TGA) of bag house dust from Neenah Foundry as shown in Figure 4-26 and 4-27.

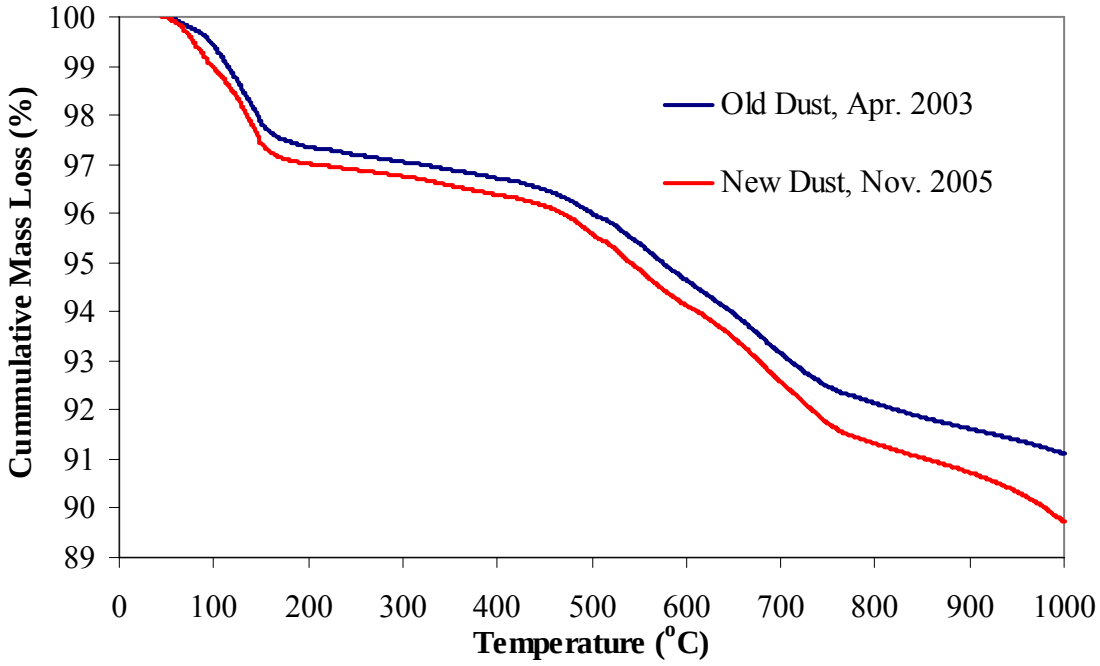

Figure 4-26 Cumulative mass loss for bag house dusts that contain old and new core binder residues

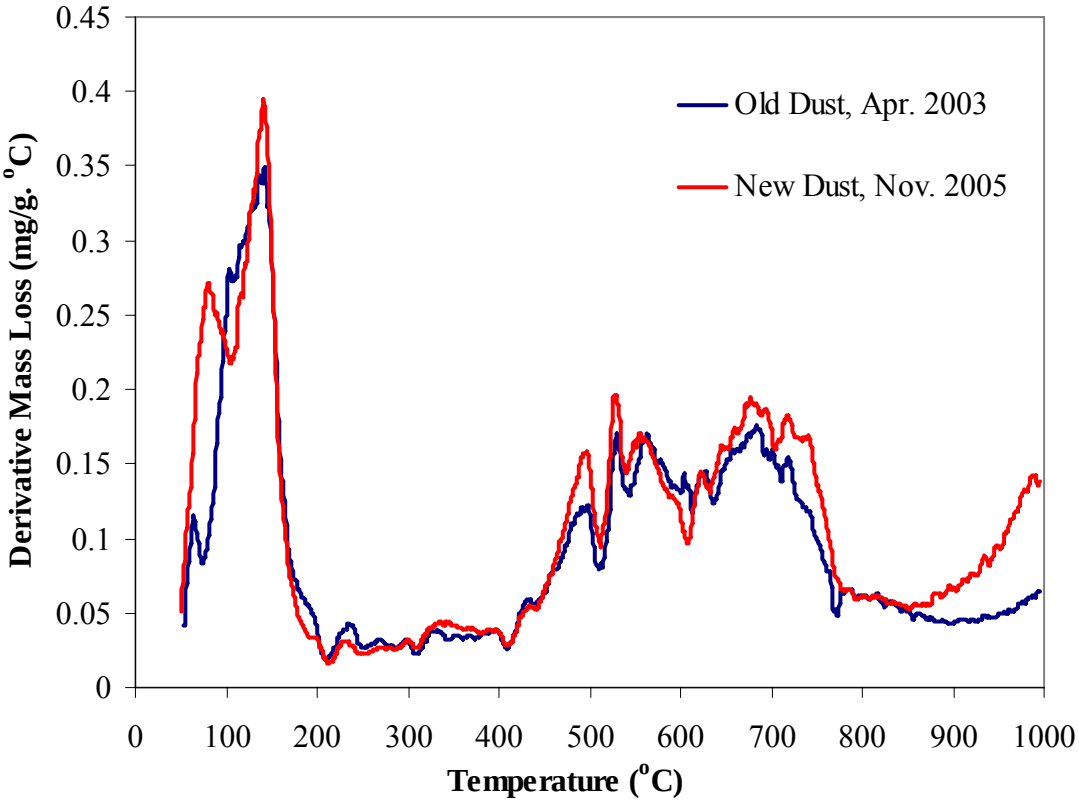

Figure 4-27 Derivative mass loss for bag house dusts that contain old and new core binder residues

Neenah Foundry experienced an increase in gas-related casting defects after they employed a new core binder. One possible reason could be due to the abrupt release of excessive gases from the new core binder when the core was in contact with the molten metal. When compared the mass loss curve of an old bag house dust sample (Apr. 2003) and the new bag house dust (Nov. 2005), one could discern that the new bag house dust released more mass as gaseous products, especially above 850^{o}C. This result suggests that it is true that the new core binder releases more gases when exposed to intense heat that might lead to the casting defects.

4.3 On Searching the Optimal Pyrolysis Conditions Using Lignite as the Raw Material of in-situ Pyrolyzed Carbon

4.3.1 The Optimal Pyrolysis Temperature

In previous study, pyrolysis temperatures at 600 °C, 800 °C and 900 °C were tested for all the coals used in the experiments. The results indicate that all raw materials produced their highest pore volume and surface area at 800 °C. In order to confirm this found, two more temperature points, 700 °C and 850 °C, were selected to pyrolyze the Red Hills lignite. The result is shown in Figure 4-28.

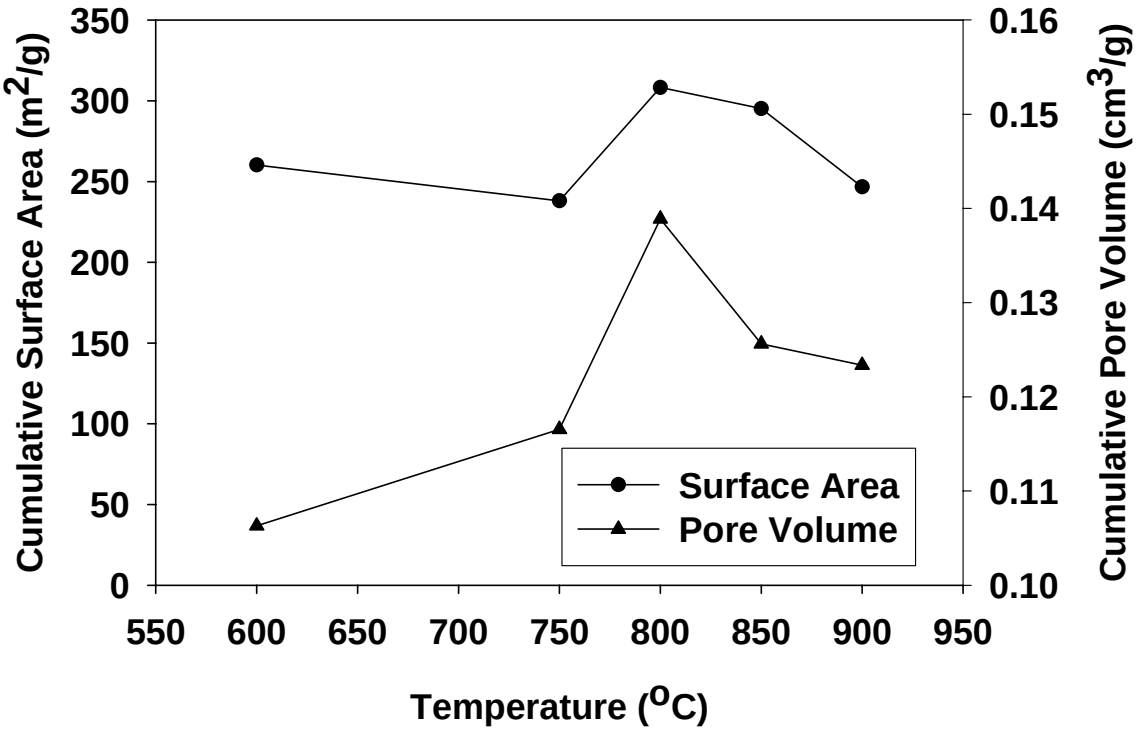

Figure 4-28 The effect of temperature on cumulative pore volume and cumulative surface area of pyrolyzed Red Hills lignite

It can be seen from Figure 4-28 that within the temperature range tested, which is also similar to the possible temperature range in the heat exchange tube, the maximum values for pore volume and surface area of pyrolyzed lignite both appear at 800 °C. At temperatures higher than 800 °C, the pyrolyzed lignite will also lose a part of its pore volume and surface area. Although the pore volume and surface area lost in pyrolyzed lignite at higher temperature is much smaller than that in pyrolyzed highly volatile bituminous coal, and also the temperature in heat exchange tube system is hard to control, it may still be favorable to design the heat exchange tube system carefully to avoid higher pyrolysis temperatures.

4.3.2 Effect of Different Lignite Resources on the Final Product

Mass Loss

The mass loss profiles of the lignites are shown in Figure 4-29.

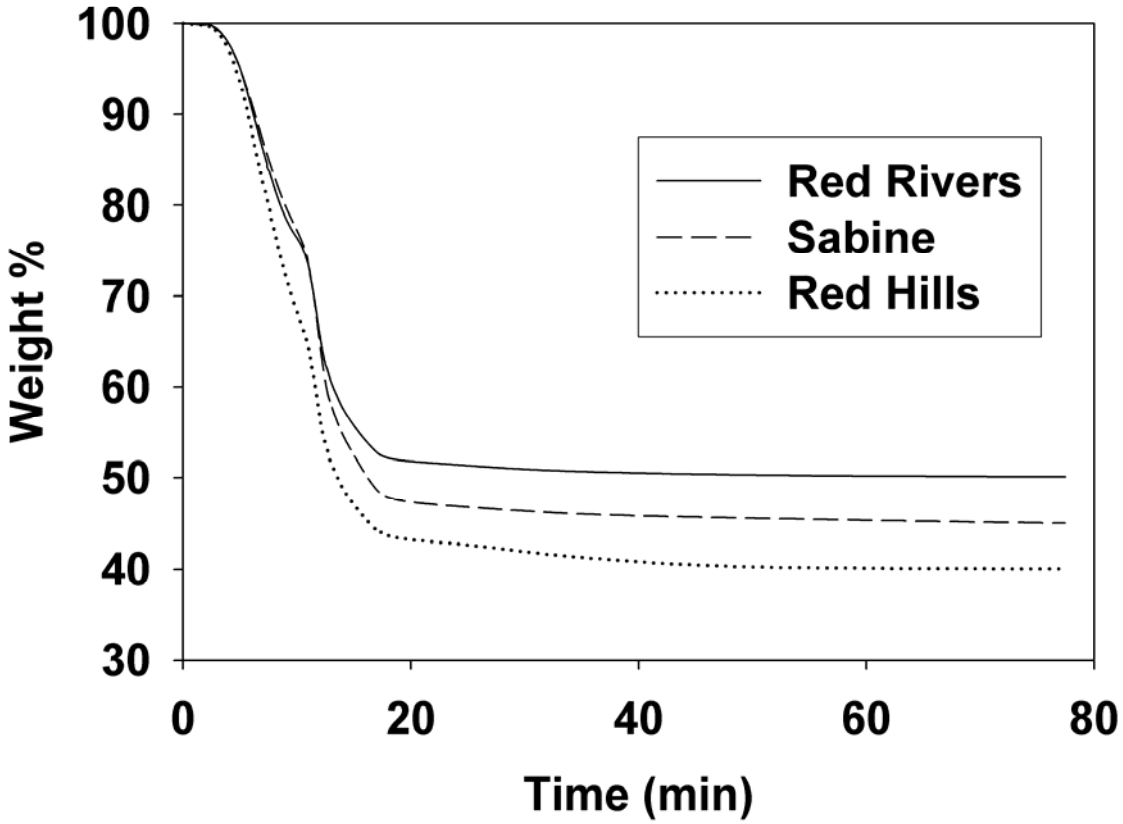

Figure 4-29 Mass loss profiles of the lignites during pyrolysis

It can be seen that the mass loss profiles of these lignite are similar to each other in their shapes. But they are different in the final mass loss amount, which is about 60% for Red Hills lignite, about 55% for Sabine lignite and about 50% for Red Rivers lignite. And the difference in mass loss amount is mainly from their difference in moisture and VOCs contents.

Physical Properties of Pyrolyzed Lignites

The pore volume distributions and surface area of the three different lingnites pyrolyzed under same conditions (800 °C for 1 hour) are shown in Figure 4-30 and Table 4-3 respectively.

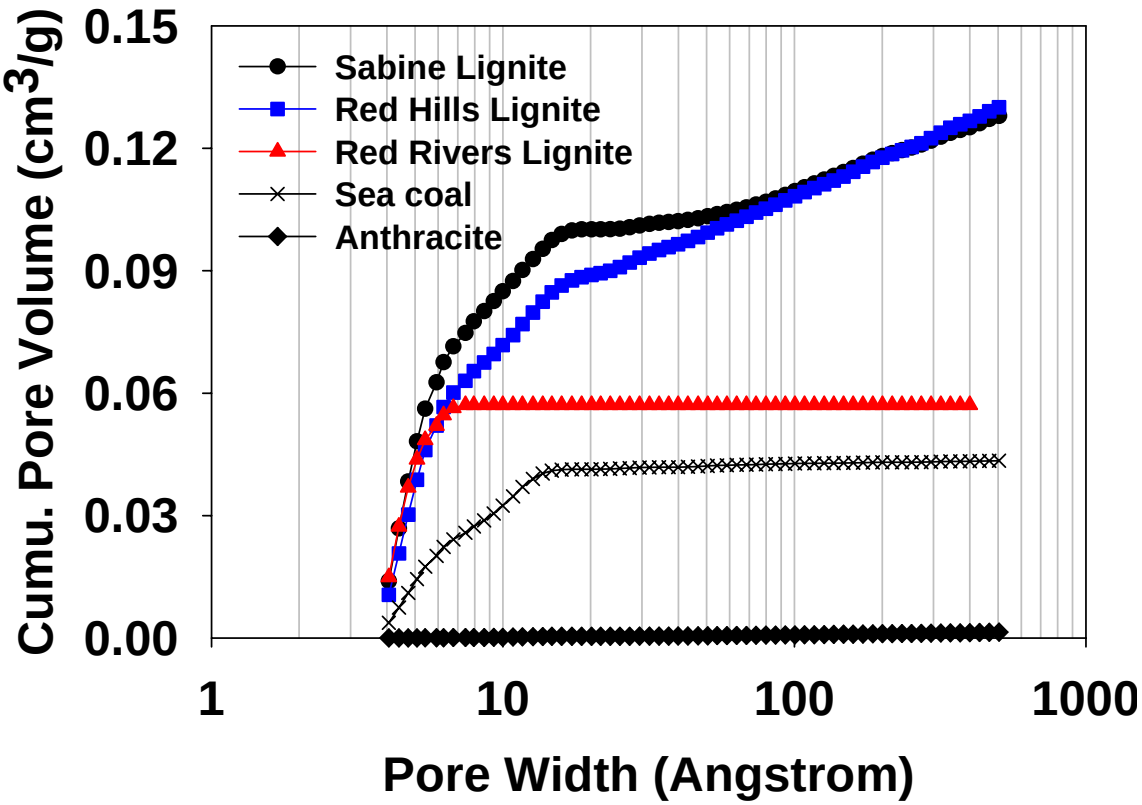

Figure 4-30 Pore volume distribution of in-situ pyrolyzed carbon from different raw materials

Table 4-3 Cumulative surface area of in-situ pyrolyzed carbon from different raw materials

Raw Material	Sabine Lignite	Red Hills Lignite	Red Rivers Lignite	Highly volatile bituminous coal	Anthracite
Surface Area (m^2/g)	342	308	246	131	1

It was found that Sabine lignite provides the highest micro-pore volume after being pyrolyzed. Therefore, Sabine lignite also contains the highest surface area, which is more favorable for adsorbing VOCs. It was noticed that Sabine lignite also do not have the largest mass loss among these three lignites, hence it is hard to conclude that the higher pore volume in pyrolyzed Sabine lignite is due to higher burn off rate. One possible reason for this may be that the Sabine lignite contains more fixed carbon than other two lignites, and it can be verified by elemental analysis of the pyrolyzed lignites.

Elemental Analysis of Pyrolyzed Lignites

Elemental analysis of pyrolyzed lignites was performed on a CHN600 carbon-hydrogen-nitrogen determinater (LECO Co., St. Joseph, MI) and the data are shown in Table 4-4.

Table 4-4 Elemental analysis of pyrolyzed lignites

Lignite	C	H	N	S	Ash
Sabine	73.1	0.84	1.28	0.65	23.9
Red Hills	61.7	0.67	1.13	0.52	~28
Red Rivers	57.2	0.66	0.93	0.54	~27

From Table 4-4, it is clear that Sabine lignite contains the highest amount of fixed carbon, while Red Rivers lignite has the lowest fixed carbon content. This trend is same as the surface area contained in the pyrolyzed lignites.

4.3.3 Effect of Pyrolysis Time on the Final Products

Sabine lignite was pyrolyzed at 800 °C for 15, 30 and 60 minutes respectively to study the effect of pyrolysis time on the pore volume distribution of the final products. The results are shown in Figure 4-31.

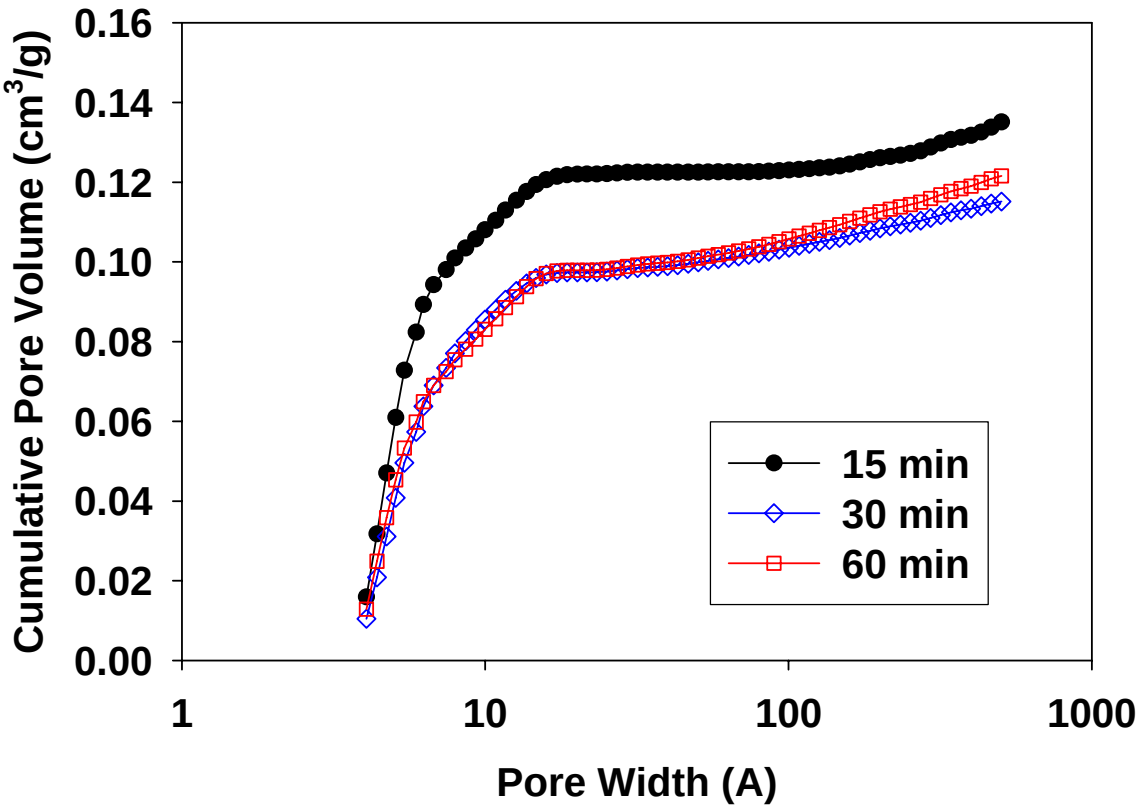

Figure 4-31 Effect of pyrolysis time on the pore volume distribution of in-situ pyrolyzed Sabine lignite

It can be seen from Figure 4-31 that when Sabine lignite has more micro-pore volume (about 0.12 cm^3/g) when it was pyrolyzed at 800 °C for only 15 minutes. After being pyrolyzed for 30 minutes, some of the micro-pores were lost. However, almost no change on pore volume distribution was noticed after another 30 minute' pyrolysis. It is speculated that the pore structure formation in the lignite has already accomplished after 30 minutes' pyrolysis.

4.3.4 In-situ Pyrolyzed Carbon V.S. Commercial Activated Carbon

Lignite is a common raw material for activated carbon manufacture. Therefore, it is valuable to compare the properties of in-situ pyrolyzed carbon with the lignite-based commercial activated carbon. The lignite-based commercial activated carbon used here is Hydrodarco 4000 (HD4000), a steam-activated carbon by NORIT America. The pore volume distributions of HD4000 and in-situ pyrolyzed carbon from Sabine lignite (pyrolyzed at 800 °C for 15 minutes) are shown in Figure 4-32.

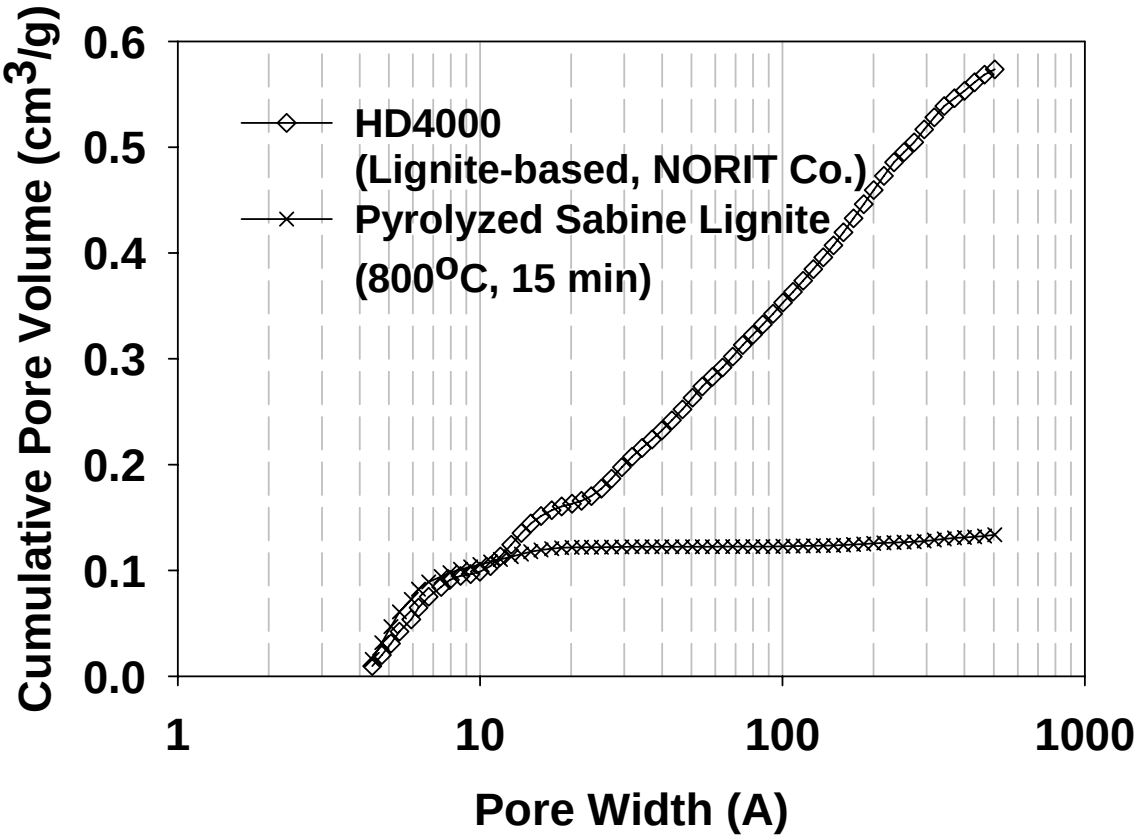

Figure 4-32 Pore volume distribution of HD4000 and pyrolyzed Sabine lignite

It can be seen from Figure 4-32 that HD4000 has a much higher pore volume than the pyrolyzed Sabine lignite. The reason for this difference is that HD4000 was activated by steam in well controlled conditions, while the in-situ pyrolyzed Sabine lignite was not.

However, by checking the pore volume distribution profile carefully it can be found that the micro-pore volume of in-situ pyrolyzed Sabine lignite is only slightly smaller than that of HD4000. Rendered from this high micro-pore volume, the surface area of the pyrolyzed Sabine lignite is 438 m^2/g and about 82% of HD4000's surface area, which is 535 m^2/g. Therefore, predicted from the amount of surface area, the in-situ pyrolyzed lignite has a promising VOCs adsorption capacity.

4.3.5 Preliminary Test on Adsorption of VOCs on in-situ Pyrolyzed Lignite

In the preliminary adsorption experiment Sabine lignite pyrolyzed at 800 °C for 1 hour was packed in the first section of the column. The proposal of this experiment is to test the feasibility of using the in-situ pyrolyzed carbon as adsorbent for VOCs adsorption. Meanwhile, the types of VOCs from the highly volatile bituminous coal emission can also be verified. Figure 4-33 shows the results of the adsorption experiments.

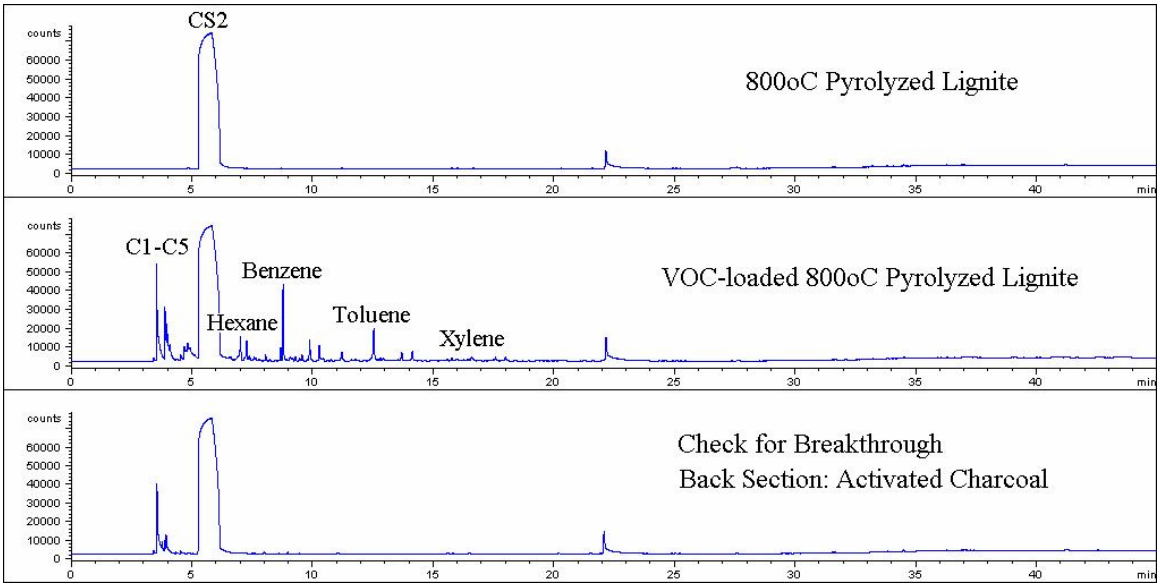

Figure 4-33 Adsorption of VOCs on pyrolyzed lignite

It can be seen from Figure 4-33 that after been pyrolyzed, there is no VOCs left in the lignite. However, after the adsorption experiment, some VOCs were loaded onto the pyrolyzed lignite and only some small size VOCs were detected in the second section. The results indicate that the in-situ pyrolyzed lignite is feasible for adsorbing the VOCs from green sand mode emission. The breakthrough of the small size VOCs may due to either the capacity of the in-situ pyrolyzed carbon to adsorb these small size VOCs has already been exhausted, or the rate of the in-situ pyrolyzed carbon to adsorb these small size VOCs is not fast enough to separate all these compounds from the gas flow.

4.4 Evaluation of hydrocarbon emission characteristics of typical carbonaceous additives in green sand foundries

4.4.1 TGA Pyrolysis of Carbonaceous Additives.

The TGA profiles of the four samples are shown in Figure 4-34. The anthracite lost the lease mass and its mass loss mainly occurred above 600 ^{o}C. The highly volatile bituminous coal lost its mass mainly within the temperature range of 400-600 ^{o}C where the active thermal decomposition of coal occurred. The lignite lost its mass more gradually than the highly volatile bituminous coal. The cellulose lost most of its mass at 200-400 ^{o}C.

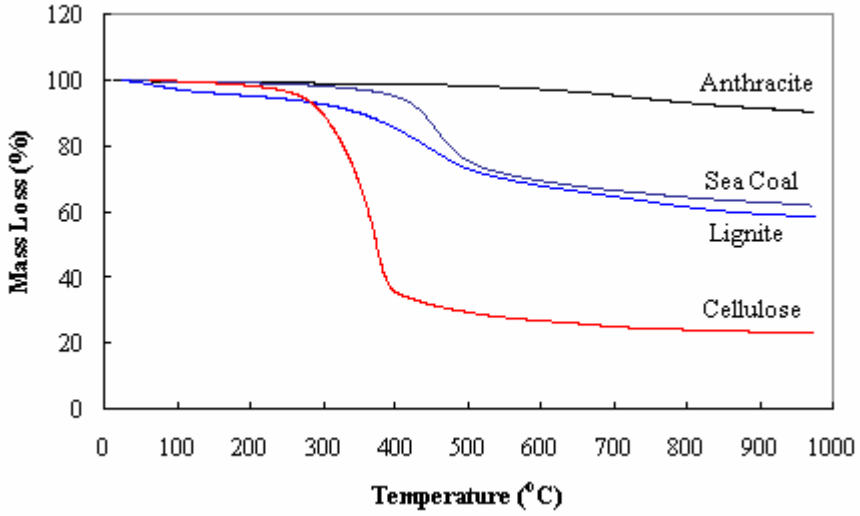

Figure 4-34 TGA profiles of the carbonaceous additives.

Mass spectroscopy (MS) revealed the temperature ranges where the major hydrocarbon gas products (methane) and HAPs released from the carbonaceous additives during the TGA slow heating (see Figure 4-34). The MS responses to the anthracite are relatively weak compared with other materials tested herein. No apparent peaks were detected for the anthracite except methane that shows a peak between 600-800 ^{o}C. Most of the hydrocarbon gases and major HAPs are released from the highly volatile bituminous coal in the temperature range of 400-600 ^{o}C, with the exception of benzene that exhibited a considerable increase above 800 ^{o}C. Lignite releases hydrocarbon gases at a relative wide temperature range (300-800 ^{o}C) compared with the highly volatile bituminous coal. The cellulose released methane and HAPs at relative lower temperature range (200- 600 ^{o}C). It is noted that for the coals of different ranks, i.e. the anthracite, highly volatile bituminous coal and lignite tested herein, the MS responses correlated well with the TGA test. Most of the HAPs are released in the same temperature range where the coals lost most of their mass. In comparison, the cellulose lost most of its mass before 400 ^{o}C (see Figure 4-34), while most of its HAPs are generated above 400 ^{o}C. This reflected the different pyrolysis mechanisms of the coals and the cellulose. When the coals are progressively heated, they will lose chemically combined H_2O, CO, CO_2 and some occluded species at relative low temperatures (<350^{o}C). Then suddenly, considerable tar

and hydrocarbon gases simultaneously begin to expel from the coals when the coals are heated to their active thermal decomposition temperature (350-400 ^{o}C, except anthracite) (Speight et al., 1994; Berkowitz et al., 1985). In comparison, the cellulose undergoes primary pyrolysis in the range of 200-400 ^{o}C that produces tar, H_2O, CO and CO_2. The hydrocarbon gases and HAPs primarily come from the secondary thermolyisis of the tar at higher temperature (>400 ^{o}C) (Fisher et al., 2002; Li et al., 2001; Fushimi et al., 2003; Banyasz et al., 2001).

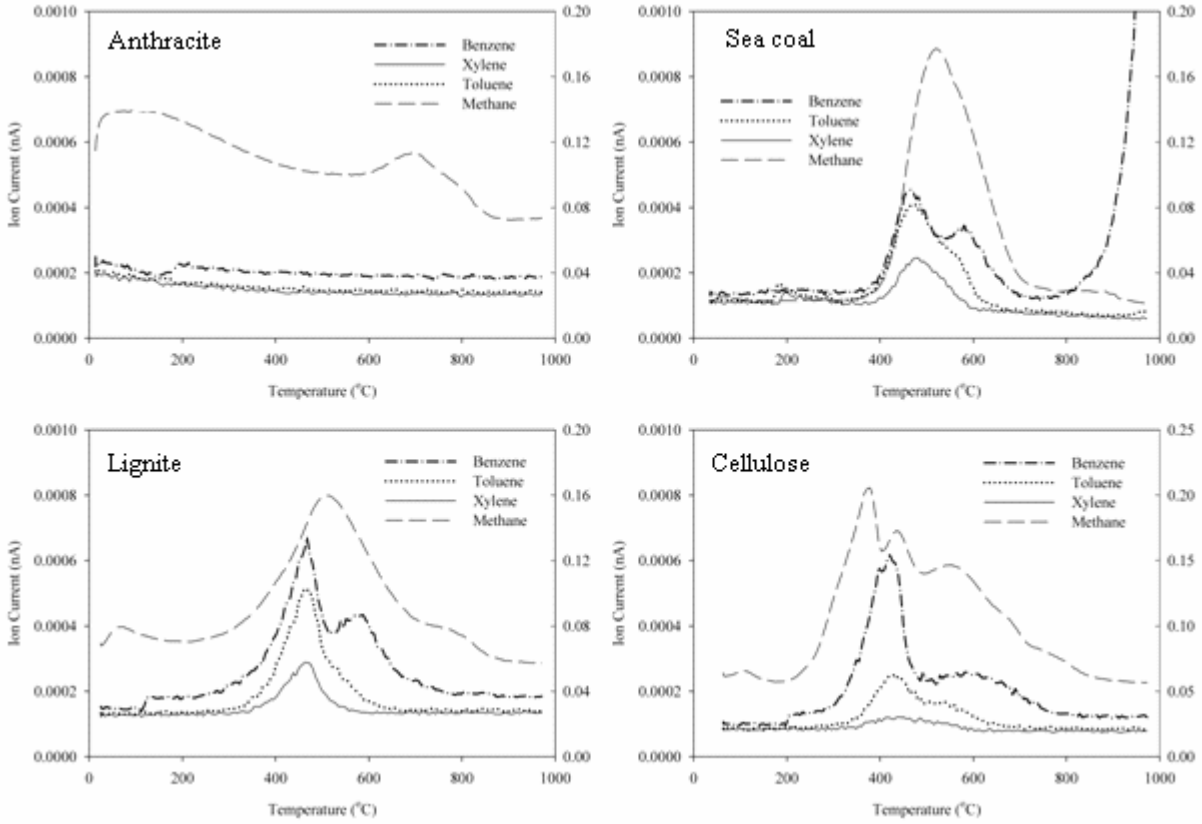

Figure 4-35 MS response to the HCG emissions during TGA pyrolysis

Previous research has indicated that volatiles that evolved from highly volatile bituminous coal below 400 ^{o}C did not help the formation of lustrous carbon and good casting peel (Green et al., 1980). And the best casting quality were obtained when the highly volatile bituminous coal thermal decomposition took place at above 400 ^{o}C and the volatiles contained aromatics (Stanbridge, 1974). It could be seen from Figure 4-35b that 400 ^{o}C is the temperature that large amount of hydrocarbon gases begin to evolve from the highly volatile bituminous coal. Thus, the authors herein proposed that it is the hydrocarbon portion of the volatiles that are of most importance for the casting qualities. And for the production of quality castings, a certain amount of hydrocarbon gases (not the total volatiles) must be present at the metal-mold interface following the metal pouring.

To quantify the amount of hydrocarbon emissions, the emissions from the TGA were captured by activated charcoal, and then extracted by CS_2 solvent and analyzed with the GC-FID. The emission analysis results were summarized in Table 4-5. In the table, the

hydrocarbons of C1-C5 are normalized to the standard of methane, and the C6-C16 are normalized to the standard of benzene. As shown, the highly volatile bituminous coal has the highest HCG yields in the slow TGA heating situation, followed by the lignite, cellulose and anthracite.

Table 4-5 Hydrocarbon Emissions (mg/g) of the carbonaceous additives during the TGA pyrolysis

Sample	Hydrocarbon (mg/g)				Representative HAPs (mg/g)					
	C1-C5		C6-C16		Benzene		Toluene		Xylene	
	mean	SD	mean	SD	mean	SD	mean	SD	mean	SD
Anthracite	0.105	0.036	0.374	0.103	0.072	0.027	0.021	0.007	0.005	0.002
Highly volatile bituminous coal	10.093	0.086	8.499	0.751	0.406	0.021	0.783	0.065	0.384	0.059
Lignite	5.274	0.621	4.572	0.177	0.351	0.002	0.413	0.006	0.160	0.004
Cellulose	3.838	0.466	2.602	0.297	0.213	0.015	0.298	0.038	0.077	0.009

4.4.2 Flash Pyrolysis of Carbonaceous additives.

During the flash pyrolysis, the carbonaceous additives were completely devolatilized. The remaining char or ash of the anthracite, highly volatile bituminous coal, lignite and cellulose was 89.5%, 56.3%, 47.2%, and 7.8%. Practically, the cellulose left the least amount of ash content that are usually undesirable in the casting process; and in full-scale foundries, this means that less new sand addition is needed to dilute these ash fines in the green sand system (Lafay et al., 1987). This, in turn, decreases the amount of waste sand that needs to be landfilled.

A typical GC-FID response to the hydrocarbon emissions from the flash pyrolysis is shown in Figure 4-36. As shown, the hydrocarbon emission characteristics of these carbonaceous additives are very similar. This is possibly the reason that all these carbonaceous additives are capable of producing quality castings (LaFay et al., 2004; Thiel et al., 2005). Large amount of hydrocarbon emitted as methane (and ethane); benzene, toluene, xylene (BTX) compounds composed the major part of the HAP emissions. Although the compositions of the hydrocarbon emissions were similar for the four samples tested herein, the yields of the hydrocarbons varied considerably, which were summarized in Table 4-6. In the table, the hydrocarbons of C1-C5 are normalized to the standard of methane, and the C6-C16 are normalized to the standard of benzene. As shown, the cellulose has the highest HCG yields in the flash pyrolysis situation, followed by the highly volatile bituminous coal, lignite and anthracite.

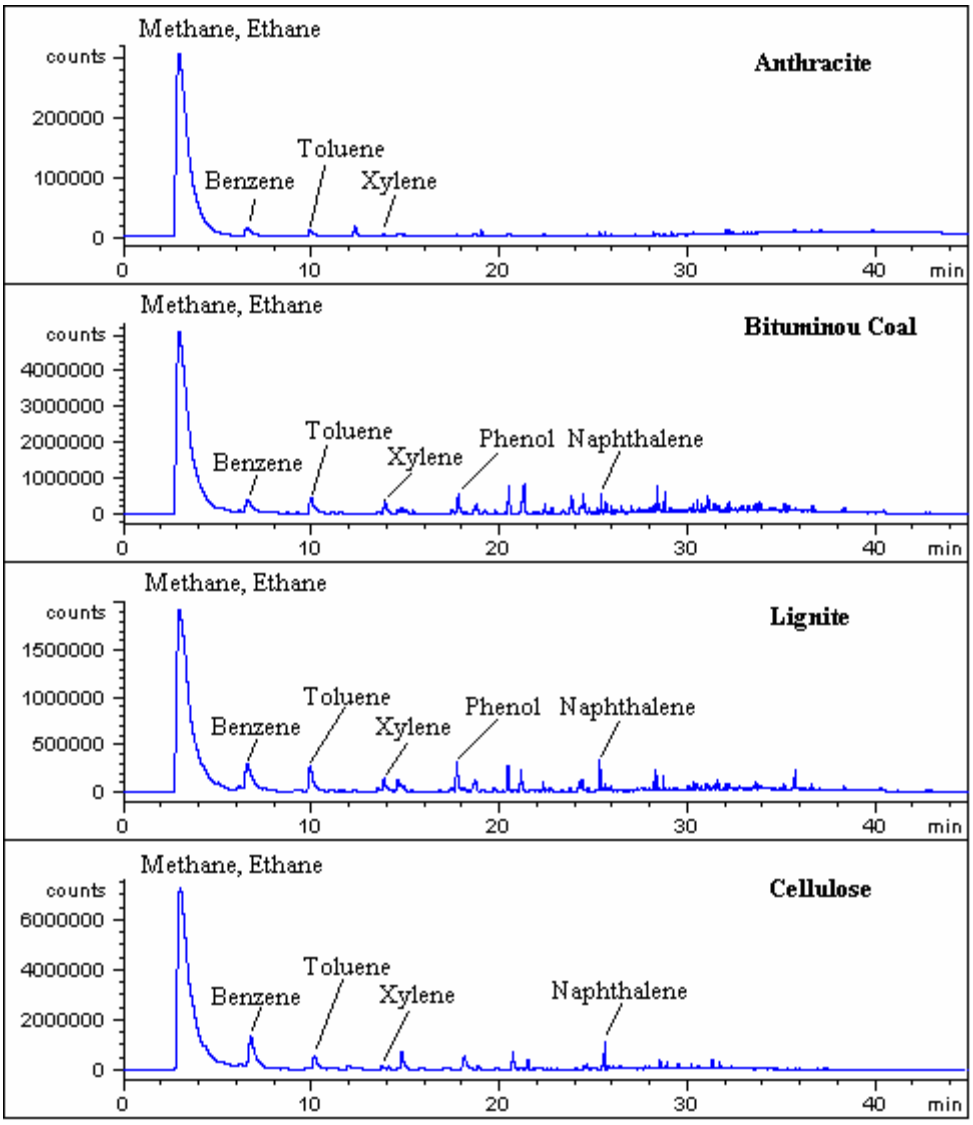

Figure 4-36 GC-FID responses to the hydrocarbon emissions of the carbonaceous additives during the flash pyrolysis.

Table 4-6 Hydrocarbon Emissions (mg/g) of the carbonaceous additives during the flash pyrolysis

Sample	Hydrocarbon (mg/g)				Representative HAPs (mg/g)					
	C1-C5		C6-C16		Benzene		Toluene		Xylene	
	mean	SD	mean	SD	mean	SD	mean	SD	mean	SD
Anthracite	2.25	0.18	0.81	0.02	0.14	0.01	0.11	0	0.04	0
Highly volatile bituminous coal	58.33	2.54	27.27	1.23	1.49	0.13	1.33	0.05	0.65	0.01
Lignite	36.98	3.37	17.36	1.84	2.11	0.15	1.25	0.11	0.47	0.05
Cellulose	80.66	14.94	37.56	2.76	4.45	0.62	1.38	0.06	0.22	0.02

4.4.3 Discussion

As mentioned before, a certain amount of HCGs are needed at the metal-mold interface to prevent the sand adherence to the casting surface. Thus, in full-scale foundries, this means that the amount of the carbonaceous additives in the green sand must be adjusted according to their capacity to release HCGs. The anthracite seems not an ideal carbonaceous additive in the green sand since it has very low HCG yield unless very large amount of anthracite is used in the green sand.

It is noted that lustrous carbon film is formed at the metal-mold interface instantly as the molten metal is poured into the green sand mold (Naro, 2002). And rationally, the role of the volatiles and lustrous carbon film in preventing sand grains from sticking to the casting surface is only effective before the casting develops a solid skin that usually takes less than one minute after metal pouring (Hsiau et al., 1998; Shih et al., 1996). Thus, it is inferred that the lustrous carbon film is formed from the HCGs that are released from the flash pyrolysis of carbonaceous additives at the very vicinity of the metal-sand interface. The HCGs released from the slow heating of carbonaceous additives that are further away from the metal-mold interface do not help develop the lustrous carbon film and prevent sand adherence to the casting surface, while they could contain significant amount of HAPs. For example, Hsiau and Shih showed that it took about 3 and 10 minutes respectively for the green sand that was 1.0 cm and 1.5 cm away from the metal-mold interface to be heated to 400 ^{o}C, and thus to release HCGs (Hsiau et al., 1998; Shih et al., 1996). But at the moments, the solidification of the casting surface has well completed.

Thus, the authors herein proposed that only the HCGs that are released from the flash pyrolysis of carbonaceous additives at the metal-mold interface are of great importance for the casting process. The HCGs released from the slow heating of carbonaceous additives at further away from the metal-mold interface has limited value in improving casting surface quality, while they may contribute the major HAP emissions.

It could be seen from Figure 4-36 that HAP emissions from these carbonaceous additives mainly occur above 400 ^{o}C. And in casting practice, green sand molds are usually kept intact for about 30-60 min for casting solidification and mold cooling after the molten metal is poured in the mold. During this period, as the casting heat dissipates from the metal-mold interface outwards through the green sand mold, a considerable fraction of the green sand mold can be slowly heated to temperatures above 400 ^{o}C, and thus release HAPs (Dempsey et al., 1997; LaFay et al., 1998).

From this perspective, the ideal carbonaceous additives should be able to release sufficient HCGs during the flash pyrolysis at the metal-mold interface, and release the least of HAPs during the slow heating at the major part of the green sand mold. And the authors herein perceive that the cellulose is a potential ideal carbonaceous additives as discussed below.

Figure 4-37 shows the ratio of hydrocarbon gas yields of the TGA pyrolysis and flash pyrolysis. It is found that the hydrocarbon gas yields in the TGA slow pyrolysis are much lower than them in the flash pyrolysis for all the samples tested herein. The yields of lower molecular weight hydrocarbon (C1-C5) in the TGA pyrolysis are about 5-20% of the yields in the flash pyrolysis. For larger molecular hydrocarbons (C6-C16), the ratio is about 10-50%. Also, it is found that the heating rates have a more pronounced effect on the cellulose compared with other carbonaceous additives. For the cellulose, the yield of C6-C16 that contains most of the major HAPs is decreased more than 90% by decreasing the heating rate, while it only decreased about 55-75% for the other materials tested herein.

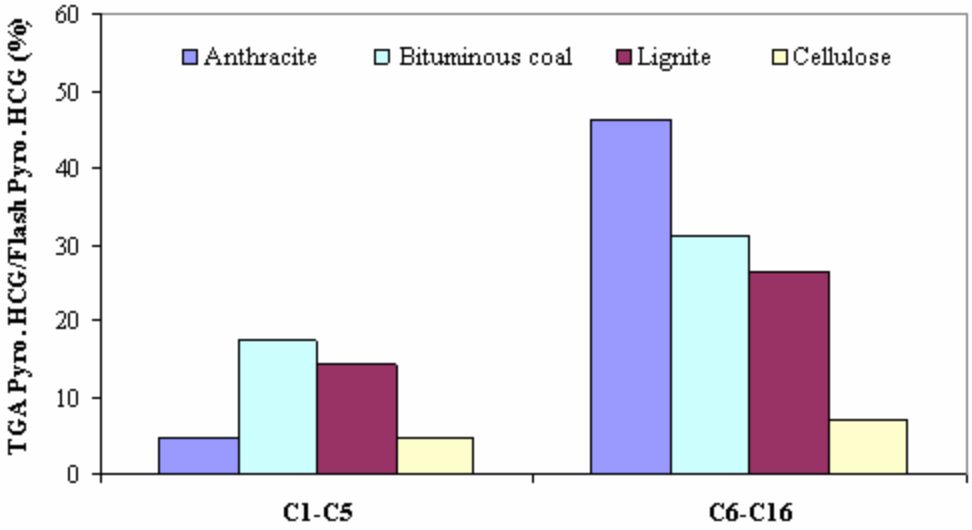

Figure 4-37 Ratio of HCG yields in the TGA pyrolysis and in the flash pyrolysis

It is well known that the heating rates profoundly affect the hydrocarbon gas yields of the coals. Very fast heating (i.e. the flash pyrolysis) causes more extensive thermal fragmentation of coal molecules, thus can produce much higher volatiles (especially lower molecular weight hydrocarbons) compared with the slow TGA heating (Speight et al., 1994; Berkowitz et al., 1985). In comparison, flash pyrolysis dramatically enhanced cellulose's hydrocarbon gas production via a different mechanism. Unlike the coals, the cellulose pyrolysis consists of two stages. The first stage (200-400 ^{o}C) primarily produces tar, H_2O, CO and CO_2. The hydrocarbon gases are generated from the secondary thermolysis of the tar at higher temperatures (>400 ^{o}C) (Fisher et al., 2002; Li et al., 2001; Fushimi et al., 2003; Banyasz et al., 2001). However, cellulose's tar is easily volatilized below 400 ^{o}C. Thus, when the cellulose is slowly heated, as in the TGA pyrolysis, the tar quickly escapes from the TGA reactor before the temperature goes up. This prevented the tar from further pyrolysis to form hydrocarbon gases. In contrast, when the cellulose is flash pyrolyzed, the tar can be decomposed into hydrocarbon gases before it escapes from the reactor due to the very high heating rate. This characteristic of the cellulose makes it a ideal carbonaceous additive for diminishing HAP emissions from the foundry.

As mentioned before, during the casting solidification and mold cooling, a considerable fraction of the green sand mold can be slowly heated to temperatures above 400 ^{o}C, and

thus release HAPs. However, when the cellulose is used, the slow heating would allow the tar released from the cellulose at 200-400 ^{o}C to move outwards from the hot region and then re-condense at the cool region of the green sand mold. This prevents the cellulose tar from further pyrolysis (that occurs above 400 ^{o}C) to form HAPs. In contrast, the highly volatile bituminous coal and lignite generate tar and volatiles simultaneously when slowly heated to above 350-400 ^{o}C; and the tar is much less volatile compared with the cellulose tar. So the tar of highly volatile bituminous coal and lignite stays in the hot region and is further pyrolyzed to from volatiles (and HAPs) as the temperature goes up. In practice, this means that HAP emissions from the major part of the green sand mold that is slowly heated would be greatly reduced when the cellulose is used instead of the other carbonaceous additives tested herein.

Based on the notion that a certain amount of hydrocarbon gases (HCGs) is needed at the metal-mold interface to ensure the casting quality, and these HCGs are released from the flash pyrolysis of carbonaceous additives that are at the very vicinity of the interface, the usage of the carbonaceous additives in the green sand must be adjusted according to their capacity to release hydrocarbons per mass during the flash pyrolysis. Thus, due to the different pyrolysis mechanisms of the coals and the cellulose, when they produce the same amount of total hydrocarbon gases during the flash pyrolysis, the amount of HAPs released from the major part of the green sand mold that is slowly heated could vary dramatically. Figure 4-38 shows the ratio of HAPs released during the slow TGA heating to the total HCGs (C1-C16) released during the flash pyrolysis.

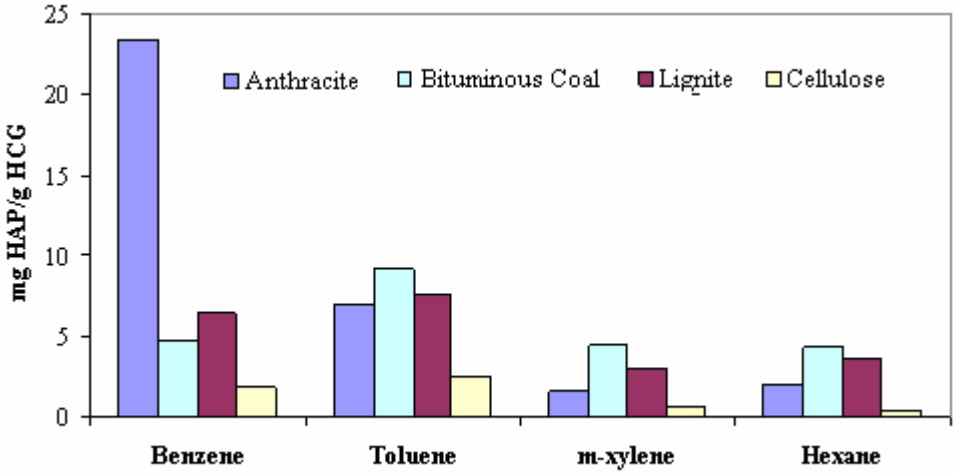

Figure 4-38 Ratio of HAPs released during TGA Pyrolysis to the total HCGs released during flash pyrolysis

As shown, the cellulose HAP emissions are much lower than them of other carbonaceous additives tested herein. This would offer a great opportunity for the foundry to cut down the HAP emissions.

5. Conclusion

ESEM and EDS measurements confirmed that AO and sonication treatments greatly separate surface clays from the large particles of silica and coal and reduce the size of the clay agglomerates. The physical characteristics of baseline bituminous coal particles in these baghouse dust suspensions have been characterized so that the relative performance of anthracite-based green sand mixtures can be similarly characterized in the later portions of the study.

Experimental results revealed that use lignite as raw material to produce in-situ pyrolyzed carbon by reclaiming the waste heat from foundry is promising. An in-situ pyrolyzed carbon contains surface area as much as 80% of the commercial lignite-base activated carbon can be produced. And it takes much less effort and cost to produce this in-situ activated carbon than the commercial activated carbon. The result of adsorption test indicates the in-situ pyrolyzed carbon is also a good adsorbent for VOCs adsorption.

It is found that the hydrocarbon gas yields in the TGA slow pyrolysis are much lower than them in the flash pyrolysis for all the samples tested herein. Also, it is found that the heating rates have a more pronounced effect on the cellulose compared with other carbonaceous additives. Knowledge of this would help the foundry personnel to choose the proper material, and provide guidance for process modifications in the foundry to minimize their HAP emissions. As shown, the cellulose HAP emissions are much lower than them of other carbonaceous additives tested herein. This would offer a great opportunity for the foundry to cut down the HAP emissions.

6. Reference

Allen, G. R.; Archibald, J. J.; Keenan, T. Hazardous air pollutants: a challenge to metal casting industry. *Am. Foundry Soc. Transactions.* **1991**, *99*, 585-593.

American Foundrymen's Society, Inc., Back to the Basics: A Green Sand Primer, **1994**.

American Foundrymen's Society, Inc., Green Sand Additives, 2nd Edition, **2000**.

American Foundrymen's Society, Inc., Guide to Sand Additives, **1976.**

Andrews, J. ,Neenah Foundry, personal communication, **2004**.

Bachmann, J.; Baier, D. Some aspects of gas evolution from carbonaceous materials used in foundry molding sands. *Am. Foundry Soc. Transactions.* **1982**, 90, 465-471.

Banyasz, J. L.; Li, S.; Lyons-Hart, J.; Shafer, K. H. Gas evolution and the mechanism of cellulose pyrolysis. *Fuel* **2001**, *80*, 1757-1763.

Berkowitz, N. *The chemistry of coal*; Elsevier Science Inc.: New York, 1985.

Chen, J. H.; Tsai, H. L. An efficient and accurate numerical algorithm for multi-dimensional modeling of casting solidification, Part I: control volume method. *Am. Foundry Soc. Transactions.* **1990**, *98*, 527-537.

Cannon, F. S.; Furness, J. C. Jr. and Voigt, R. C. "Economical Use of Advanced Oxidation Systems for Green Sand Emission Reductions," 12th AFS International Environmental, Health & Safety Conference, Lake Buena Vista, FL, Oct. 9-11, **2000**, pp. 317-332.

Cartage.org, "The Properties of Coal Macerals," http://www.cartage.org.lb/en/themes/Sciences/Earthscience/Geology/Coal/MoreaboutCoal/CoalMacerals/PropertiesofCoal/PropertiesofCoal.htm, viewed 2005; sketch modified from J. Shinn, Fuel, v. 63, **1984**, 1190.

Dempsey, T. C.; LaFay, V. S.; Neltner, S. L.; Taulbee, D. N. Understanding properties of carbonaceous additives and their potential to emit benzene. *Am. Foundry Soc. Transactions.* **1997**, *105*, 109-117.

Fisher, T.; Hajaligol, M.; Waymack, B.; Kellogg, D. Pyrolysis behavior and kinetics of biomass derived materials. *J. Anal. Appl. Pyrolysis* **2002**, *62*, 331-349.

Fox, J. R.; Adamovits, M.; Henry, C. Strategies for reducing foundry emissions. *Am. Foundry Soc. Transactions.* **2002**, *110*, 1299-1309.

Furness, J. Jr., Furness-Newburge, Inc., personal communication, **2004-2005**.

Fushimi, C.; Araki, K.; Yamaguchi, Y.; Tsutsumi, A. Effect of heating rate on steam gasification of biomass. 2. thermogravimetric-mass spectrometric (TG-MS) analysis of gas evolution. *Ind. Eng. Chem. Res.* **2003**, *42*, 3929-3936.

Glowacki, C. R. ; Crandell, G. R. ; Cannon, F. S. ; Clobes, J. K. ; Voigt, R. C. ; Furness, J. C. ; McComb, B. A. and Knight, S. M. "Emissions Studies at a Test Foundry using an Advanced Oxidation-Clear Water System," *AFS Trans.,* v. **2003**,111.

Goodzwaard, J. E. ; Kurtti, C. M. ; Andrews, J. H. ; Cannon, F. S. ; Voigt, R. C. ; Firebaugh, J. E. ; Furness, J. C. and Sipple, D. L. "Foundry Emissions Effects with an Advanced Oxidation Blackwater System," *AFS Trans.,* v. **2003**,111.

Green, R. A.; Olender, A. L. An evaluation and comparison of foundry carbonaceous materials. *Am. Foundry Soc. Transactions.* **1980**, *88*, 817-822.

Hsiau, S. S.; Chang, W. J. Cooling analysis of castings in green sand molds. *Am. Foundry Soc. Transactions.* **1998**, *106*, 595-600.

LaFay, V. S.; Neltner, S. L. The value of seacoal and seacoal supplements in today;s foundry industry. *Am. Foundry Soc. Transactions.* **1987**, *95*, 133-138.

LaFay, V. S.; Neltner, S. L.; Dempsey, T. C.; Wellbrock, R.; Ashburn, C. Analysis of residual characteristics of carbonaceous additives. *Am. Foundry Soc. Transactions.* **1998**, *106*, 301-303.

LaFay, V. S.; Neltner, S. L. Green sand without seacoal. *Am. Foundry Soc. Transactions.* **2004**, *112*, 671-681.

LaFay, V. S.; Neltner, S. L.; Taulbee, D. N.; Wellbrock, R. J. Evaluating emission characteristics of seacoal and seacoal supplements using advanced analytical techniques. *Am. Foundry Soc. Transactions.* **2000**, *108*, 713-718.

Li, S.; Lyons-Hart, J.; Banyasz, J.; Shafer, K. Real-time evolved gas analysis by FTIR method: an experimental study of cellulose pyrolysis. *Fuel* **2001**, *80*, 1809-1817.

Mckinley, M. D.; Jefcoat, I. A.; Herz, W. J.; Frederick, C. Air emissions from foundries: a current survey of literature, suppliers and foundrymen. *Am. Foundry Soc. Transactions.* **1993**, *101*, 979-990.

Naro, R. L. Formation and control of lustrous carbon surface defects in iron and steel castings. *Am. Foundry Soc. Transactions.* **2002**, *110*, 815-834.

Schifo, J. F.; Radia, J. T.; Crandell, G. R.; Mosher, G. Iron foundry hazardous air pollutants "what we know and what we don't". *Am. Foundry Soc. Transactions.* **2003**, *111*, 1173-1190.

Neill, D.A.; Cannon, F.S.; Voigt, R.C.; Furness, J. and Bigge, R. "Effects of Advanced Oxidants on Green Sand System Performance in a Black Water System," *AFS Trans.,* v. , **2001**,109, 937-955.

Shih, T. S.; Hsiua, S. S.; Hong, C. H. Movements of vaporization interface and temperature distributions in green sand molds. *Am. Foundry Soc. Transactions.* **1996**, *104*, 481-489.

Speight, J. G. *The chemistry and technology of coal*; Marcel Dekker: New York, 1994.

Stanbridge, R. P. The replacement of seacoal in iron fourndry molding sands. *Am. Foundry Soc. Transactions.* **1974**, *82*, 169-180.

Technikon Environmental Development Center™. Pre-production air emission test report. Parts 1-3, McClellan, CA, 2000.

Thiel, G.; Giese, S. R. Effects of using causticized lignite as a seacoal replacement on mold gas emissions. *Am. Foundry Soc. Transactions.* **2005**, *113*, 471-484.

Volkmar, A. P.; Galloway III, H. J.; La Forest, L. T. Results of efforts to reduce benzene emissions during four years of production in an iron foundry. *Am. Foundry Soc. Transactions.* **2000**, *108*, 663-666.

Wang, C.; Heine, R. W.; Schumacher, J. S.; Green R. A. What's the story on seacoal replacements in foundry sands? *Am. Foundry Soc. Transactions.* **1973**, *81*, 496-502.

Wang, Y. J.; Cannon, F. S.; Neill, D.; Crawford, K.; Voigt, R. C.; Furness, J. C.; Glowacki, C. R. Effects of advanced oxidation treatment on green sand properties and emissions. *Am. Foundry Soc. Transactions.* **2004**, *112*, 635-648.

Wang, Y. J.; Cannon, F. S.; Voigt, R.C.; Komarneni, S.; Furness, J.C. Effects of advanced oxidation on green sand properties via iron casting into green sand molds. *Environ. Sci. Technol.* **2006**, *40*, 3095-3101.

Zeng, X. C.; Pehlke, R. D. Analysis of heat transfer at metal-sand mold boundaries and computer simulation of solidification of a gray iron casting. *Am. Foundry Soc. Transactions.* **1985**, *93*, 275-282

Premium Carbon Products from Coal: A Sulfur-Based Approach

Final Report

3/1/2005 – 06/30/2006

Principle Authors: P.C. Painter, J. Larsen, H. Schobert
June 14, 2006

DOE Award Number: Subcontract # 2874-TPSU-DOE-1874 under DOE Prime DE-FC26-03NT4187

The Energy Institute
Penn State University
University Park, PA 16802

Disclaimer

Abstract

The goal of this research is to develop methods for producing marketable forms of carbon from coals using a sulfur dehydrogenation process. If successful, this work could have considerable impact, allowing the development of a new, environmentally cleaner process for coke and carbon production, expanding the number of coals that can be used to make these products and allowing the development of a CO_2 free, carbon neutral, source of H_2.

Initial work focused on fundamental research to establish feasibility and an understanding of the relationships between processing conditions, coal structure, the mechanism of dehydrogenation, and the nature of the carbon being produced. While a continuous flow apparatus was being assembled, batch reactions were performed. Two coals were reacted with sulfur under a range of processing conditions. FTIR spectra of the products yielded some unexpected results, showing the formation of carbon disulfide and some carbonyl containing functional groups. The formation of carbon disulfide was suppressed by processing the coal under pressure (an initial pressure of 100 psi nitrogen), while at the same time these conditions resulted in the surprising formation of carbonyl groups.

Recent work has focused on flow reactor experiments. The results demonstrate that the extent of dehydrogenation by sulfur at 500°C appears comparable to that obtained in the absence of sulfur, only at much higher temperatures. This is broadly consistent with the findings of Jusino and Schobert (2006) who produced a product much like metallurgical coke but at much lower temperatures than in a conventional coke oven. Flow-reactor tests at 700°C also produced coke cenospheres, which may have interesting potential applications.

Table of Contents

Graphical Materials

Introduction

There is much discussion of the prospect of a "hydrogen economy", in which hydrogen would serve as a primary energy carrier. In the short-term, it is envisioned that hydrogen will be produced "from coal", which actually means that coal, i.e., the carbon in coal, will be used as the reagent for splitting water molecules in gasification processes. This is mature and well-known technology that produces a carbon monoxide/hydrogen mixture; subsequent reaction via the water-gas shift converts the carbon monoxide to the dioxide. Various separation processes allow removal of the carbon dioxide leaving fairly pure hydrogen as the desired product (Kohl and Riesenfeld, 1985). However, the stoichiometry is such that the majority of the hydrogen has actually come from water, not from coal.

In the research reported here, a much different approach has been taken. This involves removing the hydrogen from coal itself—that is, literally, a hydrogen *from* coal process. The world's recoverable coal reserves are thought to be about 10^{12} tonnes (Schobert and Song, 2002). Assuming an average hydrogen content of 3%, not including hydrogen in moisture or mineral matter, this amount of coal represents a source of $3x10^{10}$ tonnes of hydrogen. One requirement for recovering this hydrogen is a reagent that effectively dehydrogenates the various organic structures that are present in coals. While many reagents could, in principle, be used, sulfur is particularly attractive because it will dehydrogenate alkanes, cycloalkanes, and hydroaromatics at relatively low temperatures (Bloxam, 1913; Turner et al., 1936; Fieser and Fieser, 1944; Rasmussen et al., 1946; Fuson, 1950; Szmant, 1957; Kleinberg et al., 1960; Bordwell, 1963; Cram and Hammond, 1964). The dehydrogenation product is H_2S. Various methods, including pyrolysis, are available for subsequently splitting H_2S to H_2 and S (Roscoe and Schorlemmer, 1911; Müller, 1931; Thau, 1932; Sneed and Maynard, 1944; Sidgwick, 1950; Reeve, 1958). Separation then allows recovery of the desired hydrogen with recycle of sulfur back through the reactor. Cox et al. (1998) estimated that hydrogen could be produced from H_2S at a cost of USD 727/ton (1997 dollars), but added that, with improvements in heat transfer and gas separation, the process could become competitive with conventional steam-reforming of methane. We suggest that even at this estimated price, the process would be economically attractive if high-value carbon products were being obtained at the same time.

Jusino and Schobert (2006) reported preliminary work on this process. Using a medium-volatile bituminous coal from Virginia, 70–75% of the hydrogen in the coal could be removed as H_2S, with 97% conversions of S to H_2S. The carbonaceous solid remaining had volatile matter, fixed carbon, ash, and friability comparable to standard samples of metallurgical coke, even though it was produced at temperatures of only 700–800°C (*vs.* 950–1050°C in slot-type coke ovens). This work suggests the potential of making both a valuable carbon product and hydrogen from coal in a single, relatively simple process in which the active reagent can be recycled.

The goal of the research reported here is to develop methods for producing hydrogen and marketable forms of carbon from coals using this sulfur dehydrogenation process. Initial work has focused on fundamental research to establish feasibility and an understanding of the relationships between processing conditions, coal structure, the mechanism of dehydrogenation, and the nature of the carbon being produced. To this end, both batch reactions and dehydrogenation reactions in a continuous flow reactor have been performed.

Executive Summary

This is the first year of work on this research program and initial work involved the assembly of a continuous flow reactor. While this reactor was being assembled, results were obtained using batch reactors. Initially, two coals were reacted with sulfur under a range of processing conditions. FTIR spectra of the products yielded some unexpected results, showing the formation of carbon disulfide and some carbonyl containing functional groups. The formation of carbon disulfide was suppressed by processing the coal under pressure (100 psi nitrogen), while at the same time these conditions resulted in the surprising formation of carbonyl groups. Because the chemical changes that occur in the 400˚C–500˚C range are crucial in determining the characteristics of the carbons produced in subsequent processing, a systematic study of the changes occurring in this temperature range was initiated and remains incomplete, as we thought it more crucial to commence work with the continuous flow reactor. The results obtained in these latter experiments demonstrate that the extent of dehydrogenation by sulfur at 500°C appears comparable to that obtained in the absence of sulfur, only at much higher temperatures. This is broadly consistent with the findings of Jusino and Schobert (2006) who produced a product much like metallurgical coke but at much lower temperatures than in a conventional coke oven. Flow-reactor tests at 700°C also produced coke cenospheres, which may have interesting potential applications.

Experimental

The coal selected for this study was a medium-volatile bituminous coking coal, DECS-30, from Virginia, USA. On an as-received basis, this coal has an ash content of 3.81%, with 29.51% volatile matter, 64.62% fixed carbon and a sulfur content of 0.77%. This coal was selected in part for its low ash yield and sulfur content, so that the effect of coal minerals and initial sulfur content on the results would be minimized.

For the batch reactions, the coal was mixed with sulfur (S/coal ~0.56) and loaded to the reaction vessel. Reactors were weighed empty and after loading. After loading, the reactors were purged with nitrogen and checked for leaks, then the gas was slowly released, valves were fastened and the reactors were then heated to the required temperature in a sand bath (400 or 500˚C) and kept at this temperature for 30 min. The reactors were then quenched in water, dried and weighed before and after the release of gases to special bags. The bags were also weighed empty and after filling with the gaseous product. Experiments were performed under atmospheric pressure (initial), at 100 psi and at 500 psi (initial pressure) of nitrogen.

For the continuous flow studies, a reactor similar to that described by Jusino and Schobert (2006) was built and is shown in figure 1. In the continuous flow experiments, the Pyrex glass tube (about 1 m long, 5 cm diameter) was heated in an electric furnace. The ends of the reactor were closed with stoppers that have provisions for an inert gas sweep inlet tube and an exist tube. The inert gas sweeps the sulfur vapor, as it is formed in a separate “boat”, through a bed of coal, and prevents the vapor from diffusing away from the coal. This procedure also allowed the hydrogen sulfide produced to be swept out of the reactor into gas wash bottles that contain a solution of cadmium chloride. These solutions were used to determine the amount of hydrogen sulfide generated. Weighed quantities of coal and sulfur were placed in the reactor. The ratio of sulfur to coal was 0.50.

Figure 1. Pictures of the continuous flow reactor

The reactor was heated to the desired test temperature and allowed to run for the desired test duration (usually 1 hour, but in one case the reaction time was prolonged to 2 hours). At the end of the reaction, nitrogen flow through the reactor was continued for several additional minutes, to insure that all the hydrogen sulfide in the reactor was swept through the wash bottles. The contents of the gas wash bottles were then filtered to remove precipitated cadmium sulfide. The amount of cadmium remaining in solution was determined by atomic absorption spectroscopic analysis of the filtrate. Given the known amount of cadmium in solution at the start of a test, and that remaining in solution at the end, the amount of cadmium sulfide formed, and hence the amount of hydrogen sulfide generated, was determined by straightforward stoichiometric calculations.

Proximate analysis of the samples (volatile matter, VM; ash; and fixed carbon, FC) were performed using a LECO MAC-400 Proximate Analyzer. Sulfur content was determined using a Leco SC-32 analyzer. Fourier transform infrared (FTIR) spectra were obtained using a Digilab FTS 45 spectrometer and a diffuse reflectance attachment. A Hitachi S-35000N scanning electron microscope (SEM) with a Princeton Gamma-Tech (PCT) energy dispersive X-ray spectrometer (EDS) was used for analysis of selected samples.

Results and Discussion

Batch reactor results

The chemical reactions that occur in the temperature range 350˚C to 500˚C are crucial to the subsequent formation of carbons with desirable properties. In traditional carbon formation processes, there is a competition between condensation and cracking reactions that goes a long way toward determining the characteristics of the final carbon product (Loison et al., 1989). Accordingly, in initial work (while the continuous flow reactor was being assembled) we focused on batch reactions in this temperature range and performed an FTIR analysis of the products. We found that for reactions of DECS 30 conducted under a zero initial applied pressure of nitrogen:

- After 30 minutes at 400˚C approximately 50% of the aliphatic carbon had been removed from the coal.
- After 30 minutes at 500˚C approximately 90% of the aliphatic carbon had been removed from the coal.
- The aromatic hydrogen appeared unaltered in both reactions.
- A band due to carbon disulfide became apparent in the spectrum of the sample reacted at 500˚C.

A set of experiments was also performed at an initial pressure of 100 psi of nitrogen. This suppressed the formation of CS_2, but surprisingly resulted in the appearance of a carbonyl band, probably due to an aldehyde, in reactions performed at 500˚C.

Given these initial results, we undertook a systematic set of batch experiments, reacting the coal with sulfur for 30 minutes at various temperatures under 0 psi initial pressure of nitrogen. The same coal was also reacted at 500˚C for various times under an initial pressure of 100 psi nitrogen. Proximate analysis of these samples has been completed; elemental analysis of the samples is presently being performed.

The moisture content of the carbon products increased sharply with temperature in the samples reacted for 30 minutes at temperatures in the range 400˚–550˚C, indicating that in addition to dehydrogenation by sulfur, some condensation reactions have occurred (Loison et al., 1989):

$$R - OH + R'H \rightarrow R - R' + H_2O \qquad [1]$$

The fixed carbon content of these carbons increased with reaction temperature, leveling off at a value of 73%. The sulfur content of the product diminishes significantly with increasing temperature, from an initial value of 37% in the coal plus sulfur charge to the reactor, to values of less than 10% in the sample processed at 550˚C. We anticipated significant sulfur retention in these batch reactor studies, since the sulfur is necessarily trapped somewhere in the system. Sulfur incorporation from H_2S into coal has been reported (Polansky et al., 1961; Blayden and Patrick, 1970); but this appears to be significant only at the last stages of reaction (Larsen and Li, 1998; Larsen et al., 2001). The most interesting questions for flow reactor work being what is the form of this sulfur (e.g., is it residual un-reacted material?), and what is its distribution? These questions are being addressed in on-going work. Because some of these results are intriguing and promise to throw light on the mechanism of dehydrogenation, systematic studies involving batch reactions will still be performed in future work, in order to elucidate the role of carbonyl formation at intermediate times and temperatures and the mechanism and role of CS_2 formation.

Flow reactor results

Turning now to the initial results obtained using a continuous flow reactor, two sets of reactions were performed. First, the coal was heated under a flow of nitrogen alone at temperatures of 500˚C, 600˚C and 700˚C, for one hour. The experiments were then repeated with sulfur in the reaction vessel (in a separate vessel to the coal), so that dehydrogenation by sulfur vapor could occur. The reaction conditions and amount of H_2S formed (in the latter reactions) are summarized in Table 1.

There are distinct differences in the visual appearance of the products. We will start by considering the samples formed by heating in the absence of sulfur. The coal heated to 500˚C and held at that temperature for one hour passed through the anticipated fluid stage and reformed into a very, brittle, porous carbonaceous mass that broke into smaller particles on being removed from the reaction vessel. At 600˚C, the product consisted of two phases. One phase consisted of large lumps of material that had a coke-like appearance, while the second phase was similar to that formed at 500˚C. As an example, a picture of these products is shown in figure 2. At 700˚C only large lumps of material that had a coke like appearance were formed.

FTIR spectra of these samples were obtained. It is important to first note that infrared spectra cannot be obtained from a highly carbonaceous material like coke; all one obtains is a sharply sloping baseline and noise. Accordingly, we could not obtain spectra from the coke-like lumps formed at 700˚C, but did manage to obtain spectra from the smaller, broken-up particles formed

Table1. Summary of experimental results for selected reactions of coal alone and with sulfur vapor.

Run	Maximum temp. ˚C	Time at t_{max}. min	Heat-up rate. ˚C/min	Heat-up time. (min.)	Total reaction time. (min.)	Weight of coal charged. (gm)	H_2S, Produced. (gm)	Ratio of produced H_2S to charged coal
Coal	500	60	5	100	165	50.493		
Coal	600	60	5	130	190	50.521		
Coal	700	60	5	140	210	50.513		
Coal + Sulfur	500	60	5	100	165	30.453	3.621	0.118
Coal + Sulfur	600	60	5	130	190	30.624	3.246	0.106
Coal + Sulfur	700	60	5	140	205	30.531	3.725	0.122
Coal + Sulfur	600/2h	120	5	130	250	30.548	2.4770	0.161

Figure 2. Products formed at 600˚C. The product consisted of two phases. One phase consisted of large lumps of material that had a coke-like appearance, while the second phase was a powder similar to that formed at 500˚C

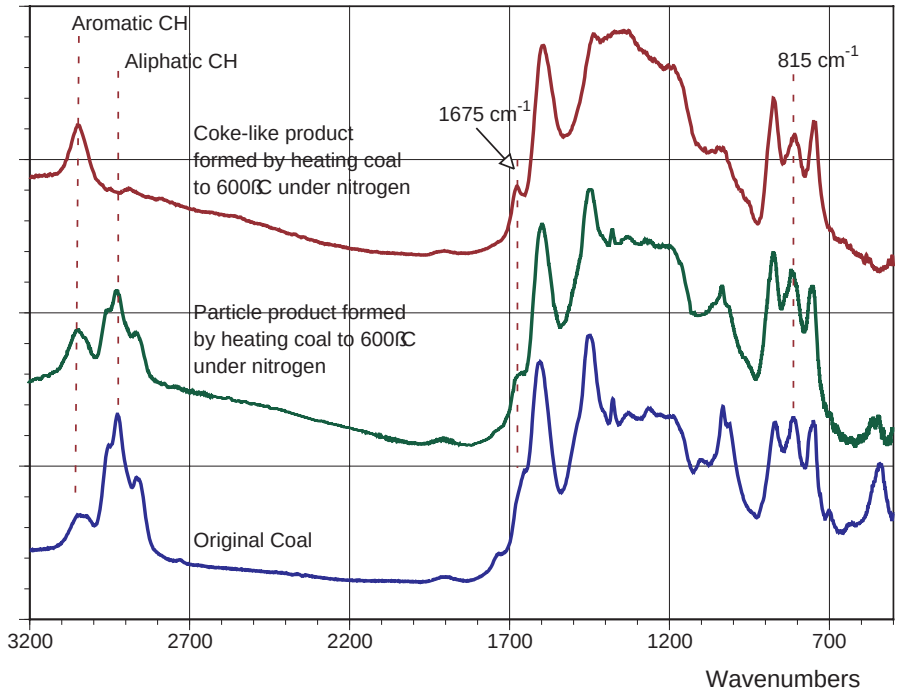

Figure 3. FTIR spectra of the original coal, DECS 30 (bottom); broken-up particulate material produced at 600˚C (middle); and the coke-like material also formed at 600˚C (top).

at lower temperatures and one of the coke-like lumps formed at 600˚C. The spectra of the products formed at this latter temperature are shown in Figure 3, where they are compared to the spectra of the original coal. The spectra show that dehydrogenation occurs primary through the

loss of aliphatic CH groups. In the broken-up smaller particle, the aliphatic CH content (as measured by the stretching modes near 2900 cm^{-1}) is less than half that of the original coal. In the coke-like product, the aliphatic stretching modes have essentially been eliminated. The aromatic CH groups appear to be only slightly affected by heating to this temperature, however. In addition, a band near 1670 cm^{-1}, possibly due to quinone- or semiquinone-like structures, becomes more prominent in the spectra of the products. (This latter mode may also be an overtone or combination mode of the out-of-plane aromatic CH bending vibrations between 700 cm^{-1} and 900 cm^{-1}.) Finally, if the spectra are carefully examined in the 700 cm^{-1} to 900 cm^{-1} region of the spectrum, it can be seen that the band at 815 cm^{-1}, assigned to out-of-plane motions of two adjacent aromatic CH, groups has a lower relative intensity than its two immediate neighbors, near 975 cm^{-1} and 775 cm^{-1}, assigned to isolated CH vibrations and vibrations of three adjacent CH groups, respectively. This suggests that such groups, presumably on the edge of aromatic clusters, are involved in the formation of the larger molecules that, in turn, could lead to mesophase formation.

The samples dehydrogenated by sulfur at these temperatures had a different character. At 500˚C, a two-phase system consisting of larger lumps of a product with a coke-like appearance were formed, together with what appeared to be small particles formed by a degree of “melting” and fusing of the even smaller coal particles originally present. Visually, these have the appearance of a roughly ground coal. At 600˚C a similar two-phase system was occasionally observed, although in some experiments the smaller particles were obtained with some larger lumps. These larger lumps are extremely brittle, unlike the lumps formed in the absence of sulfur at the same temperature. These can fall apart upon simply being touched. They look like an agglomeration of bigger particles that are only weakly attached to one another. Similar results were obtained for samples heated to 700˚C.

Only the FTIR spectra of samples obtained at 500˚C could be obtained and these are shown in Figure 4, where they are compared to the spectrum of the powder-like product formed at this temperature in the absence of sulfur.

Comparing these spectra to those shown in Figure 1, it can be seen that in the presence of sulfur, the extent of dehydrogenation at 500˚C appears comparable to that obtained at higher temperatures in the absence of sulfur. The fact that spectra of samples obtained by heating to higher temperature could not be obtained at all also implies that there is a greater degree of dehydrogenation. This conclusion is supported by the results of proximate analysis, shown in Table 2, where it can be seen that the amount of fixed carbon is higher in the samples dehydrogenated in the presence of sulfur.

SEM micrographs of the samples heated in the absence of sulfur are shown in figure 5. The continuous structure that appears in the micrographs of the coke-like lumps formed by heating in the absence of sulfur are presumably what one would expect if the coal forms a mesophase through the condensation of aromatic molecules. Such large, continuous structures are not formed by sulfur dehydrogenation *under these conditions* (see below). However, it is worth noting that the dehydrogenative dimerization or oligomerization of aromatic ring systems with sulfur can be facilitated in *other reaction systems* (Short et al., 1936; Fieser and Fieser, 1944; Whitmore, 1951; Álvarez et al., 1989). Is the extent of condensation limited by sulfur dehydrogenation? What would happen if we use less sulfur initially, essentially feeding it in a more piecemeal-like fashion? Clearly, under the conditions used in these initial studies we would not get the mechanical properties characteristic of a metallurgical coke. However, what is really

interesting are the particles formed by sulfur dehydrogenation SEM micrographs of these samples are shown in figure 6.

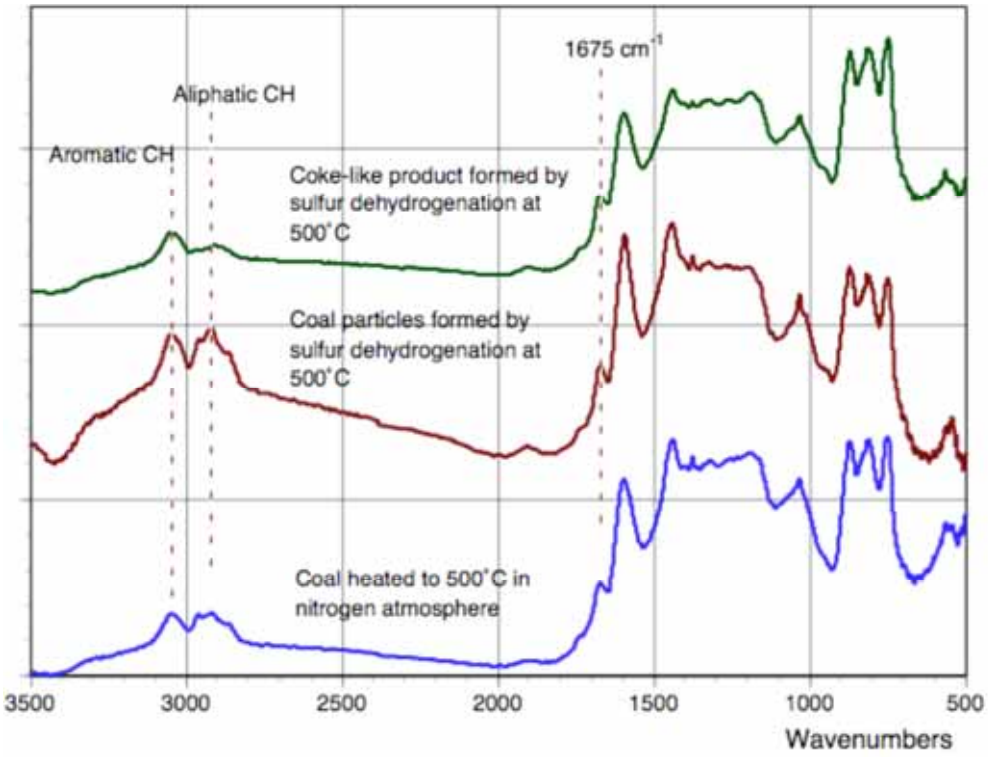

Figure 4. FTIR spectra of the coke-like product obtained by sulfur dehydrogenation at 500˚C (top), powder-like product (middle) and, for comparison, the spectrum of the melted porous mass from heating to 500˚C in the absence of sulfur (bottom).

Table 2. Proximate analysis of carbon products

Run	Sample	Moisture	Volatile matter	Fixed carbon	Ash	Sulfur
Coal	500°C	1.93	17.46	76.05	6.49	0.47
Coal	600°C,"coke"	1.32	15.41	78.76	5.83	0.53
	600°C, "particles"	1.12	17.01	77.01	5.78	0.58
	700°C,"coke"	1.23	11.47	83.06	5.47	0.45
Coal + sulfur	500°C, "particles"	0.41	14.6	80.78	4.62	4.15
	500°C,"coke"	0.49	13.75	81.17	5.08	0.81
Coal + Sulfur	600°C "particles"	0.65	13.89	81.34	4.74	3.10
	600°C,"coke"	0.60	12.37	83.01	4.56	0.80
Coal + sulfur	700°C, "particles"	0.63	10.99	84.68	4.33	2.89
	700°C, "coke"	0.26	9.89	86.50	4.06	0.75
Coal + sulfur	600°C/2h, particles	0.61	12.99	82.45	4.56	3.00
	600°C/2h,"coke"	0.58	11.98	83.92	4.10	0.76

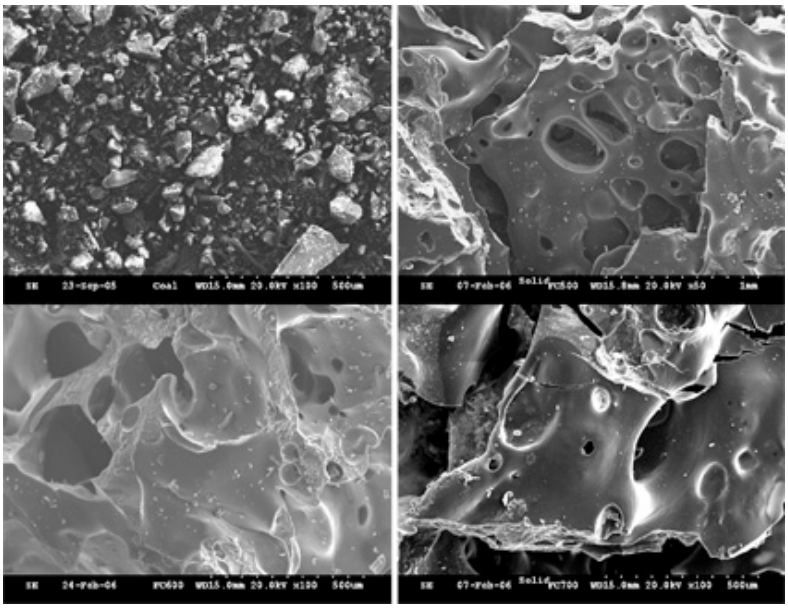

Figure 5. SEM of original coal (top left) and clockwise broken-up particles formed at 500˚C, coke-like lumps formed at 700˚C and coke-like lumps formed at 600˚C.

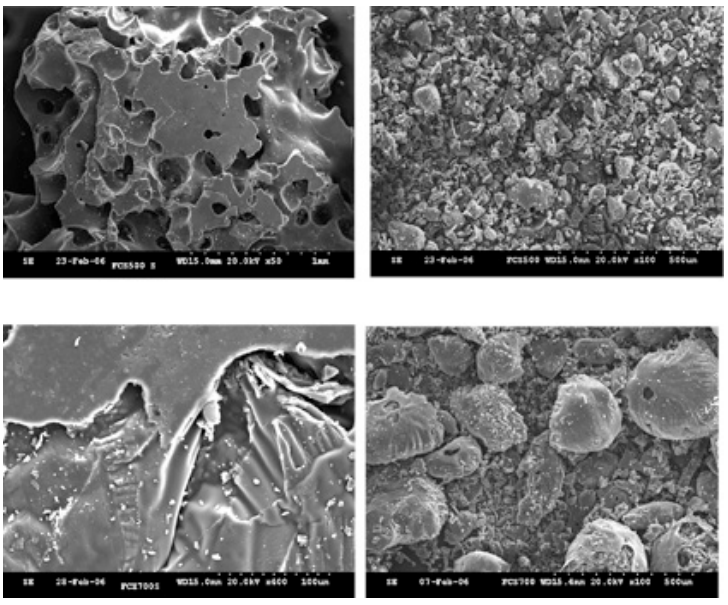

Figure 6. The SEM of carbon products formed at 500˚C (top two micrographs) and 700˚C (bottom two micrographs) by sulfur dehydrogenation. On the left side are the micrographs of the coke like lumps cokes, on the right side are micrographs of the powder or particle fractions.

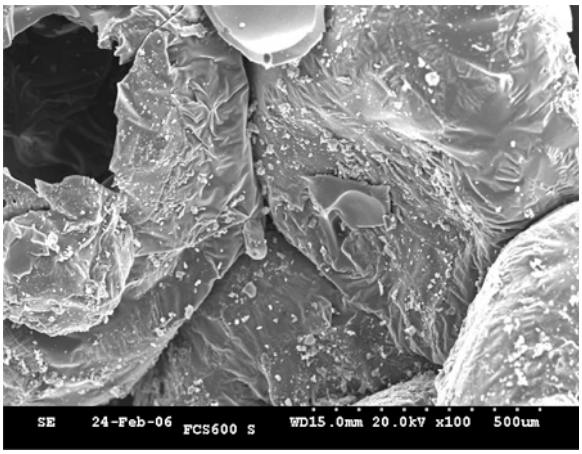

Figure 7. Hollow spheres obtained by dehydrogenating coal with sulfur at 700˚C.

The particles formed at 500˚C are smaller and "more solid" than those formed at 700˚C. The latter appear to be hollow, as shown in Figure 7. The formation of such coke cenospheres has been discussed by Gray (1989). Their formation is attributed to swelling of plasticized particles of coal by gases trapped inside the particle. This is particularly the case when the heating of the coal is relatively rapid and the coal particles are unconfined (Gray and Krupinski, 1997). Hollow carbon spheres might prove to be useful products and we are proposing to investigate their properties in future work.

Conclusions

In batch reactions with sulfur, 90% of the aliphatic carbon is removed in 30 minutes' reaction time. The aromatic hydrogen does not react at these conditions. Dehydrogenation is accompanied by condensation reactions that likely involve oxygen functional groups, as indicated by the formation of water in these reactions. In flow reactor experiments, the extent of dehydrogenation by sulfur at 500°C appears comparable to that obtained in the absence of sulfur only at much higher temperatures. This is broadly consistent with the findings of Jusino and Schobert (2006) who produced a product much like metallurgical coke but at much lower temperatures than in a conventional coke oven. Flow-reactor tests at 700°C also produced coke cenospheres, which may have interesting potential applications.

References.

Álvarez, R., Barriocanal, C., Canga, C., Canga, J.S., Diez, M.A., Gaejol, O.M., Miyar, E.A., 1989. Coke oven gas control by online gas chromatography. Chromatographia. 27, 611-616.
Blayden, H.E., Patrick, J.W., 1970. Studies of organic sulfur in coke: sulfur-carbons formed by pyrolysis in condensed phases. Fuel. 49, 257-270.
Bloxam, C.L., 1913. Chemistry. Blakiston: Philadelphia; p. 151ff.
Bordwell, F.G., 1963. Organic Chemistry. Macmillan: New York; Chapter 23.
Cox, B.G., Clarke, P.F., Patrick, F., Pruden, B.B., 1998. Economics of thermal dissociation of H_2S to produce hydrogen. Intl. J. Hydrogen Energy. 23. 531-544.
Cram, D.J.; Hammond, G.S., 1964. Organic Chemistry. McGraw-Hill: New York; Chapter 23.

Fieser, L.F., Fieser, M. Organic Chemistry. Heath: Boston; Chapter 37.
Gray, R.J., 1989. Coal to coke conversion. In: Introduction to Carbon Science (Marsh, H., Ed.) Butterworths: London; pp. 286-321.
Gray, R.J., Krupinski, K.C., 1997. Pitch production: Supply, coking, microscopy and applications. In: Introduction to Carbon Technologies (Marsh, H., Heintz, E.A., Rodríguez-Reinoso, F., Eds.). University of Alicante: Alicante; Chapter 7.
Jusino, A., Schobert, H.H., 2006. The use of sulfur to extract hydrogen from coal. Intl. J. Coal Geol. 65, 223-234.
Kleinberg, J.; Argersinger, W.J., Griswold, E., 1960. Inorganic Chemistry. Heath: Boston; Chapter 15.
Kohl, A.L., Riesenfeld, F.C., 1985. Gas Purification. Gulf: Houston.
Larsen, J.W., Azik, M., Lapucha, A., Li, S., Kidena, K., Nomura, M., 2001. Coal dehydrogenation using quinones or sulfur. Energy Fuels. 15, 801-806.
Larsen, J.W., Li, S., 1998. Measuring the hydrogen donor reactivity and capacity of coals. Energy Fuels. 12, 830-831.
Loison, R., Foch, P., Boyer, A., 1989. Coke: Quality and Production. Butterworths: London. Chapter 4.
Müller, H., 1931. The liquid purification plant for removal of sulfur at the Hamburg Gas Works. Gas. Wasserf. 74, 653-657.
Polansky, T.S., Knapp, E.C., Kinney, C.R., 1961. J. Inst. Fuel. 34, 245-246.
Rasmussen, H.E., Hansford, R.C., Sachanen, A.N., 1946. Reactions of aliphatic hydrocarbons with sulfur. Ind. Eng. Chem. 38, 376-382.
Reeve, L., 1958. Desulphurization of coke oven gas at Appleby-Frodingham. J. Inst. Fuel. 31, 319-324.
Roscoe, H.E.; Schorlemmer, C., 1911. A Treatise on Chemistry, vol. I. Macmillan: London; p. 386ff.
Schobert, H.H., Song, C., 2002. Chemicals and materials from coal in the 21st century. Fuel 81, 15-32.
Short, W.F., Stromberg, H., Wiles, A.C., 1936. Syntheses in the phenanthrene series. II. 7-Methoxy-1-methylphenanthrene and a new route to phenanthrene. J.Chem. Soc. 319-322.
Sidgwick, N.V., 1950. The Chemical Elements and Their Compounds, vol. II. Clarendon Press: Oxford; p. 879ff.
Szmant, H.H., 1957. Organic Chemistry. Prentice Hall: Englewood Cliffs; Chapter 5.
Thau, A., 1932. Chemical utilization of coke oven gas. Gas World. 97, 92-98.
Turner, E.E., Hirst, E.L., Peat, S., Haworth, R.D., Baker, W., Linstead, R.P., Cook, J.W., 1936. Organic chemistry. Ann. Rep. Prog. Chem. 33, 228-382.
Whitmore, F.C., 1951. Organic Chemistry. Van Nostrand: New York.; Part III, Chapter I.

NANOCARBONS FROM ANTHRACITE COAL

Final Report

Start Date: March 1, 2005

End Date: June 30, 2006

Principle Investigator: Dr. Caroline E. Burgess Clifford

Co-Principal Investigator: Dr. Angela Lueking

Contributors: Apurba Sakti. Puja Jain, Humberto Guitierrez, Dania Fonseca Alvarez

Report Issue: July 31, 2006

Internal Agreement No. 2875-TPSU-DOE-1874,

For Award No.: DE-FC26-03NT41874

The Energy Institute

Penn State University

C205 Coal Utilization Laboratory

University Park PA 16802

DISCLAIMER

ABSTRACT

Anthracite can be processed to make several different types of carbon materials. Based on previous research of thermally annealed ball-milled Buck Mountain anthracite coal, SEM micrographs of the samples indicated carbon-based tubes. Initially it was thought that these tubes could be multi-wall or single-wall carbon nanotubes, but the SEM data were not conclusive. The goal of this project was to more thoroughly characterize the products from the process in order to begin to understand the reaction process.

In this final report, we report information with regards to product characterization and how it has benefited identification of various nanocarbons in ball milled anthracite coal. Buck Mountain anthracite coal was milled, with and without cyclohexene, and was thermally annealed at 1400°C. Several carbons have been identified in our samples, particularly the sample milled in cyclohexene and thermally annealed. Several characterization techniques were used to identify these structures, including X-ray diffraction spectroscopy, temperature programmed oxidation, temperature programmed desorption, Raman spectroscopy, scanning electron microscopy, and transmission electron microscopy. While nanotubes have not been specifically identified, we have identified nanographene ribbons, graphitic carbon, precursors to nanocrystalline diamond (NCD), NCD, hydrogen, and metal alloys of Fe, C, and Si. We believe that milling in cyclohexene is causing the anthracite to react with cyclohexene, causing some sp^2 carbon to become sp^3 and forming "seed" crystals for NCD formation. Some of the carbon becomes more amorphous upon milling, but after thermal annealing, the samples become more crystalline and even graphitic in some cases, with greater formation of NCD. Most interesting is the production of hydrogen during the thermal annealing. We also believe that differences in the graphitic nature of the thermally annealed samples may be due to structural changes caused by the milling.

TABLE OF CONTENTS:

INTRODUCTION

Anthracite coal is an abundant and inexpensive natural resource. Whereas initially its main use was for home heating, its carbon content is high and could be useful to produce premium carbon materials. Most anthracites contain 92–98% carbon, virtually all of which is present as aromatic carbon in large polycyclic sheets.[1-5] These sheets may contain thirty or more fused aromatic rings,[1,2] but unlike graphite, anthracite is a non-graphitic carbon (although highly ordered carbon) that may graphitize upon thermal annealing. For many years, researchers at Penn State have been exploring modifying the structure of anthracite to produce value-added marketable products. The range of projects includes the use of anthracite in synthetic graphite production,[3-9] the possibility of making an anthracite-based pitch,[9,10] and processes to produce activated carbons and other materials.[9,11-17]

Along with these materials, anthracite has been explored as a carbon precursor for hydrogen storage materials.[18] Ball milling of carbon materials has been used as a strategy to produce carbon-based hydrogen storage materials,[19-22] and carbon-metal hydrogen storage composites.[23-37] The performance of ball milled carbon composites is generally a function of ball-milling time, the presence of a solvent during processing,[23-27] and the breakdown of the graphitic structure.[25, 31, 38] Graphitic carbon becomes rapidly amorphitized during milling, evidenced by a rapid decrease in the characteristic graphite 002 ($2\theta=26^{o}$) reflection in X-ray diffraction (XRD).[39] It is thought that any chemical transformations that occur in a ball milling process are due to a liquefaction at the interface to facilitate reaction,[40, 41] although this is not generally agreed upon. The initial objectives of this research were to explore the substitution of highly graphitic anthracite coal into both carbon- and carbon-metal composites formed via a high energy ball milling process.[18] The use of anthracite carbon is based on its similarity to graphite and polycondensed ring compounds (e.g., anthracene, perylene and chrysene). Anthracite coals are known to be somewhat crystalline in nature compared to lower rank coals and thus have similarities to graphite in terms of structure and thermodynamics, yet the substitution of heteroatoms and certain cross-linkages within anthracite make anthracite slightly less stable than true graphite. In our analysis of these ball-milled anthracite products we have observed the formation of several carbonaceous compounds, including nanographene ribbons, graphitic carbon, metal composites and nanocrytalline diamond (NCD). We also observed hydrogen produced during the formation of these composites.

In this final report, we are reporting the results of characterization of ball milling the coal (with and without cyclohexene). We have identified the following in our samples: (1) before thermal annealing, we observe unusual XRD, Raman spectra and temperature programmed oxidation (TPO) as well as incorporation of cyclohexene into the structure, and (2) after thermal annealing, we observe tubular structures, graphitic carbon, nanographene ribbons, and NCD. Initially, from SEM, we thought we might be forming multi-wall nanotubes (MWNT) or single-wall nanotubes (SWNTs), but with further characterization, we have not been able to establish that these samples contain MWNTs or SWNTs. The work will be discussed with respect to four projects that took place simultaneously: (1) observation of the graphitizing behavior to monitor structural changes,[42] (2) observation of the NCD formation, (3) observation of the hydrogen production as NCD forms, and (4) observations of changes to the solvent interaction before and after milling.

EXECUTIVE SUMMARY

The major accomplishments in the project have been to identify most of the major products in the samples produced from the ball-milling of Buck Mountain coal with and without cyclohexene and after thermally annealing the sample at 1400°C. In a separate CPCPC project, we are varying the process conditions to determine of how the milling and thermal treatments affect the coal structure.

Several carbons have been identified in our samples, particularly the sample milled in cyclohexene and thermally annealed. While nanotubes have not been specifically identified, we have identified nanographene ribbons, graphitic carbon, precursors to NCD, NCD, hydrogen, and metal alloys of Fe, C, and Si. We believe that milling in cyclohexene is causing the anthracite to react with cyclohexene, causing some sp^2 carbon to become sp^3 and forming "seed" crystals for NCD formation. Some of the carbon becomes more amorphous upon milling, but after thermal annealing, the samples become more crystalline and even graphitic in some cases. Most interesting is the production of hydrogen during the thermal annealing. We also believe that differences in the graphitic nature of the thermally annealed samples may be due to structural changes caused by the milling.

EXPERIMENTAL

Synthesis of Samples – Materials, Ball Milling and Heat Treatment:

The coal used is PSOC-1468, from the Penn State University coal sample bank. The coal is an anthracite coal from the Buck Mountain seam, bottom of the Llewellyn formation, collected from Luzerne Co., PA, near Eckley. Henceforth, it will be labeled as BMT. It is a fairly low ash content coal, with low volatile matter content and high fixed carbon content. Details of the ultimate and proximate analysis are included in Table 1. Cyclohexene (99 % purity) was purchased from JT Baker.

In the literature, it was reported that samples of graphite needed to be ball-milled for 150 h or longer in order to obtain carbon nanotubes during heat treatment.[43, 44] BMT was milled both under dry conditions and in the presence of a cyclohexene solvent as a wetting agent. All milling occurred with an argon purge to minimize oxidation effects and water contamination during processing. Ball milling was done on a Fritsch Pulveristte LC-106A at 400 rpm, using 6 g of BMT and 20 mL of cyclohexene solvent in the 250 mL bowl and 15 balls (each 15 mm diameter) in the mill. The grinding bowl and balls were made of 316 Stainless Steel. The coal was ball-milled for 80 h, with and without cyclohexene, and denoted as BMT-dry and BMT-wet, respectively. The ball milling time was selected based on work with a different focus, in order to create defects within the anthracite structure.[18, 19, 25]

Ball-milled samples were then heated in a tube furnace using a 2.5°C/min heating rate, holding at 1400°C for 3 h, and under 1 L/min of argon. The 1400°C annealing temperature was selected based on previous reports of annealing ball-milled graphite to form multi-wall nanotubes (MWNTs).[43,44] The thermally-annealed samples are labeled BMT-dry-HT and BMT-wet-HT, respectively. Selected samples were purified using: 4 M HCl for 24 h at room temperature, extensive washing with deionized water, a 10 M NaOH treatment for 24 h at room temperature followed by extensive washing with deionized water. A schematic of the work done on this project is shown in Figure 1.

Modifications to Synthesis:

Removal of Volatile Components After Ball-Milling: Approximately 0.5 g of BMT-wet was ground in a mortar and pestle and vacuum treated at 80-100°C for 24 h.

Soxthlet extraction was carried out on ~1 g of BMT-wet, using ~250 mL of dichloromethane for 24 h. The liquid sample was removed from the extractor, the solvent was removed by rotoevaporation and blowing nitrogen through the sample. The liquid was analyzed by gas chromatography/mass spectrometry (GC/MS) using a temperature program of a temperature program of 40 °C for 5 min, with a ramp rate of 4°C/min to 320°C for 15 min. The remaining solid matrix was analyzed by pyrolysis GC/MS, using 710°C for the pyrolysis temperature and a temperature program of 40 °C for 5 min, with a ramp rate of 4°C/min to 320°C for 10 min.

Modification to Cyclohexene to Coal Ratio: During ball milling, the solvent concentration was varied by keeping the amount of coal constant (6 g) and using 10 mL, 20 mL, and 40 mL of cyclohexene.

Characterization of Samples:

Electron Spectroscopy and Analysis:

Several electron spectroscopy methods were used to examine the ball-milled samples. In previous work, scanning electron microscopy (SEM) was used for analysis of ball-milled coal.[18] Samples were analyzed on a Hitachi S 3000-H, under high vacuum and 20 eV. Transmission electron microscopy was done on a JEOL 2020F 200kV field emission transmission electron microscope (TEM) at the Materials Research Institute at the Penn State University for more detailed analysis of selected products.

Temperature Programmed Oxidation

Temperature programmed oxidation (TPO) is a technique used to determine carbon morphology and may be helpful in distinguishing between carbons that are graphite (crystalline), amorphous, nanofiber, or nanotubes, as each carbon may have distinctive temperatures of burn-off. TPO could also be used to purify samples that could have more than one type of carbon, along with other methods of purification processes.[45-47] Several samples were used as standards to distinguish potential types of carbons in produced samples. Samples were analyzed on a Perkin Elmer 7 thermogravimetric analyzer (TGA) using purified air as the oxidant and an initial heating rate of 10°C/min. All graphs of TPO are of the derivative of the mass versus the temperature in order to enhance areas of oxidation.

Temperature Programmed Desorption Coupled With Mass Spectrometer

Temperature programmed desorption (TPD) is a thermal method used to observe gases evolving from a sample, with the mass spectrometer the method to identify the gases evolving. This technique was mainly used to observe the loss of hydrogen from our samples. The instrument used was a TGA 2050 coupled with a Pfeiffer Thermostar D-35614 mass spectrometer. The sample was heated under argon, although the system still may have contained very small quantities of water that might have affected the outcome of results. A heating rate of 10°C/min from 30-1000°C was used.

Raman Spectroscopy

Raman spectroscopy was performed using an instrument in the Chemistry Department at Penn State, under the supervision of Dr. John Badding and Jacob Calkins. Raman spectroscopy was done on a Renishaw inVia spectrometer with a confocal Leica DM LM microscope and a Peltier cooled RenCam dd-CCD. It is currently equipped with both a green (514 nm) Ar ion and a red (633 nm) HeNe laser. The software for the instrument is WiRE 2.0. Additional spectra were obtained using UV Raman with a laser at 257 nm wavelength.

XRD

X-Ray diffraction (XRD) was performed on raw and thermally annealed samples in order to monitor changes in both the carbon structure and metals inherent in the coal. XRD measurements were taken with a Scintag Model X2 θ/θ goniometer with Cu radiation Ka1/Ka2 with Si(Li) Peltier detector operated at 30 kV and 50 mA.

Proximate and Ultimate Analyses

Proximate analysis was done on a Thermogravimetric Analyzer LECO MAC 400, and was used to determine the ash and volatile content of the coal and products. The moisture temperature was set at 105ºC, the temperature for measurement of volatiles was wet at 950 ºC, and the ash temperature was set at 750 ºC.

Neutron activation analysis (NAA) was done using the following procedure. The sample was placed near the reactor core so that could be bombarded by a beam of neutrons. After a predetermined amount of time, the sample was removed and taken to the counting laboratory. Measurements were taken using a multi-channel analyzer HPGe detector system and the unknown elements were determined using the gamma ray energies detected. A comparative method was used to convert the output of the analyzer, which is in gamma ray energies, to parts per million (ppm) or weight percent. The coal samples were transferred from the sealed packaging to clean Pyrex evaporating bowls and dried in an oven for approximately 2 hours; the samples were then placed into clean, pre-weighed polyethylene vials and the weight of each sample determined. Depending on the sample, the irradiation time used was 30 seconds or 1 h, the reactor power was set at 25, 50, or 200 kW, and the reactor flux was set at 1.7×10^{12} - 8.5×10^{11} n/cm^2-sec. The decay time was 10 minutes or 7 days and the count time was 2, 4, or 167 minutes.

RESULTS AND DISCUSSION

As mentioned in the introduction, anthracite has been explored as a carbon precursor for hydrogen storage materials;[18] we observed carbon tubes in SEM micrographs of BMT-wet-HT. Based on these results, further work was done to characterize the produced samples. The work will be discussed in four different parts.

1. Graphitization behavior of milled anthracite: Contributions by C.E. Burgess-Clifford, D.L. Narayanan, D.T. Van Essendelft, P. Jain, A. Sakti, and A.D. Lueking (see acknowledgements)

Background

It has been known for many years that, while anthracite is a non-graphitic carbon, anthracites will graphitize.[2-17,48-60] Most researchers have suggested that two factors must be present for anthracite to graphitize: 1) the carbon structure in the anthracite, while non- graphitic, must have some sort of alignment to allow for graphitization and 2) certain minerals must be present to catalyze graphitization of anthracite by carbide formation and decompostion. Franklin first classified anthracite as a special non-graphitic carbon that would graphitize upon thermal annealing at temperatures of 1700-2500°C.[48,49] As suggested in her work, a non-graphitic carbon that can graphitize must have an inherent structure that will be amenable to graphitization, more alignment than a non-graphitizing carbon will have. Figure 2 represents the basic differences in these structures, where 2A represents the structure of a graphitizing (but non-graphitic) carbon and 2B represents the structure of a non-graphitizing carbon, showing significantly more cross-links that occur between layers. Oberlin et al. built upon this theory suggesting that how well anthracite graphitizes depends mainly on pore shape (anthracite with spherical pores would not graphitize as well as an anthracite with flattened pores) and possibly on the catalytic graphitization (carbide crystal formation and decomposition).[50-52] Bustin et al.[58] and Cohaut et al.[59] supported the pore shape theory by examining the pore shape and microtexture of anthracites. They found that the weakly graphitizing coals were isotropic with spherical pores and the strongly graphitizing coals were anisotropic with flattened pores. Evans et al. suggested an alternative theory, that minerals may play the dominant role in graphite formation from anthracite, using XRD and transmission electron microscopy (TEM) to monitor the onset of graphitization at 1400°C.[60] Recent work by Pappano et al. and González et al. supported the catalysis theory.[3-5,9,55-57] They both report that one of the critical factors in anthracite graphitizing was related to mineral matter content in the coal. [3-5,9,55-57] González et al. reported the minerals of illite (clay), ankerite (iron carbonate), and siderite (iron carbonate) were the major contributors to graphite formation.[57] In particular, Pappano et al. reported the silica, iron, and titanium in minerals of the raw coal would form carbides during heating.[3-5,9] Pappano's work showed that the best graphitizing anthracite coal out of four coals had a higher percentage of volatile matter (hence a greater amount of "fragmented" carbon, ~10% of the organic matter) and a high mineral matter content, particularly silica (18%). They showed that addition of the minerals to a non-graphitizing coal allowed it to graphitize, and that removal of the minerals from a strongly graphitizing coal caused it to become non-graphitizing. They were not able to correlate how the pore shape may relate to graphitization, but thought an important factor was that anthracite coals have the basic structural units that could align as well as a mechanism for cross-links and "fragments" of carbon to interact with the catalyst.

While anthracite is known to graphitize upon thermal annealing, it is not used as a component in synthetic graphite production commercially because of a lack of knowledge about the quality of graphite that can be produced from anthracite. Atria took a different approach, by adding a processing step in order to increase the quality of graphite produced from anthracite.[7,8] He did so by hydrogenating anthracite with hydrogen donor solvents and suggested this approach increased the available carbon by hydrogenating and liquefying fragments of the anthracite.[7,8] Atria found that the hydrogenated anthracites graphitized better than the non-hydrogenated

anthracites. He also found that lower oxygen content could lead to greater degrees of graphitization, and suggested that reduced particle size could lead to greater anthracite hydrogenation and therefore a higher degree of graphitization. González et al. found that an increased H/C ratio in the coal appeared to improve the graphitization of the coal, but found that reduced particle size slightly inhibited graphite formation.[55-57]

This project explored how milling anthracite with or without solvent affects the graphitization behavior upon thermal annealing.[61-65] The work presented here reports significant differences in graphitization behavior upon thermal annealing depending on whether milling the anthracite with and without cyclohexene.

Results and Discussion for Graphitization of Milled Anthracite Coal

Figure 1 is a schematic of the experimental process. The discussion will focus on examining the products of the coal before and after heat treatment, by separating the discussion into the different milling parameters, i.e., before milling (BMT and BMT-HT), after milling 80 h (BMT-dry and BMT-dry-HT), and after milling 80 h in cyclohexene (BMT-wet and BMT-wet-HT).

Examination of BMT and BMT-HT

The nominal particle size of BMT as received is–60 mesh, or 250 μm and smaller. SEM (Figure 3a and b) of the surface of the particles indicates that after thermal annealing, gases have evolved and the surface is rougher.

The XRD of BMT and BMT-HT are in Figure 4a, and parameters for the XRD are shown in Table 2. For BMT, the spectrum is fairly typical for an anthracite coal, with broad peaks at 26, 40-45, 53, and 78º representing carbon. The other peaks are representative of mineral matter inherent in the coal and could represent a variety of minerals, including silica and iron sulfide or oxide. The carbon peaks are broad, an indication of the sample containing amorphous carbon, with a d-spacing of 3.42 Å, L_c of 12 Å, and a L_a of 38 Å. When the sample is heated to 1400 ºC, the d-spacing does not change significantly (3.41 Å), and L_c (20 Å) and L_a (40 Å) increase a little as would be expected with heating, but the sample is still not considered graphitic. The mineral peaks have been preliminarily identified; the candidate minerals include SiO_2, SiC, Fe_xO_y, Fe_xSi_y, Fe_xC_y and other minerals that could be composites of the elements associated in the sample.

The TPO of BMT and BMT-HT are in Figure 5a. As mentioned in the experimental section, the TPO figures shown are graphs of the negative of the derivative of the mass loss over time. TPO shown this way indicates where there are maxima and minima in the loss of sample, which includes CO, CO_2, and H_2O. For BMT, the sample oxidizes from 500-750 ºC, a relatively broad oxidizing region and the oxidation occurring at a temperature higher than coals of lower rank. The major peak occurs at ~575 ºC, but there are numerous peaks in this sample. Since the sample is relatively heterogeneous, this was not unexpected. However, after thermal annealing at 1400 ºC, the oxidation curve of BMT-HT shifts to 600-1000 ºC, the major peak at ~900 ºC, even higher than a typical peak for graphite at ~850 ºC.

Examination of BMT-dry and BMT-dry-HT

Milling BMT-dry produced a typical particle size of ~5 μm (SEM micrographs in Figure 3c). After heat treatment (BMT-dry-HT, Figure 3d), some of the smaller particles agglomerated to form large particles, on the order of 100 μm. One interesting feature was the formation of small rod-like spikes, although very few.

The XRD of BMT-dry and BMT-dry-HT are in Figure 4b, and parameters for the XRD are shown in Table 2. For BMT-dry, the spectrum is similar to BMT, with broad peaks at 26, 40-45, 53, and 78º representing carbon; however, the mineral peaks that were in the BMT spectrum are not there, so minerals have become more amorphous. For this sample, the d-spacing (3.40 Å), L_c (18 Å), and L_a (36 Å) is not significantly different from the raw coal, BMT. However, after thermal annealing (BMT-dry-HT), there are more mineral peaks, but the d-spacing (3.45 Å) suggests the sample is less graphitic than the sample before heating or BMT-HT, an indication that milling may be destroying any crystalline structure within the coal. The mineral peaks have been preliminarily identified; the candidate minerals include SiO_2, SiC, Fe_xO_y, Fe_xSi_y, Fe_xC_y and other minerals that could be composites of the elements associated in the sample.

The TPO of BMT-dry and BMT-dry-HT are in Figure 5b. For BMT-dry, the sample oxidizes from 450-600 ºC, the oxidizing region much less broad than BMT. The major peak occurs at ~540 ºC. The sample appears less heterogeneous, and as this sample has been milled and has smaller particles, this was not unexpected. After thermal annealing at 1400 ºC, the oxidation curve of BMT-HT shifts to 500-900 ºC, with two major peaks at ~650 and 825 ºC. The sample has become more crystalline, with one peak similar to graphite at 850 ºC, but the other peak at 650 ºC suggests this sample is less crystalline, and the XRD supports this. BMT-dry-HT also has a significantly higher metal content at 13.10 wt% and a slightly higher iron content at ~0.8 wt%. These metals are known to catalyze oxidation, and could explain why the temperatures have shifted a little compared to BMT-HT.

Examination of BMT-wet and BMT-wet-HT

Milling BMT-wet produced particles on the order of 100-200 μm (SEM in Figure 3e),[18, 61] much larger than BMT-dry and approximately the same as the as received material. However, agglomeration appeared to be taking place, and several smaller size particles seem to be attached to the large particle surface, particles less than 1 μm. After thermal annealing (BMT-wet-1400, SEM in Figure 3f), the surface of the larger particles looked very different.[18, 61-62] Upon closer examination, there are amorphous, round (denoted on micrograph as *1), and tubular particles (*2, *3). The tubular particles appear to be attached to the round particles, and vary in size from ~50-500 nm. EDS of the sample indicated the round particles are iron, the tubes are carbon, and background particle is silicon.[18, 61-62] Figure 6 is an EDS map showing this.

The XRD of BMT-wet and BMT-wet-HT are in Figure 4c, and parameters for the XRD are shown in Table 2. For BMT-wet, the spectrum is similar to BMT, with broad peaks at 26, 40-45, 53, and 78º representing carbon; however, the mineral peaks that were in the BMT spectrum are not there, so minerals have become more amorphous, and the carbon peaks appear broader. For this sample, the d-spacing (3.49 Å) is different, suggesting the sample has become more amorphous; however, L_c (12 Å), and L_a (40 Å) are not significantly different. After thermal annealing (BMT-wet-HT), there are more mineral peaks, but the d-spacing (3.39 Å)

suggests the sample is becoming more graphitic than the sample before heating or the other two heat treated samples. The mineral peaks have also become much more prominent in this sample. The mineral peaks have been preliminarily identified; the candidate minerals include Fe_xO_y, Fe_xSi_y, Fe_xC_y SiO_2, SiC, and other minerals that could be composites of the elements in the original sample. BMT-wet and BMT-wet-HT both have significantly higher metal contents, as evidenced by the ash contents listed in Table 3. For BMT-wet, the ash content is 10.82 wt%, with NAA showing the increase in metal almost entirely iron, with an iron content for BMT ~0.5 wt% increasing to 3.84 wt% in BMT-wet. It is evident that significant attrition of the milling container occurred in BMT-wet. The metal content could also have affected the graphitic nature of the heat treated sample, as it has been suggested that these minerals participate in catalyzing the graphitizing of carbon.

The TPO of BMT and BMT-HT are in Figure 5c. For BMT-wet, the sample oxidizes in two regions, from 150-400 ºC and from 450-700 ºC (this region appears to have two maxima), the oxidizing region is broader than BMT and BMT-dry. The major peaks occur at ~275, 550, and 650 ºC. The sample appears more heterogeneous. The peak at 275 ºC indicates either a more amorphous carbon or evolution of volatiles. In a recent publication, we report a loss of hydrogen at this temperature in temperature programmed desorption.[66] This aspect will be discussed in greater detail in the next section. After thermal annealing at 1400 ºC, the oxidation curve of BMT-wet-HT shifts to 450-775 ºC, with no low temperature peak. There again appear to be two major peaks, in this case at ~550 and 700 ºC. The sample has become more crystalline, as evidenced by XRD, but the lower temperature of oxidation can suggest a less crystalline material. As discussed in the previous paragraph, the metal content of both BMT-wet and BMT-wet-HT is significantly higher, 10.82 and 22.20 wt% These metals are known to catalyze oxidation, and could explain why the temperatures have shifted compared to the other samples. Further characterization with TEM was done on this sample because of the unusual structures seen in SEM.

BMT-wet-1400 was selected for TEM characterization due to the variety of structures. TEM of BMT-wet-1400 (Figure 7) has confirmed many types of structures, including nanographene ribbons.[41] In addition to the nanographene ribbons represented, TEM images indicated several other graphitic forms of carbon, such as multiwalled nanopolyhedral particles, a common byproduct in nanotube formation[42] and curved graphitic regions (Figure 5b-c). In many of the TEM images, it was impossible to distinguish between the different types of graphitic carbon due to sample overlap (Figure 3f). Tubes (~100 nm) were also observed in the sample via TEM (Figure 5e), and energy loss spectroscopy (EELS) distinguished these as silicon carbide based tubes. These silicon carbide tubes were highly irregular with variable diameter along the tube length. Other carbons have been identified in the sample by TEM, such as nanocrystalline diamond (NCD), and will be discussed in greater detail in the next section.

Raman Spectroscopy of BMT and Heat-treated Samples

The Raman spectra of BMT and the heat-treated samples are shown in Figure 8. We focus here on the thermally annealed samples. Raman indicates that BMT-dry-HT and BMT-wet-HT are more crystalline than BMT-HT, as evidenced by the I_D/I_G ratios of 0.5, 0.5, and 1.2 respectively. However, Raman focuses on much smaller areas than XRD or TPO, so it is difficult to assess the Raman compared to XRD and TPO. In subsequent sections, Raman is used

to identify other carbon and metal components in thermally annealed samples and will be discussed in greater depth.

Effect of Milling With and Without Cyclohexene Solvent

It is evident that both the milling and thermal annealing play different roles in the formation of the nanocarbons, depending on whether or not a hydrocarbon solvent in involved in the milling process. This study examined how the ball milling may be participating in the reaction process.

In ball milling, as with any grinding process, both physical and chemical changes take place.[67] From the physical perspective, particles can agglomerate, particularly with grinding of coal into hyperfine particles. SEM micrographs indicate that the physical agglomeration of particles is facilitated in the presence of cyclohexene; the resulting particles of BMT-wet are approximately 200 μm, significantly larger than the particles resulting from dry grinding BMT-dry particles estimated at 1-5 μm. The particle morphology of BMT-wet suggests that several smaller particles have become agglomerated or accreted in the presence of the solvent. Some of the smaller particles that appear as "bumps" on the surface of BMT-wet are as small as 1 μm, the size of the particles in BMT-dry. Agglomeration occurs due to particle-particle interactions such as van der Waals forces, electrostatic interactions, or capillary phenomena. A solvent can coat the particle, cause "cold welding," and even pelleting.[67]

Mechanochemistry, or chemistry brought about by mechanical milling, also plays a role in mechanical grinding of organic materials.[67-68] Bond scission can occur during mechanical action that can lead to breaking bonds to reduce the molecular weight and even to cross-linking, a suggestion of free radical chemistry.[67] Improved hydrogenation and/or liquefaction occurs upon mechanochemical activation of a lower rank coal with iron-based catalysts in a ball-milling process;[69] ball-milling participated by breaking down the coal structure and possibly activating new sites for further processing. However, anthracite coals may behave differently than coals used for liquefaction, mainly because anthracite coal structure is much less amenable to liquefaction.

Anthracites are characterized by high carbon content and low volatile matter content, with low H/C and O/C ratios. The precursor BMT was of low volatile matter content (3.65 wt %, dry) and high fixed carbon content (89.52 wt %, dry, see Table 1). BMT anthracite was chosen for the milling study due to its more crystalline nature (compared with other anthracites), and previous studies have demonstrated formation of MWNTs, graphite nanofibers (GNF) and other curved graphite structures from ball-milled graphite.[43-44] The graphite structure breaks down during ball milling, with the characteristic XRD reflection of graphite (i.e. 2θ~26°) decreasing significantly,[23-27] with a corresponding increase of the disordered to graphitic carbon ratio in Raman spectroscopy.[23-27] However, anthracites are known to contain relatively stable free radical systems due to the large condensed ring systems within highly aromatic coals,[70-71] which could provide active sites for solvent to interact with during milling. Milling anthracite may expose these stable free radicals and/or create new free radical sites.

Cyclohexene was introduced into the milling process based on similar studies of ball milling of graphite.[23-27] These studies showed the presence of a solvent inhibited the degradation of the graphite in the ball milling process. In these previous studies, solvent inhibited the amorphitization process of graphite upon milling; in the absence of a solvent, ball milling of

graphite led to complete amorphitization (evidenced by the 002 XRD peak) within ~1 hour, whereas the addition of a solvent increased this time to more than 30 h.[19, 25] This effect was dependent upon the chemical identity of the solvent.[19, 25] We have generally observed the opposite effect for milled anthracite -- the 002 XRD reflection (Figure 4) is not significantly changed in the milling of anthracite unless there is solvent present.[18]

Graphitizing versus non-graphitizing behavior of milled anthracite

As suggested in the background section, Franklin has shown that with thermal annealing, some non-graphitic carbons will graphitize and others are non-graphitizing.[48-49] She suggested that the hard, non-graphitic carbon can only graphitize and turn into a soft carbon if the crystallites have cross-links that will break upon thermal anneal at 1700-2500°C; others suggest that there must be a catalyst available to promote crystallite growth through carbide formation and decomposition.[3-5, 55-57, 60] Graphitization is much less likely to occur if the cross-links are numerous and between layers, even with available catalyst. We examined our data in comparison with this work.

When coal was thermally annealed without any milling, there is evidence that while the material may be losing volatile matter and becoming more difficult to oxidize, it is a non-graphitizing material, probably due to cross-links inherent in the coal.

When milling the coal without solvent (BMT-dry), the particle size of the coal is reduced. Upon thermal annealing at 1400°C (BMT-dry-1400), it clearly evident from XRD and TPO that the carbon is beginning to crystallize, although the carbon is non-graphitic carbon.

However, when milling the coal in cyclohexene (BMT-wet), our particle size is significantly larger, the result of agglomeration and possibly reaction of cyclohexene with the coal. Upon thermal annealing at 1400°C (BMT-wet-HT), it is evident from XRD that carbon is more crystalline and approaching graphite. Silicon carbides and iron silicides are clearly observed in XRD in BMT-wet-HT, materials known to catalyze graphite formation and even overcome barriers to graphite formation.[3-5,9,55-57,60] However, TPO indicates a less crystalline material. Clearly there are structural differences in the three thermally annealed samples. And as shown in SEM and TEM, other types of graphitic carbons are forming in BMT-wet-HT, such as nanographene ribbons, multiwalled nanopolyhedral particles, curved graphitic regions, silicon carbide tubes, and possibly sp^3 based carbons.[61-66] These types of carbons will oxidize at a lower temperature than graphite. We also believe the high metal content in BMT-wet-HT that may be catalyzing graphite formation (XRD) can also be catalyzing oxidation as seen in TPO and why the results appear contradictory.

The key seems to be with the addition of cyclohexene and the interaction during ball milling. If anthracene (3-ring aromatic carbon compound) were reacted with cyclohexene, it may be possible to react as in a Diels-Alder reaction. If the center ring reacted with cyclohexene, a sp^2 carbon could form a sp^3 carbon and could be creating a relatively unreactive type of crosslink.[55] Upon thermal annealing, this could explain the formation of more graphitic carbon, retrogressive Diels-Alder to produce vapors that could form nanographene ribbons and other carbons.[55]

Thermal annealing of anthracite coal that has been ball-milled in cyclohexene leads to a variety of nanocarbons, including non-graphitic carbon and nanographene ribbons. Minerals present in the coal and introduced during milling form metal complexes that crystallize during thermal annealing, as noted by XRD. These crystalline metals appear to catalyze graphitic

carbon formation and nanographene ribbon formation in BMT-wet-HT. Milling BMT without solvent reduced the particle size of the coal (SEM, TPO) and led to a decrease in graphitic carbon upon thermal annealing; milling dry may increase the incidence of forming cross-links that do not break easily and therefore reduce the coal's ability to graphitize. Milling in cyclohexene modified the products after thermal annealing. The materials in BMT-HT and BMT-dry-HT are non-graphitic when compared to BMT-wet-HT according to XRD, and while TPO indicates BMT-wet-HT may be less crystalline than the other heat treated samples, the sample contains graphitic nanocarbons and metals that can decrease the oxidation temperature. Milling in cyclohexene appears to cause an increase in quasi-graphitic carbon upon thermal annealing. This appears to be due increased attrition of metals into the sample when the anthracite was milled with cyclohexene, metals that have been shown to catalyze graphitization.

2. Synthesis of Nanocrystalline Diamond (NCD), Bucky Diamond, and Hydrogen From Milled Anthracite Coal: Contributions by A.D. Lueking, H.R. Gutierrez, D.L. Narayanan, C.E.B. Clifford, D. Van Essendelft (see acknowledgements)

Background

Natural diamond is produced in high pressure and high temperature volcanic shafts, and the scarcity and cost of natural diamond has stimulated synthetic diamond research for over 100 years. Diamond synthesis requires high energy inputs, as diamond is not the thermodynamically stable form of carbon at ambient conditions. Diamond is, however, more thermodynamically stable than amorphous carbon. Generally, diamond is synthesized at high pressure (~1-10 GPa) where diamond is the thermodynamically preferred form of carbon, and at high temperatures (T>2000 K) to overcome the kinetic barriers of the solid-phase conversion of graphite to diamond. In addition to the high-pressure, high-temperature conversion from graphite into diamond, synthetic diamond is currently produced via either chemical vapor deposition or explosive detonation. There have been some reports of low-pressure diamond synthesis via hydrothermal processing,[72] but these methods are not commercialized. In 1992, the estimated production of synthetic diamond was 70 tons at an estimated market value of $500 million.[73]

Synthetic diamond that is less than 1 mm is used for grinding and polishing due to the high strength of diamond;[73] likewise, nanocrystalline diamond (NCD) is used in high-precision polishing applications and, when combined with polymers, as surface coatings for aircrafts, cars, and ships. Chemical vapor deposition (CVD) diamond is used to make diamond coatings for improved electrical, optical, mechanical, and chemical properties.[73] NCD is used in the electronics industry: as an additive to magnetic recording systems to reduce friction and increase the wear resistance of the magnetic materials[74], in field electron emission materials (i.e. flat panel displays)[75-80], in nanoelectro-mechanical resonant structures (NEMS), [81-83] and in biosensors.[84]

One route for NCD formation is currently the explosive detonation process (commercialized by Dupont), as it leads to diamond particles generally on the order of 5-60 nm. The explosive detonation process for diamond synthesis relies on a 20–30 GPa shock wave over a 10^{-6} to 10^{-7} second duration for the essentially immediate conversion of graphite into diamond.[85] This high energy process may also cause the curvature of the graphite to form graphite ribbons. NCD content of 'as synthesized' NCD formed via explosive detonation are on the order of 1-9 % by weight NCD.[85] Commercial NCD is further purified via acid oxidation to remove amorphous carbon.

Ball milling of carbon materials has been used as a strategy to produce carbon-based hydrogen storage materials,[19-22] and carbon-metal hydrogen storage composites.[23-37] The performance of ball milled carbon composites is generally a function of ball-milling time, the presence of a solvent during processing,[23-27] and the breakdown of the graphitic structure.[25, 31, 38] Graphitic carbon becomes rapidly amorphitized during milling, evidenced by a rapid decrease in the characteristic graphite 002 ($2\theta=26^{o}$) reflection in XRD.[39] It is thought that any chemical transformations that occur in a ball milling process are due to a liquefaction at the interface to facilitate reaction,[40, 41] although this is not generally agreed upon. Previously, the objective of this research was to explore the substitution of highly graphitic anthracite coal in place of graphite into both carbon- and carbon-metal composites formed via a high energy ball milling process;[18] the current objective is to identify the carbons structures formed as they appear to be different than expected. The use of anthracite carbon was based on its similarity to graphite and polycondensed ring compounds (e.g., anthracene, perylene and chrysene). Anthracite coals are known to be more crystalline in nature than coals of lower rank and thus have some similarities to graphite in terms of structure and thermodynamics, yet the substitution of heteroatoms and certain cross-linkages within anthracite make anthracite less stable than true graphite (but much harder). In our analysis of these ball-milled anthracite products, we have observed the formation of NCD, and this part of the report discusses these initial observations as well as complementary data to support these findings. To explain the unusual and unexpected observation of NCD after a low-temperature and low-pressure (but high energy) synthesis route, we propose a preliminary reaction pathway based on the findings to date.

Results and Discussion for NCD and Hydrogen Production

Evidence for the formation of NCD via High Energy Ball Milling

Nanocrystalline diamond (NCD) particles are observed in HRTEM images of the highly graphitic anthracite coal precursor after 80 hours of milling in a cyclohexene wetting agent (BMT-wet) (Figures 9a and b). The NCD particle is embedded in a region of amorphous carbon; during HRTEM analysis, this amorphous carbon region was converted to the graphitic nanocarbon onions, similar to that reported previously (Figure 9c).[66] The lattice spacing in the HRTEM images is 2.0 Å, characteristic of diamond, and EDS spectra indicated that this sample was primarily carbon. Only limited TEM analysis was performed on these samples, with more complete characterization performed on the more stable thermally annealed samples. However, the presence of the NCD (surrounded by amorphous carbon) in the sample *prior to thermal annealing* indicates that the NCD is formed in the ball milling process, rather than the subsequent processing steps.

After thermal annealing at 1400 °C (i.e. BMT-wet-HT), observed NCD particles were encapsulated in a graphitic carbon outer-layer (Figure 10). This type of carbon structure, with a sp^3 hybridized carbon core surrounded by a sp^2 hybridized fullerene-like coating has been previously referred to as bucky diamond.[86] Once again, the lattice spacing in the HR-TEM images is characteristic of diamond (2.0 Å), and the reciprocal-space lattice corresponds to the diamond crystal structure with the 3.57 Å lattice constant (Figure 11). Several NCD particles were observed in this sample, with particle sizes ranging from approximately 5 to 35 nm (Figure 10a-d). The high contrast of these images indicates the NCD particles have an equal dimension parallel to the electron beam, and are thus approximately spherical. Additional thin regions

(evidenced by low contrast via TEM) of NCD regions were also observed in this material (Figure 10e).

In addition to the graphitic coating observed on the NCD particles, other graphitic regions include nanographene ribbons and polyhedral graphitic region, as discussed previously.[66] The 1400 °C thermal anneal at 1 bar likely converted some of the NCD generated by the ball mill into graphitic carbon, and we observe regions of transition between sp^2 and sp^3 hybridized carbon, with a variation in lattice spacing from 2.0 Å to 3.33 Å (Figure 12). The transformation of diamond into nanographene ribbons at high temperature is well documented,[87-92] and the expected direction of the graphite to diamond phase transition at this temperature. However, directly after milling, the NCD was surrounded by amorphous carbon (Figure 9a), and it is possible that the NCD formed during milling acted as a 'seed' for the conversion of amorphous carbon into diamond. Complementary analysis (discussed below) indicates that the NCD purity increased upon the thermal anneal.

The XRD spectra of the ball milled anthracite samples were discussed previously in the context of the graphitizability and cross-linking of the anthracite coal upon milling time, and the effect of the cyclohexene wetting agent which appeared to lead to cross-linking.[66] In a previous report, we have discussed the reduction in the graphite (002) peak upon milling for both a graphite powder and the BMT anthracite coal.[18] There are significant differences in the 002 peak reduction upon milling: the 002 peak for graphite samples is still detectable after 20 hours of milling, whereas the 002 peak of the anthracite coal is non-detectable after one hour of milling.[66] The amorphitization of the graphite powder is consistent with previously reported data under similar conditions.[39, 93, 94] In our previous report, we also identify the formation of several iron species during the thermal anneal, including both iron silicides and iron carbides.[18, 61-66] We claim that the iron is introduced primarily during the milling process, and becomes crystalline during the thermal annealing. The formation of iron carbides (particularly Fe_3C) was also observed by Ichikawa et al. for graphite ball milled in high-pressure hydrogen.[22] The formation of Fe_3C in Ichikawa et al's report is related to the dehydrogenation of the ball milled graphite upon heating.[22]

The observation of NCD in HR-TEM has led us to reanalyze our previous XRD reports. Diamond has a characteristic XRD peak at $2\theta=43.89^{\circ}$, corresponding to diffraction of the 2.06 Å spacing of the (111) crystal structure. The (220) and (311) diamond peaks are at 2θ of 75.4° and 91.6°, respectively. Any evidence of *nano-crystalline* diamond would be reflected in a very broad and disperse XRD peak, following from the Scherrer equation. For example, the (111) XRD at $2\theta=44°$ is very weak and broad for NCD materials synthesized via explosive detonation, until the samples are further purified.[85] In our annealed samples, analysis of the XRD spectra in the 40-45° range is complicated by iron carbides, iron silicides (discussed previously) and possible NCD. However, upon revisiting our XRD data, we do note a broad and disperse XRD peak in several of our samples at $2\theta=44°$ (Figure 13) which can be resolved to differentiate from the iron-based peaks. We attribute this broad XRD peak to the NCD, due to the parallel observation of NCD in HR-TEM micrographs of these samples. We do not disagree nor dispute Ichikawa's[15] XRD interpretation, but believe our XRD spectra are due to a combination of iron carbides and nano-diamond, based on the observation of NCD via HRTEM. Both Ichikawa et al. and Orimo et al. report high hydrogen incorporation into graphite (up to 7.4%), when the graphite is milled in the presence of high-pressure hydrogen,[22, 106] but do not include TEM micrographs of their sample which may indicate the presence of NCD. Our preparation method does not use high-pressure hydrogen, but rather, the milling is conducted under 1 bar argon.

Either anthracite or cyclohexene may provide a ready source of hydrogen in our process, but it is not yet clear if this is a necessary step of the NCD preparation.

Analysis of the XRD spectra has allowed us to use the (111) diamond reflection to track the formation of NCD in our ball milled coal and graphite samples. Currently, we observe this broad XRD peak after eighty hours of milling BMT with cyclohexene (BMT-wet). We also observe this XRD peak for samples annealed at 1400 °C, regardless of whether they were milled in cyclohexene (BMT-dry-HT and BMT-wet-HT). We do not observe the XRD peak for graphite ball milled in the presence of cyclohexene for 1-20 hours. The XRD peak is also observed for a second preparation of BMT-wet-HT, giving an indication of the reproducibility of this processing method.

Raman spectroscopy of sp^2 hybridized carbons gives rise to characteristic D (defect) and G (graphite) peaks at 1350 cm^{-1} and 1600 cm^{-1}, respectively. Diamond has a sharp D (diamond) peak at 1333 cm^{-1}. Thus, the D peak for diamond and the D peak for sp^2 hybridized carbons are separated by only ~17 cm^{-1}, and are normally distinguishable by the very sharp and narrow character of the diamond D peak at 1333 cm^{-1}. Raman spectroscopy of BMT-wet-HT indicates the characteristic D and G peaks at 1333 cm^{-1} and 1584 cm^{-1} (Figure 14a), respectively, but the 1333 cm^{-1} D peak is too broad to be conclusively assigned to diamond. It has been demonstrated that as diamond particles reach nanometer scale, the Raman band broadens and shifts to lower frequency.[95] An additional prominent feature in the BMT-wet-HT Raman spectra is a split G peak with an unusual high-energy shoulder, which can be resolved to two peaks at 1585 cm^{-1} and 1618 cm^{-1} (Figure 13a). The strength of the 1618 cm^{-1} peak would be highly unusual for sp^2 hybridized carbon, but possibly related to the strong intensity of the disordered 'D' peak at 1350 cm^{-1}.[96] It is however more likely, given the observation of NCD in TEM, that the strong peak located at 1618 cm^{-1} is due to NCD, as a peak at 1620 cm^{-1} has been previously reported for NCD and assigned to a localized (100) sp^2 bonded pair of carbons within the diamond, the so-called "dumbbell defect".[93] It is of note that a peak at 1620 cm^{-1} was also observed in ball milled graphite, and attributed to sp^2-hybridized carbon (i.e., graphite rather than diamond) defects introduced during ball milling;[19] but again, HRTEM analysis of the resulting carbonaceous materials was not included as part of the analysis. We also note several low frequency Raman modes in BMT-wet-HT-P (which become apparent after purification), including peaks at 225, 292, 410, 496 cm^{-1} (Figure 14b). The assignment of these peaks is unfortunately complicated by the natural mineral matter present in the material, the formation of FeSi and FeC during thermal anneal, and possible precipitation reactions that occur during the pretreatment.[18, 66] We do however note the broad peak at 496 cm^{-1} may correspond with a theoretically predicted 'characteristic fingerprint' of NCD.[100] Although amorphous silicon exhibits a broad Raman peak at 480 cm^{-1}, the silicon peak generally sharpens and shifts toward crystalline silicon band at 520 cm^{-1} after thermal annealing[97] (at 1000 °C, whereas our sample was annealed at 1400 °C). The other peaks present in the low frequency Raman may arise due to the natural mineral matter in the sample. Our work in a closely related project is looking at the effect of demineralization of the samples at several points in the synthesis process to more conclusively assign these low frequency Raman modes.

The corroborating evidence of NCD in our samples provided by Raman spectroscopy and XRD analysis is complicated by the natural mineral matter present in the BMT coal and the metal introduced during the milling process. Our previous study[18,66] discussed evidence that the mineral matter changes chemically during both thermal annealing and during subsequent purification steps. Our previous work discussed the dissolution of carbon in the introduced iron

particles during thermal annealing.[18, 66] Our speculation on the role of this mineral matter in the formation of NCD is discussed below. Due to the complicating interplay of NCD with natural mineral matter, the Raman and XRD data provide corroborating evidence of the TEM, but not 'stand alone' evidence of NCD in our sample. The excitation frequency of visible Raman spectroscopy is resonant with sp^2 hybridized carbon, therefore the Raman scattering efficiency in the visible range is more than 50 times the scattering efficiency of sp^3 regions. In contrast, the excitation frequency of UV-Raman is resonant with the sp^3 bond, and is therefore much more sensitive to diamond samples.

Proposed Reaction Pathway for NCD via High Energy Ball Milling

The presence of a NCD particle in the BMT-wet sample (prior to thermal annealing) indicates that it is the high energy ball milling process that leads to the formation of seeds of NCD, and the subsequent thermal annealing step helps to promote the formation of the NCD. However, the amount of NCD in this sample is apparently low as there is no evidence of a characteristic XRD peak in this sample. In contrast, there is evidence of a NCD characteristic XRD peak in the corresponding sample milled in the presence of cyclohexene. It has been previously suggested that solid-solid reactions observed in ball milling occur via liquefaction of the solids at the interface during the high energy impact,[40, 41] and we generally observe a greater increase in ash content for samples milled in the presence of the wetting agent. Alternatively, the presence of cyclohexene may lead to a Diels Alder condensation reaction that facilitates the formation of sp^3 hybridized carbon: the 'diene' nature of the cyclohexene molecule, combined with the aromatic nature of the anthracite coal, may lead to a three-dimensional sp^3 diamond precursor (Figure 15). However, as there is XRD evidence of the NCD in the BMT-80-1400 sample, the cyclohexene seems to facilitate the formation of NCD, but is not necessarily required for the formation of NCD. The increase in the XRD evidence of NCD after thermal anneal suggests that the NCDs may grow from amorphous carbon during the high temperature annealing; however, graphite is also formed during this thermal anneal as evidenced by increased graphitization and the formation of graphene ribbons.

We have no analytical evidence that diamondoids were present in the BMT coal precursor. Diamondoids, hydrocarbon molecules with a characteristic diamond structure, have been isolated from petroleum.[98] Diamondoids are hydrocarbon molecules with the same 'unit cell' of the diamond molecule and lower diamondoids have a diameter of <1 nm. Generally speaking, NCD are classified as diamond particles with a diameter >2 nm, and the NCD observed in our sample range from 5-35 nm. Although diamondoids can be isolated from petroleum, there have been no previous reports (to the best of our knowledge) of diamondoids isolated from coal, although there has been a previous report of NCD / bucky diamond synthesized via explosion of a coal precursor.[99] Rather, the data suggest the observed NCD is a result of the high energy ball mill process. Amorphous carbon is the least thermodynamically stable form of carbon, or the highest energy form of carbon. Therefore, the amorphitization of graphite requires more energy input than the conversion of graphite into diamond. Previous observations of amorphitziation of graphite via ball milling provide corroborating evidence that the ball milling process provides enough energy input to convert graphite into amorphous carbon, and therefore by deduction, the ball milling process provides enough energy to convert graphite into diamond (as this is less energy). Ball milling is a high energy process, although the *system* temperature and pressure remain mild (e.g. ~100 °C and 0-7 bar), the instantaneous

and localized forces present in the ball mill provide high energy collisions. In this sense, ball milling may be not unlike the explosive detonation processes used to form diamond in which 20-30 GPa are typical over the course of 10^{-6} to 10^{-7} seconds.[85] It is of note that iron catalysts facilitate diamond synthesis via explosive detonation and significant iron is introduced to our samples via break down of the stainless steel milling materials. As discussed above, the formation of iron carbides has been observed previously in the dehydrogenation of graphite ball milled in high-pressure hydrogen.[22] It is also of note that the hydrothermal diamond growth has been reported at low pressures, in which a diamond phase "precipitates out" of a metal carbon due to a change in solubility or electrochemical potential. For example Zhao et al. report diamond nucleation upon diamond seeds in a carbon, water, and metal environment.[72] It is not currently clear what role the metals—either inherent to the coal or introduced via the breakdown of the stainless steel milling materials—play in the formation of NCD in our samples. Visually, however, observed NCD particles are not found adjacent to the many metal particles observed in the HRTEM micrographs of the various samples.

A sufficient energy input to convert graphite into thermodynamically less stable forms does not explain the apparent entropy increase in forming diamond preferentially (or in addition to) the more disordered amorphous carbon. However, the traditional conceptualizations of thermodynamic carbon stability ($G_{f,graphite} < G_{f,diamond} < G_{f,amorphous\ C}$), or the carbon phase diagram, are currently being reexamined at the nanoscale. Barnard has theoretically predicted that NCD is the most stable form of carbon in the range of 1.9-5.2 nm: below 1.9 nm fullerene type carbons become the most stable form, whereas above 5.2 nm graphite is the most thermodynamically stable form of carbon. Other experimental observations indicate that the transition of nanocrystalline diamond into carbon onions appears to be a function of the particle size: NCD is readily transformed into carbon onions at high temperature,[90] the reverse transformation from onions into nanocrystalline diamond has been observed upon electron irradiation.[101-104] Kuznetsov et al. have extensively studied the mechanism of the nanocrystalline diamond to carbon onion transition, and proposed a mechanism for this transition.[92] Experimentally, the number of observations of graphite encapsulated nanodiamonds, or bucky diamonds, exceeds the number of observations of 'true' NCD or carbon onions. Recently, the conversion of carbon nanotubes directly into nanocrystalline diamond has been observed at high pressure.[105]

In conclusion, we have observed nanocrystalline diamond formation via high energy ball milling of a highly graphitic anthracite precursor. Direct evidence for NCD may be provided by HRTEM and FT of the HRTEM images, while corroborating supporting evidence of NCD is provided via XRD and Raman spectroscopy. The formation of nanocrystalline diamond in the particle size of 5 to 35 nm provides experimental support of a recent theoretical prediction that nanocrystallline diamond is the most stable form of carbon on the nanoscale, in a particular stability region. The NCD are formed during the high energy ball milling, but corroborating analytical evidence suggests the NCD content of the samples increase via thermal anneal. The thermal anneal also serves to increase the stability of the NCD via the formation of encapsulating fullerene-like graphitic onions, otherwise known as bucky diamonds. Although the ball milling process is high energy, the *overall system* can be considered a low temperature, low-pressure process. Thus, a novel method to synthesize nano-crystalline diamond from graphitic precursors has been outlined. The precursor material is naturally occurring anthracite coal, suggesting a low cost feedstock for the formation of NCD. Although the exact synthesis pathway needs further

elucidation, a wetting agent during milling and natural or introduced transition metals (particularly iron) appear to play a role in synthesis.

3. Combined Hydrogen Production and Storage with Subsequent Carbon Crystallization: Contributions by A.D. Lueking, H.R. Gutierrez, D.A. Fonseca, D.L. Narayanan, D.T. Van Essendelft, P Jain, and C.E. Burgess-Clifford (see acknowledgements)

Background

Development of a hydrogen economy will require significant advances in methods by which to produce, store, transport, and distribute hydrogen in an economically viable manner. Centralized hydrogen production methods currently in use are limited by an inefficient means to transport hydrogen to its point of use.[107] Compressed and cryogenic storage methods do not meet density targets and incremental advances in candidate solid-state storage materials are not likely to meet density or cost targets. [108] Here we provide evidence of a combined hydrogen production and storage process that utilizes a low cost carbon precursor that slowly evolves hydrogen at room temperature. Our process draws hydrogen from dehydrogenation of a hydrocarbon donor, with simultaneous trapping of molecular hydrogen, as evidenced by Raman-active molecular hydrogen vibrations. The evolution of the trapped hydrogen is kinetically-limited and continues in excess of one year; heating the material to modest temperatures accelerates hydrogen evolution. The presence of a nanocrystalline diamond by-product suggests hydrogen-induced carbon crystallization and corroborates theoretical predictions[109-112] of sp^3-rehybridization of nanocarbon structures upon hydrogen exposure.

Results and Discussion of Hydrogen Production

Reactive ball milling of Buck Mountain anthracite coal (BMT) with a cyclohexene hydrogen donor led to a carbon structure (referred to as BMT-wet) that decomposes upon heating to give molecular hydrogen. The term 'hydrogen donor' is applied to cyclohexene as its dehydrogenation during milling leads to the following observations of molecular hydrogen evolution via temperature desorption spectroscopy (TDS) measurements. The TDS indicates the following qualitative hydrogen evolution (m/z=2) for three samples (Figure 16): an immediate increase in the hydrogen baseline (Type I) [113], followed by an increase at ~60 °C with a local maxima at ~150 °C (Type II), and a third increase at ~300 °C with a maxima at ~400 °C (Type III). Samples were exposed to air during sample transfer and/or during storage. The Type III hydrogen evolution is similar to previous reports of carbons ball milled in high-pressure molecular hydrogen: Hydrogen evolved from milled graphite at ~330°C,[21, 114] activated carbon at ~300 °C[22], and SWNT at ~230 °C.[21] No previous report showed evidence of low temperature hydrogen evolution (Types I and II), and this may be due in part to cyclohexene desorption and subsequent catalytic dehydrogenation, although the active catalytic sites have not yet been determined. Type I and II hydrogen evolution at atmospheric pressure from the various BMT-wet samples ranges from 0.4 wt%-0.8% depending on sample age (inset, Figure 16); however these quantifications do not capture hydrogen evolution during storage and sample transfer. Overall hydrogen evolution from the onset of sample heating to 750 °C is as much as 2.1 wt% after 3 days of storage under atmospheric conditions (inset, Figure 16). In comparison, hydrogen

evolution from the BMT precursor ensues at 550 °C, and is 0.5 wt%, with no significant Type I baseline increase (Figure 16d).

After heating, crystalline regions are observed at several locations in BMT-wet and range in size from 5-35 nm. The crystalline regions are embedded in a graphitic carbon outer-layer (Figure 17), and Fourier transform (FT) reveals a reciprocal-space lattice corresponding to the diamond crystal structure observed along the [011] zone axis and a lattice constant of 3.57 Å (Figures 17c-d). The 3.3 Å spacing of the shells surrounding the core are consistent with graphite, but discontinuities with periodicity of 2.0 Å (close to the (111) interplanar distance of diamond) suggest a sp^2-sp^3 hybridization transition. These diamond-graphite structures are similar to those reported previously after electron irradiation,[89, 104] and have been referred to as bucky diamond. Transition regions similar to Figure 17a are also observed that lack the inner core structure. Corresponding changes in the visible Raman spectra (633 nm, Figure 17e) may be attributed to structural doping (increased D' reflection at 2652 cm^{-1}) and localized sp^2 defects within sp^3 hybridized carbon, the so-called "dumbbell defect" (at 1620 cm^{-1}).[93-94] Low frequency Raman modes arise that are consistent with the 'characteristic fingerprint' of NCD at 496 cm^{-1},[100] and the low energy tail for tetrahedral carbon at ~600 cm^{-1}.[115, 116] Although diamondoids[22] and nanocrystalline diamond (NCD)[89] have been isolated from petroleum, there have been no previous reports of the isolation from coal. No analytical evidence was found for NCD in the BMT precursor and quasi-amorphous carbon structures (see Figure 18d) are typical for BMT-wet immediately directly after milling, prior to heating.

Re-hybridization of sp^2 nanocarbons upon the introduction of hydrogen has been theoretically predicted: Hydrogen adsorption on planar graphite leads to distortion,[117] doped nanocarbons will restructure and partially re-hybridize to sp^3 carbon upon hydrogen exposure[109, 110] leading to an increased adsorption energy and stretching of the molecular hydrogen bond.[118] These effects may be more pronounced upon the application of high pressure[111] or resulting from hydrogen chemisorption.[112] These prior results are based on molecular simulations, and sp^3 re-hybridization due to hydrogen exposure in carbon has not been previously observed experimentally although hydrogen-induced crystallization has been reported for amorphous silicon.[119]

Photoluminescence of BMT-wet (Figure 18a-b) in visible Raman relative to the coal precursor (Figure 18c) is consistent with hydrogenation, as photoluminescence has been empirically correlated to hydrogen content.[45] BMT-wet samples continue to fluoresce in visible Raman one year after preparation, but with decreased intensity. A perturbed Q branch vibration for molecular hydrogen (Figure 18e, near 4161 cm^{-1}) is present after one year, despite storage and measurement in air. The Q branch hydrogen peak is perturbed (to 4125, 4166, and 4377 cm^{-1}) due to interactions of hydrogen with the material, similar to that demonstrated with *in situ* Raman hydrogen adsorption studies with carbon at cryogenic temperatures in a pressurized hydrogen atmosphere.[46-47] The hydrogen vibrations in Figure 18e are a clear indication of both hydrogen production and hydrogen trapping within the material, with slow diffusion-limited evolution in excess of one year.

Although not graphitic, forthcoming graphitization studies with BMT coal[42] demonstrate its quasi-crystalline nature that may graphitize upon heating. The formation of cross-linkages upon milling in cyclohexene likely promote NCD formation, as the formation of sp^3 cross-linkages has previously been used to explain diamond nucleation via electron irradiation of carbon onions.[104] Defects containing dangling carbon bonds are also theoretically predicted to promote NCD nucleation[120] and anthracite coal is known for discontinuities and dangling bonds

within its quasi-graphite structure. BMT coal contained inherent mineral matter, and transition metals were introduced by the milling process (i.e. Fe, Ni, and Cr). Transition metals not only migrate within a ball mill to form alloys, but are known hydrogen dissociation catalysts. These metals likely catalyze cyclohexene dehydrogenation, cross-linking, and hydrogen trapping. Iron, in particular, catalyzes the graphite to diamond phase transition, and is used in the catalytic deposition of carbon to form both synthetic diamond and carbon nanotubes. Capturing carbon-metal synergy to optimize hydrogen storage is the focus of on-going hydrogen storage activities,[121] including work by the authors. The metals clearly play a catalytic role at various stages; however, the 1-2% by weight hydrogen evolution can not be attributed solely to metals which make-up only 5-10% of the sample. The Raman-active molecular hydrogen vibrations in air and room temperature hydrogen evolution are atypical of metal hydrides and physical adsorption to carbon.

A crystalline carbon structure embedded in amorphous carbon (Figure 19a) was observed via HRTEM in BMT-wet prior to heat treatment, suggesting that crystallinity—at least in part—arises due to the high impact collisions in the mill. The sample had a sharp Raman peak at ~1090 cm^{-1}, similar to that attributed previously to NCD[93]; the low frequency peaks (e.g. 155, 278, 714 cm^{-1}) may be associated with metal oxides from the milling materials (Figure 19d). The six-fold symmetry of the FT from this crystalline region (Figure 19c) correlates with either a face centered cubic structure (zone axis [111]) or a close packed hexagonal structure (zone axis [0001]). The d_{hkl} spacing of 1.99 Å does not match graphite, diamond, or lonsdaleite. EDX analysis indicates this region is primarily carbon-based (Figure 19b), as EDX is insensitive to light elements and the bulk material evolved hydrogen upon heating, the structure may be a crystalline carbon-hydrogen structure, but we are unable to conclusively identify the carbon, or carbon-hydrogen, structure of this region. The expansion of graphite along the c-axis was first proposed for hydrogen interaction with graphite nanofibers,[122] and there has been some TEM and XRD evidence for c-axis expansion by another group.[123] The d_{hkl} spacing of 1.99 Å (Figure 19) is inconsistent with expansion only in the c-axis direction of graphite. Interstitial hydrogen atoms in diamond (H_2* defects) are known: molecular modeling of H_2* leads to a bond-inserted hydrogen atom, a second hydrogen in an "antibonding" site,[124] and reduces the carbon-carbon bond order to ½, leaving to no net C-H bond.[125] These particular studies do not allow carbon-carbon expansion in the model. An alternative explanation of H_2* involves off-axis hydrogen-hydrogen interaction and has found carbon-carbon bond expansion.[126] It remains an open question whether H_2 can intercalate carbon materials and whether H_2 has unique adsorption properties due to its small size and inherent ability to penetrate pores.[127] Quinn has shown that under conditions of corresponding state (i.e. constant P/Pc and T/Tc), hydrogen is adsorbed to a greater extent than other gases, an observation which can be attributed only in part to its decreased molecular diameter.[127] However, we suspect that hydrogen in BMT-wet is not a result of true pore penetration, but rather, hydrogen released from cyclohexene dehydrogenation is trapped as structural changes in the carbon during milling occur. On-going work is seeking to increase and understand the occurrence of Figure 19 type regions, and parallel modeling studies are underway to help characterize the structure.

In conclusion, we have evidence of trapped molecular hydrogen, slow room temperature hydrogen evolution, and subsequent carbon crystallization. Carbon crystallization has previously been tied to nanocarbon hydrogenation via molecular simulations. Samples continue to evolve hydrogen and contain Raman-active hydrogen vibrations in excess of one year, despite storage in air. The hydrogen evolution can be accelerated with moderate sample heating. The hydrogen is

derived from dehydrogenation of the cyclohexene additive, as molecular hydrogen was not added to the process. A combined hydrogen production-storage process may offer improved *overall* system efficiency, as separately, both hydrogen production and hydrogen storage come at an energy penalty. Modification of low-cost anthracite coals into materials that evolve hydrogen and rearrange into value-added crystalline carbon products may provide a viable alternative to solid-state hydrogen storage materials that rely on reversible thermodynamics, for which DOE storage targets are difficult, if not impossible, to achieve. A separate and unique solid-state adsorption material may be an unnecessary step for the ultimate goal of a ready supply of hydrogen to the fuel cell.

4. Modifications of Process Parameters, Contributions by C.E. Burgess Clifford, D. T. Van Essendelft, P. Jain, and A.D. Lueking

Background

The work described in the following section discusses initial tests to attempt to determine the interaction between the coal and cyclohexene during ball milling, first by removing the solvent by extraction, then by vacuum, and then changing the solvent to coal milling ratio.

Results and Discussion

Several modifications have been done during the ball milling stage to elucidate coal and cyclohexene interactions. This work presented is preliminary.

Removal of Volatile Components After Ball-Milling

A second sample of BMT-wet was produced and is labeled BMT-wet2. The sample was vacuum-dried as described in the experimental section and named BMT-wet2-Vac. TPO was done on each sample and is shown in Figure 20. BMT-wet-Vac is plotted with BMT-wet2. TPO of BMT-wet2 does not look the same as BMT-wet. There is oxidation occurring at ~80°C (versus about 250°C for BMT-wet), the boiling point of cyclohexene, and the high temperature oxidation is 400-585°C, whereas previously, it was ~400-700°C. This indicates much less interaction of the cyclohexene with the coal in this second run. After vacuum treatment of BMT-wet2, TPO reveals changes in the oxidation profile, with no low temperature oxidation taking place and at high temperature, two definite peaks with oxidation from ~400-550°C. The profile suggests that loosely bound cyclohexene and possibly other degradation products are removed during vacuum treatment as well as a loss of other possible volatiles in the coal.

BMT-wet was extracted by dichloromethane as described in the experimental section. GC/MS of the extracted liquid (Figure 21) is mainly oxygenated derivatives of cyclohexene. As dichloromethane was removed, the sample was not protected from the atmosphere, therefore it is difficult to determine if cyclohexene was oxygenated during ball milling or during evaporation of the solvent. The low cyclohexene content in the sample may have been are result of evaporation. Another problem is dichloromethane typically contains a small amount of the stabilizer of cyclohexane, which could interfere with the products upon evaporation of the solvent.

Py-GC/MS was done on the remaining solid matrix and the chromatogram is shown in Figure 22. The main products of pyrolysis are benzene, cyclohexene and derivatives, biphenyl, and phenol. Some of the smaller peaks were identified as butylenes. We believe ethylene would be generated during pyrolysis, but was not identified as a product and may be too small a molecule to be detected in this system. This indicates a possible reaction of cyclohexene with the coal matrix, most likely due to the ball milling process. If butylenes and ethylene are formed during pyrolysis at 710°C, these are compounds that are typical feeds for chemical vapor deposition (CVD) formation of nanotubes and nanographene ribbons and may have contributed to these compounds.

Modification to Cyclohexene to Coal Ratio

BMT was ball-milled with cyclohexene at two additional cyclohexene to coal ratios, at 10 mL/6 g (BMT-wet10) and 40 mL/6g (BMT-wet40). From visual inspection, BMT-wet10 looked very similar to BMT-wet, with larger agglomerated particles. However, BMT-wet40 looked very different to the other two samples, like a cyclohexene/coal slurry. The sample was removed from the ball mill and filtered to remove the excess cyclohexene. TPO of BMT-wet40 is shown in Figure 23 with BMT-dry and can be compared to BMT-wet in Figure 20. The TPO of BMT-wet40 looked very similar to BMT-dry rather than BMT-wet, an indication that with excess cyclohexene, much less interaction occurred between the coal and cyclohexene.

CONCLUSIONS

In this final report, we report information with regards to product characterization and how it has benefited identification of various nanocarbons in ball milled anthracite coal. Buck Mountain anthracite coal was milled, with and without cyclohexene, and was thermally annealed at 1400°C. Several carbons have been identified in our samples, particularly the sample milled in cyclohexene and thermally annealed. Several characterization techniques were used to identify these structures, including X-ray diffraction spectroscopy, temperature programmed oxidation, temperature programmed desorption, Raman spectroscopy, scanning electron microscopy, and transmission electron microscopy. While nanotubes have not been specifically identified, we have identified nanographene ribbons, graphitic carbon, precursors to nanocrystalline diamond (NCD), NCD, hydrogen, and metal alloys of Fe, C, and Si. We believe that milling in cyclohexene is causing the anthracite to react with cyclohexene, causing some sp^2 carbon to become sp^3 and forming "seed" crystals for NCD formation. Some of the carbon becomes more amorphous upon milling, but after thermal annealing, the samples become more crystalline and even graphitic in some cases, with greater formation of NCD. Most interesting is the production of hydrogen during the thermal annealing. We also believe that differences in the graphitic nature of the thermally annealed samples may be due to structural changes caused by the milling.

ACKNOWLEDGEMENTS

The authors wish to acknowledge Dr. Joe Kulik of the Penn State Materials Research Institute and Dr. Humberto Gutierrez of the Penn State Physics Department for assistance in obtaining TEM micrographs, and Dr. John Badding and Mr. Jacob Caulkins of the PSU Chemistry Department for equipment time and assistance to obtain the Raman images. The authors would like to acknowledge the help of Dr. John W. Larsen and Dr. Harold H. Schobert, who participated in useful discussions about how cyclohexene might interact with coal.

The work in this project has been supplemented by another CPCPC project that was funded a few months after this project, "Mechano-Thermal Method To Produce Carbon Nanotubes," for Award No. DE-FC26-03NT41874, Internal Agreement No. 2985-TPSU-DOE-1874. The second project provided funding for interpretation of the characterization and to understand the reactions that are taking place, which are being used to determine the limits of reactions and to help optimize the reaction conditions. Some data reported in this final report will also be included in the second project final report for purposes of cohesiveness.

REFERENCES

1. Gerstein, B.C., Murphy, P.D., Ryan, L.M., In: *Coal Structure.* Academic Press, New York, 1982, Chapter 4.
2. van Krevelen, D.W., *Coal: Typology–Chemistry–Physics–Constitution.* Elsevier, Amsterdam, 1981.
3. Pappano, P.J., Mathews, J.P., Schobert, H.H., *Preprints, Amer. Chem. Soc. Div. Fuel Chem.* **44** (1999) 567.
4. Pappano, P.J., M.S. Thesis, The Pennsylvania State University, University Park, PA, 2000.
5. Pappano, P.J., PhD. Thesis, The Pennsylvania State University, University Park, PA, 2003.
6. Zeng, S., Rusinko, Jr., F., Schobert H.H., Penna. Energy Devel. Auth. Report, PEDA 9303-4019, 1996.
7. Atria, J.V., M.S. Thesis, The Pennsylvania State University, University Park, PA, 1995.
8. Atria, J.V., Ruskino, F., Schobert, H.H., *Energy Fuels,* **16** (6), 1343-1347, 2002.
9. Andrésen, J.M., Burgess, C.E., Pappano, P.J., Schobert, H.H., *Fuel Proc. Tech.,* **85** (12), 1373-1392, 2004.
10. Andrésen, J.M., Zhang, Y., Burgess, C.E., and Schobert, H.H., *Fuel Proc. Tech.,* **85** (12), 1361-1372, 2004.
11. Bessant, G.A.R., Walker Jr., P.L. *Carbon,* **32** 1171, 1994.
12. Walker Jr., P.L., Almagro, A., *Carbon*, **33,** 239, 1995.
13. Walker Jr., P.L., Imperial, G.R., *Fuel,* **74**, 179, 1995.
14. Gergova, K., Eser, S., Schobert, H.H., *Energy Fuels*, **7,** 661, 1993.
15. Gergova, K., Eser, S., Schobert, H.H., Klimkiewicz, M., Brown, P.W., *Fuel*. **74** 1042, 1995.
16. Maroto-Valer, M.M., Tang, Z., Zhang, Y.Z., *Fuel Proc. Tech.,* **86** (14-15), 1487-1502, 2005.
17. Burgess-Clifford, C.E., Maroto-Valer, M.M., Hsaio, E., Tang, Z., and Weiss, B., Final Report, Consortium for Premium Carbon Products from Coal, "Understanding Anthracite Properties Towards Its Use as Intumescent Material for Polyurethane Foams," DOE Award number: DE-FC26-03NT41874, Internal Agreement Number: 2689-TPSU-DOE-1874, August 31, 2005.
18. Lueking, A.D., Principal Investigator, Final and Quarterly Reports for "Nanostructured Anthracite-Metal Composites for Hydrogen Storage," Internal Agreement No. 2670-TPSU-DOE-1874, for US DOE Prime Award No.: DE-FC26-03nt41874, (a) 1st Quarterly Report, June 15, 2004 (b) 2nd Quarterly Report, Sept. 15, 2004, (c) 3rd Quarterly Report, Dec. 15, 2004, (d) 4th Quarterly Report, March 31, 2005, and (e) Final Report.
19. Orimo, S., Matsushima, T., Fujii, H., Fukunaga, T., Majer, G. *J Appl Phys,* **90**, 1545, 2001**.**
20. Hirscher, M., Becher, M.; Haluska, M., von Zeppelin, F., Chen, X. H., Dettlaff-Weglikowska, U., Roth, S., *J Alloy Compd,* **356**, 433, 2003.

21. Hirscher, M., Becher, M., Haluska, M., Quintel, A., Skakalova, V., Choi, Y. M., Dettlaff-Weglikowska, U., Roth, S., Stepanek, I., Bernier, P., Leonhardt, A., Fink, J., *Journal of Alloys and Compounds*, **330**, 654, 2002.
22. Ichikawa, T., Chen, D. M., Isobe, S., Gomibuchi, E., Fujii, H., *Materials Science and Engineering B*, **108,** 138, 2004.
23. Imamura, H., Sakasai, N., Kajii, Y., *J Alloy Compd*, **232**, 218, 1996.
24. Imamura, H., Sakasai, N., Fujinaga, T., *Journal of Alloys and Compounds*, **253**, 34, 1997.
25. Imamura, H., Takesue, Y., Tabata, S., Shigetomi, N., Sakata, Y., Tsuchiya, S., *Chem Commun*, 2277, 1999.
26. Imamura, H., Tabata, S., Takesue, Y., Sakata, Y., Kamazaki, S., *International Journal of Hydrogen Energy*, **25**, 837, 2000.
27. Imamura, H., Tabata, S., Shigetomi, N., Takesue, Y., Sakata, Y., *J Alloy Compd*, **330**, 579, 2002.
28. Iwakura, C., Inoue, H., Furukawa, N., Nohara, S., *Mater Trans*, **43**, 2706, 2002.
29. Iwakura, C., Inoue, H., Furukawa, N., Nohara, S., *Electrochemistry*, **71**, 776, 2003.
30. Janot, R., Aymard, L., Rougier, A., Nazri, G. A., Tarascon, J., M. *J Mater Res*, **18**, 1749, 2003.
31. Bouaricha, S., Dodelet, J. P., Guay, D., *Journal of Materials Research*, **16**, 2893, 2001.
32. Bouaricha, S., Dodelet, J. P., Guay, D., Huot, J., Boily, S., Schulz, R., *J Alloy Compd*, **307**, 226, 2000.
33. Imamura, H., Usui, Y., Takashima, M., *J Less-Common Met*, **175**, 171, 1991.
34. Imamura, H., Nakamura, M., *Z Phys Chem*, **183**, 157, 1994.
35. Wu, F., Zhu, J., Ibe, K., Oikawa, T., *Compos Sci Technol*, **58**, 77, 1998.
36. Bobet, J. L., Grigorova, E., Khrussanova, M., Khristov, M., Stefanov, P., Peshev, P., Radev, D., *J Alloy Compd*, **366**, 298, 2004.
37. Dal Toe, S., Lo Russo, S., Maddalena, A., Principi, G., Saber, A., Sartori, S., Spataru, T., *Materials Science and Engineering B*, **108**, 24, 2004.
38. Bobet, J.-L., *Journal of Alloys and Compounds* 2003, *In Press*.
39. Fukunaga, T., Itoh, K., Orimo, S., Aoki, M., Fujii, H., *J Alloy Compd*, **327**, 224, 2001.
40. Shantha, K., Varma, K. B. R., *Mat Sci Eng B-Solid*, **60**, 66, 1999.
41. Bennett, K., Varma, R., Von Dreele, R. B., *Scripta Mater*, **40**, 825, 1999.
42. Burgess-Clifford, C. E., Narayanan, D., Van Essendelft, D. T., Jain, P., Sakti, A., Lueking, A. D. *Carbon,* 2006, *In Preparation*.
43. Chen, Y., Conway, M.J., and Fitzgerald, J.D., *Appl. Phys. A*, **76**, 633-636, 2003.
44. Chen, Y., Conway, M.J., Fitzgerald, J.D., Williams, J.S., and Chadderton, L.T., *Carbon,* **42**, 1543-1548, 2004.
45. Casiraghi, C., Ferrari, A.C., Robertson, *J., Phys. Rev. B*, **72**, 085401, 2005.
46. Pradhan, B.K., Sumanasekera, G.U., Adu, K., Romero, H.E., Williams, K.A., Eklund, P.C., *Physica B*, **323**, 115, 2002.
47. Centrone, A., Brambilla, L., Zerbi, G., *Phys. Rev. B*, **71**, 245406, 2005.
48. Franklin, R., *Acta Cryst.,* **4,** 253, 1951.
49. Franklin, R., *Proc. Roy. Soc. Ser. A.,* **209**, 196, 1951.
50. Oberlin, A., Terriere, G., *Carbon*, **13** 367, 1975.
51. Oberlin, A., *Carbon*, **17**, 7, 1979.

52. Oberlin, A., *Carbon*, **22**, 521, 1984.
53. Conrad, B., Principal Investigator, Final Report for "Anthracite Feedstocks for Specialty Graphite Production," CPCPC, DOE Prime Award No.: DE-FC26-98FT40350, July 1, 2000.
54. Stansberry, P., Principal Investigator, Final Report for "Anthracite Filler and Coal Extract Binder for Development of Isostatically-Molded Graphite," CPCPC, DOE Prime Award No.: DE-FC26-98FT40350, July 1, 2003.
55. González, D., Montes-Morán, M.A., Garcia, A.B., *Energy Fuels,* **17**, 1324, 2003.
56. González, D., Montes-Morán, M.A., Suárez-Ruiz, I., Garcia, A.B., *Energy Fuels,* **18**, 365, 2004.
57. González, D., Montes-Morán, M.A., Garcia, A.B., *Energy Fuels,* **19**, 263, 2005.
58. Bustin, R., Rouzaud, J.N., Ross, J., *Carbon*, **33**, 679, 1995.
59. Couhaut, N., Blanche, C., Dumas, D., Guet, J.M., Rouzaud, J.N., *Carbon*, **38**, 1391, 2000.
60. Evans, E., Jenkins, J., Thomas, J., *Carbon*, **10**, 637, 1972.
61. Burgess-Clifford, C.E., Lueking, A.D., Naranayan, D., 1st Quarterly Report, "Nanocarbons from Anthracite Coal," Internal Agreement No. 2875-TPSU-DOE-1874, for Award No.: DE-FC26-03NT4187, June 15, 2005
62. Burgess-Clifford, C.E., Lueking, A.D., Jain, P., Van Essendelft, D.T., Naranayan, D., 2nd Quarterly Report, "Nanocarbons from Anthracite Coal," Internal Agreement No. 2875-TPSU-DOE-1874, for Award No.: DE-FC26-03NT4187, September 15, 2005.
63. Burgess-Clifford, C.E., Lueking, A.D., Jain, P., Van Essendelft, D.T., Naranayan, D., 3rd Quarterly Report, "Nanocarbons from Anthracite Coal," Internal Agreement No. 2875-TPSU-DOE-1874, for Award No.: DE-FC26-03NT4187, December 15, 2005.
64. Burgess-Clifford, C.E., Lueking, A.D., Jain, P., Van Essendelft, D.T., Naranayan, D., 1st Quarterly Report, "Mechano-Thermal Method to Produce Carbon Nanotubes from Coal," Internal Agreement No. 2875-TPSU-DOE-1874, for Award No.: DE-FC26-03NT4187, October 15, 2005.
65. Burgess-Clifford, C.E., Lueking, A.D., Jain, P., Van Essendelft, D.T., Naranayan, D., Gutierrez, H., Fonseca Alverez, D., 2nd Quarterly Report, "Mechano-Thermal Method to Produce Carbon Nanotubes from Coal," Internal Agreement No. 2875-TPSU-DOE-1874, for Award No.: DE-FC26-03NT4187, January 15, 2005.
66. Lueking, A.D., Gutierrez, H.R., Fonseca, D.A., Narayanan, D.L., Van Essendelft, D.T., Jain, P., Clifford, C.E.B., *J. Amer. Chem. Soc.,* **128** (24), 7758-7760, 2006.
67. Dyrkacz, G.R., Bloomquist, C.A.A., *Energy Fuels*, **8**, 680-689, 1994.
68. Barambiom, N.K., In *Mechanochemistry of Polymers*, Ed. W.F. Watson, Macalaren: London, 1964.
69. Kuznetsov, P.N., Kuznetsova, L.I., Chumakov, V.G., Moiseeva, G.A., *Mat Res Innovat,* **3**, 340-346, 2000.
70. Sanada, Y. Sasaki, M., Kumagai,H. Aizawa, S., Nishizawa, T., Mineo, T., Chiba, T., *Fuel*, **81**, 1397-1402, 2002.
71. Sanada, Y., Kumagai, H., Sasaki, M., *Fuel*, **73**, 840, 1994.
72. Zhao, X. Z., Roy, R., Cherian, K. A., Badzian, A., *Nature***, 385**, 513, 1997.
73. Pierson, H. O., Handbook of Carbon, Graphite, Diamond and Fullerenes: Properties, Processing and Applications. ed.; Noyes Publications: Mill Road, Park Ridge, New Jersey, 1993.

74. Kurmashev, V.I., Timoshkov, Y.V., Orehovskaja, T.I., Timoshkov, V.Y., *Physics of the Solid State*, **46**, 696, 2004.
75. Zhang, W.J., Wu, Y., Chan, C.Y., Wong, W.K., Meng, X.M., Bello, I., Lifshitz, Y., Lee, S.T., *Diam. Relat. Mater.*, **13**, 1037, 2004.
76. Alimova, A. N., Chubun, N.N., Belobrav, P. I.; Detkov, P. Y.; Zhirnov, V. V., *J. Vac. Sci. Technol. B*, **17**, 715, 1999.
77. Show, Y., Witek, M. A., Sonthalia, P., Swain, G. M., *Chem. Mater.*, **15**, 879, 2003.
78. Choi, W. B., Cuomo, J. J., Zhirnov, V. V., Myers, A. F., Hren, J. J., *Appl. Phys. Lett.*, **68**, 720, 1996.
79. Ralchenko, V., Karabuto, A., Vlasov, I., Frolov, V., Konov, V., Gordeer, S., Zhukov, S., Dementjev, A., *Diamond Relat. Mater.*, **8**, 1496, 1999.
80. Jiang, N., Eguchi, K., Noguchi, S., Inaoka, T., Shintani, Y., *J. Cryst. Growth*, **236**, 577, 2002.
81. Wang, J., Butler, J. E., Hsu, D. S., Nguyen, C.T.-C., *15th IEEE Int. Conf. Micro Electromechan. Syst*, 657, 2002.
82. Sekaric, L., Parpia, J. M., Craighead, H. G., Feygelson, T., Houston, B. H., Butler, J., E. *Appl. Phys. Lett.*, **81**, 4455, 2002.
83. Philip, J., Hess, P., Feygelson, T., Butler, J. E., Chattopadhyay, S., Chen, K. H., Chen, L.C., *J. Appl. Phys..*, **93**, 2164, 2003.
84. Yang, W., Auciello, O., Butler, J. E., Cai, W., Carlisle, J. A., Gerbi, J. E., Gruen, D. M., Knickerbocker, T., Lasseter, T. L., Russel, J. N., Jr., Smith, L. M., Hamers, R. J., *Nat. Mater.*, **1**, 253, 2002.
85. Chen, P. W., Huang, F. L., Yun, S. R., *Carbon*, **41**, 2093, 2003.
86. Raty, J. Y., Galli, G., Bostedt, C., van Buuren, T. W., Terminello, L. J., *Phys Rev Lett*, **90**, 2003.
87. Affoune, A. M., Prasad, B. L. V., Sato, H., Enoki, T., Kaburagi, Y., Hishiyama, Y., *Chem Phys Lett*, **348**, 17, 2001.
88. Kuznetsov, V. L., Chuvilin, A. L., Moroz, E. M., Kolomiichuk, V. N., Shaikhutdinov, S. K., Butenko, Y. V., Malkov, I. Y., *Carbon*, **32**, 873, 1994.
89. Kuznetsov, V. L., Chuvilin, A. L., Butenko, Y. V., Malkov, I. Y., Titov, V. M., *Chem Phys Lett*, **222**, 343. 1994.
90. Kuznetsov, V. L., Chuvilin, A. L., Butenko, Y. V., Stankus, S. V., Khairulin, R. A., Gutakovskii, A. K., *Chem Phys Lett*, **289**, 353, 1998.
91. Kuznetsov, V. L., Zilberberg, I. L., Butenko, Y. V., Chuvilin, A. L., Segall, B., *J Appl Phys*, **86**, 863, 1999.
92. Kuznetsov, V. L., Butenko, Y. V., Zaikovskii, V. I., Chuvilin, A. L., *Carbon*, **42**, 1057–1061, 2004.
93. Prawer, S., Nugent, K. W., Jamieson, D. N., Orwa, J. O., Bursill, L. A., Peng, J. L., *Chem Phys Lett*, **332**, 93, 2000.
94. Orwa, J. O., Nugent, K. W., Jamieson, D. N., Prawer, S., *Phys Rev B*, **62**, 5461, 2000.
95. Wen, C., Jin, Z. H., Liu, X. X., Li, X., Guan, J. Q., Sun, D. Y., Lin, Y. R., Tang, S. Y., Zhou, G., Lin, J. D., *Spectrosc Spect Anal*, **25**, 681, 2005.
96. Dresselhaus, M. S., Dresselhaus, G., Pimenta, M. A., Eklund, P. C., Raman Scattering in Carbon Materials. In *Analytical Applications of Raman Spectroscopy*, ed.; Pelletier, M. J., Eds., Blackwell Science: Ann Arbor, 1999; pp 367.
97. Ribeiro, M., Pereyra, I., Alayo, M. I., *Thin Solid Films*, **426**, 200, 2003.

98. Dahl, J. E., Liu, S. G., Carlson, R. M. K., *Science*, **299**, 96, 2003.
99. Donnet, J.B., Lemoigne, C., Wang, T.K., Peng, C.M., Samirant, M., Eckhardt, A., *BULLETIN DE LA SOCIETE CHIMIQUE DE FRANCE*, **134**, 875, 1997.
100. Zhang, D. J., Zhang, R. Q., *J Phys Chem B*, **109**, 9006, 2005.
101. Banhart, F., Ajayan, P. M., *Nature*, **382**, 433, 1996.
102. Banhart, F., Ajayan, P. M., *Adv Mater*, **9**, 261, 1997.
103. Zaiser, M., Lyutovich, Y., Banhart, F., *Phys Rev B*, **62**, 3058, 2000.
104. Zaiser, M., Banhart, F., *Phys Rev Lett*, **79**, 3680, 1997.
105. Yusa, H., *Diam Relat Mater*, **11**, 87, 2002.
106. Orimo, S., Majer, G., Fukunaga, T., Zuttel, A., Schlapbach, L., Fujii, H., *Appl Phys Lett*, **75**, 3093, 1999.
107. U.S. Department of Energy, Office of Hydrogen, Fuel Cells and Infrastructure Technologies. Fact Sheet Series: Hydrogen Production from Coal.
108. U.S. Department of Energy, Office of Hydrogen, Fuel Cells and Infrastructure Technologies. Hydrogen Storage "Think Tank" Report.; Washington, DC, March 14, 2003.
109. Froudakis, G. E., *J Phys-Condens Mat*, **14**, R453, 2002.
110. Dillon, A.C. et al., Nanostructured Carbon and Carbon/Metal Hybrid Materials for Vehicular Hydrogen Storage.
111. Yildirim, T., Gulseren, O., Kilic, C., Ciraci, S., *Phys Rev B*, **62**, 12648, 2000.
112. Yildirim, T., Gulseren, O., Ciraci, S., *Phys Rev B*, **6407**, 075404, 2001.
113. No increase in baseline is observed upon loading the TiH_2 calibration standards nor the BMT coal precursor.
114. Orimo, S., Zuttel, A., Schlapbach, L., Majer, G., Fukunaga, T., Fujii, H., *J Alloy Compd*, ***356***, 716, 2003.
115. Bacsa, W. S., Lannin, J. S., Pappas, D. L., Cuomo, J., *J. Phys Rev B*, **47**, 10931, 1993.
116. Ferrari, A. C., Robertson, J., *J. Phys Rev B*, **64**, 075414, 2001.
117. Ferro, Y., Marinelli, F., Allouche, A., *J Chem Phys*, **116**, 8124, 2002.
118. Cheng, H., Pez, G. P., Cooper, A. C., *J. Am. Chem. Soc.*, **123**, 5845, 2001.
119. Sriraman, S., Agarwal, S., Aydil, E. S., Maroudas, D., *Nature*, **418**, 62, 2002.
120. Barnard, A. S.;, Terranova, M. L., Rossi, M., *Chemistry of Materials*, **17**, 527, 2005.
121. Zhao, Y. F., Kim, Y. H., Dillon, A. C., Heben, M. J., Zhang, S. B., *Phys Rev Lett*, **94**, 155504, 2005.
122. Chambers, A., Park, C., Baker, R. T. K., Rodriguez, N. M., *J Phys Chem B*, **102**, 4253, 1998.
123. Gupta, B. K., Srivastava, O. N., *Int J Hydrogen Energ*, **26**, 857, 2001.
124. Anderson, A. B., Kostadinov, L. N., Angus, J. C., *Phys Rev B*, **67**, 233402, 2003.
125. Mehandru, S. P., Anderson, A. B., Angus, J. C., *J Mater Res*, **7**, 689, 1992.
126. Saada, D., Adler, J., Kalish, R., *Phys Rev B*, **61**, 10711, 2000.
127. Quinn, D. F., *Carbon*, **40**, 2767, 2002.

Table 1: Ultimate and proximate analysis of Buck Mountain (BMT) anthracite coal, provided by the Penn State coal sample bank.

Analytical Method	Value
Moisture, as received	6.53
Ash, wt %, dry	6.83
Volatile Matter, wt %, dry	3.65
Fixed Carbon, wt%, dry	89.52
Carbon, wt %, dmmf	88.85
Hydrogen, wt %, dmmf	1.29
Nitrogen, wt %, dmmf	0.78
Sulfur, wt %, dmmf	0.49
Oxygen (by difference), wt %, dmmf	1.76
Vitrinite reflectance, %	5.45
Inertinite reflectance, %	14.1

Table 2: XRD parameters of BMTsamples, before and after milling, before and after heat treatment.

Processing Method	d-spacing (Å)	Lc (Å)	La (Å)
BMT	3.42	12	38
BMT-HT	3.41 (±0.4)	20	40
BMT-dry	3.40	18	36
BMT-dry-HT	3.45	29	40
BMT-wet	3.49	12	44
BMT-wet-HT	3.39	50	44

Table 3: Ash content of BMT samples, before and after milling, before and after heat treatment.

Processing of PSOC 1468	**Total Ash (wt%)**	**Iron[c] (wt%)**	**Magnesium[c] (wt %)**	**Aluminum[c] (wt%)**
BMT	6.60[a]	0.494	0.060	1.337
BMT-1400	8.23	n.d.	n.d.	n.d.
BMT-80	6.80[a]	0.78	0.027	1.200
BMT-80-1400	13.10	n.d.	n.d.	n.d.
BMT-80CH	10.82[a]	3.84	0.041	0.982
BMT-80CH-1400	22.20	n.d.	n.d.	n.d.

a Ash content measured by Proximate Analysis on different sample than earlier PSU characterization
b Ash content measured by TGA
c Individual metal content measured by Neutron Activation Analysis

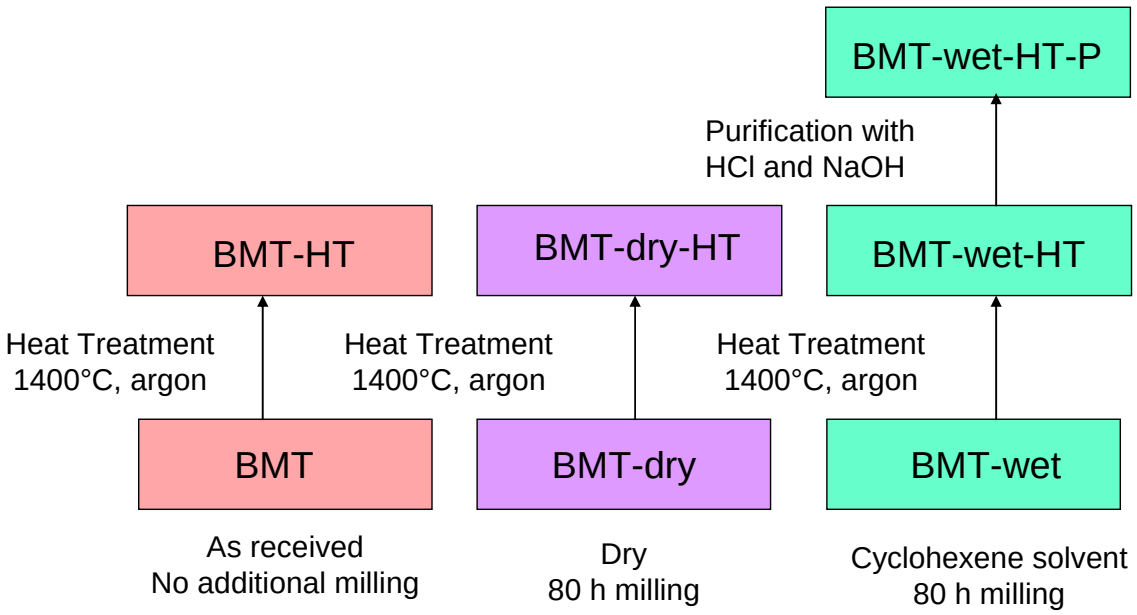

Figure 1: Schematic of process conditions.

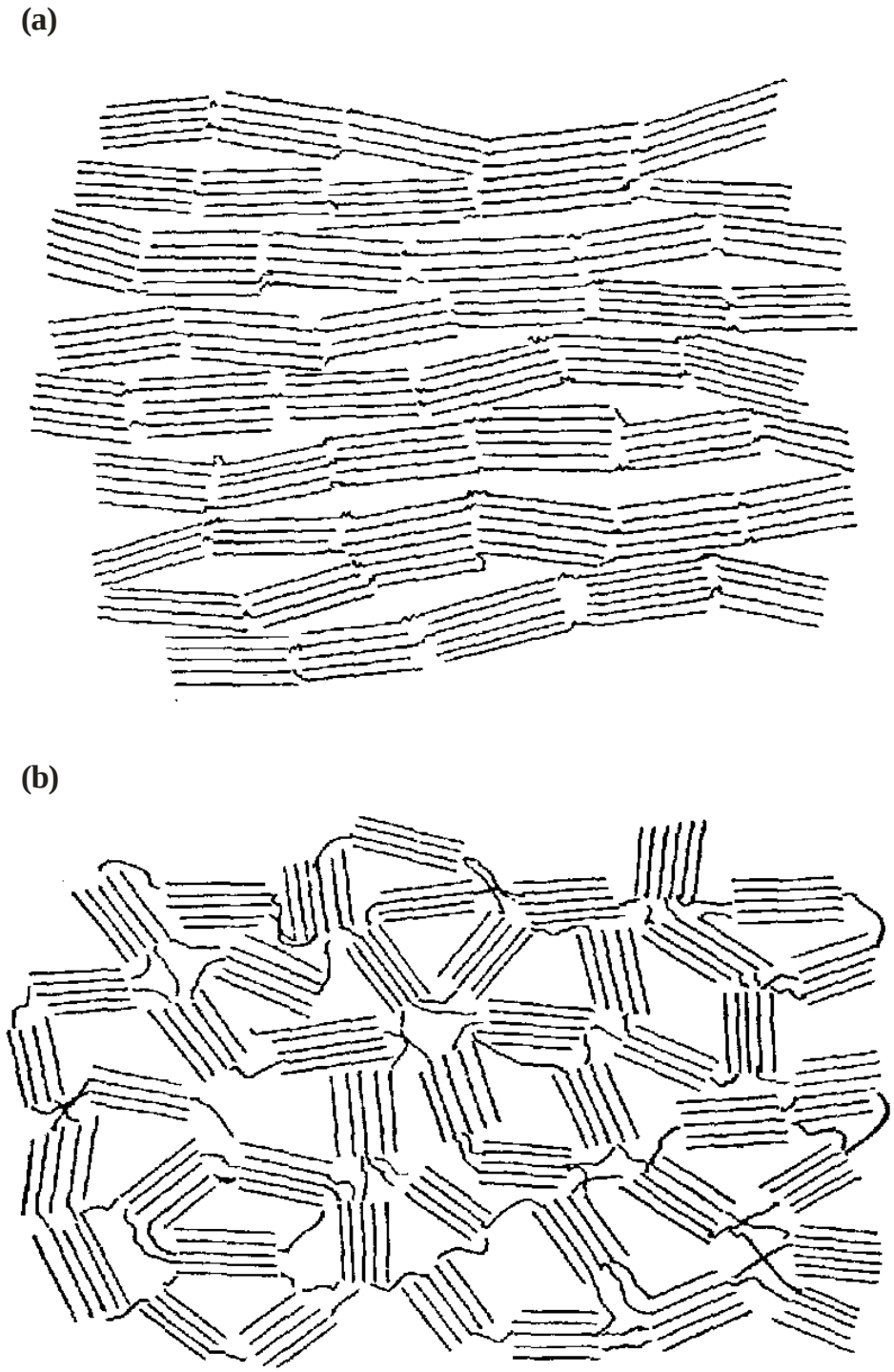

Figure 2: Schematic of (a) non-graphitic carbon that can graphitize and (b) non-graphitizing carbon, as depicted by R. Franklin.[48-49]

(a)

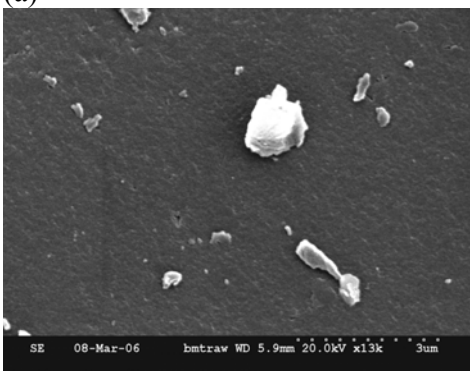

(b)

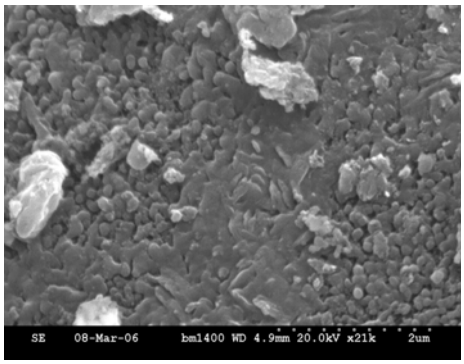

(c)

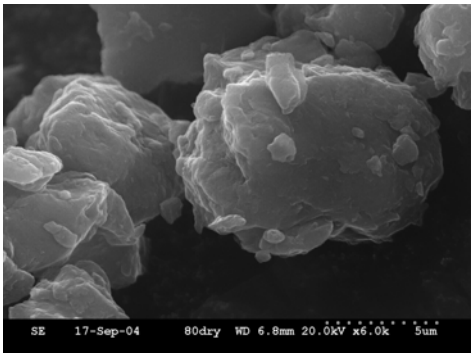

(d)

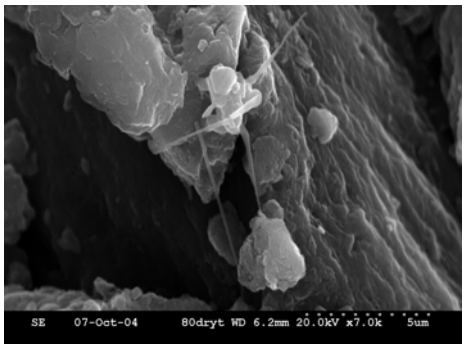

(e)

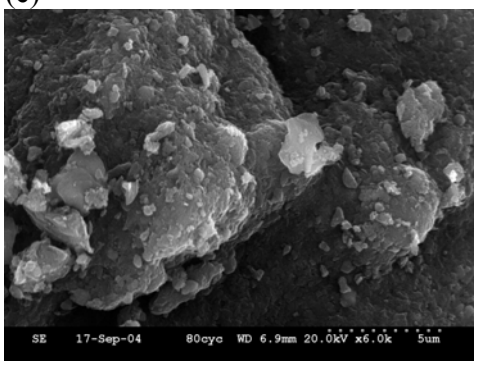

(f)

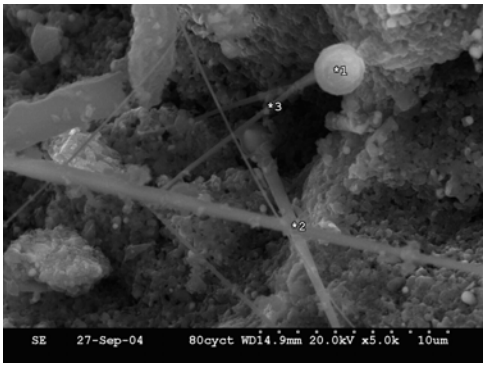

Figure 3: SEM micrographs of sample with no milling (a) before (BMT) and (b) after heat treatment at 1400 °C (BMT-HT), sample ball milled without solvent for 80 h (c) before (BMT-dry) and (d) after heat treatment at 1400 °C (BMT-dry-HT), sample ball milled with solvent for 80 h (e) before (BMT-wet) and (f) after heat treatment at 1400 °C (BMT-wet-HT).

(a)

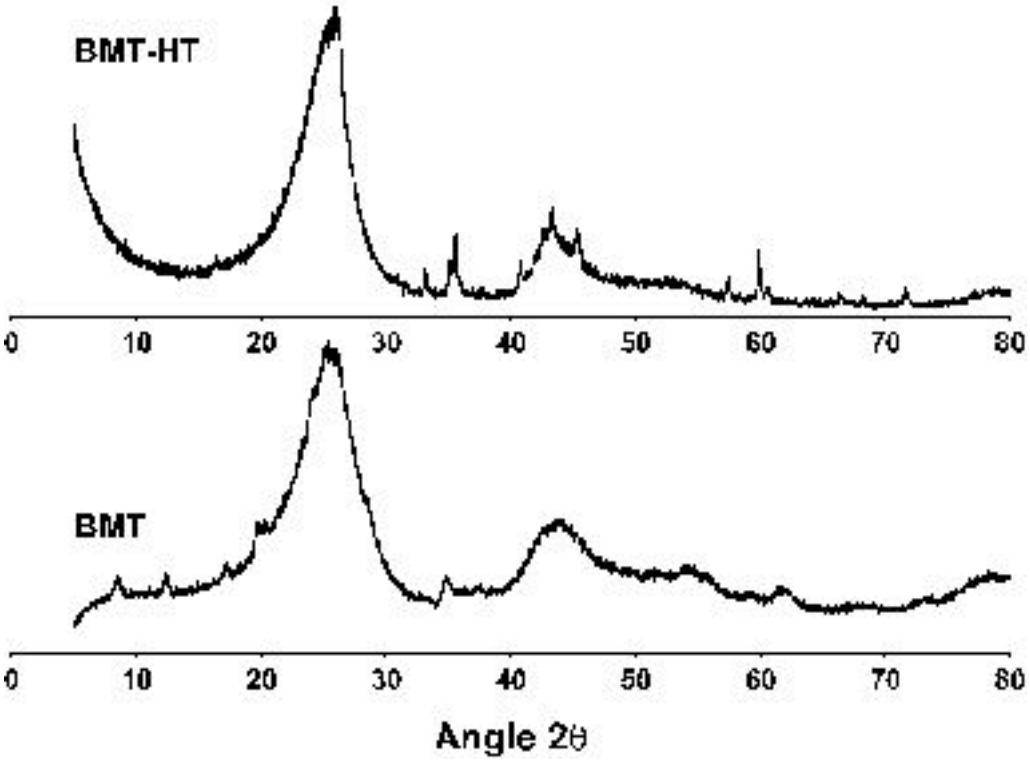
BMT-HT
0
10
20
30
40
50
60
70
80
BMT
0
10
20
30
40
50
60
70
80
Angle 2θ

(b)

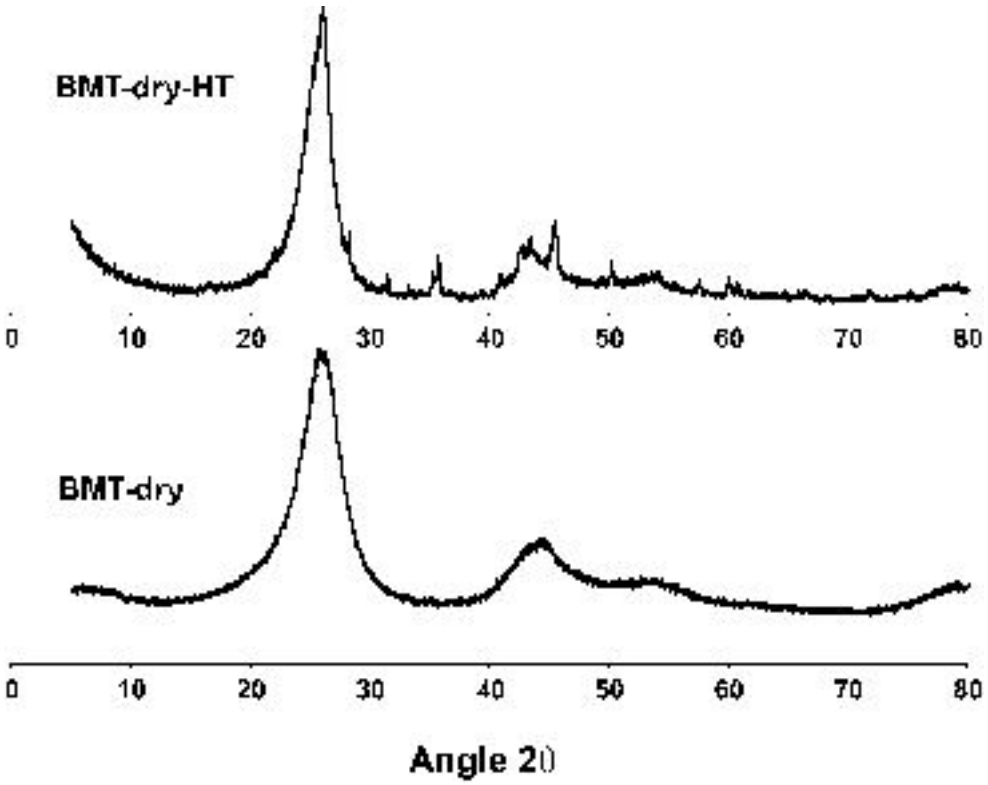
BMT-dry-HT
0
10
20
30
40
50
60
70
80
BMT-dry
0
10
20
30
40
50
60
70
80
Angle 2θ

(c)

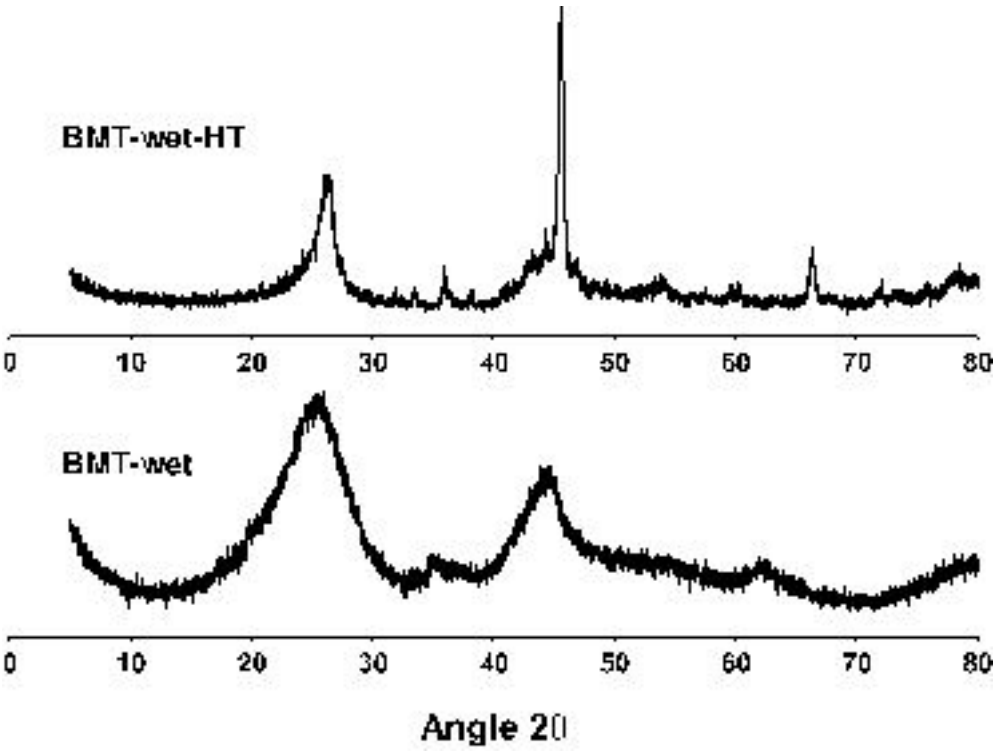

Figure 4: XRD spectra of (a) BMT and BMT-HT, (b) BMT-dry and BMT-dry-HT, and (c) BMT-wet and BMT-wet-HT.

(a)

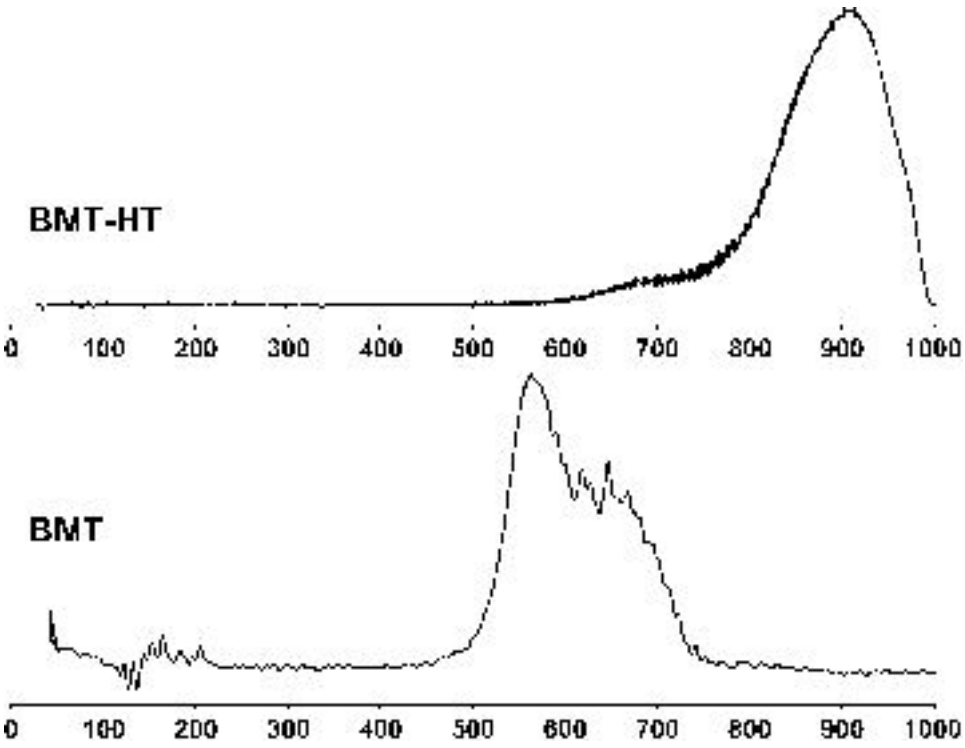
BMT-HT
0
100
200
300
400
500
600
700
800
900
1000
BMT
0
100
200
300
400
500
600
700
800
900
1000

(b)

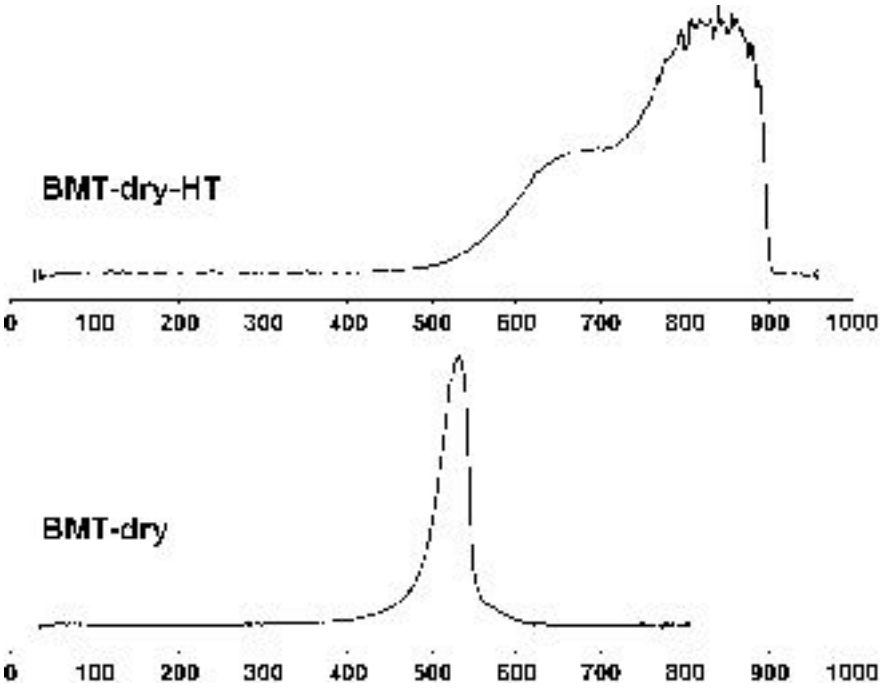
BMT-dry-HT
0
100
200
300
400
500
600
700
800
900
1000
BMT-dry
0
100
200
300
400
500
600
700
800
900
1000

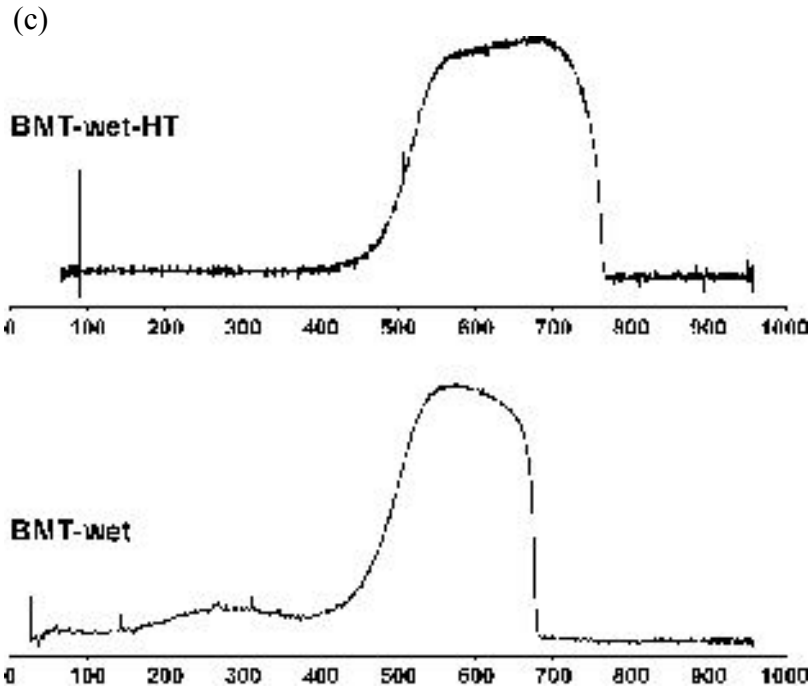

Figure 5: TPO, the derivative of the mass loss for (a) BMT and BMT-HT, (b) BMT-dry and BMT-dry-HT, and (c) BMT-wet and BMT-wet-HT.

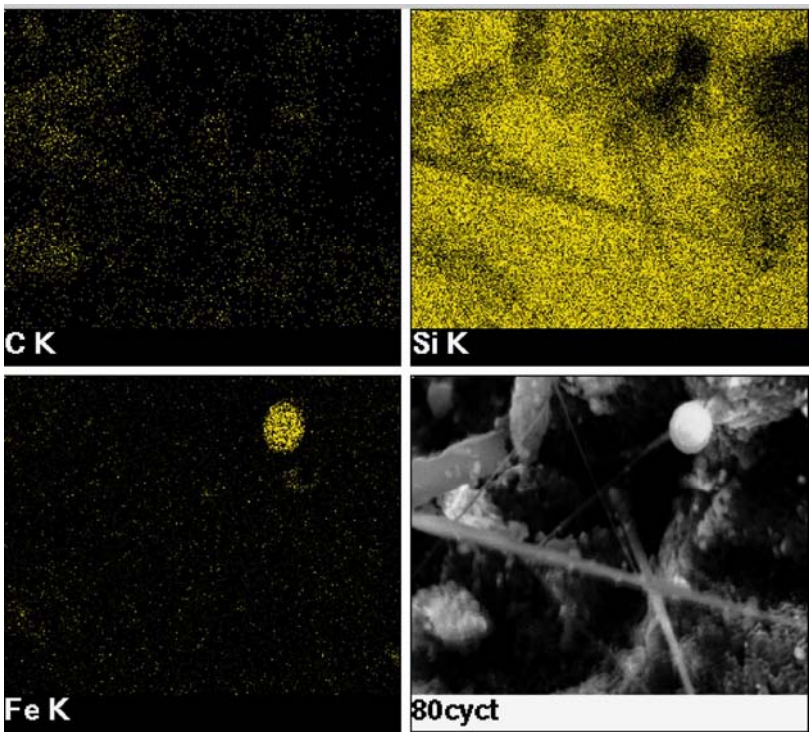

Figure 6: EDS map of elements for sample BMT-wet-HT (based on SEM in Figure 3f). The elements mapped are Fe, Si, and C.

(a)

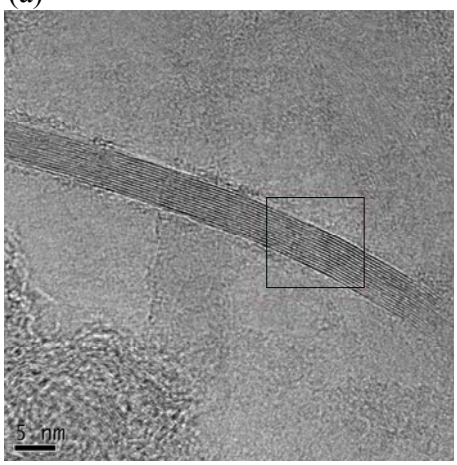

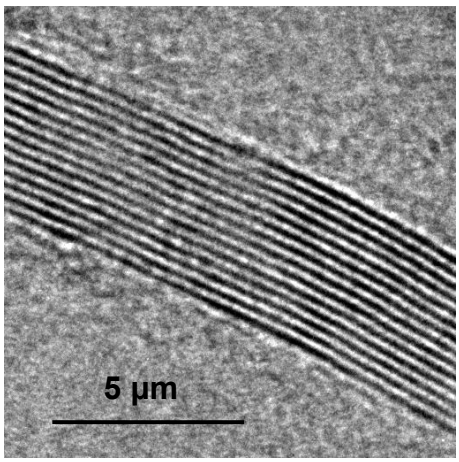

(b)

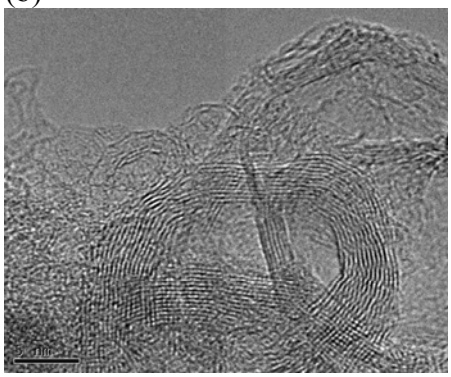

(c)

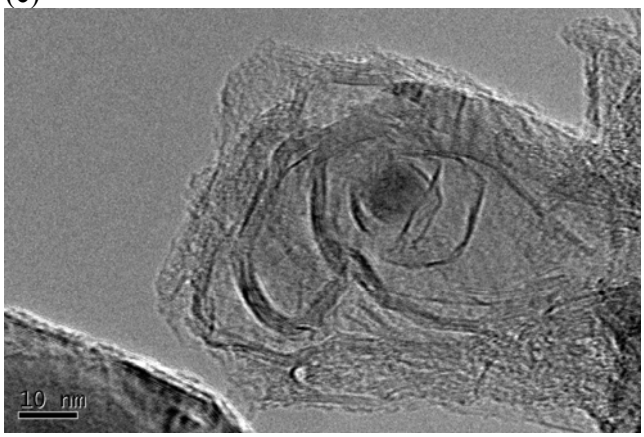

(d)

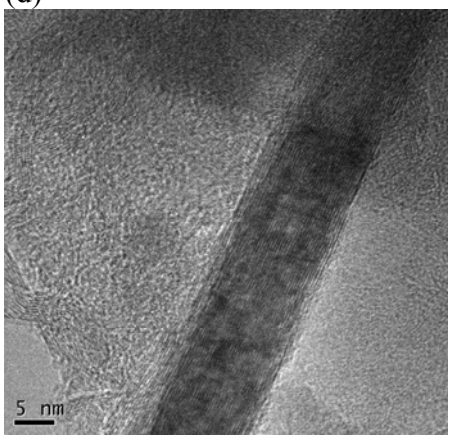

(e)

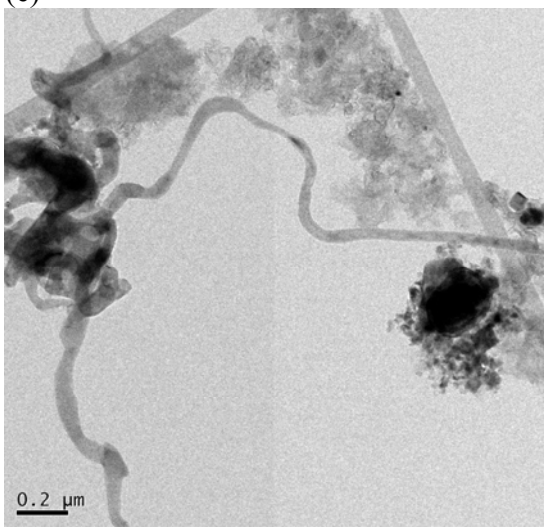

Figure 7: Structures formed upon mechano-thermal processing of anthracite sample BMT-80CH-1400. The technique resulted in range of graphitized and tubular structures, including (a) nanographitic ribbons at 5 nm and expansion of highlighted portion, (b) highly graphitic, curved regions, (c) graphitic tubes; (d) overlapping graphitic tubes; and (e) larger diameter tube representative of silicon-based structure.

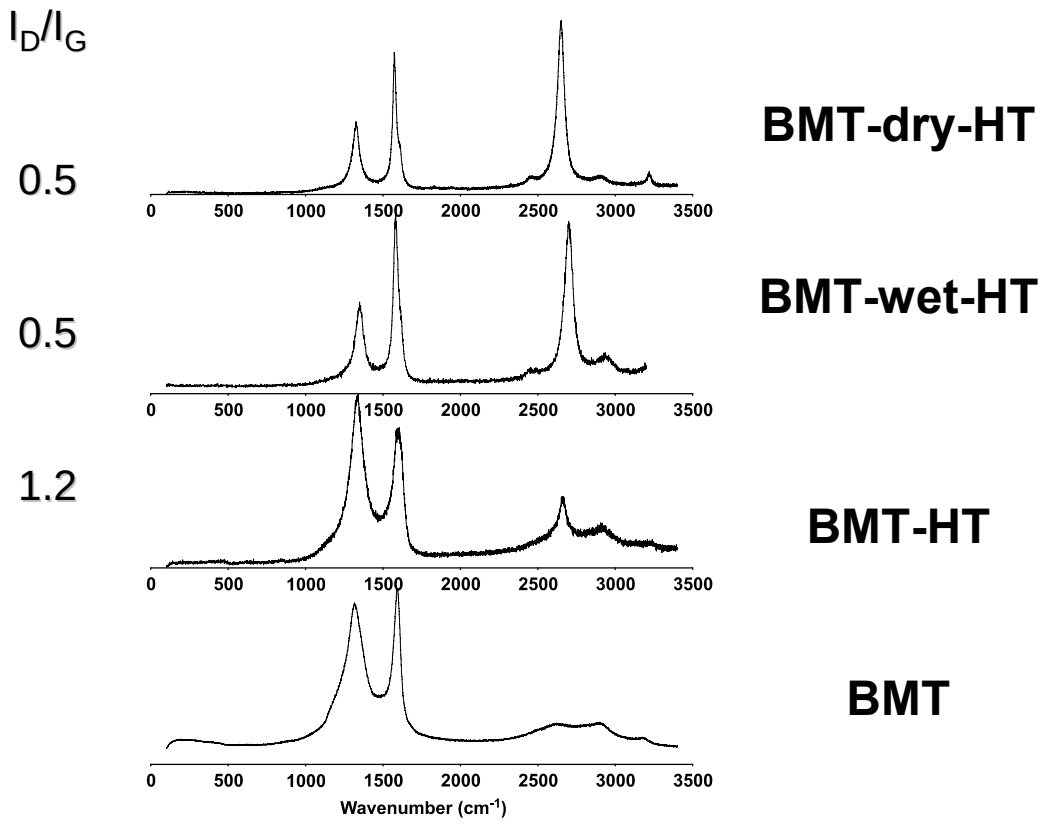

Figure 8: Raman spectra of BMT and heat-treated samples.

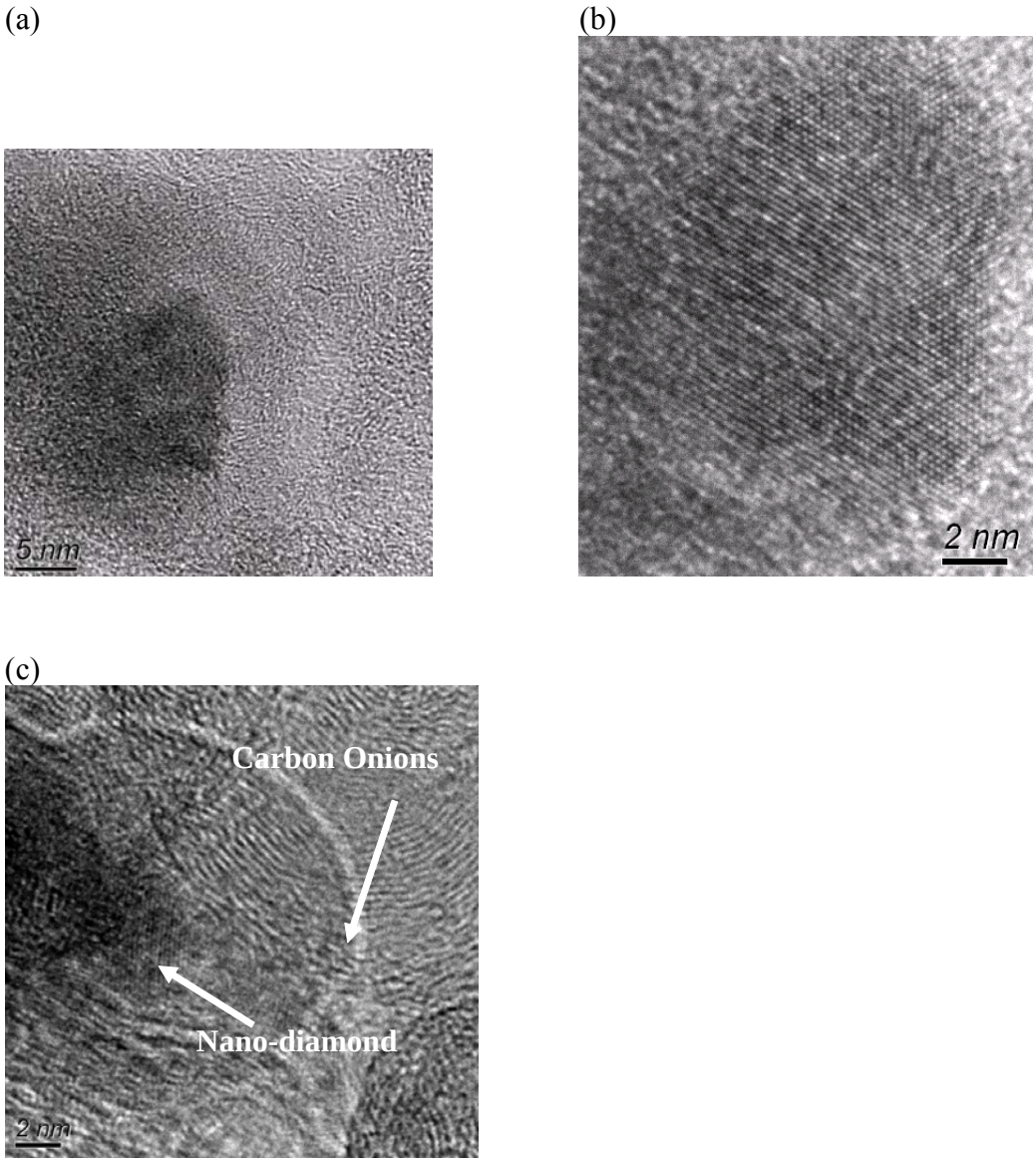

Figure 9: HR-TEM observation of nanocrystalline diamond (NCD) in a ball milled anthracite coal directly after milling suggests the high energy ball mill provides the needed energy to convert the graphitic coal into diamond. (a) NCD surrounded by amorphous carbon; (b) high resolution of NCD shows characteristic diamond structure with corresponding Fourier transform of the image (inset); (c) the amorphous carbon surrounding the NCD was converted to graphite onions after exposure to the electron beam.

(a)

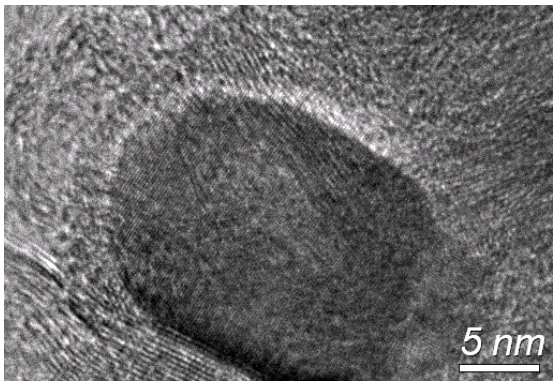

(b)

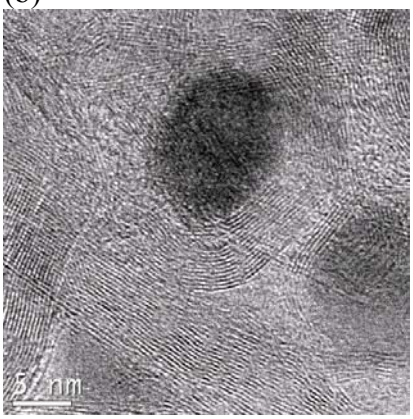

(c)

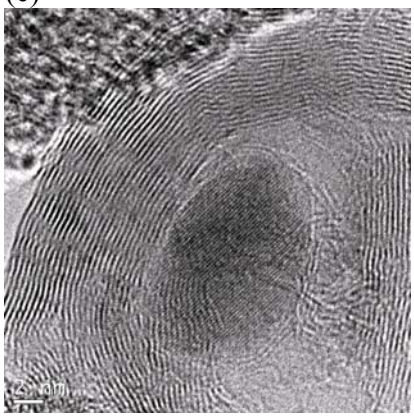

(d)

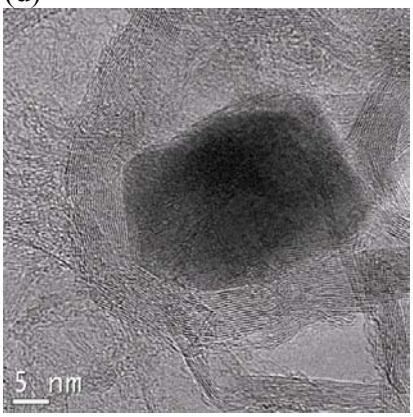

(e)

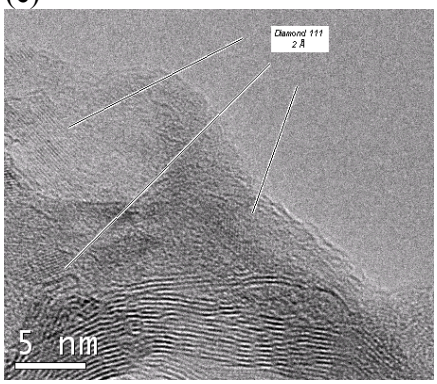

Figure 10: HR-TEM observations of NCD in ball milled anthracite coal after a subsequent thermal anneal. Particle sizes ranged from approximately 5 to 35 nm. The dark contrast of many of the images (a-d) suggests the NCD particles are spherical, whereas other NCD particles were present as a thin sheet, indicated by the light contrast of these regions (e).

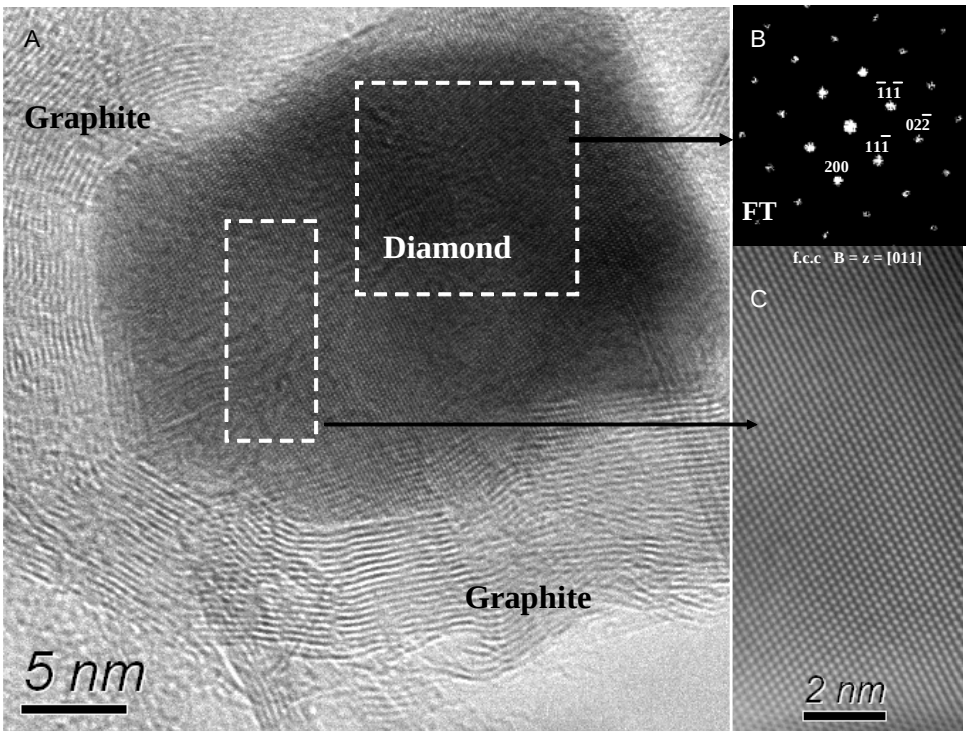

Figure 11: HR-TEM of a NCD particle surrounded by a fullerene carbon onion (a). Fourier Transform of the image indicates the characteristic diamond structure (b), and high-resolution of the NCD indicates the characteristic 2.06 Å lattice of diamond.

(a) (b)

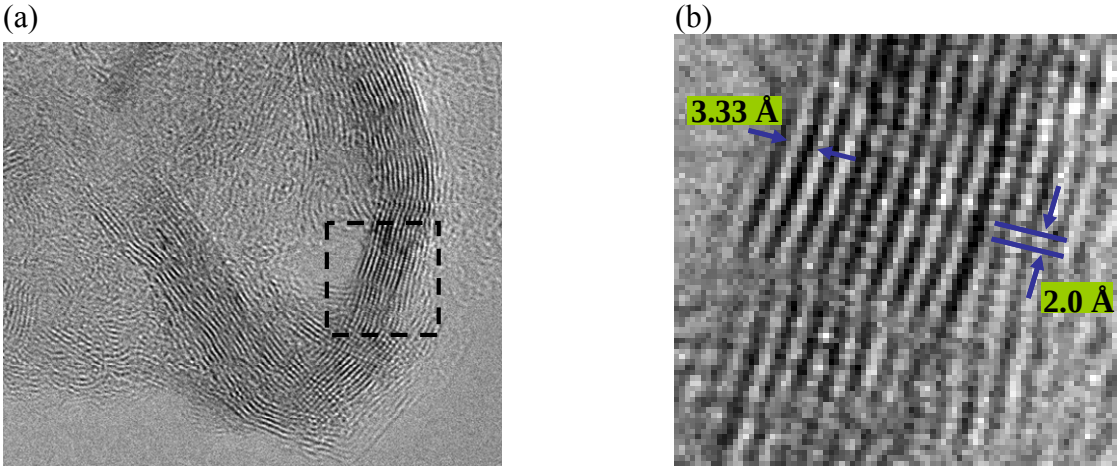

Figure 12: Region showing transition from sp^3-hybridized carbon to sp^2-hybridized carbon. The boxed area in (a) is shown in high resolution in (b).

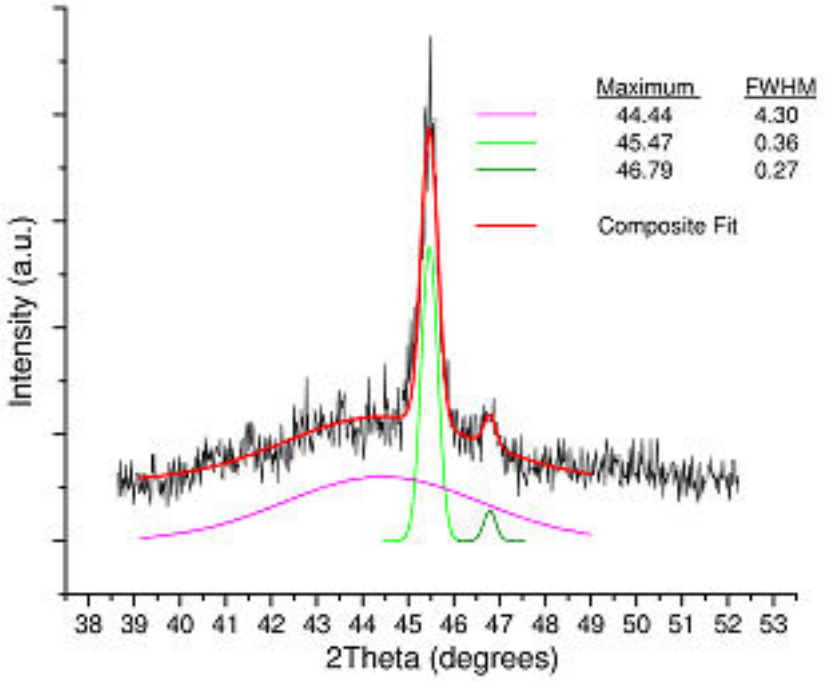

Figure 13: Additional analysis of previously reported XRD data show the samples in which NCD is observed via TEM have a broad peak at 2□=44º, corresponding to the expected location of the (111) reflection of diamond. The peak is broad due to the small particle size of the NCD, and deconvolution of the peak allows quantification of this XRD peak. This is the XRD data of BMT-wet-HT, and this broad XRD peak was observed also in BMT-wet, BMT-dry-HT, and an additional sample prepared under the same conditions as the first BMT-wet-HT.

(a) (b)

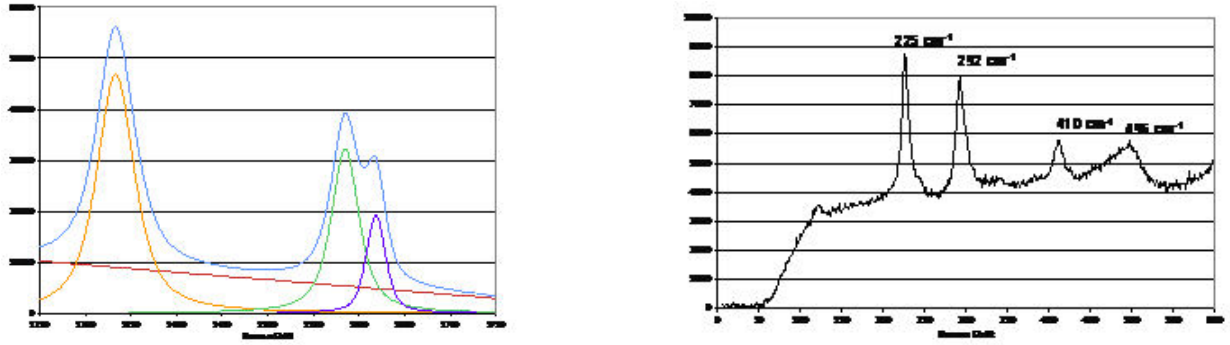

Figure 14: Raman spectroscopy of BMT-wet-HT-P provided corroborating evidence for the formation of NCD. The D (diamond) peak at 1333 cm^{-1} is too broad to be conclusively assigned to diamond, however a peak at 1620 cm^{-1} has been previously observed in NCD, and a peak at 480 cm^{-1} has been claimed to be the 'signature peak for NCD. The analysis of the low frequency Raman peaks is complicated by the presence of the natural mineral matter of the coal.

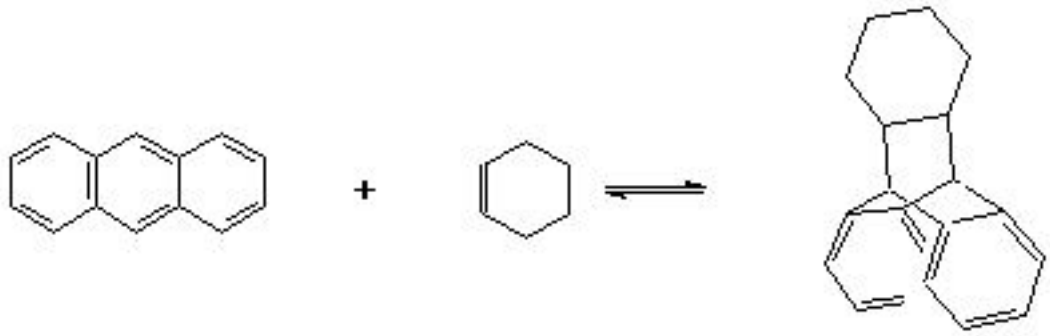

Figure 15: Schematic of the Diels Alder Condensation Reaction as one possible contributor to NCD formation. An olefin can add 1,4 across the central ring of acenes as shown for anthracene. The cyclohexene wetting agent may have precipitated with the sp^2 hybridized coal end groups to provide a three-dimensional sp^3 structure that lead to NCD formation. Particles milled with cyclohexene have appear to have more NCD (based on XRD), but NCD is also observed for samples milled without cyclohexene after annealing (contributions by Dr. John W. Larsen and Dr. Harold H. Schobert).

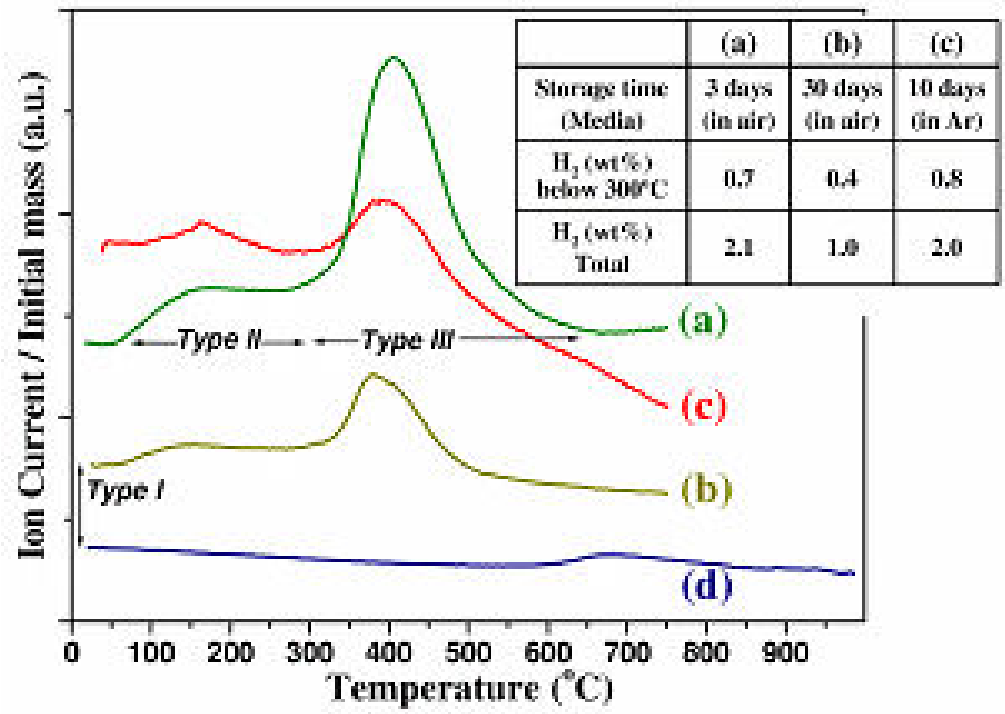

Figure 16. TDS Hydrogen evolution for several preparations of BMT-wet (a-c) relative to the BMT coal precursor (d). The table (inset) summarizes the released hydrogen amount and the storage conditions. All samples were exposed to air prior to H_2 TDS.

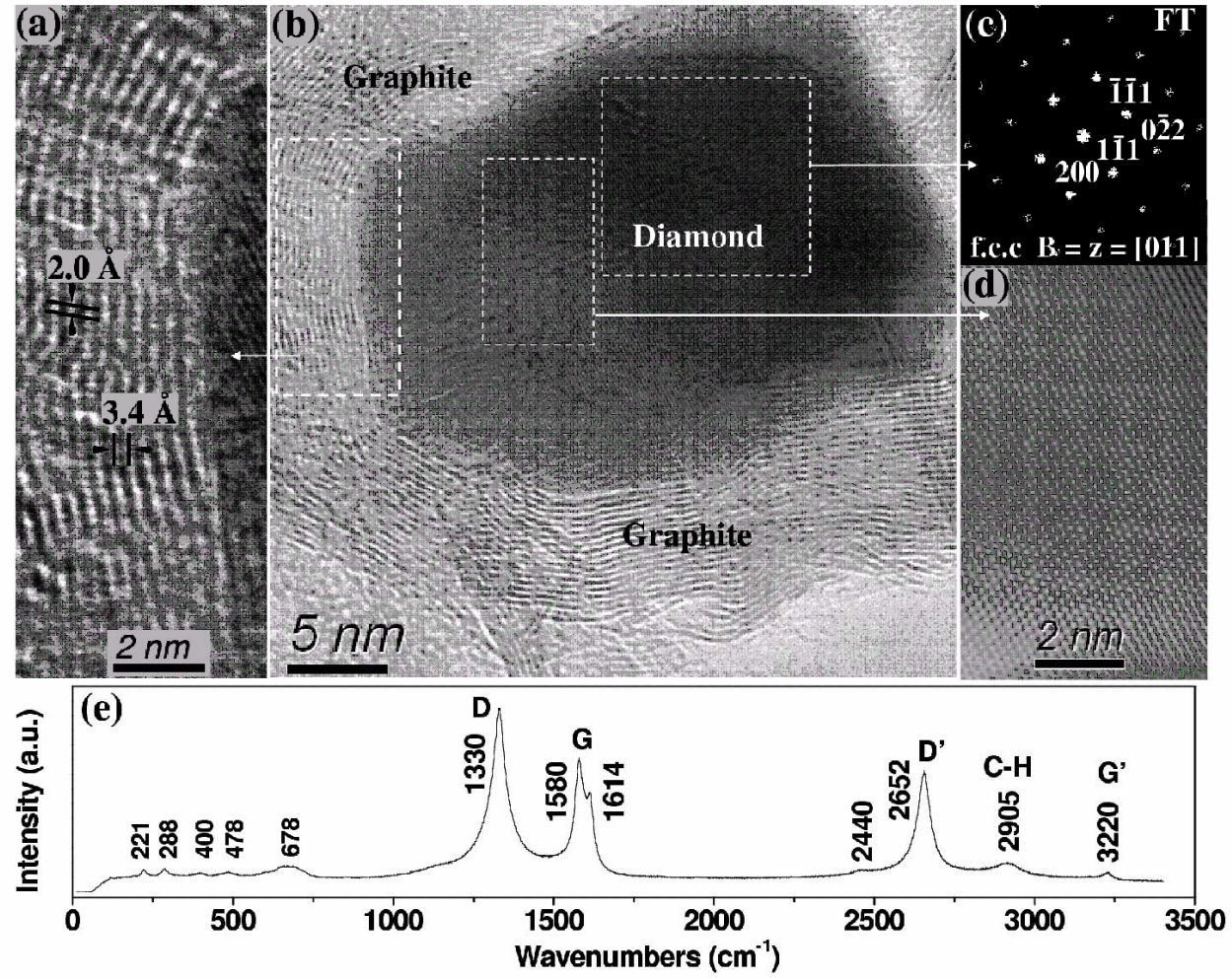

Figure 17: Representative HR-TEM of observed crystalline regions (a-b) for BMT-wet-HT-P. FT (c) and high-resolution (d) indicate a highly crystalline structure with a 3.56 Å lattice parameter. Visible Raman (633 nm) shows a split G peak (1580 and 1614), increased D' peak (2652), and several low frequency peaks (e).

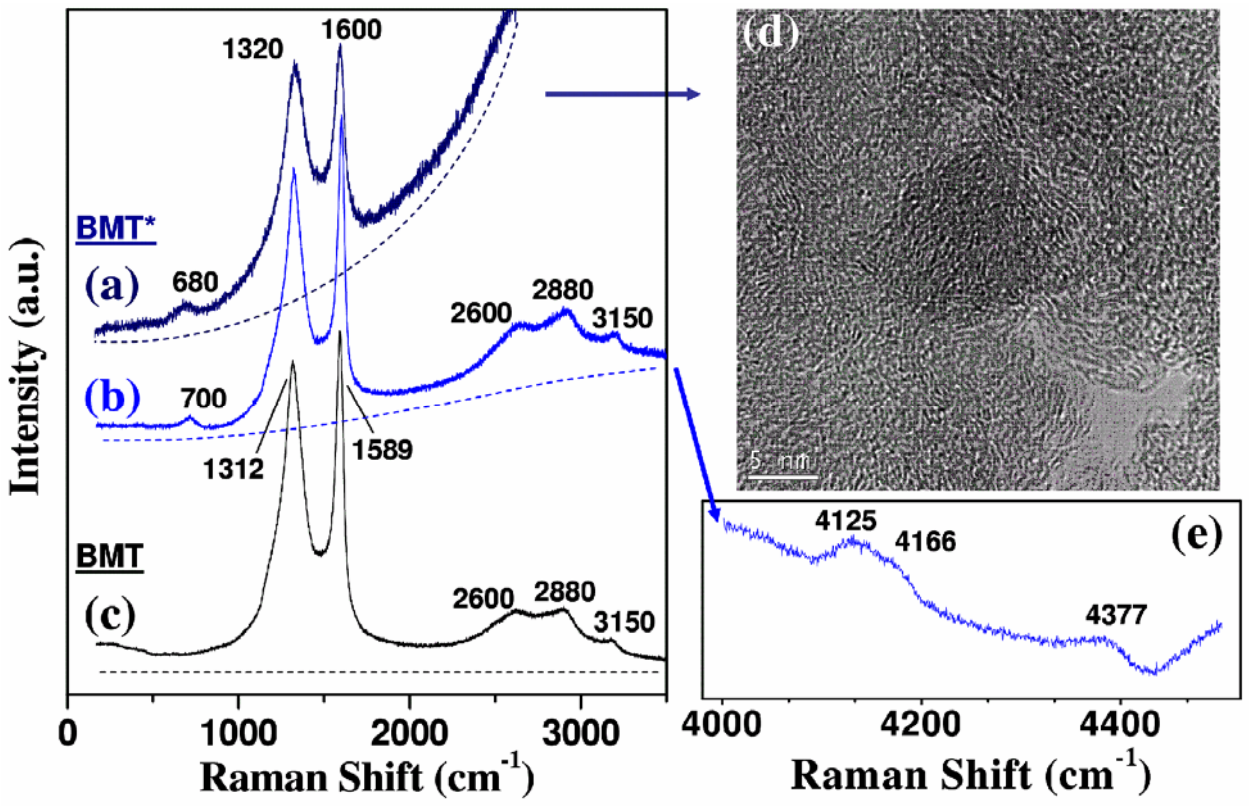

Figure 18: Visible Raman (633 nm) of BMT* samples after (a) 3 days and (b,e) 1 year, relative to (c) the BMT precursor. Dashed lines reflect observed background photoluminescence. (d) A representative HRTEM of the BMT* sample shows a defective (quasi-amorphous) carbon structure.

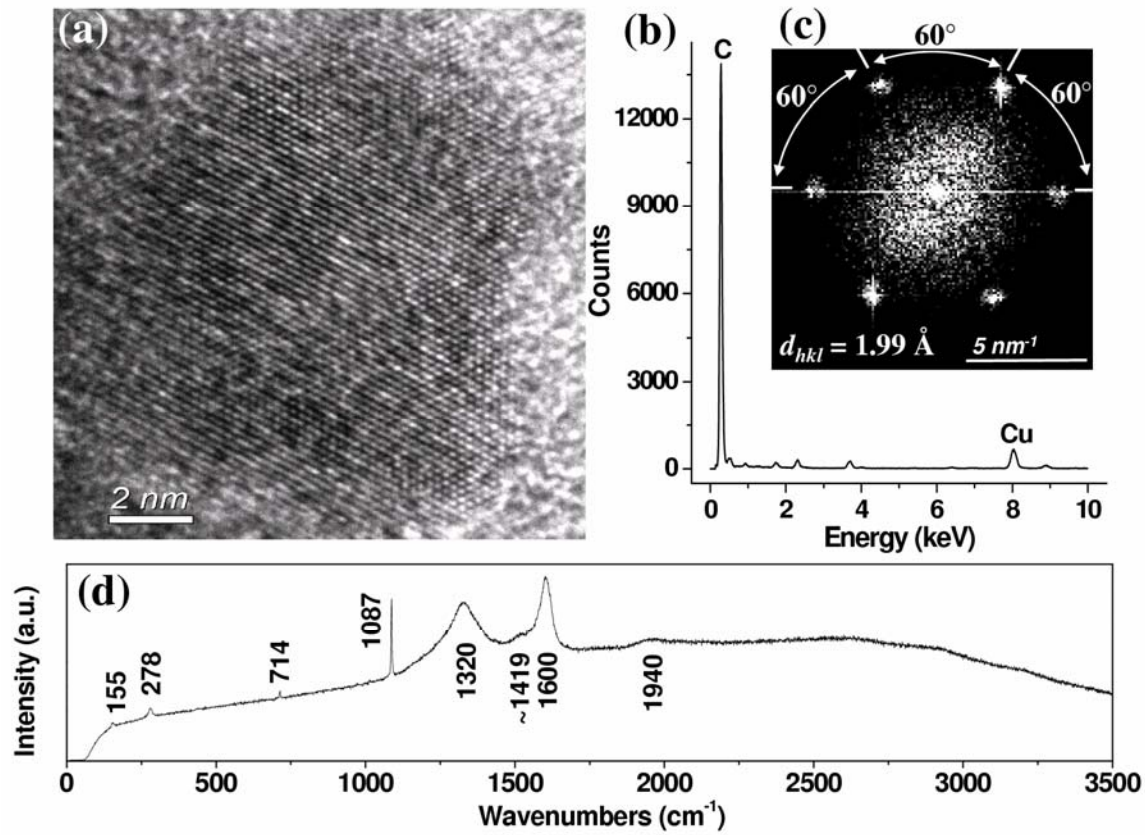

Figure 19: (a) HR-TEM observation of crystalline carbon in BMT-wet surrounded by amorphous carbon. FT of this image (b) presents a six-fold symmetry, corresponding to crystalline planes with a 1.99 Å (d_{hkl}) spacing. EDX data (c) indicates the region is carbon based. Visible Raman spectra (d) of this sample indicates a broad D peak and several additional peaks relative to the BMT precursor.